CONSTITUTIVE CORRELATIONS FOR WIRE-WRAPPED SUBCHANNEL ANALYSIS UNDER FORCED AND MIXED CONVECTION CONDITIONS

by

SHIH-KUEI CHENG

B. S. National Tsing-Hua University
(1975)

M. S. National Tsing-Hua University
(1979)

Submitted to the Department of
Nuclear Engineering
in Partial Fulfillment of the
Requirements for the Degree of

DOCTOR OF PHILOSOPHY

at the

© MASSACHUSETTS INSTITUTE OF TECHNOLOGY

August 1984

Signature of the Author Shih-Kuei Cheng
Department of Nuclear Engineering
July 24, 1984

Certified by Neil E. Todreas
Professor Neil E. Todreas
Thesis Supervisor

Accepted by A. F. Henry
Allen F. Henry
Chairman, Departmental
Graduate Committee

MASSACHUSETTS INSTITUTE
OF TECHNOLOGY

OCT 29 1984

LIBRARIES

CONSTITUTIVE CORRELATIONS FOR WIRE-WRAPPED SUBCHANNEL ANALYSIS UNDER FORCED AND MIXED CONVECTION CONDITIONS

by

Shih-Kuei Cheng

Submitted to the Department of Nuclear Engineering
on July 24, 1984 in partial fulfillment of the
requirements of the degree of Doctor of Philosophy
in Nuclear Engineering.

ABSTRACT

A simple subchannel analysis method based on the ENERGY series of codes, ENERGY-IV, has been established for predicting the temperature field in a single isolated wire-wrapped Liquid Metal Fast Breeder Reactor (LMFBR) subassembly under steady state forced and mixed convection conditions. The ENERGY-IV is a totally empirical code employed for fast running purposes and requires well calibrated lead length averaged input parameters to achieve satisfactory predictions. These input parameters were identified to be the inlet flow split parameters, the subchannel friction factors, the interchannel mixing parameters, the conduction shape factor, and the transverse velocity at the edge gap.

Experiments were performed in a 37-pin wire-wrapped rod bundle with a geometry between that of a typical LMFBR fuel subassembly and blanket subassembly for filling the gap in the available data base for the input parameters. The isokinetic extraction method for measuring subchannel velocity, the pitot-static probe for measuring pressure drop, and the salt tracer injection method for estimating the interchannel mixing, were used in these experiments.

Models accounting for both the geometry and flow regime effects have been developed for all input parameters. Correlations based on these models were then calibrated from the available data base. The proposed correlation can predict the data within ±5% for flow split parameter, ±14% for bundle average friction factor, ±25% for the wire sweeping and turbulent mixing and ± 15% for the transverse velocity at the edge gap.

Validation studies for the simple subchannel analysis model together with the proposed constitutive correlations were performed using temperature data from out of pile sodium cooled heated pin experiments. An additional mixing mechanism due to thermal plume effects was found to exist in the mixed convection condition. A correlation has been developed to quantitatively estimate this mixing effect on energy transfer. The predictions of the ENERGY-IV code were verified to be more or at least as accurate as those of the COBRA-WC

code, while the ENERGY-IV running time is dramatically reduced in comparison, e.g. 1 minute versus hours in the mixed convection condition. Different energy transfer mechanisms were compared to each other using the proposed correlations. The operation regions at which these mechanisms are important were then identified on Grashof versus Reynolds flow maps.

Thesis Supervisor: Professor Neil E. Todreas
Title: Head, Department of Nuclear Engineering

Thesis Reader: Professor Andrei L. Schor
Title: Assistant Professor
Department of Nuclear Engineering

ACKNOWLEDGEMENTS

I wish to express my deep graditude to Professor Neil E. Todreas for his guidance throughout the course of the work. Professor K. Rehme at KfK, West Germany is also acknowledged for many helpful discussions and suggestions. Dr. D. Rector at BNWL and R. Siever at WARD are also thanked for providing COBRA runs for this work.

Thanks are due to Yee-Ning Chan, Joseph Caloggero and Ray Johnson for their assistances in the experimental work. Special thanks are also due to my associates, Tolis Efithimiadis, Jim Robinson, and Victor Iannello for discussing and correcting the English in the draft of the thesis. Typing of the thesis by Cher-Jean Lee and Judy Bolger is warmly appreciated.

TABLE OF CONTENTS

page

Abstract i

Acknowledgement iii

Table of Contents iv

List of Figures x

List of Tables xviii

Nomenclature xx

CHAPTER 1 INTRODUCTION 1

1.1 Overview 1

1.2 Previous Work and Motivation 10

1.3 Objective 17

CHAPTER 2 SIMPLE SUBCHANNEL ANALYSIS METHOD: THE ENERGY-IV CODE 20

2.1 General Equations for Subchannel Analysis 20

2.2 Simple Subchannel Analysis Model for Wire-Wrapped LMFBR Subassembly 28
2.2.1 Two-Region Approach 28
2.2.2 Treatment of Continuity Equation 30
2.2.3 Treatment of Energy Equation 31
2.2.4 Treatment of Axial Momentum Equation 37

2.3 Finite Difference Equations for the ENERGY-IV Code 39
2.3.1 Finite Difference Equations for the Forced Convection Condition 39
2.3.2 Finite Difference Equations for the Mixed Convection Condition 46

2.4 Empirical Parameters for the ENERGY-IV Code 51

CHAPTER 3 HYDRODYNAMIC EXPERIMENTS IN A 37-PIN WIRE-WRAPPED ROD BUNDLE 52

3.1 Introduction 52

3.2 Test Section 54
3.2.1 Test Section Design and Fabrication 54
3.2.2 Test Loop 57

3.3 Experimental Methods 62

page

3.3.1 Flow Split Experiment..... 62
3.3.2 Pressure Drop Experiment..... 64
3.3.3 Mixing Experiment..... 67

3.4 Experimental Results and Discussions..... 70
3.4.1 Flow Split Experiment..... 72
3.4.1.1 Experimental Results..... 72
3.4.1.2 Discussion..... 79
3.4.2 Pressure Drop Experiment..... 81
3.4.2.1 Experimental Results..... 81
3.4.2.2 Discussion..... 84
3.4.3 Mixing Experiment..... 89
3.4.3.1 Experimental Results..... 89
3.4.3.2 Discussion..... 95

CHAPTER 4 SUBCHANNEL FRICTION FACTOR CORRELATIONS..... 96

4.1 Introduction..... 96

4.2 Literature Review..... 97
4.2.1 Bundle Average Friction Factor Data..... 97
4.2.2 Flow Split Data..... 101
4.2.3 Correlations for Friction Factor and Flow Split Parameter..... 102

4.3 Subchannel Friction Factor Formulations..... 106
4.3.1 Subchannel Friction Factor Models..... 106
4.3.1.1 Interior Subchannel..... 107
4.3.1.2 Edge Subchannel..... 112
4.3.1.3 Corner Subchannel..... 116
4.3.2 Formulations and Empirical Constants for the Laminar and Turbulent Regions..... 117
4.3.3 Formulations and Empirical Constants for the Transition Region..... 120
4.3.3.1 Reynolds Numbers at Transition Points..... 120
4.3.3.2 Formulations and Empirical Constants..... 126
4.3.4 Flow Split Parameters and Bundle Average Friction Factor..... 128
4.3.4.1 Turbulent and Laminar Regions..... 129
4.3.4.2 Transition Region..... 131
4.3.5 Summary..... 134

4.4 Empirical Constants for Bare Rod Subchannel Friction Factor.. 135
4.4.1 Introduction..... 135
4.4.2 Laminar Flow Subchannel Friction Factor..... 137
4.4.2.1 Interior Subchannel..... 137
4.4.2.2 Edge and Corner Subchannels..... 138
4.4.2.3 Equations for Determining K_{ij}..... 138
4.4.2.4 Comparison Between Experimental Data and Correlation..... 138

page

4.4.3 Turbulent Flow Subchannel Friction Factor..... 143
4.4.3.1 Theoretical Work on Turbulent Subchannel Friction Factor..... 143
4.4.3.2 The G*-Method..... 146
4.4.3.3 Comparison between Experimental Data and Correlation..... 152
4.4.4 Summary..... 157

4.5 Empirical Constants for Wire-Wrapped Subchannel Friction Factor..... 166
4.5.1 Empirical Constants for the Turbulent Region..... 167
4.5.2 Empirical Constants for the Laminar Region..... 175
4.5.3 Empirical Constants for the Transition Region..... 181

4.6 Summary of Correlations..... 187
4.6.1 Summary..... 187
4.6.2 Parametric Behavior for Bare Rod Bundles..... 188
4.6.3 Parametric Behavior for Wire-Wrapped Rod Bundles..... 190
4.6.3.1 Bundle Friction Factor Constants..... 190
4.6.3.2 Flow Split Parameters..... 196
4.6.4 Conclusion..... 198

CHAPTER 5 DATA REDUCTION FOR MIXING EXPERIMENTS..... 199

5.1 Introduction..... 199
5.1.1 Validity of Salt injection Experiment..... 199
5.1.2 Data Reduction Version of the ENERGY Code..... 204

5.2 Data Reduction for the Mixing Experiments..... 207
5.2.1 Introduction..... 207
5.2.2 Data Reduction for 37-pin mixing Experiments..... 208
5.3.2.1 DEED, ε^*_{ln}..... 208
5.3.2.2 ETVR, C_{ll}..... 220
5.2.3 Data Reduction for 61-pin Mixing Experiments..... 230
5.2.4 Discussion..... 245

5.3 Error Analysis of Mixing Parameters Results..... 245
5.3.1 Error Involved in C_i^* : Experimental Error..... 246
5.3.1.1 Error Caused by Misdetermination of C_i..... 247
5.3.1.2 Error Caused by Misdetermination of Flow Split Parameters..... 249
5.3.2 Error Involved in ther Code Calibration..... 249
5.3.2.1 Interior Injection Case..... 250
5.3.2.2 Edge Injection Case..... 250
5.3.3 Error Involved by Metho lology..... 251
5.3.4 Conclusion..... 251

CHAPTER 6 MIXING PARAMETER CORRELATIONS..... 253

6.1 Physical Meaning of Mixing Parameters..... 253

page

6.2 Recommended Value for $\varepsilon^*_{2\eta}$ 259

6.3 modles for DEED and ETVR 263
6.3.1 Literature Review 263
6.3.2 Models for the Transverse Velocity 266
6.3.3 Formulations for DEED and ETVR 269

6.4 Empirical Contants for DEED and ETVR 271
6.4.1 Empirical Constants for the Turbulent Region 271
6.4.2 Empirical Constants for the Laminar Region 282
6.4.3 Empirical Constants for the Transition Region 284

6.5 Correlation for Conduction Shape Factor, κ 290
6.5.1 Introduction 290
6.5.2 Conduction Shape Factor in the Literature 291
6.5.3 Recommended Correlation for Conduction Shape Factor 294

6.6 Summary of mixing Parameter Correlations 294

CHAPTER 7 THE ENERGY-IV CODE 297

7.1 Structure of the ENERGY-IV Code 297

7.2 Numerical Method for the Forced Convection Option 303

7.3 Numerical Method for the Mixed Convection Option 305

CHAPTER 8 VALIDATION OF THE ENERGY-IV CODE 312

8.1 Introduction 312

8.2 Description of the Tests Used for Validation 315

8.3 Validation of the ENERGY-IV in the Forced Convection Condition 325
8.3.1 Comparison between Data and Predictions for WARD Bundle 327
8.3.2 Comparison between Data and Predictions for ORNL Bundles 336
8.3.3 Comparison between Data and Predictions for Toshiba Bundle 344
8.3.4 Conclusion 344

8.4 Validation of the ENERGY-IV in the Mixed Convection Condition 348
8.4.1 Phenomena Caused by Buoyancy Effects in the Mixed Convection Condition 352
8.4.1.1 Subchannel Friction Factors 352
8.4.1.2 Flow Redistribution 354
8.4.1.3 Mixing Enhanced by Thermal Plumes Effects 356
8.4.2 Comparisons between Data and Prediction in the Mixed Convection Condition 357

page

8.4.2.1 WARD Bundle..... 357
8.4.2.2 ORNL-61 pin Bundle..... 371
8.4.2.3 Toshiba Bundle..... 375
8.4.2.4 Grenoble (FETUNA) Bundle..... 381
8.4.3 Conclusions..... 381

8.5 Relative Importance of Energy Transfer Mechanisms in the Mixed Convection Condition..... 384

CHAPTER 9 SUMMARY, CONCLUSION AND RECOMMENDATION..... 397

9.1 Introduction..... 397
9.1.1 Formulation of a Simple Subchannel Analysis Code, the ENERGY-IV..... 397
9.1.2 Data Base for Imput Parameters..... 398
9.1.3 Models ano Correlation for Input Parameters..... 398
9.1.4 Validation of the ENERGY-IV Code..... 399

9.2 Summary..... 399
9.2.1 Experimetal Results..... 399
9.2.2 Models and Correlations of Input Parameters..... 400
9.2.2.1 Subchannel Friction Factor and Flow Split Parameter..... 402
9.2.2.2 Dimensionless Effective Eddy Diffusivity and Edge Transverse Velocity Ratio..... 406
9.2.2.3 Dimensionless Eddy Diffusivity for the Edge Region..... 408
9.2.2.4 Conduction Shape Factor..... 408
9.2.2.5 Thermal Plume Mixing Parameter..... 409
9.2.3 Validation of the ENERGY-IV Code..... 409
9.2.4 Mechanisms for Energy Transfer in the Mixed Convection Condition..... 410

9.3 Recommendation..... 411
9.3.1 Conduction Shape Factor..... 411
9.3.2 Thermal Plume Mixing Parameter..... 411

References..... 412

Appendix A1 Normalized Flow Split Maps from Flow Split Experiments..... A1

Appendix A2 Dimensionless Salt Concentration Maps from Mixing Experiments..... A18

Appendix B1 Data Base for Bundle Average Friction Factor and Flow Split Parameters..... B1

		page
Appendix B2	Input and Listing for WWCR Program.....	B7
Appendix C1	Revised DRV Code Listing.....	C1
Appendix D1	Input and Output Formulations for ENERGY-IV.....	D1
Appendix D2	ENERGY-IV Code Listing.....	D5
Appendix E1	Simple Model for Thermal Plumes Mixing Parameter....	E1

LIST OF FIGURES

Figure		page
1.1	Typical LMFBR Wire-Wrapped Assembly and Rod Configuration...	3
1.2	Number of Blanket Assemblies at Various Reynolds Number for Full and Partial Load Operation.....	5
1.3	Comparison between Experimental Data and Prediction of Old Correlations for Laminar $f_b Re_b$.....	14
2.1	Typical Subchannels in LMFBR Wire-Wrapped Bundle.....	21
2.2	Subchannel Control Volume for Continuity Equation.....	25
2.3	Subchannel Control Volume for Energy Equation.....	26
2.4	Subchannel Control Volume for Axial Momentum Equation.....	27
2.5	Two Region Approach for LMFBRE Subchannel Analysis.....	29
2.6	Difference between the Subchannel Centroid to Centroid Distance and Laminar Mixing Length.....	34
2.7	Control Volumes and Noding Scheme for Different Kinds of Subchannels.....	41
3.1	Relations Among Flow Split Experiment, Mixing Experiment and Pressure Drop Experiment.....	53
3.2	37-Pin Bundle Design Configuration.....	56
3.3	As built Geometry at Exit Plane.....	58
3.4	Layout of the Test Loop.....	60
3.5	Calibration Curve for Rotometer M3.....	61
3.6	Flat to Flat Measuremment Scheme and Wire Positions in Two Different Types of Interior Subchannel.....	63
3.7	Design Configuration of Instrumentation Rod and Injector....	65
3.8	Structure of Probe Supporter.....	68
3.9	Interior Subchannel Flow Split Parameter X_1 versus Re_b.....	76
3.10	Edge Subchannel Flow Split Parameter X_2 versus Re_b.....	77
3.11	Normalized Subchannel Flow Split Map at Re_b = 10480.....	78

LIST OF FIGURES (cont'd)

		page
3.12	Bundle Average Friction Factor Data Form Pressure Drop Experiment	86
3.13	Interior Subchannel Friction Factor versus Interior Subchannel Reynolds Number	87
3.14	Edge Subchannel Friction Factor versus Edge Subchannel Reynolds Number	88
3.15	Salt Concentrations and Flowrates in the Mixing Experiment	91
3.16	Typical Measured Dimensionless Salt Concentration at Re_b = 22100	93
3.17	Subchannel Numbering Scheme for 37-pin Bundle	94
4.1	Velocity Components and Schematic Configuration of an Interior Subchannel	108
4.2	Velocity Components and Schematic Configuration of an Edge Subchannel	113
4.3	Ramm and Johannsen Correlation and Yang Correlation for Reynolds Number at Transition Points	123
4.4	Data and Proposed Correlations for the Transition Reynolds Number	124
4.5	Illustration of Re_{bL} and Re_{bT} from Friction Factor Data	125
4.6	Theoretical Results of Laminar fRe for Different Subchannels	142
4.7	Comparison between Experimental and Predicted Bare Rod Bundle Laminar Friction Factor Constant fRe	144
4.8	Theoretical Work and Experimental Data for Interior Subchannel Friction Factor at $Re=10^5$ as compared to Circular Tube Values	148
4.9	G^*-method f/f_{ct} at Re = 10^5 for Interior, Edge, and Corner Subchannel	153
4.10	Comparison between Experimental and Predicted Bare Rod Bundle Turbulent Friction Factor Constand $C_{fbT}(=fRe^{0.18})$	158

LIST OF FIGURES (cont'd)

page

4.11 Calibration Procedure for Empirical Constants W_{dT} and W_{sT} in Turbulent Region..... 168

4.12 Wire Drag Constant W_{dT}..... 170

4.13 Swirl Flow Constant W_s..... 172

4.14 Prediction Error for Wire-Wrapped Turbulent Bundle Friction Factor Constant C_{fbT}..... 173

4.15 Comparison Between Experimental Data and Predictions for Wire-Wrapped Edge Subchannel Flow Split Parameter..... 174

4.16 Drag Coefficient for Circular Cylinder..... 178

4.17 Comparison between Experimental Data and Predictions for Wire-Wrapped Laminar Bundle Average $f_b Re_b$..... 180

4.18a Comparison between Experimental Data and Predictions for Wire-Wrapped Bundle Friction Factor (P/D>1.1)..... 183

4.18b Comparison between Experimental Data and Predictions for Wire-Wrapped Bundle Friction Factor (P/D$\leq$1.1)..... 184

4.19 Comparison between Wire-Wrapped Edge Flow Split Data and Predictions in the Transition Region..... 185

4.20 Comparison between Experimental Data and Predictions for Bare Rod 37-pin Turbulent Friction Factor Constant..... 189
$C_{fbt}(=f_b Re_b^{0.18})$

4.21 Predictions for Bare Rod 37-pin Laminar Friction Factor Constant $C_{fbL}(=f_b Re_b)$..... 191

4.22 Predicted Edge Subchannel Flow Split Parameter for 61-pin Bare Rod Bundle..... 192

4.23 Comparison Between Experimental Data and Predictions for Wire-Wrapped 37-pin Turbulent Friction Factor Constant.. 193
$C_{fbT}(=fRe^{0.18})$

4.24 Comparison between Experimental Data and Predictions for Wire-Wrapped 37-pin Laminar Friction Factor Constant.... 194
$C_{fbL}(=fRe)$

4.25 Predictions of Edge Flow Split Parameter for Wire-Wrapped 61-pin Rod Bundle..... 197

LIST OF FIGURES (cont'd)

		page
5.1	Turbulent Mixing Parameter (M_{ij}'/μ) from Ramm et al Correlation.....	203
5.2	Injection Flow Path Near Injection Position.....	210
5.3	Mean Square Indicator for Interior Injection Case.....	211
5.4	Comparison between DRV Calculation at Minimun MSI and Data for 37-pin Interion Injection Cases.....	214
5.5	Sensitivity of the Predicted Dimensionless Salt Concentration to DEED.....	219
5.6	Reduced Dimensionless Effective Eddy Diffusivity for 37-pin Experiment.....	221
5.7	Mean Square Indicator for the Edge Injection Case.....	222
5.8	Comparison between DRV Calculations at Minimum MSI and Data for 37-pin Edge Injection Cases.....	224
5.9	Sensitivity of the Predicted Dimensionless Salt Concentration to C_{1L}.....	229
5.10	Reduced Edge Transverse Velocity Ratio C_{1L} for the 37-pin Experiment.....	231
5.11	As Built Geometrty at Exit Plane for Chiu's 61-pin Bundles.....	232
5.12	Subchannel Numbering Scheme for 61-pin Bundle.....	233
5.13	Comparison between DRV Calculations at Minimum MSI and Data for 61-pin H/D=8 Interior Injection Cases.....	237
5.14	Comparison between DRV Calculations at Minimum MSI and Data for 61-pin H/D = 4 Interior Injection Cases.....	238
5.15	Comparison between DRV Calculations at Minimum MSI and Data for 61-pin H/D = 8 Edge Injection Cases.....	239
5.16	Comparison between DRV Calculations at Minimum MSI and Data for 61-pin H/D = 4 Edge Injection Cases.....	240
5.17	Reduced Mixing Parameters for 61-pin H/D = 8 Bundle.....	241
5.18	Reduced Mixing Parameters for 61-pin H/D = 4 Bundle.....	242

LIST OF FIGURES (cont'd)

		page
5.19	Comparison between New (This Study) and old (Chiu) Mixing Parameters for 61-pin H/D = 8 Bundle.....	243
5.20	Comparison between New (This Study) and Old (Chiu) Mixing Parameters for 61-pin H/D = 4 Bundle.....	244
6.1	Typical Transverse Velocity at the Interior Gap as a Function of Wire Position.....	255
6.2	Typical Transverse Velocity at the Edge Gap (19-pin, P/D = 1.19, H/D = 18.75, H = 15 cm, from Lafay and Benant (1975).....	258
6.3	Turbulent Interchange Mixing Parameter for Bare Rod Bundle.....	262
6.4	Pressure Distribution Relative to Wire Position.....	267
6.5	Data and Calibrating Results for C_{m1T} (i.e., $\varepsilon^*_{1\eta}$) in the Turbulent Region.....	274
6.6	Data and Calibrating Results for C_{m2T} (i.e., C_{1L}) in the Turbulent Region.....	278
6.7	Parametric Behavior of DEED in the Turbulent Region.....	280
6.8	Paeametric Behavior of ETVR in the Turbulent Region.....	281
6.9	Comparison between Proposed Correlation and Data for DEED of 37-pin Results.....	286
6.10	Comparison between Proposed Correlation and Data for C_{1L} of 37-pin Results.....	287
6.11	Comparison between Proposed Correlation and Data for DEED of 61-pin Results.....	288
6.12	Comparison between Proposed Correlation and Data for C_{1L} of 61-pin Results.....	289
6.13	Available Investigations and Fitting Result for Conduction Shape Factor.....	295
7.1	Flow Chart for the ENERGY-IV Code.....	298
7.2	Fuctions of the Subroutines in ENERGY-IV.....	311

LIST OF FIGURES (cont'd)

		page
7.3	Rod Identification Number Assigned by Subroutine NUMB.....	302
7.4	Equation in Matrix Form for Mixed Convection Option.....	306
7.5	Flow Chart of Subroutine MIXED.....	309
8.1	Power Regions and Thermocouple Locations for WARD and ORNL Bundles.....	317
8.2	Subchannel Identification Number for a 61-pin Bundle (by Subroutine NUMB).....	319
8.3	Test Section and Thermocouple Positions for WARD 61-pin Bundle Tests.....	320
8.4	Rod and Subchannel Identification Number and Thermocouple Locations for ORNL 19-pin THORS 2A Bundle.....	322
8.5	Thermocouple Locations and Power Regions for Toshiba 37-pin Bundle.....	324
8.6	Measured and Predicted Temperature Rise for WARD Run 223....	328
8.7	Measured and Predicted Temperature Rise for WARD Run 403....	329
8.8	Measured and Predicted Temperature Rise for WARD Run 226....	330
8.9	Sensitivity of the ENERGY-IV Results to $\varepsilon^*_{1\eta}$ for WARD Run 223.....	331
8.10	Sensitivity of the ENERGY-IV Results to $\varepsilon^*_{1\eta}$ for WARD Run 403.....	332
8.11	Sensitivity of the ENERGY-IV Results to $\varepsilon^*_{1\eta}$ for WARD Run 226.....	333
8.12	Measured and Predicted Temperature Rise in Edge Subchannels for WARD Bundle.....	335
8.13	Measured and Predicted Temperature Rise for ORNL 19-pin 3/1 Power Skew.....	337
8.14	Measured and Predicted Temperature Rise for ORNL 19-pin Uniform Power Distribution.....	338
8.15	Measured and Predicted Temperature in the Edge Subchannel for ORNL 19-pin Bundle.....	341

LIST OF FIGURES (cont'd)

		page
8.16	Measured and Predicted Temperature Rise for ORNL 61-pin Run 19-101	342
8.17	Measured and Predicted Temperature Rise for ORNL 61-pin Run 1-4	343
8.18	Sensitivity of the ENERGY-IV Results to $\varepsilon^*_{l\eta}$ for ORNL 61-pin Run 19-101	345
8.19	Measured and Predicted Temperature Rise for Toshiba 37-pin Bundle	346
8.20	Velocity Distributions Calculated by COBRA-WC and ENERGY-in the Mixed Convection Condition	355
8.21	Measured and Predicted Temperature Rise for WARD Run 221	357
8.22	Sensitivity of $\varepsilon^*_{\eta M}$ to ENERGY IV Results for WARD Run-221	360
8.23	Measured and Predicted Temperature Rise for WARD Run 229	361
8.24	Sensitivity of the ENERGY IV Results to $\varepsilon^*_{\eta M}$ for WARD Run 229	362
8.25	Measured and Predicted Temperature Rise for WARD Run 231	363
8.26	Sensitivity of ENERGY-IV Results to $\varepsilon^*_{\eta M}$ for WARD Run 231	364
8.27	Measured and Predicted Temperature for WARD Run 401	366
8.28	Measured and Predicted Temperature Rise for WARD Run 731	367
8.29	Measured and Predicted Temperature Rise for WARD Run 720	368
8.30	Measured and Predicted Temperature Rise for WARD Run 227	369
8.31	Measured and Predicted Temperature Rise for WARD Run 732	370
8.32	Measured and Predicted Temperature Rise for ORNL 61-pin Bundle Test 19 Run 105	372
8.33	Measured and Predicted Temperature Rise for ORNL 61-pin Bundle Test 18 Run 105	373
8.34	Measured and Predicted Temperature Rise for ORNL 61-pin Bundle Test 17 Run 105	374

LIST OF FIGURES (cont'd)

		page
8.35	Comparsion among Data, ENERGY-IV Results ($\varepsilon^*_{\eta F}$ only) and COBRA-WC Results for Test 19 Run 105	376
8.36	Measured and Predicted Temperature Rise for ORNL 61-pin Bundle Test 12 Run 114	377
8.37	Measured and Predicted Temperature Rise for Toshiba 37-pin Test at Re = 3000	378
8.38	Sensitivity of the ENERGY-IV Results to $\varepsilon^*_{\eta M}$ for Toshiba Tests	379
8.39	Measured and Predicted Temperature Rise for Toshiba Low Flow Tests	380
8.40	Measured and Predicted Temperature Rise for FETUNA Tests with Uniform Power Skew	382
8.41	Measured and Predicted Temperature Rise for FETUNA Tests at Re = 1740	383
8.42	Relative Importance of Energy Transfer Mechanisms for Blanket Assembly	390
8.43	Relative Importance of Energy Transfer Mechanisms for Blanket Assembly with Different $Gr_{\Delta T}$	391
8.44	Relative Importance of Energy Transfer Mechanisms for Fuel Assembly	392
8.45	α^*_l Effect on the Energy Transfer	393
8.46	Operation Regions in which Different Energy Transfer Mechanisms Are Important for Blanket Assembly	394
8.47	Operation Regions in which Different Energy Transfer Mechanisms Are Importrant for Fuel Assembly	395

LIST OF TABLES

Table		page
1.1	Subchannel Analysis Codes Developed in USA	7
1.2	Status of Old Correlation (Chiu-Hawley-Burns)	18
3.1	Subchannel Geometric Parameters	59
3.2	ν: Kinematic Viscosity of Water	71
3.3	Predicted Parameters by Chiu, Hawley and Burns' Correlations for This Bundle	73
3.4	Flow Split Experimental Results	75
3.5	Experimental Results of Pressure Drop Experiment	82
3.6	Results of f_b, f_1 and f_2	85
3.7	Mass Balance Ratio for Mixing Experiment	92
4.1	Fitting Results of Laminar KL= f^*Re for Triangular Array (KL from Axford and Rehme's results)	139
4.2	f/fct for Bare Rod Interior Subchannel in Turbulent Flow by Different Investigators	147
4.3	G*-Method Fitting Results	150
4.4	Data for Bare Rod Interior Subchannel Friction Factor in Turbulent Region	154
4.5	Data for Bare Rod Edge Subchannel Friction Factor in Turbulent Region	156
4.6	Fitting Results of Turbulent $KT=fRe^{0.18}$ for Triangular Array	159
4.7	Fitting Results of Laminar KL=fRe for Square Array	162
4.8	Fitting Results of Turbulent $KT=fRe^{0.18}$ for Square Array	164
4.9	Comparison between Data, Predictions of the Proposed Correlation and Predictions of Westinghouse Correlation	176
5.1	Reduced ε^*_{in} for 37-pin Interior Injection Experiments	212

LIST OF TABLES (Cont'd)

		page
5.2	Reduced C_{1L} for 37-pin Edge Injection Experiments.....	223
5.3	Reduced $\varepsilon^*_{1\eta}$ and C_{1L} for 61-pin Bundle with H/D = 8.....	235
5.4	Reduced $\varepsilon^*_{1\eta}$ and C_{1L} for 61-pin Bundle with H/D = 4....	236
5.5	Summarization of Errors Associated with Mixing Parameters.....	252
6.1	Available Data for $\varepsilon^*_{\eta M}$ in the Turbulent Region.....	272
6.2	Available Data for C_{1L} in the Turbulent Region.....	276
6.3	Available Data for C_{mLT}.....	283
6.4	Theoretical Results for Asymptotic (fully developed) L_{ij}	293
8.1	Characteristics of Test Bundles.....	316
8.2	Normalized Power Factor for Different Power Skew in WARD and ORNL Bundles Tests.....	318
8.3	Cases Used for Forced Convection Validation.....	326
8.4	Input Parameters for COBRA-WC (or -IV).....	339
8.5	Input Parameters used in COBRA-IV for Toshiba Tests.....	347
8.6	Sensitivity of $\varepsilon^*_{1\eta}$ to the ENERGY-IV Calculation.....	349
8.7	Cases Used for Mixed Convection Validation.....	351
8.8	Comparisons among $\varepsilon^*_{1\eta}$, α^*_1 and $\varepsilon^*_{\eta M}$ for Blanket and Fuel Assemblies.....	386
8.9	Relative Importance on Energy Transfer of Flow Redistribution to $\varepsilon^*_{1\eta}$.....	388
9.1	Coefficients for Bare Rod Friction Factor Constants K_i..	405

NOMENCLATURE

A	Axial average flow area (mm^2)
A_r	Projected area of wire in a subchannel (mm^2)
c	Gap between rods (mm)
C_D	Drag coefficient for circular cylinder
C_d	Drag coefficient for wires
C_f	Friciton factor constant defined in equation (4.38)
C_i	Salt concentration measured by resistance probe
C_m	Constants for mixing parameters
C_s	Swirl flow ratio defined in equation (4.20)
C_{lL}	Edge transverse velocity ratio
D	Rod diameter (mm)
D_e	Equivalent hydraulic diameter (mm)
D_w	Wire diameter (mm)
$\hat{e}$	Total mechanical energy loss per unit fluid volume caused by drag loss (erg/mm^3)
f	Fricition factor
G^*	Constant defined in G^*-method equation (4.59)
$Gr_{\Delta T}$	Grashof number defined as $g\beta(\Delta T_b/L)De_b^4/\nu^2$
Gr_q	Grashof number defined as $g\beta De^4 q''/k\nu^2$
H	Wire lead length (mm)
h	Enthalpy
K	Subchannel friciton factor constants for bare rod bundles
L	Axial (heated) length(mm)
m	Reynolds number exponent in expressions for turbulent or laminar
N	Number of subchannels in the bundle

N_r Number of fuel pins in the bundle

P Rod pitch (mm)

P Pressure

P_r Prandtl number

P_w Wetted perimeter (mm)

Q Average volumetric heat source

q" Heat flux

Re Reynolds number

S Parameter defined in equation (2.28)

v Subchannel velocity (mm/sec)

V_T Transverse velocity inside the edg subchannel

$V_T\big|_{gap}$ Transverse velocity at the gap of the edge region

W Edge Pitch parameter ≡ D + gap between rod and bundle wall

W_d Wire drag constant

W_s Swirl flow constant

W'^{T}_{ij} Total effective interchange mass flow rate per unit lenght (g/cm-sec)

W'_{ij} Interchange mass flow rate for turbulent interchange

W'^{W}_{ij} Effective interchange mass flow rate for wire sweeping

X Flow split parameter

ΔT_b Bundle average temperature rise from inlet to outlet

ΔT^* Normalized temperature rise defined in equation (8.1)

$\varepsilon^*_{l\eta}$ Dimensionless effective eddy diffusivity for the interior region

$\varepsilon^*_{2\eta}$ Dimensionless eddy diffusivity for the edge region

$\varepsilon^*_{\eta F}$ DEED for the forced convection condition

$\varepsilon^*_{\eta M}$ Thermal plume mixing parameter

$\varepsilon^*_{\eta T}$ Dimensionless eddy diffusivity for turbulent interchange

α^*_1	Dimensionless conduction parameter defined in eq. (8.7)
α	Thermal diffusivity (cm^2/sec)
η	Subchannel Centroid to centroid distance
ℓ	Parameter introduced in equation (1.4)
ℓ_{ij}	Laminar Mixing Length between subchannels i and j
ρ	Coolant density (g/cm^3)
μ	Dynamic viscosity (g/cm-sec)
ν	Kinematic viscosity (cm^2/sec)
ψ	Intermittency factor defined in equation (2.26)
θ	Angle which the wire makes with respect to vertical
γ	Exponent in intermittence factor in transition friction factor equation

Subscripts

i	1,2,3, or b which denote interior, edge, and corner subchannel types, and bundle average, respectively
L	Denotes laminar region
T	Denotes turbulent region

Superscripts

'	Denotes equivalent bare rod values

CHAPTER 1

INTRODUCTION

1.1 Overview

The economic performance of a Liquid Metal Fast Breeder Reactor (LMFBR) is closely linked to the endurance of the reactor core fuel assemblies. The fuel assembly life is affected by peak cladding temperature and the temperature distributions in the coolant, fuel, and assembly structures. These temperature distributions should be such that burnup goals can be met without seriously impairing core life and performance. An example of temperature-affected performance is that estimates for existing LMFBR designs indicate that pin burnup might be increased by about 500 to 600 MWD/T for each degree Fahrenheit reduction in hot spot cladding temperature. Since temperature levels thus constrain the design, it is important that the fuel assembly temperature distributions be accurately predicted and the governing thermal-hydraulic phenomena be understood.

Fuel and blanket assemblies in an LMFBR are quite different in geometry and are subjected to a wide range of operating conditions. Therefore, methods developed for predicting temperature distributions should be capable of accounting for the effects of geometrical differences and a wide range of coolant flow and thermal convection regimes which include laminar, transition, and turbulent flow, and natural, forced and mixed (forced and natural) convection.

The key geometric parameters are: number of fuel pin, N_R, rod diameter, D, centroid to centroid distance between adjacent rod (rod pitch), P, and the spacer type. Although various spacer designs have been proposed for LMFBR subassemblies such as wire-wrap, grid spacer, and helical fin, helical wire-wraps are most widely used for maintaining proper spacing between fuel rods and promoting coolant mixing. The wire are all wrapped around rods in a helix of lead length H in the same direction and at any cross section are all at the same position relative to the rod. Figure 1.1 illustrates a typical LMFBR wire wrapped assembly and rod configuration. For a fuel assembly, the geometric parameters are N_R = 217 or 271, D = 0.23", P/D = 1.25, H/D = 50.0; for a blanket assembly, N_R = 61, D = 0.5", P/D = 1.07, H/D = 8.0; and for a control assembly, N_R = 37, D = 0.6", P/D = 1.05, H/D = 20.0. Therefore, the range of geometric differences might be : N_R = 37 - 271; P/D = 1.05 - 1.30; H/D = 8.0 - 50.0.

The coolant flow and thermal convection regimes are strongly related to the bundle Reynolds number. For flow in a wire-wrapped LMFBR rod bundle, there is a broad transition regime, and the flow will not reach fully laminar until the bundle Reynolds number is sufficiently low (around 400~1000). At high Reynolds number operation, the flow redistribution within an assembly is small as compared to the axial flow. Consequently, the buoyancy effects can be neglected. However, at low Reynolds number operation, buoyancy effects must be taken into account. The regime of operation of an assembly where forced flow enters an assembly and is redistributed within the assembly to cause reduction in the transverse temperature gradient, is called

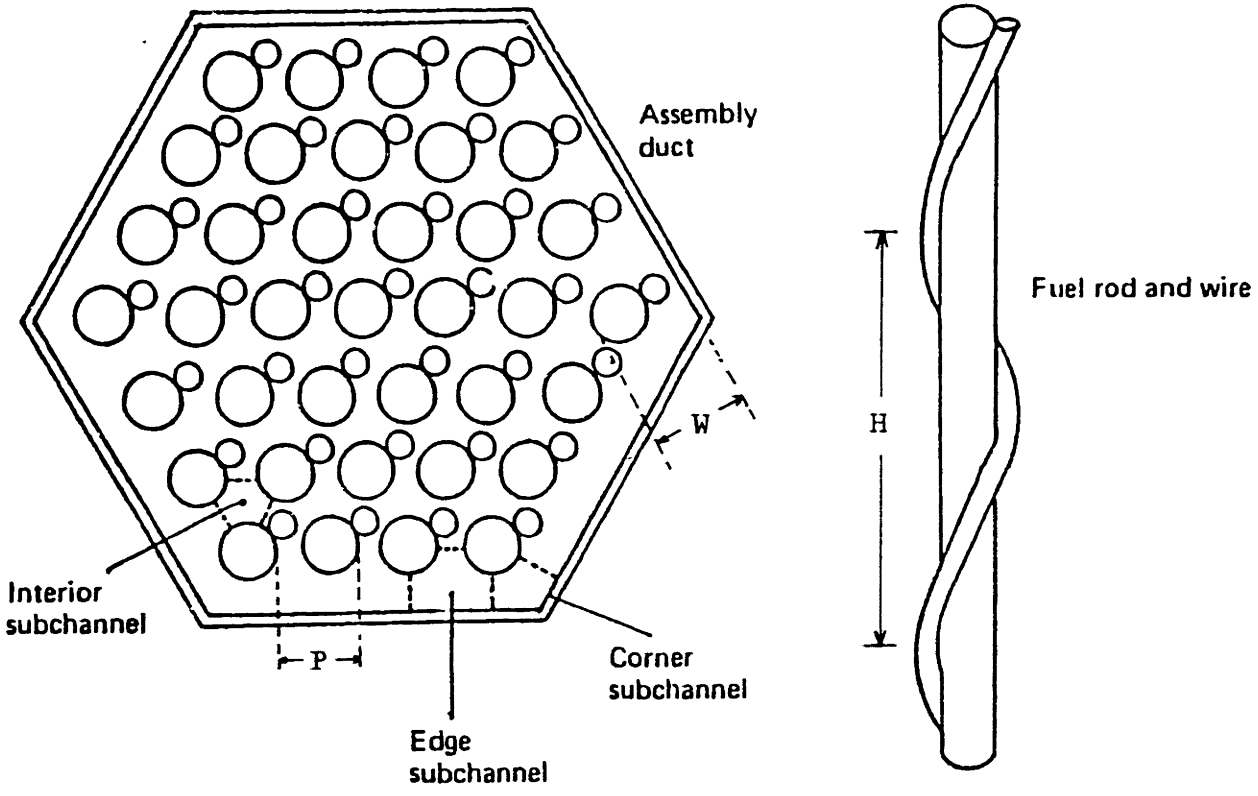

Figure 1.1 Tpypical LMFBR Wire-Wrapped Assembly and Rod Configuration

the mixed convection regime of operation of an assembly. Since LMFBRs are expected to operate both at full as well as part loads, a few fuel assemblies and a significant number of blanket assemblies may operate in the mixed convection regime. Figure 1.2 taken from [Biancheria et al. (1973)] gives an indication of the number of blanket assemblies that may be expected to operate at low Reynolds numbers during full and part load operation of the reactor.

Investigators have developed a number of analytical methods for predicting LMFBR core thermal-hydraulics. Because of core geometrical complexities, various physical approximations are required to develop tractable analytical models that can be readily solved on high-speed computers. These approximations reduce model complexity and computational resource needs, but they also reduce model generality. A large degree of empiricism is necessary, and the range of application of an analytical method for different geometric and operating conditions must be validated by in-pile or out-of-pile experiments from which the empiricism was reduced.

For the thermal-hydraulic analysis of a single assembly, the subchannel analysis method is commonly used. A bulk average value characterizes the hydrodynamic and thermal coolant conditions in each subchannel. An alternate method for thermal-hydraulic analysis of an assembly is the porous body method, in which the whole assembly is treated as a homogeneous continuum. With experimental support, subchannel analysis can predict the peak coolant temperature in a typical LMFBR rod assembly within approximately ±7% [Khan (1980)] of the assembly mixed-mean (axial) temperature rise. In the forced

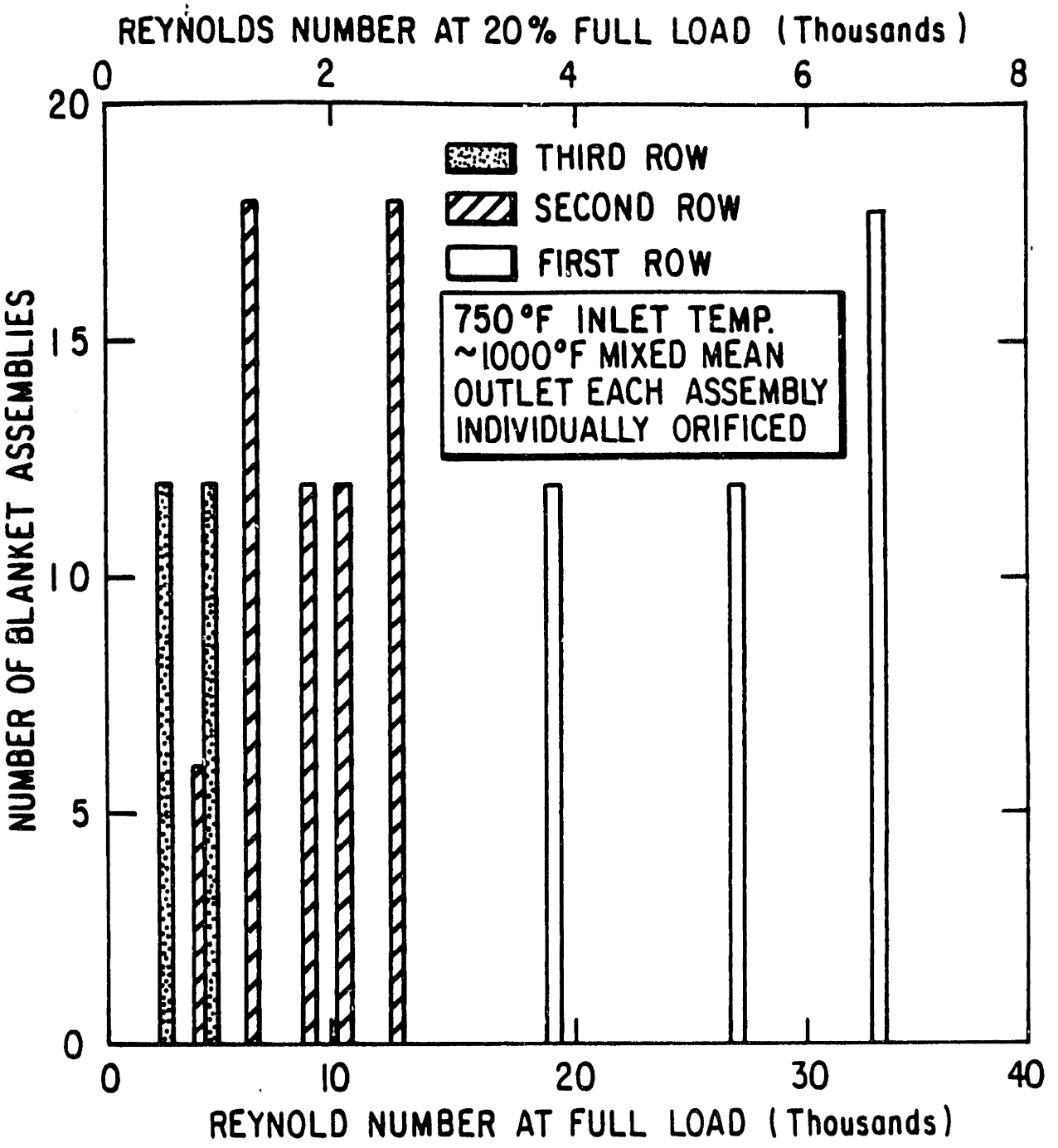

Figure 1.2 Number of Blanket Assemblies at Various Reynolds Number for Full and Partial Load Operation.

convection, the major emphasis in subchannel analysis is on the solution of the energy equation and on the evaluation of empirical constants from existing data, which are needed to match predictions with data. This approach is possible because the hydrodynamic and thermal fields are not strongly coupled in the forced convection regime. In the mixed convection regime, these fields are strongly coupled, hence the mass, momentum, and energy equations need to be solved simultaneously. Table 1.1 lists the available subchannel analysis and porous body analysis codes developed in the United States. In addition to these codes, some comparable codes have also been developed in other countries, such as MISTRAL-II [Baumann (1972)] and ARTIS [Straub (1976)] in Germany, HAMNA [Cooper (1981)] and SABRE [Potter (1976)] in Great Britian, SWIRL [Miyaguchi et al. (1979)] and ASFRE [Yoshikawa et al. (1981)] in Japan, and FLICA [Fajeau (1969)] in France.

Of the codes listed in Table 1.1, the COBRA code is the most widely used. The validation of the COBRA code has been performed by Donovan et al. (1979) and Khan et al. (1982) by comparing the predictions to the available in-pile and out-of-pile data. Statistical analysis of all data showed that the code predicts coolant temperature to within ±25 °F of measured temperature at a 95% confidence level. Because of its generality in solving all the conservation equations, COBRA code is believed to be applicable outside its calibration range.

There are two numerical schemes in COBRA-IV (or -WC), one for high flow rate, and one for low flow rate at which flow reversal might

Table 1.1 Subchannel Analysis Codes Developed in USA

Code	Reference and Originator[a]	Approach[b]	Application[c]	Features
COBRA-IV	Wheeler et al. (1976) PNL	SC, BV; C, AM, TM, E	BR, GS, WW; FC, MC	transient, two phase extensive experience throughout U.S.
COBRA-WC	George et al. (1980) PNL	SC, BV; C, AM, TM, E	BR, GS, WW; FC, MC	same as COBRA IV detailed whole-core coolant temp.
COMMIX	Domanus et al. (1977) ANL	PB, BV; C, SM, TM, E	BR, GS, WW; other components; FC, MC	3-D transient, two phase
COTEC	Novendstern (1972a) ARD	SC, MT; C, E	WW; FC	empirical, fast running extensive verified/calibrated
ENERGY I, II III	Khan et al. (1975) M.I.T.	SC and PB, MT; E for I; C, AM, E for II, III	WW; FC, MC	empirical, Simple model fast running
FULMIX-II	Wei (1979) GE	SC, BV; C, AM, TM, E	WW; FC, MC	little experience
ORRIBLE	Wantland (1974) ORNL	SC, MT; C, AM, TM, E	WW; FC	sweeping flow model for 19 pin only
Simple-2	Jones et al. (1976) ANL	SC, MT; C, AM, E	WW; FC	no empirical coefficients for wire sweeping model
THI-3D	Sha et al. (1975) ANL	SC, BV; C, AM, TM, E	BR, GR, WW; FC, MC	3D axial flow area variation, detailed control assembly model, little experience

Table 1.1 continue

a. PNL = Pacific Northwest Laboratory
ANL = Argonne National Laboratory
ARD = Westinghouse Advanced Reactor Division
GE = General Electric Company
MIT = Massachusetts Institute of Technology
ORNL = Oak Ridge National Laboratory

b. SC = Subchannel Analysis approach
PB = Porous Body approach
BV = Boundary Value problem
MT = Marching Type initial value problem
C = Continuity equation
AM = Axial Momentum equation
TM = Transverse Momentum equation
E = Energy equation

c. BR = Bare Rod bundle
GS = Grid Spaced bundle
WW = Wire-Wrapped bundle
FC = Forced Convection condition
MC = Mixed Convection condition

occur during iteration. The running time for the first scheme for a 61-pin bundle with 120 subchannels (no corner subchannels) is about 10 minutes, while the second one will take hours because of the sophisticated solution method. This makes it very expensive if not impossible to run large bundles in low flow rate transient cases, without introduction of some coarser mesh. However, coarser mesh will decrease the accuracy of the predicting peak temperature. Hence, a fast running, more empirical code is desirable.

The ENERGY series of codes developed at MIT is one kind of subchannel analysis code to complement the COBRA code. Basically, the ENERGY code adopts the simplest model one can imagine to physically simulate a wire-wrapped rod bundle. It is a totally empirical code, in which empirical parameters are input to reduce the complexity in solving conservation equations. These empirical parameters, however, have to be calibrated from the experimental data by matching the code predictions. Furthermore, models and correlations should be developed for these parameters over the calibration range to account for geometric effects and flow regime effects.

Although the ENERGY code and the correlations for its input parameters have been investigated at MIT over the last several years, they are still not fully developed and the application of this code to mixed convection situations is not complete. The objective of this study is to complete these tasks. The derivation of the equations for the code will be thoroughly discussed. While they are very similar to the old equations, some modifications are included and the derivation

is reduced from general subchannel equations on a clear and sound basis. One experiment will be performed to fill the gap in data required for developing the input parameters of the code. The models and correlations for the input parameters will be redeveloped or vastly revised and then calibrated from the available world data. Finally, the code will be validated by comparing its predictions to the sodium cooled temperature data in forced and mixed convection in wire-wrapped rod bundles. The capability in the range of application of this approach will then be established.

1.2 Previous Work and Motivation

The ENERGY series of codes, ENERGY I, II, III, were first developed by Khan et al. (1975). They were formulated particularly for calculating the sigle phase coolant temperature distribution in a nominal hexagonal wire-wrapped rod bundle under both the forced convection regime (ENERGY I) and the mixed convection regime (ENERGY II, III). For the forced convection regime, only the energy equation is solved by a marching type technique. For the mixed convection regime, the axial momentum, energy and total mass balance equations are solved simultaneously at one axial level to obtain the cross flow due to buoyancy effects. Properites are updated at the end of each axial node and used as the inlet properties for the next axial step. The difference between ENERGY II and III is that ENERGY II neglects the convective terms in the axial momentum equation.

Greene (1980) consolidated ENERGY I and ENERGY III into a single code with an option to use the forced convection or mixed convection solution. Greene also improved the numerical efficiency of the mixed convection option, which effectively eliminated the need for ENERGY II. Kim (1982) later corrected some errors in Greenes version of the code. Both Greene and Kim compared the code predictions with some available temperature data.

Two kinds of representation, i.e., porous body and subchannel, have been formulated in the ENERGY codes. However, the porous body representation has never been exercised. All the cases run by ENERGY have used the subchannel representation. In this study, only the subchannel representation will be used. The reason for this choice will be discussed in Chapter 2.

Although the ENERGY codes had been studied as described above there are still many improvements needed to be done. First, the equations and the input parameters derived for the code are not clearly documented. Second, the code will not converge in the mixed convection solution scheme unless the terms related to the swirl flow in the edge channels are set to be zero as pointed out by the former investigators. And third, the tedious input information and format are not necessary. Therefore, all of the equations, numerical scheme, and code formulation need to be re-established or modified.

Since the ENERGY code is an extremely empirical code, the accuracy of the input parameters is the most important factor in determining the prediction capability of the code. The input parameters for the ENERGY

code were discussed by Chan et al. (1980). As will be derived in Chapter 2, the input parameters required are: flow split parameters, X_i, subchannel friction factors, f_i, and mixing parameters. We next discuss the previous work done for modelling these parameters.

Over the last several years, subchannel friction factor and mixing parameter models for wire-wrapped LMFBR subassemblies have been developed by Chiu (1980d, 1980e), Hawley (1980), and Burns (1980a) at MIT. A two region approach, which assumed that the velocity in the corner subchannels is the same as that in the edge subchannels, was used in these models. Under the assumption of equal pressure drop over the same axial distance in all subchannels, i.e.,

$$\Delta P = f_i \frac{L}{De_i} \frac{\rho V_i^2}{2} \qquad (1.1)$$

for i = b, 1, 2

where b = bundle average

1 = interior subchanel

2 = edge subchannel

they obtained

$$\frac{f_b}{De_b} = \frac{f_1}{De_1} X_1^2 = \frac{f_2}{De_2} X_2^2 \qquad (1.2a,b)$$

and under the mass continuity condition, they got

$$S_1 X_1 + S_2 X_2 = 1.0 \qquad (1.3)$$

where $S_1 \equiv \frac{N_1 A_1}{A_b}$, $S_2 \equiv \frac{N_2 A_2 + N_3 A_3}{A_b}$

From equations (1.2a and b) and (1.3), any three of the five parameters f_b, f_1, f_2, X_1 and X_2 could be determined provided the other two were given. The final approach evolved by Hawley utilizing the earlier work of Chiu (1978d) was to formulate phenomenological models for subchannel friction factors f_1 and f_2. These parameters were then utilized to compute f_b, X_1 and X_2 from this equation set.

The accuracy of the subchannel friction factor/flow split correlations developed by Hawley and Chiu is reasonable in the turbulent region (about ± 20% for bundle average friction factor and ± 5% for flow split parameters). However, significant discrepancies between the predictions and recent data were found in the laminar region as shown in Figure 1.3 which compares this new data with the associated predicted value for bundle friction factor in the laminar region. The predicted values are apparently too high.

The reason for the inability of these correlations to satisfactorily predict recent laminar data is due to the insufficient data base available when the correlations were originally developed. The empirical constants in the subchannel friction factor correlation were calibrated with the bundle average friction factor data and flow split data of each bundle, since only the bundle friction factor and flow splits had been measured in the experiments. At the time that Hawley calibrated his laminar friction factor correlations, only three bundle friction factor data had been measured, as also shown in Figure 1.3. Even worse, the only laminar flow split data were for two bundles measured at MIT by Chen (1974) using the Laser Doppler Anemometer

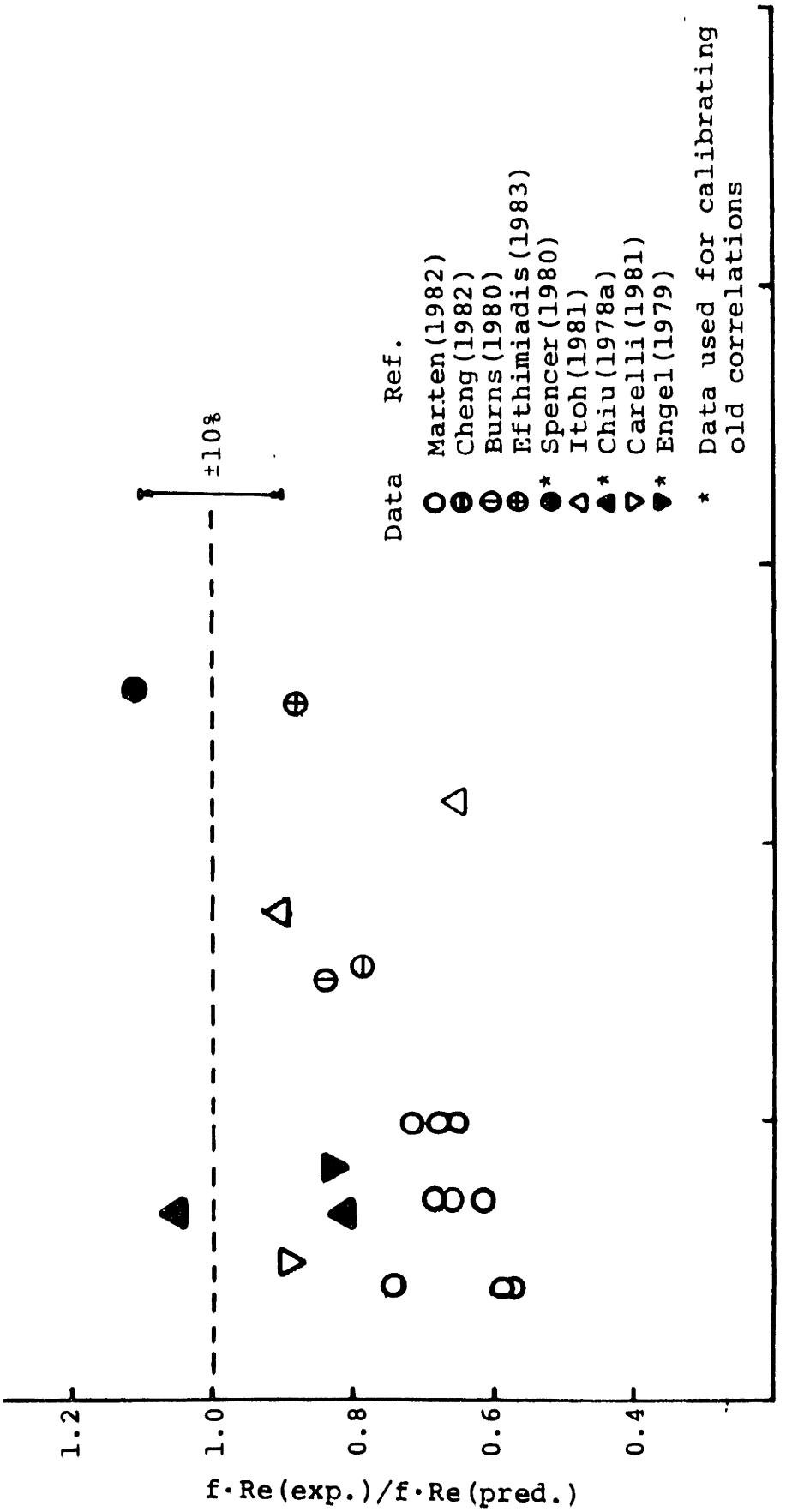

Figure 1.3 Comparison between Experimental Data and Prediction of Old Correlations for Laminar $f_b \cdot Re_b$

technique. Hawley used those three bundle friction factor data, and estimated the laminar flow split values for each of them by extrapolating from the transition regime to calibrate his empirical constants. As new pressure drop data were measured, it became clear that these three data sets did not represent the right data trend. Hence the correlations could not correctly predict the new data.

The transition friction factors were formulated by Hawley as

$$f_{itr} = \left[\left(\frac{C_{fiL}}{Re_i} \right)^{\ell_i} + \left(\frac{C_{fiT}}{Re_i^m} \right)^{\ell_i} \right]^{1/\ell_i} \tag{1.4}$$

where i = b, 1, 2; C_{fiL}/Re_i and C_{fiT}/Re_i^m were the friction factor equations for the laminar and turbulent regions, respectively; and ℓ_i was to be determined.

Based on the available bundle friction factor data, ℓ_b was calibrated by Hawley to be 1.49. Hawley assumed that $\ell_1 = \ell_2 = \ell_b$ for simplicity. The transition flow split parameters were then calculated by equation (1.2) to be

$$X_{itr} = \left[\frac{f_{btr}}{f_{itr}} \left(\frac{De_i}{De_b} \right) \right]^{0.5} \tag{1.5}$$

where i =1,2

These X_{1tr} and X_{2tr} values calculated from equation (1.5) utilizing friction factors from equation (1.4) taking $\ell_1 = \ell_2 = \ell_b$ would not satisfy the mass balance, equation (1.3). This occurred because only two of the five parameters f_b, f_1, f_2, X_1, and X_2 are needed to calculate the other three by equations (1.2a,b) and (1.3). Since

equation (1.4) gives f_b, f_1, and f_2, one redundant equation had been imposed to replace the mass balance equation. This can be eliminated if one calculates X_{itr} by using mass balance equation (1.3) and only f_1 and f_2 from equation (1.4).

Even in the turbulent region where the correlations are sufficiently accurate, two problems still exist. The major one is that the correlations cannot be reduced to bare rod cases. This is undesirable because bare rod cases are good benchmark points for the correlations, and it is convenient to have a single correlation which can cover both cases. In the friction factor case, no bare rod data were used to calibrate any empirical constants.

The second problem is the inconsistency between the Reynolds number exponent in the original [Chiu(1978e)] friction factor equations used to derive flow split parameters (-0.25) and that used in the recent [Hawley(1980)] friction factor equations (-0.18). This inconsistency exists because the formulations were developed at different times and on different data bases.

Regarding the mixing models, Chiu et al. (1978d) developed a sweeping flow model to formulate correlations for those parameters. The calibration result for the sweeping flow falls into the ±35% range of the experimental data for the interior gap and ±25% for the edge gap. Later, Burns (1980a) utilized a single phenomenological model in both the laminar and transition flow regimes. Whenever the value calculated by this laminar/transition correlation is higher than the turbulent value, the turbulent value is used. However, it was found

that the transition correlation could not predict the trend of the data correctly. Also, this model was not developed to be consistent with the model developed for friction factors. Since all these parameters are essentially related to the same hydraulic characteristics, we would like to have consistent models for all of them. A transition mixing parameter model which is consistent with the friction factor model is therefore required. This consistent model is expected to fit the data better than the old one.

Table 1.2 depicts the status of the old correlations and summarizes the problems associated with them. Recently, new data from pressure drop measurements and mixing experiments have become available. In order to correct the inconsistencies new models for friction factor and revised models for mixing parameters will be proposed. The new data will also be used in calibrating the empirical constants of these models. The usefulness of these correlations for the ENERGY code will be validated by comparing the predictions to the sodium cooled temperature data.

1.3 Objective

The objective of this work is to develop a final and conclusive set of equations and input parameters for the ENERGY code by using the experience obtained over the last several years. Specifically, the following areas are the major concerns:

1) Derive subchannel equations and empirical parameters in a clear and sound manner and revise the ENERGY code (ENERGY-IV). (Chapters 2,7).

TABLE 1.2

Status of Old Correlation (Chiu-Hawley-Burns)

	Turbulent ($Re_i \geq 100,000$)	Transition ($400 < Re_i < 100,000$)	Laminar ($Re_i \leq 400$)
FLOW SPLIT	GOOD • exponent of Re used is inconsistent with friction factor model	POOR • mass balance not satisfied	POOR • no data base • low values assumed for calibration
FRICTION FACTOR	FAIR • cannot be reduced to bare rod case	FAIR • discontinuity near Re = 400 and 100,000	POOR • insufficient data base, overpredict new data
MIXING PARAMETER	FAIR • can be improved by revised model	FAIR • model not consistent with friction factor model	FAIR • no model, new model needed.

2) Perform experiments in a wire-wrapped bundle to obtain the data to fill the gap of the available data required for the input parameters. (Chapters 3, 5)
3) Develop consistent models and correlations for those input parameters and calibrate them by the data base available. (Chapters 4,6)
4) Validate the ENERGY model and the input parameter correlation by comparing the predictions to the real case temperature data, i.e., sodium cooled experiments (Chapter 8) in both the forced and mixed convection regimes.

CHAPTER 2

SIMPLE SUBCHANNEL ANALYSIS METHOD: THE ENERGY CODE

2.1 General Equations for Subchannel Analysis

Generally, all thermal analysis methods for rod bundles start from the basic governing equations for mass, momentum and energy balance. These equations are then integrated over control volumes used for the method and simplified by some assumptions. This is the typical so-called lumped parameter method. Two kinds of approaches are currently prevalent, one is the subchannel approach; the other is the porous body approach. The subchannel approach uses control volumes defined by the typical subchannel in rod bundles, as shown in Figure 2.1 for a hexagonal LMFBR subassembly while the porous body approach treats the rod bundles as a porous medium, approximating it as a continuum. Hence the control volumes in the porous body approach can theoretically be any size as long as their porosity and permeability can be calculated.

Major benefit for the porous body approach is that the mesh size can be enlarged to be more than a conventional subchannel, hence reducing the computational time for large bundles. In addition, it might be easier to understand some assumptions by imagining a complicated wire-wrapped rod bundle as a homogeneous continuum. However, the final equations for the porous body approach are essentially the same as the subchannel approach if the control volumes are defined in the same conventional way. Lumping many subchannels into one bigger subchannel can also be done in the subchannel approach.

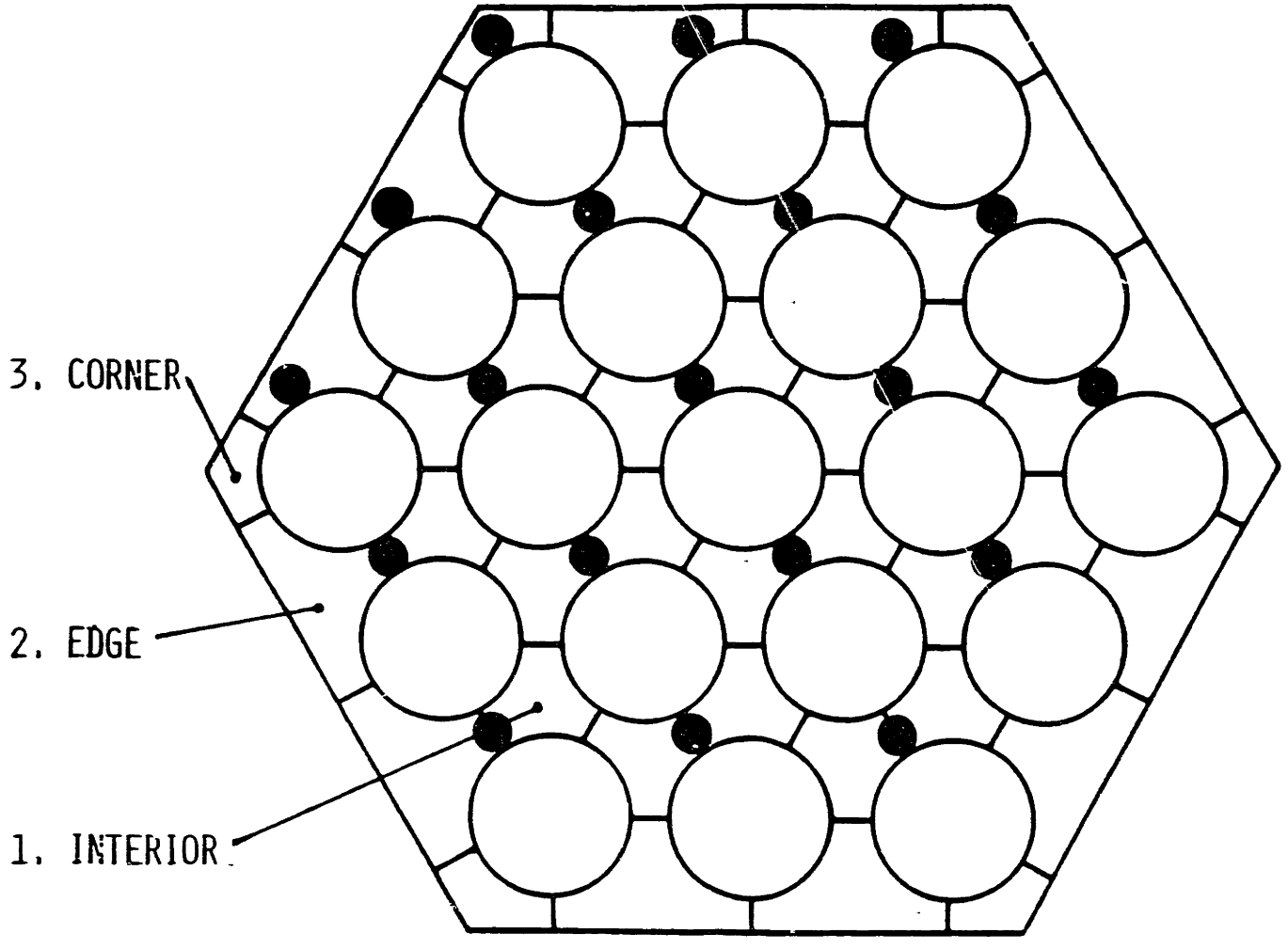

Figure 2.1 Typical Subchannels in LMFBR Wire-Wrapped Bundle

Since all the empirical parameters introduced later in this study are reduced by the subchannel approach, their application to the porous body approach using a different mesh geometry is doubtful. On the other hand, the introduction of porous body representation introduces complexity and confusion in the notation. Therefore, in this study, the subchannel approach will be used.

The general integral equations for the subchannel approach for axially dominant flow have been derived by Todreas (1984). The subchannel equations were presented in the following form.

Continuity

$$A_i \Delta z \frac{\partial}{\partial t} \langle \rho_i \rangle + \Delta \dot{m}_i = - \Delta z \sum_{j=1}^{J} W_{ij} \tag{2.1}$$

Energy

$$A_i \Delta z \frac{\partial}{\partial t} \left[\langle \rho h \rangle_i \right] + \Delta \left[\dot{m}_i \{h_i\} \right] = A_i \Delta z Q_i$$

$$- \Delta z \sum_{j=1}^{J} W_{ij}^{*H} (h_i - h_j) - \Delta z \sum_{j=1}^{J} W_{ij} \{h^*\} + A_i \Delta z \left\langle \frac{dP_i}{dt} \right\rangle \tag{2.2}$$

Axial Momentum

$$\Delta z \frac{\partial}{\partial t} \langle \dot{m}_i \rangle + \Delta \left[\dot{m}_i \{v_i\} \right] = -A_i \Delta z \langle \rho_i \rangle g$$

$$-A_i \Delta \{P\} - \Delta z \sum_{j=1}^{J} W_{ij}^{*M} (v_i - v_j) - \Delta z \sum_{j=1}^{J} W_{ij} \{v^*\} - \{F_{iz}\} \tag{2.3}$$

Transverse Momentum

$$\frac{\partial}{\partial t} \langle W_{ij} \rangle + \frac{\Delta}{\Delta x'} \left[W_{ij} \{u\} \right] + \frac{\Delta}{\Delta z} \left[W_{ij} \{v\} \right]$$

$$= - \left[s_{ij} \frac{\Delta}{\Delta x'} \{P\} \right] - \left\{ \frac{F_{ix}}{\Delta x' \Delta z} \right\} \tag{2.4}$$

where $\langle\ \rangle$ = indicates volume average over a control volume V_f

$$\langle\Psi\rangle \equiv \frac{1}{V_f}\int_{V_f}\Psi dV$$

$\{\ \}$ = indicates area average over a flow area A_f

$$\{\Psi\} \equiv \frac{1}{A_f}\int_{A_f}\Psi dA$$

$\Delta\Psi \equiv \Psi$ at $z+\Delta z$ - Ψ at z

z = axial direction

x = transverse direction

v = local axial velocity

u = local transverse velocity

h = local enthalpy

ρ = local fluid density

P = static pressure

$\dot{m} = \{\rho vA\}$

A_i = axial subchannel flow area

s_{ij} = gap between subchannel i and j

Δz = axial length of control volume used

$\Delta x'$ = transverse characteristic length

$v_i = \langle v_i \rangle$

$h_i = \langle h_i \rangle$

W_{ij}^{*H} = effective mass exchange rate per unit length between subchannel i and j for energy transfer

W_{ij}^{*M} = effective mass exchange rate per unit length between subchannels i and j for momentum transfer

W_{ij} = transverse mass flow rate per unit length from subchannel i to j = $s_{ij} \{\rho u\}$

$\{h^*\}$ = effective enthalpy transported by transverse flow

$\equiv \{\rho uh\}/\{\rho u\}$

$\{v^*\}$ = effective velocity transported by transverse flow

$\equiv \{\rho uv\}/\{\rho u\}$

F_{ix}, F_{iz} = total force on the fluid at x, z direction due to fluid-solid interaction

Q_i = equivalent dispersed heat source per unit volume

Figures 2.2, 2.3 and 2.4 illustrate the control volume and most of the terms for the continuity, energy and axial momentum equations, respectively. The transverse momentum equation is not used in our model as will be discussed in the next section.

Using this set of equations and some assumptions, a set of subchannel equations will be adopted for a simple computer code, ENERGY-IV.

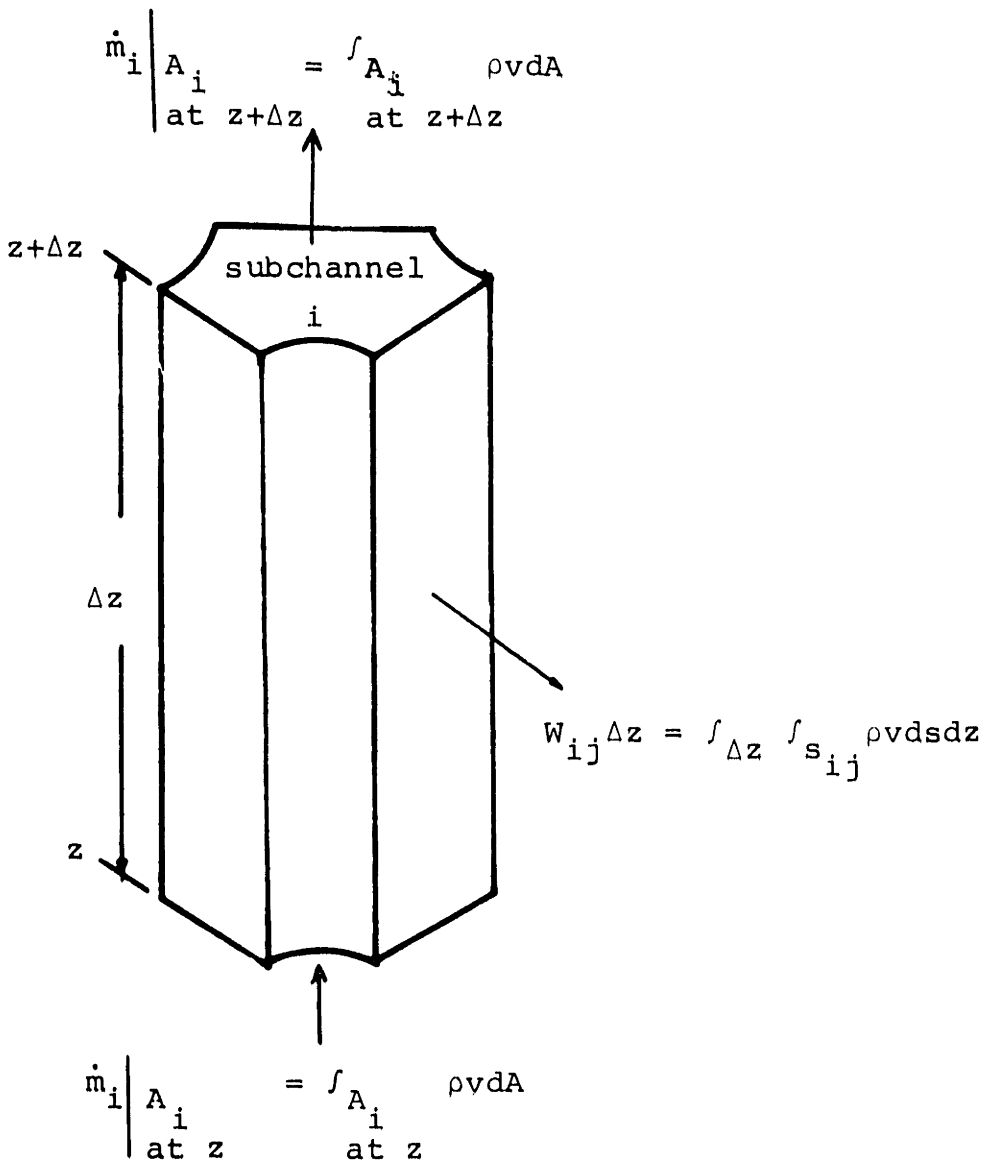

Figure 2.2 Subchannel Control Volume for Continuity Equation

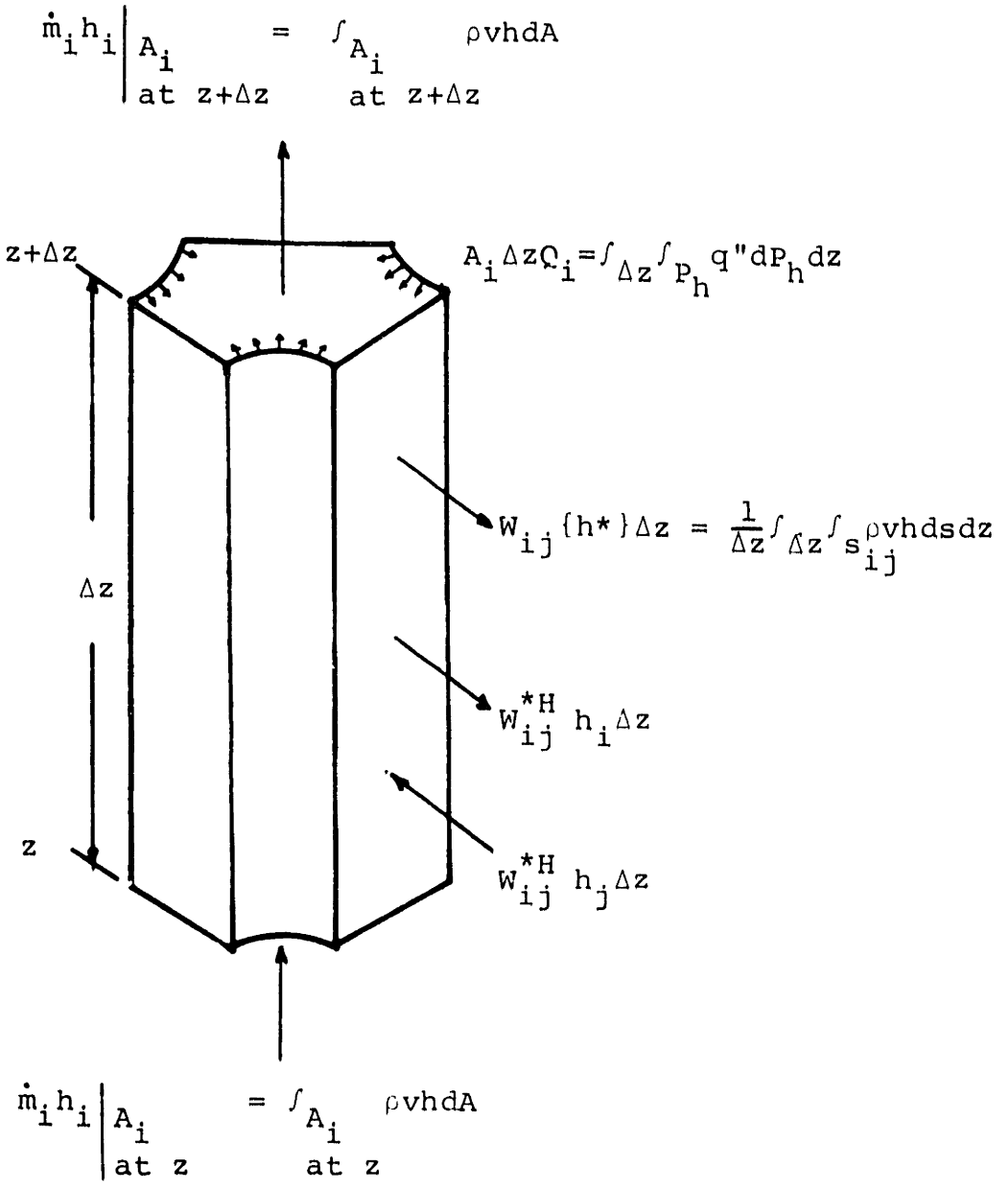

Figure 2.3 Subchannel Control Volume for Energy Equation

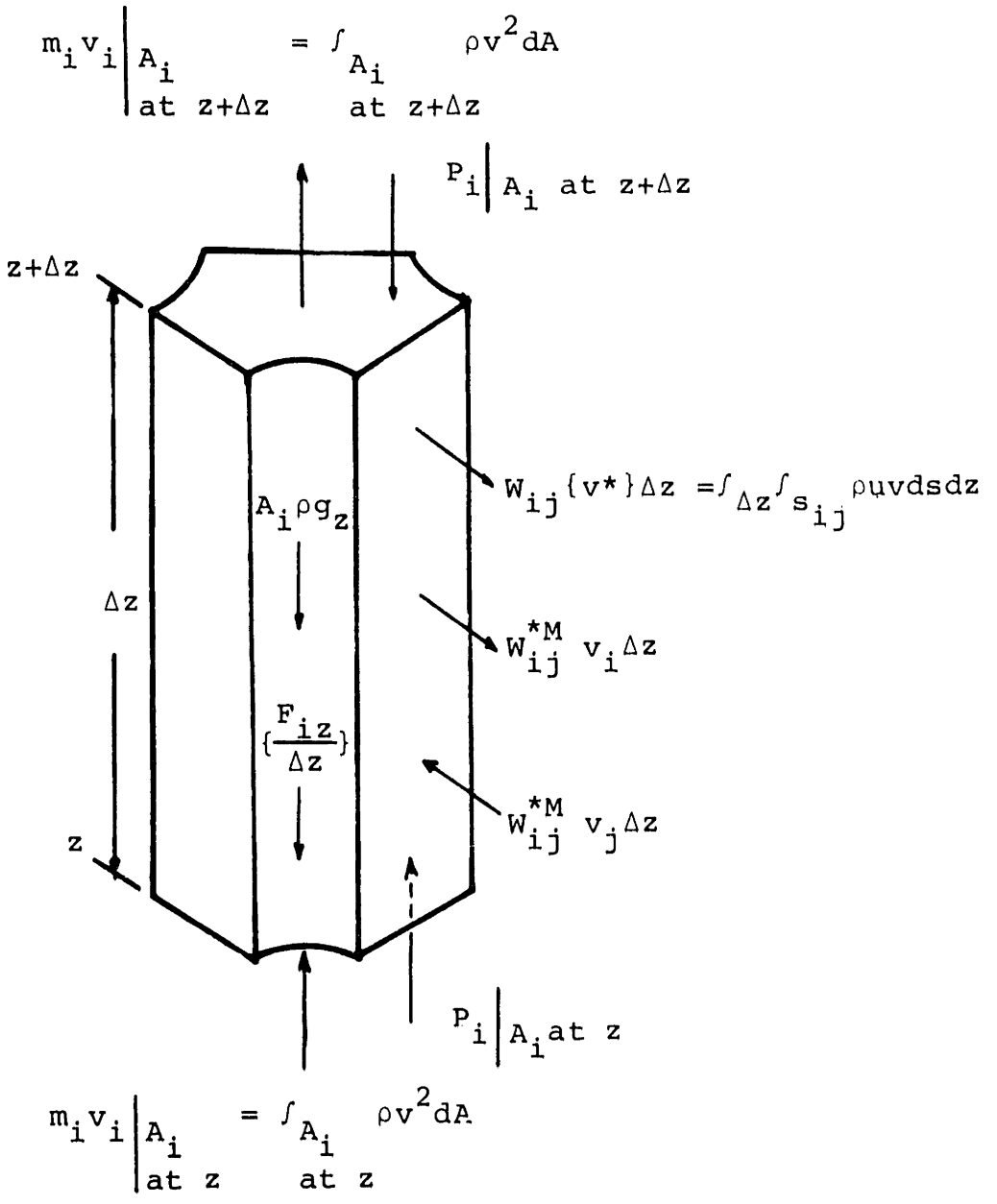

Figure 2.4 Subchannel Control Volume for Axial Momentum Equation

2.2 Simple Subchannel Analysis Model for Wire-Wrapped LMFBR Subassembly

2.2.1 Two Region Approach

In a wire-wrapped LMFBR subassembly, the wire-wrapped rods are packed in an array which is enclosed by a flow duct. As a result there is a region of flow next to the duct wall which is quite different in character from the flow in the interior region. In the interior region the mean flow oscillates around each rod while progressing in an axial direction. This oscillation of flow may be imagined to contribute an effective eddy diffusivity superimposed on the normal eddy diffusivity associated with turbulent interchange. In the outer region near the wall, i.e., the edge region, since the wire wrap is spiralled around each rod in the same direction, the flow progresses with both an axial component and a tangential component parallel to the wall.

Thus, a basis of our simple model is the existence of a uniform lateral effective enhanced (by the wire) eddy diffusivity for the heat transfer in the interior region and a uniform transverse velocity, V_T along the duct wall in the edge region. These two parameters are integral values averaged over a wire lead length. The local wire position effect is therefore not modeled. In our model these two parameters will be empirically determined and treated as input parameters to the code. Figure 2.5 illustrates the two regions and these two parameters.

Regarding conservation equations used in our model, the first simplifying assumption is that the pressure is uniformly distributed across the assembly. This gives constant pressure in each axial plane of the bundle and enables us to discard the transverse momentum

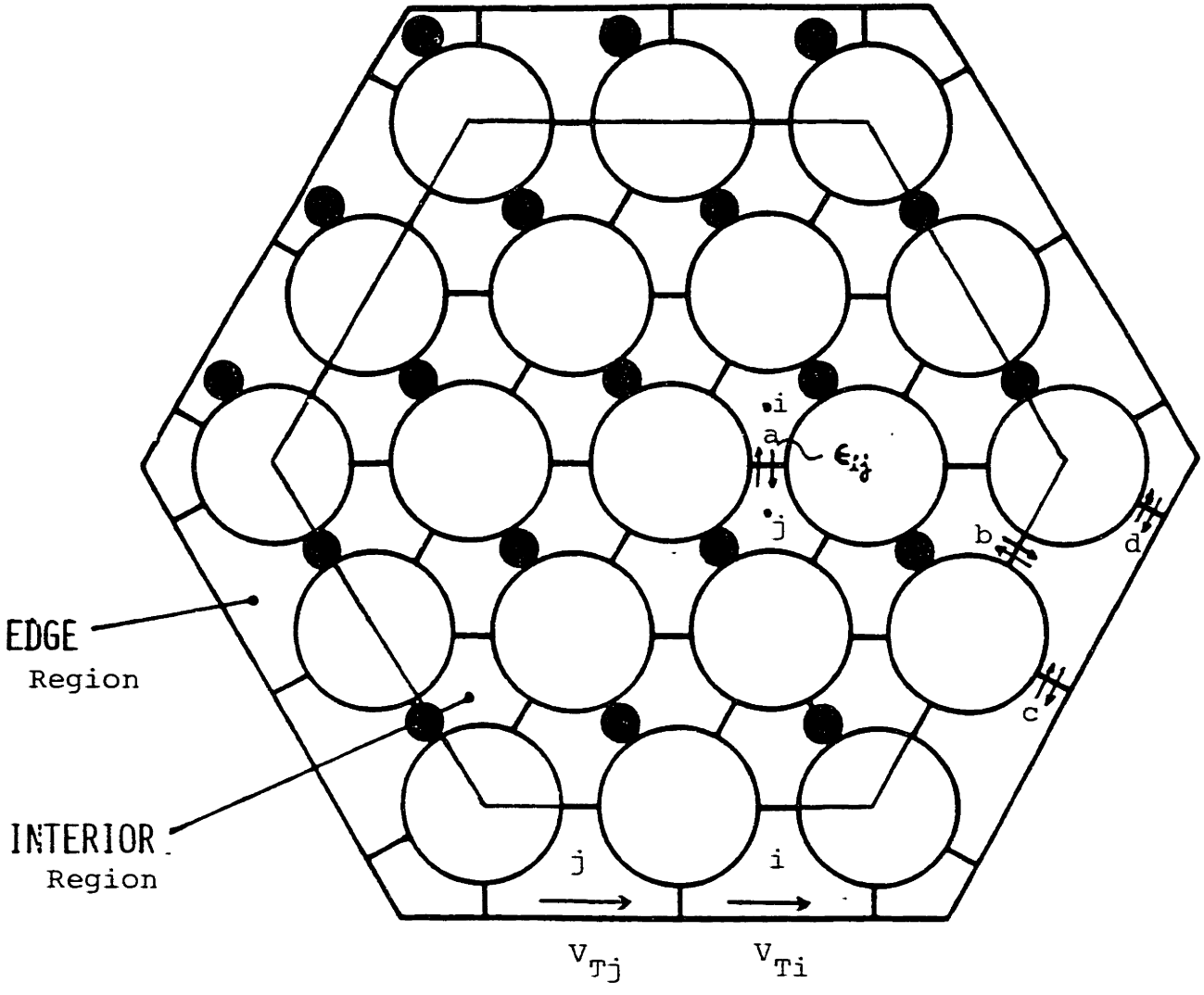

Figure 2.5 Two Region Approach for LMFBR Subchannel Analysis

equation. Because no transverse momentum equation is used, the cross flow can not be calculated at each gap. Only the total cross flow for each subchannel can be calculated by substituting the crossflow terms

$$\sum_{j=1}^{J} W_{ij} \{h^*\} \text{ and } \sum_{j=1}^{J} W_{ij} \{v^*\}$$

into the energy and momentum equations respectively, from the continuity equation.

To compensate for the equal pressure drop assumption the bundle inlet flow distribution must be empirically supplied as an input parameter for the code. In this study, the inlet velocity field is assumed to consist of three constant values for three kinds of subchannels i.e., V_1 for the interior subchannel, V_2 for the edge subchannel, and V_3 for the corner subchannel. Specifically, we define three flow split input parameters X_1, X_2, and X_3 as V_1/V_2, V_2/V_b, and V_3/V_b respectively where V_b is the bundle average velocity.

2.2.2 Treatment of Continuity Equation

Since only the steady state condition is considered in this work, all time dependent terms in the conservation equation are dropped. The continuity equation then becomes:

$$\frac{\Delta \dot{m}_i}{\Delta z} = - \sum_{j=1}^{J} W_{ij} \tag{2.5}$$

where W_{ij} is the transverse mass flow rate per unit length from subchannel i to j. In the interior region, since the wire sweeping flow is modelled by an effective eddy diffusivity, no net crossflow will be

introduced by wire. However, in the edge region, a uniform transverse velocity is assumed to model the wire sweeping effect. hence, there is a net cross flow transported by this velocity, in addition to the cross flow caused by the requirement to keep subchannel axial pressue drops equal.

As shown in Figure 2.5, subchannel i in the edge region gains mass at flow rate $\Delta z D_g \rho_j V_{Tj}$ from subchannel j and transports mass at flow rate $\Delta z D_g \rho_i V_{Ti}$ to subchannel k where Dg is the gap between subchannels in the edge region. Hence, the continuity equation for subchannels in the edge region becomes

$$\frac{\Delta \dot{m}_i}{\Delta z} = - \sum_{j=1}^{J} W_{ij} + D_g \left[\rho_j V_{Tj} - \rho_i V_{Ti} \right] \tag{2.6}$$

Note that W_{ij} always denotes the cross flow caused by momentum balance.

2.2.3 Treatment of Energy Equation

For the steady state condition, the subchannel energy conservation equation for an interior subchannel, equation (2.4), becomes

$$\frac{\Delta}{\Delta z} \left[\dot{m}_i \{h_i\} \right] = A_i Q_i - \sum_{j=1}^{J} W_{ij}^{*H} \left[h_i - h_j \right] - \sum_{j=1}^{J} W_{ij} \{h^*\} \tag{2.7}$$

The term $W_{ij}^{*H} (h_i - h_j)$ is the total effective energy exchange rate per unit length contributed by both the effective conduction due to the molecular effects and the effective mixing due to wire sweeping and turbulent interchange which we label "mixing."

$$W_{ij}^{*H}(h_i - h_j) = q''_{ij}\, s_{ij}\Big|_{\text{conduction}} + q''_{ij}\, s_{ij}\Big|_{\text{mixing}} \qquad (2.8)$$

In a hexaganal rod bundle, there are four kinds of subchannel pairs. As also illustrated in Figure 2.5, in which gap a is between interior and interior subchannels; gap b is between interior and edge subchannels; gap c is between edge and edge subchannels; and gap d is between edge and corner subchannels. The s_{ij} in equation (2.8) is the gap between rods for a, b and gap between rod and wall for c, d. In gaps c, d, the wires sweep flow in the same direction which is modelled by a uniform transverse velocity. Hence the wire-sweeping effects are not included in $q''_{ij}\, s_{ij}\Big|_{\text{mixing}}$, and only the natural turbulence interchange is counted. In gaps a, b, the wire sweeping effects are the major contributions to $q''_{ij} s_{ij}\Big|_{\text{mixing}}$.

The effective conduction between subchannels can be formulated as

$$q''_{ij} s_{ij}\Big|_{\text{conduction}} = \int_{s_{ij}} \left[- k \frac{\partial T}{\partial n}\Big|_{\text{gap}}\right] ds$$

$$= k \frac{T_i - T_j}{\ell_{ij}} S_{ij} \qquad (2.9)$$

where ℓ_{ij} is an effective mixing length defined by equation (2.9) which allows the gradient across the gap to be expressed in terms of the available subchannel average temperatures T_i and T_j, i.e.,

$$\ell_{ij} \equiv \frac{k(T_i - T_j)}{\frac{1}{s_{ij}} \int_{s_{ij}} \left[- k \frac{\partial T}{\partial n}\Big|_{\text{gap}}\right] ds} \qquad (2.10)$$

These parameters are shown in Figure 2.6 which illustrates the difference between the subchannel centroid to centroid distance, η_{ij}, and the effective mixing length, ℓ_{ij}. Now a parameter called the conduction shape factor, κ, is defined as

$$\kappa \equiv \frac{\eta_{ij}}{\ell_{ij}} \tag{2.11}$$

The contribution of energy transfer by effective conduction can be then formulated as

$$q_{ij}s_{ij}\Big|_{\text{conduction}} = \kappa k \left(\frac{T_i - T_j}{\eta_{ij}}\right) s_{ij} = \rho s_{ij} \kappa \left(\frac{\alpha}{\eta_{ij}}\right) (h_i - h_j) \tag{2.12}$$

where α = thermal diffusivity $\equiv k/\rho Cp$

The contribution of energy transfer due to wire sweeping and turbulent interchange effects will be combined as one term and modelled by an enhanced eddy diffusivity. Usually, the energy transfer by turbulent interchange only is written as

$$q''_{ij}\, s_{ij}\Big|_{\substack{\text{turbulent} \\ \text{interchange}}} = W'_{ij}\,(h_i - h_j) \tag{2.13a}$$

where W'_{ij} is the effective mass exchange rate between subchannel i and j due to turbulent interchange. Assuming that the sweeping flow caused by wire can also be treated as an uniform bidirectional transverse flowrate just as that of the turbulent interchange, the effective wire effect can be written as

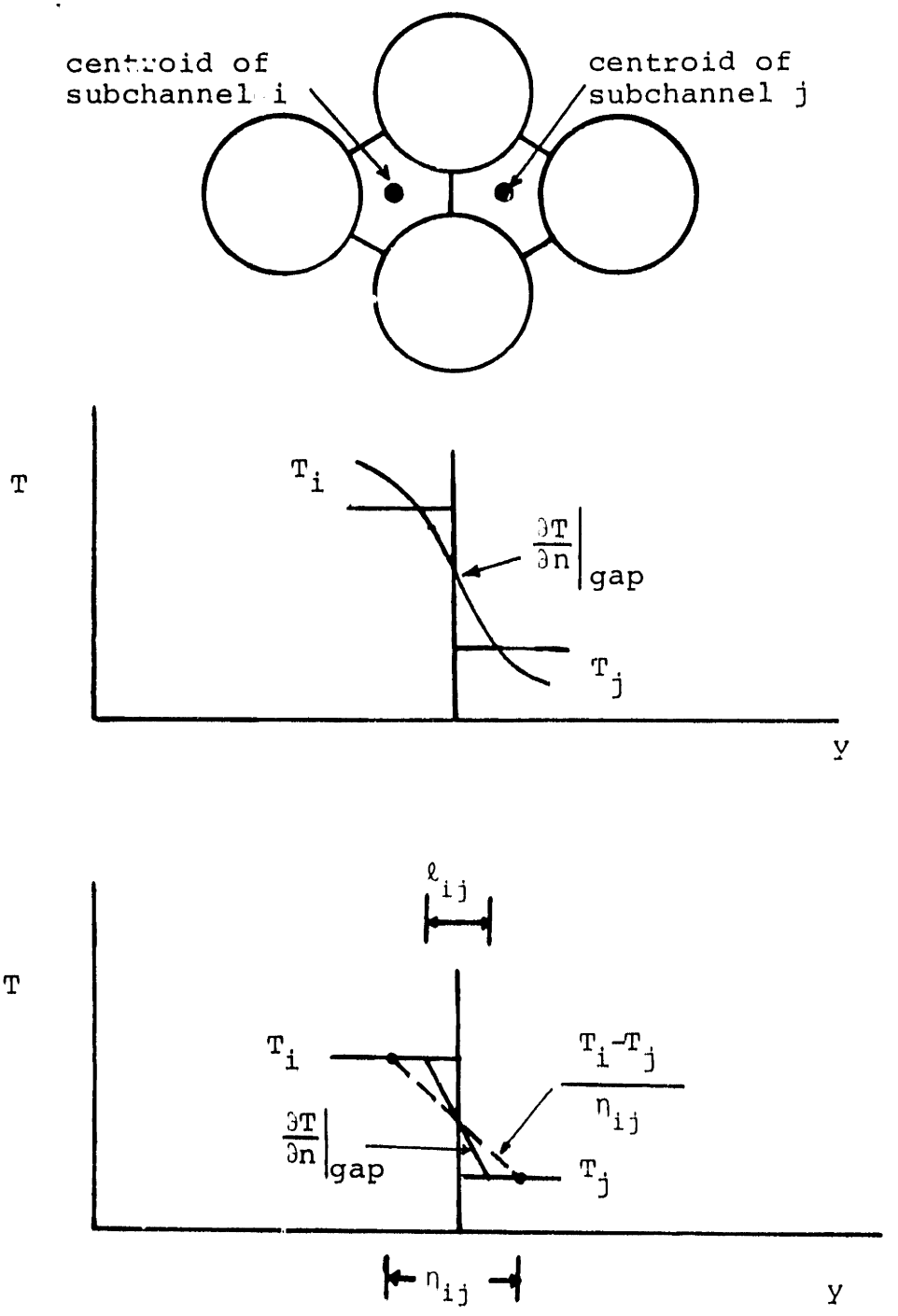

Figure 2.6 Difference between the Subchannel Centroid to Centroid Distance and Laminar Mixing Length

$$q''_{ij}\, s_{ij}\Big|_{\text{wire}} = W'^{W}_{ij}\,(h_i - h_j) \tag{2.13b}$$

where W'^{W}_{ij} represents the effective mass exchange rate due to the effects of wire sweeping. Combining equations (2.13a) and (2.13b) we obtain the total mixing effect as

$$q''_{ij}\, s_{ij}\Big|_{\text{mixing}} = W'^{T}_{ij}\,(h_i - h_j) \tag{2.14}$$

where $W'^{T}_{ij} \equiv W'_{ij} + W'^{W}_{ij}$;

Note that for gaps c and d, $W'^{W}_{ij} = 0$.

Using the eddy diffusivity concept, one can alternatively formulate this total mixing energy transfer as

$$q''_{ij}\, s_{ij}\Big|_{\text{mixing}} = \rho\, s_{ij}\, \varepsilon_{ij}\left(\frac{h_i - h_j}{\eta_{ij}}\right) \tag{2.15}$$

where

ε_{ij} = the effective eddy diffusivity defined by equation (2.15)

η_{ij} = subchannel centroid to centroid distance

ρ = coolant density at the gap

The physical meaning of ε_{ij} can be made clear by comparing equation (2.15) to equation (2.14), i.e.,

$$\rho\frac{\varepsilon_{ij}}{\eta_{ij}} = \frac{W'^{T}_{ij}}{s_{ij}} \tag{2.16}$$

Hence $\rho(\varepsilon_{ij}/\eta_{ij})$ is the mass exchange rate per unit area at the gap, and $(\varepsilon_{ij}/\eta_{ij})$ represents the transverse velocity for this exchange.

From equations (2.12) and (2.15), the total energy transfer between subchannel i and j is finally written as

$$W_{ij}^{*H}(h_i - h_j) = \left[\rho s_{ij}\kappa\left(-\frac{\alpha}{\eta_{ij}}\right) + \rho s_{ij}\left(\frac{\varepsilon_{ij}}{\eta_{ij}}\right)\right](h_i - h_j) \qquad (2.17)$$

Similar to the argument for the continuity equation, the transverse flow caused by the wire sweeping effect should be included in W_{ij} in the last term of equation (2.7) for the edge region. Hence for the edge region the last term of equation (2.7) becomes

$$\sum_{j=1}^{J} W_{ij}\{h^*\} + D_g\left[\rho_j V_{Tj} h_j - \rho_i V_{Ti} h_i\right]$$

The term $\sum_{j=1}^{J} W_{ij}\{h^*\}$ will be treated next. The enthalpy carried by cross flow, $\{h^*\}$, should be different for different gaps of a subchannel. However, in the final equations of our work, only the total cross flow rate $\sum_{j=1}^{J} W_{ij}$ will be calculated for each subchannel, and the energy transported by this total cross flow is approximated by multiplying it by a cross flow enthalpy H_i^* i.e.,

$$\sum_{j=1}^{J} W_{ij}\{h^*\} \approx H_i^* \sum_{j=1}^{J} W_{ij} \qquad (2.18)$$

The necessary value of H_i^* is a weighted average value determined from the average enthalpies of each subchannel and its adjacent subchannels.

The defining equation for H_i^* is

$$H_i^* \equiv \frac{\sum_{j=1}^{J} \left[\left| X_{ij} \right| (h_i + h_j) - X_{ij}(h_i - h_j) \right]}{2 \sum_{j=1}^{J} \left| X_{ij} \right|} \tag{2.19}$$

where $X_{ij} \equiv \Delta\dot{m}_i - \Delta\dot{m}_j$

$$\Delta\dot{m}_i \equiv \dot{m}_i \Big|_{z+\Delta z} - \dot{m}_i \Big|_z \qquad (\dot{m}_i \text{ is the mass flow rate of subchannel i})$$

The weighting factor X_{ij} represents the net gain in the rate of mass flow per unit cell between subchannel i and j along the length step Δz. With this definition the value of H_i^* is bounded by the least and greatest values of h for subchannel i and subchannels j.

Finally, the energy equation becomes

$$\frac{\Delta}{\Delta z}\left[\dot{m}_i\{h_i\}\right] = A_i Q_i - \sum_{j=i}^{J} \rho s_{ij} \left[\kappa\left(\frac{\alpha}{\eta_{ij}}\right) + \left(\frac{\varepsilon_{ij}}{\eta_{ij}}\right) \right](h_i - h_j)$$

$$- H_i^* \sum_{j=1}^{J} W_{ij} + D_g\left[\rho_j V_{Tj} h_j - \rho_i V_{Ti} h_i\right] \tag{2.20}$$

Note that for the interior region, there is no V_{Ti} or V_{Tj}, hence the last term is zero.

2.2.4 Treatment of Axial Momentum Equation

For the steady state condition, the axial momentum equation, equation (2.3), becomes

$$\frac{\Delta}{\Delta z}\left[\dot{m}_i\{v_i\}\right] = A_i\langle\rho_i\rangle g - A_i\frac{\Delta\{p\}}{\Delta z} - \sum_{j=1}^{J} W_{ij}^{*M}(v_i - v_j)$$

$$- \sum_{j=1}^{J} W_{ij}\{v^*\} - \frac{\{F_{iz}\}}{\Delta z} \qquad (2.21)$$

The effective momentum transfer rate per unit axial length $W_{ij}^{*M}(v_i - v_j)$ can be treated similarly to that in the energy equation. We further assume that the molecular contribution, i.e., viscous effect, is negligible compared to the effective mixing contribution. Therefore, this term can be written as

$$\text{Momentum transfer} = \rho\, s_{ij}\, \varepsilon_{ij}^{m}\left(\frac{v_i - v_j}{\eta_{ij}}\right) \qquad (2.22)$$

The effective eddy diffusivity for momentum transfer ε_{ij}^{m} is assumed to be the same as ε_{ij} for energy transfer since both the mass exchange rates for momentum and energy transfer come mainly from the same wire sweeping flow effects.

The term $W_{ij}\{v^*\}$ can also be treated similarly to that in the energy equation. The definition for the velocity transported by cross flow is exactly the same as equation (2.19) except that v is used in place of h. The same weighting factor X_{ij} is used. The momentum transported by cross flow is then

$$- V_i^* \sum_{j=1}^{J} W_{ij} + D_g\left[\rho_j V_{Tj} v_j - \rho_i V_{Ti} v_i\right]$$

The last term in equation (2.21) is the force per unit length on the fluid at x direction due to fluid-solid interaction. If τ is the average shear stress including both rod surface friction loss and wire drag loss, then the force per unit length is $\tau \cdot P_w$, where P_w is the

wetted perimeter for that subchannel. But τ is usually calculated by

$$\tau = \left(\frac{f_i}{4}\right)\left(\frac{\rho_i v_i^2}{2}\right) \tag{2.23}$$

where f_i is the subchannel friction faction, hence

$$\frac{\{F_{iz}\}}{\Delta z} = \tau \cdot P_w = f_i \frac{P_w}{4} \frac{\rho_i v_i^2}{2}$$

$$= A_i f_i \frac{P_w}{4A_i} \frac{s_i v_i^2}{2} = A_i \frac{f_i}{De_i} \frac{\rho_i v_i^2}{2} \tag{2.24}$$

where De_i = subchannel hydraulic equivalent diameter $\equiv P_w/4A_i$

Finally, the axial momentum equation becomes

$$\frac{\Delta}{\Delta z}\left[\dot{m}_i\{v_i\}\right] = -A_i\langle\rho_i\rangle g - A_i \frac{\Delta\{p\}}{\Delta z} - A_i \frac{f_i}{De_i} \frac{\rho_i v_i^2}{2}$$

$$- \sum_{j=1}^{J} s_{ij}\left(\frac{\varepsilon_{ij}}{\eta_{ij}}\right)(v_i - v_j) - V_i^* \sum_{j=1}^{J} W_{ij} + D_g\left[\rho_j V_{Tj} v_j - \rho_i V_{Ti} v_i\right] \tag{2.25}$$

2.3 Finite Different Equations for the ENERGY-IV Code

2.3.1 Finite Different Equations for the Forced Convection Condition

In the forced convection regime, the buoyancy-induced cross flow is negligible. The velocity distribution is assumed to be constant throughout the length of the bundle. Thus, only the energy equation needs to be solved to determine the temperature distribution.

In addition to the fixed velocity distribution assumption, the following assumptions are used to simplify the final energy equation for the forced convection condition.

1) constant density and thermal properties throughout the bundles.

By constant density and constant velocity, the cross flow $\sum_{j=1}^{J} W_{ij}$ is forced to be zero since the axial mass flow distribution does not change with position from the prescribed inlet distribution.

2) in calculating the energy transfer, the average enthalpy of each node is approximated by the enthalpy at the exit of the last axial step of that node. Hence no iteration will be needed for calculating the enthalpy at the exit of each step.

3) the transverse velocity is the same for all the subchannels in the edge region.

By the above assumptions, the energy equation, equation (2.20) will be written as finite different equations for different kinds of subchannels. In the following equations, the subscripts 1, 2, 3, refer to interior, edge and corner subchannels, respectively. The subscript ij refers to the quantity relating to subchannel types i and j.

Interior Subchannels

A control volume and noding scheme for an interior subchannel is illustrated in Figure 2.7a. In this case, equation (2.20) becomes

$$\rho A_1 v_1 \frac{\Delta h_1}{\Delta z} = A_1 Q_1 + \rho c \left[\kappa_{11}\left(\frac{\alpha}{\eta_{11}}\right) + \left(\frac{\varepsilon_{11}}{\eta_{11}}\right)\right](h_i + h_j - 2h_1)$$

$$+ \rho c \left[\kappa_{1x}\left(\frac{\alpha}{\eta_{1x}}\right) + \left(\frac{\varepsilon_{1x}}{\eta_{1x}}\right)\right](h_k - h_1) \qquad (2.26)$$

where c = gap between rods, i.e., s_{11} or s_{12} = P - D

x = 1 if the third adjacent subchannel is an interior subchannel

= 2 if the third adjacent subchannel is an edge subchannel

Dividing equation (2.26) by $\rho A_1 v_1$, we have

a. Interior Subchannel

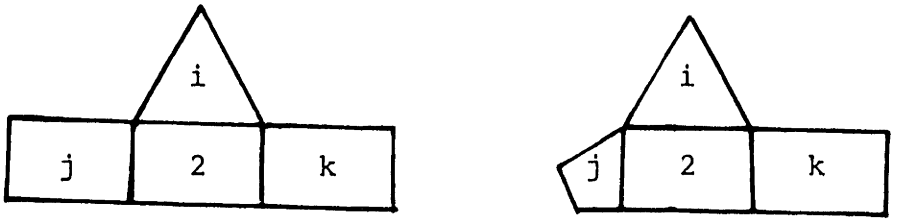

b. Edge Subchannel

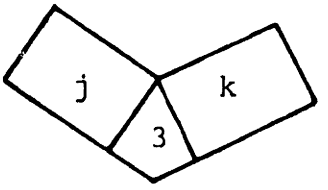

c. Corner Subchannel

Figure 2.7 Control Volumes and Noding Scheme for Different Kinds of Subchannels

$$\frac{\Delta h_1}{\Delta z} = \frac{Q_1}{\rho v_1} + \frac{c}{A_1}\left[\kappa_{11}\left(\frac{\alpha}{v_1 \eta_{11}}\right) + \left(\frac{\varepsilon_{11}}{v_1 \eta_{11}}\right)\right](h_i + h_j - 2h_1)$$

$$+ \frac{c}{A_1}\left[\kappa_{1x}\left(\frac{\alpha}{v_1 \eta_{1x}}\right) + \left(\frac{\varepsilon_{1x}}{v_1 \eta_{1x}}\right)\right](h_k - h_1) \qquad (2.27)$$

Edge Subchannel

A control volume and noding scheme for an edge subchannel is illustrated in Figure 2.7b. An edge subchannel has three neighbors. One is always an interior subchannel, and the other two may be either edge or corner subchannels. In this case, after dividing $\rho A_2 v_2$ equation (2.20) becomes

$$\frac{\Delta h_2}{\Delta z} = \frac{Q_2}{\rho v_2} + \frac{c}{A_2}\left[\kappa_{12}\left(\frac{\alpha}{v_2 \eta_{12}}\right) + \left(\frac{\varepsilon_{12}}{v_2 \eta_{12}}\right)\right](h_i - h_2)$$

$$+ \frac{D_g}{A_2}\left[\kappa_{2x}\left(\frac{\alpha}{v_2 \eta_{2x}}\right) + \left(\frac{\varepsilon_{2x}}{v_2 \eta_{2x}}\right)\right](h_j - h_2)$$

$$+ \frac{D_g}{A_2}\left[\kappa_{2y}\left(\frac{\alpha}{v_2 \eta_{2y}}\right) + \left(\frac{\varepsilon_{2x}}{v_2 \eta_{2y}}\right)\right](h_k - h_2)$$

$$+ \frac{D_g}{A_2}\left(\frac{V_T}{v_2}\right)(h_j - h_2) \qquad (2.28)$$

where

D_g = gap between rod and wall

x (or y) = 2 if node j (or k) is an edge subchannel

= 3 if node j (or k) is a corner subchannel

Corner Subchannel

A control volume and noding scheme for a corner subchannel is illustrated in Figure 2.7c. A corner subchannel is always adjacent to two edge subchannels. In this case, after dividing by $\rho A_3 v_3$, equation (2.20) becomes

$$\frac{\Delta h_3}{\Delta z} = \frac{Q_3}{\rho v_3} + \frac{D_g}{A_3}\left[\kappa_{23}\left(\frac{\alpha}{v_3 \eta_{23}}\right) + \left(\frac{\varepsilon_{23}}{v_3 \eta_{23}}\right)\right](h_j + h_k - h_3)$$

$$+ \frac{D_g}{A_3}\left(\frac{V_T}{v_3}\right)(h_j - h_3) \qquad (2.29)$$

In these different equations, equations (2.27), (2.28), and (2.29), the following nondimensional parameters need to be inputted:

a) Flow split parameters X_1, X_2, X_3 for calculating v_1, v_2, and v_3 at a given bundle flow rate,

b) Conduction shape factors, κ_{11}, κ_{12}, κ_{22}, κ_{23}, for interior to interior subchannel, interior to edge subchannel, edge to edge subchannel and edge to corner subchannel.

c) Mixing parameters, related to eddy diffusivity,

$$\left(\frac{\varepsilon_{11}}{v_1 \eta_{11}}\right),\ \left(\frac{\varepsilon_{12}}{v_1 \eta_{12}}\right),\ \left(\frac{\varepsilon_{12}}{v_2 \eta_{12}}\right),\ \left(\frac{\varepsilon_{22}}{v_2 \eta_{22}}\right),\ \left(\frac{\varepsilon_{23}}{v_2 \eta_{23}}\right),\ \left(\frac{\varepsilon_{23}}{v_3 \eta_{23}}\right)$$

related to transverse velocity,

$$\left(\frac{V_T}{v_2}\right),\ \left(\frac{V_T}{v_3}\right)$$

Note that in our two region approach, ε_{11}, ε_{12} and V_T are related to the wire sweeping effects, while ε_{22} and ε_{23} are only related to the conventional turbulent interchange between subchannels in the edge region.

The forms of above mixing parameters suggest defining the following dimensionless parameters for use in these equations:

Dimensionless effective eddy Diffusivity (DEED), $\varepsilon^*_{1\eta}$ for the interior region

$$\varepsilon^*_{1\eta} \equiv \frac{\varepsilon_{11}}{v_1 \eta_{11}} \tag{2.30}$$

Edge Transverse Velocity Ratio (ETVR), C_{1L}, for the edge region

$$C_{1L} \equiv \frac{V_T}{v_2} \tag{2.31}$$

The physical meaning of $\varepsilon^*_{1\eta}$ is easy to understand if one remembers that $(\varepsilon_{ij}/\eta_{ij})$ represents the transverse velocity at the interior gap from equation (2.16). Therefore,

$$\varepsilon^*_{1\eta} = \frac{W'^T_{ij}/s_{ij}}{\rho v_1} = \frac{\text{Transverse mass flux}}{\text{Axial mass flux}} \tag{2.32}$$

From this physical meaning, $\varepsilon^*_{1\eta}$ actually represents a transverse mass exchange rate. Note that if one enlarges the mesh size, the mass exchange rate per unit area at the mesh boundary should not be changed and no η_{ij} effect should show in the heat transfer by the mixing effect. This is one major merit of using $\varepsilon^*_{1\eta}$ which uses η_{ij} as the characteristic length in its definition, hence, η_{ij} correctly does not appear in the effective mixing term in the final energy equation.

Similar to the definition for DEED, a dimensionless eddy diffusivity, $\varepsilon^*_{2\eta}$ can also be defined for the edge region as

$$\varepsilon^*_{2\eta} \equiv \frac{\varepsilon_{22}}{v_2 \eta_{22}}$$

To simplify those mixing parameters, the following two assumptions will be adopted,

1) The transverse velocity for the effective mixing between interior and edge subchannels $\varepsilon_{12}/\eta_{12}$ is the same as that between interior and interior subchannels, $\varepsilon_{11}/\eta_{11}$.

2) Similarly the transverse velocity between edge and corner is the same as between edge subchannels, $\varepsilon_{23}/\eta_{23} \approx \varepsilon_{22}/\eta_{22}$

By the above definitions and assumptions, these mixing parameters become

$$\frac{\varepsilon_{11}}{v_1\eta_{11}} = \varepsilon^*_{1\eta}, \quad \frac{\varepsilon_{12}}{v_1\eta_{12}} = \varepsilon^*_{1\eta}, \quad \frac{\varepsilon_{12}}{v_2\eta_{12}} = \left(\frac{v_1}{v_2}\right)\left(\frac{\varepsilon_{12}}{v_1\eta_{12}}\right) = \left(\frac{X_1}{X_2}\right)\varepsilon^*_{1\eta},$$

$$\frac{\varepsilon_{22}}{v_2\eta_{22}} = \varepsilon^*_{2\eta}, \quad \frac{\varepsilon_{23}}{v_2\eta_{23}} = \varepsilon^*_{2\eta}, \quad \frac{\varepsilon_{23}}{v_3\eta_{23}} = \left(\frac{v_2}{v_3}\right)\left(\frac{\varepsilon_{23}}{v_2\eta_{23}}\right) = \left(\frac{X_2}{X_3}\right)\varepsilon^*_{2\eta},$$

$$\frac{V_T}{v_2} = C_{1L}, \quad \frac{V_T}{v_3} = \left(\frac{v_2}{v_3}\right)\left(\frac{V_T}{v_2}\right) = \left(\frac{X_2}{X_3}\right)C_{1L}$$

The finite different equations for the forced convection condition then become,

Interior subchannel

$$\frac{\Delta h_1}{\Delta z} = \frac{Q_1}{\rho v_1} + \frac{c}{A_1}\left[\kappa_{11}\left(\frac{\alpha}{v_1\eta_{11}}\right) + \varepsilon^*_{1\eta}\right](h_i + h_j - 2h_1)$$

$$+ \frac{c}{A_1}\left[\kappa_{1x}\left(\frac{\alpha}{v_1\eta_{1x}}\right) + \varepsilon^*_{1\eta}\right](h_k - h_1) \qquad (2.34)$$

Edge subchannel

$$\frac{\Delta h_2}{\Delta z} = \frac{Q_2}{\rho v_2} + \frac{c}{A_2}\left[\kappa_{12}\left(\frac{\alpha}{v_2 \eta_{12}}\right) + \left(\frac{X_1}{X_2}\right)\varepsilon^*_{1\eta}\right](h_i - h_2)$$

$$+ \frac{D_g}{A_2}\left\{\left[\kappa_{2x}\left(\frac{\alpha}{v_2 \eta_{2x}}\right) + \varepsilon^*_{2\eta}\right](h_j - h_2) + \left[\kappa_{2y}\left(\frac{\alpha}{v_2 \eta_{2y}}\right) + \varepsilon^*_{2\eta}\right](h_k - h_2)\right\}$$

$$+ \frac{D_g}{A_2} C_{1L}(h_j - h_2) \qquad (2.35)$$

Corner Subchannel

$$\frac{\Delta h_3}{\Delta z} = \frac{Q_3}{\rho v_3} + \frac{D_g}{A_3}\left[\kappa_{23}\left(\frac{\alpha}{v_3 \eta_{23}}\right) + \left(\frac{X_2}{X_3}\right)\varepsilon^*_{2\eta}\right](h_j + h_k - 2h_3)$$

$$+ \frac{D_g}{A_3}\left(\frac{X_2}{X_3}\right) C_{1L}(h_j - h_3) \qquad (2.36)$$

The empirical parameters which need to be determined are then:

- Flow split parameters: X_1, X_2, X_3
- Conduction shape factor: κ_{11}, κ_{12}, κ_{22}, κ_{23}
- Mixing parameters: $\varepsilon^*_{1\eta}$, $\varepsilon^*_{2\eta}$, C_{1L}

2.3.2 Finite Different Equations for the Mixed Convection Condition

At low flow rate, the net crossflow driven from the hot region to the cold region due to the buoyancy effect may be significant. This crossflow not only carries cold fluid to the hot region but also increases (decreases) the flow rate in the hot (cold) region. Therefore, the temperature distribution in the mixed convection

condition will be flatter than that in the forced convection condition in which this crossflow is negligible. Criteria for determining when the flow is in mixed convection have been proposed by Engel et al. (1982) and Symolon (1982).

To model this crossflow, the continuity, energy and momentum equations, equations (2.6), (2.20) and (2.25) must be simultaneously solved. However, the continuity equation is only used to obtain the net cross flow rate $\sum_{j=1}^{J} W_{ij}$ in terms of other quantities for each subchannel which are then utilized in the energy and momentum equations. These two conservation equations are coupled with one total mass balance equation

$$\sum_{i=1}^{I} \Delta\dot{m}_i = 0 \tag{2.37}$$

where I = total number of subchannels, and solved numerically.

From equation (2.6),

$$\Delta z \sum_{j=1}^{J} W_{ij} = -\Delta\dot{m}_i + D_g\left[\rho_j V_{Tj} - \rho_i V_{Ti}\right] \tag{2.38}$$

where for the interior subchannels the term in [ ] is zero. Substituting equation (2.38) and the following identities,

$$\Delta\dot{m}_i = (\rho_i v_i A_i)_{z+\Delta z} - (\rho_i v_i A_i)_z \tag{2.39}$$

$$\Delta\left[\dot{m}_i\{h_i\}\right] = (\rho_i v_i A_i h_i)_{z+\Delta z} - (\rho_i v_i A_i h_i)_z \tag{2.40}$$

where $z+\Delta z$ and z are the axial positions at inlet and exit of each node, into equation (2.20), the energy equation becomes,

$$\left[(\rho_i v_i A_i h_i)_{z+\Delta z} - (\rho_i v_i A_i h_i)_z\right] - H_i^* \left[(\rho_i v_i A_i)_{z+\Delta z} - (\rho_i v_i A_i)_z\right] =$$

$$A_i \Delta z Q_i - \Delta z \sum_{j=1}^{J} \rho s_{ij} \left[\kappa\left(\frac{\alpha}{\eta_{ij}}\right) + \left(\frac{\varepsilon_{ij}}{\eta_{ij}}\right)\right](h_i - h_j) +$$

$$D_g \Delta z \left[\rho_j V_{Tj}(h_j - H_i^*) - \rho_i V_{Ti}(h_i - H_i^*)\right] \tag{2.41}$$

Similarly, substituting equations (2.38), (2.39) and the following identities

$$\Delta\left[m_i\{v_i\}\right] = (\rho_i A_i v_i^2)_{z+\Delta z} - (\rho_i A_i v_i^2)_z \tag{2.42}$$

$$\Delta\{P\} = P_{z+\Delta z} - P_z \equiv \Delta P \tag{2.43}$$

into equation (2.25), the momentum equation becomes,

$$\left[(\rho_i A_i v_i^2)_{z+\Delta z} - (\rho_i A_i v_i^2)_z\right] - V_i^* \left[(\rho_i v_i A_i)_{z+\Delta z} - (\rho_i v_i A_i)_z\right] =$$

$$- A_i \Delta z \rho_i g - A_i \Delta z \frac{f_i}{De_i} \frac{\rho_i v_i^2}{2} - A_i \Delta P - \Delta z \sum_{j=1}^{J} \rho s_{ij} \left(\frac{\varepsilon_{ij}}{\eta_{ij}}\right)(v_i - v_j)$$

$$+ Dg \Delta z \left[\rho_j V_{Tj}(v_j - V_i^*) - \rho_i V_{Ti}(v_i - V_i^*)\right] \tag{2.44}$$

Now the following definitions and approximations are introduced

$$\Delta\rho = \rho_{z+\Delta z} - \rho_z, \text{ i.e., } \rho_{z+\Delta z} = \rho_z + \Delta\rho \tag{2.45a}$$

$$\Delta v = v_{z+\Delta z} - v_z, \text{ i.e., } v_{z+\Delta z} = v_z + \Delta v \tag{2.45b}$$

$$\Delta h = h_{z+\Delta z} - h_z, \text{ i.e., } h_{z+\Delta z} = h_z + \Delta h \tag{2.45c}$$

and

$$\Delta h \simeq R\Delta\rho, \text{ where } R \equiv \left(\frac{\partial h}{\partial \rho}\right)_p \text{ (at constant pressure)} \tag{2.45d}$$

$$\rho_i = \rho_{z+\Delta z/2} \simeq \rho_{iz} + \frac{\Delta\rho_i}{2} \tag{2.46a}$$

$$v_i = v_{z+\Delta z/2} \simeq v_{iz} + \frac{\Delta v_i}{2} \tag{2.46b}$$

The terms in the left hand side of equations (2.41) and (2.44) are expanded using equations (2.45a, b, c, d). The parameters ρ_i and v_i in the first two terms of the right hand side of equation (2.44) are substituted by equations (2.46a, b). After these arrangements and dividing by A_i , equations (2.41) and (2.44) become,

Energy equation

$$S_i \Delta\rho_i + T_i \Delta v_i = Q_i \Delta z + EEX_i \tag{2.47}$$

where

$$S_i = (v_{iz} + \Delta v_i)\left[R_i(\rho_{iz} + \Delta\rho_i) + h_{iz} - H_i^*\right] \tag{2.47a}$$

$$T_i = \rho_{iz}(h_{iz} - H_i^*) \tag{2.47b}$$

$$EEX_i = -\frac{\Delta z}{A_i} \sum_{j=1}^{J} \rho s_{ij}\left[\kappa\left(\frac{\alpha}{\eta_{ij}}\right) + \left(\frac{\varepsilon_{ij}}{\eta_{ij}}\right)\right](h_i - h_j)$$

$$+ \frac{Dg\ \Delta z}{A_i}\left[\rho_j V_{Tj}(h_j - H_i^*) - \rho_i V_{Ti}(h_i - H_i^*)\right] \tag{2.47c}$$

and Momentum Equation

$$E_i \Delta\rho_i + F_i \Delta v_i + \Delta P = G_i + MEX_i \tag{2.48}$$

where

$$E_i = (v_{iz} + \Delta v_i)(v_{iz} + \Delta v_i - V_i^*) + \frac{f_i \Delta z}{16De_i}(2v_{iz} + \Delta v_i)^2 + \frac{g\Delta z}{2} \tag{2.48a}$$

$$F_i = \rho_{iz}\left[\left(2 + \frac{f_i \Delta z}{2De_i}\right) v_{iz} + \left(1 + \frac{f_i \Delta z}{8De_i}\right) \Delta v_i - V_i^*\right] \tag{2.48b}$$

$$G_i = -\rho_{iz}\left(g\Delta z + \frac{f_i \Delta z}{2De_i} v_{iz}^2\right)$$

$$MEX_i = -\frac{\Delta z}{A_i} \sum_{j=1}^{J} \rho s_{ij} \left(\frac{\varepsilon_{ij}}{\eta_{ij}}\right)(v_i - v_j)$$

$$+ \frac{Dg\Delta z}{A_i}\left[\rho_j V_{Tj}(v_j - V_i^*) - \rho_i V_{Ti}(v_i - V_i^*)\right] \qquad (2.48d)$$

The total mass balance equation, equation (2.37) can be written in a similar form,

$$\sum_{i=1}^{I} A_i (v_{iz} + \Delta v_i)\Delta\rho_i + \sum_{i=1}^{I} A_i \rho_{iz} \Delta v_i = 0 \qquad (2.49)$$

Equations (2.47) and (2.48) when written for each subchannel and equation (2.49) form a system of 2I + 1 equations (I being the number of subchannels) in the 2I + 1 unknown $\Delta\rho_i$, Δv_i and Δp.

We now consider the empirical parameters for the mixed convection condition. In addition to the inlet flow distribution which is provided as three constant velocitites, v_1, v_2, v_2 as in the forced convection condition, the subchannel friction factor f_i, interior transverse mass flux $\rho(\varepsilon_{ij}/\eta_{ij})$ and edge transverse velocity V_{Ti} are the parameters required in equations (2.47) and (2.48).

From the definition of $\varepsilon^*_{l\eta}$, equation (2.32), $\rho(\varepsilon_{ij}/\eta_{ij})$ can be written as

$$\rho \frac{\varepsilon_{ij}}{\eta_{ij}} = \rho v \varepsilon^*_{l\eta} \qquad (2.50)$$

Since now ρ and v are not same values between subchannel i and j, average values of these two subchannel should be used to evaluate this parameter. As for the edge transverse velocity, V_{Ti}, it can be

calculated by

$$V_{Ti} = v_i C_{1L} \tag{2.51}$$

The parameters $\varepsilon^*_{1\eta}$ and C_{1L} are assumed to be constant values for the subchannels in the interior regions and the subchannels in the edge region at one operation condition, respectively. These parameters are reduced from the forced convection data. The validation of their application in the mixed convection condition will be discussed in chapter 8.

2.4 Empirical Parameters for the ENERGY Code

In summary, the following empirical parameters are required for our model,

a) Flow slip parameters: X_1, X_2, X_3

b) Subchannel friction factors: f_1, f_2, f_3

c) Dimensionless Effective Eddy Diffusivity (DEED): $\varepsilon^*_{1\eta}$

d) Dimensionless eddy diffusivity for the edge region : $\varepsilon^*_{2\eta}$

e) Edge Transverse Velocity Ratio (ETVR): C_{1L}

f) Conduction shape factor: κ_{11}, κ_{12}, κ_{22}, κ_{23}

These parameters are functions of bundle geometry and operation conditions. The major work of this study will be developing models and correlations for these parameters. After implementing these correlations into ENERGY code, recent temperature data will be used to validate our subchannel analysis method.

CHAPTER 3

HYDRODYNAMIC EXPERIMENTS IN A 37-PIN WIRE-WRAPPED ROD BUNDLE

3.1 Introduction

Experimental studies with wire-wrapped bundles using either tracers or heated pins have been conducted by many investigators to understand the mixing phenomena in these bundles. Most of these experiments were designed to simulate either the fuel assembly with pitch to diameter ratio (P/D) near 1.25 and wire lead length to diameter ratio (H/D) near 48.0 or the blanket assembly with P/D near 1.07 and H/D near 8.0. Because it is not a typical U.S. reactor design, a bundle with P/D between these two extremes, say near 1.15, has not been investigated at M.I.T. before. To fill this gap in the data base, a 37-pin bundle with P/D equal to 1.154 and H/D equal to 13.4 was fabricated and studied.

Flow split, pressure drop and mixing experiments were performed in this mock-up to obtain flow split parameters, friction factor and mixing parameters for this geometry. The isokinetic extraction method, pitot-static probe pressure measurement method and salt tracer injection method were used for these experiments. The results of flow split experiments can be used with the data from the other two experiments to reduce the subchannel friction factors and mixing parameters. Figure 3.1 shows the relationship among these experiments.

The flow split and bundle friction factor data will be used together with other available data to calibrate the empirical constants

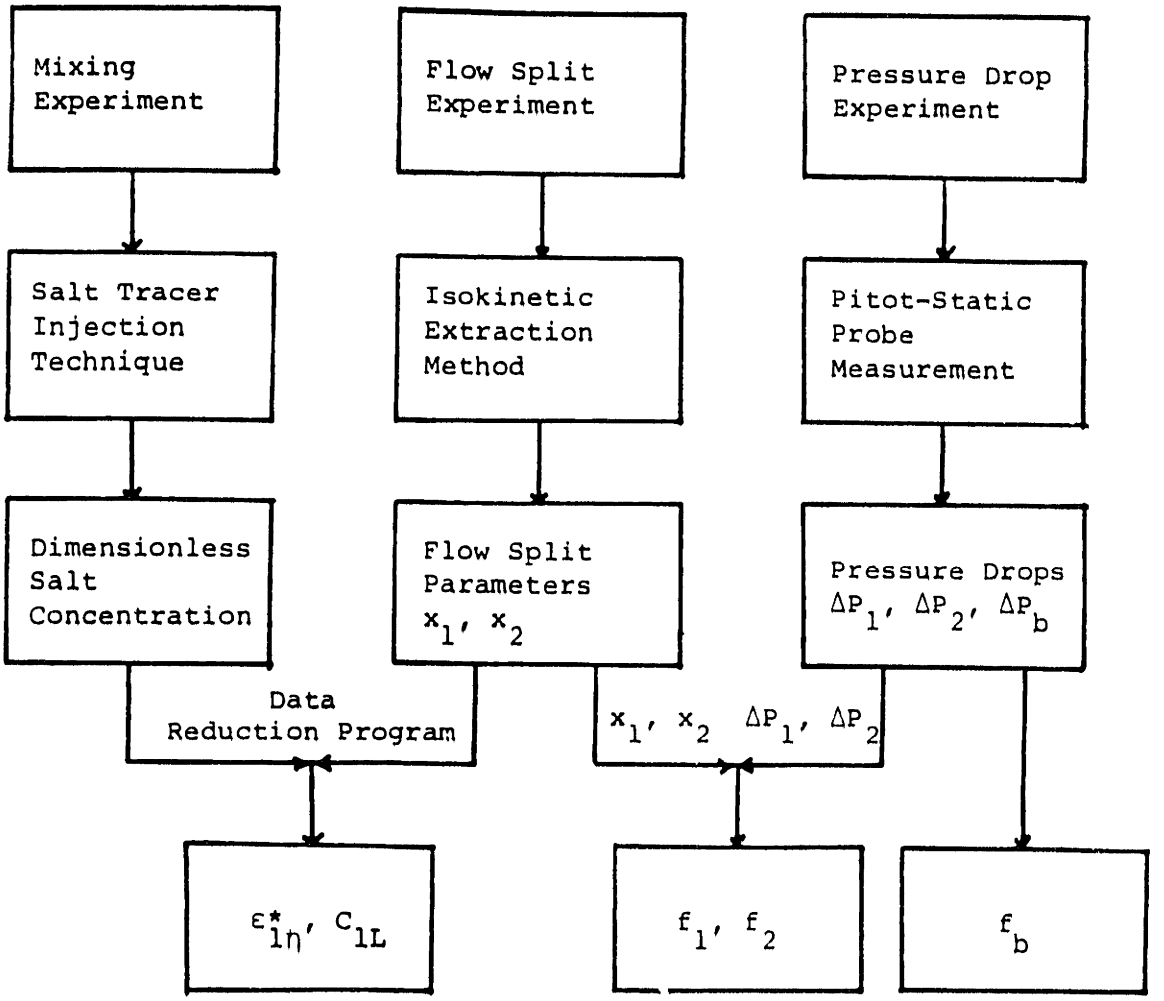

Figure 3.1 Relations Among Flow Split Experiment, Mixing Experiment and Pressure Drop Experiment

in subchannel friction factor correlations which will be developed in the next chapter. The necessary values for flow split used in reducing the mixing parameters, $\varepsilon^*_{l\eta}$ and C_{lL}, are calculated from these correlations. Hence the data reduction for the mixing experiment will be carried out (in chapter 5) after the subchannel friction factor correlations are obtained.

Previous experiments of a similar geometry (P/D = 1.15, H/D = 21.0) have been performed by Chiu (1979) and Burns (1980), but their data were flawed due to the degraded dimensional control in the bundle housings which were salvaged from previous blanket geometry tests. In this attempt a new, well-controlled housing is used. No new experimental methods were introduced except for some minor modifications which will be elaborated in the next section.

3.2 Test Section

3.2.1 Test Section Design and Fabrication

The design and fabrication of this 37-pin bundle test section is very similar to the previous one [Chiu(1979)], except for the housing, rod diameter and wire diameter. The dimensions of the previous aluminum and plexiglass housing were found to be non-uniform. Since it was too expensive to build new housing, the new 37-pin assembly was designed to fit an extruded, hexagonal housing originally used for a 217-pin bundle. A non-standard rod diameter of 0.592 inch was selected which called for modifications to the collars and clamps originally machined in accordance with the procedure documented by Chiu (1979a). The wire-wrapping device was also modified to wrap with an

8-inch lead length.

The hexagonal mounting device used for the previous 217-pin experiment conducted by Symolon (1981) was inverted and drilled to accomodate seven 1/4-inch rods. These seven rods were aligned horizontally to secure the 37 rods of the bundle vertically. The rods were assembled onto the hexagonal mounting device and then the whole assembly was inserted into the housing until the ends of the rods were flush with the housing exit plane. The hexaganol mounting was then fastened securely to the housing with six screws. Figure 3.2 illustrates the relative positions of housing, hexagonal mounting device and rods and some design parameters.

Two hollow rods, one in the center position and the other adjacent to the wall, were installed in this bundle. These are the instrumentation rods used for inserting the injector to measure the pressure drop in the pressure drop experiment and to inject the saline solution in the mixing experiment. Two stainless steel plugs were fabricated to plug the exit end of these two hollow rods when they were not in use.

The average flat to flat distance of the housing, D_F was 4.336". With 0.592" rod diameter and 0.089" wire diameter, the tolerance was calculated to be 0.027". After the assembly was mounted in place, the distances between each adjacent pair of rods and between the edge rods and duct at the exit plane were measured. The average gaps between rods and between rod and duct were 0.0913" and 0.0964" respectively. The looseness factor was

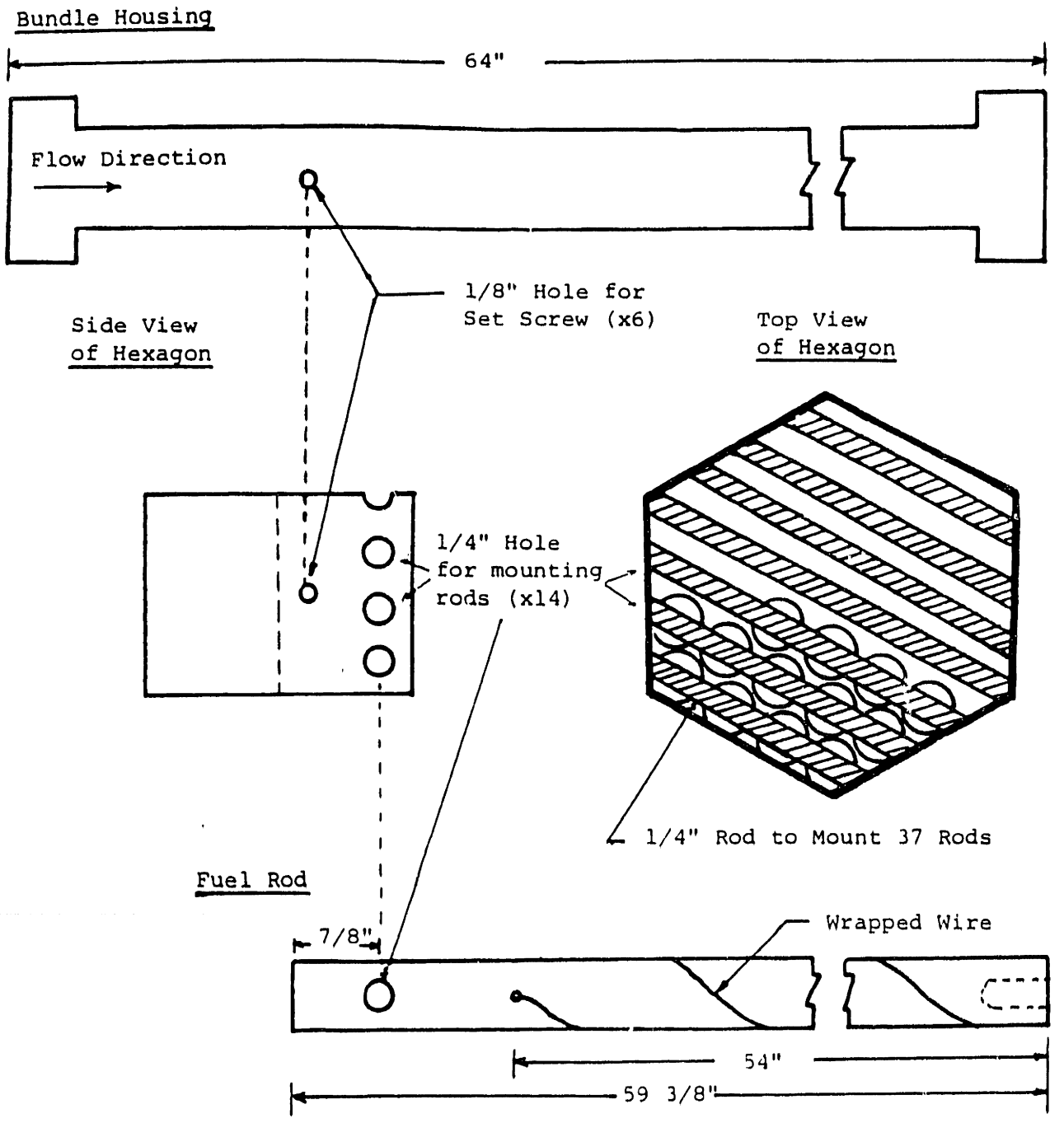

Figure 3.2 37-Pin Bundle Design Configuration

$$F \equiv (P-D-D_w) \times \sqrt{3} \times N_{RING}/T_{ff} = 0.447$$

where

$$T_{ff} \equiv D_F - (\sqrt{3}\, N_{RING} + 1)\,(D+D_w)$$

$$N_{RING} \equiv \{[3 + (12N_R - 3)^{1/2}]/6\} - 1$$

The design value of the wire lead length was 8". However, after the rod was wrapped with wire, a lead length of a little less than 8" was shown by the wire position at the exit plane. The correct value was calculated to be 7.935". This may be attributed to the precision of the wire-wrapping device.

The bundle geometry and some important as-built geometrical parameters at the exit plane are shown in Figure 3.3 and some subchannel based geometrical parameters are tabulated in Table 3.1.

3.2.2 Test Loop

The test loop of this experiment was exactly the same as the one used before. Figure 3.4 shows this loop. For flow rates higher than 56 GPM, flowmeter M3 was used. Otherwise, flowmeters M1 and M2 were used.

Flowmeter M3 (40-300 GPM) was calibrated using the technique discussed in Appendix A of [Chiu(1979)]. However, the calibrated values were found to be in error at the low flow rates (from 40 to 70 GPM). The readings in M1 (0-14 GPM) and M2 (0-37 GPM) were accurate. Since the same pressure drop implies the same flow rate, the readings of M1 plus M2 can be used to calibrated M3 at low flow rates from 40 to 56 GPM with the help of pressure drop data. The new calibration curve of M3 is shown in Figure 3.5.

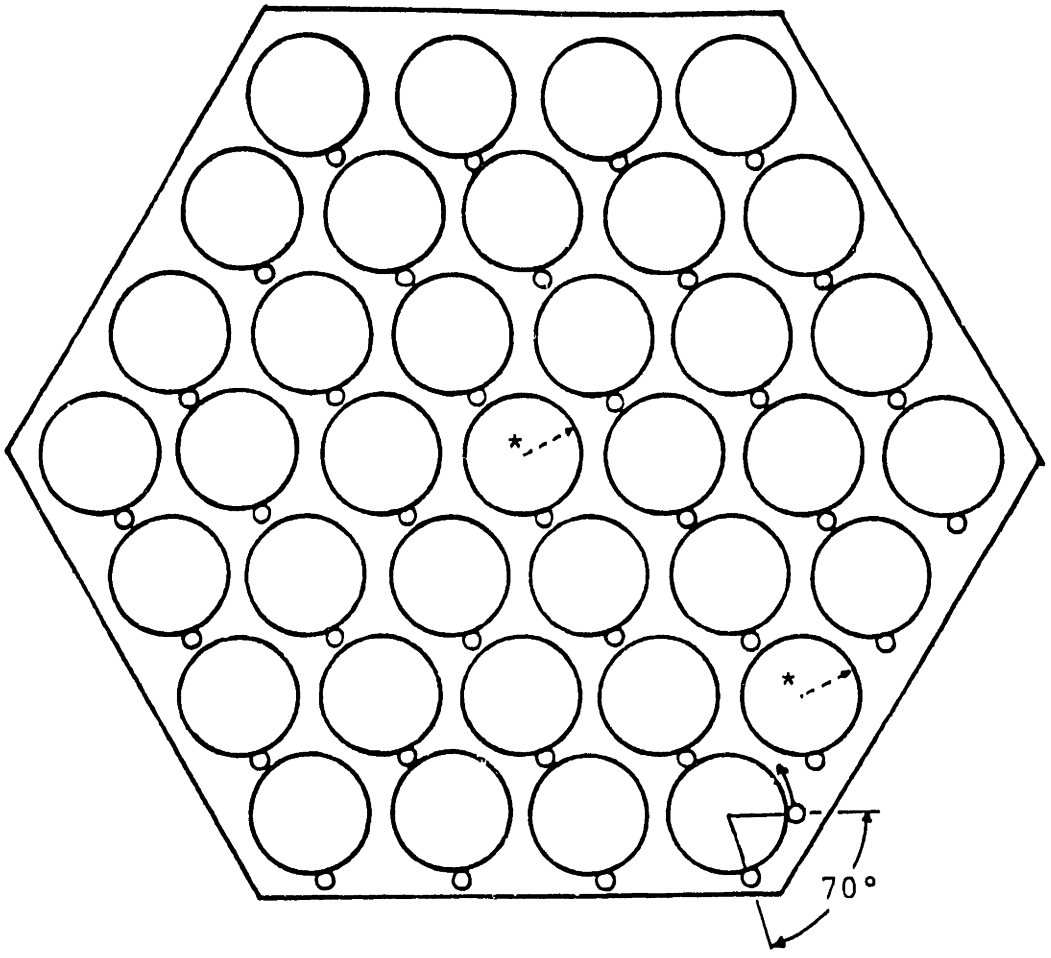

wire start position

* instrumentation rod

---> 30° hole position

37-pin P/D = 1.154 H/D = 13.4 Design Parameters	
D = 0.592"	P = 0.683"
D_w = 0.089"	H = 7.935"
D_F = 4.336"	F = 0.447
D_g = 0.097"	θ = 16.8°
T_{ff} = 0.027"	S = 0.7675

Figure 3.3 As built Geometry at Exit Plane

Table 3.1

Subchannel Geometric Parameters

	Subchannel Numbers	Flow Area (in^2)	Equiv. Dia. (in)
Bundle average		5.856	0.248
Interior Subchannel Average	54	0.0613	0.228
With wire inside		0.0597	
Without wire inside		0.0630	
Edge Subchannel Average	18	0.1273	0.290
With wire inside		0.1257	
Without wire inside		0.1289	
Corner Subchannel	6	0.0420	0.207

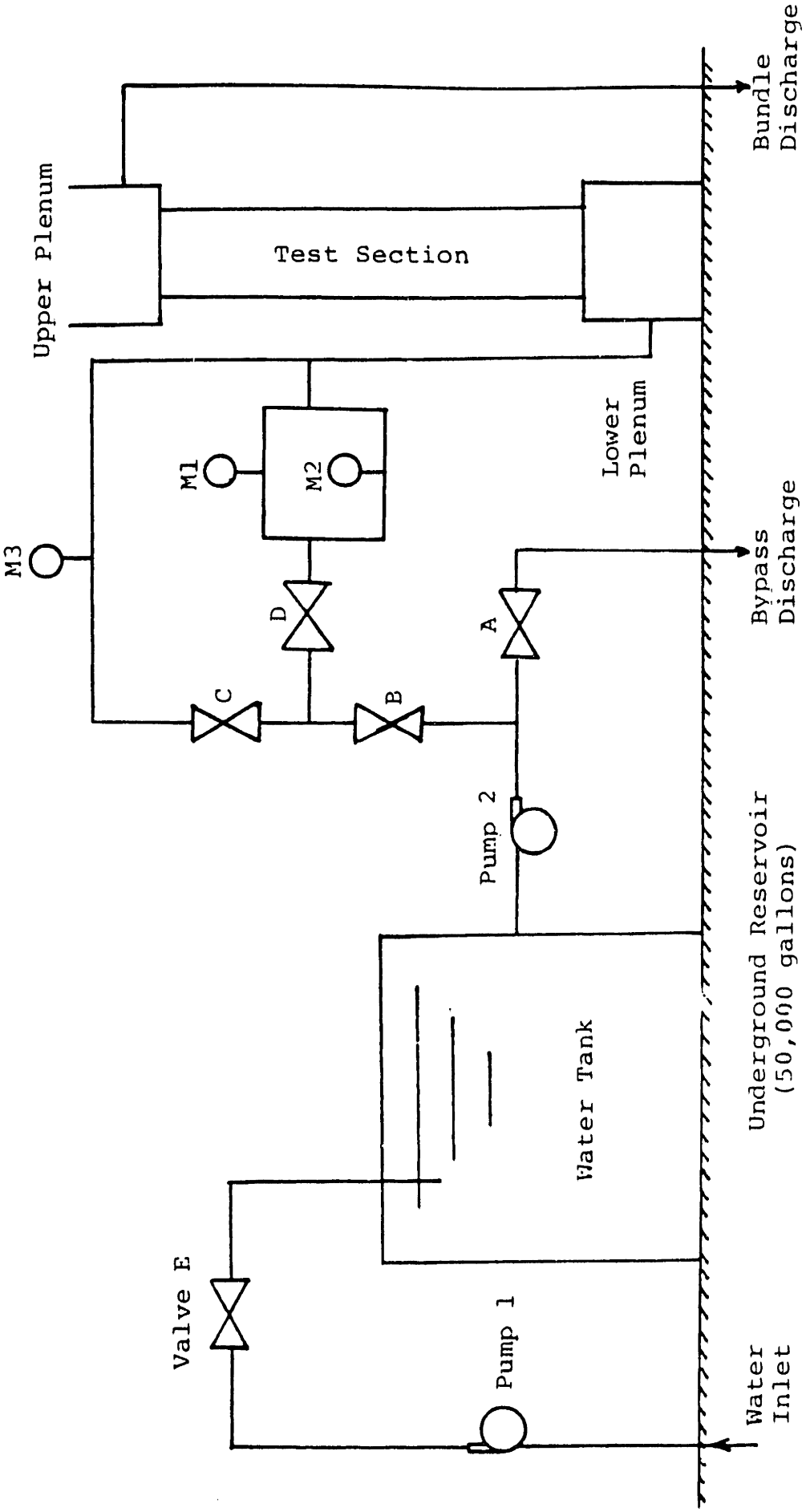

Figure 3.4 Layout of the Test Loop

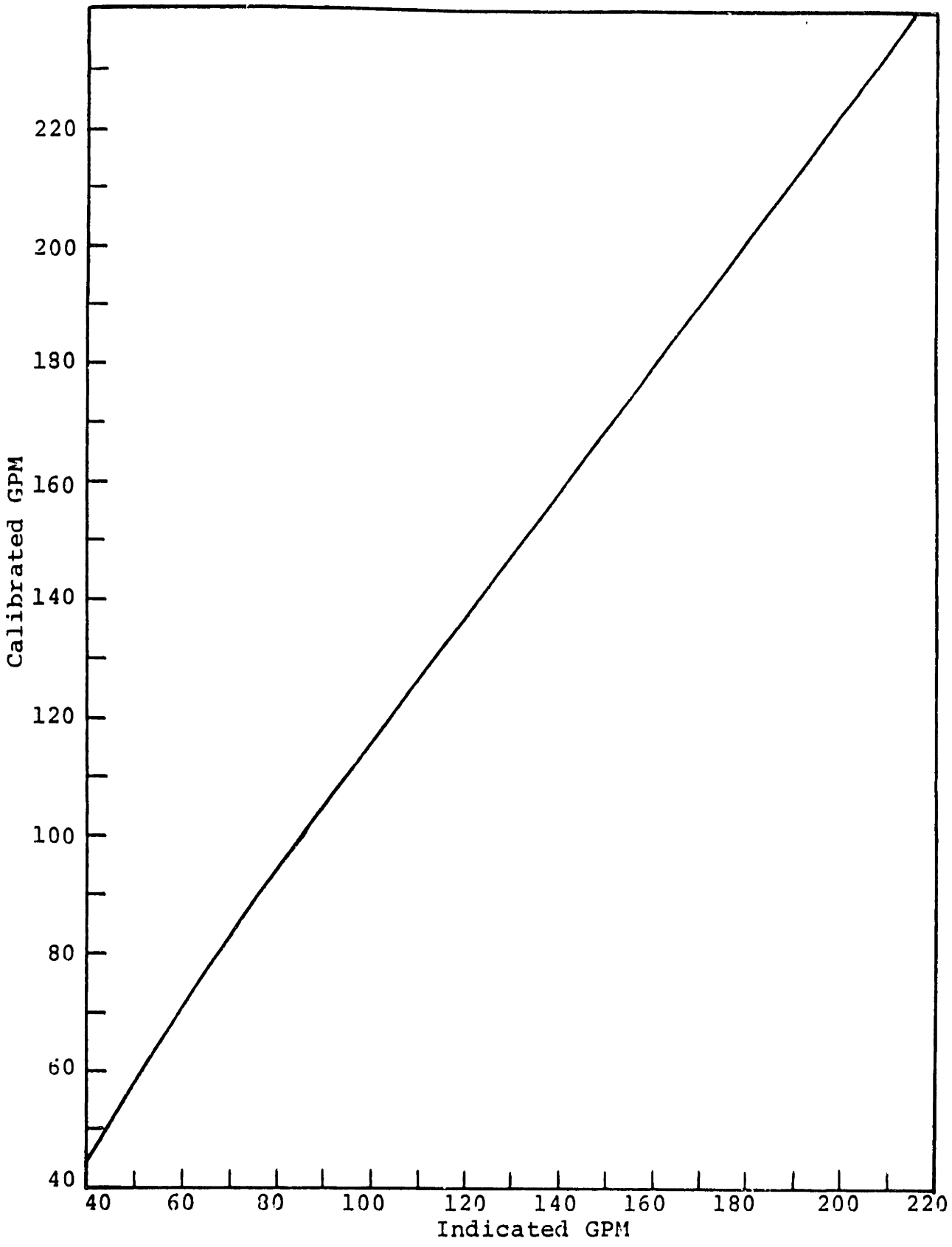

Figure 3.5 Calibration Curve for Rotometer M3

3.3 Experimental Methods

3.3.1 Flow Split Experiment

The flow extraction by the isokinetic condition measurement method discussed by Hawley et al. (1980a) was used in the flow split experiment. No attempt was made to measure the corner subchannel flow rates because it was not practical to fabricate a small collector to collect the individual corner subchannel flows. The flow velocity of the corner subchannel was assumed to be the same as that of the edge subchannel.

The flat to flat measuring technique [Chiu(1979)] was used in collecting interior subchannel flow to reduce experimental time. Therefore, instead of the entire 54, only the 18 interior subchannels which are numbered in Figure 3.6 were measured. Also shown in this figure are the three rings of measured interior subchannels and the wire position in two different types of interior subchannels. The effect of the wire was eliminated when the flow rates of all 6 subchannels in each ring were measured and averaged. Therefore, an average interior flow rate over one lead length was obtained by averaging 18 interior flow rates. A similar situation was afforded by the 18 edge subchannels except that there is only one ring, and the wire positions were the same in the three subchannels of each face. For each run, i.e., at each bundle flow rate, these 36 subchannel flow rates were collected to provide a data set at a given flow condition.

The isokinetic method was not applicable at low bundle flow rates because the siphon head was not maintainable while attempting to reach

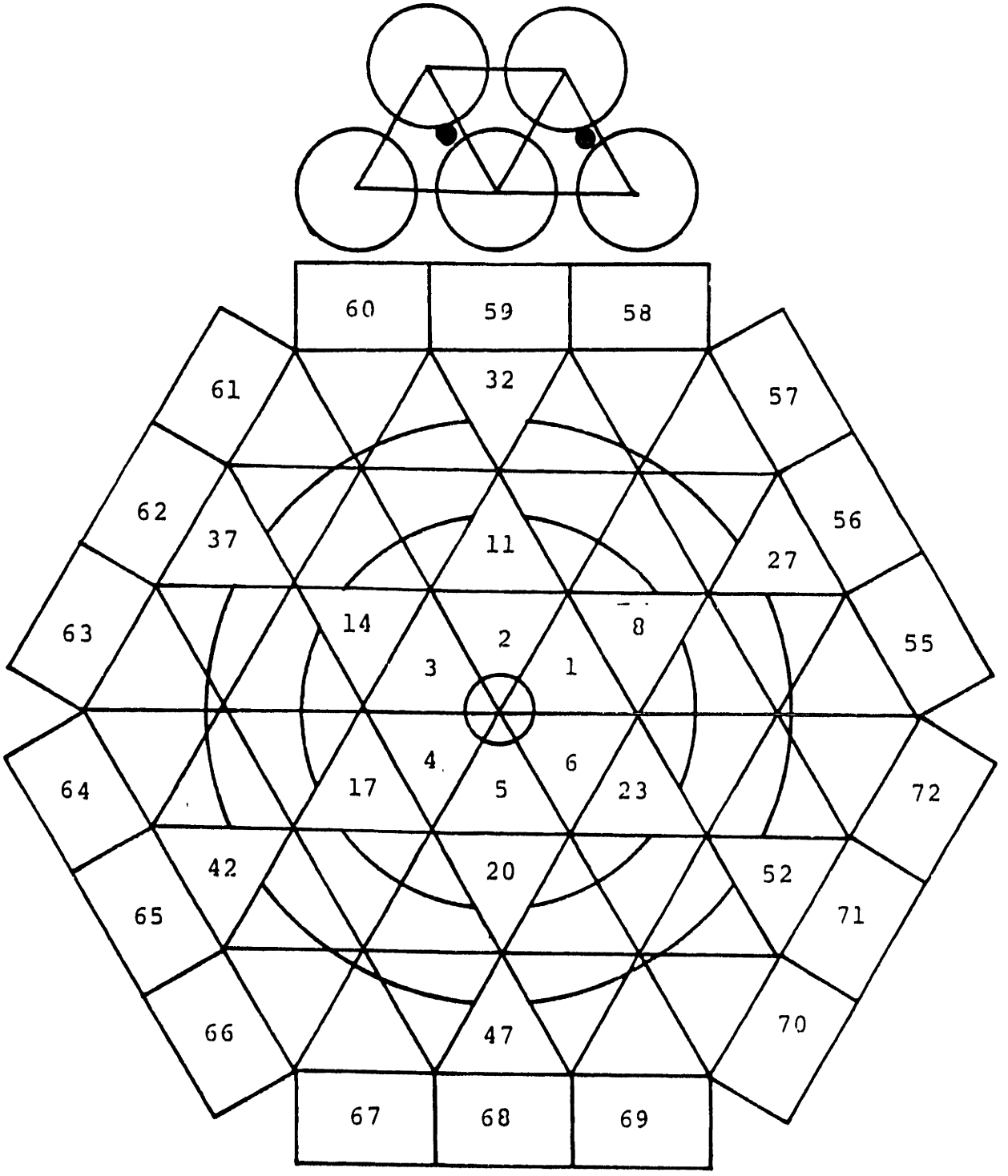

Figure 3.6 Flat to Flat Measurement Scheme and Wire Positions in Two Different Types of Interior Subchannel

the isokinetic condition. For this bundle, this condition was observed at flow rates lower than 70 GPM. A short stainless steel rod was inserted into the sampling tube to decrease the collecting flow area so as to prevent the loss of siphon head. Even with this modification, the lowest flow rate at which the isokinetic condition was attainable was 32.5 GPM, which corresponds to Re_b = 3470 and is still in the transition flow regime.

The highest flow rate attainable was about 220 GPM. To extend the data to higher Reynolds numbers, steam was injected into the water tank to increase the water temperature and hence decrease its kinetic viscosity. However, only 10°C difference was obtained, and kinetic viscosity decreased only to about 0.8 of its initial value.

3.3.2 Pressure Drop Experiment

The pressure drop experiment was discussed in detail by Burns (1980a). Pressure drops were measured by a pressure tap inserted inside two instrumentation rods: one in the interior region, the other in the edge region. Two collinear 30° holes with respect to rod vertical axis were drilled on each of the two instrumentation hollow rods: one is 8" below the exit end and the other is 32" below the exit end. Figure 3.7 shows an instrumentation rod, the 30° holes and the injector which was used as a pressure tap in the pressure drop experiment. The center instrumentation rod was aligned such that the 30° holes were directed into subchannel 1 to measure the interior subchannel pressure drop. For the edge one, the holes were directed into subchannel 71 to measure edge subchannel pressure drop (c.f.

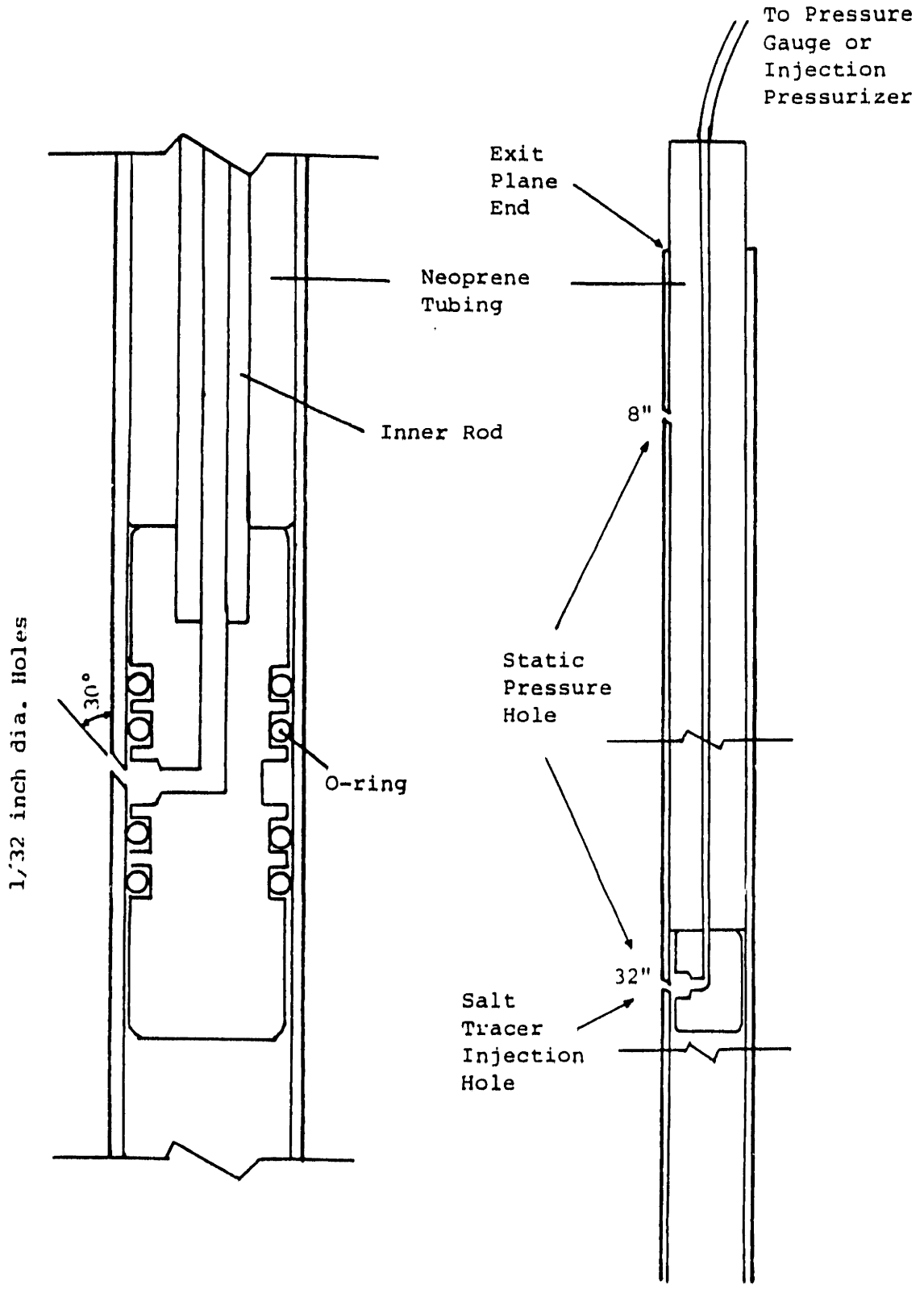

Figure 3.7 Design Configuration of Instrumentation Rod and Injector

Figures 3.3 and 3.6).

The 30° hole was selected by the trade-off between easy manufacture and less disturbance to the flow condition. Ideally, the hole should be zero degrees to prevent any horizontal velocity of the injection tracer in the mixing experiment. However, this was impossible to fabricate, and hence 30° was selected to make a drilling possible.

The 8" and 32" depths were selected because the pressure drop across several integral numbers of lead lengths was desired. Pressure drop across these three lead lengths would not be affected by the disturbance of pressure field caused by wire present, and would reduce the percentage measuring error.

Originally, the pressure was measured by two differential pressure gauges with ranges of 0-50 inches of water and 0-150 inches of water respectively. It was found that in the laminar flow, the pressure drop was so small (~ 0.1 inch of water) that it was not resolvable by the pressure gauge. To improve the resolution, a one meter long manometer was implemented to measure the static pressure at low and intermediate flow rates. When the flow rate was higher than 100 GPM, the pressure at the 32" depth was higher than the 100 cm of water. Then the pressure had to be measured by a 0-150 inch pressure gauge.

The manometer was constructed simply by attaching a glass tube to a meter stick. It was mounted such that the bottom end of the glass tube was a little lower than the water level in the upper plenum. A clear plastic tube connected this bottom end to the upper end of the injection tube. The hydrostatic head at the pressure tap drove the

water to a level, and the reading was recorded as the static pressure.

Pressure at different flow rates were first measured at one position. Then the pressure tap was slid to the other position, and the pressure at the same flow rates were measured. The difference between these two readings is the static pressure drop across the distance between two positions.

3.3.3 Mixing Experiment

In the mixing experiment, a tracer substance (salt) which changes the electrical resistance of water was injected at a known location within the mock-ups through which the water flow was forced. Resistance measurements made at the outlet of the test section by the resistance probes would then indicate the salt concentration in each subchannel at the bundle exit plane. These probes were held in place by a probe support structure located at the top of rod bundle. A flow separator is not required in this 37-pin bundle because the subchannel flow area is large enough for the platinum tips of the probes to be inserted directly in the subchannel without electrically shorting them by inadvertant conduct with the rods. The probes and probe support structure relative to the bundle exit are illustrated in Figure 3.8.

The data acquisition system developed by Glazer et al. (1977) was used to find the salt concentration level for each subchannel characterized by a particular resistance signal. However, the data storage function of that system was not working, and the data sets had to be recorded manually. The data sets were first photographed and then transcribed by hand with the help of a microfiche reader.

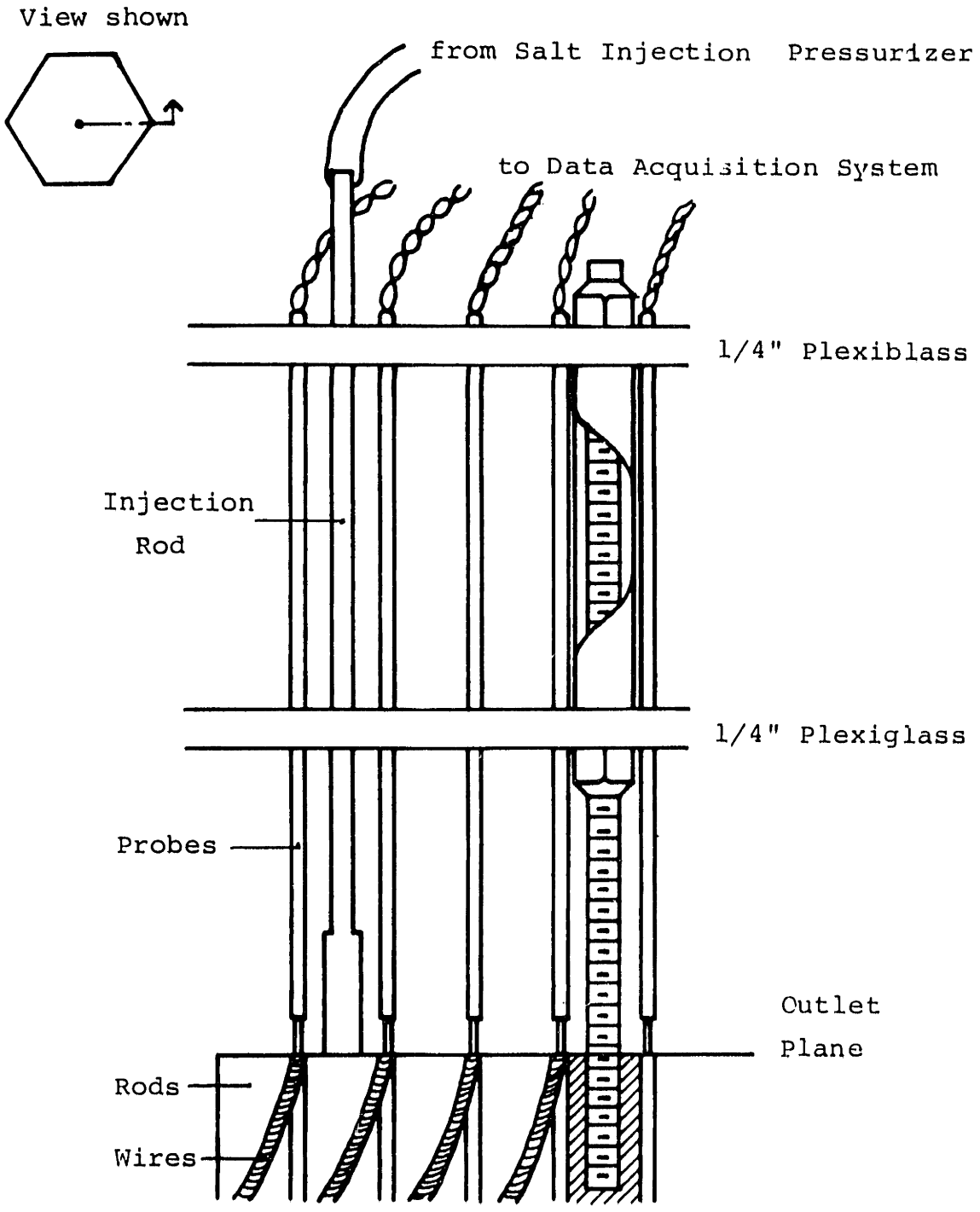

Figure 3.8 Structure of Probe Supporter

Only the 32" depth holes of the two injection rods shown in Figure 3.7 were used to inject saline water. The selection of this depth was based on past experience which indicated that a 3-5 lead length injection depth would give the best result for the mixing parameters [Symolon(1982a)]. The interior injection rod was designed to inject saline water into subchannel 1; and the edge injection rod, subchannel 71.

Since the calibration data were the base for transfering the probe resistances detected in the mixing step to the salt concentrations in each subchannel, the probe calibration step was the most important step in this experiment. An error in the reading of one probe for one calibration data set would cause an error in all the subsequent concentrations of the mixing result for the subchannel measured by that probe. Therefore, several data sets were taken at each calibration concentration to prevent any possible flawed data.

Following the recommendations of Chan et al.(1980a), the calibration concentrations were selected to be 0, 2, 4, 8, 12, 16 and 20 grams of salt per 100 lbm of water, and the concentration of the saline injection water was set at 800 grams/100 lbm. It was later found that for this injection concentration, salt concentrations of less than 2.0 grams/100 lbm were detected in practically all the subchannels. This meant that only two calibration points, i.e., 0 and 2 grams/100 lbm, could be used for calibrating data. Since the calibration curve (probe resistance vs salt concentration) is concave [Glazer et al. (1977)], the use of linear calibration curve based on these two points would give higher detected concentration than it

should be, and hence make the mass balance ratio higher than 1. However, the relative dimensionless ratios of salt concentration were only slightly affected because all the probes were calibrated this way and boosted to a higher level by the same factor.

In the mixing step, the injection flow rate was calculated at each bundle flow rate by equating the axial component of the injection velocity with the bundle average axial velocity to minimize the disturbance to the flow. Background calibration correction data were taken for each flow rate before the salt tracer was injected. This calibration correction data not only eliminated the discrepancy caused by the flow effect, but also compensated the decreasing sensitivity of each probe with time due to degradation of the platanized probe surface. Mixing data were then taken after the injected flow rate was steady at a present value.

3.4 Experimental Results and Discussion

The bundle average Reynolds number, Re_b, is given by

$$Re_b = \frac{V_b D_{eb}}{\nu}$$

Substituting the numerical value of De_b and conversion factor for flow rate, we get

$$Re_b = 4.07 \frac{G}{\nu}$$

where G is in GPM and ν is in ft^2/hr. The kinematic viscosity ν as a function of temperature is tabulated in Table 3.2 for water at 1 atm.

Both the flow split and pressure drop experiments were performed

Table 3.2

ν: Kinematic Viscosity of Water*

Temperature		ν ft^2/hr
°F	°C	
40	4.4	0.05993
45	7.2	0.05501
50	10.0	0.05073
55	12.8	0.04694
60	15.6	0.04363
65	18.3	0.04064
70	21.1	0.03802
75	23.9	0.03563
80	26.7	0.03350
85	29.4	0.03139
90	32.2	0.02978

*Source: F.M. White, "Viscous Fluid Flow," McGraw-Hill, New York (1974)

over a range of flow rates. In the pressure drop experiments, data were taken from very low flow rates (~2 GPM, Re_b~100) to the highest flow rate allowed by the overflow capacity of the upper plenum (~230 GPM, Re_b~23,000). However, as mentioned in Section 3.3, flow split experiments were not possible at low flow rates ($\leq$ 30 GPM, $Re_b \leq 3{,}000$). Therefore, laminar flow split data were not available.

In the mixing experiments, data were taken for bundle flow rates from ~ 2 GPM to ~ 250 GPM, corresponding to $Re_b \simeq$ 200 to 30,000 for the interior injection position. The difference in Re_b for the same bundle flow rate (e.g., 2 GPM) between this experiment and the pressure drop experiment was caused by differences in the water temperature on the dates that were performed. For the edge injection position, the data were taken form $Re_b \simeq 400$ to $Re_b \simeq 26{,}000$. Higher flow rates were attainable in the mixing experiments because the probe supporter placed at the bundle exit plane reduced the flow impulse, thereby increasing the effective overflow capacity of the existing upper plenum.

The experimental results will be compared with the Chiu, Hawley and Burns correlations which are the basis of the WIWRAP code [Wang(1981)]. Table 3.3 lists all the predicted parameters calculated by the WIWRAP code as functions of Re_b for this bundle.

3.4.1 Flow Split Experiment

3.4.1.1 Experimental Results

Let m_1 and m_2 be the average volumetric flow rate of eighteen

Table 3.3

Predicted Parameters by Chiu, Hawley and Burns' Correlations for This Bundle

Re_b	X_1	X_2	f_1	f_2	f_b	ε^*_{1L}	C_{1L}
200	0.840	1.208	0.799	0.490	0.612	0.0693	0.107
400	0.840	1.189	0.400	0.275	0.332	0.0884	0.136
700	0.858	1.175	0.256	0.173	0.204	0.108	0.165
1,000	0.865	1.163	0.189	0.132	0.153	0.122	0.187
2,000	0.884	1.135	0.112	0.0860	0.0948	0.154	0.239
3,000	0.897	1.119	0.0867	0.0706	0.0757	0.154	0.265
4,000	0.906	1.109	0.0742	0.0628	0.0660	0.154	0.265
5,000	0.912	1.102	0.0667	0.0579	0.0602	0.154	0.265
6,000	0.917	1.098	0.0616	0.0545	0.0562	0.154	0.265
7,000	0.920	1.094	0.0579	0.0520	0.0532	0.154	0.265
8,000	0.923	1.091	0.0551	0.0500	0.0510	0.154	0.265
10,000	0.927	1.087	0.0510	0.0471	0.0476	0.154	0.265
12,000	0.930	1.085	0.0482	0.0450	0.0453	0.154	0.265
15,000	0.933	1.082	0.0452	0.0427	0.0427	0.154	0.265
18,000	0.935	1.080	0.0431	0.0410	0.0409	0.154	0.265
21,000	0.937	1.079	0.0414	0.0396	0.0394	0.154	0.265
>100,000	0.944	1.073	--*	--	--	0.154	0.265

*This is Re_b dependent value.

interior and eighteen edge subchannels, respectively. Under the assumption that $X_3 = X_2$, the collected bundle flow rate is

$$m_b = 54m_1 + 18m_2 + 6\left(\frac{A_3}{A_2} m_2\right)$$

$$= 54m_1 + 20m_2$$

since $A_3 = 0.0420\ in^2$ and $A_2 = 0.1273\ in^2$.

The average velocities of bundle, interior and edge subchannels are

$$V_b = \frac{m_b}{A_b}, \qquad V_1 = \frac{m_1}{A_1}, \qquad V_2 = \frac{m_2}{A_2}$$

The flow split parameters were then obtained directly from their definitions:

$$X_1 \equiv \frac{V_1}{V_b}, \qquad X_2 \equiv \frac{V_2}{V_b}$$

To check the validity of the isokinetic technique, the total collected flow rate m_b was compared with the calibrated (measured) flow rate m_L, and their difference was expressed as the mass balance error:

$$\text{mass balance error} = \frac{m_b - m_L}{m_L}$$

Table 3.4 shows the experimental results of sixteen runs of flow split experiments. The flow split parameters versus bundle Reynolds number are illustrated in Figures 3.9 and 3.10. Figure 3.11 shows a typical collected normalized flow split map for eighteen interior and eighteen edge subchannels at $Re_b = 10480$. The normalized flow split

Table 3.4

Flow Split Experimental Results

Run #	Flow Rate GPM	Re_b	X_1	X_2	Mass Balance Error
1	32.5	3,470	0.763	1.307	-12%
2	42.8	4,570	0.800	1.259	-5.0%
3	52.4	5,600	0.841	1.206	-3.5%
4	56	5,950	0.864	1.175	-1.6%
5	70	7,440	0.875	1.161	-2.2%
6	70	7,630	0.879	1.155	-1.4%
7	81	8,620	0.894	1.136	-2.8%
8	100	10,480	0.915	1.110	-3.7%
9	105	11,380	0.916	1.109	-3.5%
10	121	10,740	0.939	1.079	-3.6%
11	142	12,840	0.936	1.082	-4.4%
12	173	16,170	0.934	1.085	-2.8%
13	197	18,960	0.939	1.078	-3.4%
14	200	21,600	0.962	1.048	-2.2%
15	220	22,510	0.953	1.060	-2.0%
16	215*	26,300	0.967	1.042	+0.9%

*Steam injected into tank to heat the water, hence Reynolds number increased.

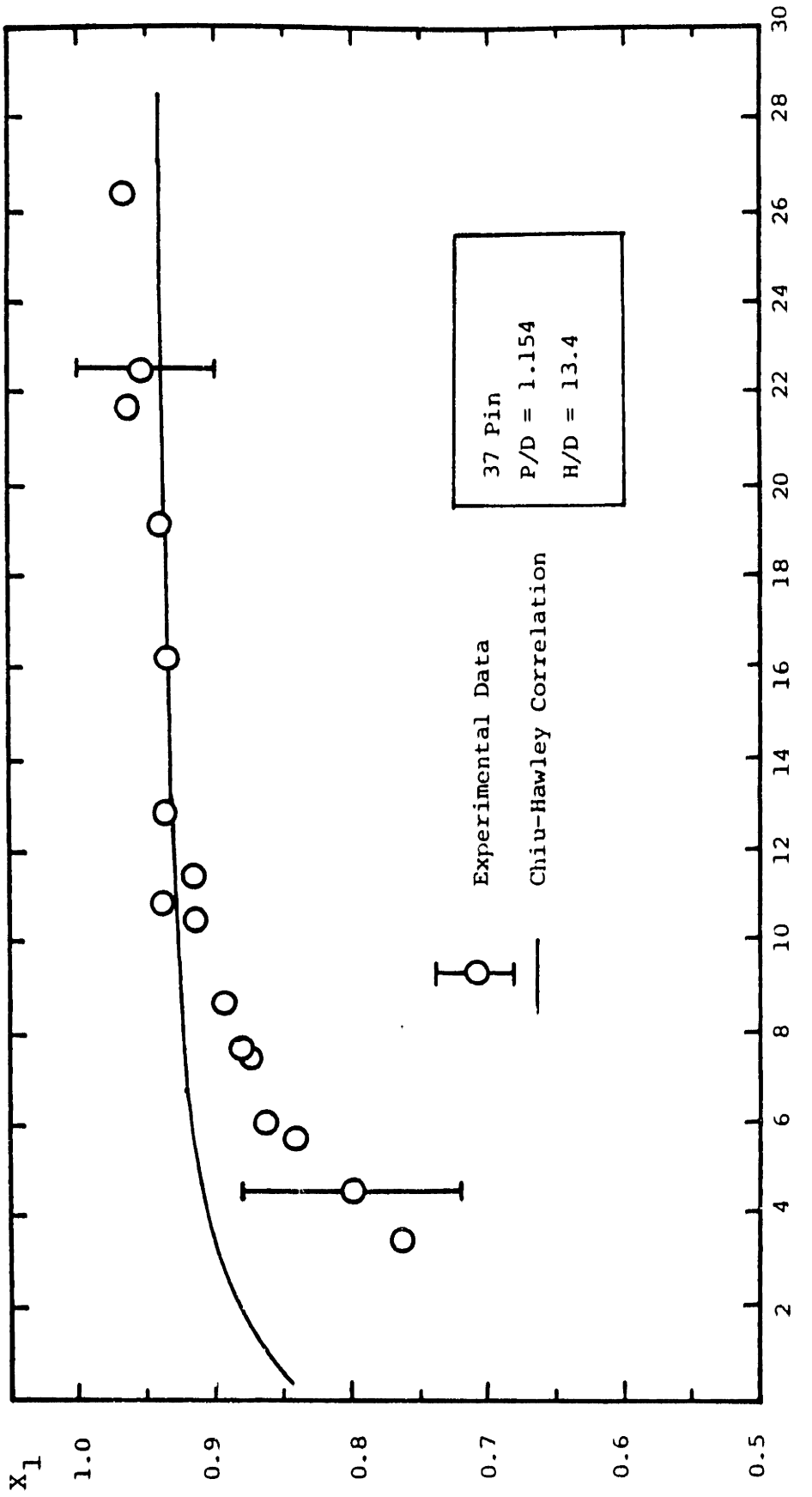

Figure 3.9 Interior Subchannel Flow Split Parameter X_1 versus Re_b

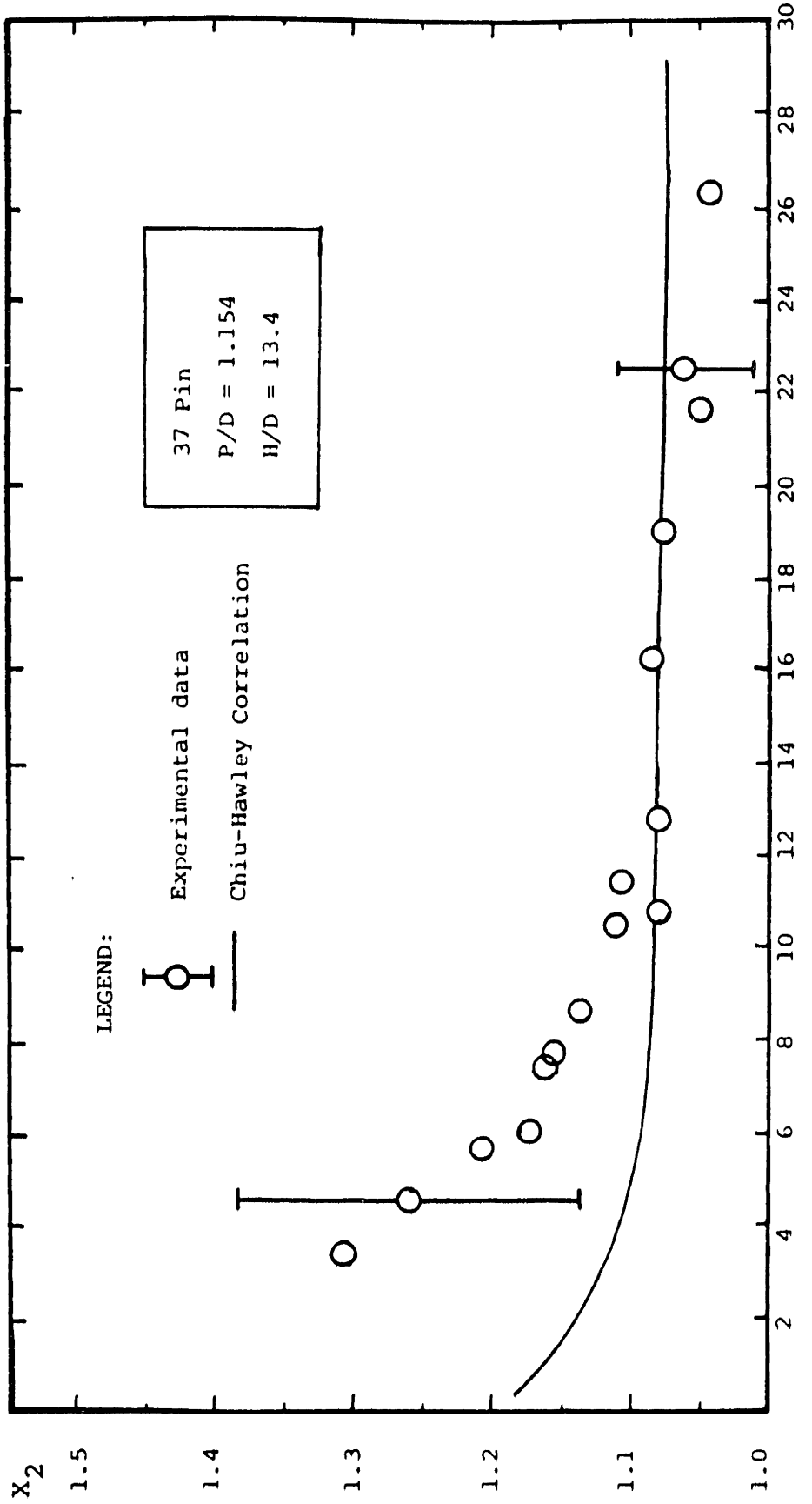

Figure 3.10 Edge Subchannel Flow Split Parameter X_2 versus Re_b

37-Pin P/D = 1.154 H/D = 13.4

M_L = 100 GPM

Re_b = 10480

X_1 = 0.915

X_2 = 1.110

Mass Balance Error = -3.7%

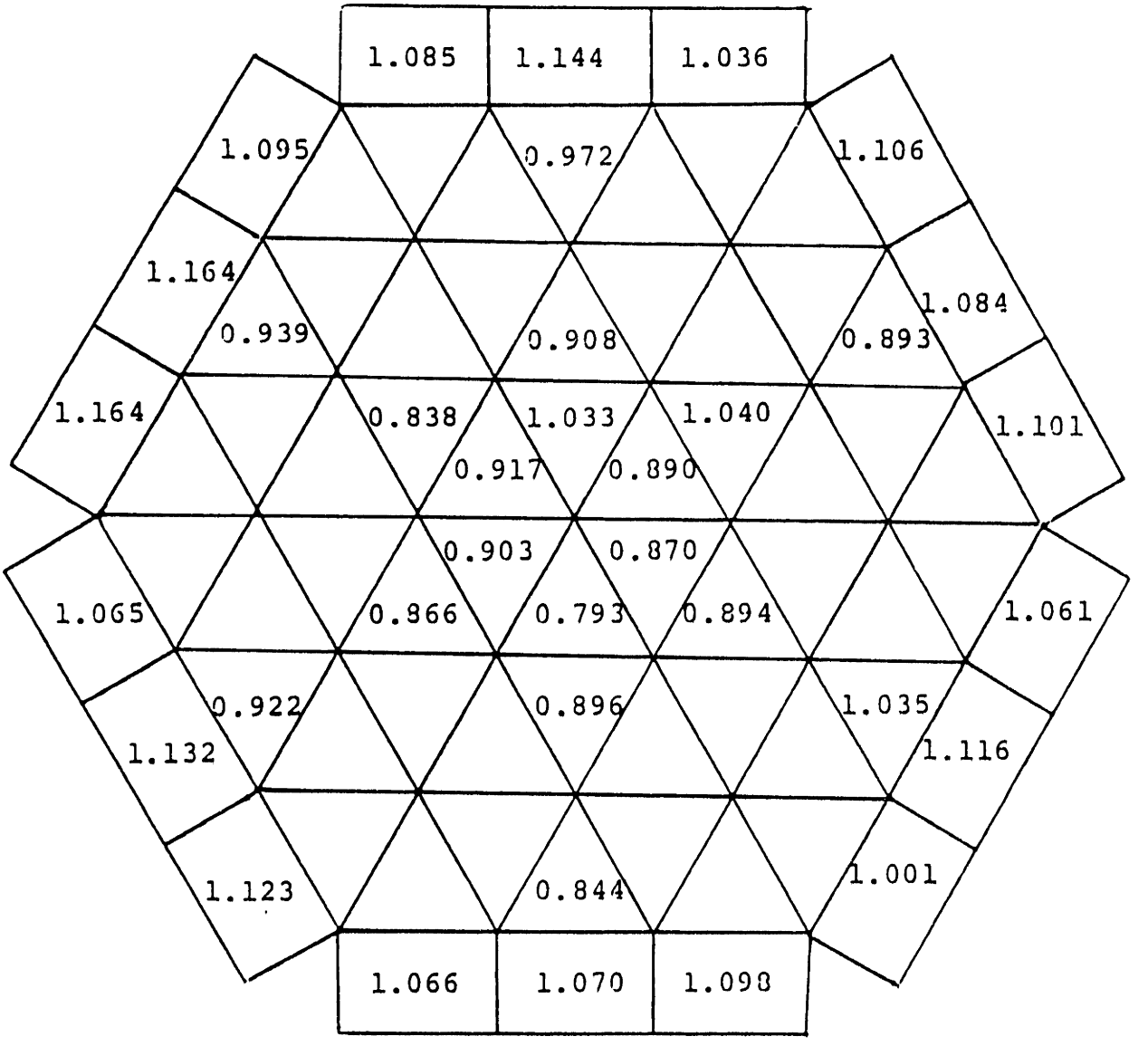

Figure 3.11 Normalized Subchannel Flow Split Map at Re_b = 10480

maps for all sixteen runs are presented in Appendix A1. Note that in all these figures the flow split value in each subchannel was the average velocity in each subchannel divided by bundle average velocity, where subchannel average velocity was calculated by the collected subchannel flow rate divided by its actual (i.e., with or without wire) flow area.

The error associated with the experimental results of flow split parameters by using this isokinetic extraction method was estimated to be ±5% in the turbulent flow regime [Hawley et al. (1980a)]. For the transition flow regime (say, $Re_b < 6,000$), the isokinetic condition is difficult to achieve, so that the uncertainty in data would increase. The error would conservatively be estimated to be doubled, i.e., ±10% for Re_b <6,000. These errors were illustrated in Figures 3.9 and 3.10 by the error bars associated with the two data points: one in the turbulent flow regime, the other in the transition/laminar flow regime.

3.4.1.2 Discussion

As tabulated in Table 3.4, all the mass balance errors are less than 5% except the one at the lowest flow rate. This was expected because at that flow rate, the isokinetic condition was very difficult to achieve, hence the larger percentage error.

Mass balance error is not only caused by the error inherent in the isokinetic technique, but also by the error in recording the indicated flow rate and by the accuracy of the calibration curve. All the mass balance errors except that for the highest flow rate are negative,

indicating that either the calibration curve of flow meter is not accurate or that there is a systematic error in the measuring technique. However, all these factors lead only to a mass error of 5% or less. This accuracy in mass balance serves to establish confidence in the isokinetic procedure.

Figures 3.9 and 3.10 show that the transition flow split behavior starts from Re_b = 12,000. This is consistent with data from Chiu's (1978) 61-pin bundle with P/D = 1.067 and H/D = 8. Also, the trends of this transition phenomenon are quite similar in these two bundles. Thomas Chiu's (1979) 37-pin data were considered to be flawed because the bundle dimensional symmetry was poor and the transition phenomenon was not shown. Symolon's (1981) 217-pin bundle data (P/D = 1.25, H/D = 52) also shown this transition phenomenon, but considerable scatter existed.

Figures 3.9 and 3.10 show excellent agreement of data with the Chiu-Hawley correlations in the turbulent flow regime. Flow split experiments of Symolon's 217-pin bundle also confirmed the validity of the correlations at the turbulent flow regime. Note that the correlations for turbulent flow split were calibrated before Symolon's experiment and the present work were done. However, significant discrepancy between the experimental results and predictions was found in the transition/laminar flow regime for all these bundles. The correlations for the transition/laminar flow regime need to be revised and/or recalibrated.

Figure 3.10 as well as the results of Chiu's 61-pin bundle (H/D=8) and Symolon's 217-pin bundle show that X_2 decreases with Re and

exhibits asymptotic behavior. However, some bundle data show a different trend: X_2 increases with Re before it saturates, e.g., Chiu's (1978a) 61-pin with P/D = 1.067, H/D = 4 and Wang's (1980) shaved-wire 61-pin with P/D = 1.067, H/D = 8. Besides, some investigators' data show that X_2 is less than X_1, e.g., Lorenz's (1977) isokinetic sampling results and some unpublished Japanese data. These might be caused by experimental error, which would introduce these opposite results since X_1 and X_2 were quite close to 1.0.

3.4.2 Pressure Drop Experiment

3.4.2.1 Experimental Results

The purpose of this experiment was to find the bundle average and subchannel friction factors. Table 3.5 shows the pressure drop experimental data, where the bundle average pressure drop ΔP_b was simply determined from a force balance which averages the pressure drop data for interior (ΔP_1) and edge (ΔP_2) subchannel as follows:

$$\Delta P_b = \frac{N_1 A_1 \Delta P_1 + N_2 A_2 \Delta P_2}{N_1 A_1 + N_2 A_2} \qquad (3.1)$$

$$= 0.591\ \Delta P_1 + 0.409\ \Delta P_2$$

The relationship between the pressure drop data and the friction factors are

$$\Delta P_i = f_i \frac{L}{De_i} \frac{\rho V_i^2}{2g_c} \qquad (3.2)$$

where L is the distance across which the pressure drops were measured.

Table 3.5

Experimental Results of Pressure Drop Experiment

Bundle flow rate (GPM)	ΔP_1 (interior) cm of water	ΔP_1 (interior) in of water	ΔP_2 (edge) cm of water	ΔP_2 (edge) in of water	ΔP_b in of water
1.93	0.2	0.079	0.2	0.079	0.079
2.90	0.3	0.118	0.4	0.158	0.134
3.86	0.4	0.158	0.5	0.197	0.174
4.83	0.5	0.197	0.6	0.236	0.213
5.79	0.7	0.276	0.8	0.315	0.292
6.76	0.9	0.354	1.1	0.433	0.386
7.72	1.1	0.433	1.3	0.512	0.465
7.40	1.0	0.394	1.2	0.472	0.426
9.25	1.3	0.512	1.5	0.591	0.544
11.1	1.8	0.709	2.0	0.787	0.741
13.0	2.2	0.866	2.5	0.984	0.914
14.8	2.8	1.102	3.0	1.181	1.134
16.7	3.3	1.299	3.5	1.378	1.331
18.5	3.9	1.535	4.0	1.575	1.551
20.4	4.6	1.811	4.6	1.811	1.811
22.2	5.2	2.047	5.4	2.126	2.079
25.9	6.6	2.598	6.7	2.638	2.614
29.6	8.2	3.228	8.2	3.228	3.223
33.3	9.8	3.858	9.8	3.858	3.858
37.0	11.7	4.606	11.8	4.646	4.622
40.8	13.7	5.394	13.9	5.472	5.426
44.6	15.9	6.260	15.7	6.181	6.223
48.4	18.1	7.126	17.9	7.047	7.094
52.2	20.6	8.110	20.1	7.913	8.029
56.0	22.8	8.976	22.5	8.858	8.928
50.0	19.5	7.68	18.5	7.28	7.52
56.0	22.8	8.98	22.2	8.74	8.88
63.0	25.8	10.16	25.2	9.92	10.06
70.0	30.5	12.00	28.6	11.26	11.70
76.0	34.2	13.46	32.9	12.95	13.25
81.0	39.5	15.55	36.1	14.21	15.00
95.0	49.5	19.49	45.2	17.80	18.80
105.0	58.1	22.87	54.1	21.30	22.23
115.0	67.4	26.54	63.7	25.08	25.94
126.0	--	31.4	--	30.1	30.9
137.0	--	35.8	--	35.2	35.6
147.0	--	42.9	--	41.1	42.2
160.0	--	48.4	--	46.5	47.6
170.0	--	53.9	--	52.7	53.4
180.0	--	59.4	--	56.8	58.3
190.0	--	65.0	--	63.5	64.4
201.0	--	72.0	--	70.0	71.2
212.0	--	78.0	--	77.0	77.6
223.0	--	86.0	--	84.0	85.2
233.0	--	93.0	--	91.0	92.2
244.0	--	101.0	--	101.0	101.0
254.0	--	108.0	--	111.0	109.0

It is three lead lengths, i.e., 24" in this experiment.

Substituting L, De_i, and some conversion factors into equation (3.2), we get the following formulae:

$$f_b = 18.45 \frac{\Delta P_b}{G^2}$$

$$f_1 = 17.01 \frac{\Delta P_1}{(X_2 G)^2}$$

$$f_2 = 21.58 \frac{\Delta P_2}{(X_2 G)^2}$$

where ΔP_i is in inches of water, G is in GPM, and X_i are the experimental flow split results.

To investigate the subchannel friction factor as a function of subchannel Reynolds number, a knowledge of the subchannel Reynolds numbers in terms of the measured bundle Reynolds number measured flow split and bundle geometry is required. They are calculated simply from

$$Re_i = Re_b \frac{De_i}{De_b} X_i$$

i.e.,

$$Re_1 = 0.92\ Re_b X_1$$

$$Re_2 = 1.17\ Re_b X_2 \qquad (3.4)$$

As previously mentioned, the flow split parameters were not available for $Re_b \leq 3{,}500$; hence, the subchannel friction factors and Reynolds numbers are not calculable for this range unless the flow split parameters are estimated. We simply assume that the flow split parameters are constant for $Re_b \leq 3{,}500$.

Table 3.6 tabulates the calculated results of Re_i and f_i. Figures 3.12, 3.13 and 3.14 illustrate f_b, f_1 and f_2 versus Re_b, Re_1 and Re_2, respectively.

The error associated with this pressure drop experiment was discussed in detail by Burns (1980b). According to this reference, the errors involved in friction factors are about ±60% at Re_b = 200, 30% at Re_b = 500 and 20% for $Re_b \geq 6{,}000$, as illustrated by the error bars in Figures 3.12, 3.13 and 3.14.

3.4.2.2 Discussion

Equations (3.1) and (3.3) show that the bundle friction factor is determined only by experimental subchannel pressure drop data. On the other hand, the subchannel friction factors were determined by both subchannel pressure drop and flow split data. Note that the flow split behavior and hence the subchannel friction factors are determinable only from experimental flow split data.

A transition regime of bundle friction factor was observed to start from $Re_b \simeq 600$ in Figure 3.12 as well as all the other wire wrapped bundle data. One might arbitrarily define $Re_b < 600$ as the laminar flow regime and high Re_b (say 10,000) as the turbulent flow regime for this bundle friction factor behavior.

In the laminar flow regime, f_b was observed to behave as C_{fL}/Re_b. The constant C_{fL} for this bundle was calculated to be 94.2 as shown in Figure 3.12. C_{fL} was 90 and 160 for Chiu's H/D = 8 and 4 bundles, respectively; 70 for Symolon's 217-pin, and 85 for T. Chiu's 37-pin (P/D = 1.15, H/D = 21.0).

Table 3.6

Results of f_b, f_1 and f_2

Re_b	f_b	X_1	Re_1	f_1	X_2	Re_2	f_2
226	0.3913	0.76	158	0.6246	1.30	344	0.2704
340	0.2940	0.76	238	0.4132	1.30	517	0.2395
452	0.2155	0.76	317	0.3123	1.30	687	0.1689
565	0.1685	0.76	395	0.2487	1.30	859	0.1292
678	0.1607	0.76	474	0.2424	1.30	1,040	0.1200
791	0.1558	0.76	554	0.2281	1.30	1,200	0.1210
904	0.1440	0.76	633	0.2139	1.30	1,370	0.1097
866	0.1435	0.76	607	0.2119	1.30	1,310	0.1101
1,080	0.1173	0.76	757	0.1762	1.30	1,640	8.82 -2
1,300	0.1110	0.76	910	0.1694	1.30	1,970	8.15 -2
1,520	9.98 -2*	0.76	1,064	0.1503	1.30	2,310	7.44 -2
1,730	9.52 -2	0.76	1,210	0.1482	1.30	2,630	6.88 -2
1,960	8.80 -2	0.76	1,370	0.1371	1.30	2,980	6.31 -2
2,170	8.36 -2	0.76	1,520	0.1321	1.30	3,300	5.87 -2
2,390	8.02 -2	0.76	1,670	0.1282	1.30	3,630	5.56 -2
2,600	7.79 -2	0.76	1,820	0.1233	1.30	3,950	5.51 -2
3,030	7.18 -2	0.76	2,120	0.1141	1.30	4,610	5.02 -2
3,470	6.80 -2	0.76	2,430	0.1085	1.30	5,280	4.70 -2
3,900	6.42 -2	0.79	2,840	9.48 -2	1.28	5,840	4.58 -2
4,330	6.23 -2	0.80	3,190	8.94 -2	1.26	6,380	4.58 -2
4,780	6.02 -2	0.81	3,570	8.40 -2	1.25	6,970	4.52 -2
5,220	5.78 -2	0.83	3,990	7.77 -2	1.22	7,460	4.52 -2
5,670	5.58 -2	0.84	4,390	7.33 -2	1.21	8,020	4.47 -2
6,110	5.44 -2	0.85	4,790	7.01 -2	1.20	8,570	4.42 -2
6,560	5.25 -2	0.87	5,260	6.43 -2	1.17	8,970	4.50 -2
7,380	4.70 -2	0.88	5,980	5.62 -2	1.16	10,000	4.01 -2
8,190	4.41 -2	0.89	6,720	5.26 -2	1.14	10,900	3.82 -2
8,900	4.25 -2	0.90	7,380	4.89 -2	1.13	11,800	3.79 -2
9,480	4.22 -2	0.91	7,940	4.87 -2	1.12	12,500	3.73 -2
11,100	3.84 -2	0.92	9,410	4.33 -2	1.10	14,300	3.53 -2
12,300	3.72 -2	0.93	10,500	4.08 -2	1.09	15,700	3.51 -2
13,500	3.61 -2	0.94	11,700	3.86 -2	1.08	17,000	3.52 -2
14,400	3.59 -2	0.95	12,600	3.73 -2	1.07	18,100	3.56 -2
15,800	3.60 -2	0.95	13,800	3.70 -2	1.07	19,800	3.64 -2
17,200	3.60 -2	0.95	15,100	3.74 -2	1.06	21,300	3.65 -2
18,700	3.43 -2	0.96	16,600	3.49 -2	1.06	23,200	3.50 -2
19,900	3.41 -2	0.96	17,600	3.44 -2	1.05	24,400	3.57 -2
21,100	3.32 -2	0.96	18,700	3.39 -2	1.05	25,900	3.43 -2
22,200	3.39 -2	0.96	19,600	3.33 -2	1.05	27,300	3.44 -2
23,500	3.25 -2	0.96	20,800	3.29 -2	1.05	28,900	3.39 -2
24,800	3.19 -2	0.96	21,900	3.21 -2	1.05	30,400	3.36 -2
26,100	3.16 -2	0.96	23,100	3.20 -2	1.05	32,000	3.31 -2
27,300	3.13 -2	0.96	24,100	3.16 -2	1.05	33,500	3.29 -2
28,600	3.13 -2	0.96	25,300	3.13 -2	1.05	33,510	3.32 -2
29,700	3.12 -2	0.96	26,200	3.09 -2	1.05	36,500	3.37 -2

* $\underline{-2} \equiv \times 10^{-2}$

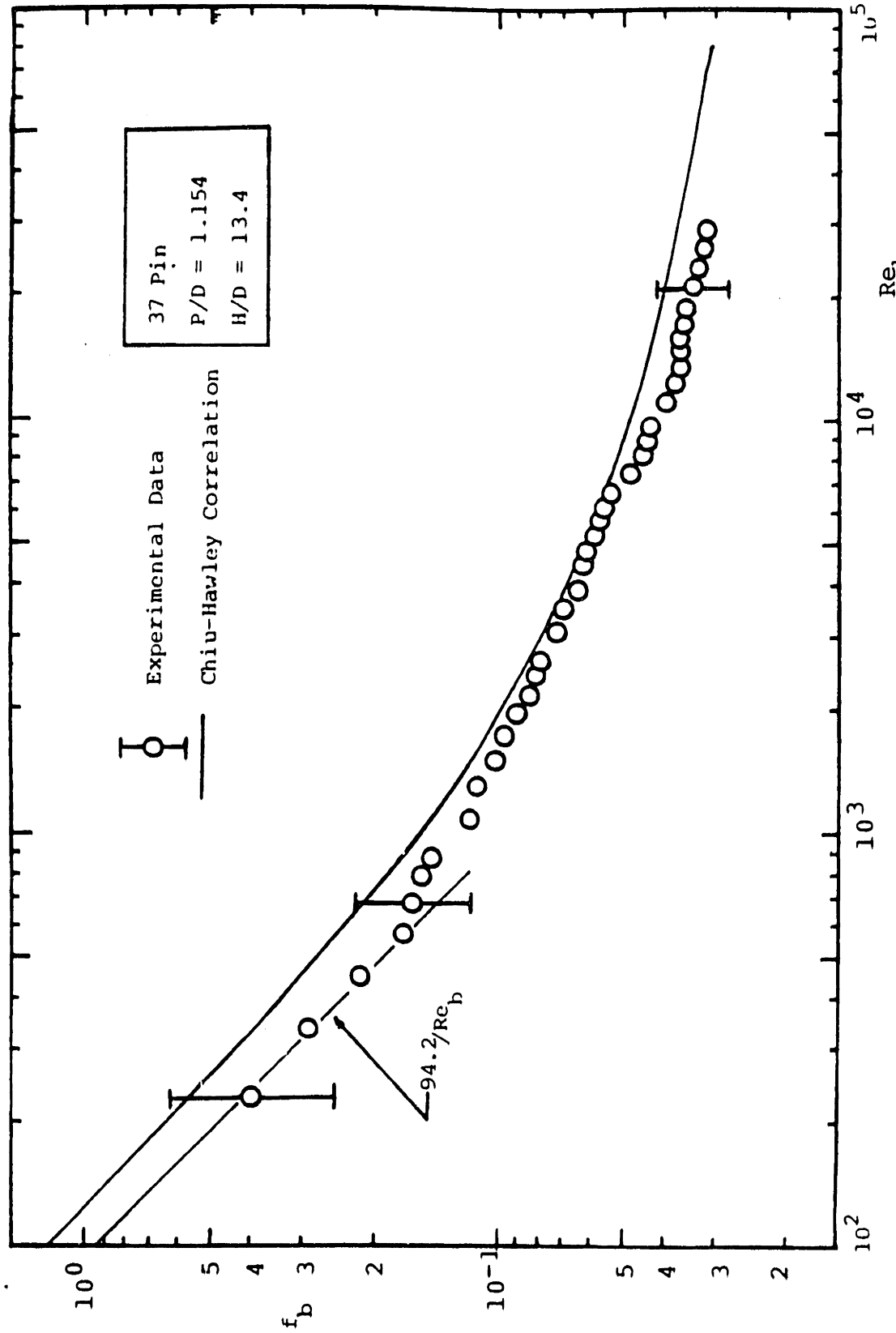

Figure 3.12 Bundle Average Friction Factor Data form Pressure Drop Experiment

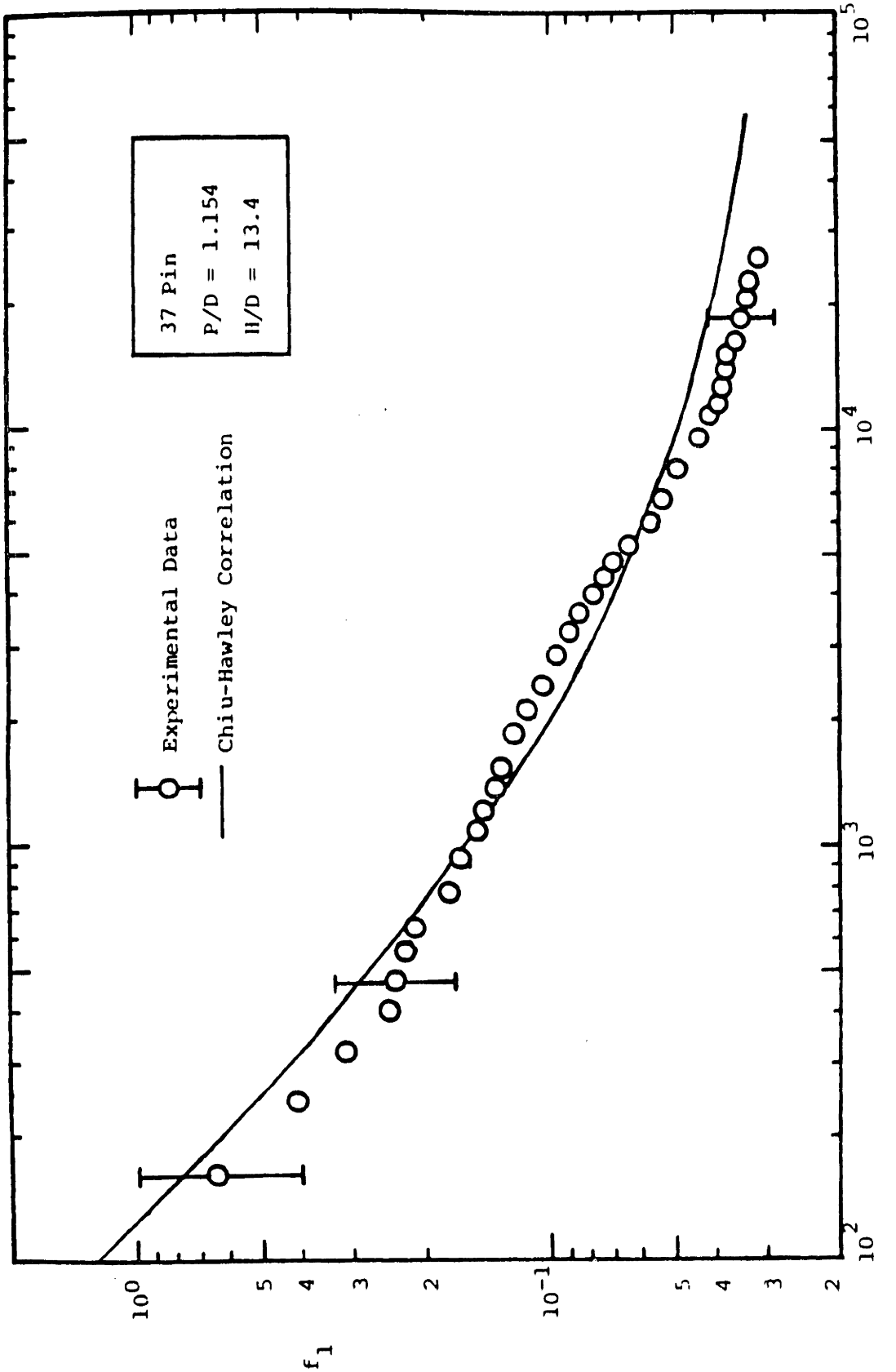

Figure 3.13 Interior Subchannel Friction Factor versus Interior Subchannel Reynolds Number

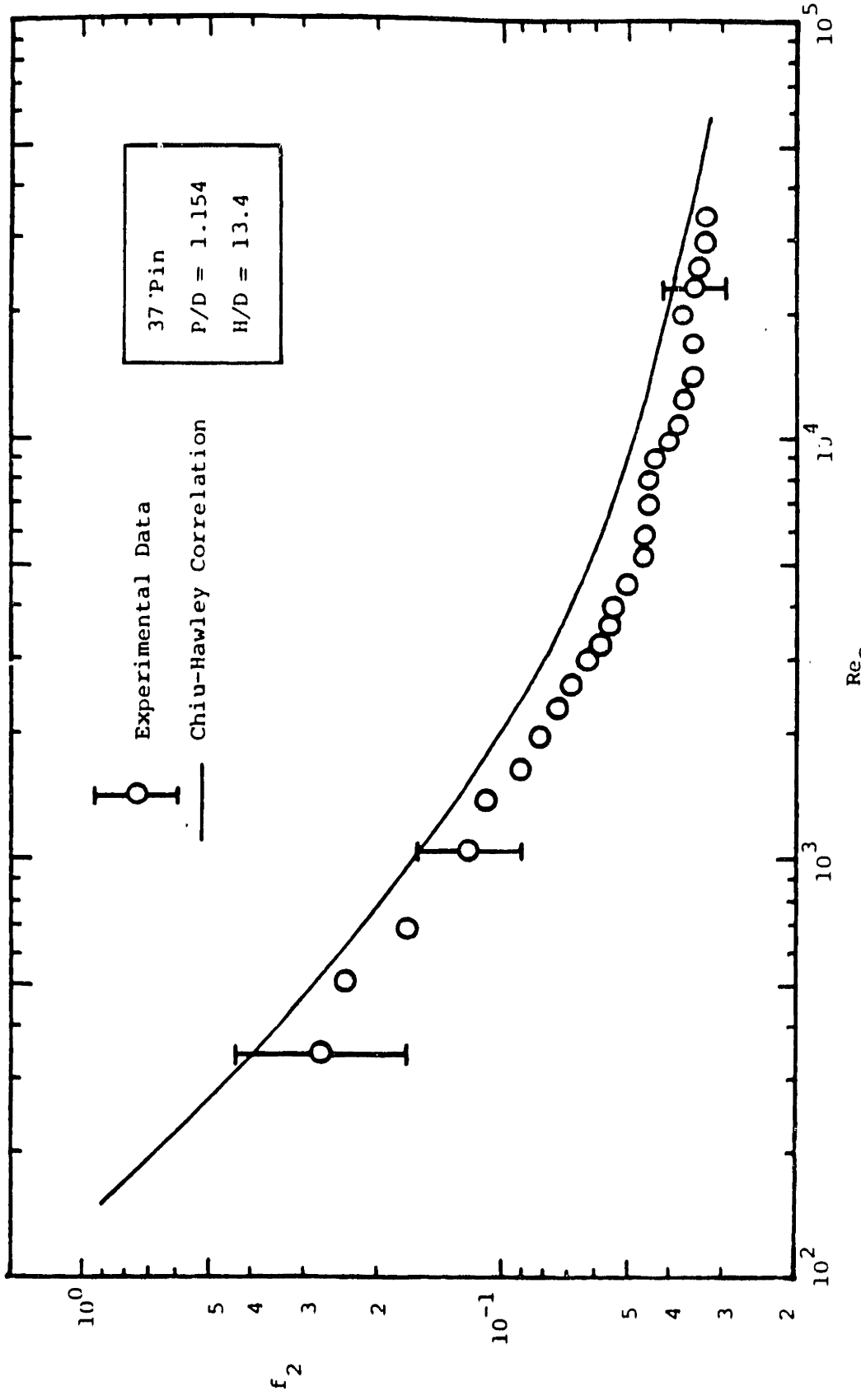

Figure 3.14 Edge Subchannel Friction Factor versus Edge Subchannel Reynolds Number

As for the turbulent flow regime, the data for $Re_b > 10{,}000$ show $f_b = 0.20/Re_b^{0.18}$ or $0.40/Re_b^{0.25}$, depending on which relation was used. The second one was a better fit. Since there is error associated with the data, it is difficult to ascertain which relation is more accurate. However, Hawley correlated the world data into $f_b = C_{fT}/Re_b^{0.18}$ in his correlation. If $f_b = C_{fT}/Re_b^{0.25}$, then the following C_{fT} values apply: 0.48 and 0.90 for Chiu's H/D = 8 and 4 bundles, respectively; 0.29 for Symolon's 217-pin, and 0.31 for Chiu's 37-pin.

Figure 3.12 shows that Chiu-Hawley's friction factor correlations slightly overpredict f_b, especially in the laminar flow regime.

3.4.3 Mixing Experiment

3.4.3.1 Experimental Results

The measured raw data in the mixing experiment were the resistances for probes located at the bundle exit plane detected by the data acquisition system. These resistances were then transformed to salt concentrations according to the calibration curves for each probe (i.e., each subchannel), respectively. The final data, however, are presented as dimensionless salt concentrations for each subchannel i which are defined by

$$C_i^* \equiv \frac{C_i}{\frac{1}{m_o}\left[\sum_{j=\text{interior}} m_j C_j + \sum_{k=\text{edge}} m_k C_k\right]} \tag{3.5}$$

where m_j, m_k = interior and edge subchannel flow rates

m_o = injection subchannel flow rate

$= m_j$ for interior injection

$= m_k$ for edge injection

C_i, C_j, C_k = detected subchannel salt concentration

In calculating C_i^*, the flow split parameters measured in the flow split experiments were used for determining m_o, m_j and m_k. Note that the denominator in definition (3.5) means the salt concentration in the injection subchannel at the injection position based on the total subchannel flow rate. This concentration is less than the salt concentration in the stream which is injected into the subchannel. Fig. 3.15 illustrates these two sets of concentrations and flowrates.

An indication of the quality of the detected salt concentrations is the mass balance ratio between the total detected salt divided by injected salt, i.e.,

$$\text{mass balance ratio} \equiv \sum_i m_i c_i / m_{inj} C_{inj} \tag{3.6}$$

where m_i, C_i same as in equation (3.5)

m_{inj} = injection flow rate

C_{inj} = injection salt concentration

Table 3.7 lists the Reynolds numbers, the flow split parameters used and the mass balance ratios for all 30 runs in the mixing experiment. Figure 3.16 illustrates a typical dimensionless salt concentration map at $Re_b = 22100$ for both interior and edge injections. The subchannel numbering scheme for Figure 3.16 is shown in Figure 3.17. The dimensionless salt concentration maps for all 30 runs are included in

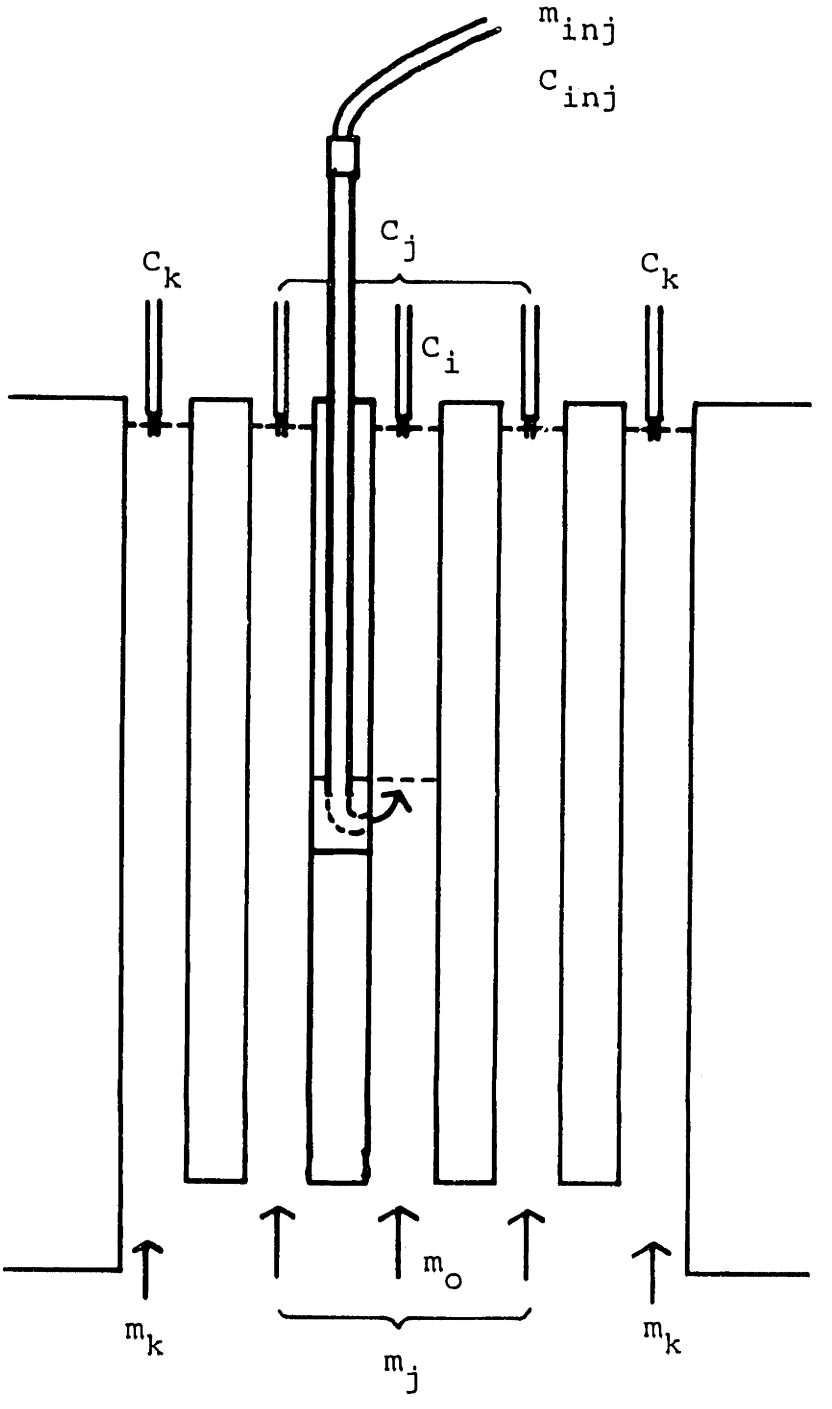

Figure 3.15 Salt Concentrations and Flowrates in the Mixing Experiment

Table 3.7 Mass Balance Ratio for Mixing Experiment

Interior Inj.					Edge Inj.				
Run	Re_b	X_1	X_2	Mass Balance Ratio	Run	Re_b	X_1	X_2	Mass Balance Ratio
1	220	0.76	1.30	1.70					
2	430	0.76	1.30	1.81	17	430	0.76	1.30	2.01
3	860	0.76	1.30	1.35	18	860	0.76	1.30	1.53
4	1,500	0.76	1.30	1.39	19	1,500	0.76	1.30	1.05
5	2,200	0.76	1.30	1.15	20	2,200	0.76	1.30	1.27
6	3,200	0.76	1.30	1.36	21	3,200	0.76	1.30	1.34
7	4,300	0.80	1.26	1.13	22	4,300	0.80	1.26	0.94
8	5,400	0.84	1.20	1.31	23	5,400	0.84	1.20	1.38
9	6,500	0.86	1.17	1.44	24	6,500	0.86	1.17	1.11
10	9,400	0.91	1.11	1.58	25	9,400	0.91	1.11	1.20
11	12,200	0.94	1.08	1.57	26	12,200	0.94	1.08	1.20
12	14,800	0.95	1.07	1.67	27	14,800	0.95	1.07	1.62
13	18,600	0.96	1.06	1.58	28	18,600	0.96	1.06	1.40
14	22,100	0.96	1.05	1.42	29	22,100	0.96	1.05	1.50
15	26,000	0.96	1.05	1.42	30	26,000	0.96	1.05	1.22
16	29,600	0.96	1.05	1.43					

37 pin p/d= 1.154 h/d= 13.40
inj. subchannel = 1
inj. depth (in) = 32.0
bundle reynolds no.= 22100
mass balance ratio = 1.423
dimensionless ratios of salt concentration*100.0:

0.3 0.5 0.8 0.6 0.4
0.1 0.8 2.8 1.4 0.2
0.5 1.3 2.3 1.7
0.3 1.3 3.8 4.2 1.0 0.0
1.0 3.1 4.4 4.0 1.5
0.1 1.3 4.2 5.5 3.7 1.3 0.3
0.4 1.6 3.6 (3.9) 2.8 0.7
0.2 0.0
0.5 2.7 4.1 3.2 0.9 0.1
0.0 0.1 2.1 4.0 2.2 0.9 0.0
0.6 1.3 0.9 0.7 0.0
0.0 0.3 1.5 1.2 0.5 0.1
0.0 0.2 0.3 0.2
0.1 0.1 0.4 0.0 0.0
0.1 0.1 0.1 0.0 0.0

37 pin p/d= 1.154 h/d= 13.40
inj. subchannel = 71
inj. depth (in) = 32.0
bundle reynolds no.= 22100
mass balance ratio = 1.222
dimensionless ratios of salt concentration*100.0:

7.6 7.8 6.8 7.4 8.0
3.6 1.1 1.5 6.2 6.2
1.7 1.3 0.9 5.8
1.6 1.0 0.2 3.2 7.4 4.4
0.0 0.5 0.8 3.0 6.6
0.5 0.0 0.2 0.2 3.3 5.8 3.6
0.0 0.4 0.0 0.9 3.0 5.8
0.5 3.0
0.0 0.0 0.6 1.9 3.4 6.0
0.0 0.0 0.0 0.3 1.7 7.5 2.5
0.0 0.4 1.3 4.3 4.1
0.0 0.0 0.0 1.7 4.5 (1.4)
0.0 0.9 1.8 5.0
0.0 0.0 0.7 1.9 0.6
0.0 0.0 0.0 0.0 0.3

Figure 3.16 Typical Measured Dimensionless Salt Concentration at Re_b = 22100

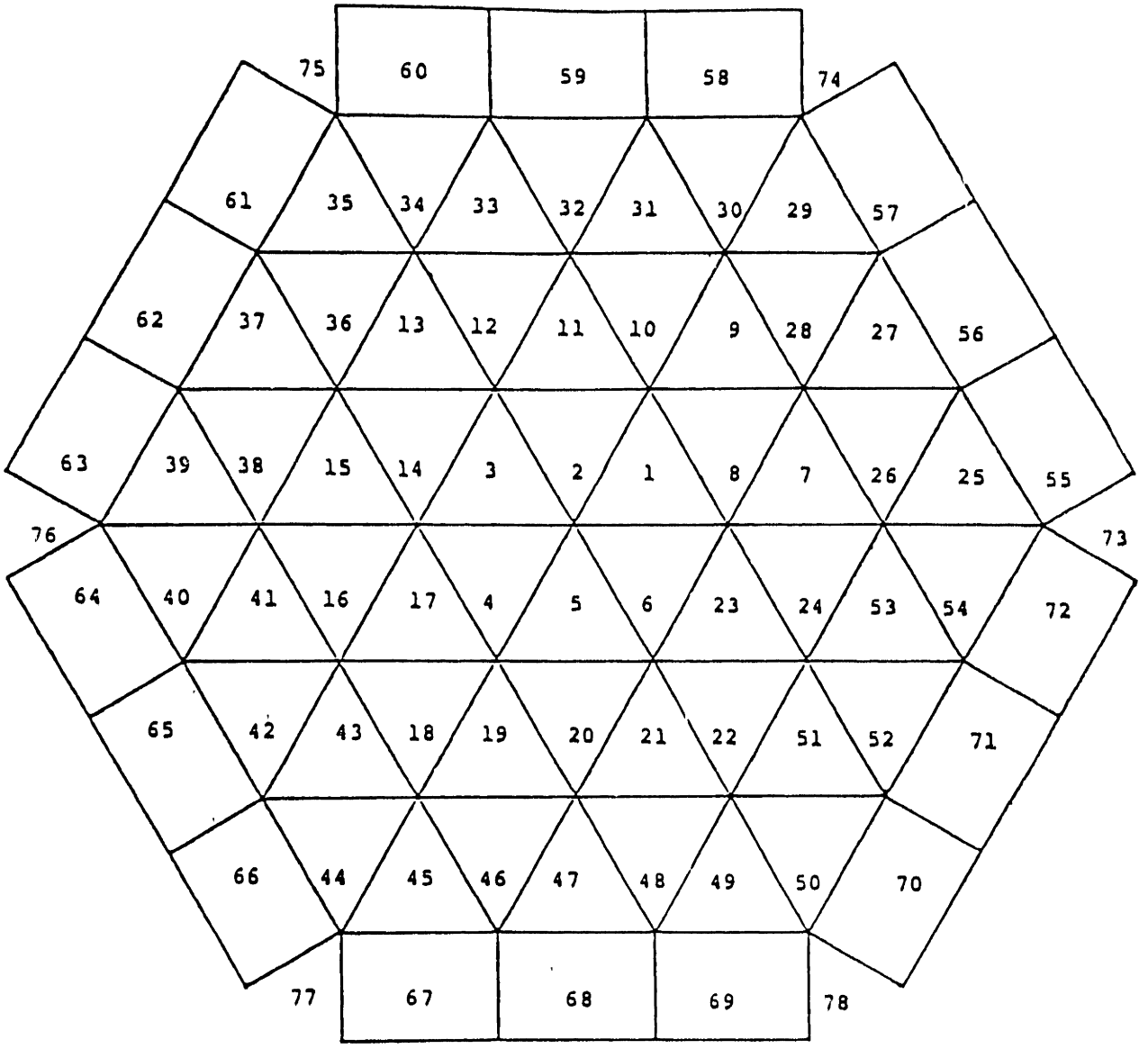

Figure 3.17 Subchannel Numbering Scheme for 37-pin Bundle

Appendix A2.

The mixing parameters, DEED, $\varepsilon^*_{l\eta}$, and ETVR, C_{lL}, will be reduced from these dimensionless salt concentration maps by a data reduction version of ENERGY code (DRV) in chapter 5.

3.4.3.2. Discussion

As shown in Table 3.7, all the mass balance ratios except run 22 are higher than 1. The average value is about 1.4. This high mass balance ratio was expected because of the calibration procedure discussed in Section 3.3.3.

For interior injection, for all runs except Re_b of 430 and 200, the peak salt concentration occured at subchannel 2 instead of the injection subchannel 1 (refer to Appendix A2). This phenomenon, namely that the maximum concentration did not occur at the injection subchannel at the bundle exit plane, had been observed before and was the motivation for the development of DRV-2 [Symolon (1980)]. This behavior is believed to be caused by wire located about 1/4 lead length downstream of the injection position. Large amounts of the salt solution were diverted into subchannel 2 right after they had been injected. However, at very low flow rates (Re_b = 220, 430), this diversion effect decreased and the peak concentration remained in subchannel 1.

CHAPTER 4

SUBCHANNEL FRICTION FACTOR CORRELATIONS

4.1 Introduction

The constitutive relations for subchannel friction factors are essential for subchannel analysis codes, either as input to those codes which solve coupled conservation equations (COBRA, COMMIX, THI-3D, and ENERGY-III) or as the means to derive flow split parameters for use as input to those codes which solve only the energy equation (COTEC, ENERGY-I). Several investigators, deStordeur (1961), Sangster (1968), Novendstern (1972), Rehme (1967), Engel et al. (1979), and Hawley et al. (1980), have suggested empirical models for correlating the bundle average friction factors as functions of the wire-wrapped subassembly geometry. Significantly, none of these investigators except Hawley et al. extended their efforts to correlate subchannel based friction factors.

Although subchannel friction factors models have been developed by Hawley et al., these models can be substantially improved. In this chapter we present new and consistent subchannel friction factor and flow split models which have been fully calibrated utilizing all old and new published data. These correlations will then be used in the ENERGY-IV code as input for flow split parameters and subchannel friction factors.

The objective of this chaper is to develop the models for drag loss in three kinds of subchannels in a typical wire-wrapped LMFBR subassembly. From these models, the equations for the average value of

subchannel friction factors over one lead length are formulated, and expressions for flow split parameters and bundle average friction factors are then derived. The empirical constants in these formulations are calibrated from bundle average friction factor data and flow split data. These subchannel friction factor models will be formulated to be,

a) applicable to both turbulent and laminar flow conditions; the transition flow region will be represented as a superposition of turbulent and laminar values weighted by some intermittency factor,

b) based on simple but sound physical concepts,

c) correctly reducible to bare rod cases, and most importantly,

d) able to satisfactorily correlate the wire-wrapped experimental data.

4.2 Literature Review

The available data for the wire-wrapped rod bundle friction factor and flow split parameter have been reviewed and collected. Appendix B1 lists all these data in addition to bare rod bundle friction factor data.

4.2.1 Bundle Average Friction Factor Data

The first systematic pressure drop experiments for wire-wrapped rod bundles with varied P/D and H/D reported were by Bishop et al. (1962) in 19-pin bundles. Since the center pin of their bundles was not wire-wrapped, their results are not appropriate for our models in which all the rods are wire-wrapped.

Rehme (1967) performed pressure drop experiments for over seventy-four wire-wrapped rod bundles with different combinations of geometrical parameters (N_r = 7, 19, 37, 61; P/D = 1.125, 1.233, 1.275, 1.343, 1.417; and H/D = 8.33, 12.5, 16.67, 25.0, 50.0). Because of their consistent characteristics, Rehme's data have been widely used for calibrating models.

Bauman et al. (1968) measured pressure drop in several hexagonal bundles with different kinds of spacers. Four of them were wire-wrapped bundles, two of which were 61-pin, P/D = 1.167 and H/D = 16.7, 25.0, while the other two were 19-pin, P/D = 1.227 and H/D = 15.1, 22.7.

Reihman (1969) measured pressure drop in fourteen wire-wrapped rod bundles, most of them were 37-pin. The reported geometry of these bundles showed that the tolerances were quite large. Since no value for the looseness factor has been reported, average values calculated by assuming that the tolerance is uniformly distributed are used. This makes the P/D values of these bundles in Appendix B1 different from the reported values which were $(D+D_w)/D$. This may be the reason why Reihman's data are almost consistently higher than Rehme's correlation using the reported P/D.

Okamoto (1970) and Wakasugi (1971) performed pressure drop measurements in their JEFR 91-pin bundles with one P/D (=1.221) combined with four H/D values (=14.3, 20.6, 30.2, 41.3). Davidson (1971) measured pressure drop in a 217-pin bundle with P/D = 1.283 and H/D = 48.0. Hoffmann (1973) measure pressure drop in three 61-pin bundles with P/D =1.317 and H/D = 16.67, 33.33, and 50.0. Sodium was

used as the working fluid in Hoffmann's bundles.

At MIT, Chiu (1978b) measured pressure drop in two 61-pin simulated LMFBR blanket assemblies with P/D = 1.067 and H/D = 4.0 and 8.0. Although Chiu has measured the pressure drop at low flow rate, only two data points were in the laminar region (Re < 400). The f•Re value of 160 for the H/D = 4.0 bundle and 90 for the H/D = 8.0 bundle are believed to be too high based on our comparison, reported here, with the latest Marten (1982) data. After Chiu, the author performed a pressure drop experiment in a 37-pin bundle with P/D = 1.154 and H/D = 13.4 to fill the gap in the available data as described in Chapter 3. Recently, Efthimiadis (1983) measured pressure drop in a 19-pin bundle with P/D = 1.245 and H/D = 35.2 at very low flow rate (Re = 30 to 800).

Engel et al. (1979) measured pressure drop in four 61-pin blanket bundles, two of which were cooled by sodium and two by water. The averaged geometrical parameters of these four blanket bundles are P/D = 1.082 and H/D = 7.78. The friction factor has been correlated in a simple form. However, the correlated constants were later corrected by the authors. The reported revised form is [Markley (1982)]

$$\text{for } Re \leq 400 \qquad f = \frac{99}{Re} \tag{4.1a}$$

$$400 < Re < 5000 \qquad f = \frac{99}{Re}(1-\psi)^{1/2} + \frac{0.48}{Re^{0.25}}\psi^{1/2} \tag{4.1b}$$

$$\text{where } \psi \equiv \frac{Re-400}{4600}$$

$$5000 \leq Re \leq 4\times10^{4} \qquad f = \frac{0.48}{Re^{0.25}} \tag{4.1c}$$

Spencer (1980) measured the friction factor of several fuel bundles with N_r = 217, P/D = 1.252 and H/D = 51.74, and correlated all the data in a simple form. Carrelli et. al. (1981) measured pressure drop in a 61-pin absorber bundle which has low P/D (=1.05) and medium H/D (= 20.0).

Marten and Yonekawa (1982) recently carried out pressure drop experiments in nine 37-pin low P/D (= 1.041, 1.072, 1.101) and H/D (≃ 8.3, 12.5, 16.7) bundles. Marten's data are very valuable not only because their P/D is very low but also because very low flow rate (down to Re ≃ 50) data were measured. In these experiments, the same bundle housing was used for all nine bundles, hence the rod and wire diameters were changed to obtain the desired P/D. Excellent tolerance control resulted in very tight geometry. To evaluate the influence of the dynamic pressure caused by crossflow in the edge region, Yonekawa (1982) examined five different measuring methods in one bundle. All results were in good agreement within a deviation of only ±2%; therefore, one standard method was confirmed to be sufficient. The method used to measure all nine bundles was that of interconnecting all six pressure taps in each face such that the orientations of the wire spacers at the measuring planes need not be the same.

In addition to all the data above, data from some new test bundles of the Japanese JOYO and MONJU assemblies are also available. [Itoh (1981)].

4.2.2 Flow Split Data

Most of the flow split experiments were only performed in the turbulent flow condition. Davidson (1971) measured these parameters in a 217-pin fuel bundle (P/D = 1.283, H/D = 48.0) by the time of flight technique. Ginsberg (1973) and Lorentz (1977) investigated 7-pin (P/D = 1.2, H/D = 48.0) and 91-pin (P/D = 1.24, H/D = 48.0) bundles respectively by the isokinetic extraction method. Pederson (1974) used the time of flight method to measure flow split in another 91-pin bundle (P/D = 1.21, H/D = 48.0)

At MIT, Chen (1974) used a laser doppler anemometer to measure edge subchannel transverse and vertical flow velocities in two 61-pin bundles with the same P/D (= 1.25) but different H/D (= 24.0, 48.0). Two flow rates corresponding to Re = 640 and 4500 were performed. Chen's low flow rate data at Re = 640 were the only available laminar flow split data for low flow rate until recent work performed by Efthimiadis. Efthimiadis (1983) measured the velocity distribution in subchannels at very low flow rates with a hot wire anemometer in a 19-pin bundle (P/D = 1.245, H/D = 35.2). The detailed velocity distribution was measured at three Reynolds numbers, 80, 158 and 316, at which the flow is purely laminar.

Also, the isokinetic extraction method (IEM) was used to measure flow split parameters by Chiu (1978a) in two blanket bundles (N_r = 61, P/D = 1.067, H/D = 4.0, 8.0), by Symolon (1981) in a fuel bundle (N_r = 217, P/D = 1.25, H/D = 51.72) and by the author in a bundle with medium geometry (N_r = 37, P/D = 1.154, H/D = 13.4). The drawback of the IEM is that there is a flow rate below which no flow can be

extracted from interior subchannels while flow can still be extracted from edge subchannels. The Reynolds number corresponding to this limiting flow rate is around 3000.

In addition to these experiments, some investigators, e.g., Ohtake (1976) and Bartholet (1976), used a pitot tube to measure the detailed air flow velocity distribution in large simulated bundles.

These flow split experiments together with their data are also listed in Appendix B1.

4.2.3 Correlations for Friction Factor and Flow Split Parameter

de Stordeur (1961) investigated the drag coefficient of fuel element spacers. This method correlated data from both square and triangular rod arrays with both spiral wire and grid type spacers. His drag coefficient is around 0.4 at Re = 2×10^4 and is a slightly decreasing function of Re. The pressure drop is calculated by superimposing the drag loss and the conventional rod surface friction loss.

Sangster (1968) proposed an equivalent bundle friction factor calculated by multiplying the smooth tube friction factor from Blasius' equation by two correction factors Y and Z. The Y factor accounts for rod spacing effect and the Z factor is the spiral wire spacer effect. Sangster's method was later improved by Magee and Nilsson (1971) by using Ibragimov's (1967) results for the Y factor and by making the Z factor a function of both H/D and Reynolds number.

Novendstern (1972) developed a semiempirical model to predict pressure losses in wire-wrapped rod bundles. The model theoretically

determines the flow distribution within the fuel array and multiplies the pressure drop for a smooth pipe, using equivalent diameter techniques, by an empirical correlation factor (M) which accounts for wire effects. The M factor is able to correlate the experimental data of Reihman, Rehme and Baumann to an accuracy of ±14%.

The most widely used correlation for calculating bundle friction factor is Rehme's (1973a) model. The correlation of Rehme is based on an effective velocity to take into account the swirl flow velocity around the rods. The square of the ratio of this effective velocity (V_{eff}) to the bundle average axial velocity (V_b), F, was correlated to be

$$F \equiv \left(\frac{V_{eff}}{V_b}\right)^2 = \left(\frac{P}{D}\right)^{0.5} + \left[7.6 \left(\frac{d_m}{H}\right) \left(\frac{P}{D}\right)^2\right]^{2.16} \qquad (4.2)$$

where d_m is the wrapping diameter of spacers; for wire-wrapped bundles, $d_m = D+D_w$.

The pressure drop of a rod bundle was hypothesized by Rheme to be proportional to the square of this effective velocity and a parameter which accounts for the influence of the number of rods, i.e., the ratio of the wetted perimeter of the rod bundles (rods and wires) S_b to the total wetted perimeter S_t,

$$\Delta P = f \frac{L}{De} \frac{\rho V_b^2}{2} = \left(f' \frac{S_b}{S_t}\right) \frac{L}{De} \frac{\rho V_{eff}^2}{2} \qquad (4.3)$$

where $V_{eff} = \sqrt{F}\ V_b$

The modified friction factor f' was then calibrated as a function of the modified Reynolds number Re' using V_{eff} as the characteristic velocity to be

$$f' = \frac{64}{Re'} + \frac{0.0816}{Re'^{0.133}} \tag{4.4}$$

$$\text{where } Re' \equiv \frac{V_{eff} De}{\nu} = \frac{V_b De}{\nu}\sqrt{F} = Re\sqrt{F}$$

Expressing the pressure drop in the conventional form using the bundle average axial velocity as the characteristic velocity yields

$$\Delta p = f\frac{L}{D_e}\frac{\rho V_b^2}{2} \tag{4.5}$$

The bundle friction factor, f, of equation (4.5) can be expressed utilizing equations (4.2) and (4.3) as,

$$f = f'F\frac{S_b}{S_t}$$

$$= \left(\frac{64}{Re}\sqrt{F} + \frac{0.0816}{Re^{0.133}} F^{0.9335}\right)\frac{N_r\pi(D+D_w)}{S_t} \tag{4.6}$$

This correlation is valid for $2\times10^3 \leq Re \leq 3\times10^5$, $1.1 \leq P/D \leq 1.42$, $8 \leq H/D \leq 50$, $7 \leq N_r \leq 217$ as later confirmed by the author from the available data in Appendix B. The accuracy of this correlation is around ±8% in the turbulent region.

For $Re > 2\times10^4$, a simpler version of the modified friction factor, f', was reported by Hoffmann (1973),

$$f' = 0.1317Re'^{-0.17} \tag{4.6}$$

The above correlations are applicable primarily in the turbulent region, although Rehme's correlation is valid down to Re = $2x10^3$. For the laminar flow condition, Engel et al. (1979) developed a simple correlation based upon the very limited data base available at that time [Chiu(1978b): P/D = 1.067, H/D = 4.0, Engel(1979): P/D =1.082, H/D =7.78, Spencer(1980): P/D = 1.252, H/D =51.74]; the proposed correlation was

$$f \cdot Re = \frac{320}{\sqrt{\bar{H}}} \ (P/D)^{1.5} \qquad (4.7)$$

where H is in cm.

Note that the application of this correlation appears limited to the two extreme geometry conditions of the data base, and the laminar friction factor constant f•Re is not expressed as a function of the nondimensional parameter H/D.

Hawley, Chiu and Todreas (1980) are the first investigators to develop friction factor models from the subchannel point of view. The flow split parameters can be calculated from the subchannel friction factors. These are the 1980 MIT correlations, and they have been discussed in detail in the first chapter.

Recently, Carajilescov and Fernandez(1982) developed a semi-empirical model for subchannel friction factors and flow split parameters. However, their data base is very limited.

4.3 SUBCHANNEL FRICTION FACTOR FORMULATIONS

4.3.1 Subchannel Friction Factor Models

The definition of the friction factor, f, in our models is in terms of the total loss of mechanical energy per unit volume, $\hat{e}$, caused by the total drag force over a length L. This energy loss $\hat{e}$ is defined as

$$\hat{e} \equiv f \frac{L}{De}\left(\frac{\rho V^2}{2}\right) \tag{4.8}$$

where De (equivalent hydraulic diameter) $\equiv 4A/P_w$. Note that the parameters A and P_w, and hence D_e, include the presence of the wire in the subchannel, axially averaged over one lead length. The subchannel friction factors can then be formulated from equation (4.8), if one can express the total mechanical energy loss, $\hat{e}$, by some models for each type of subchannel.

Since the flow phenomena in a wire-wrapped LMFBR subassembly are very complicated, no simple models such as those we are going to propose can precisely simulate the drag loss. On the other hand, the models themselves must reflect physical reality; otherwise, they may not be able to correlate the experimental data. Therefore, we try to include the most important physical effects by geometrical factors within these models, and incorporate all the other effects of the presence of the wire into the empirical constants.

In our approach for a wire-wrapped subassembly there are two regions with different flow characteristics: an interior region with an

axial velocity for all interior subchannels, and an edge region with a constant swirl velocity along the assembly wall and one axial velocity for all edge subchannels. However, we will not assume that the corner subchannel axial velocity equals the edge subchannel axial velocity. Consequently, three friction factor equations, i.e., interior, edge, and corner, need to be formulated.

4.3.1.1 Interior Subchannel

Figure 4.1 schematically shows an interior subchannel. Although the real flow direction should be slightly inclined to the wire direction, the effective transverse velocity component should not be significant due to the fact that the the wires change direction every one-third of a lead length. Hence, we assume that the axial velocity, V_1, shown in Figure 4.1, can be used as the characteristic velocity in modeling the drag loss.

The total mechanical energy loss in the interior subchannel is comprised of two parts: a) the friction loss caused by the fuel rod surface and b) the drag loss caused by the wire, i.e.,

$\hat{e}_1 = \hat{e}_f + \hat{e}_d$.

The friction loss along the fuel rod surface can be calculated by:

$$\begin{aligned}\hat{e}_f &= F_f(\text{force caused by friction})/A_1(\text{average flow area}) \\ &= [\tau(\text{average shear stress})\cdot P'_{w1}(\text{wetted perimeter of fuel rod surface})\cdot L] \,/\, A_1 \end{aligned} \qquad (2.2)$$

where $\tau = (\frac{f'_1}{4})(\frac{\rho V_1^2}{2})$

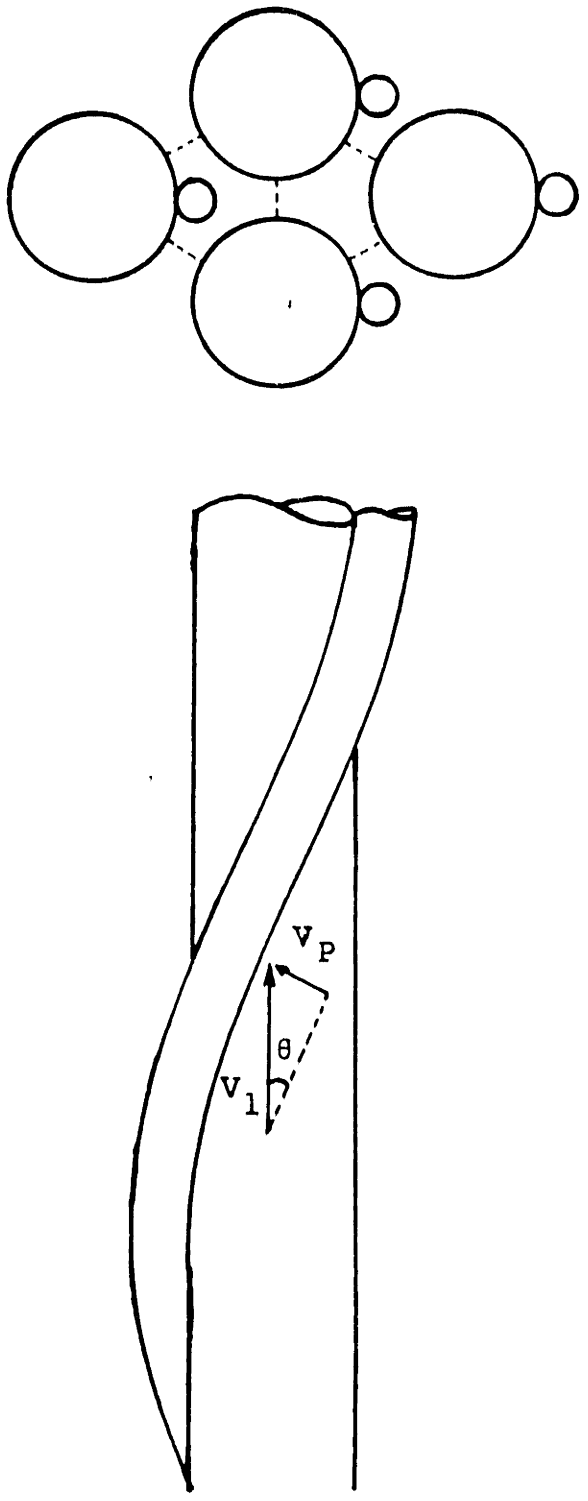

Figure 4.1 Velocity Components and Schematic Configuration of an Interior Subchannel

and $P'_{wl} = \frac{\pi D}{2}$, where the super prime notation refers to the convention that the parameter is calculated based on a bare rod geometry; i.e., the wire presence is not included.

Therefore,

$$\hat{e}_f = (\frac{f'_l}{4})(\frac{\rho V_l^2}{2})P'_{wl}L/A_l \qquad (4.10)$$

$$= f'_l(\frac{P'_{wl}}{P_{wl}})[\frac{L}{De_l}\frac{\rho V_l^2}{2}]$$

where P_{wl} = wetted perimeter of interior subchannel including the averaged wire surface effect

$$= \frac{\pi D}{2} + \frac{\pi D_w}{2\cos\theta}$$

In calculating the average shear stress around fuel rod surface, τ, we assume that the bare rod friction factor formulation can be used to calculate f'_l, i.e.,

$$f'_l = K_l \; / \; Re_l^{\,m} \qquad (4.11)$$

where K_l is derived from bare rod results.

Re_l = interior subchannel Reynolds number

$\rho V_l De_l/\mu$

m = exponent which depends on flow region;

This assumption is made for two reasons: 1) the effect of wire on the spatial distribution of the velocity field, hence the average shear

stress, hence the real friction factor, is not clear; for simplicity, the wire effect is neglected; and 2) equation (4.10) and (4.11) can be easily reduced to the bare rod case as the wire diameter goes to zero.

For the drag loss of the wire, since the wire covers the flow region from the wall to a position near which the velocity is maximum, the average velocity striking the wire can be taken as approximately the same as the average subchannel velocity. Hence the axial average velocity V_l is used as the characteristic velocity. The drag loss experienced by the fluid slipping over the wire can be represented as

$$\hat{e}_d \propto C_d\left(\frac{\rho V_l^2}{2}\right) \tag{4.12}$$

where C_d is a proportional constant; formally a drag coefficient. Note that here we simply use the subchannel average velocity V_l as the characteristic velocity rather than that of the wall velocity, V_w, as in Chiu's model. The geometrical influence on this flow phenomena will be included in C_d, which is a function of both geometrical parameters and flow regime. Since only fluid encountering the wire experiences this drag loss, the average drag loss for a single crossing of a wire for the total flow in the interior subchannel should be

$$\hat{e}_d = \left(\frac{A_{rl}}{A_l'}\right)C_d\left(\frac{\rho V_l^2}{2}\right) \tag{4.13}$$

where $A_{rl} = \dfrac{\pi(D+D_w)D_w}{6}$ (projected area of wire wrap)

$A_l' = \dfrac{\sqrt{3}}{4}P^2 - \dfrac{\pi D^2}{8}$ (bare subchannel flow area)

Alternatively, one might use the perpendicular velocity, V_p ($=V_1 \sin\theta$) to calculate the drag force exerting on the fluid in the direction perpendicular to the wire wrap,

$$F_D = A_{r1} C_D \left(\frac{\rho V_p^2}{2}\right) \tag{14.14}$$

Projecting this force into the axial direction and dividing by the axial area for flow, we have the mechanical energy loss per unit volume in the axial direction caused by this drag force

$$\hat{e}_d = \frac{F_D \sin\theta}{A_1'} = \frac{A_{r1}}{A_1'} (C_D \sin^3\theta)\left(\frac{\rho V_1^2}{2}\right) \tag{4.15}$$

According to the independence principle, C_D can be taken as the conventional value for a circular cylinder for flow in a inclined (bare) rod bundle [Ebeling-Koning(1983)]. The reason that this argument is not used is that helical wire wrap is much more complicated than a straight circular rod, hence the independence principle and the conventional C_D might not valid in this case. On the other hand, equation (4.15) is similar to equation (4.13) except that $C_D \sin^3\theta$ is combined into one constant C_d. It is later found that C_d is easier to correlate than C_D, not to mention that C_D could be a single constant.

Over length L, the fluid will encounter wire 3(L/H) times; therefore, the total wire drag loss over L is,

$$\hat{e}_d = 3\left(\frac{L}{H}\right)\left(\frac{A_{r1}}{A_1'}\right) C_d \left(\frac{\rho V_1^2}{2}\right)$$

$$= \left[3C_d \left(\frac{A_{r1}}{A_1'}\right)\left(\frac{De_1}{H}\right) \right] \frac{L}{De_1} \frac{\rho V_1^2}{2} \tag{4.16}$$

The total mechanical energy loss for an interior subchannel is

$$\hat{e}_1 = \hat{e}_f + \hat{e}_d$$

$$= \left[f_1' \left(\frac{P_{w1}'}{P_w}\right) + C_d \left(\frac{3A_{r1}}{A_1'}\right)\left(\frac{De_1}{H}\right) \right] \frac{L}{De_1} \frac{\rho V_1^2}{2} \tag{4.17}$$

The interior subchannel friction factor is then formulated as

$$f_1 = f_1' \left(\frac{P_{w1}'}{P_{w1}}\right) + C_d \left(\frac{3A_{r1}}{A_1'}\right)\left(\frac{De_1}{H}\right) \tag{4.18}$$

4.3.1.2 Edge Subchannel

As described earlier, because the wires are in the same direction, the flow in the edge subchannel is assumed to have a constant helical velocity which is more or less following the wire. Figure 4.2 schematically depicts this situation. In this case, it is reasonable to assume that the form drag loss of wire is negligible compared to the skin friction associated with the swirl velocity since only a very small velocity component slips over the wire.

Seban and Hunsbedt (1973) performed water experiments in an annulus in which swirl flow was produced by a single helical vane. They found that the friction force can be predicted by utilizing the helical path length and hydraulic diameter. For an edge subchannel defined as one in the upper part of Figure 4.2, one finds that the flow characteristics in this subchannel are very similar to the annular swirl flow channel. The drag loss in the edge subchannel can then be calculated as

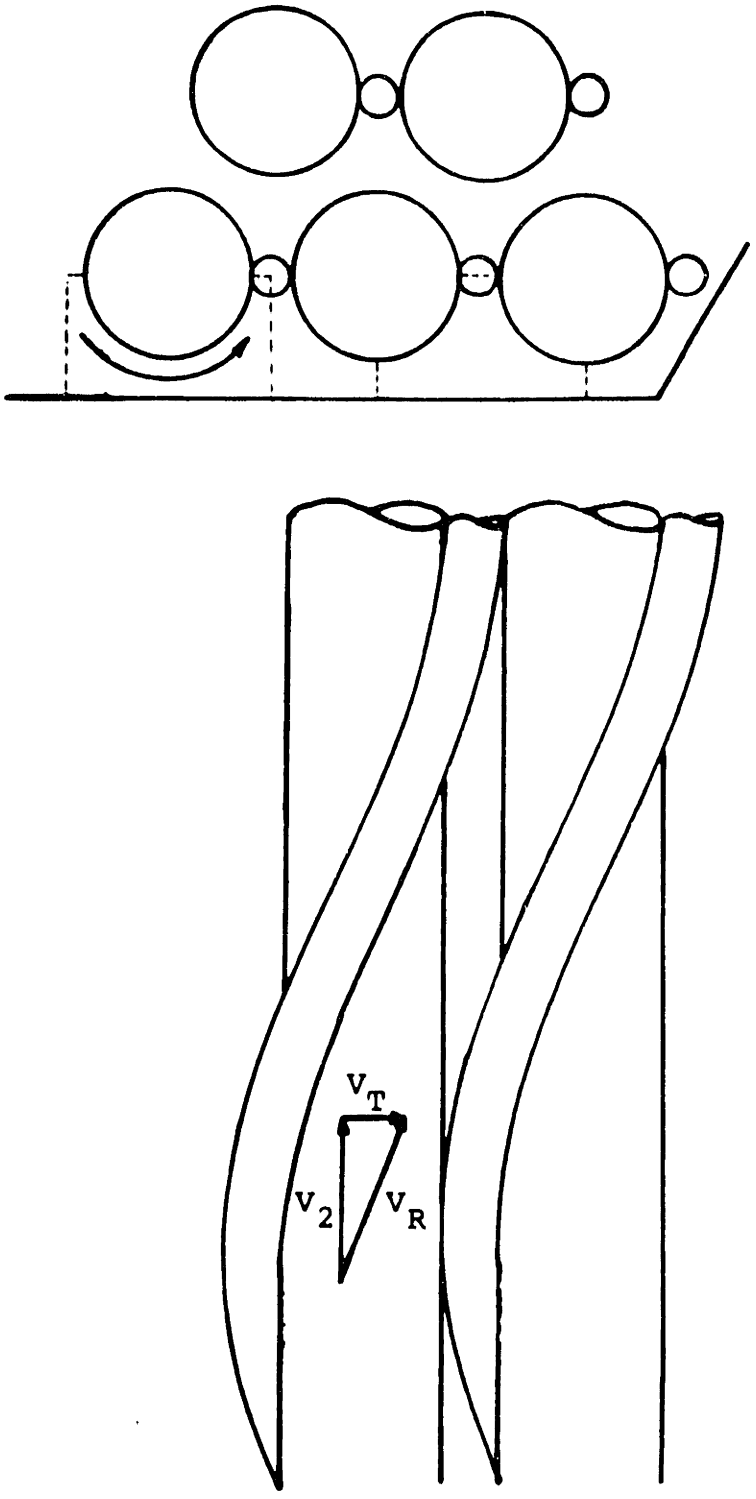

Figure 4.2 Velocity Components and Schematic Configuration of an Edge Subchannel

$$\hat{e}_{friction} = f_R \frac{L_R}{De_R} \frac{\rho V_R^2}{2} \tag{4.19}$$

where R denotes the parameters based on the swirl flow path

L_R = flow path travelled by the swirl flow for an axial length, L

V_R = resultant velocity of the swirl flow

f_R = friction factor corresponding to the swirl flow

De_R = equivalent hydraulic diameter corresponding to the swirl flow

To find V_R and L_R, one needs to know the transverse velocity V_T. If the flow follows the wire exactly, the transverse velocity V_T should be $V_2 \tan\theta$. However, according to some investigators (e.g., Ginsberg and Lorentz(1973)), the flow direction is not exactly following the wire direction, but slightly deviating from it. Nevertheless, it is reasonable to assume that the ratio V_T/V_2 is proportional to $\tan\theta$. Further, the ratio of transverse velocity head to axial velocity head is assumed to be proportional to the ratio of flow area covered by the wire to the total bare subchannel flow area, which reduces to zero when the wire diameter goes to zero. This will be discussed in more detailed in Chapter 6 when the model for transverse velocity at the gap is derived. Hence,

$$(\frac{V_T}{V_2})^2 = C_s(\frac{A_{r2}}{A_2'}) \tan^2\theta \tag{4.20}$$

Where C_s = constant of proportionality, a function of geomery

$A_{r_2} = \pi(D + D_w)D_w/4$

$A2' = P(W-D/2) - \pi D^2/8$

$$\tan\theta = \pi(D+D_w)/H$$

The resultant velocity V_R and the swirl flow path L_R can then be calculated as (refer to Figure 4.2)

$$V_R = V_2 F_R \tag{4.21a}$$

and

$$L_R = L\ F_R \tag{4.21b}$$

where

$$F_R \equiv \left[\ 1 + \left(\frac{V_T}{V_2}\right)^2\ \right]^{\frac{1}{2}}$$

$$= \left[\ 1 + C_s\left(\frac{A_{r2}}{A_2}\right)\tan^2\theta\ \right]^{\frac{1}{2}}$$

The friction factor f_R can be calculated by

$$f_R = \frac{C}{Re_R^{\,m}} \tag{4.22}$$

where C is a function of both geometry and flow regime and m is function of flow regime only. Now we approximate the equivalent hydraulic diameter for the swirl flow, De_R, to be the axial value, De_2. This approximation is close because of the canceling effects of changes in the flow area and wetted perimeter which are both projected to a new plane perpendicular to the swirl flow direction. Hence

$$f_R = \frac{C}{\left(\frac{\rho V_R De_R}{\mu}\right)^m} \simeq \frac{C}{Re_2^m F_R^m} \tag{4.23}$$

where $Re_2 = \rho V_2 De_2/\mu$

The constant C is assumed to be the same as that in the bare rod edge subchannel friction factor for the same reasons as described for interior subchannel case. Thus equation (4.23) can be written as

$$f_R = f'_2 / F_R^m \tag{4.24}$$

where $f'_2 = K_2/Re_2^m$, and K_2 is derived from bare rod results.

Substituting V_R, L_R, and f_R into equation (4.19), we have

$$\hat{e}_2 \equiv \hat{e}_{friction}$$

$$= f'_2\left[1 + C_s\left(\frac{A_{r2}}{A'_2}\right)\tan^2\theta\right]^{\frac{3-m}{2}} \frac{L}{De_2} \frac{\rho V_2^2}{2} \tag{4.25}$$

The edge subchannel friction factor is then formulated as

$$f_2 = f'_2\left[1 + C_s\left(\frac{A_{r2}}{A'_2}\right)\tan^2\theta\right]^{\frac{3-m}{2}} \tag{4.26}$$

4.3.1.3 Corner Subchannel

Since the flow characteristics in the corner subchannel are the same as those in the edge subchannel, we assume that equation (4.26) can also be used in this case, except that the bare rod subchannel friction factor constant and geometrical factors should be changed to the corresponding corner subchannel values. Therefore,

$$f_3 = f'_3\left[1 + C_s\left(\frac{A_{r3}}{A'_3}\right)\tan^2\theta\right]^{\frac{3-m}{2}} \tag{4.27}$$

where $A_{r3} = \dfrac{\pi(D + D_w)D_w}{6}$

$$A'_3 = \frac{(W - \frac{D}{2})^2}{\sqrt{3}} - \frac{\pi D^2}{24}$$

4.3.2 Formulations and Empirical Constants for the Laminar and Turbulent Regions

The subchannel friction factor models, equations (4.18), (4.26) and (4.27), are applicable to all flow regimes since no special flow condition restriction has been imposed. The flow regime effect, which is essentially the Reynolds number dependence, appears in the constants f'_1, f'_2, f'_3, m, C_d and C_s. Next formulations for each of these necessary constants are presented.

For the laminar and turbulent regions, the friction factor data show a simple dependence on Reynolds number, i.e., f = constant/Re^m. Hence we will formulate f'_i in this form for laminar and turbulent flow regimes. The exponent m in laminar flow is 1.0, which is obtained from the analytically derived behavior of a simple geometrical flow channel. In turbulent flow for Reynolds numbers higher than 20,000, this exponent is around 0.2 for smooth tubes; however, the bundle average friction factor results derived from pressure drop data show that the average exponent is around 0.18 in this flow regime. The averaged value for m considering the bundle friction factor data for 122 wire-wrapped bundles is 0.1798 as shown in Appendix B. This low value might be caused by the surface roughness of the simulated rods in the experiments. The bare rod subchannel friction factors can then be expressed as

$$\text{Laminar region:} \quad f'_i = \frac{K_{iL}}{Re_i} \tag{4.28a}$$

$$\text{Turbulent region:} \quad f'_i = \frac{K_{iT}}{Re_i^{0.18}} \tag{4.28b}$$

where K_{iL} and K_{iT} are functions of P/D for the interior subchannel, and W/D for the edge or corner subchannel.

The drag coefficient C_d is not exactly the same as that usually seen in the literature; rather, it is a proportional constant for our models. Rehme (1973a,1980b) did some measurements for the drag coefficient of the grid spacer bundles and found that it was a slightly decreasing function of Reynolds number at high Reynolds number flow conditions. For simplicity, we assume that C_d has the same Reynolds number dependence as f_1' in the turbulent region. In the laminar flow condition, C_d is expected to have (1/Re) dependence from both theoretical derivation and experimental results. Hence

$$\text{Laminar region:} \quad C_d = \frac{W_{dL}}{Re_{D_w}} = \frac{W_{dL}}{Re_1 (\frac{D_w}{De_1})} \tag{4.29a}$$

$$\text{Turbulent region:} \quad C_d = \frac{W_{dT}}{Re_{D_w}^{0.18}} = \frac{W_{dT}}{Re_1^{0.18} (\frac{D_w}{De_1})^{0.18}} \tag{4.29b}$$

where the constants W_{dL} and W_{dT} are directly related to the wire effect which should be influenced by both the wire diameter and wrapping angle; therefore, we expect that the W_d's are functions of both Dw/D and H/D. Note that the Reynolds number calculated by using D_w as the characteristic length is used for this wire drag coefficient.

The constant C_s is the empirical factor which accounts for the assumptions used in deriving the edge subchannel friction factor. In addition to this function, C_s is the proportionality factor between

the real $(V_T/V_2)^2$ and the geometrical factor in equation (4.20). However, one should realize that (V_T/V_2) in equation (4.20) is not exactly the same as the edge transverse velocity ratio C_{1L} reduced from mixing experiments. The edge transverse velocity ratio C_{1L} only accounts for the flow transported from one edge subchannel to the adjacent one rather than the swirl flow along the rod as the formulation leading to equation (4.20) assumed. Nevertheless, the behavior of the edge transverse velocity ratio could indicate the characteristics of C_s, i.e., constant value in the turbulent flow regime but a decreasing function of Reynolds number in the transition region leading to another constant value in the laminar region. Therefore, we expect that C_s's are constants in the turbulent and laminar regions, but they should be different values. On the other hand, the edge transverse velocity ratio is a strong function of H/D, hence we expect that C_s might also be a function of H/D. By analogy with equation (4.29) for C_d, we write C_s in terms of W_s/Re^n where here n = 0 since there is no Re variation in the laminar or turbulent regions, i.e.,

$$\text{Laminar region:} \quad C_s = W_{sL} \tag{4.30a}$$

$$\text{Turbulent region:} \quad C_s = W_{sT} \tag{4.30b}$$

where W_{sL} and W_{sT} are functions of H/D.

Substituting equations (4.28), (4.29), (4.30) into equations (4.18), (4.26) and (4.27), we have the final forms for the subchannel friction factors equations,

$$f_1 = \frac{1}{Re_1^m}\left[K_1\left(\frac{P'_{w1}}{P_{w1}}\right) + W_d\left(\frac{3A_{r1}}{A'_1}\right)\left(\frac{De_1}{H}\right)\left(\frac{De_1}{D_w}\right)^m\right] \quad (4.31)$$

$$= C_{f1}/Re_1^m$$

$$f_2 = \frac{1}{Re_2^m}\left[K_2\left(1 + W_s\left(\frac{A_{r2}}{A'_2}\right)\tan^2\theta\right)^{\frac{3-m}{2}}\right] \quad (4.32)$$

$$= C_{f2}/Re_2^m$$

$$f_3 = \frac{1}{Re_3^m}\left[K_3\left(1 + W_s\left(\frac{A_{r3}}{A'_3}\right)\tan^2\theta\right)^{\frac{3-m}{2}}\right] \quad (4.33)$$

$$= C_{f3}/Re_3^m$$

where m = 1.0 for the laminar flow region

m = 0.18 for the turbulent flow region

K_1 = function of P/D

K_2, K_3 = function of W/D

W_d = function of D_w/D and H/D

W_s = function of H/D

4.3.3 Formulation and Empirical Constants for the Transition Region

4.3.3.1 Reynolds Numbers at Transition Points

Unlike the circular tube case, in which an obvious transition from laminar to turbulent flow conditions occurs around Re = 2,300, the transition within a rod bundle occurs as early as Re_b around 400 to 1000 with only slight deviation from laminar behavior as Re_b

increases. The log-log plot of the friction factor curve gradually changes its slope at a Re_{bL}, which depends on the P/D of the rod bundle, until $Re_b \simeq 12000$ to 20000. After this Re_{bT} the slope is nearly a constant. The flow behavior in the transition range can be explained by the assumption that turbulence first appears in the center region of the subchannel and spreads progressively in the radial and circumferential directions with sufficient increase in Reynolds number, until laminar flow eventually disappears [Panknin et al. (1974)]. The Reynolds numbers for laminar-transition, Re^{bL}, and transition-turbulent, Re_{bT}, are required for the application of our model. These two values will be determined next.

Correlations that are assumed to qualitatively estimate the transition Reynolds number at the turbulent-transition and laminar-transition points for infinite bare triangular rod array have been proposed by Ramm et al. (1974) and Yang (1976) respectively. Ramm et al. calculated average value of the eddy diffusivity of momentum along the gap, $(\bar{\varepsilon}_{Mr}/\nu)_{\phi=0}$ and assumed that at $(\bar{\varepsilon}_{Mr}/\nu)_{\phi=0} = 0.2$ onset of laminarization starts at the gap region, i.e., the flow transits from the turbulent to the transition regime. A value of 0.3 for $(\bar{\varepsilon}_{Mr}/\nu)_{\phi=0}$ was later proposed by Johannsen (1981) to improve the correlation. Yang (1976) used a certain average value of the eddy diffusivity of momentum over the whole subchannel, $(\bar{\varepsilon}_{Mr}/\nu)$, as the criterion for the inception of flow transition and applied Ramm's (1975) Model to compute the transition Reynold's number. For the onset of transition from laminar to turbulent flow, he chose a value of 0.5 for the space-averaged eddy diffusivity $(\bar{\varepsilon}_{Mr}/\nu)$ as the qualitative criterion.

Figure 4.3 illustrates the Reynolds numbers from these two correlations as functions of P/D of an infinite triangular rod array.

Figure 4.4 shows the values of bundle Reynolds number for onset of transition from laminar to turbulent flow, Re_{bL}, from the friction factor data obtained by Rehme (1972) for bare rod bundles and other investigators for wire-wrapped rod bundles. The Reynolds number at which friction factor deviates from 1/Re behavior is assumed to be the laminar-transition point as illustrated in Figure 4.5 for bundles with P/D = 1.1. For $P/D \leq 1.1$ the data show that Re_{bL} is nearly a constant around 400. For $P/D > 1.1$, $\log (Re_{bL})$ is proportional to P/D. As shown in Figure 4.3 Yang's correlation for onset of transition can not predict the trend of data. The reasons for this inability might be : 1) the inception of turbulence is a local effect which will occur at $\phi = 30°$ of the characteristic geometry (c.f. Figure 4.3). Hence, chosing the eddy of diffusivity at $\phi = 30°$ would be more appropriate than an average value over whole subchannel, and 2) the application of the adopted eddy diffusivity expressions from Ramm's model far below their stated range of applicability regarding the Reynolds number which is $10^4 \leq Re \leq 2x10^5$ is questionable. Since Yang's model can not predict the data, we develop a purely empirical correlation to calculate Re_{bL} from these data, (c.f. Figure 4.4)

$$\log(\frac{Re_{bL}}{300}) = 1.7\ (\frac{P}{D} - 1.0) \qquad (4.34a)$$

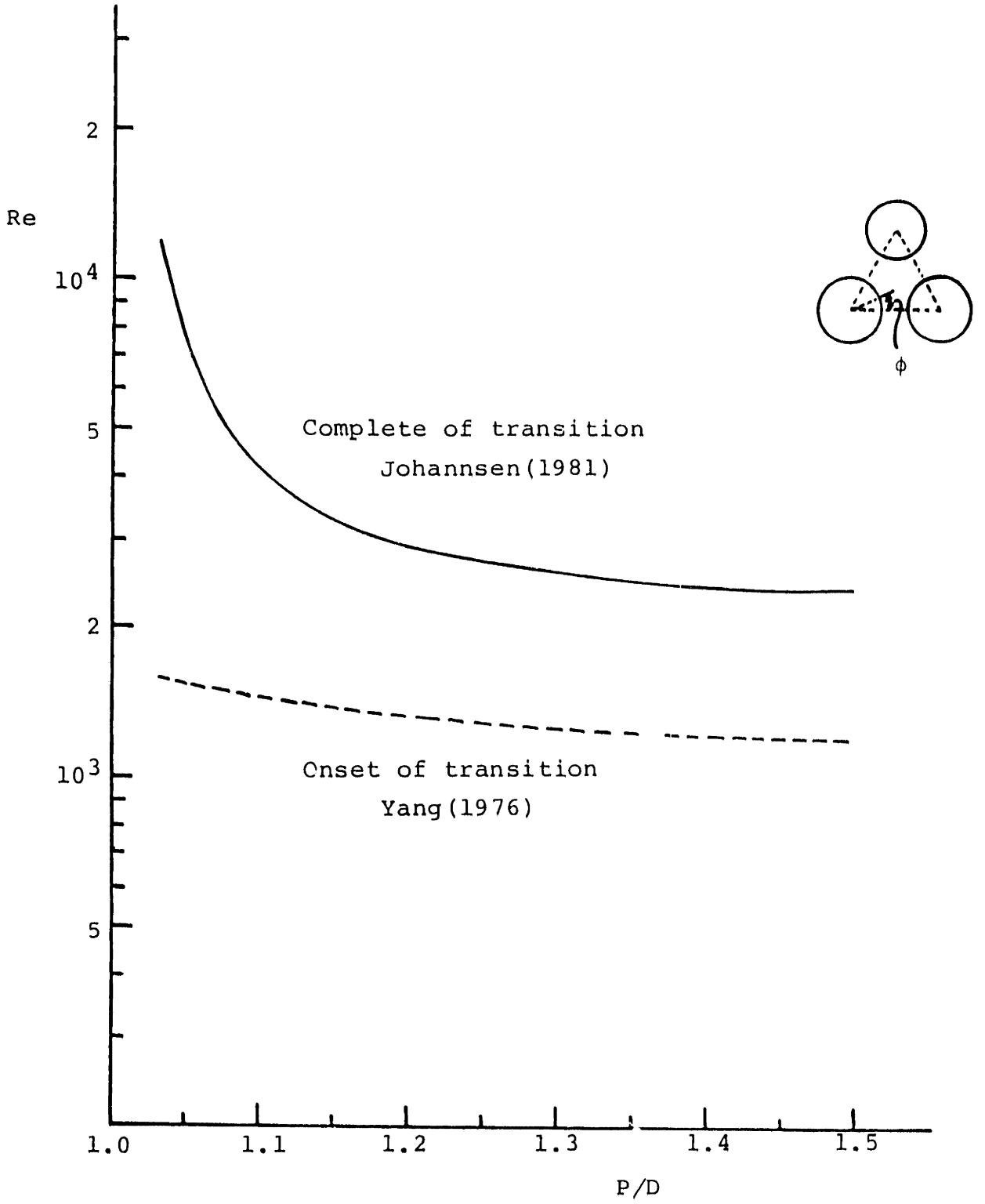

Figure 4.3 Ramm and Johannsen Correlation and Yang Correlation for Reynolds Number at Transition Points

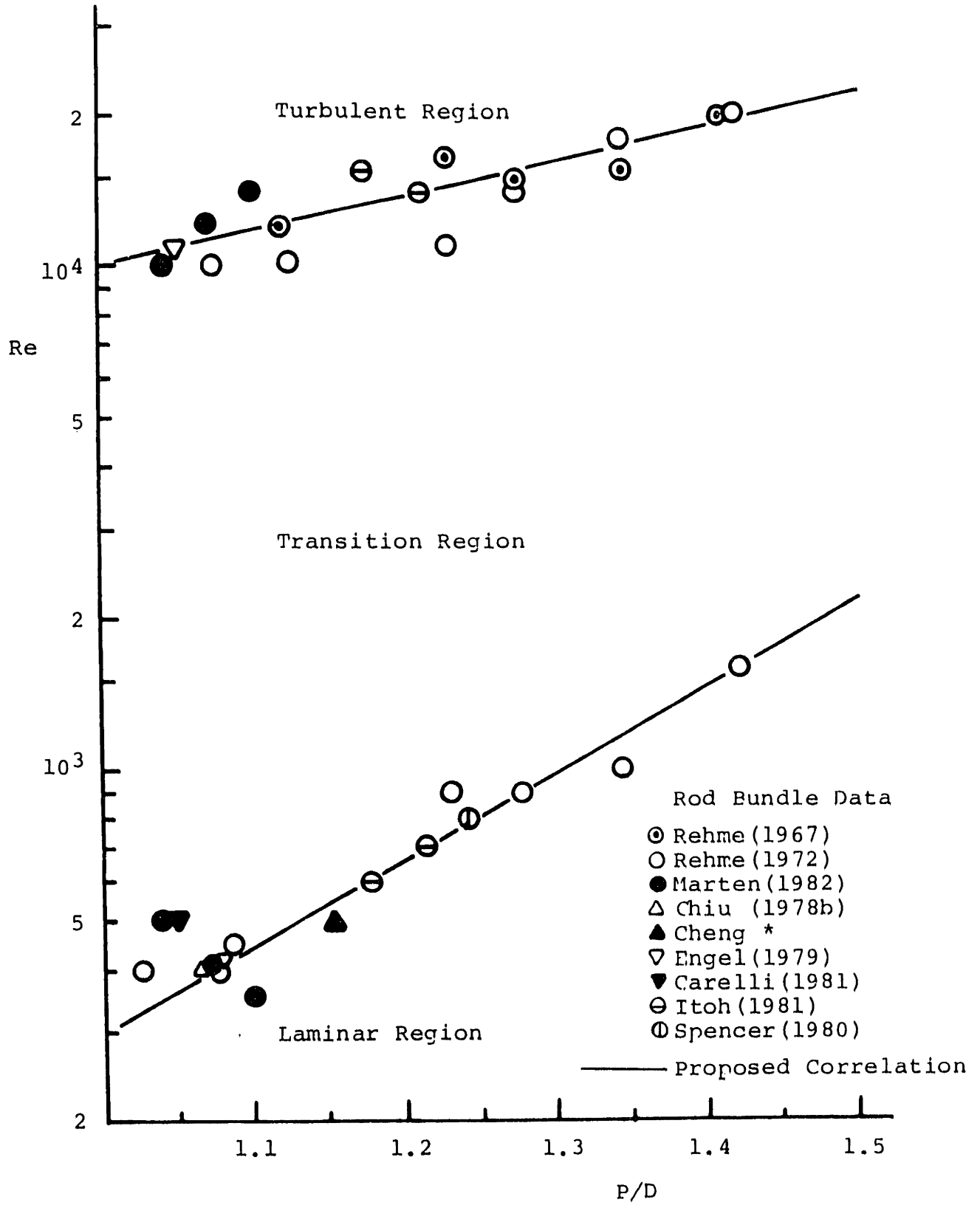

Figure 4.4 Data and Proposed Correlations for the Transition Reynolds Number

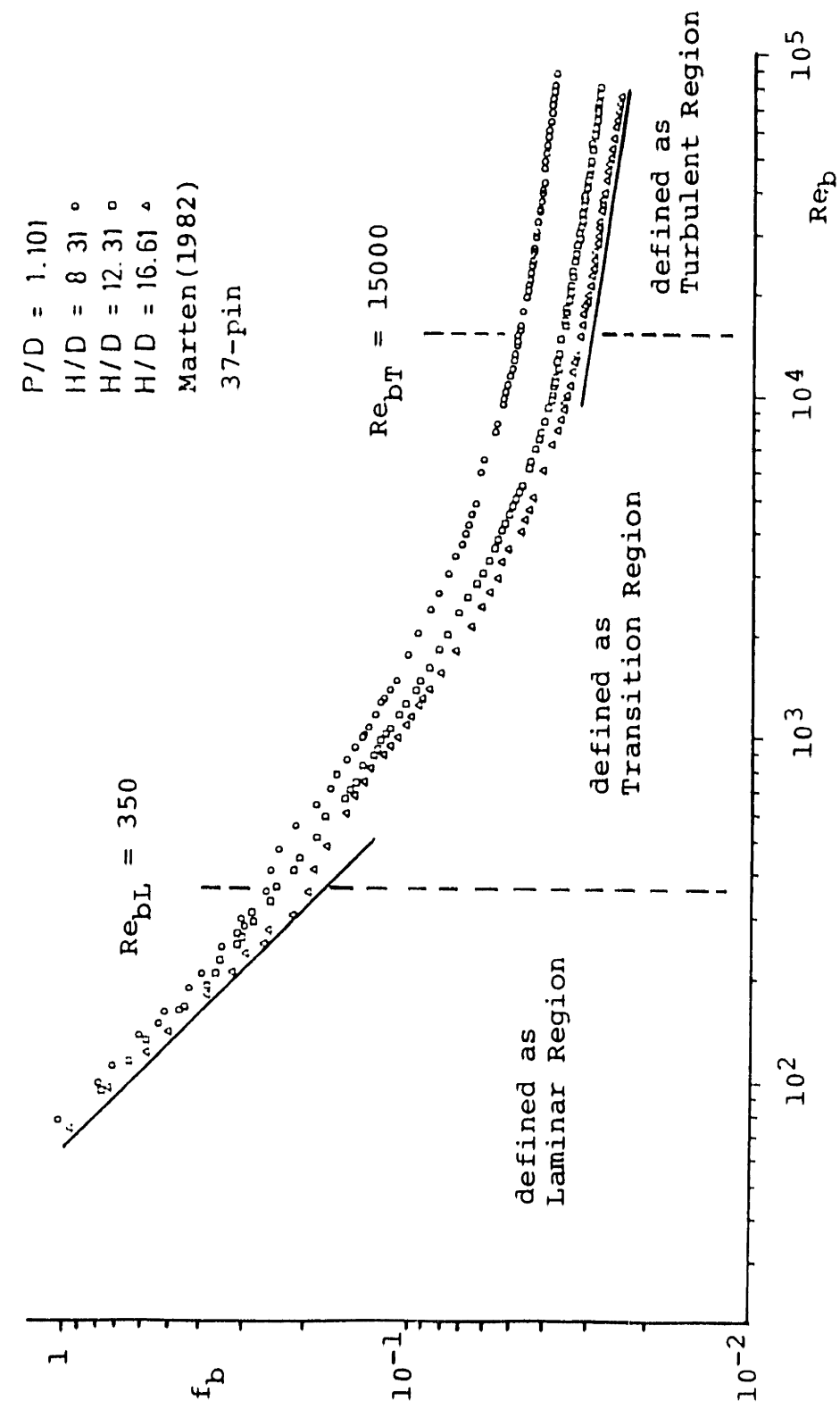

Figure 4.5 Illustration of Re_{bL} and Re_{bT} from Friction Factor Data

Although fully turbulent flow may be achieved much earlier than Re_b = 12000 to 20000 as predicted by Johannsen's model, the slope for log(f) vs. log (Re_b) shows a constant value after a Re_{bT} = 12000 to 20000 from almost all the rod bundles friction factor data. For easy formulation of the correlations, a constant exponent for Reynolds number in the friction factor formulation in the turbulent flow regime is required. Hence a Re_{bT} after which the slope is constant is artifically set to be the point beyond which we call the turbulent flow regime. These Re_{bT}'s are also shown in Figure 4.4. The way to get this Re_{bT} is also illustrated in Figure 4.5. Similar to Re_{bL} a purely empirical correlation is developed to calculate Re_{bT} from these data,

$$\log(\frac{Re_{bT}}{10000}) = 0.7\ (\frac{P}{D} - 1.0) \qquad (4.34b)$$

The subchannel transition region for each kind of subchannel is calculated based on the laminar and turbulent flow split values together withthe Re_{bL} and Re_{bT} criteria. That is we assume that all subchannels start transition at $Re_b = Re_{bL}$ and reach the fully turbulent condition at $Re_b = Re_{bT}$.

4.3.3.2 Formulation and Empirical Constant

For the transition region, we cannot simply formulate the constants m, f'_i, C_d, and C_s, since m and C_s as well as the constants in the numerator of f'_i and C_d are functions of Reynolds number.

Spriggs (1973) successfully used an intermittency factor as a weighting factor to linearly combine the laminar value and the turbulent value for calculating the friction factor for transition flow regime in a circular tube. The intermittency factor, whose value ranges from zero to unity, can be considered to represent that fraction of the flow field which is turbulent in a specified flow subchannel. Based on this argument, we propose the transition subchannel friction factors to be

$$f_{itr} = f_{iL}(1 - \psi_i)^{\gamma} + f_{iT}\psi_i^{\gamma} \qquad (4.35)$$

where $f_{iL} = C_{fiL}/Re_i$

$f_{iT} = C_{fiT}/Re_i^m$

γ = exponent fitted from data

ψ_i = intermittency factor

$$\equiv \frac{\log Re_i - \log Re_{iL}}{\log Re_{iT} - \log Re_{iL}}$$

Re_{iL} = subchannel Reynolds number at which flow starts transition for subchannel i

$= Re_{bL}(De_i/De_b)X_{iL}$

Re_{iT} = subchannel Reynolds number at which flow reaches full turbulence for subchannel i

$= Re_{bT}(De_i/De_b)X_{iT}$

The exponent of ψ_i and $(1 - \psi_i)$, γ, is the empirical constant implemented in the correlation in order to fit the data. Engel et al. (1979) successfully used equation (2.26) with $\gamma = 0.5$ to fit their blanket subassemblies' bundle average friction factor; however, their

definition of intermittency factor is different from our definition. (see equation (4.1)) Differences exist in the criteria for turbulent Reynolds number and the use of a log function in our definition of ψ_i. Note that $\gamma = 1$ means a linear combination of f_{iL} and f_{iT}, while a higher γ value gives a lower f_{itr}; and a lower γ value gives a higher f_{itr}.

4.3.4 Flow Split Parameters and Bundle Average Friction Factor

The subchannel friction factor formulae have been derived in the last two sections. From these equations one can derive the formulae for flow split parameters and bundle average friction factor. For fully developed flow over a length L which is several lead lengths long, the momentum transfer between subchannels can be assumed to be negligible; therefore, the pressure drop along this length for each kind of subchannel can be calculated from the momentum balance:

$$\Delta P_i = f_i \frac{L}{De_i} \frac{\rho V_i^2}{2}$$

By the equal subchannel pressure drop assumption and the mass continuity requirement, one has

$$\frac{f_b}{De_b} = \frac{f_1}{De_1} X_1^2 = \frac{f_2}{De_2} X_2^2 = \frac{f_3}{De_3} X_3^2 \qquad (4.36)$$

and

$$S_1 X_1 + S_2 X_2 + S_3 X_3 = 1 \qquad (4.37)$$

where $S_1 = \frac{N_1 A_1}{A_b}$, $S_2 = \frac{N_2 A_2}{A_b}$, $S_3 = \frac{N_3 A_3}{A_b}$

These are similar to equations (1.2) and (1.3), except that X_3 is also an unknown rather than assumed to equal X_2. Now we have four equations with seven parameters, f_1, f_2, f_3, X_1, X_2, X_3 and f_b. Since the three parameters, f_1, f_2, and f_3 were given, we can solve equations (4.36) and (4.37) to get the remaining four parameters, X_1, X_2, X_3 and f_b.

4.3.4.1 Turbulent and Laminar Regions

For turbulent and laminar regions, f_i (i = b, 1, 2 or 3) can be simply expressed as (cf. equations (4.31), (4.32), (4.33))

$$f_i = \frac{C_{fi}}{Re_i^m} \tag{4.38}$$

Substituting equation (4.38) into equation (4.36) and assuming that the kinetic viscosity, ν, is constant over the bundle cross section, we have

$$\begin{aligned} \frac{C_{fb}}{De_b}\left[\frac{1}{De_b}\right]^m &= \frac{C_{f1}}{De_1}\left[\frac{1}{De_1 X_1}\right]^m X_1^2 \\ &= \frac{C_{f2}}{De_2}\left[\frac{1}{De_2 X_2}\right]^m X_2^2 \\ &= \frac{C_{f3}}{De_3}\left[\frac{1}{De_3 X_3}\right]^m X_3^2 \end{aligned} \tag{4.39}$$

The ratio between velocities, (X_i/X_j), ($X_b = 1.0$ by definition), is

$$\frac{X_i}{X_j} = \left[\frac{De_i}{De_j}\right]^{\frac{1+m}{2-m}} \left[\frac{C_{fj}}{C_{fi}}\right]^{\frac{1}{2-m}} \tag{4.40}$$

From the mass continuity equation (4.37), the edge subchannel flow split parameter is

$$X_2 = \frac{1}{S_2 + \left[\frac{X_1}{X_2}\right]S_1 + \left[\frac{X_3}{X_2}\right]S_3} \tag{4.41}$$

where from equation (4.40)

$$\frac{X_1}{X_2} = \left[\frac{De_1}{De_2}\right]^{\frac{1+m}{2-m}}\left[\frac{C_{f2}}{C_{f1}}\right]^{\frac{1}{2-m}} \tag{4.42}$$

$$\frac{X_3}{X_2} = \left[\frac{De_3}{De_2}\right]^{\frac{1+m}{2-m}}\left[\frac{C_{f2}}{C_{f3}}\right]^{\frac{1}{2-m}} \tag{4.43}$$

Equations (4.41), (4.42) and (4.43) are the formulae for flow split parameters in the turbulent and laminar regions. After the constants C_{f1}, C_{f2} and C_{f3} are determined, they can be used to calculate X_i.

For bundle average friction factor, the constant C_{fb} can be derived by substituting X_i/X_b, $i = 1, 2, 3$, from equation (4.40) into equation (4.37), that is,

$$\sum_{i=1}^{3} S_i \left[\frac{De_i}{De_b}\right]^{\frac{1+m}{2-m}}\left[\frac{C_{fb}}{C_{fi}}\right]^{\frac{1}{2-m}} = 1$$

Hence

$$C_{fb} = De_b\left\{\sum_{i=1}^{3} S_i\left[\frac{De_i}{De_b}\right]^{\frac{m}{2-m}}\left[\frac{C_{fi}}{De_i}\right]^{\frac{1}{m-2}}\right\}^{m-2} \qquad (4.44)$$

4.3.4.2 Transition Region

Theoretically, the transition bundle average friction factor and flow split parameters can also be determined from subchannel friction factor equations by substituting equation (4.35) into equation (4.36) together with mass balance equation (4.37). However, the resultant equations are highly nonlinear, hence no simple equation can be derived for those parameters in the transition region. They can only be found by numerical iteration. On the other hand, we would like to have closed form expressions for bundle average friction factor and transition flow split parameters for easy calculation.

Therefore, we assume that an expression for bundle average friction factor in the transition region can take the same form as equation (4.35).

$$f_{btr} = f_{bL}(1-\psi_b)^{\gamma} + f_{bT}\psi_b^{\gamma} \qquad (4.45)$$

where $f_{bL} = C_{fbL}/Re_b$

$f_{bT} = C_{fbT}/Re_b^m$

The constants C_{fbL} and C_{fbT} are determined by equation (4.44).

The transition flow split parameters are considered next. Although the exact solution for flow split parameters from equations (4.36) and (4.37) does not have closed form, we can derive desired expressions as functions of bundle average Reynolds number by some

approximations. The first approximation involves the intermittency factors. Although the intermittency factors ψ_i for different kinds of subchannels at one bundle average Reynolds number are different, they are approximately equal to the bundle value ψ_b, i.e.,

$$\psi_i = \frac{\log(Re_i/Re_{iL})}{\log(Re_{iT}/Re_{iL})} = \frac{\log(Re_b X_i/Re_{bL} X_{iL})}{\log(Re_{bT} X_{iT}/Re_{bL} X_{iL})}$$

$$\simeq \psi_b \equiv \log(Re_b/Re_{bL})/\log(Re_{bL}/Re_{bT}) \tag{4.46}$$

Note that as $Re_b \to Re_{bL}$ or $Re_b \to Re_{bT}$, $\psi_i \to \psi_b$. Therefore, taking $\psi_i = \psi_b$, equation (4.35) can be written as

$$f_i = \frac{C_{fiL}}{Re_i}(1-\psi_b)^\gamma + \frac{C_{fiT}}{Re_i^m}\psi_b^\gamma$$

$$= \left[\frac{C_{fiL}\left(\frac{De_b}{De_i}\right)}{Re_b}(1-\psi_b)^\gamma\right]\left(\frac{1}{X_i}\right) + \left[\frac{C_{fiT}\left(\frac{De_b}{De_i}\right)^m}{Re^m}\psi_b^\gamma\right]\left(\frac{1}{X_i}\right)^m \tag{4.47}$$

Substituting equation (4.47) into the portion of equation (4.36), applicable to two subchannels, i and j, we have

$$\left[C_{fiL}\left(\frac{De_b}{De_i}\right)\right]\left[\frac{(1-\psi_b)^\gamma}{Re_b}\right]\left(\frac{X_i}{De_i}\right) + \left[C_{fiT}\left(\frac{De_b}{De_i}\right)^m\right]\left[\frac{\psi_b^\gamma}{Re_b^m}\right]\left[\frac{X_i^{2-m}}{De_i}\right]$$

$$= \left[C_{fjL}\left(\frac{De_b}{De_j}\right)\right]\left[\frac{(1-\psi_b)^\gamma}{Re_b}\right]\left(\frac{X_j}{De_j}\right) + \left[C_{fjT}\left(\frac{De_b}{De_j}\right)^m\right]\left[\frac{\psi_b^\gamma}{Re_b^m}\right]\left[\frac{X_j^{2-m}}{De_j}\right] \tag{4.48}$$

Equation (4.48) expresses the general relation between X_i and X_j. We next desire to specialize this to yield X_1/X_2 and X_3/X_2. Equation (4.48) can be used to find the approximate equations of these parameters.

Since X_i's are not far away from unity, in the first approximation, let us assume that

$$X_i^{2-m} = X_i^{1.82} \simeq X_i$$

then equation (4.48) becomes

$$\frac{X_j}{X_i} \simeq \frac{\left\{C_{fiL}\left[\frac{De_b}{De_i}\right]\left[\frac{(1-\psi_b)^{\gamma}}{Re_b}\right] + C_{fiT}\left[\frac{De_b}{De_i}\right]^m\left[\frac{\psi_b^{\gamma}}{Re_b^m}\right]\right\}\frac{1}{De_i}}{\left\{C_{fjL}\left[\frac{De_b}{De_j}\right]\left[\frac{(1-\psi_b)^{\gamma}}{Re_b}\right] + C_{fjT}\left[\frac{De_b}{De_j}\right]^m\left[\frac{\psi_b^{\gamma}}{Re_b^m}\right]\right\}\frac{1}{De_j}} \qquad (4.49)$$

On the other hand, if we replace X_i by X_i^{2-m} in equation (4.48), then

$$\frac{X_j}{X_i} \simeq \left[\text{ right side term of equation (4.49) }\right]^{\frac{1}{2-m}} \qquad (4.50)$$

As $Re_b \to Re_{bL}$, equation (4.49) gives the exact solution since equation (4.49) equals equation (4.48) and $\psi_b \to \psi_i$. On the other hand equation (4.50) does not give the exact solution. Analogously as $Re_b \to Re_{bT}$, equation (4.50) gives the exact solution but equation (4.49) does not. The exact solution in the transition region should not be far away from either equation (4.49) or equation (4.50). To give the correct limiting solutions, a good approximation might be

$$\frac{X_j}{X_i} = \frac{C_{fiL}\left[\frac{De_b}{De_i^2}\right]\left[\frac{(1-\psi_b)^\gamma}{Re_b}\right] + \beta\left\{C_{fiT}\left[\frac{De_b}{De_i}\right]^m \frac{1}{De_i}\left[\frac{\psi_b^\gamma}{Re_b^m}\right]\right\}^{\frac{1}{2-m}}}{C_{fjL}\left[\frac{De_b}{De_j^2}\right]\left[\frac{(1-\psi_b)^\gamma}{Re_b}\right] + \beta\left\{C_{fjT}\left[\frac{De_b}{De_j}\right]^m \frac{1}{De_j}\left[\frac{\psi_b^\gamma}{Re_b^m}\right]\right\}^{\frac{1}{2-m}}} \qquad (4.51)$$

where β is the constant which makes equation (4.51) approach the exact solution or the experimental data, depending on which one we want.

The empirical constants in the transition region are then γ and β. γ is determined from the bundle average friction factor data, while β is determined by the exact solutions or the experimental data of the flow split parameters.

4.3.5 Summary

The formulae for subchannel friction factors and flow split parameters have been derived in this section. In summary,

For the turbulent and laminar regions,

f_1, f_2, f_3 from equations (4.31), (4.32), (4.33), respectively

X_1, X_2, X_3 from equations (4.42), (4.41), (4.43), respectively

f_b from equations (4.38) and (4.44)

For the transition region,

f_1, f_2, f_3 from equation (4.35)

X_1, X_2, X_3 from solving equations (4.36) and (4.37), or from equations (4.41) and (4.51)

f_b from equation (4.45)

The next step will be calibrating the empirical constants K_1, K_2, K_3, W_d, W_s, γ, and β by the available data from bare rod bundles and wire-wrapped rod bundles.

4.4 Empirical Constants for Bare Rod Subchannel Friction Factor

4.4.1 Introduction

Although many investigators have carried out both theoretical and experimental work on the friction factor of bare rod bundles, none have tried to develop subchannel friction factors for use in calculating the average bundle friction factor. The reason may lie in the fact that the bundle pressure drop data can only give us the bundle average friction factor, hence one tends to correlate the data in a bundle sense. However, as we discussed before, subchannel friction factors are essential in subchannel analysis. In this section, the subchannel friction factors for bare rod bundle in both laminar and turbulent flow will be determined.

Since the flow subchannels in an assembly communicate with their neighbors, their flow patterns will be affected by this interaction. Hence the friction factors of these subchannels are not easy to define. We define the interior subchannel friction factor for simplicity to be that of an infinite triangular rod array. The influence of the adjacent duct walls on the flow field in an interior subchannel had been investigated by Schmid (1966). Schmid showed that velocity changes due to the presence of walls was less than 1% for $P/D < 2.5$ if the hydraulic diameter of the individual channels were not markedly different. The friction factor of an interior subchannel inside a rod bundle can then be assumed to be the same as that of an infinite rod array. For edge and corner subchannels with $P/D = W/D$,

the effect of rod number will be assumed to be negligible. Since we are only interested in fast breeder reactor application, the P/D and W/D will be restricted to be within 1.5.

In laminar flow, the bare rod friction factor can be represented as

$$f'_{iL} = \frac{K_{iL}}{Re_i} \tag{4.52}$$

where i = 1 means interior subchannel

= 2 means edge subchannel

= 3 means corner subchannel

= b means bundle average

In turbulent flow, the friction factor can be represented as

$$f'_{iT} = \frac{K_{iT}}{Re_i^m} \tag{4.53}$$

The constants K_{iL} and K_{iT} are functions of P/D or W/D. In order to calculate them easily, simple but accurate equations should be developed. After some tries in determining these equations, we find the best and simplest way is to separate the effect of the P/D (or W/D) into two regions, one of which is in the range of $1.0 \leq P/D \leq 1.1$, while the other is $1.1 < P/D \leq 1.5$. In either region, K_{iL} and K_{iT} are represented by a simple two degree polynomial equation:

$$K_{iL}(\text{or } K_{iT}) = a + b_1(\frac{P}{D} - 1.0) + b_2(\frac{P}{D} - 1.0)^2 \tag{4.54}$$

The objective of this section is to determine the constants a's, b_1's and b_2's.

4.4.2 Laminar Flow Subchannel Friction Factor

4.4.2.1 Interior Subchannel

Sparrow and Loeffler (1959) were the first to publish the velocity field in an infinite triangular rod array. They truncated the series representation of their velocity solution by utilizing a point matching technique (6 points) along the boundary of the triangular sector. By this method, they were able to get the value, fRe_D, as a function of P/D, which is easy to transform to fRe_{De} (i.e., K_{iL}) by

$$fRe_{De} = fRe_D\left[\frac{2\sqrt{3}}{\pi}\left(\frac{P}{D}\right)^2 - 1\right] \tag{4.55}$$

While analyzing the multiregion temperature problem, Axford (1964, 1967) also solved the velocity problem for longitudinal laminar flow over an infinite triangular bundle. He employed a finite Fourier Cosine Transform and a point matching method for the solution. He used 6 to 15 boundary points to obtain the unknown coefficients of the series. Axford's results agree with those of Sparrow and Loeffler.

Rehme (1971,1980) used the so-called method of cyclic reduced block overrelaxation to obtain a finite difference solution to the flow problem in a 7-pin hexaganol bare rod bundle. For the interior subchannel, his results are within 2% with those of the infinite triangular array. This validates our assumption described in the last section, i.e., infinite triangular array results can be used with little error for the interior subchannel of a bundle.

Ullrich (1974) also investigated the finite triangular rod array in laminar flow by a highly sophisticated method. His results are in excellent agreement with Sparrow and Loeffler's results (±2%). Rehme's

fRe factors based on his combination method for the 19-pin and 37-pin bundles are also in excellent agreement (within 1.4%) with the results of Ullrich.

4.4.2.2 Edge and Corner Subchannel

Only Rehme (1971,1980) has solved the flow problem in these two kinds of subchannels in a 7-pin bare rod bundle. According to Rehme's results, K_{iL} will vary with P/D for a fixed value of W/D. However, since we are interested in LMFBR application, at which W/D ≈ P/D, the value at which P/D = W/D will be used for each W/D.

Table 4.1 lists K_{iL}'s in which the interior results are from Axford (1964, 1967), while edge and corner results are from Rehme (1971, 1980). Figure 4.6 compares these three K_{iL} values as a function of P/D.

4.4.2.3 Equation for Determining K_{iL}

The table form of Table 4.1 is not easy to use for determining K_{iL} at one arbitrary P/D (or W/D). As described in section 4.4.1 equation (4.54) is used to fit the values in Table 4.1 in two P/D regions. The results are also depicted in Table 4.1. The values calculated by these coefficients and equation (4.54) are listed in Table 4.1 for comparison. The calculated values (from equation (4.54)) differ from the theoretical values by not more than 1.5%.

4.4.2.4 Comparison between Experimental Data and Correlation

Subchannel friction factor data from only one laminar flow experiment is known to the author. That is Gunn's (1963) edge flow channel with W/D = 1.0. The experimental f•Re is 26.0, which is within 1% of the theoretical value.

Table 4.1
Fitting Results of Laminar KL= f*Re
for Triangular Array
(KL from Axford and Rehme's results)

Calculated KL=a+b(1)*(P/D-1)+b(2)**(P/D-1)**2

Interior subchannel
for 1.0<=P/D<=1.1 the coefficients are
a= 0.2600E+02 b(i)= 0.8882E+03 -0.3334E+04

P/D	KL	cal.KL	%error
1.0000	26.0120	25.9974	-0.1
1.0040	29.4000	29.4970	0.3
1.0100	34.5360	34.5464	0.0
1.0200	42.5160	42.4287	-0.2
1.0300	49.7640	49.6444	-0.2
1.0400	56.2200	56.1932	-0.0
1.0500	61.9120	62.0754	0.3
1.1000	81.5080	81.4854	-0.0

for 1.1<P/D<=1.5 the coefficients are
a= 0.6297E+02 b(i)= 0.2169E+03 -0.1902E+03

P/D	KL	cal.KL	%error
1.1000	81.5080	82.7600	1.5
1.1500	92.5640	91.2299	-1.4
1.2000	99.8000	98.7489	-1.1
1.2500	105.2040	105.3169	0.1
1.3000	109.6680	110.9341	1.2
1.5000	124.1400	123.8941	-0.2

Table 4.1 cont.

Edge subchannel
for 1.0<=W/D<=1.1 the coefficients are
a= 0.2618E+02 b(i)= 0.5545E+03 -0.1480E+04

W/D	KL	cal.KL	%error
1.0000	26.2400	26.1777	-0.2
1.0200	36.6000	36.6764	0.2
1.0500	50.0800	50.2046	0.2
1.0710	58.3000	58.0894	-0.4
1.1000	66.7600	66.8320	0.1

for 1.1<W/D<=1.5 the coefficients are
a= 0.4440E+02 b(i)= 0.2567E+03 -0.2676E+03

W/D	KL	cal.KL	%error
1.1000	66.7600	67.3857	0.9
1.1480	77.0000	76.5192	-0.6
1.2000	85.5600	85.0220	-0.6
1.4020	103.5000	104.3198	0.8
1.5000	106.2400	105.8132	-0.4

Table 4.1 cont.

Corner subchannel
for 1.0<=W/D<=1.1 the coefficients are
a= 0.2698E+02 b(i)= 0.1636E+04 -0.1005E+05

W/D	KL	cal.KL	%error
1.0000	26.7200	26.9840	1.0
1.0250	62.3200	61.6160	-1.1
1.0500	83.1600	83.6880	0.6
1.1000	90.2400	90.1520	-0.1

for 1.1<W/D<=1.5 the coefficients are
a= 0.8726E+02 b(i)= 0.3859E+02 -0.5512E+02

W/D	KL	cal.KL	%error
1.1000	90.2400	90.5640	0.4
1.1500	92.3600	91.8046	-0.6
1.2500	93.2000	93.4592	0.3
1.5000	92.8000	92.7722	-0.0

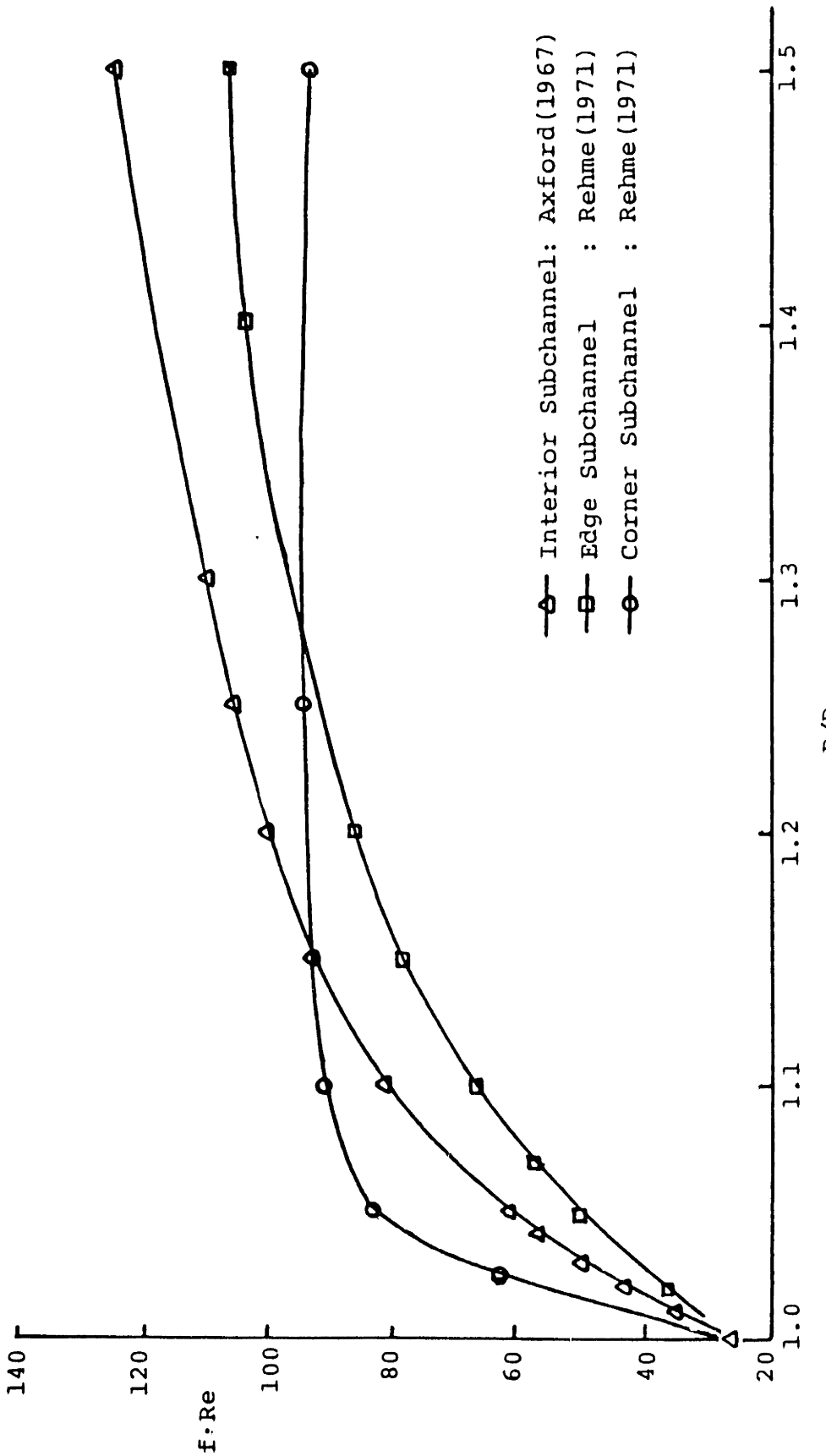

Figure 4.6 Theoretical Results of Laminar f·Re for Different Subchannels

Rehme (1972), and Galloway (1965) have measured the bundle averaged friction factor in their bare rod experiments in laminar flow region. The predicted bundle average friction factors can be calculated from equation (4.44) if one uses the K_{iL} calculated from equation (4.54). Figure 4.7 illustrates this comparison and shows that the correlation can predict the laminar data within 3% except for one point which is still within 10% of the prediction value. Note that the error might be caused by experimental error rather than by theoretical prediction.

4.4.3 Turbulent Flow Sunchannel Friction Factor

The most widely used turbulent flow friction factor for a smooth circular tube is Prandtl's universal law of friction,

$$\frac{1}{\sqrt{f_{ct}}} = 2.0 \log(Re\sqrt{f_{ct}}) - 0.8 \qquad (4.56)$$

Some investigators, e.g., Rehme, however used Maubach's equation to determine the circular tube turbulent friction factor,

$$\frac{1}{\sqrt{f_{ct}}} = 2.035 \log(Re\sqrt{f_{ct}}) - 0.989 \qquad (4.57)$$

For consistency, equation (4.56) will be used to calculate f_{ct} in thiswork.

The turbulent subchannel friction factor investigated below will be represented by the ratio between it and the circular tube value.

4.4.3.1 Theoretical Work on Turbulent Subchannel Friction Factor

The first fundamental theoretical work on the infinite triangular rod array friction factor in turbulent flow was done by Deissler and

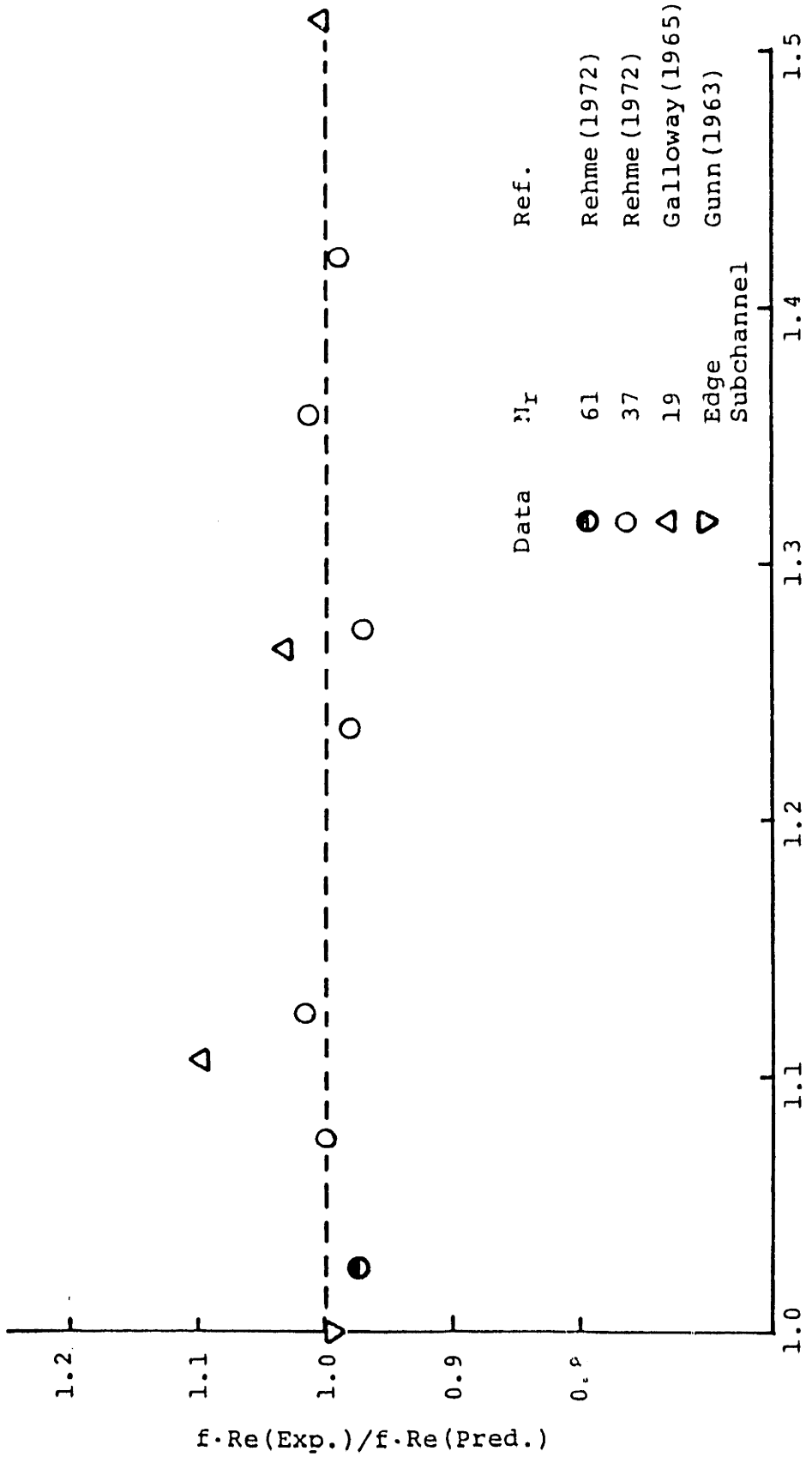

Figure 4.7 Comparison between Experimental and Predicted Bare Rod Bundle Laminar Friction Factor Constant f·Re

Taylor (1957). Deissler's velocity profile, which differs only slightly from Nikuradse's universal velocity profile, was used in their approach.

Ibragimov (1967) developed a fairly complicated method to calculate the friction factor for turbulent flow in channels of non-circular crosssection. His results were used by Magee and Nilsson (1971) as the Y parameter in their bundle friction factor correlation.

Dwyer and Berry (1972) used Nikuradse's universal velocity profile, which has been proved by Eifler (1967) and Levchenko (1967) to describe quite accurately the velocity profile in rod array channels if the local value of wall shear stress $\tau_w(\theta)$ is known, to calculate the friction factor of an interior subchannel in turbulent flow. The friction factor is varied until the average linear velocity calculated from the local velocity distribution equals the average linear velocity corresponding to the Reynolds number on which the local linear velocity was based.

Malak (1975) developed a relation between the turbulent friction factor and a geometrical parameter L* for non-circular flow channels. However, the data used to establish the correlation are restricted. After some arithmetic calculation, the f/f_{ct} for different P/D can be determined from his empirical equation.

Finally and most importantly, Rehme (1972) developed a G*-method to predict the friction factor for turbulent flow through non-circular channels on the basis of the f•Re value for laminar flow. Because of its accuracy, this method will be discussed in some detail in the next section. As for edge and corner subchannel friction factor in turbulent

flow, the only applicable theoretical method known to the author is the G*-method. Although Malak's method can also calculate these values, it is not used because of its restricted data base and difficulty in getting the L* parameter.

The results of the above five investigators for f/f_{ct} at Re = 10^5 are listed in Table 4.2 as a function of P/D. They are also illustrated in Figure 4.8 for comparison.

4.4.3.2 The G*-Method

Maubach (1970) used the "equivalent" annular zone concept for a hexagonal elementary cell around each rod and the universal velocity profile,

$$v^+ = 2.5 \ln y + 5.5$$

where $v^+ \equiv v/v^*$, $y^+ \equiv yv^*/\nu$, $v^* \equiv \sqrt{\tau_w/\rho}$

to obtain a friction factor correlation for an equivalent annular zone:

$$\sqrt{\frac{8}{f}} = 2.5 \ln\left(Re\sqrt{\frac{f}{8}}\right) + 5.5 - \frac{3.966+1.25X}{1+X} - 7.2 \ln 2(1+X) \qquad (4.58)$$

where $X \equiv \sqrt{\frac{2\sqrt{3}}{\pi}} \frac{P}{D} \simeq 1.05 \frac{P}{D}$

This "equivalent" annular zone is a good approximation to rod arrays with large rod distance ratios (P/D > 1.2) for which the wall shear stress is relatively constant around the perimeter of the rod.

Rehme (1972) assumed that the friction factor for non-circular flow channels can be represented in the same form as Maubach's theory to be

$$\sqrt{\frac{8}{f}} = A \left[2.5 \ln\left(Re\sqrt{\frac{f}{8}}\right) + 5.5\right] - G^* \qquad (4.59)$$

TABLE 4.2

f/fct for Bare Rod Interior Subchannel in Turbulent Flow by Different Investigators (at Re = 10^5)

P/D	Deissler (1956)	Ibragimov (1967)	Dwyer (1972)	Malak (1975)	Rehme (1972)
1.00	0.55	—	—	0.693	0.647
1.001	—	0.653	0.630	—	0.657
1.01	—	0.706	0.762	—	0.739
1.02	0.72	0.795	0.841	—	0.816
1.025	—	—	—	0.903	—
1.03	—	0.819	0.895	—	0.884
1.04	—	0.943	0.934	—	0.943
1.05	0.87	0.990	0.964	1.028	0.994
1.06	—	1.023	0.983	—	1.012
1.07	—	—	0.998	—	1.017
1.10	0.98	1.087	1.023	1.133	1.028
1.15	—	1.115	1.047	—	1.038
1.20	1.038	1.129	1.062	1.199	1.046
1.30	1.050	1.149	1.082	1.228	1.059
1.40	1.063	1.166	1.096	1.232	1.067
1.50	—	—	—	—	1.072
1.60	1.070	1.199	1.111	—	—
2.00	1.10	1.268	1.131	—	—

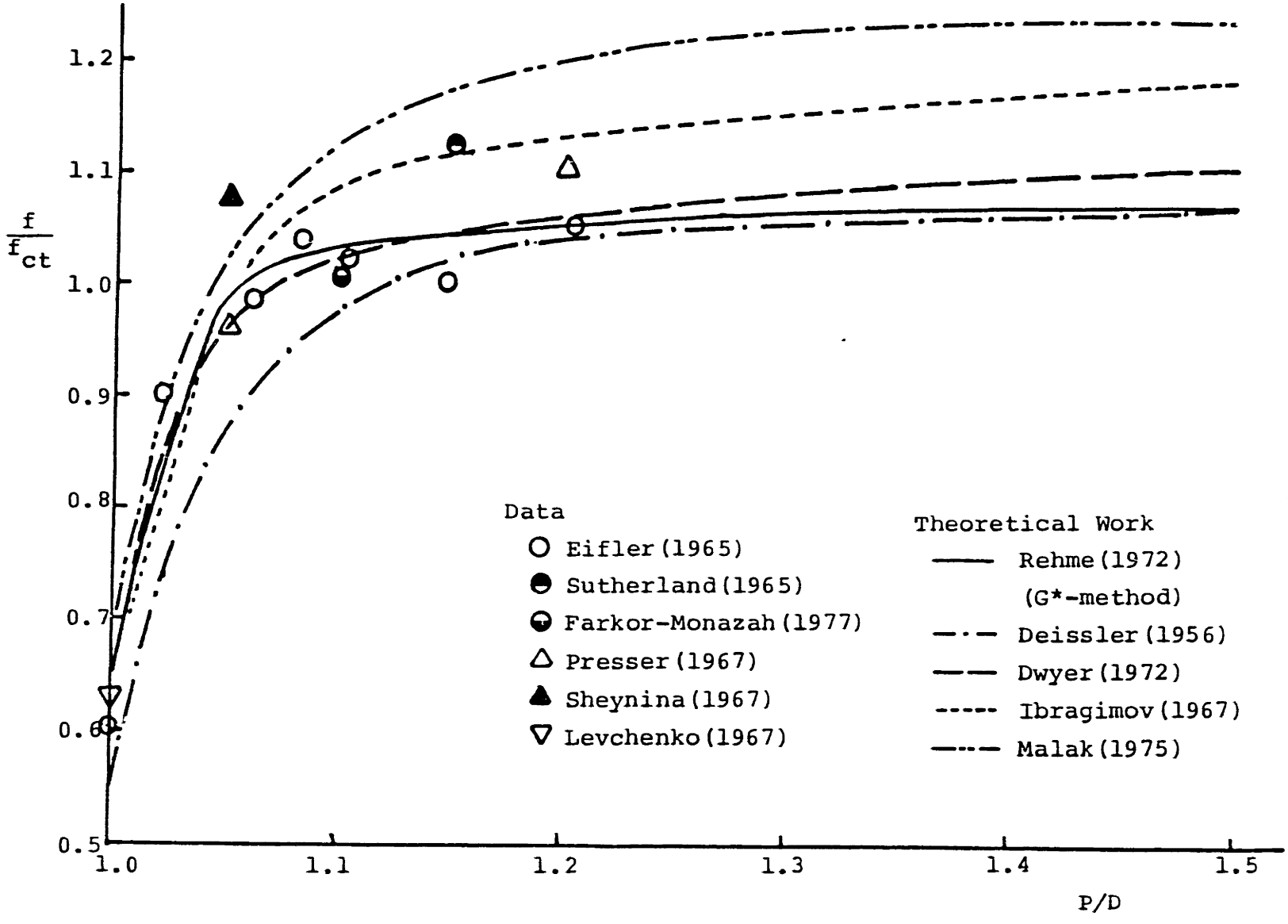

Figure 4.8 Theoretical Work and Experimental Data for Interior Subchannel Friction Factor at Re=10^5 as compared to Circular Tube Values

where A and G* are two geometrical constants which are assumed to be only functions of f•Re in laminar flow (i.e., K_L). This assumption came from the similarity between K_L/K_{Lct} (K_{Lct} = 64) and f/f_{ct} in turbulent flow, which was observed from multiple, parallel tubes by Rehme.

For K_L < 64, the values of A and G* corresponding to each K_L can be calculated from multi-tubes in parallel, at which the total (average) friction factor decreases significantly below the value of the single tube.

For K_L > 64, the relation between A, G* and K_L were determined from the annular zone solution, equation (4.58). Rehme (1971) found the laminar constant f•Re of the equivalent annular zone (AZ) to be

$$(K_L)_{AZ} = \frac{64(X^2-1)^3}{-3X^4 + 4X^2 + 4X^4 \ln X - 1} \tag{4.60}$$

where X is the same as in equation (4.58). Equations (4.58), (4.59) and (4.60) relate A, G* and K_L for the equivalent annular zone (K_L>64).

According to Rehme's results, for $K_L \leq 64$, A can be fitted to be,

$$A = 1.0 + 0.5 \log \left(\frac{64}{K_L}\right) \tag{4.61}$$

For K_L > 64, by comparing equations (4.58) and (4.59), it is clear that A = 1.0 in this case.

Table 4.3 lists the relation between G* and K_L calculated by the method described above. Separating K_L into three regions, G* can almost be exactly fitted as (within 0.5%)

Table 4.3 G*method Fitting Results

Calculated G* = a+b(1)*log(KL)+b(2)*log(KL)**2

for KL <= 64 the coefficients are
a= -.1548E+00 b(i)= 0.5126E+01 -0.1042E+01

KL	G*	cal.G*	%error
25.3800	5.0140	4.9885	-0.5
30.0000	5.1350	5.1427	0.1
30.6300	5.1430	5.1611	0.4
32.9100	5.1980	5.2233	0.5
40.4200	5.3800	5.3902	0.2
42.5100	5.4360	5.4286	-0.1
45.3400	5.4940	5.4763	-0.3
46.9100	5.5270	5.5008	-0.5
47.1600	5.5040	5.5046	0.0
48.0000	5.5210	5.5171	-0.1
48.6500	5.5200	5.5265	0.1
52.2900	5.5750	5.5759	0.0
53.6900	5.5990	5.5935	-0.1
54.4900	5.6030	5.6032	0.0
58.5900	5.6500	5.6497	-0.0
63.4800	5.6940	5.6986	0.1
63.5000	5.6950	5.6988	0.1
63.6600	5.6960	5.7003	0.1
63.7800	5.6970	5.7014	0.1

Table 4.3 cont.

for 64<KL<125 the coefficients are
a= 0.9430E+01 b(i)= -0.5976E+01 0.2159E+01

KL	G*	cal.G*	%error
64.0000	5.6988	5.6815	-0.3
66.2170	5.7020	5.7089	0.1
68.5740	5.7280	5.7381	0.2
74.8360	5.8072	5.8154	0.1
91.2000	6.0170	6.0132	-0.1
96.0000	6.0737	6.0697	-0.1
100.9120	6.1310	6.1267	-0.1
122.1830	6.3600	6.3642	0.1

for KL >= 125 the coefficients are
a= -.2344E+00 b(i)= 0.3151E+01

KL	G*	cal.G*	%error
122.1830	6.3600	6.3410	-0.3
152.0910	6.6327	6.6406	0.1
393.6380	7.9149	7.9418	0.3
993.5460	9.2245	9.2087	-0.2

$$\text{for } K_L \leq 64,$$

$$G^* = -0.1548 + 5.126(\log K_L) - 1.042(\log K_L)^2$$

$$\text{for } 64 < K_L < 125, \qquad (4.62)$$

$$G^* = 9.430 - 5.976(\log K_L) + 2.159(\log K_L)^2$$

$$\text{for } K_L \geq 125$$

$$G^* = -0.2344 + 3.151(\log K_L)$$

Now by using equations (4.61) and (4.62), one can calculate any flow channel's turbulent friction factor by equation (4.59), provided that its K_L is given. For the interior subchannel, K_L can be calculated by equation (4.54) and the coefficients in Table 4.1. Hence we can calculate f/f_{ct} for any P/D for turbulent flow. For Re = 10^5, these values are listed in Table 4.2 under the G*-method column.

For edge and corner subchannels, K_L can also be calculated by equation (4.54) and the coefficients in Table 4.1. Hence we can also calculate f/f_{ct} in turbulent flow region for edge and corner subchannel by the G*-method. Figure 4.9 illustrates f/f_{ct} for three kinds of subchannel as a function of P/D at Re = 10^5.

4.4.3.3 Comparison between Experimental Data and Correlation

Table 4.4 lists the friction factor data for interior subchannel in hexagonal array. The (f/f_{ct}) at Re = 10^5 of these data are also plotted in Figure 4.8 for comparison. It can be seen that Dwyer's method and the G*-method give the best predictions. However, selection between these methods will be defered until the bundle friction factor data is examined.

As for edge subchannel, Gunn (1963) measured the pressure drop of an edge flow channel with W/D = 1.0. Rehme (1980) measured the detail

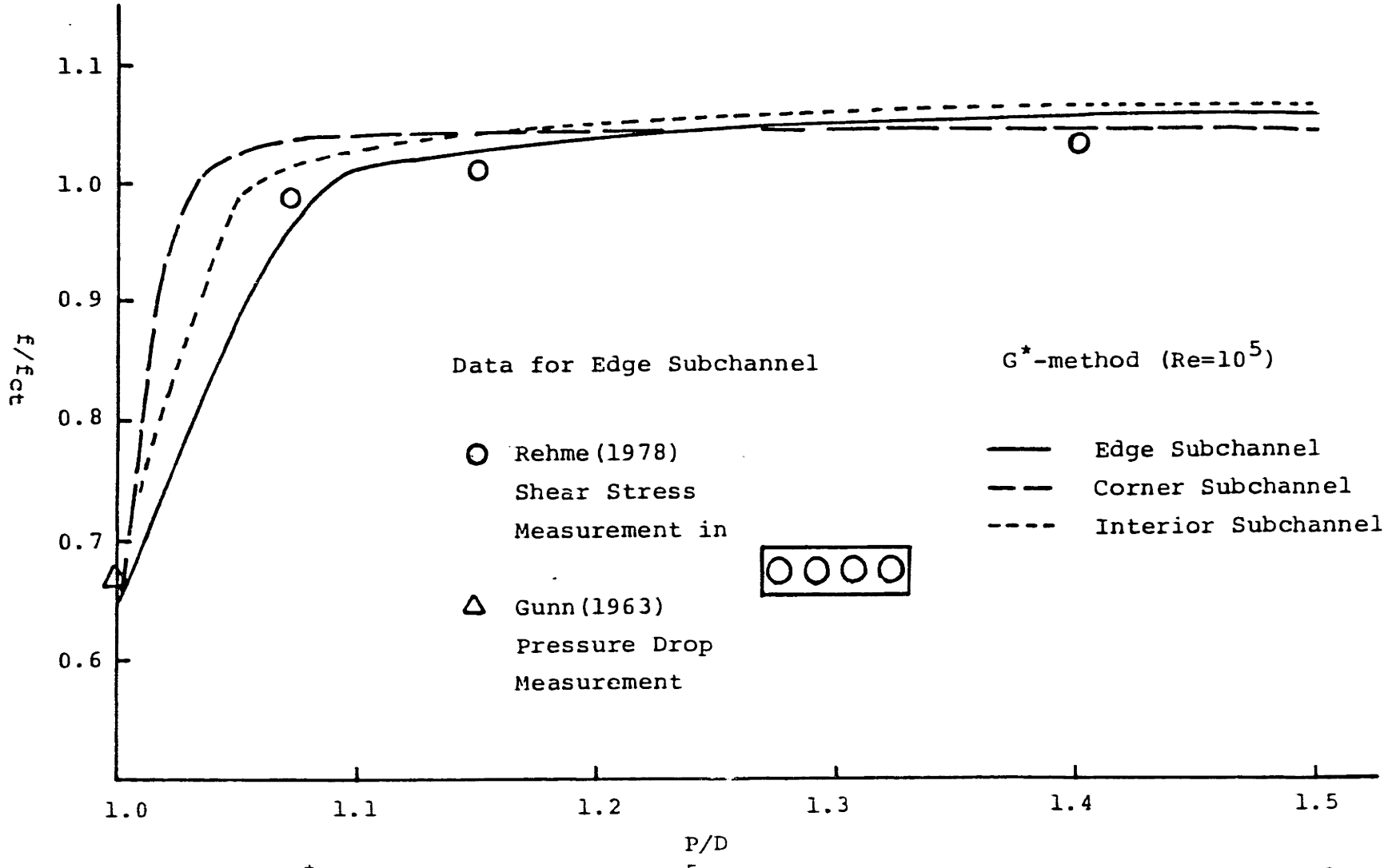

Figure 4.9 G^*-method f/f_{ct} at Re = 10^5 for Interior, Edge, and Corner Subchannel

TABLE 4.4

Data for Bare Rod Interior Subchannel
Friction Factor in Turbulent Region

Investigators	Rod Configurations	D(mm)	P/D	f @ 10^4	f @ 10^5
Eifler(1965)	4	40.0	1.00	0.0183	0.0106
"	4	40.0	1.021	0.0281	0.0162
"	4	40.0	1.059	0.0307	0.0177
"	4	40.0	1.102	0.0319	0.0184
"	4	40.0	1.147	0.0313	0.0180
"	4	40.0	1.202	0.0329	0.0189
"	4	40.0	1.08	0.0313	0.0187
Fakori-Monazah(1977)	4	38.1	1.10	0.0350	0.0181
Levchenko(1967)	3	205.0	1.00	0.0215	0.0113
Presser(1967)	1/7	74.0	1.05	0.0266	0.0173
"	7/19	15.0	1.20	0.0320	0.0198
Sheynina(1967)	19/37	14.0	1.05	0.0316	0.0195
Subbotin(1960)	1/7	12.0	1.13	0.0340	0.0225
Sutherland(1965)	7/19	25.4	1.15	0.0364	0.0202

shear stress distribution in the edge subchannel in a four rods rectangular bundle as also shown in Figure 4.9. Three different W/D's have been investigated. Table 4.5 lists these data as well as values calculated by the G*-method. They are also plotted in Figure 4.9 for comparison. Since the data are predicted within 3% accuracy by the G*-method, one can confidently use G*-method for calculating edge subchannel friction factor.

No data are available for corner subchannels. The G*-method is assumed to be valid in this case.

The available bare rod bundle friction factor data were collected and tabulated in Appendix B. These data will be examined to see which one of those five methods for calculating interior subchannel friciton factor predicts them most closely. Since the wire-wrapped bundle friction factor data show that m = 0.18, the same value is used in the bare rod case. For the G*-method, two Reynolds numbers, 5×10^4 and 10^5, are used to get K_{iT}'s. The averaged K_{iT} of these two values for each P/D (or W/D) were used to fit a polynomial equation as equation (4.54). For the other four methods, the values in Table 4.2, i.e., at $Re = 10^5$, were used to get K_{iT} and they were also fitted as equation (4.54). For each of 28 available bare rod bundle geometry for which friction factor data are available, we can calculate C_{fb}'s values utilizing K_{iT} values based on the five methods.

The prediction error of each bundle was squared, then summarized over all 28 bundles. The average square root errors, i.e., total summarized error divided by 28, then square rooted, for these 5 methods are, Malak: 10.2%, Ibragimov: 7.73%, Dwyer: 5.97%, Deissler: 5.63%, and

TABLE 4.5

Data for Bare Rod Edge Subchannel Friction Factor in Turbulent Region

Investigators	W/D	Experimental Type	Re	f	f/fct* at 10^5	Predicted f/fct at 10^5	% Error
Gunn(1963)	1.000	Pressure Drop Measurement	1.0 e5	0.0120	0.667	0.650	-2.6
Rehme(1978a)	1.071	Shear Stress Measurement	8.73e4	0.0182	0.985	0.958	-2.7
Rehme(1978b)	1.148	Shear Stress Measurement	1.23e5	0.0175	1.009	1.024	1.5
Rehme(1978c)	1.402	Shear Stress Measurement	1.94e5	0.0165	1.033	1.056	2.2

* f at Re = 10^5 is extrapolated from the experimental point by using m = 0.18 in equation (3.2).

G*-method: 5.67%.

For considerations of simplicity and consistency, we concluded that Rehme's G*-method is the best choice for calculating the interior subchannel friction factor in turbulent flow. Figure 4.10 compares the prediction results from the G*-method and the experimental data.

Table 4.6 depicts the fitting results together with the original values and fitted values for K_{iT} from the G*-method.

4.4.4 Summary

The theoretical correlations and experimental data base for hexagonal bare rod bundle have been investigated thoroughly. Correlations for bare rod subchannel friction factors have been developed. The constants K_{iL} and K_{iT} defined in equations (4.52) and (4.53), respectively, are calculated by

$$K = a + b_1(P/D - 1) + b_2(P/D - 1)^2$$

where a, b_1, and b_2 are tabulated in Table 4.1 for K_{iL} and Table 4.6 for K_{iT}.

Since square array bundles are also important in the reactor application, we also fit these constants for their three kinds of subchannels. The values used for K_{iL} were from Rehme's (1971) theoretical calculation, and for K_{iT} were also from the G*-method. Tables 4.7 and 4.8 depict the results for the laminar case and the turbulent case, respectively.

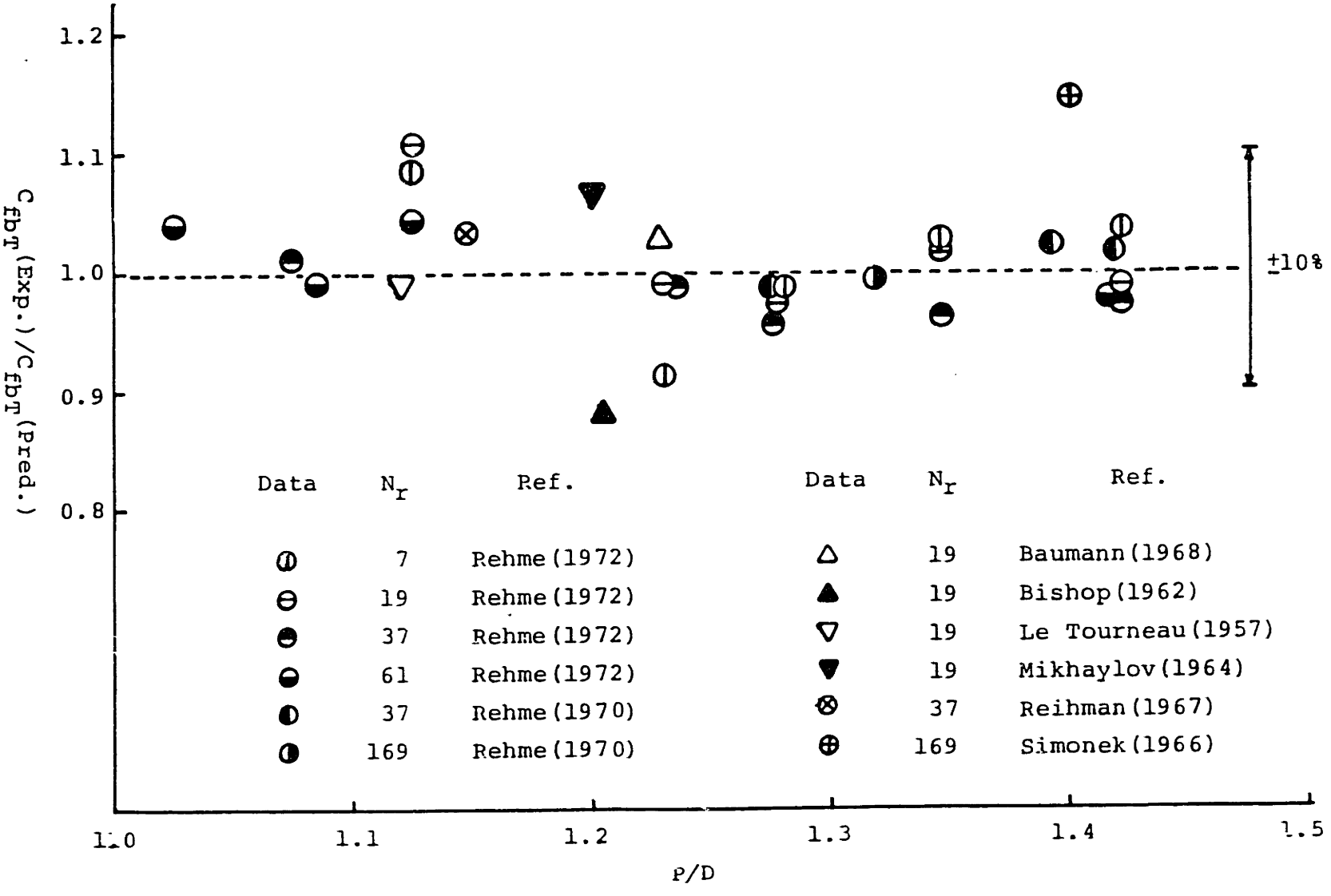

Figure 4.10 Comparison between Experimental and Predicted Bare Rod Bundle Turbulent Friction Factor Constant $C_{fbT}(=f \cdot Re^{0.18})$

Table 4.6
Fitting Results of Turbulent KT=f*Re**0.18
for Triangular Array
(KT from G* method using Re= 5e4 1e5)

Calcualted KT=a+b(1)*(P/D-1)+b(2)*(P/D-1)**2

Interior subchannel
for 1.0<=P/D<=1.1 the coefficients are
a= 0.9378E-01 b(i)= 0.1398E+01 -0.8664E+01

P/D	KT	cal.KT	%error
1.0000	0.0935	0.0938	0.3
1.0010	0.0949	0.0952	0.2
1.0100	0.1068	0.1069	0.1
1.0200	0.1182	0.1183	0.1
1.0300	0.1280	0.1279	-0.1
1.0400	0.1366	0.1358	-0.6
1.0500	0.1441	0.1420	-1.5
1.0600	0.1468	0.1465	-0.2
1.0700	0.1475	0.1492	1.2
1.0800	0.1481	0.1502	1.4
1.0900	0.1486	0.1494	0.5
1.1000	0.1490	0.1470	-1.4

for 1.1<P/D<=1.5 the coefficients are
a= 0.1458E+00 b(i)= 0.3632E-01 -0.3333E-01

P/D	KT	cal.KT	%error
1.1000	0.1490	0.1491	0.1
1.1500	0.1506	0.1505	-0.1
1.2000	0.1518	0.1518	-0.0
1.2500	0.1528	0.1528	-0.0
1.3000	0.1537	0.1537	0.0
1.3500	0.1544	0.1545	0.0
1.4000	0.1550	0.1550	0.0
1.4500	0.1554	0.1554	0.0
1.5000	0.1557	0.1557	-0.0

Table 4.6 cont.

Edge subchannel
for 1.0<=W/D<=1.1 the coefficients are
a= 0.9377E-01 b(i)= 0.8732E+00 -0.3341E+01

W/D	KT	cal.KT	%error
1.0000	0.0938	0.0938	-0.0
1.0010	0.0947	0.0946	-0.1
1.0100	0.1023	0.1022	-0.2
1.0200	0.1100	0.1099	-0.1
1.0300	0.1168	0.1170	0.1
1.0400	0.1231	0.1234	0.2
1.0500	0.1288	0.1291	0.3
1.0600	0.1339	0.1341	0.2
1.0700	0.1386	0.1385	-0.1
1.0800	0.1429	0.1422	-0.4
1.0900	0.1463	0.1453	-0.7
1.1000	0.1467	0.1477	0.7

for 1.1<W/D<=1.5 the coefficients are
a= 0.1430E+00 b(i)= 0.4199E-01 -0.4428E-01

W/D	KT	cal.KT	%error
1.1000	0.1467	0.1467	0.0
1.1500	0.1483	0.1483	-0.0
1.2000	0.1496	0.1496	-0.0
1.2500	0.1507	0.1507	-0.0
1.3000	0.1516	0.1516	0.0
1.3500	0.1522	0.1522	0.0
1.4000	0.1527	0.1527	0.0
1.4500	0.1529	0.1529	0.0
1.5000	0.1529	0.1529	-0.0

Table 4.6 cont.

Corner subchannel
for 1.0<=W/D<=1.1 the coefficients are
a= 0.1004E+00 b(i)= 0.1625E+01 -0.1185E+02

W/D	KT	cal.KT	%error
1.0000	0.0951	0.1004	5.6
1.0010	0.0977	0.1020	4.4
1.0100	0.1180	0.1155	-2.2
1.0200	0.1360	0.1282	-5.7
1.0300	0.1467	0.1385	-5.6
1.0400	0.1482	0.1465	-1.2
1.0500	0.1494	0.1521	1.8
1.0600	0.1503	0.1553	3.4
1.0700	0.1508	0.1561	3.6
1.0800	0.1510	0.1546	2.4
1.0900	0.1509	0.1507	-0.1
1.1000	0.1504	0.1445	-4.0

for 1.1<W/D<=1.5 the coefficients are
a= 0.1499E+00 b(i)= 0.6706E-02 -0.9567E-02

W/D	KT	cal.KT	%error
1.1000	0.1504	0.1505	0.0
1.1500	0.1507	0.1507	-0.0
1.2000	0.1509	0.1508	-0.0
1.2500	0.1510	0.1510	-0.0
1.3000	0.1510	0.1510	0.0
1.3500	0.1510	0.1511	0.0
1.4000	0.1510	0.1510	0.0
1.4500	0.1510	0.1510	0.0
1.5000	0.1509	0.1508	-0.0

Table 4.7
Fitting Results of Laminar KL=f*Re
for Square Array
(KL from Rehme's results)

calculated KL=a+b(1)*(P/D-1)+b(2)*(P/D-1)**2

Interior subchannel
for 1.0<=P/D<=1.1 the coefficients are
a= 0.2637E+02 b(i)= 0.3742E+03 -0.4939E+03

P/D	KL	cal.KL	%error
1.0000	26.4000	26.3711	-0.1
1.0200	33.6000	33.6578	0.2
1.0500	43.8800	43.8470	-0.1
1.1200	64.1600	64.1641	0.0

for 1.1<P/D<=1.5 the coefficients are
a= 0.3555E+02 b(i)= 0.2637E+03 -0.1909E+03

P/D	KL	cal.KL	%error
1.1200	64.1600	64.4389	0.4
1.2200	84.7600	84.3166	-0.5
1.3200	100.7200	100.3771	-0.3
1.4200	111.7200	112.6206	0.8
1.5200	121.4400	121.0469	-0.3

Table 4.7 cont.

Edge subchannel same as Triangular Array

Corner subchannel
for 1.0<=W/D<=1.1 the coefficients are
a= 0.2862E+02 b(i)= 0.7159E+03 -0.2807E+04

P/D	KL	cal.KL	%error
1.0000	28.5600	28.6189	0.2
1.0250	44.9200	44.7629	-0.3
1.0500	57.2800	57.3978	0.2
1.1000	72.1600	72.1404	-0.0

for 1.1<W/D<=1.5 the coefficients are
a= 0.5883E+02 b(i)= 0.1607E+03 -0.2035E+03

P/D	KL	cal.KL	%error
1.1000	72.1600	72.8635	1.0
1.1500	79.5600	78.3540	-1.5
1.2500	85.7200	86.2828	0.7
1.5000	88.3600	88.2997	-0.1

Table 4.8
Fitting Results of Turbulent KT=f*Re**0.18
for Square Array
(KT from G* method using Re= 5e4 1e5)

Calculated KT=a+b(1)*(P/D-1)+b(2)*(P/D-1)**2

Interior subchannel
for 1.0<=P/D<=1.1 the coefficients are
a= 0.9423E-01 b(i)= 0.5806E+00 -0.1239E+01

P/D	KT	cal.KT	%error
1.0000	0.0941	0.0942	0.1
1.0010	0.0947	0.0948	0.1
1.0100	0.1000	0.0999	-0.1
1.0200	0.1055	0.1053	-0.1
1.0300	0.1107	0.1105	-0.1
1.0400	0.1155	0.1155	-0.0
1.0500	0.1201	0.1202	0.0
1.0600	0.1245	0.1246	0.1
1.0700	0.1287	0.1288	0.1
1.0800	0.1326	0.1327	0.1
1.0900	0.1364	0.1364	0.0
1.1000	0.1400	0.1399	-0.1

for 1.1<P/D<=1.5 the coefficients are
a= 0.1339E+00 b(i)= 0.9059E-01 -0.9926E-01

P/D	KT	cal.KT	%error
1.1000	0.1400	0.1419	1.3
1.1500	0.1473	0.1452	-1.4
1.2000	0.1489	0.1480	-0.6
1.2500	0.1503	0.1503	-0.0
1.3000	0.1516	0.1521	0.3
1.3500	0.1527	0.1534	0.5
1.4000	0.1536	0.1542	0.4
1.4500	0.1544	0.1545	0.1
1.5000	0.1550	0.1543	-0.5

Table 4.8 cont.

Edge subchannel same as Triangular array

Corner subchannel
for 1.0<=W/D<=1.1 the coefficients are
a= 0.9755E-01 b(i)= 0.1127E+01 -0.6304E+01

W/D	KT	cal.KT	%error
1.0000	0.0977	0.0976	-0.2
1.0010	0.0989	0.0987	-0.2
1.0100	0.1082	0.1082	-0.0
1.0200	0.1173	0.1176	0.2
1.0300	0.1252	0.1257	0.4
1.0400	0.1321	0.1326	0.3
1.0500	0.1382	0.1382	-0.0
1.0600	0.1434	0.1425	-0.6
1.0700	0.1464	0.1456	-0.6
1.0800	0.1469	0.1474	0.4
1.0900	0.1472	0.1479	0.5
1.1000	0.1475	0.1472	-0.2

for 1.1<W/D<=1.5 the coefficients are
a= 0.1452E+00 b(i)= 0.2681E-01 -0.3411E-01

W/D	KT	cal.KT	%error
1.1000	0.1475	0.1476	0.0
1.1500	0.1485	0.1485	-0.0
1.2000	0.1493	0.1492	-0.0
1.2500	0.1498	0.1498	-0.0
1.3000	0.1502	0.1502	0.0
1.3500	0.1504	0.1504	0.0
1.4000	0.1505	0.1505	0.0
1.4500	0.1504	0.1504	0.0
1.5000	0.1501	0.1501	-0.0

4.5 Empirical Constants for Wire-Wrapped Subchannel Friction Factor

The empirical constants which need to be determined in wire-wrapped subchannel friction factor correlations are the wire drag constant W_d and swirl flow constant W_s. Since there are no subchannel friction factor data, and only bundle average friction factor and flow split parameters are measurable in wire-wrapped bundles, these two sets of data must be used simutaneously to calibrate these two constants as functions of geometrical parameters. The data reviewed in section 4.2 will be used for calibration. The parameters K_i's are determined from the fitting results of the last section.

The wire drag constant W_d and swirl flow constant W_s are both geometry and flow region dependent. They will be fitted by some functions of geometrical parameters for both laminar or turbulent region. No calibration work is needed for these two constants in the transition region since the formulation in the transition region simply combines laminar and turbulent equations weighted by a intermittency factor to a power of γ. γ is assumed to be a single value, and it is the empirical constant which needs to be calibrated in the transition region.

Since the data base in the turbulent region is vast enough for both bundle friction factor and flow split parameter, W_d and W_s can be calibrated directly from the data. However, in the laminar region, friction factor data are available for only a few bundles, and almost no flow split data are available except the three bundles of Chen

(1974) and Efthimiadis (1983). Therefore, some assumptions have to be adopted to relate these constants in the laminar region to their values in the turbulent region.

4.5.1 Empirical Constants for the Turbulent Region: W_{dT}, W_{sT}

Since there are two sets of data, i.e., around one hundred bundle friction factor data sets and around ten flow split data sets, with two constants W_{dT} and W_{sT} to be determined, a two stage iterative procedure was developed to calibrate these constants.

For hexagonal rod bundles with 19 pins or more, the number of interior subchannels is considerably more than that of edge subchannels. Hence the wire drag constant W_{dT} is more important than the swirl flow constant W_{sT} in calculating the bundle pressure loss. On the other hand, since the flow split parameter is sensitive to the edge subchannel friction factor value, W_{sT} is more important than W_{dT} in calculating the flow split parameter. For these reasons, W_{dT} is first calculated from the bundle friction factor data for each bundle with a guessed W_{sT}. These W_{dT}'s are then fitted as functions of geometrical parameters. Using this W_{dT} equation, W_{sT} is calculated from the flow split data and then fitted as another function of geometrical parameters. This new W_{sT} equation can then be used together with the friction factor data to calculate W_{dT} again. This iterative procedure is continued until a satisfactory prediction is obtained. Figure 4.11 depicts this procedure. The 'prediction O.K.?' in this figure means that if further iteration can not improve the prediction, the final results are obtained.

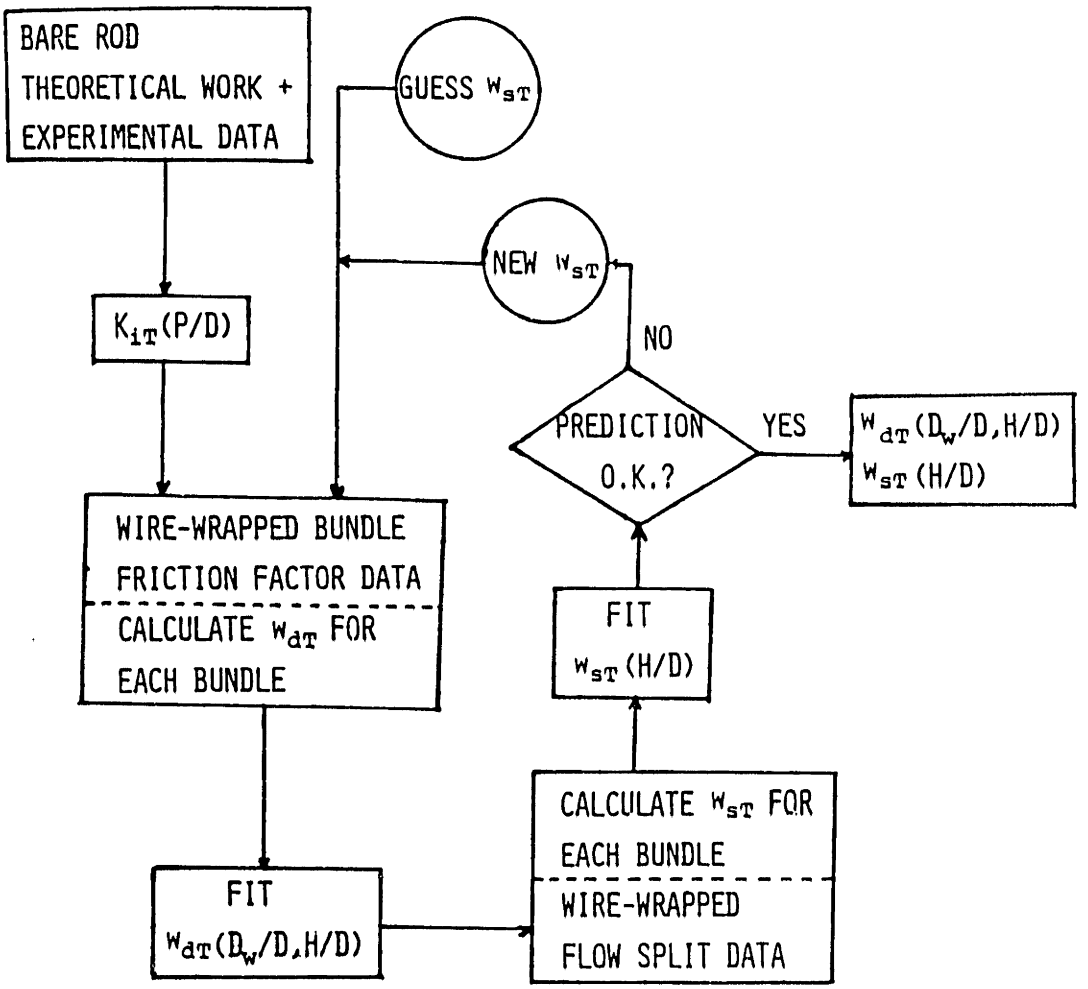

Figure 4.11 Calibration Procedure for Empirical Constants W_{dT} and W_{sT} in Turbulent Region

Since W_{dT} is essentially a wire drag coefficient, it is expected to be a function of D_w, H, and D. Several dimensionless combinations of these three geometrical parameters have been investigated, and the best two were found to be D_w/D and H/D. Since W_{sT} is related to swirl flow, which is strongly dependent on H/D, it is assumed to be function of this parameter only.

Although there are many possible fitting equations for either W_{dT}'s or W_{sT}'s, the following forms and constants were found to be satisfactory:

$$W_{dT} = [\ 29.5 - 140.0(\frac{D_w}{D}) + 401.0(\frac{D_w}{D})^2\ ](\frac{H}{D})^{-0.85} \qquad (4.63)$$

and

$$W_{sT} = 20.0\ \log(\frac{H}{D}) - 7.0 \qquad (4.64)$$

Figure 4.12 illustrates W_{dT} as functions of D_w/D and H/D. Note that the nominal value of W_{dT} is around 3.0. The drag coefficient C_D of a single elliptical shaped rod in turbulent flow is about 0.5 [Morris(1963)]. From the model, $C_d = W_{dT}/Re^{0.18}$ at $Re = 2x10^4$, taking $C_d = 0.5$, one finds that W_{dT} is 3.0. This confirms the soundness of our model.

As shown in figure 4.12, W_{dT} decreases as H/D increases as one expects; however, the dependence of D_w/D is parabolic with a minimum value around $D_w/D = 0.18$. The characteristic of the flow field apparently changes at this point. Geometrically one observes that for an interior subchannel, as D_w/D increases, the projected area of the

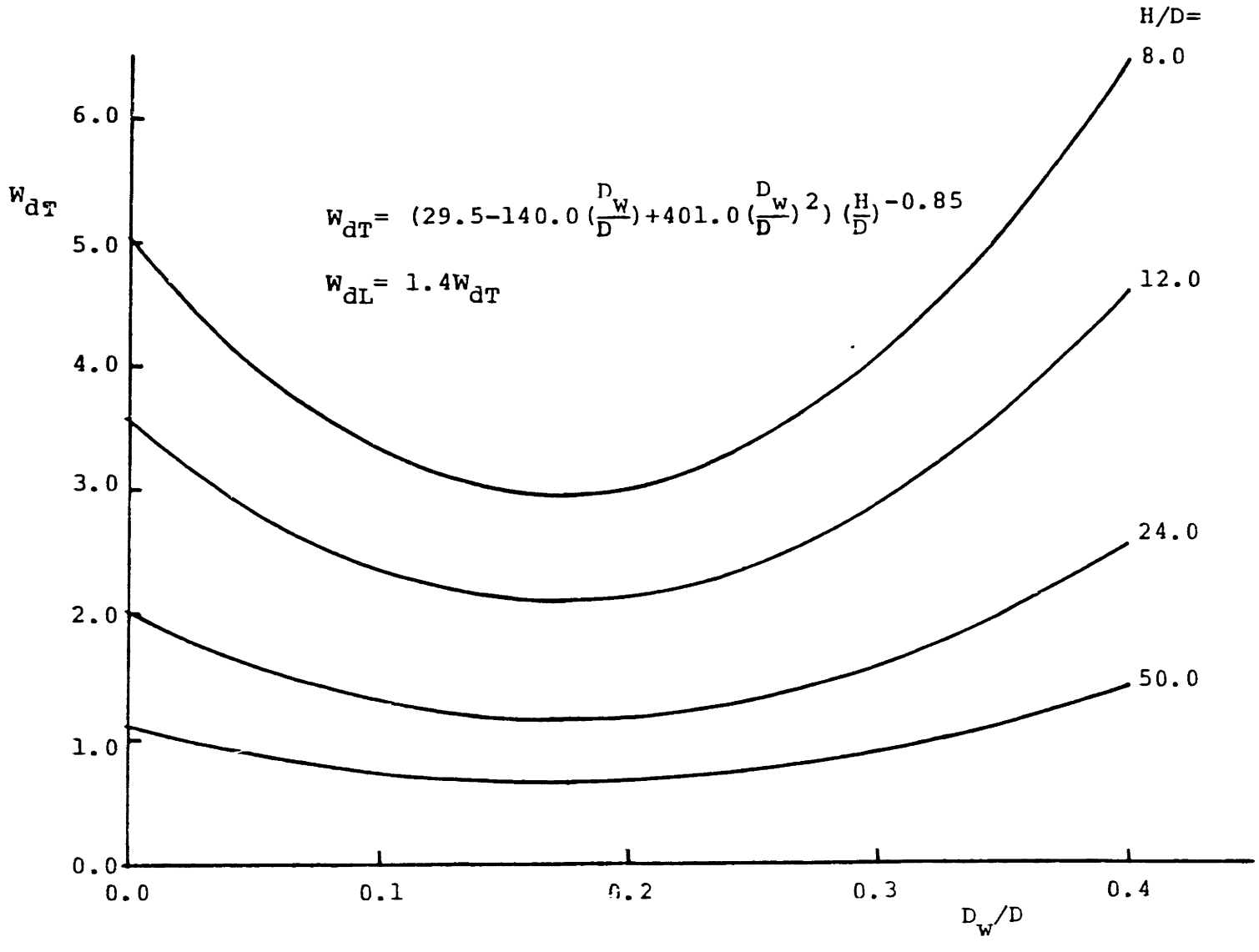

Figure 4.12 Wire Drag Constant W_{dT}

wires traversing the subchannel taken over one axial lead becomes an increasing larger fraction of the total subchannel area. Above a specific value of D_w/D (=0.183) the fraction is greater than unity. This difference in geometrical character may be the reason causing this behavior of W_{dT}.

Figure 4.13 illustrates W_{sT} as a function of H/D. W_{sT} increases as H/D increases, with a value from 5.0 to 26.6 for H/D from 4.0 to 48.0. This is consistent with the swirl flow ratio reduced from mixing experiments in which the transvese velocity in the gap is more than $V_2 \tan\theta$ for high H/D and less than $V_2 \tan\theta$ for low H/D. The trend of this constant is confirmed to be correct.

To check the accuracy of this model and calibration, Figure 4.14 shows the prediction error for overall bundle wire-wrapped turbulent friction factor constants C_{fbT} ($\equiv f_b \cdot Re_b^{0.18}$) from this correlation. The histogram in the right side of this figure is the error distribution for each 2% interval of the 101 bundle data base. Note that all data can be predicted within ±18% error. The standard deviation of this distribution is 8%. If the correlation models the subchannel friction factor accurately enough, the prediction errors for the data only come from the experimental error, which should have a normal distribution as shown by the dashed line in Figure 4.4. For a normal distribution with a standard deviation of 8%, a 92% confidence interval for prediction can be obtained with ±14% (i.e. ±1.75σ) accuracy.

As for the turbulent flow split prediction, Figure 4.15 shows the comparison between wire-wrapped edge subchannel flow split data and the

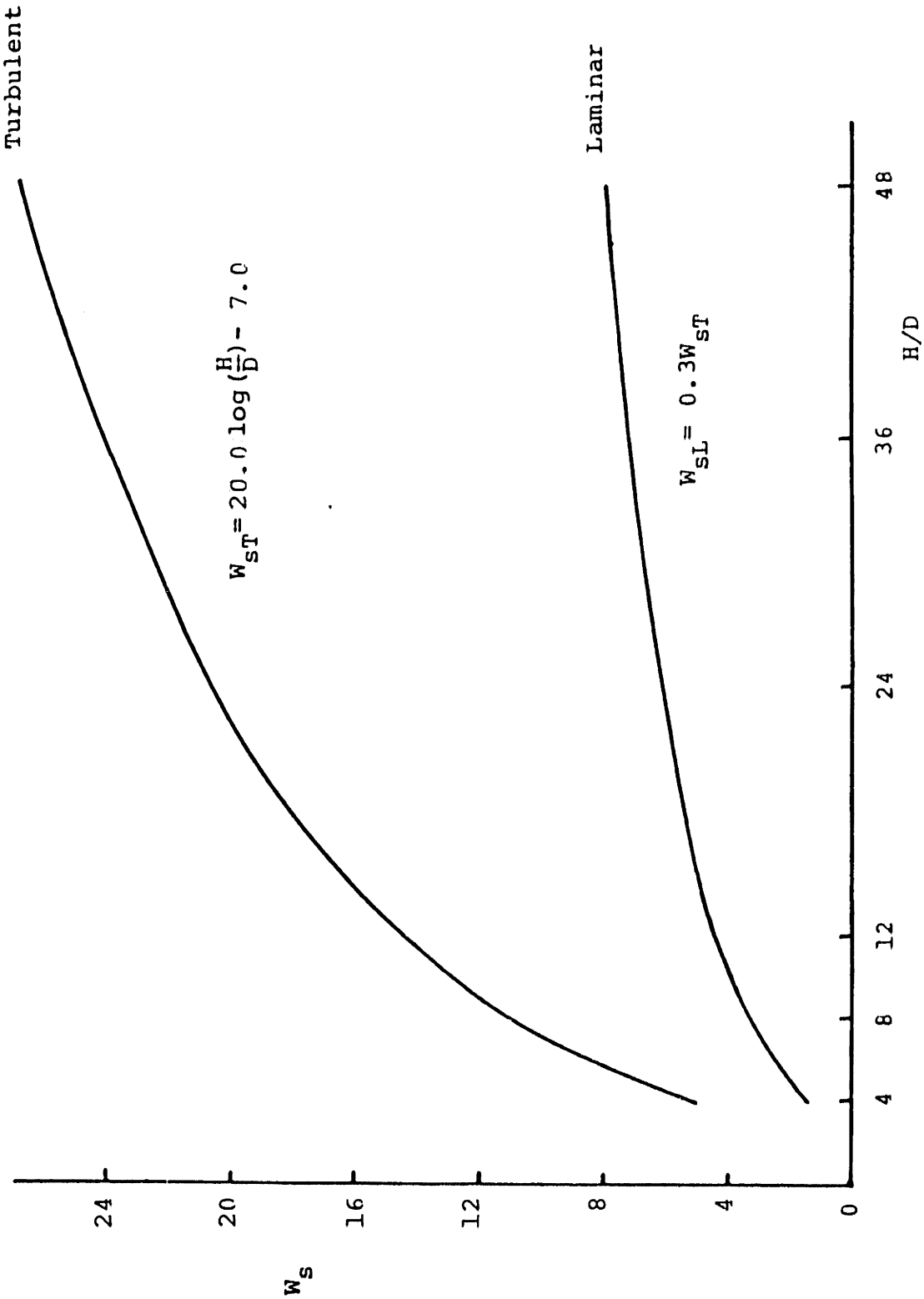

Figure 4.13 Swirl Flow Constant W_s

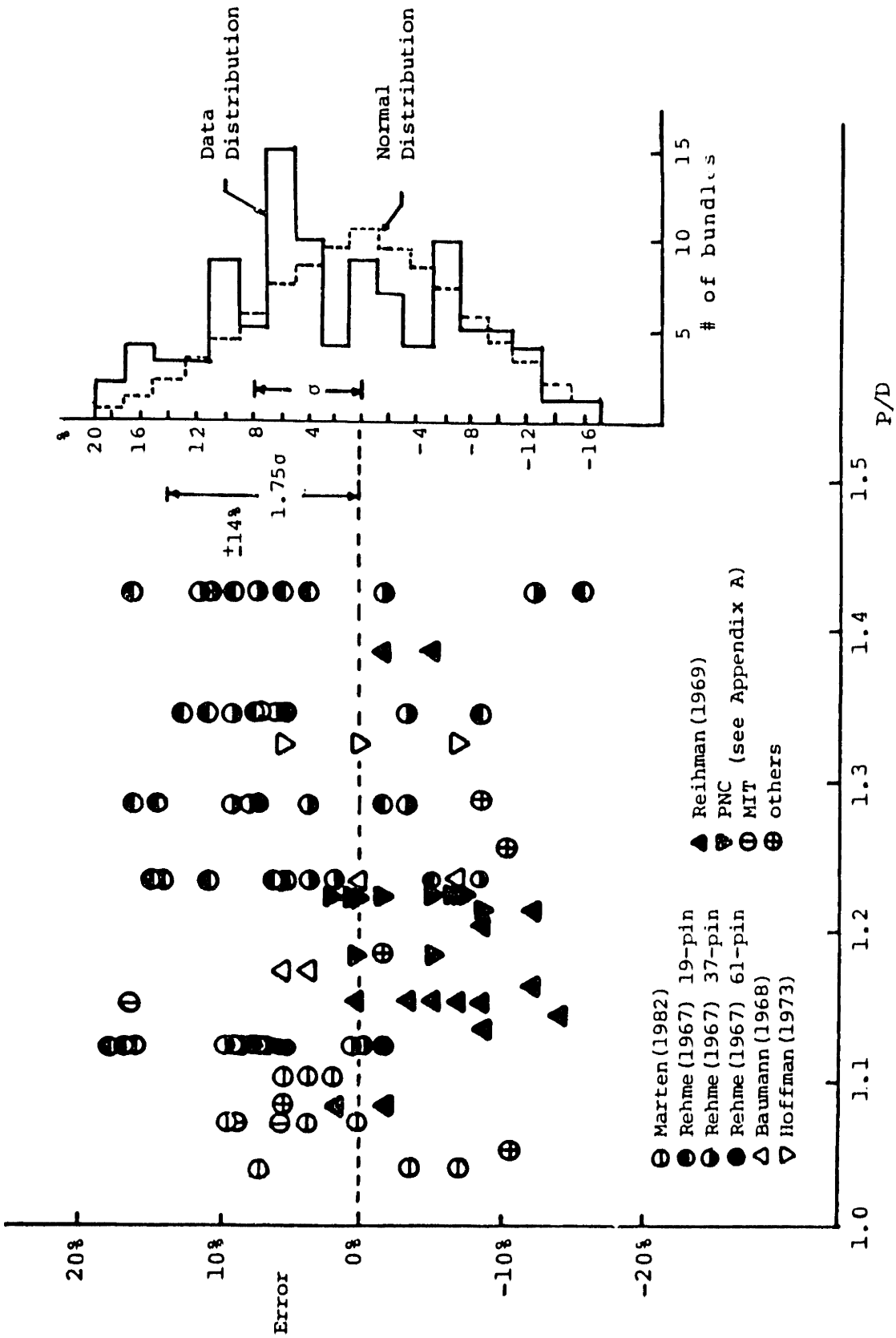

Figure 4.14 Prediction Error for Wire-Wrapped Turbulent Bundle Friction Factor Constant C_{fbT}

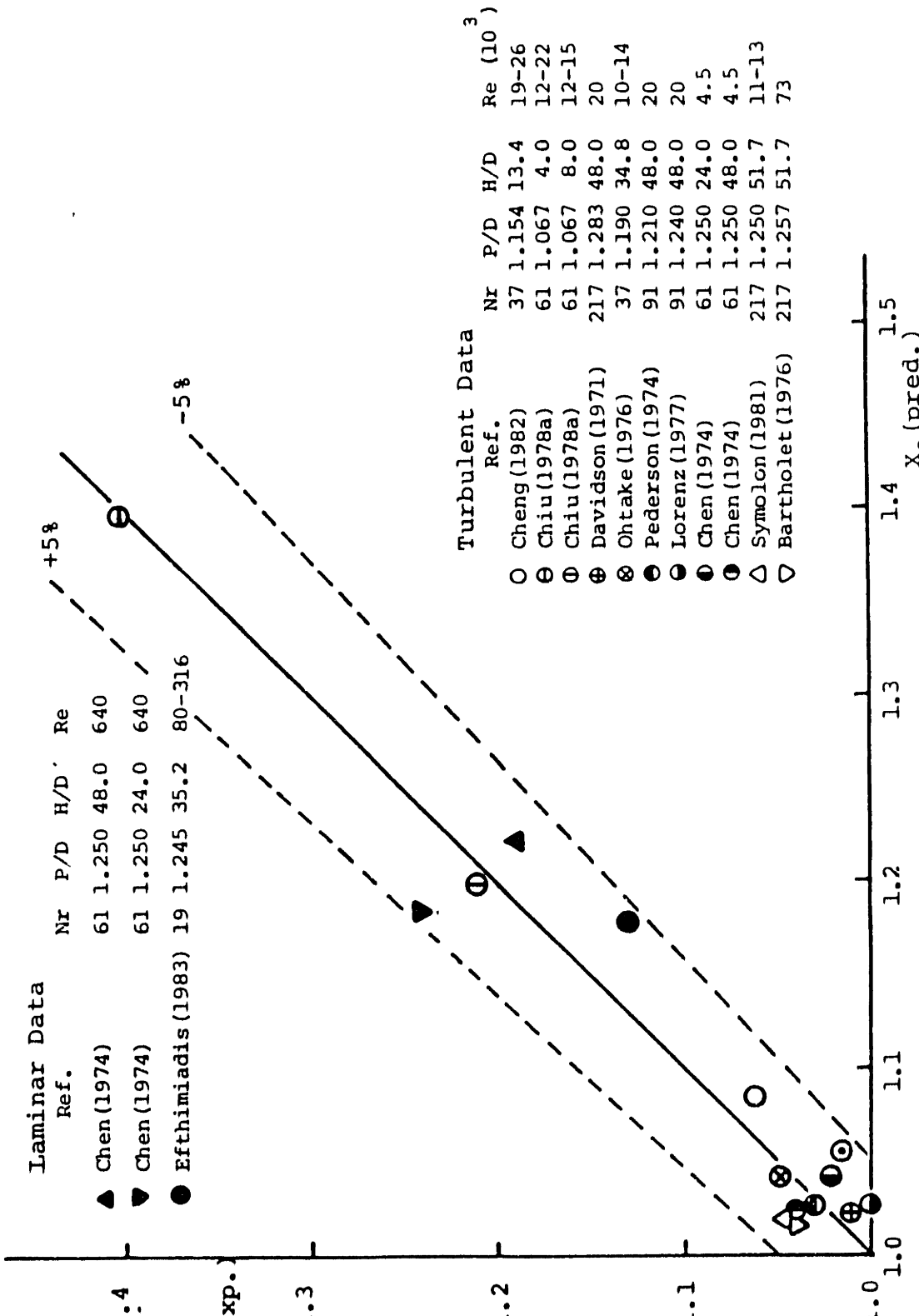

Figure 4.15 Comparison between Experimental Data and Predictions for Wire-Wrapped Edge Subchannel Flow Split Parameter

prediction values. All data are predicted within ±5% error. The accuracy of our correlations is within the experimental error of flow split experiments which are considered to be not less than 5%.

4.5.2 Empirical Constants for the Laminar Region: W_{dL}, W_{sL}

The data in the laminar region are very limited, especially for flow split data as discussed in Section 4.2. Only 19 bundles of our collected data have laminar friction factor data, 9 of which are Marten's low P/D bundles. Table 4.9 lists the investigators, geometries and laminar fRe data of these 19 bundles.

As Table 4.9 shows, there is a large inconsistency between the data for bundles with blanket assembly geometry (P/D ≈ 1.07, H/D ≈ 8.0); the fRe for Chiu's 61-pin is 90, Engel's 61-pin is 99, and Marten's 37-pin is 68. Because of this inconsistency and the lack of laminar flow split data, some assumptions have to be adopted to reduce the complexity in calibrating the laminar constants, W_{dL} and W_{sL}.

First, a similarity in geometrical dependence of W_d and W_s between the turbulent and laminar flow cases is assumed. Therefore, the variations of W_{dL} and W_{sL} as functions of geometrical parameters are the same as that of W_{dT} and W_{sT} respectively, and only two ratios, W_{dL}/W_{dT} and W_{sL}/W_{sT}, need to be determined.

Second, a similarity in Reynolds number dependence between the laminar to turbulent region regarding the relationship of the drag coefficient of a single circular cylinder to that of wires in the model is proposed, i.e.,

$$C_{dL}/C_{dT} \simeq C_{DL}/C_{DT} \qquad (4.65)$$

Table 4.9

Comparison between Data, Predictions of the Proposed Correlation and Predictions of Westinghouse Correlation Eq.(4.7) for Laminar $f_b \cdot Re_b$

Investigators	N_r	P/D	H/D	H(cm)	$f_b \cdot Re_b$	This Model	W.H. Model
Marten(1982)	37	1.041	8.38	13.4	45.0	48.4	92.9
	37	1.041	12.60	20.1	45.0	47.2	75.8
	37	1.041	17.01	27.2	45.0	46.5	65.2
	37	1.072	8.34	12.9	68.0	64.0	98.9
	37	1.072	12.54	19.5	56.0	62.0	80.4
	37	1.072	16.68	25.9	56.0	61.0	69.8
	37	1.101	8.31	12.6	80.0	74.7	104.2
	37	1.101	12.31	18.6	74.0	72.1	85.7
	37	1.101	16.61	25.1	68.0	70.7	73.8
Efthimiadis(1983)	19	1.245	35.20	66.6	82.2	87.4	54.5
Cheng(1982)	37	1.154	13.40	20.2	94.2	81.1	88.4
Itoh(1981)	127	1.176	38.00	20.9	72.7	80.5	89.3
Itoh(1981)	169	1.214	47.40	30.8	77.1	83.3	77.1
Carelli(1981)	61	1.05	20.00	25.4	60.0	51.8	68.3
Burns(1980)	37	1.156	21.00	26.7	85.0	79.4	77.0
Spencer(1980)	217	1.252	51.70	30.0	84.0*	85.5	81.8
Engel(1979)	61	1.082	7.78	10.0	99.0**	68.3	113.9
Chiu(1978b)	61	1.067	4.00	5.1	160.0*	65.7	156.0
Chiu(1978b)	61	1.067	8.00	10.2	90.0	62.5	110.5

* Data used to calibrate W.H. correlation.

** Original published value is 110.0 whichwas revised later [Markley (1982)].

where C_{dL} = drag coefficient of wires at one laminar Re_L

C_{dT} = drag coefficient of wires at one turbulent Re_T

C_{DL} = drag coefficient of circular cylinder at Re_L

C_{DT} = drag coefficient of circular cylinder at Re_T

Re_L, Re_T are both based on D_w

An approximate value for W_{dL}/W_{dT} can then be derived from the drag coefficient of a circular cylinder, which is illustrated in Figure 4.16. For turbulent flow, $C_{DT} \approx 1.2$ and $C_{dT} = W_{dT}/Re_T^{0.18}$. For laminar flow, $C_{DL} \approx 10.0/Re_L$ and $C_{dL} = W_{dL}/Re_L$. Hence,

$$C_{dL}/C_{dT} = (W_{dL}/Re_L)/(W_{dT}/Re_T^{0.18})$$

and

$$C_{DL}/C_{DT} = (10.0/Re_L)/1.2$$

Substituting these results into equation (4.65) yields

$$W_{dL}/W_{dT} = 10.0/(1.2Re_T^{0.18}) \tag{4.66}$$

Typically, for $Re_T = 10^4$, $W_{dL}/W_{dT} = 1.6$; for $Re_T = 2\times10^4$, $W_{dL}/W_{dT} = 1.4$; and for $Re_T = 5\times10^4$, $W_{dL}/W_{dT} = 1.2$; therefore, for $10^4 \leq Re_{Dw} \leq 5\times10^4$, an average value for $W_{dL}/W_{dT} = 1.4$ is obtained. W_{dL} is then found to be

$$W_{dL} = 1.4W_{dT}$$

$$= [\ 41.3 - 196.0(\frac{D_w}{D}) + 561.0(\frac{D_w}{D})^2\ ](\frac{H}{D})^{-0.85} \tag{4.67}$$

Now the only constant left to be determined is W_{sL}/W_{sT}. This ratio is calibrated from the laminar bundle friction factor constant

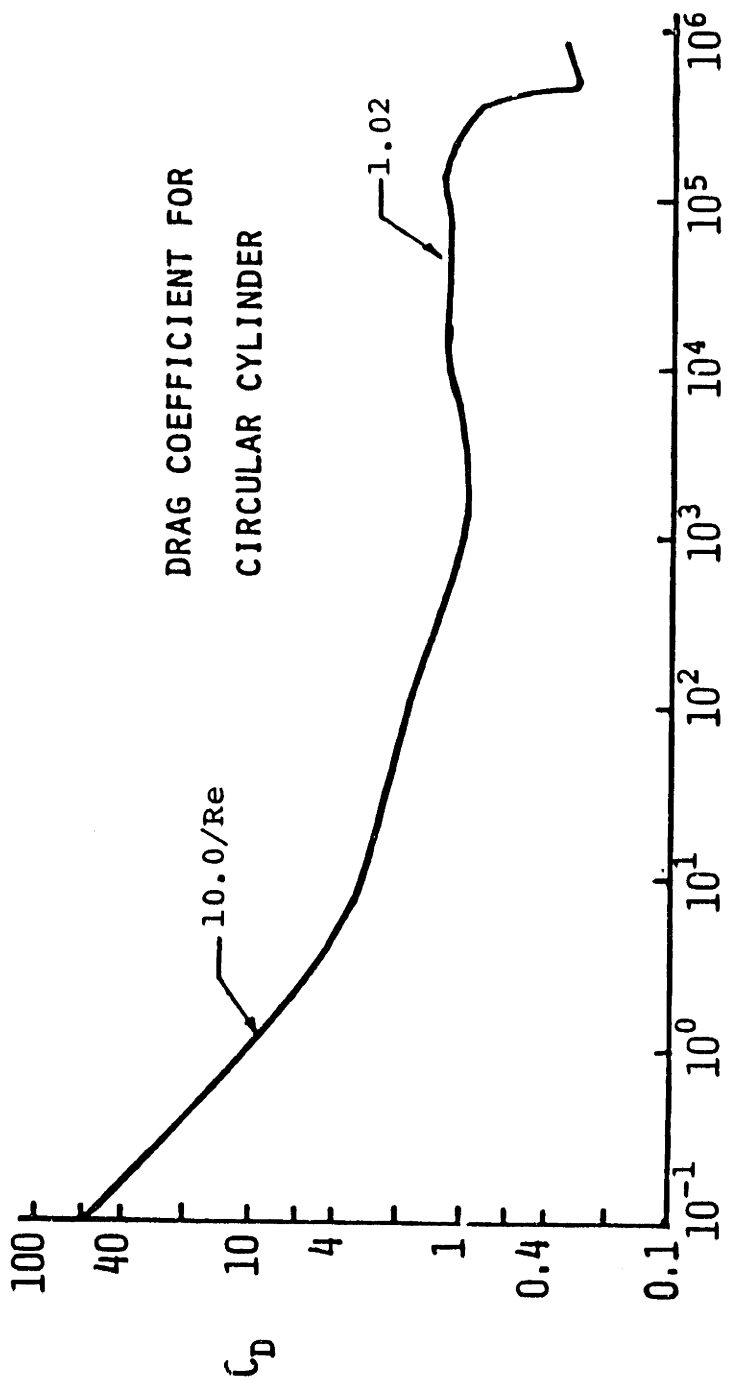

Figure 4.16 Drag Coefficient for Circular Cylinder

(f•Re) data listed in Table 4.9. The W_{sL}/W_{sT} ratio which makes the predictions for these bundles match the data is 0.3. Therefore,

$$W_{sL} = 0.3W_{sT}$$

$$= 6.0 \log(\frac{H}{D}) - 2.1 \qquad (4.68)$$

Figure 4.17 compares the predictions for laminar f•Re with the experimental values. Since only one constant, W_{sL}/W_{sT}, is calibrated by all the friction factor data and this correlation can well predict Marten's data, which are considered to be quite accurate, as well as the other high P/D (>1.1) data, the correlation for the laminar region is considerd optimum based on the existing data base.

This calibration result for W_{sL}/W_{sT}, 0.3, is very consistent with the data of local swirl flow ratio, C_{1L}, which is the ratio of the transverse velocity at the gap to average axial velocity in edge subchannels from mixing experiments i.e., $V_T\big|_{gap}/V_2$. The ratio of laminar to turbulent local swirl flow ratio, i.e.,

$$\frac{(C_{1L})_L}{(C_{1L})_T} = \frac{(V_T\big|_{gap}/V_2)_L}{(V_T\big|_{gap}/V_2)_T},$$

from these experiments varies from 0.3 to 0.6, whereas from the results just presented, the ratio of laminar (V_T/V_2) to turbulent (V_T/V_2) is $\sqrt{W_{sL}/W_{sT}}$, i.e., 0.55. Although the velocities V_T and $V_T\big|_{gap}$ are not defined identically, the ratio of their ratios with respect to V_2 in laminar and turbulent flow should be approximately the

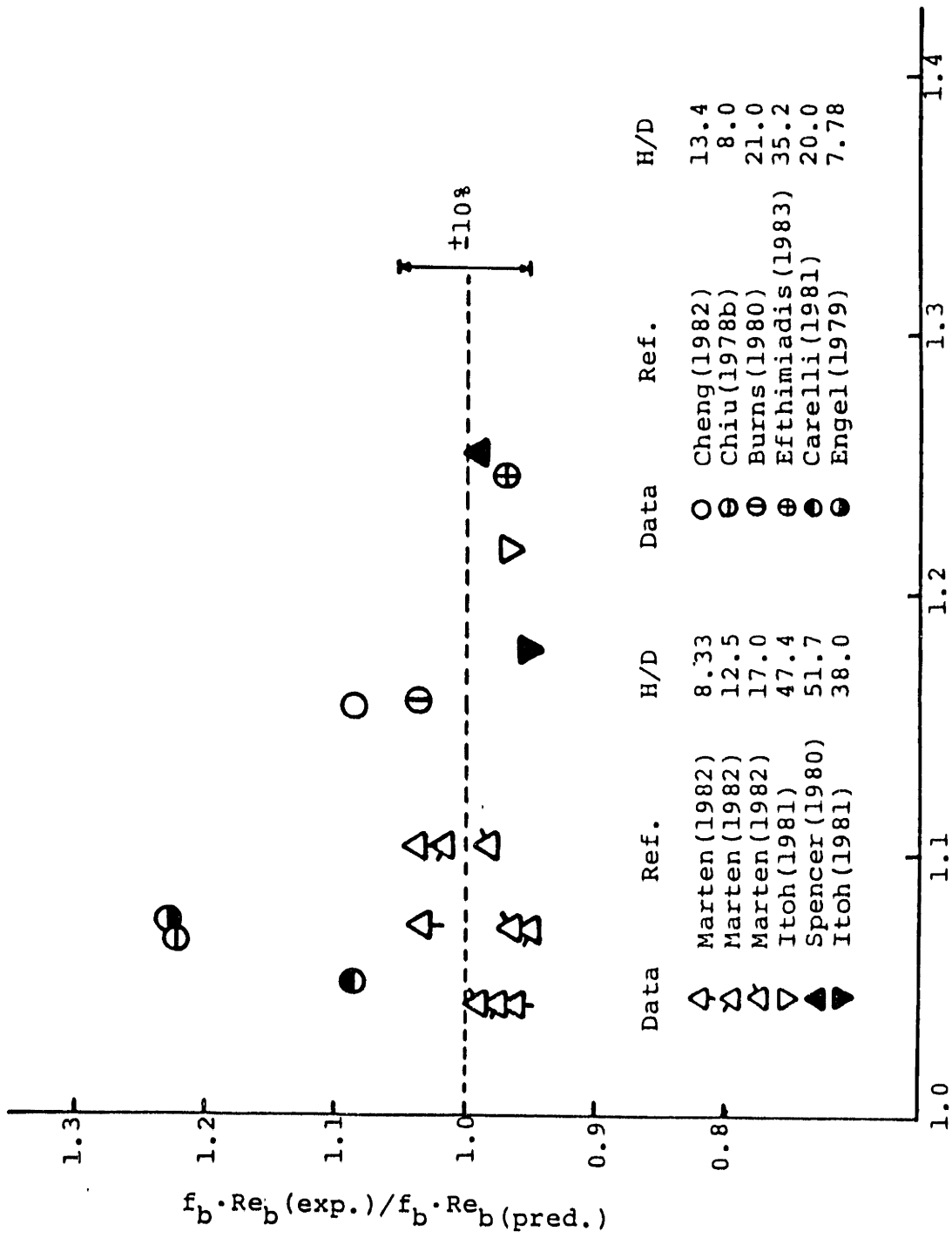

Figure 4.17 Comparison between Experimental Data and Predictions for Wire-Wrapped Laminar Bundle Average $f_b \cdot Re_b$

same, i.e.,

$$\frac{(V_T|_{gap}/V_2)_L}{(V_T|_{gap}/V_2)_T} \simeq \frac{(V_T/V_2)_L}{(V_T/V_2)_T}$$

Our values for these ratios of 0.3 to 0.6 ≃ 0.55 once again confirms the soundness of our model.

An indicator of the accuracy of these constants is the degree to which flow split predictions based on them agree with the available data existing of three bundles, i.e., Chen (1974) two cases, Efthimiadis (1983). These comparisons are also shown in Figure 4.15, which indicates that these data are predicted within 5% error. Also, for those bundles which have transition flow split data but not laminar data, the predicted laminar flow split parameters for these bundles are around the right limit of these transition data for very low flow rate.

4.5.3 Empirical Constant for the Transition Region: γ, β

In the transition region, the empirical constants which need to be calibrated are the exponent γ for the intermittency factor ψ_i in equation (4.35) and β in equation (4.51). γ is calibrated from the bundle friction factor data in the transition region ($Re_{bL} < Re_b < Re_{bT}$) and is assumed to be the same for the three kinds of subchannels. Note that in this procedure, the transition flow split data are not used to calibrate any constants. After γ is found, the flow split parameters can be calculated from the pressure drop equation (4.36) and the mass balance equation (4.37) using subchannel friction factors calculated by equation (4.35). Since these are a set nonlinear equations, Newton's iteration method is used to solve for the flow

split parameters. Note that the flow split parameters calculated by this method satisfy the mass balance requirement.

The constant γ is adjusted to minimize the root mean square of the prediction error of all transition data points. By this method, γ is calibrated to be 1/3, which yields a root mean square of the prediction error of 9.3%. To illustrate the validity of this constant, Figures 4.18a and 4.18b show the comparison between the predictions and experimental data for bundle friction factor as function of Re for several new experiments which have produced data in all three flow regions. The trend in transition region is well simulated by this transition model.

The predictions for X_2 based on the assumption that γ is the same for all three kinds of subchannels always fall below the data as illustrated in Figure 4.19 for three bundles which have transition flow split data obtained by the isokinetic extraction method; i.e., IEM, [this work, Symolon(1981), Chiu(1978a)]. Note that this means X_1 is overpredicted by this method because of the mass balance requirement. Many approaches have been investigated to eliminate this discrepancy, e.g., different γ's for different kinds of subchannels, different transition equation, e.g., the old model equation (1.4), or different γ's for laminar and turbulent components; however, no improvement could be obtained.

Since in IEM, there is a flow rate below which the flow can not be extracted from the interior subchannel, a systematic error is believed to exist in those data near that flow rate. The edge flow split

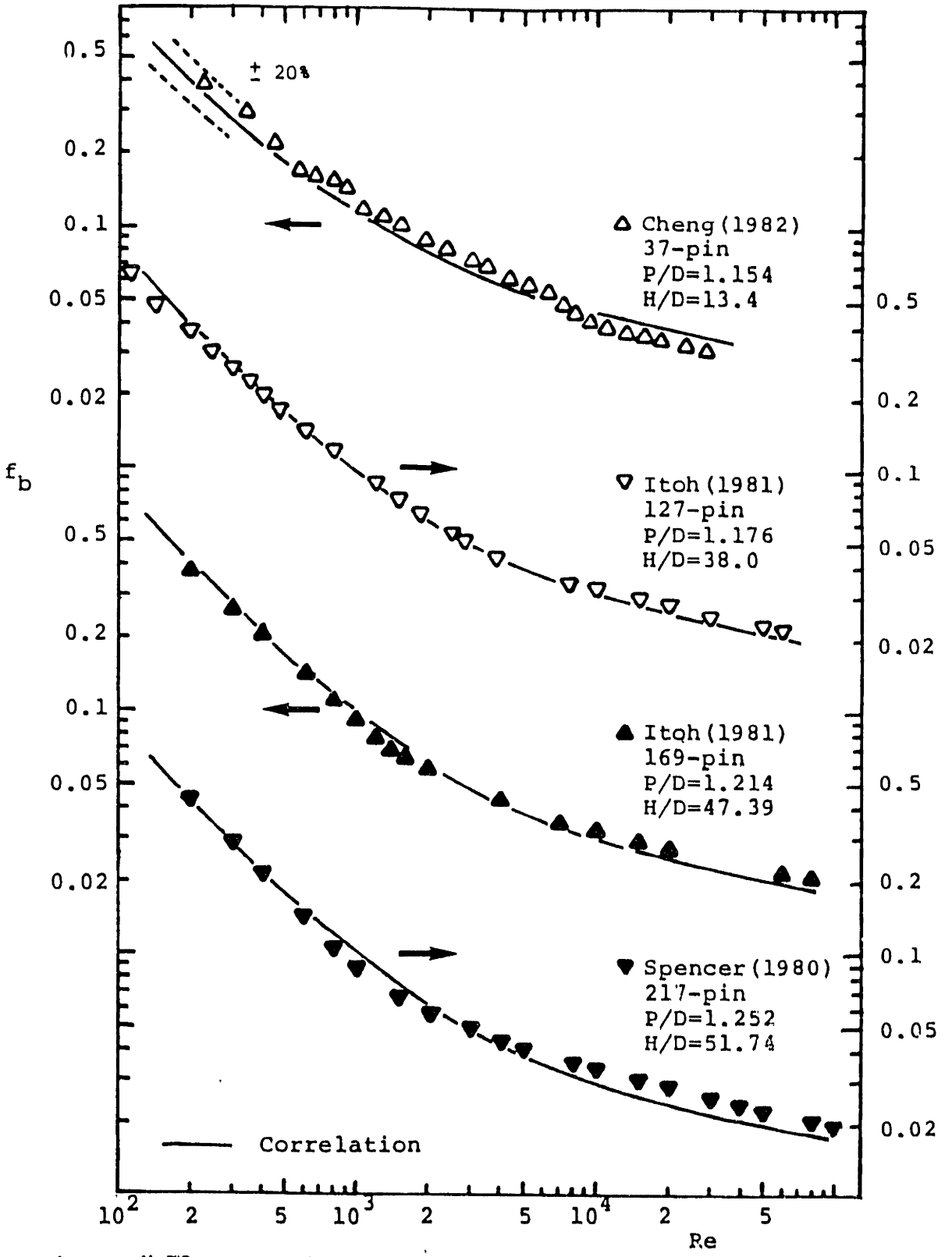

Figure 4.18a Comparison between Experimental Data and Predictions for Wire-Wrapped Bundle Friction Factor (P/D > 1.1)

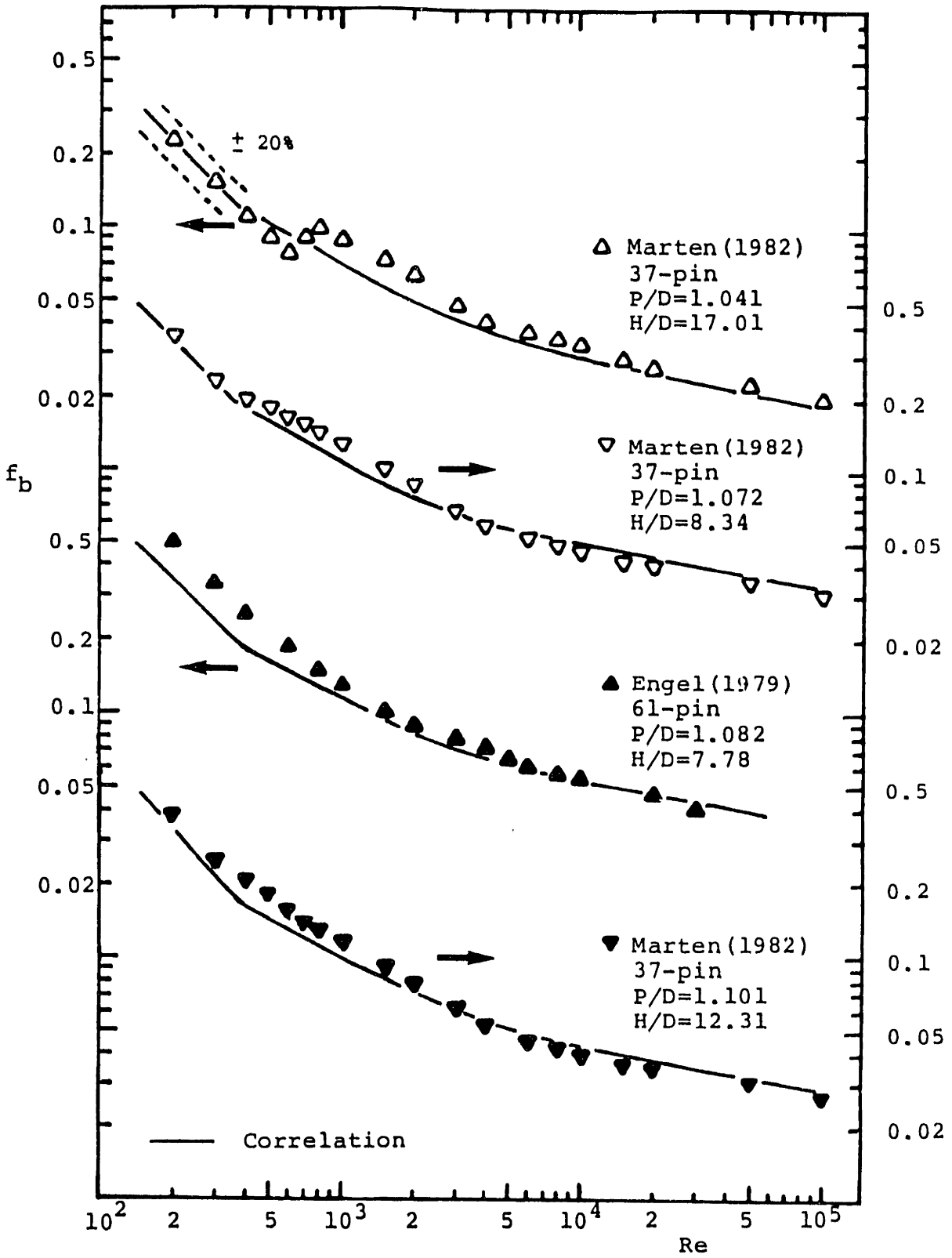

Figure 4.18b Comparison between Experimental Data and Predictions for Wire-Wrapped Bundle Friction Factor (P/D ≤ 1.1)

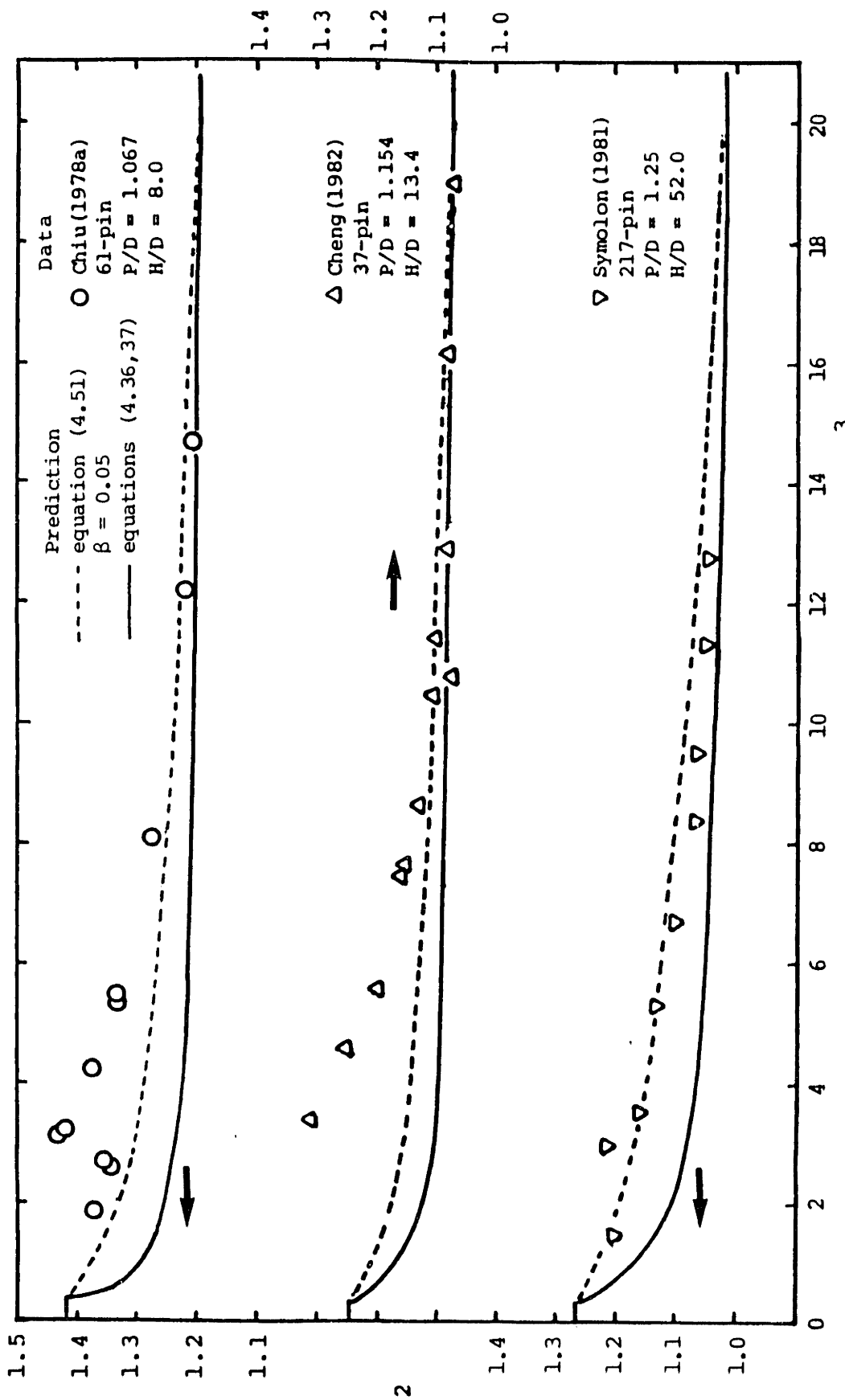

Figure 4.19 Comparison between Wire-Wrapped Edge Flow Split Data and Predictions in the Transition Region

parameter in these experiments is calculat.d by

$$X_2 = \frac{V_2}{V_b} = \frac{m_{2t}/A_{2t}}{m_t/A_t} \tag{4.69}$$

where m_{2t} = total flow rate extracted from edge subchannels

A_{2t} = total flow area for edge subchannels

m_t = total flow rate extracted from all subchannels

A_t = total bundle flow area

At this critical point $m_t = m_{2t}$ because no flow is extracted from interior subchannels. Hence

$$X_2 = \frac{A_t}{A_{2t}} \tag{4.70}$$

In the real situation, however, the flow in the interior subchannel should never be zero, and m_t is always higher than m_{2t}. Hence X_2 should be less than A_t/A_{2t}. Because of this breakdown of this technique, the flow split data obtained by IEM near this point are believed to be too high. This systematic error should gradually disappear as flow rate increases. From this point of view, the observation that the predictions fall below the edge flow split data is expected.

The approximate solution for transition flow split parameters, equation (4.51), with an empirical constant β, which adjusts the effect of the turbulent part, is one option to improve the predicitons. A β value of 0.05 gives the best match for transition flow split data. X_2 curves predicted by equation (4.51) with $\beta = 0.05$ are also shown as dash line in Figure 4.19 for comparison.

4.6 Summary of Correlations

4.6.1 Summary

The formulae for subchannel friction factors and flow split parameters have been derived in section 4.3 and summarized in section 4.3.5.

Calibration of the empirical constants, K_i, W_d, W_s, γ, and β of these correlations have been described in the last two sections. In summary,

K_{1L}, K_{2L}, K_{3L} from equation (4.54) and Table 4.1

K_{1T}, K_{2T}, K_{3T} from equation (4.54) and Table 4.6

W_{dL}, W_{dT} from equations (4.67) and (4.68), respectively

W_{sL}, W_{sT} from equations (4.68) and (4.64), respectively

$\gamma = 1/3$

$\beta = 0.05$

These correlations are valid over the following geometry and Re range for both Bare and Wire-wrapped bundles

$$19 \leq N_r \leq 217$$

$$1.0 \leq P/D \leq 1.42$$

$$4.0 \leq H/D \leq 52.0$$

$$50 \leq Re \leq 10^6$$

These correlations have been programed in a computer program WWCR which calculates the friction factors and flow split parameters for bare or wire-wrapped rod bundles. Appendix B2 presents this program

and its input and output formulations.

The parametric behavior of the bundle average friction factor and edge flow split parameter for the range of the P/D and H/D values calculated by WWCR for bare and wire-wrapped bundles in the laminar and turbulent regions will be presented in the following sections. The transition region will not be discussed since the values in this region are a combination of the laminar and turbulent values.

4.6.2 Parametric Behavior for Bare Rod Bundles

The bare rod bundle is a special case of these correlations in which the wire diameter is zero. Note that in the models, no restriction has been imposed on the wire diameter except that P should be greater than $(D+D_w)$. Hence the correlations are theoretically applicable to bundles with wire of one size whose diameter varies from zero to (P-D). However, they have only been verified at the two extreme conditions, i.e., bare rod bundles in which $D_w = 0$ and wire-wrapped rod bundles in which $D_w \simeq P-D$.

In contrast to the wire-wrapped empirical constants, which are calibrated from the data, the bare rod friction factor constants K_i's are obtained from theoretical results and then verified by comparison with subchannel and bundle friction factor data.

To illustrate the predictions for bare rod bundles, Figure 4.20 and 4.2.1 depict the bundle friction factor constants C_{fb} as function of P/D for a 37-pin bundle with W/D = P/D for turbulent and laminar cases,respectively. In both figures, the dependance of the constants as a function of P/D are quite similar to bare interior subchannels. According to the results of WWCR, these constants C_f's are a very

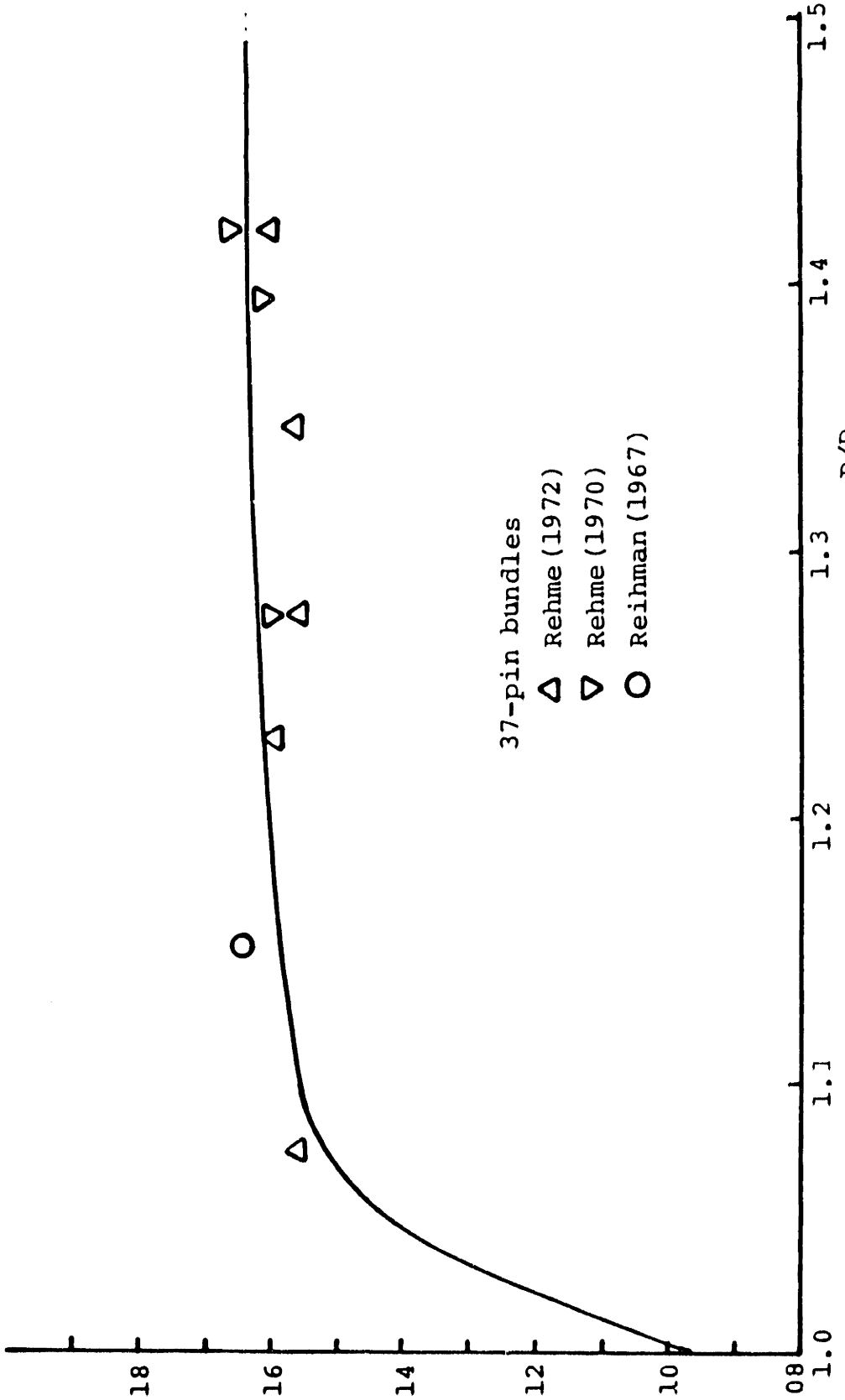

Figure 4.20 Comparison between Experimental Data and Predictions for Bare Rod 37-pin Turbulent Friction Factor Constant C_{fbT} (= $f_b \cdot Re_b^{0.18}$)

slightly increasing function of bundle pin number, N_r.

Data for 37-pin turbulent friction factor constant are also shown in Figure 4.20 for comparison; however, no low P/D bundle fricition factor data are available and the predictions for low P/D cases can only be verified by subchannel data (c.f. Figure 4.8). The data for laminar friction factor constant in Figure 4.21 are from Rehme's results for bare rod bundles which have W/D ≈ P/D. These data are well predicted by the model.

Figure 4.22 illustrates the edge flow split parameter as function of P/D for a 61-pin bare rod bundle with W/D = P/D. Because the equivalent diameter of an edge subchannel (with W/D = P/D) is always higher than that of interior subchannel, the edge flow split parameters are always higher than 1.0 as shown. The decreasing behavior of these curves is caused mainly by the difference in the change of equivalent diameter for different kinds of subchannels as P/D increases. The laminar value is consistently higher than turbulent value because of the difference in Reynolds number dependence (Re^{-1} vs. $Re^{-0.18}$) in friction factor equations.

4.6.3 Parametric behavior for Wire-Wrapped Bundles

4.6.3.1 Bundle Friction Factor Constants

Figures 4.23 and 4.24 depict the bundle friction factor constants, C_{fbT} and C_{fbL}, as functions of P/D and H/D for a 37-pin wire-wrapped bundle with W/D = P/D for the turbulent and laminar regions, respectively. The pin number effect is the same as bare rod case, i.e., these constants increases slightly as pin number

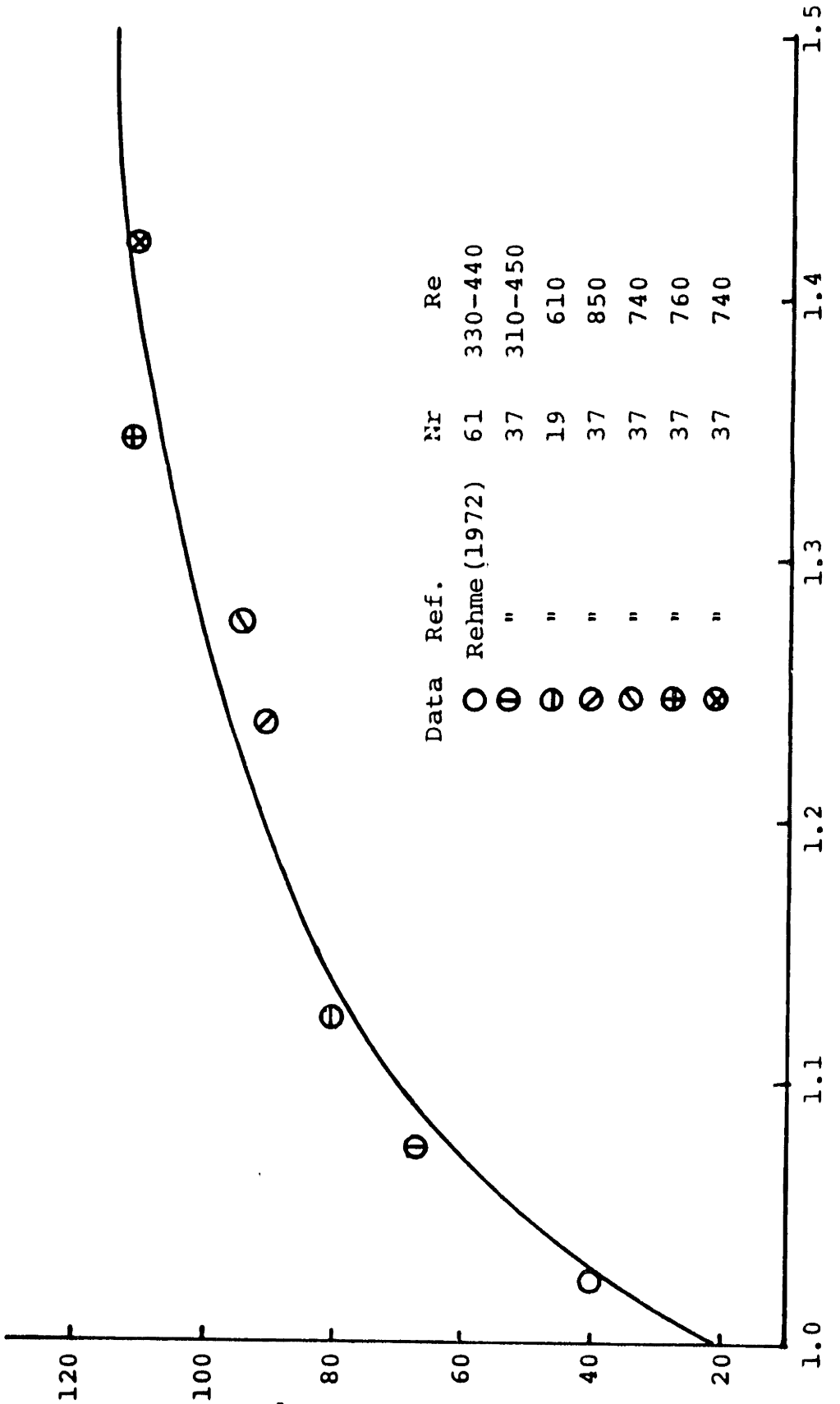

Figure 4.21 Predictions for Bare Rod 37-pin Laminar Friction Factor Constant C_{fbL} (= $f_b \cdot Re_b$)

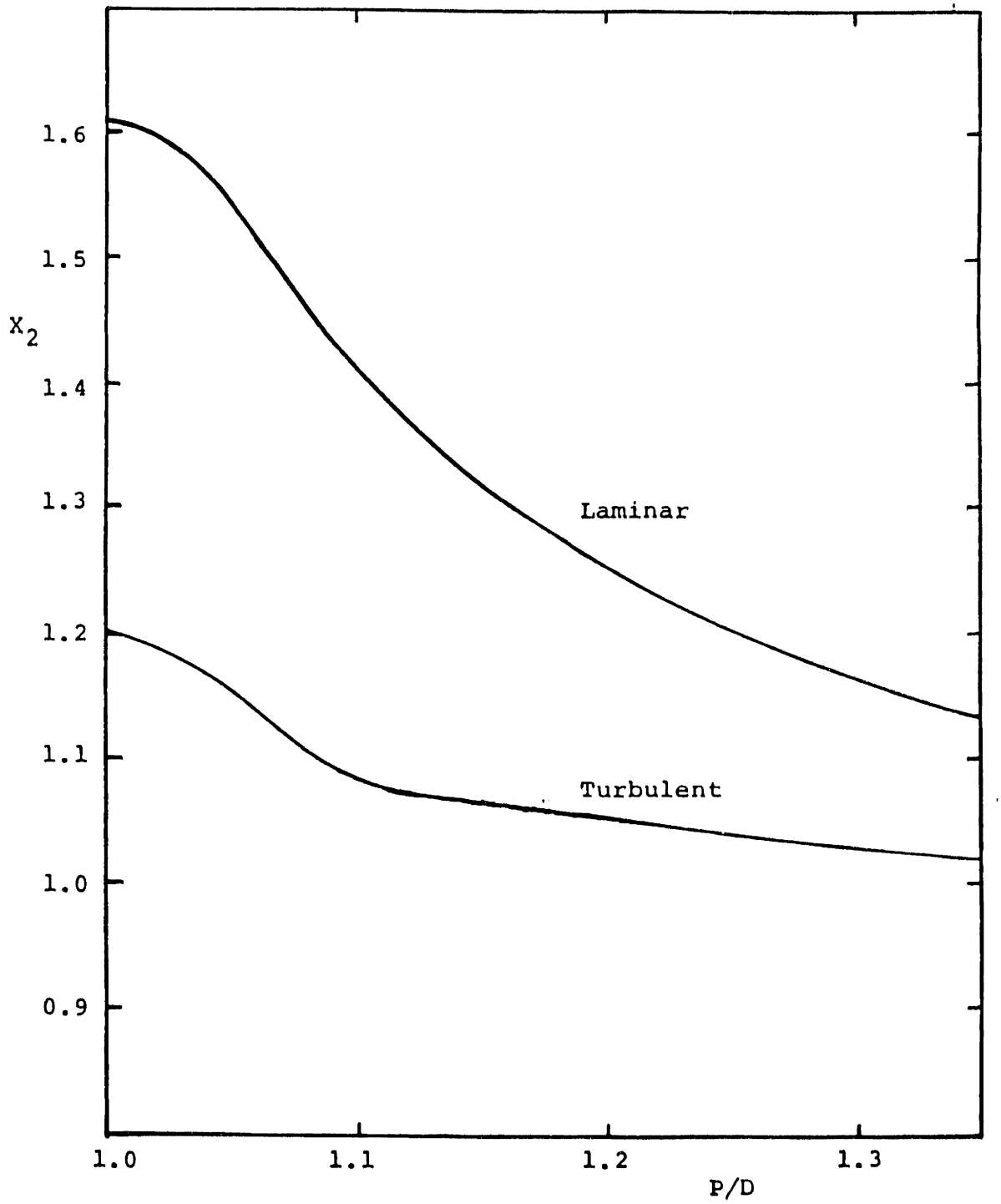

Figure 4.22 Predicted Edge Subchannel Flow Split Parameter for 61-pin Bare Rod Bundle

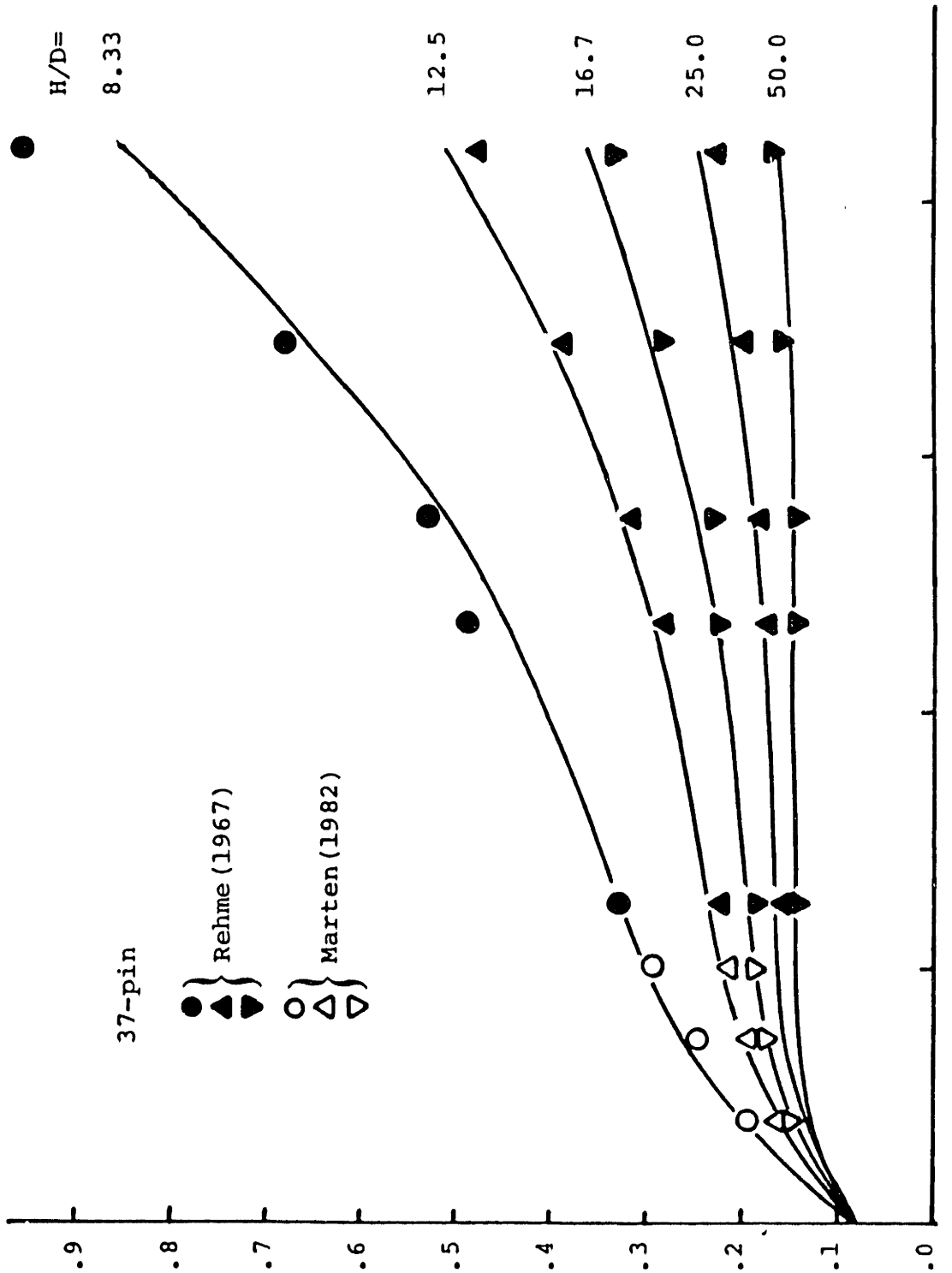

Figure 4.23 Comparison Between Experimental Data and predictions for Wire-Wrapped 37-pin Turbulent Friction Factor Constant C_{fbT} (= $f \cdot Re^{0.18}$)

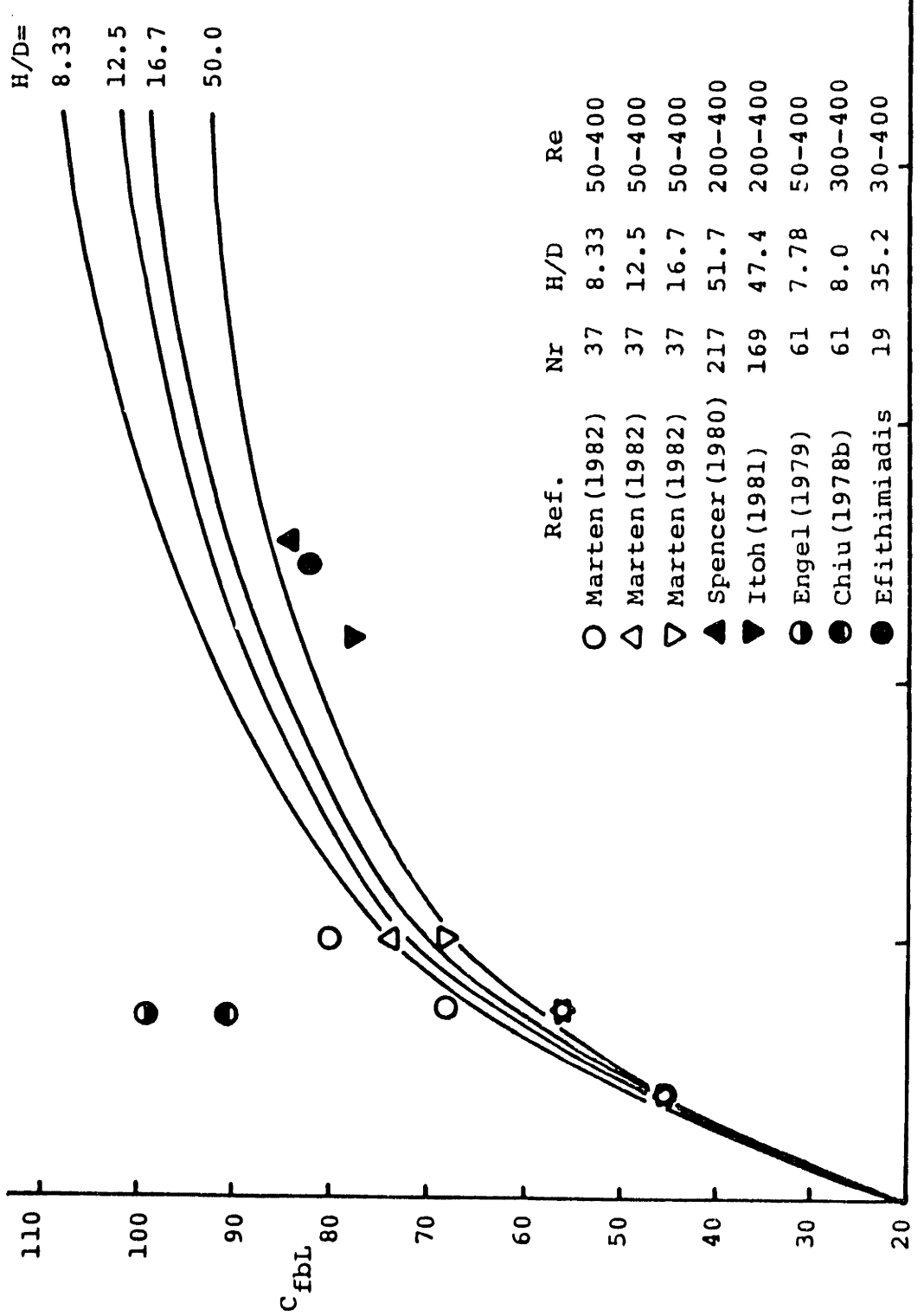

Figure 4.24 Comparison between Experimental Data and Predictions for Wire-Wrapped 37-pin Laminar Friction Factor Constant C_{fbL} (= f.Re)

increases. The P/D effect on these two constants is also similar to the bare rod case.

Although the H/D effect of these two constants is similar to each other, i.e., C_f increases as H/D decreases because of the wire drag effect, the change in absolute value is quite different from laminar to turbulent case. For the laminar case, C_f changes slightly from H/D = 50.0 to 8.0, while for turbulent case, C_f increases approximately five fold from H/D = 50.0 to 8.0. This indicates that the wire drag effect is much stronger in the turbulent region than that in the laminar region.

The turbulent data in Figure 4.23 are from Rehme's (1967) 37-pin bundles and Marten's (1982) 37-pin bundles. As shown in this figure, these correlations can predict not only Rehme's data (P/D > 1.1) but also Marten's data (P/D <1.1) which can not be well predicted by Rehme's correlation [Marten(1982)]. This confirms that the applicable range for P/D for these correlations is from 1.0 to 1.42.

The laminar data in Figure 4.24 are from Marten's (1983) 37-pin bundles together with Efthimiadis' (1983) 19-pin bundle and two high P/D, high H/D but higher N_r bundles. These data can be predicted by the correlations within 10% error, which is considered to be about the experimental error. Two other 61-pin bundle data of Chiu (1978b) and Engel (1979), are also shown for comparison. The inconsistence between data from blanket bundles is clear, and the correlations predict the value quite close to Marten's results rather than these other two data. This is because Marten's data were adopted as the basis upon which to base the correlation as discussed in Section 4.5.2.

The Westinghouse correlation, equation (4.7) can predict Chiu and Engel's data because it was calibrated by those data; however, it can not predict Marten's data and Efthimiadis data which has quite long H (66.6 cm). Table 4.9 compares the available laminar fRe data and the predictions from this correlation and Westinghouse correlation. Marten's data confirm the validity of this correlation and the lack of generality of Westinghouse correlation.

4.6.3.2 Flow Split Parameters

Figure 4.25 illustrates how the edge flow split parameter varies as a function of P/D and H/D in a 61-pin bundle with W/D = P/D for both laminar and turbulent flow conditions. Again, the P/D effect is similar to bare rod case because of the equivalent diameter effect. However, there is a minimum around P/D = 1.2 for H/D $\leq$ 24 in turbulent case. This is caused by the wire drag constant which increases as D_w/D becomes greater than 0.18. Hence the friction factor for interior subchannels increases relatively for D_w/D greater than 0.18 and this produces a higher velocity in edge subchannels.

The H/D effects for the laminar and turbulent cases are opposite to each other as shown in this figure. For the turbulent case, X_2 decreases as H/D increases, while for laminar case, X_2 increases as H/D increases. This may be explained from the effect of H/D on the interior subchannel friction factor, f_1, and the edge subchannel friction factor, f_2.

From equation (4.31), f_1 increases as wire drag effect increases, (i.e., H/D decreases). From equation (4.24), f_2 increases as swirl flow effect increases (i.e., H/D decreases). Note that although W_s

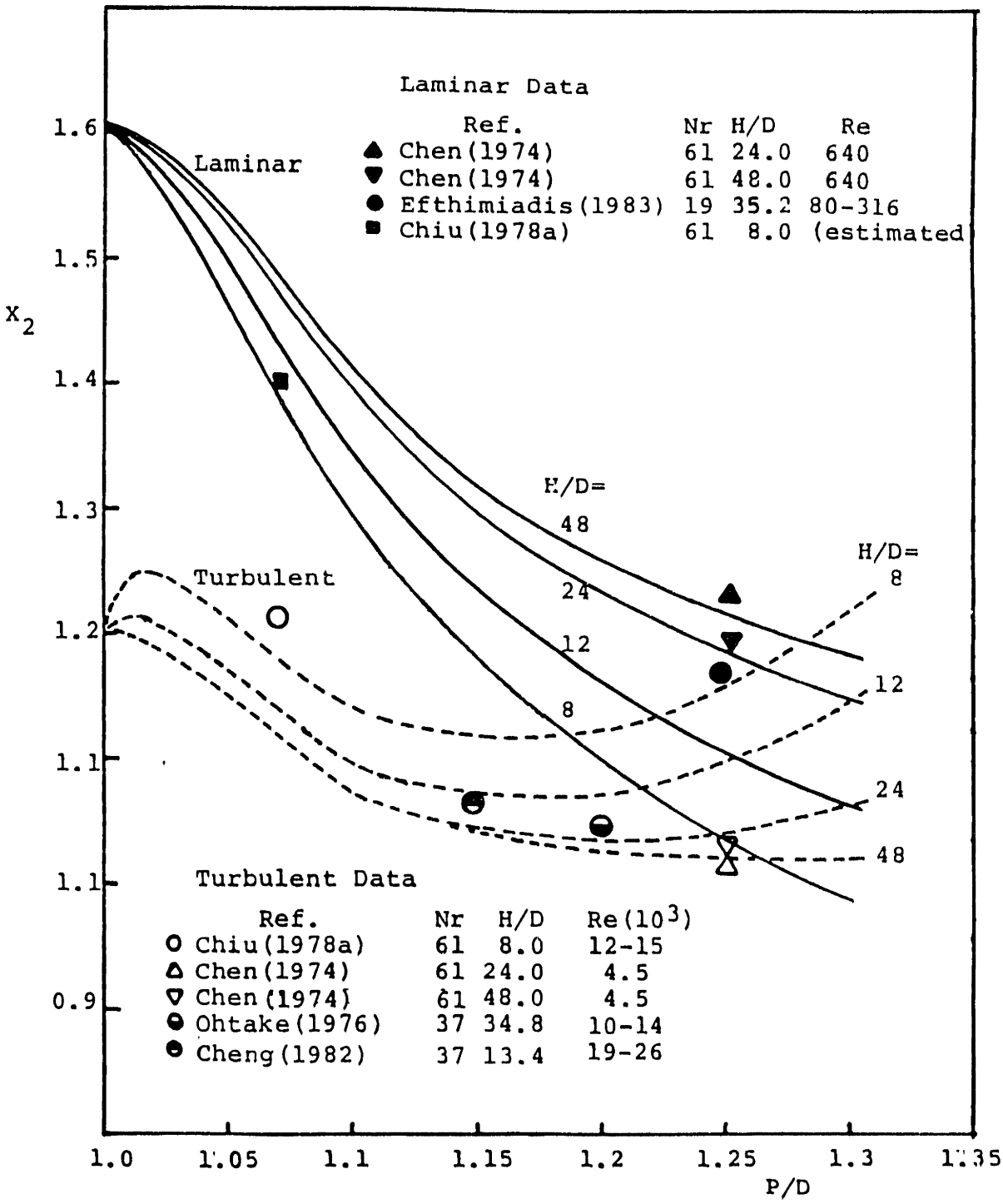

Figure 4.25 Predictions of Edge Flow Split Parameter for Wire-Wrapped 61-pin Rod Bundle

increases as H/D increases, the total swirl flow ratio, V_T/V_2 ($=\sqrt{W_s(A_r/A_l')\tan\theta}$), decreases from around 0.5 to around 0.05 as H/D increases from 8 to 48 for the turbulent case. Since in turbulent flow f_l is strongly affected by wire drag effect, this makes swirl flow effect relatively less important. Hence f_l increases more than f_2 does as H/D decreases; therefore, X_2 increases as H/D decreases. As for laminar flow, f_l is only slightly affected by wire drag effect, this makes swirl flow effect relatively more important. Hence f_l increases less than f_2 does as H/D decreases; therefore, X_2 decreases as H/D decreases.

To compare the predictions with data, some edge flow split data are also shown in Figure 4.25. The trend of these data is well predicted and all data can be predicted within 5% error.

4.6.4 Conclusion

A subchannel friction factor correlation applicable to both bare and wire-wrapped hexagonal rod bundles has been developed and calibrated. The validity of this correlation is confirmed by bare subchannel friction factor data, bare and wire-wrapped bundle average friction factor data, and wire-wrapped flow split data. The correlation can predict the bundle average friction factor data within ±14% with a 92% confidence interval and all the flow split data within ±5% except that in the transition region. This study concludes that the reported transition flow split data obtained by the isokinetic extraction method has a systematic error in this flow regime.

CHAPTER 5

DATA REDUCTION FOR MIXING EXPERIMENTS

5.1 Introduction

5.1.1 Validity of Salt Injection Experiment

The main purpose of the salt injection experiment is to simulate the coolant energy mixing process in an LMFBR bundle and to provide quantitative results for this process. The experiments employ water in place of sodium coolant. The geometrical characteristics of our bundle are similar to those of an LMFBR bundle. The question of the applicability of the mixing parameters based on salt injection into water experiments to the sodium energy mixing process has been investigated by Chiu (1978c). To investigate this question, we consider the two step process: salt mixing to heat mixing in water followed by heat mixing in water to heat mixing in sodium. Therefore, successful simulation primarily depends on the following conditions:

a) similarity between salt mixing and heat mixing due to eddy and wire sweeping effects only of a wire-wrapped subassembly in a water loop.

b) Similarity of heat mixing in water and in sodium for a given wire-wrapped bundle.

These two similarities will be investigated in this section.

From the definition of C_{1L} and $\varepsilon^*_{1\eta}$ in chapter 2, one realizes that C_{1L} represents the ratio of the actual average transverse flow rate to the average axial flow rate in the edge region while $\varepsilon^*_{1\eta}$

represents the combination of effects of turbulent interchange, W'_{ij}, which includes eddy effects only, and wire sweep flow, W'^{W}_{ij} on energy transfer between subchannels. This sweep flow is physically the lateral flow between subchannels. For a given bundle, working fluid (water) and flow condition, the edge transverse flow and the interior wire sweeping flow bear the same value for both salt mixing and heat mixing. Further, if one assumes that W'_{ij} for mass interchange equals that for heat interchange, similarity condition (a) above is easy to confirm since the salt diffusion is negligible in comparison with the total mixing (about 10^{-4} from [Chiu (1978c)]), i.e.,

$$\text{effects of diffusion} + W'_{ij} \text{ for mass} + W'^{W}_{ij} \text{ for mass}$$

$$= W'_{ij} \text{ for heat} + W'^{W}_{ij} \text{ for heat}$$

Similarity condition (b) will be investigated in detail here employing a revision of Chiu's argument. Since the velocity field in forced convection, is independent of the temperature field, it can be determined by solving the mass and momentum equations only. In nondimensional form, these equations are

$$\text{mass} \qquad \nabla^* v^* = 0 \tag{5.1}$$

$$\text{momentum} \qquad (v^* \cdot \nabla^*)v^* = -\nabla^* P^* + \frac{1}{Re} \nabla^{*2} v^* \tag{5.2}$$

where $v^* \equiv \frac{v}{U} = \frac{\rho v De}{Re \mu}$ for a given Reynolds number

where $U \equiv$ characteristic velocity and $Re \equiv \frac{\rho U De}{\mu}$

$v \equiv$ velocity vector

$$P^* \equiv \frac{P}{\rho u^2}$$

$$\nabla^* \equiv De\nabla$$

De ≡ characteristic length, usually equivalent hydraulic diameter

The only dimensionless parameter which appears in these two equations is the Reynolds number. Consequently, if this parameter is the same for the water and the sodium flow, the solution of v^* in both cases is the same. Therefore at a given bundle and a given Re, the parameter $(\rho v/\mu)$, where v represents a velocity vector, has the same value for both cases. This leads to the conclusion that C_{lL} and (W'^{W}_{ij}/μ) are the same for both cases because C_{lL} equals to V_T/V_A and W'^{W}_{ij} can be written as

$$W'^{W}_{ij} = \rho s_{ij} \tilde{V}_T \tag{5.3}$$

where s_{ij} = the gap between rods

V_T = transverse velocity at the gap

$$\tilde{V}_T = \frac{1}{H}\int_0^{H/2} V_T dz,$$

The quantitative difference between $[\varepsilon^*_{ln}]_{Na}$ and $[\varepsilon^*_{ln}]_{H_2O}$ can be represented in terms of a simulation error (S.E.)

$$S.E. = \frac{[\varepsilon^*_{ln}]_{H_2O} - [\varepsilon^*_{ln}]_{Na}}{[\varepsilon^*_{ln}]_{Na}} \tag{5.4}$$

From its definition,

$$\varepsilon^*_{ln} = \frac{(W'_{ij} + W'^{W}_{ij})/s_{ij}}{\rho V_A}$$

$$= \frac{1}{Re}\left(\frac{De}{s_{ij}}\right)\left(\frac{W'_{ij}}{\mu} + \frac{W'^{W}_{ij}}{\mu}\right) \tag{5.5}$$

Substituting equation (5.5) into equation (5.4) and using the identity, $\left[W'^{W}_{ij}/\mu\right]_{H_2O} = \left[W'^{W}_{ij}/\mu\right]_{Na}$, we get:

$$S.E. = \frac{\left[\frac{W'_{ij}}{\mu}\right]_{H_2O} - \left[\frac{W'_{ij}}{\mu}\right]_{Na}}{\left[\frac{W'_{ij}}{\mu}\right]_{Na} + \left[\frac{W'^{W}_{ij}}{\mu}\right]_{H_2O}} \tag{5.6}$$

Ramm and Johannsen (1975) proposed a theoretical correlation for (W'_{ij}/μ) as a function of geometry, Reynolds number and Prandtl number. Using this correlation Figure 5.1 was constructed to illustrate $(W'_{ij}/\mu)/(W'_{ij}/\mu)_{Pr=3}$ as a function of Pr for P/D = 1.15 bundle at $Re = 10^4$ and 10^5. The parameter (W_{ij}/μ) decreases as Pr decreases. For water, Pr≈3, while for sodium, Pr≈0.004, hence from this figure we have

$$\text{at } Re = 10^4 \qquad \left[\frac{W'_{ij}}{\mu}\right]_{Na} \approx 0.1\left[\frac{W'_{ij}}{\mu}\right]_{H_2O} \tag{5.7a}$$

$$Re = 10^5 \qquad \left[\frac{W'_{ij}}{\mu}\right]_{Na} \approx 0.3\left[\frac{W'_{ij}}{\mu}\right]_{H_2O} \tag{5.7b}$$

The simulation error of equation (5.6) can be bounded by utilizing equation (5.7a) and neglecting the quantity $\left[\frac{W'_{ij}}{\mu}\right]_{Na}$ in the denominator, i.e.,

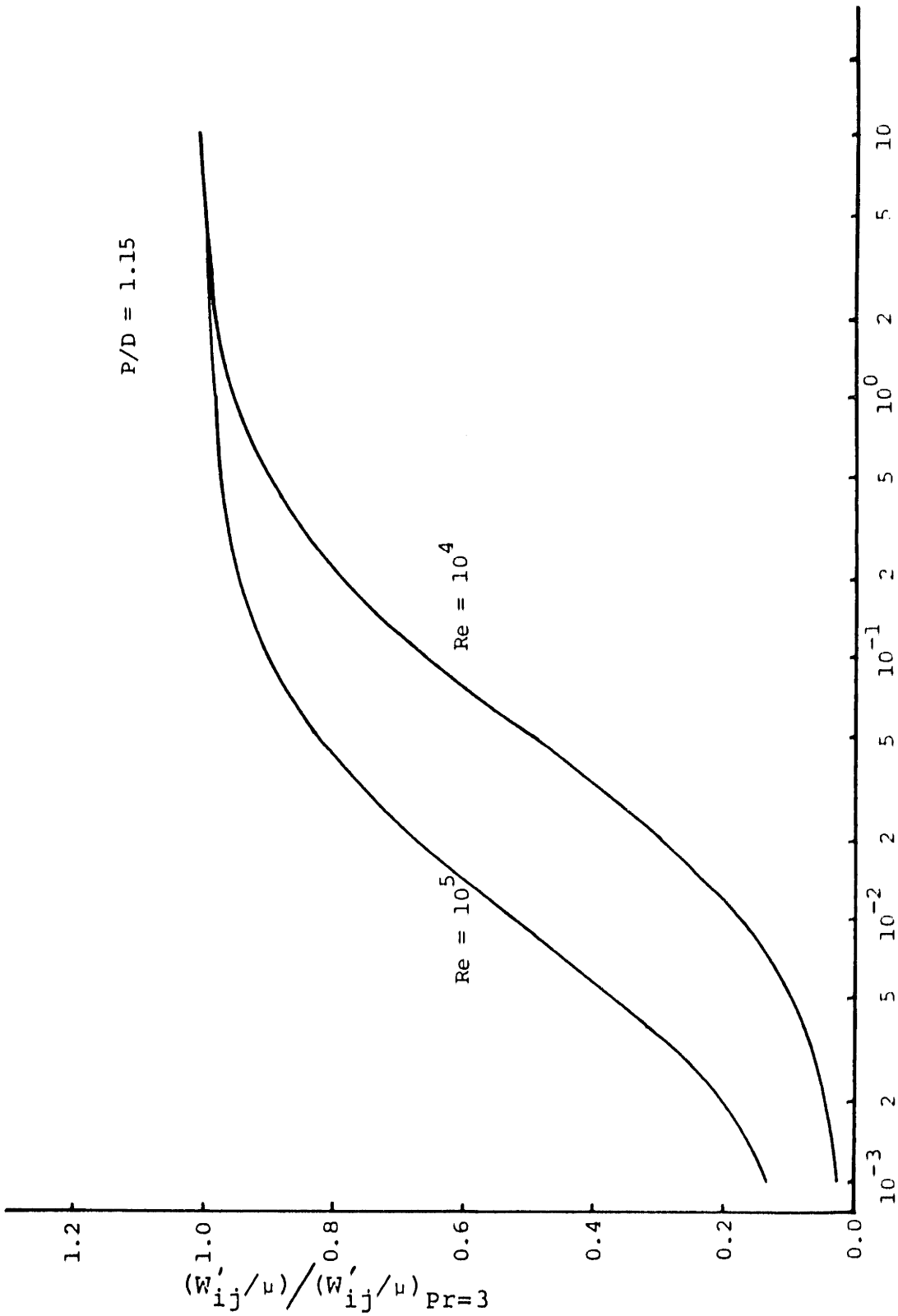

Figure 5.1 Turbulent Mixing Parameter (W'_{ij}/μ) from Ramm et al. Correlation

$$S.E. \leq \frac{0.9\left[\frac{W'_{ij}}{\mu}\right]_{H_2O}}{\left[\frac{W'^{W}_{ij}}{\mu}\right]_{H_2O}} = \frac{0.9\left[W'_{ij}\right]_{H_2O}}{\left[W'^{W}_{ij}\right]_{H_2O}} \tag{5.8}$$

Equation (5.8) shows that the similarity between $\left[\varepsilon^{*}_{l\eta}\right]_{H_2O}$ and $\left[\varepsilon^{*}_{l\eta}\right]_{Na}$ holds under the condition that $\left[W'^{W}_{ij}\right]_{H_2O}$ is much larger than $\left[W'_{ij}\right]_{H_2O}$ so that the mismatch between $\left[W'_{ij}/\mu\right]_{Na}$ and $\left[W'_{ij}/\mu\right]_{H_2O}$ can be neglected. As will be discussed in the next chapter $\left[W'_{ij}\right]_{H_2O}$ is around 10 % of $\left[W'^{W}_{ij}\right]_{H_2O}$, hence the S.E. of the mixing parameter $\varepsilon^{*}_{l\eta}$ reduced from salt injection experiment is about 9%.

5.1.2 Data Reduction Version of the ENERGY Code

The Data reduction procedure for salt tracer mixing experiments has been discussed by Symolon et al. (1980); however, different mixing parameters ε^{*}_{l} and C_l defined as

$$\varepsilon^{*}_{l} \equiv \frac{\varepsilon}{V_b De_l} \tag{5.9}$$

$$C_l \equiv \frac{V_T}{V_b} \tag{5.10}$$

where V_b is the bundle average velocity were employed. In this study, the mixing parameter derived from chapter 2 are $\varepsilon^{*}_{l\eta}$ and C_{lL} defined as

$$\varepsilon^{*}_{l\eta} = \frac{\varepsilon}{V_l \eta} \tag{5.11}$$

$$C_{lL} = \frac{V_T}{V_2} \tag{5.12}$$

where V_1 and V_2 are the interior and edge subchannel velocity, respectively.

In addition, the flow split correlation employed by Symolon et al. is different from our flow split correlation, which was presented in chapter 4. Although no appreciable difference is expected in the reduced results using either of the above correlations (see error analysis in section 5.4), our correlation is preferred in this work for consistency reasons.

Because of the above differences, a revised data reduction version (DRV) of the ENERGY code was developed. The subroutines used in this code are the same as those used in the final ENERGY-IV code described in chapter 7.

The equations used in DRV were easily obtained from equations (2.34), (2.35) and (2.36) by setting the source terms equal to zero since there is no salt generation after the injection point. These equations are:

Interior subchannel

$$\frac{\Delta C_1}{\Delta z} = \frac{(P-D)}{A_1}\left[\varepsilon^*_{1\eta} + \kappa D^*\right](C_i + C_j + C_k - 3C_1) \qquad (5.13)$$

Edge Subchannel

$$\frac{\Delta C_2}{\Delta z} = \frac{(P-D)}{A_2}\left[\left(\frac{X_1}{X_2}\right)\varepsilon^*_{1\eta} + \kappa D^*\right](C_i - C_2) +$$

$$\frac{D_g}{A_2}\left\{\left[\varepsilon^*_{2\eta} + \kappa D^*\right](C_j + C_k - C_2) + C_{1L}(C_j - C_2)\right\} \qquad (5.14)$$

Corner Subchannel

$$\frac{\Delta C_3}{\Delta z} = \frac{D_g}{A_3}\left\{\left[\left(\frac{X_2}{X_3}\right)\varepsilon^*_{2\eta} + \kappa D^*\right](C_j + C_k - 2C_3) + \left(\frac{X_2}{X_3}\right)C_{1L}(C_j - C_3)\right\} \tag{5.15}$$

where

C_i = dimensionless salt concentration

κ = shape factor for diffusion process, defined similar to equation (2.11)

$$D^* \equiv \frac{\rho D_o}{v\eta}$$

D_o = coefficient of diffusion

In salt mixing process, the contribution of salt diffusion is negligible ($D^*/\varepsilon^*_{1\eta} \approx 10^{-4}$) [Chiu (1978)]; therefore, the corresponding term in the code can be simply dropped. The $\varepsilon^*_{2\eta}$ parameter required in the above equations corresponds to the turbulent interchange between the edge subchannels. Since 0.01 is the recommended value for this parameter (see chapter 6) of the ENERGY-IV code $\varepsilon^*_{2\eta}$ is also set to 0.01 in the DRV.

The DRV calibrates the mixing parameters $\varepsilon^*_{1\eta}$ and C_{1L} by finding the values of $\varepsilon^*_{1\eta}$ and C_{1L} that generate a salt concentration distribution which most closely matches she dimensionless salt concentration distribution obtained from the mixing experiment. The predicted distribution which yields a "best fit" to the experimental distribution is determined by the mean square indicator (MSI), defined as

$$MSI = \sqrt{\sum_i (C^*_i - C^*_{ip})^2} \tag{5.16}$$

where

C_i^* = experimental dimensionless salt concentration

C_{ip}^* = predicted dimensionless salt concentration by DRV code

i = number of subchannels used for reduction

The values of $\varepsilon_{l\eta}^*$ and C_{lL} which correspond to a minimum value of MSI are the reduced results.

DRV was also modified to search for the best fit mixing parameters in an automatic way. This revised DRV requires an initial guess of $\varepsilon_{l\eta}^*$ or C_{lL}, while the old version requires the maximum and minimum bounds of these parameters. Appendix C1 lists this DRV code.

5.2 Data Reduction for the Mixing Experiments

5.2.1 Introduction

The dimensionless salt concentrations obtained in the interior and edge injection mixing experiments (chapter 3) were used to obtain the dimensionless effective eddy diffusivity (DEED), $\varepsilon_{l\eta}^*$, and the edge transverse velocity ratio (ETVR), C_{lL}, respectively. To reduce each parameter, the other parameter is used as an input into the DRV. In the interior injection case where very little salt reached the edge region of the bundle, the results of $\varepsilon_{l\eta}^*$ reduced from DRV were insensitive to the value of C_{lL} input to DRV. On the other hand, in the edge injection case, about half of the salt tracer diffused into the interior region and this must be simulated by inputing the correct $\varepsilon_{l\eta}^*$ into the DRV to reduce C_{lL}. Therefore a two step methodology was used: (a) obtain correct $\varepsilon_{l\eta}^*$ from the interior injection case by

inputting an appropriate C_{1L} into DRV, and (b) reduce C_{1L} from the edge injection case using the reduced $\varepsilon^*_{1\eta}$ from step (a) as input for the DRV.

Originally, the salt concentrations in all the subchannels were used to calculate MSI for both $\varepsilon^*_{1\eta}$ and C_{1L}. It was later found that for the edge injection case, better match could be achieved between the data and DRV results if only the concentration in the edge subchannels were used to calculate MSI.

This procedure is justified because the movement of saline solution from the edge region to the interior is governed by an eddy diffusivity parameter for edge-interior subchannels. Such a parameter is unavailable since interior injection results yield only an interior - interior subchannel diffusivity. For edge injection while the predicted interior subchannel concentration is sensitive to the value of $\varepsilon^*_{1\eta}$ used (which is not directly applicable as discussed above), the edge channel concentration is not similarly sensitive. In the following, this method of using only edge channel concentrations from edge channels injection cases is used for reducing C_{1L}.

5.2.2 Data Reduction for 37-pin Mixing Experiments

5.2.2.1 DEED, $\varepsilon^*_{1\eta}$

The required C_{1L} for reducing $\varepsilon^*_{1\eta}$ could be estimated from the Chiu-Burns mixing parameter correlations. For this 37 pin bundle (P/D = 1.154, H/D = 13.4), these correlations predict C_{1L} around 0.30 for $Re_b > 3000$, 0.20 for $Re_b = 1000$ and 0.1 for $Re_b = 200$.

To reduce $\varepsilon^*_{1\eta}$, C_{1L} was fixed at 0.3 for $Re_b > 3200$, 0.2 for $3200 \geq Re_b > 1500$ and 0.1 for $1500 \geq Re_b$.

Although in the interior injection mixing experiments the injection subchannel is subchannel 1 as shown in Figure 3.16, maximum salt concentration was detected in subchannel 2 for high flow rates. Considering the wire position at the injection level (32" below exit plane) shown in Figure 5.2, one finds that the wire it located about 1/4 lead length downstream of the injection hole. As the saline flow is injected into subchannel 1, it encounters the wire about immediately and is sweeped into subchannel 2. This flow path is illustrated by the arrow in Figure 5.2. Hence one could expect that the use of subchannel 2 as the injection subchannel in the DRV for the purpose of simulation of the mixing process might accomplish better matches between data and calculations than the use of subchannel 1. In order to investigate the effect of these phenomena, both subchannel 1 and subchannel 2 were used as injection subchannels in the DRV to reduce $\varepsilon^*_{1\eta}$.

In addition to this phenomenon, because the injection direction is 30° relative to the axial axis, a transverse velocity is associated with the injection flow. This transverse velocity will cause some error in determining the parameter $\varepsilon^*_{1\eta}$. However, this is small comparing to the sweeping phenomena as will be discussed in the error analysis section.

Figure 5.3 illustrates the MSI calculated by the DRV versus $\varepsilon^*_{1\eta}$ at three Re_b: 1500, 9400 and 22100. Similar results were obtained for all the other runs. The value of $\varepsilon^*_{1\eta}$ at which MSI reached its minimum, is the reduced value. Table 5.1 illustrates the reduced results for 16 interior injection runs. Figure 5.4 compares the calculated

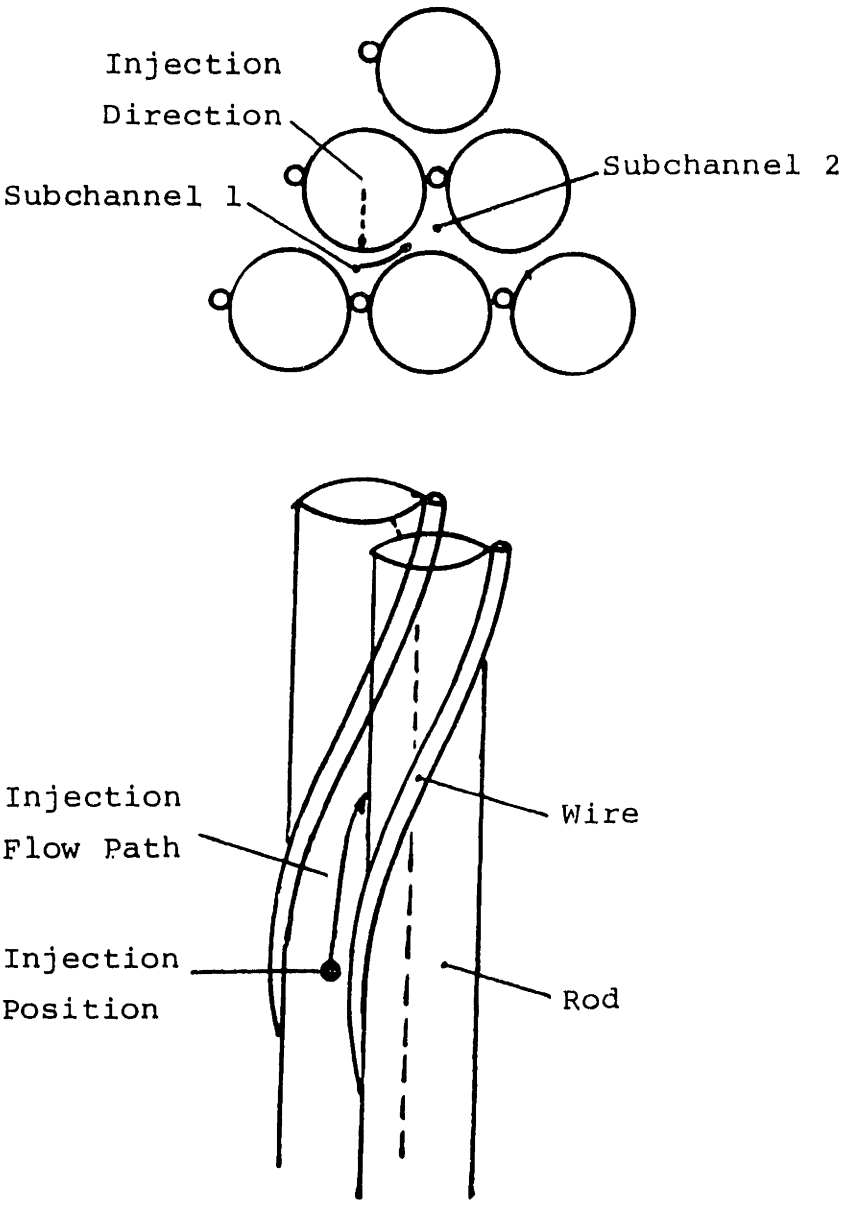

Figure 5.2 Injection Flow Path Near Injection Position

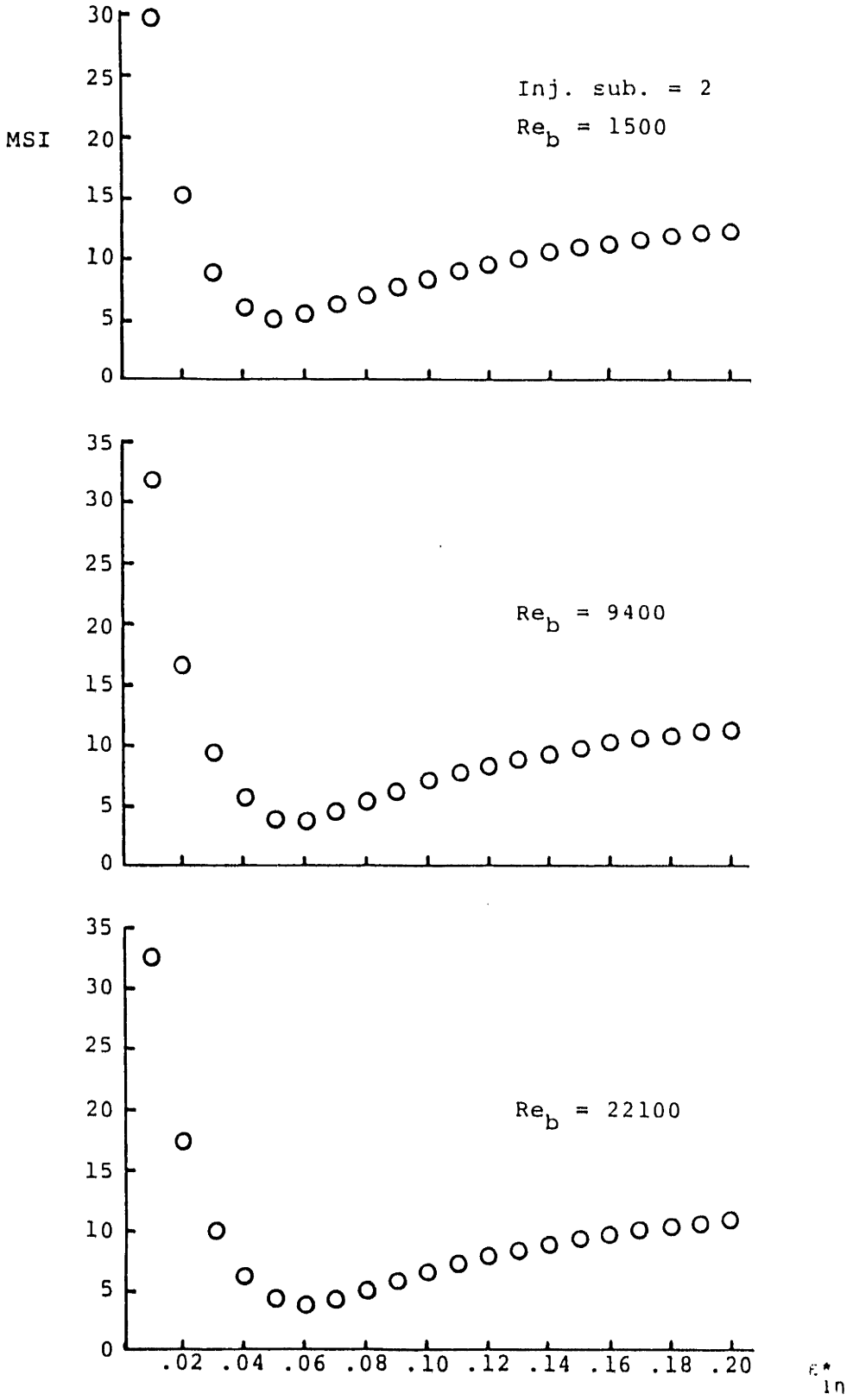

Figure 5.3 Mean Square Indicator for Interior Injection Case

Table 5.1 Reduced $\varepsilon^*_{1\eta}$ for 37-pin Interior Injection Experiments

Run	Re_b	Input C_{1L}	Inj. Subchannel = 1		Inj. Subchannel = 2		Recommended
			Minimum MSI	$\varepsilon^*_{1\eta}$	Minimum MSI	$\varepsilon^*_{1\eta}$	$\varepsilon^*_{1\eta}$
1	220	0.10	11.89	0.038	15.89	0.051	0.038
2	430	0.10	8.23	0.043	11.14	0.053	0.043
3	860	0.10	5.60	0.042	7.19	0.046	0.042
4	1500	0.10	5.64	0.051	5.11	0.050	0.051
5	2200	0.20	5.29	0.060	4.49	0.057	0.059
6	3200	0.20	5.28	0.064	4.17	0.059	0.062
7	4300	0.30	5.24	0.068	3.74	0.061	0.064
8	5400	0.30	5.83	0.061	4.47	0.057	0.059
9	6500	0.30	5.95	0.064	3.65	0.057	0.061
10	9400	0.30	5.82	0.062	3.79	0.056	0.059
11	12200	0.30	6.09	0.067	4.39	0.060	0.064
12	14800	0.30	5.71	0.067	3.81	0.060	0.064
13	18600	0.30	6.40	0.072	3.97	0.061	0.067
14	22100	0.30	6.42	0.068	3.77	0.059	0.064
15	26000	0.30	6.27	0.070	3.64	0.059	0.065
16	29600	0.30	6.43	0.066	4.16	0.059	0.063

*Injection depth = 32" for all runs.

dimensionless salt concentrations at minimum MSI and data across the bundle (flat to flat) for all 16 runs. The subchannel numbering scheme was shown in Figure 3.17. For $Re_b \geq 1500$, the match between calculations and data is excellent if subchannel 2 is selected as the injection subchannel in the DRV. For $Re_b \leq 860$, better match is found by using subchannel 1 as the injection subchannel in the DRV.

To investigate the sensitivity of MSI, Figure 5.5 shows the calculation results for three $\varepsilon^*_{1\eta}$ at Re_b = 9400 using subchannel 2 as the injection subchannel. The three $\varepsilon^*_{1\eta}$'s correspond to the value at minimum MSI for Re_b= 9400 run 0.056, its + 25% value: 0.070, and its -25% value : 0.042. The three MSI's for these three $\varepsilon^*_{1\eta}$'s are 3.79, 4.56 and 5.18, respectively. The maximum value of dimensionless salt concentration decreases 20% as $\varepsilon^*_{1\eta}$ increases 25% (MSI increases 20%) and increases 34% as $\varepsilon^*_{1\eta}$ decreases 25% (MSI increases 37%). One might conclude that the percentage change in the maximum dimensionless salt concentration is approximately the same as the percentage change in the MSI from its minimum value.

For $Re_b \leq 860$, since the data were better matched by using subchannel 1 rather than subchannel 2 as the injection subchannel in the DRV, the local wire sweeping effects at the injection position are believed to be small. Hence the $\varepsilon^*_{1\eta}$ data using subchannel 1 as the injection subchannel are recommended. For high Re_b, the difference between two sets of reduced $\varepsilon^*_{1\eta}$(injection subchannel = 1 or 2) is about 10%. This variation will be included as a component in the data reduction error discussed in the last section of this chapter.
It is recommended that for $Re_b \geq 1500$ $\varepsilon^*_{1\eta}$ is taken equal to the average

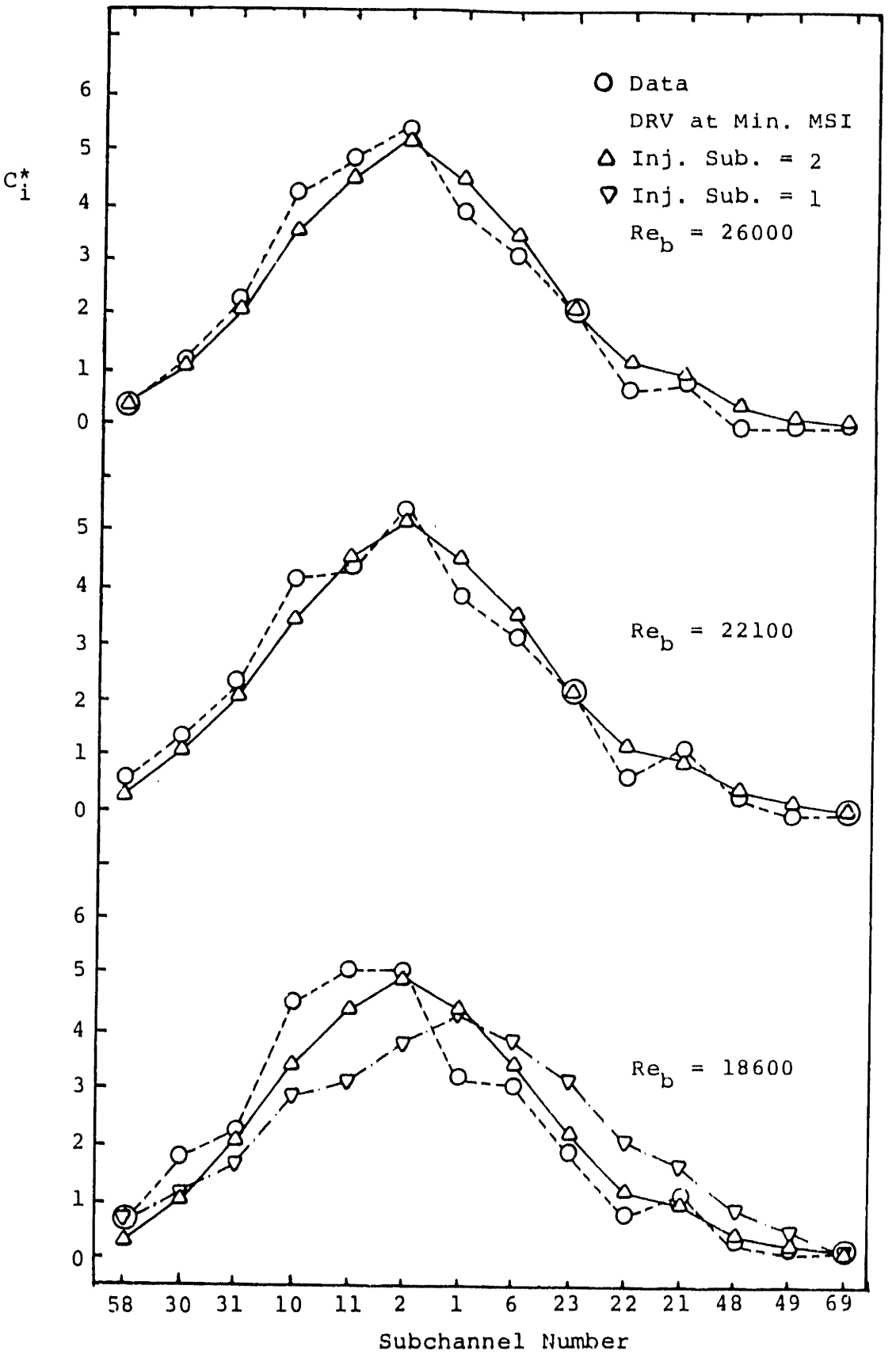

Figure 5.4 Comparison between DRV Calculation at Minimun MSI and Data for 37-pin Interion Injection Cases

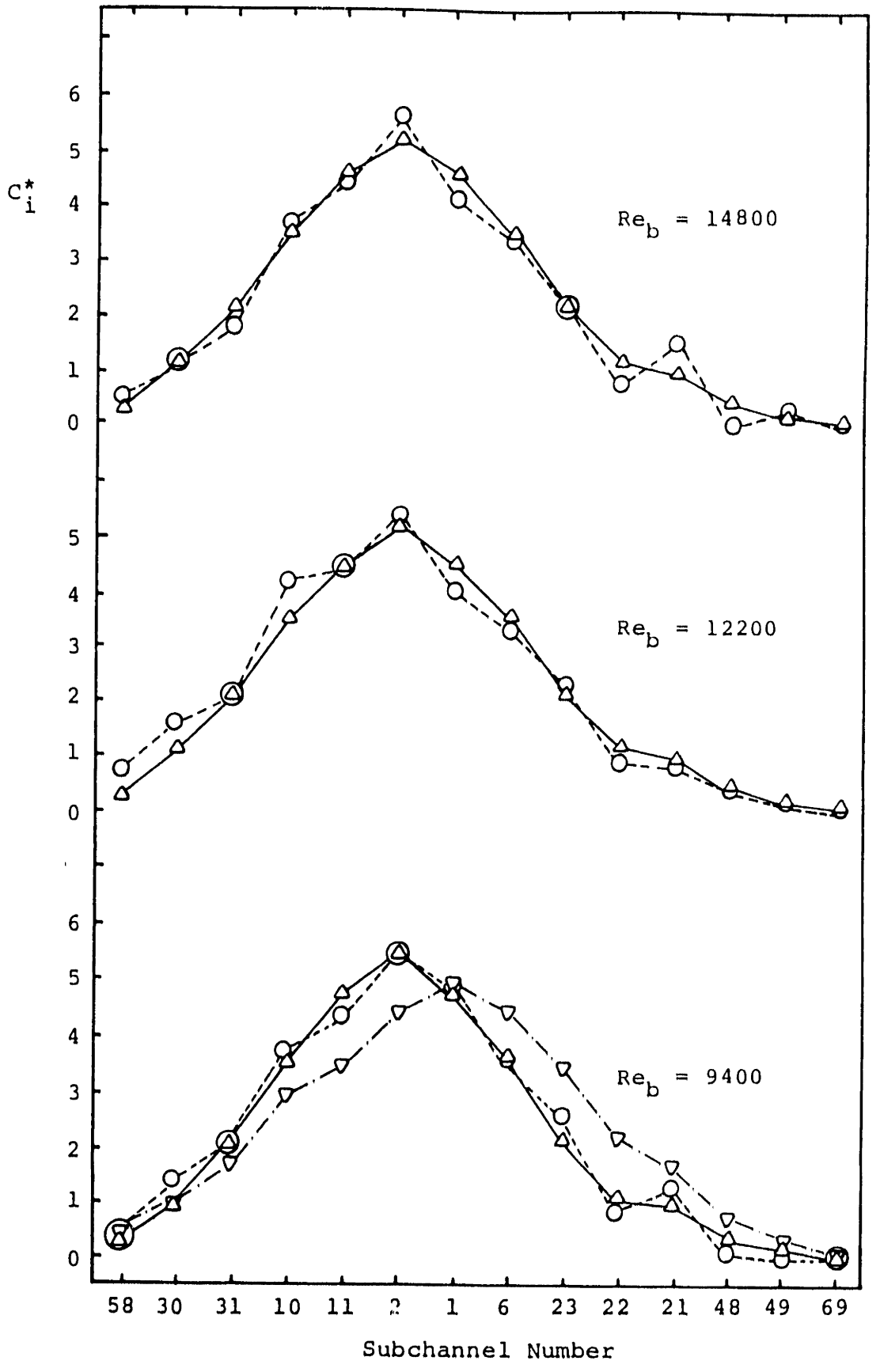

Figure 5.4 Continued

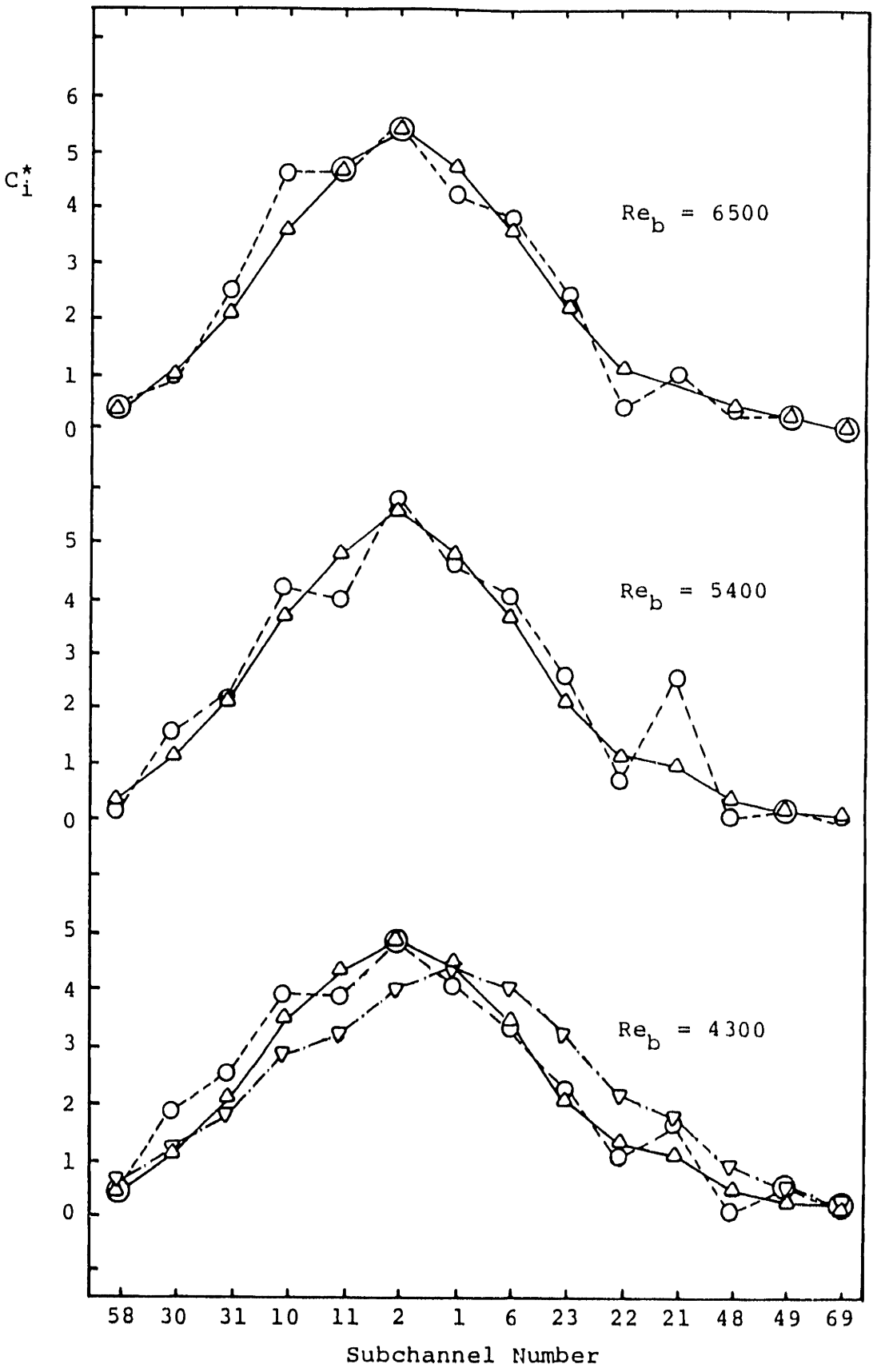

Figure 5.4 Continued

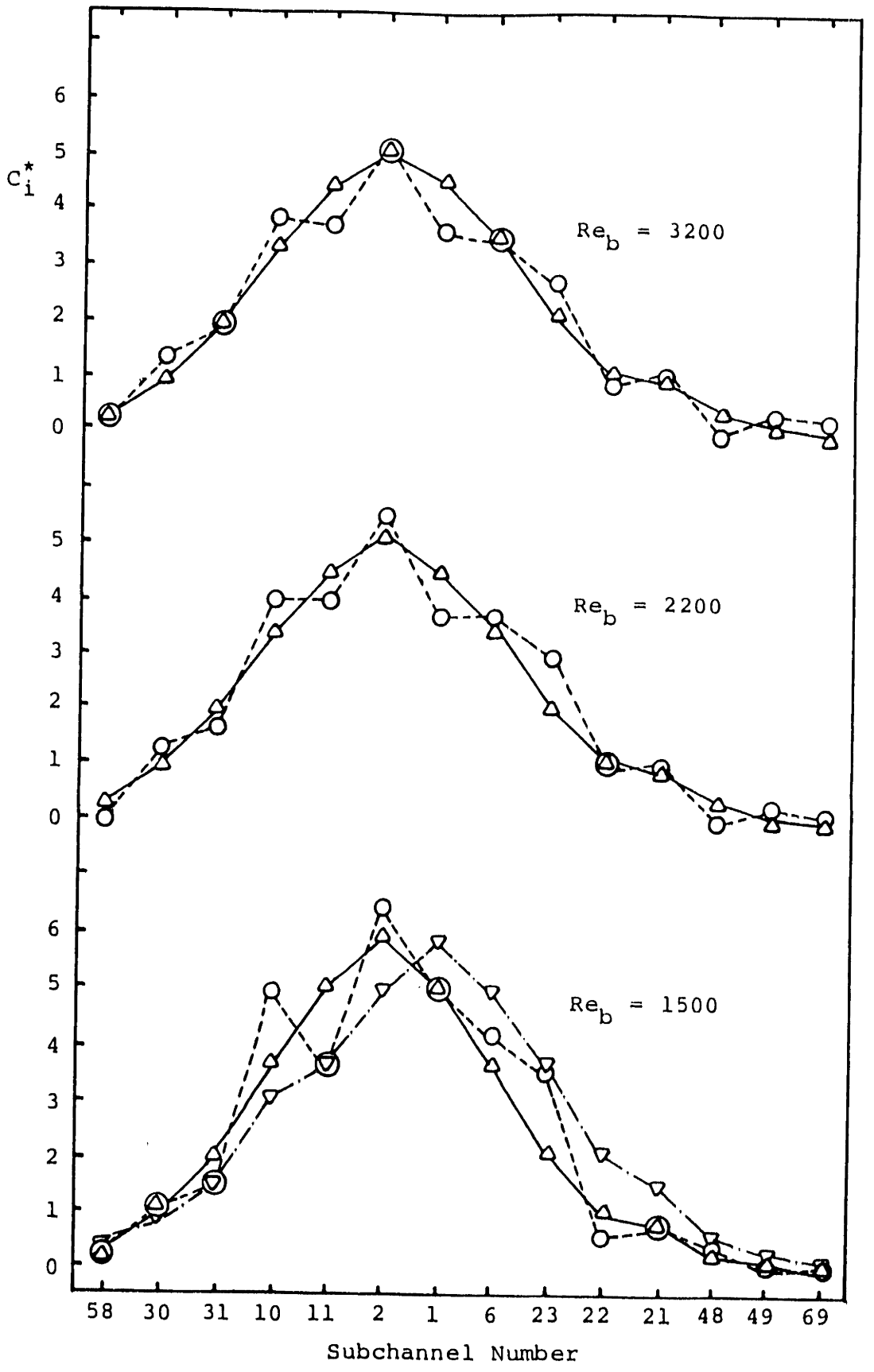

Figure 5.4 Continued

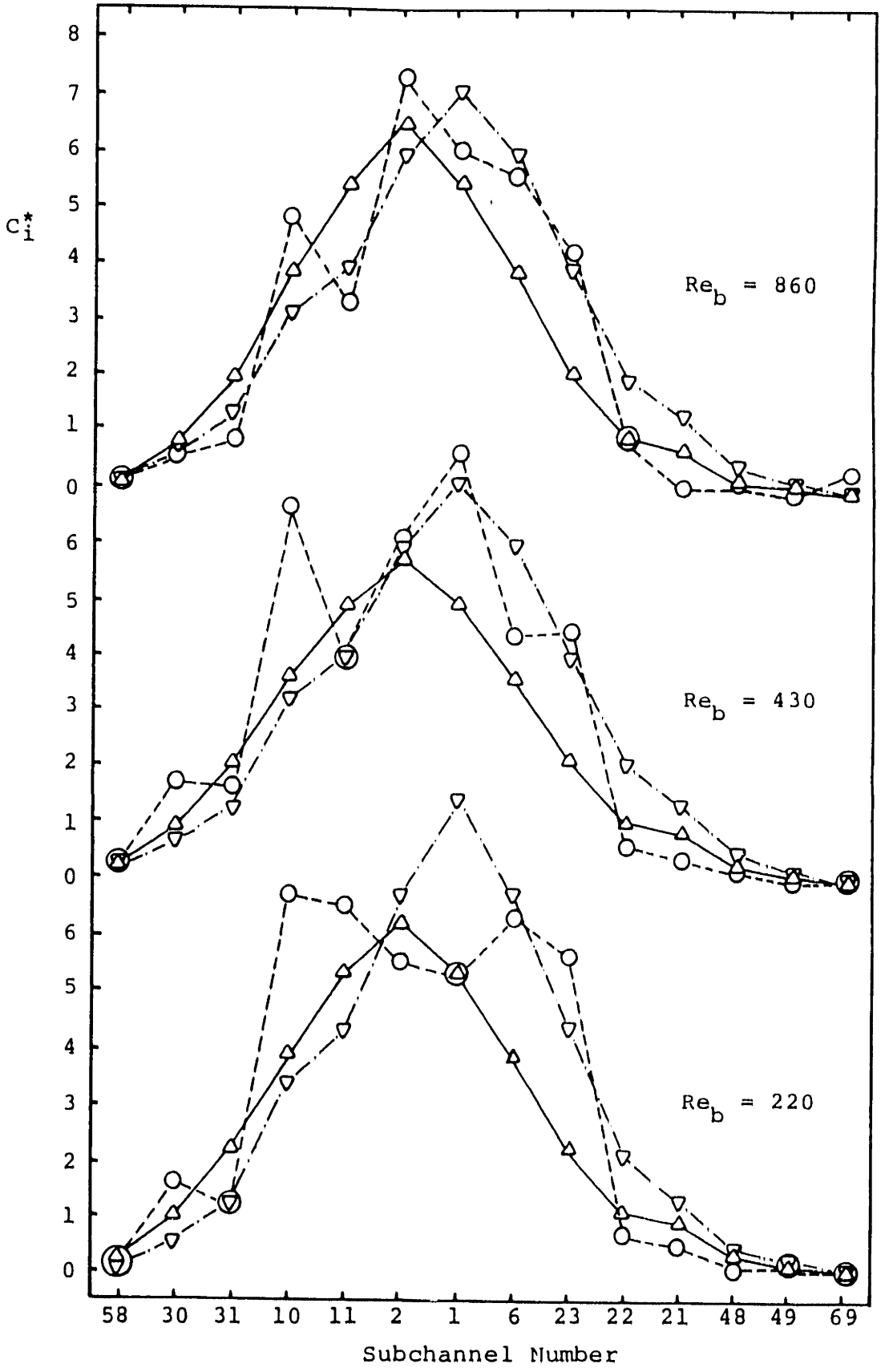

Figure 5.4 Continued

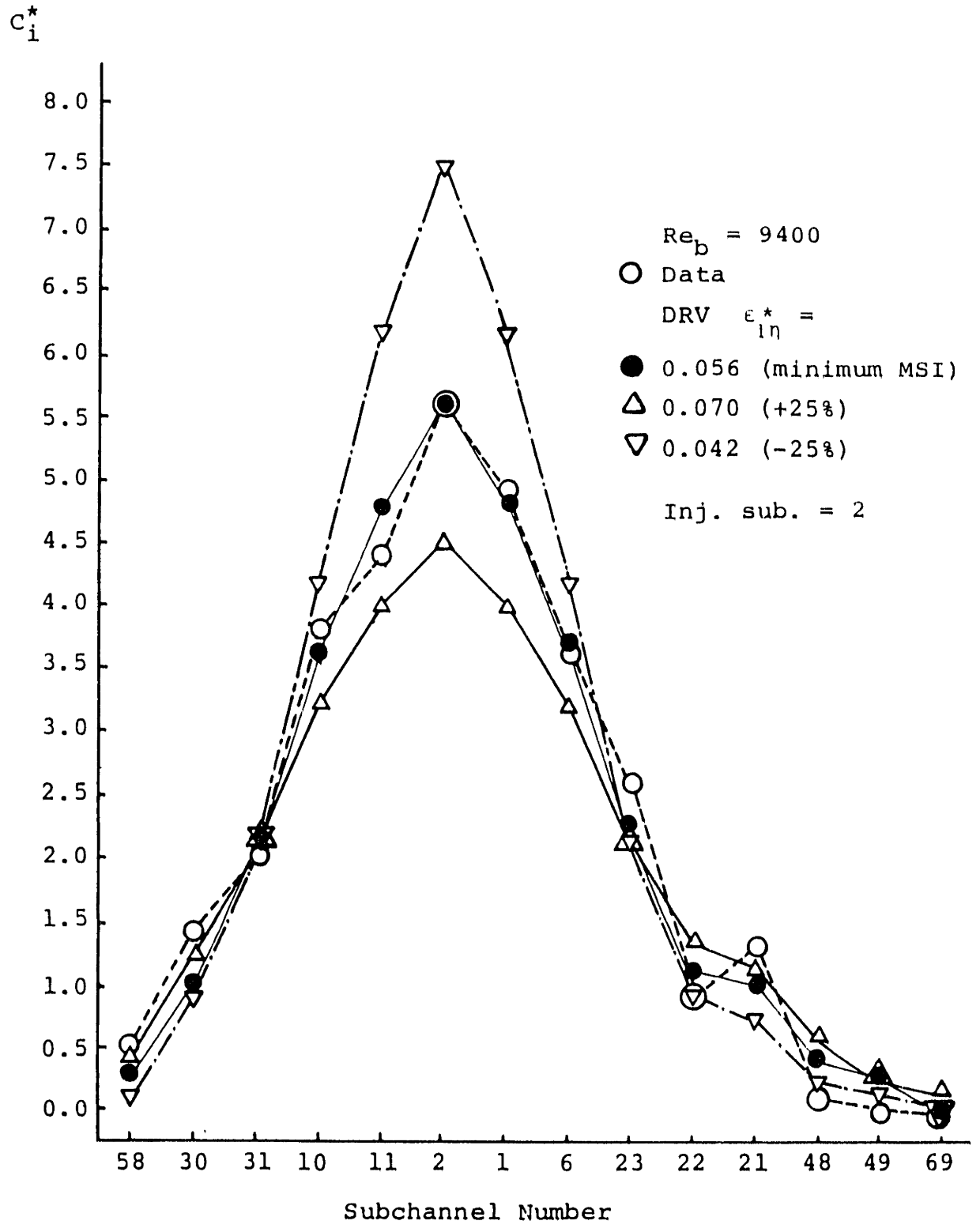

Figure 5.5 Sensitivity of the Predicted Dimensionless Salt Concentration to $\varepsilon_{i\eta}^*$

value of these two sets of reduced results as listed in the last column of Table 5.1. Figure 5.6 illustrated the recommended $\varepsilon^*_{l\eta}$ as function of Re_b.

The Chiu-Burns correlation for the mixing parameters ε^*_{lL} defined as

$$\varepsilon^*_{lL} \equiv \frac{\varepsilon}{V_l De_b} = \frac{\eta}{De_b} \varepsilon^*_{l\eta} \tag{5.17a}$$

i.e.,

$$\varepsilon^*_{l\eta} = \frac{De_b}{\eta} \varepsilon^*_{lL} \tag{5.17b}$$

is also plotted in Figure 5.6 for comparison. One observes that the prediction value, 0.097 for the turbulent region is too high, although the data (0.065) were still within the ±35% accuracy of the correlation.

5.2.2.2 ETVR, C_{lL}

The DEED $\varepsilon^*_{l\eta}$ values that were reduced in the last section were used as the required input to the DRV to reduce C_{lL} using the edge injection results. The injection subchannel is subchannel 71. Only edge subchannels dimensionless salt concentrations were used to calculated MSI's. Figure 5.7 illustrates the MSI as function of C_{lL} at three Re : 1500, 9400 and 22100. Table 5.2 depicts the C_{lL} at minimum MSI for all 14 edge injection cases. Figure 5.8 compares the DRV calculations at minimum MSI and dimensionless salt concentration data for all 14 runs of the edge injection experiment.

Similar to the interior injection case, Figure 5.9 illustrates the sensitivity of MSI at Re_b = 9400. The three C_{lL}'s correspond to the value at minimum MSI: for Re_b= 9400 run 0.244, its + 25% value: 0.305

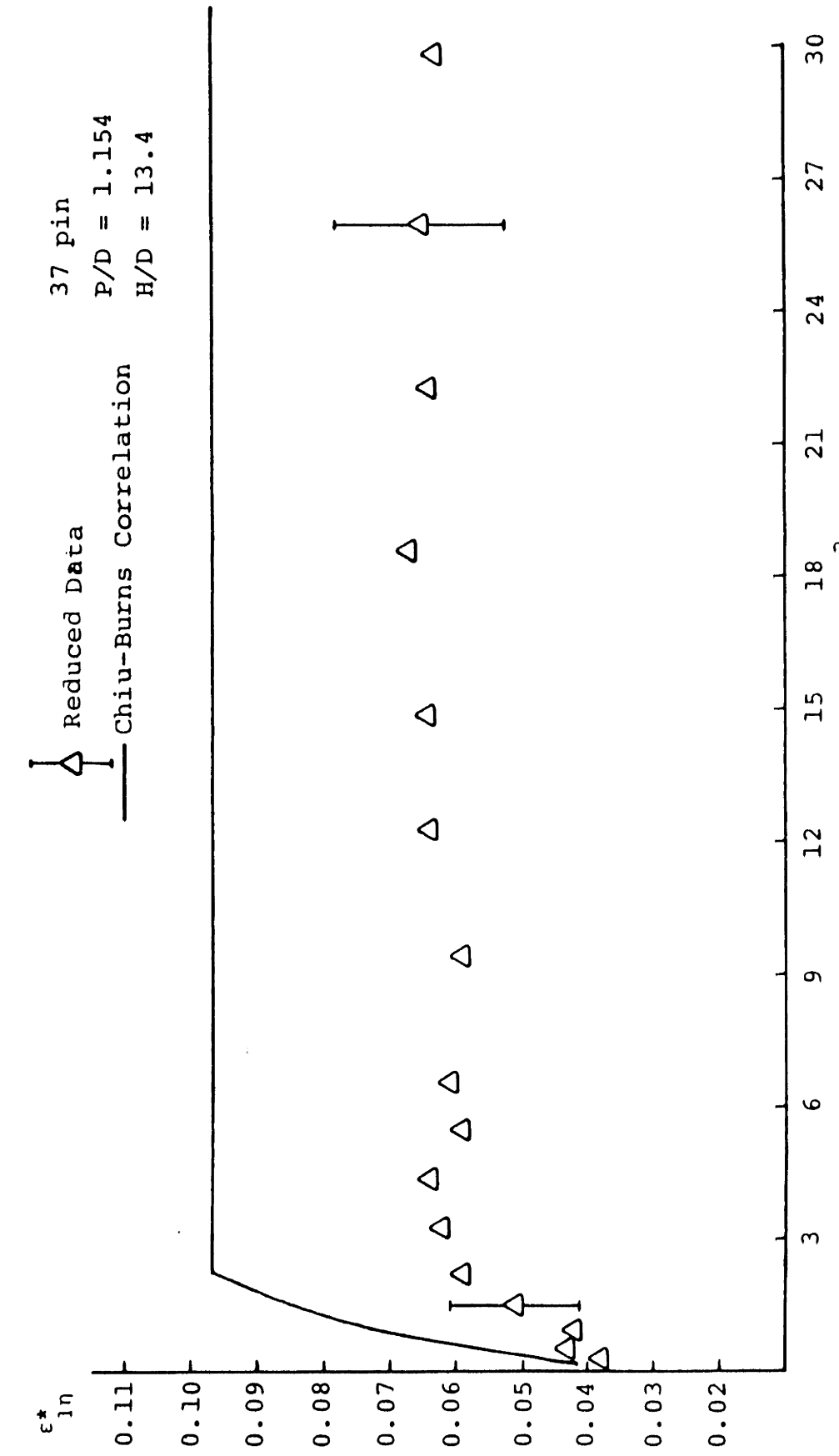

Figure 5.6 Dimensionless Effective Eddy Diffusivity $\varepsilon^*_{1\eta}$ for 37-pin Experiment

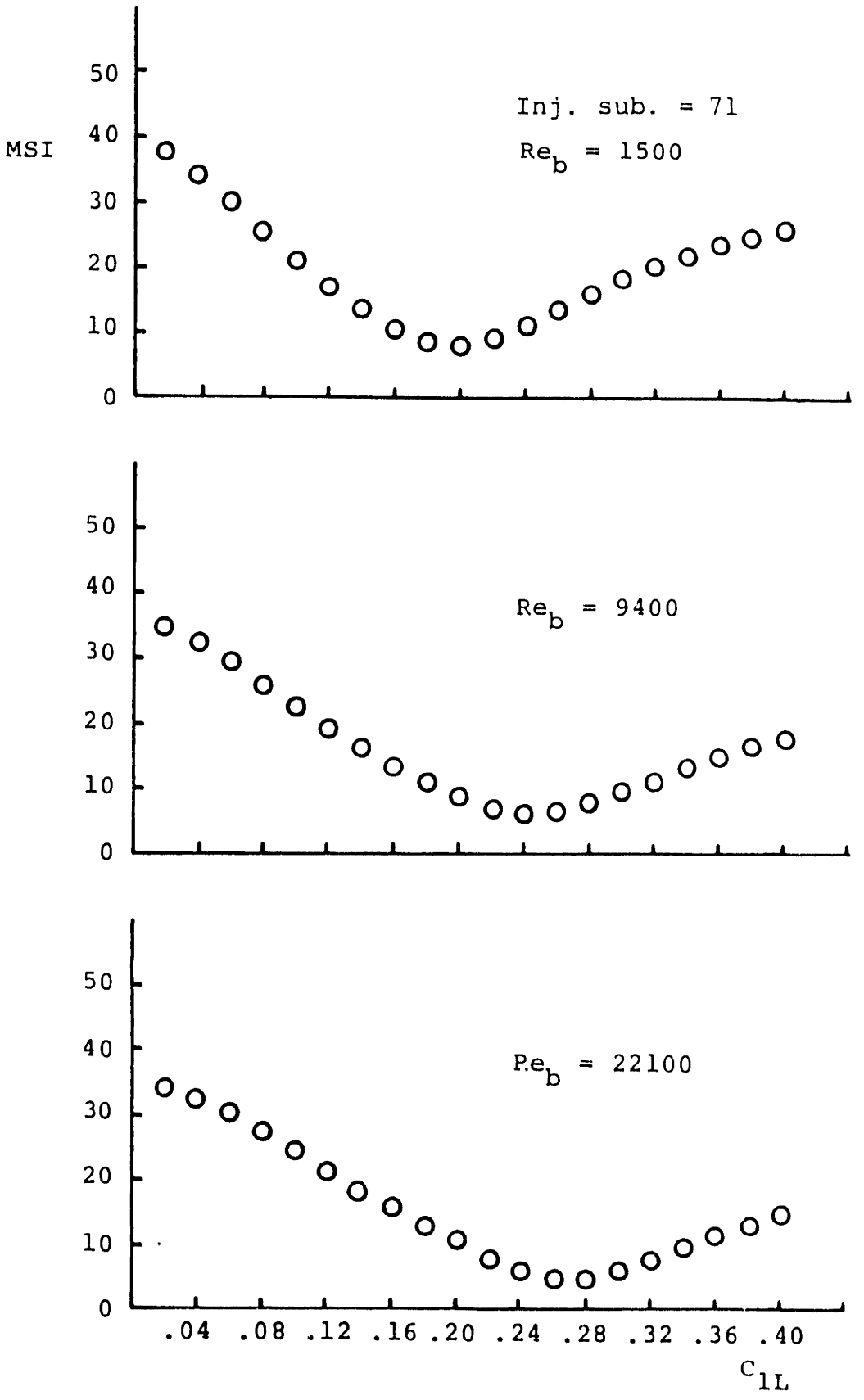

Figure 5.7 Mean Square Indicator for the Edge Injection Case

Table 5.2 Reduced C_{1L} for 37-pin Edge Injection Experiments

Run	Re_b	Input $\epsilon^*_{1\eta}$	Minimum MSI	C_{1L}
1	430	0.043	11.73	0.158
2	860	0.042	8.49	0.176
3	1,500	0.051	7.99	0.194
4	2,200	0.059	7.52	0.205
5	3,200	0.062	6.75	0.231
6	4,300	0.064	7.13	0.235
7	5,400	0.059	6.10	0.235
8	6,500	0.061	6.13	0.233
9	9,400	0.059	5.86	0.244
10	12,200	0.064	6.80	0.258
11	14,800	0.064	6.33	0.262
12	18,600	0.067	5.39	0.267
13	22,100	0.064	4.14	0.268
14	26,000	0.065	5.94	0.281

* Injection depth = 32" for all runs

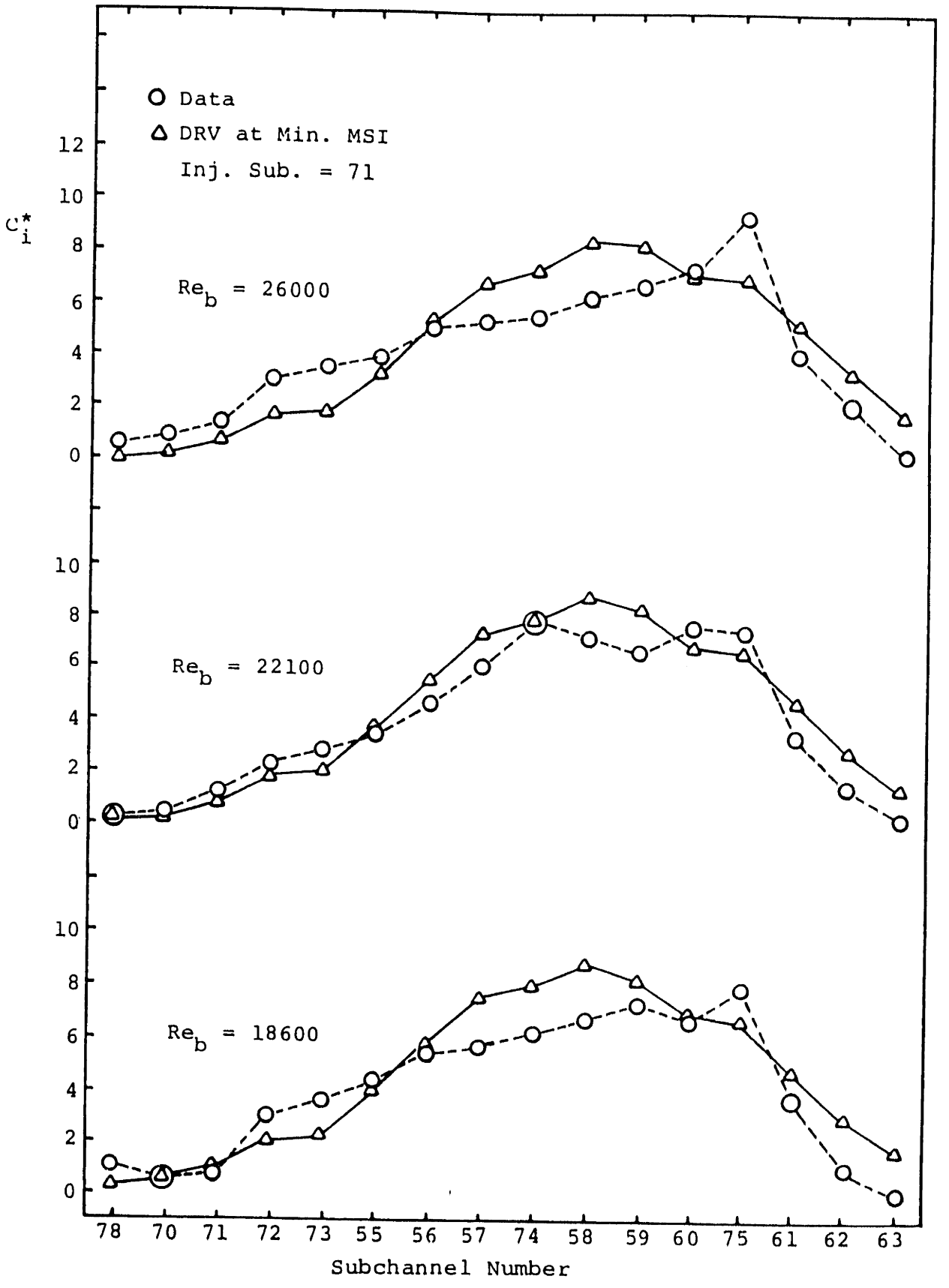

Figure 5.8 Comparison between DRV Calculations at Minimum MSI and Data for 37-pin Edge Injection Cases

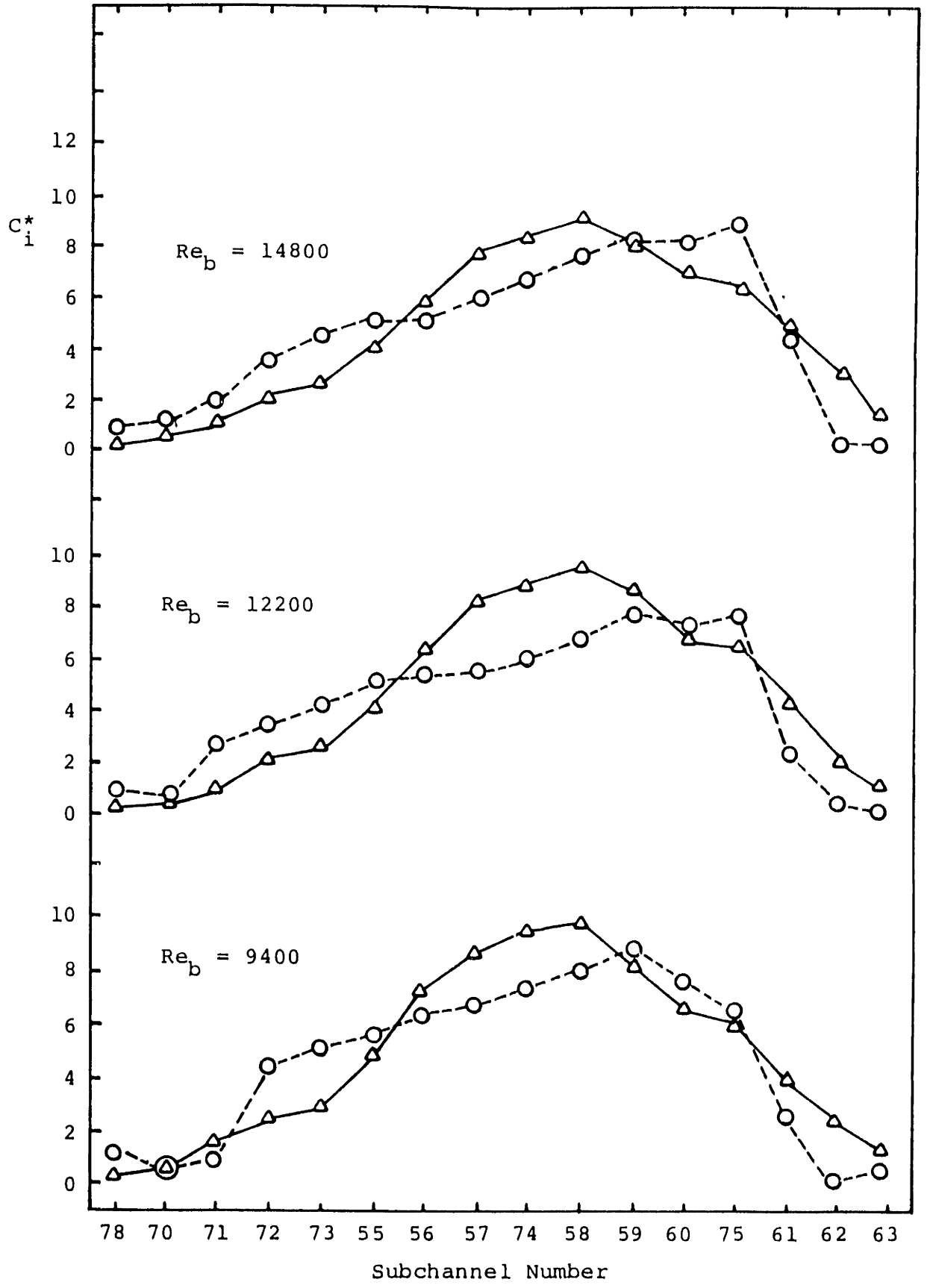

Figure 5.8 Continued

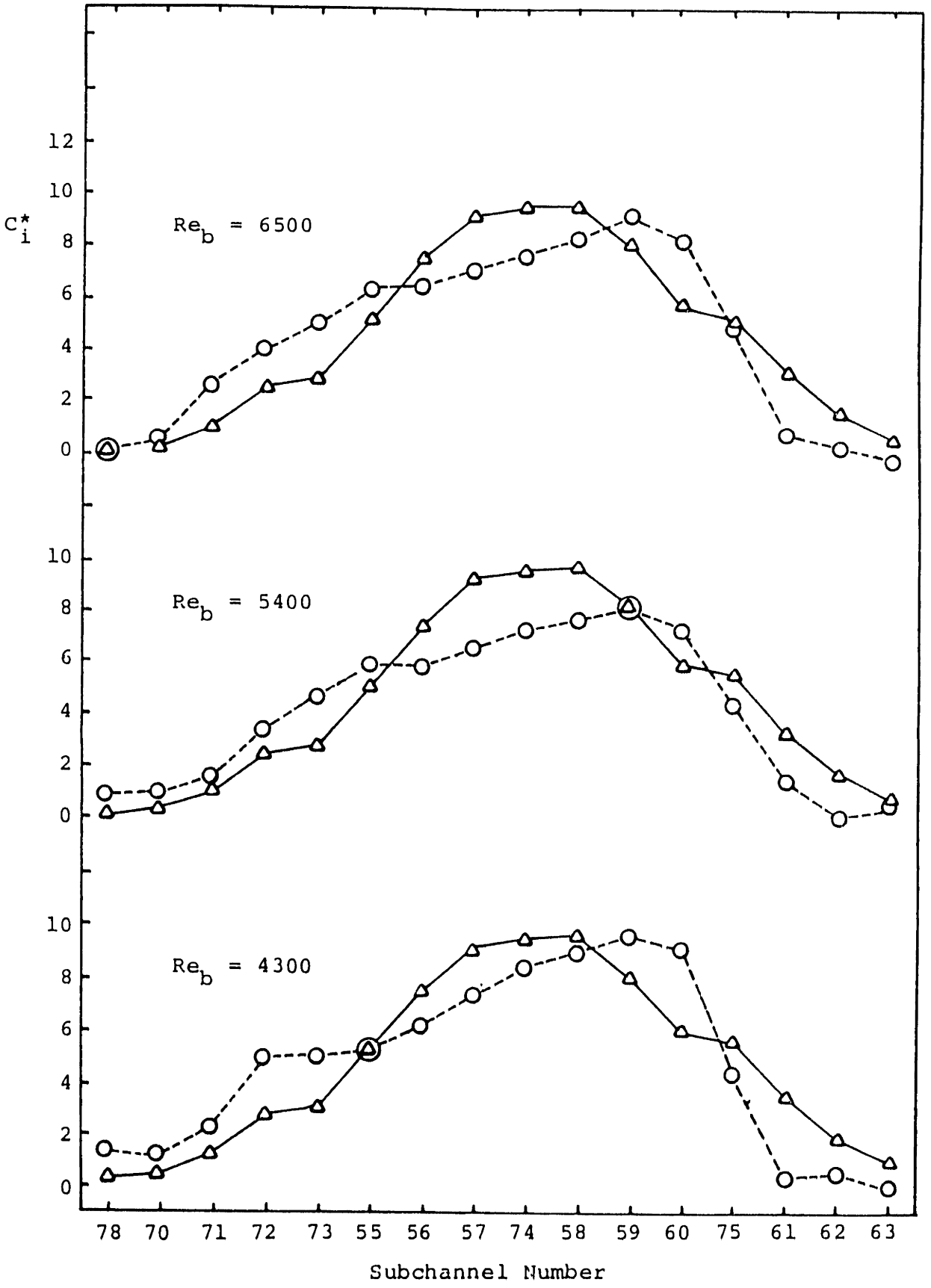

Figure 5.8 Continued

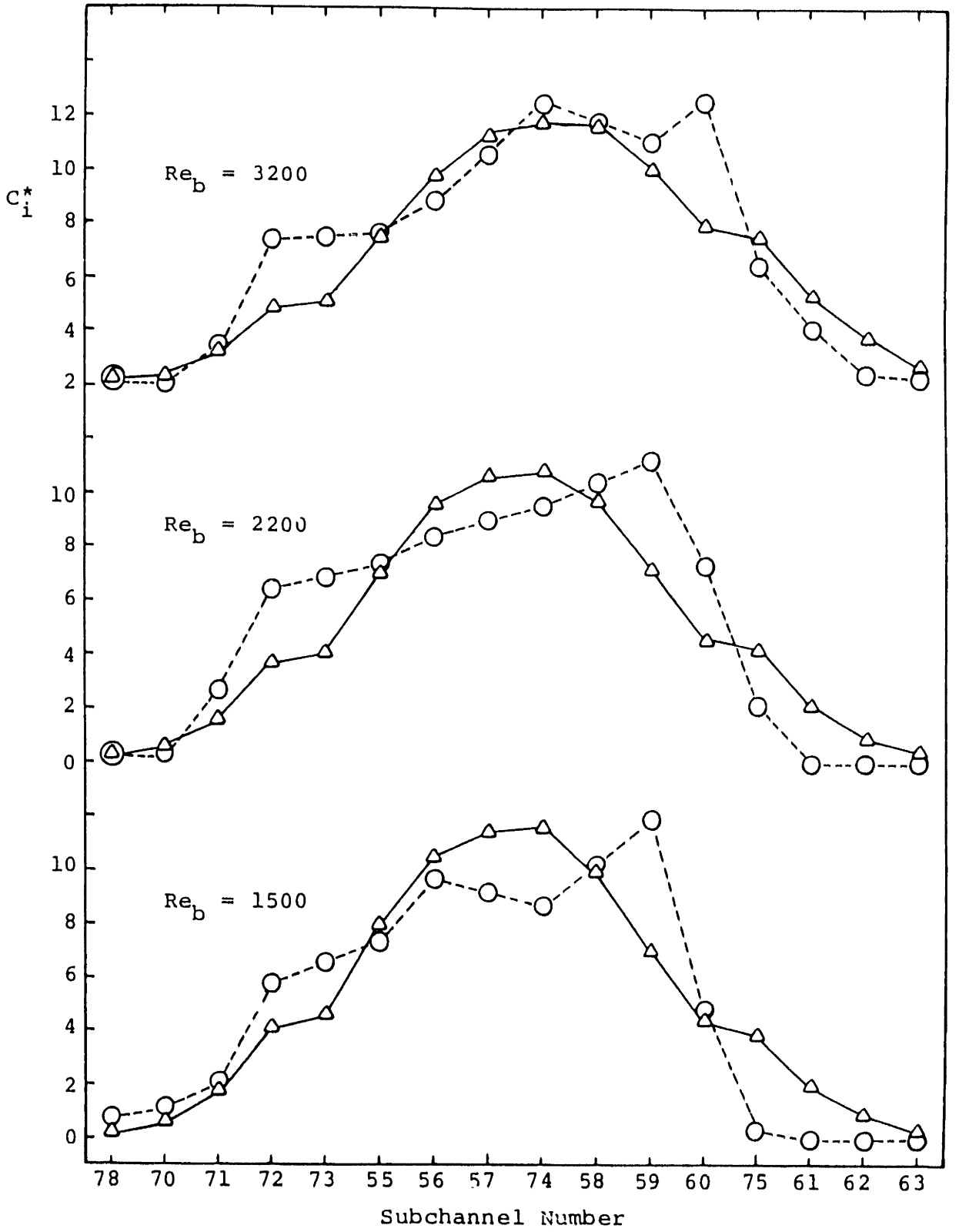

Figure 5.8 Continued

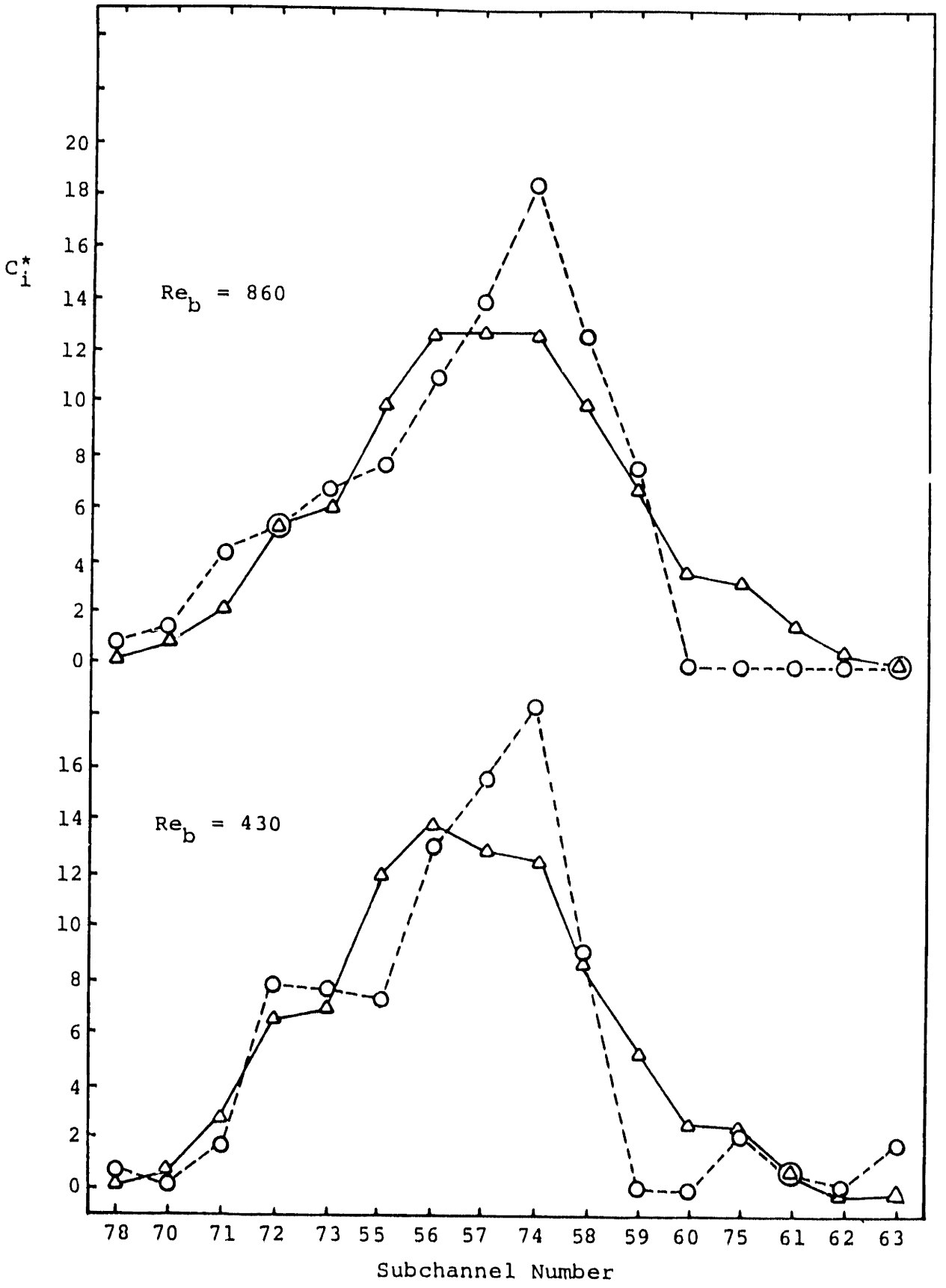

Figure 5.8 Continued

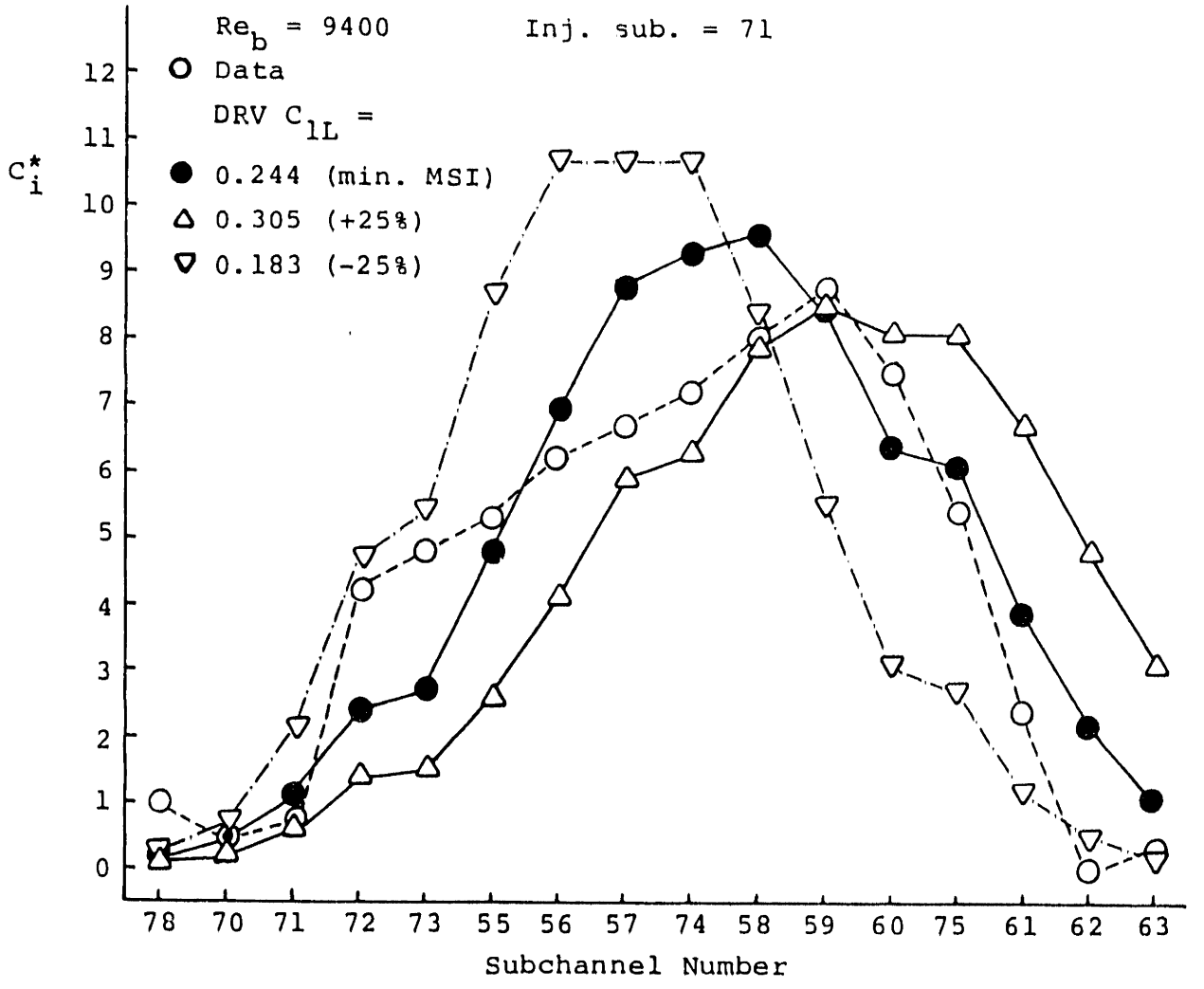

Figure 5.9 Sensitivity of the Predicted Dimensionless Salt Concentration to C_{1L}

and its -25% value: 0.183. The three MSI's for these three C_{1L}'s are 5.86, 9.95, and 10.57, respectively. The location of the maximum salt concentration moves forward one subchannel while the value decreases about 11% for each 25% increment in C_{1L}.

Figure 5.10 illustrates the C_{1L} reduced from the data as function of Re_b. The Chiu-Burns correlation for C_{1L} is also presented in Figure 5.10 for comparison. The correlation predicted the turbulent region value well, but it could not predict the trend of the data in the transition region.

5.2.3 Data Reduction for 61-pin Mixing Experiments

Chiu (1978c) performed salt tracer mixing experiments in two 61-pin bundles with P/D = 1.067 and H/D = 4.0 and 8.0. Figure 5.11 depicts the bundle geometry at the exit plane and some important geometry parameters. Figure 5.12 illustrates the subchannel numbering scheme of a 61-pin bundle. The injection subchannel of Chiu's experiments was subchannel 6 for the interior injection case and subchannel 115 for the edge injection case.

Although Chiu's mixing experiments had been reduced by the old SUPERENERGY-DRV code, we have repeated this effort here because of the following reasons: 1) the definition of DEED was changed from ε^*_{1L} to $\varepsilon^*_{1\eta}$ which caused some modifications in the new DRV code, 2) the flow split parameters used in the DRV would have to be calculated from the new flow split correlation developed in Chapter 4, and 3) the method for calculating MSI in the edge injection case was revised to use only the edge subchannel dimensionless salt concentration.

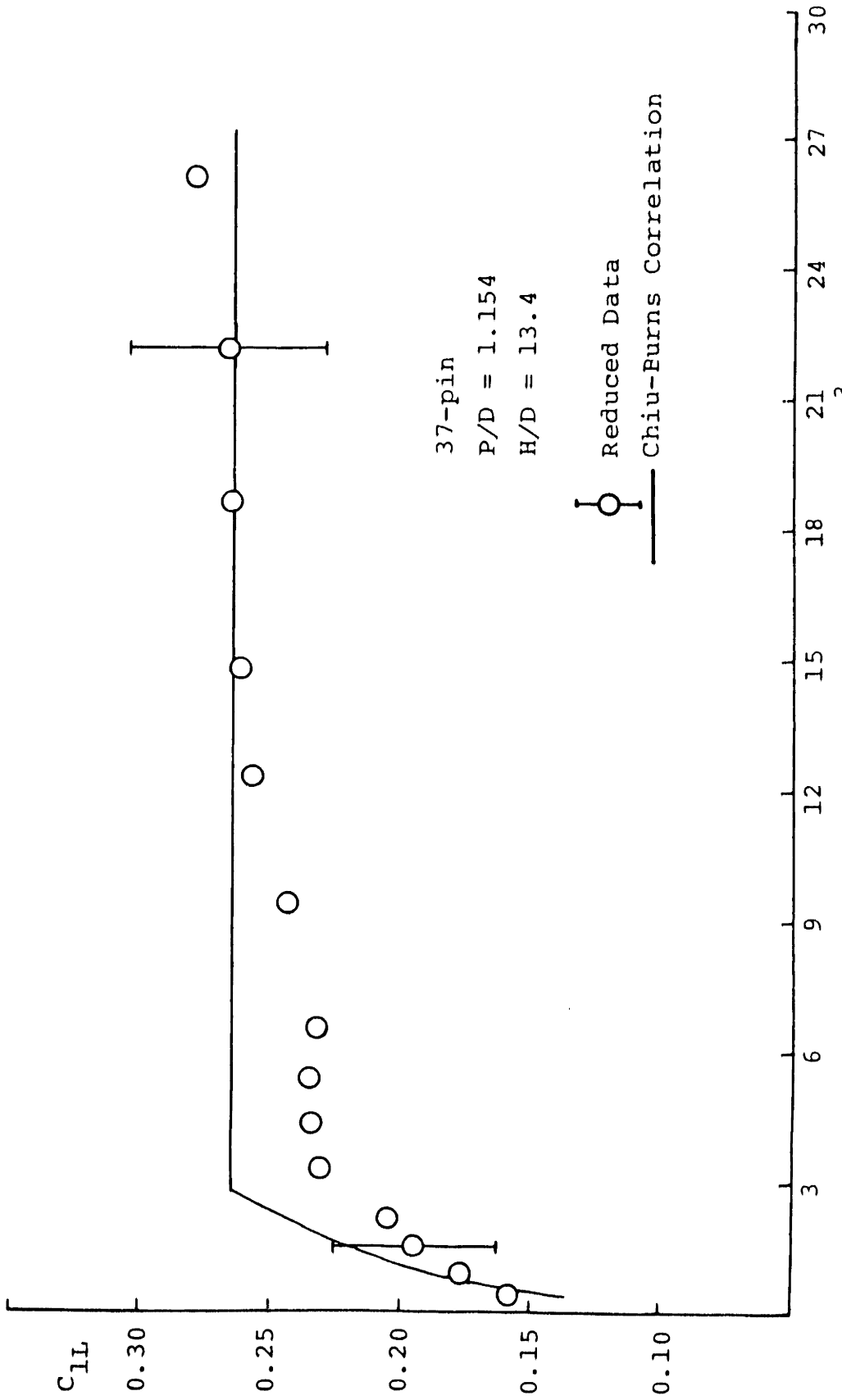

Figure 5.10 Reduced Edge Transverse Velocity Ratio C_{1L} for the 37-pin Experiment

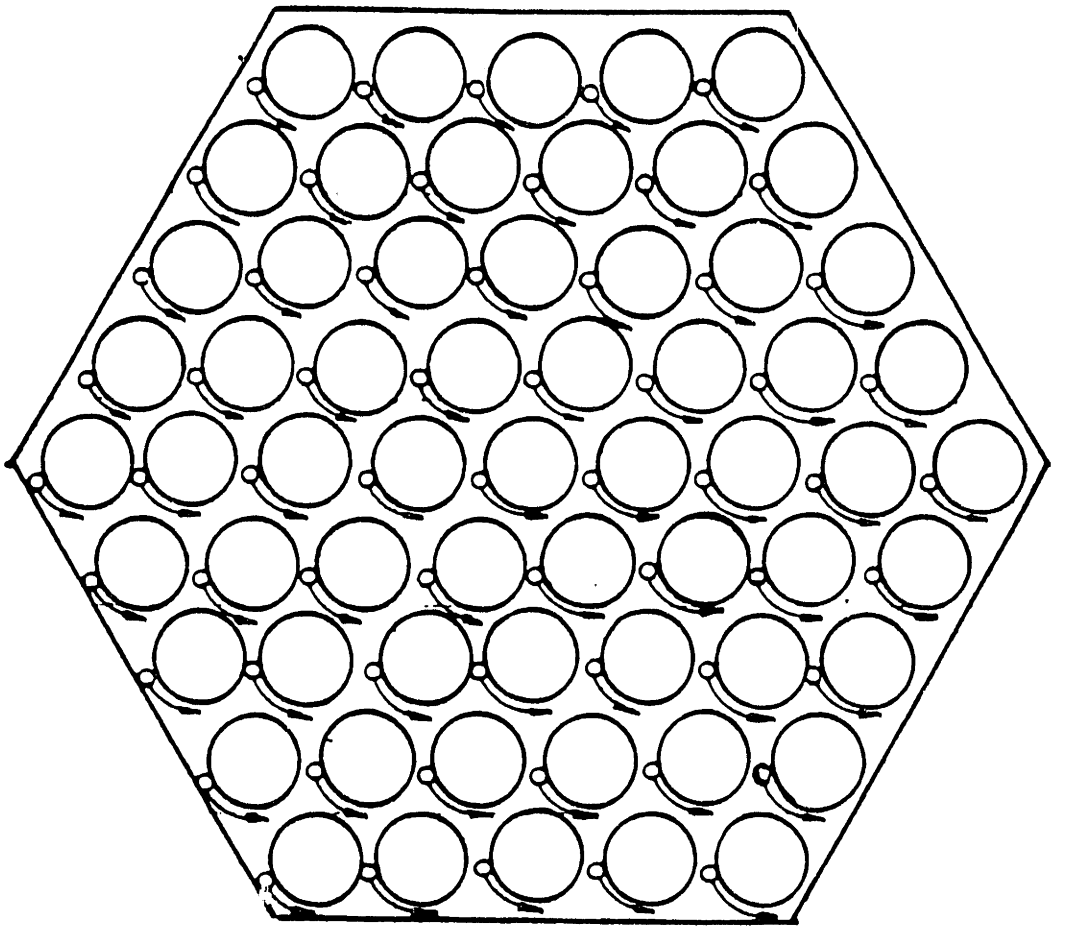

Fuel Pin and Wire Position

Figure 5.11 As Built Geometry at Exit Plane for Chiu's 61-pin Bundles

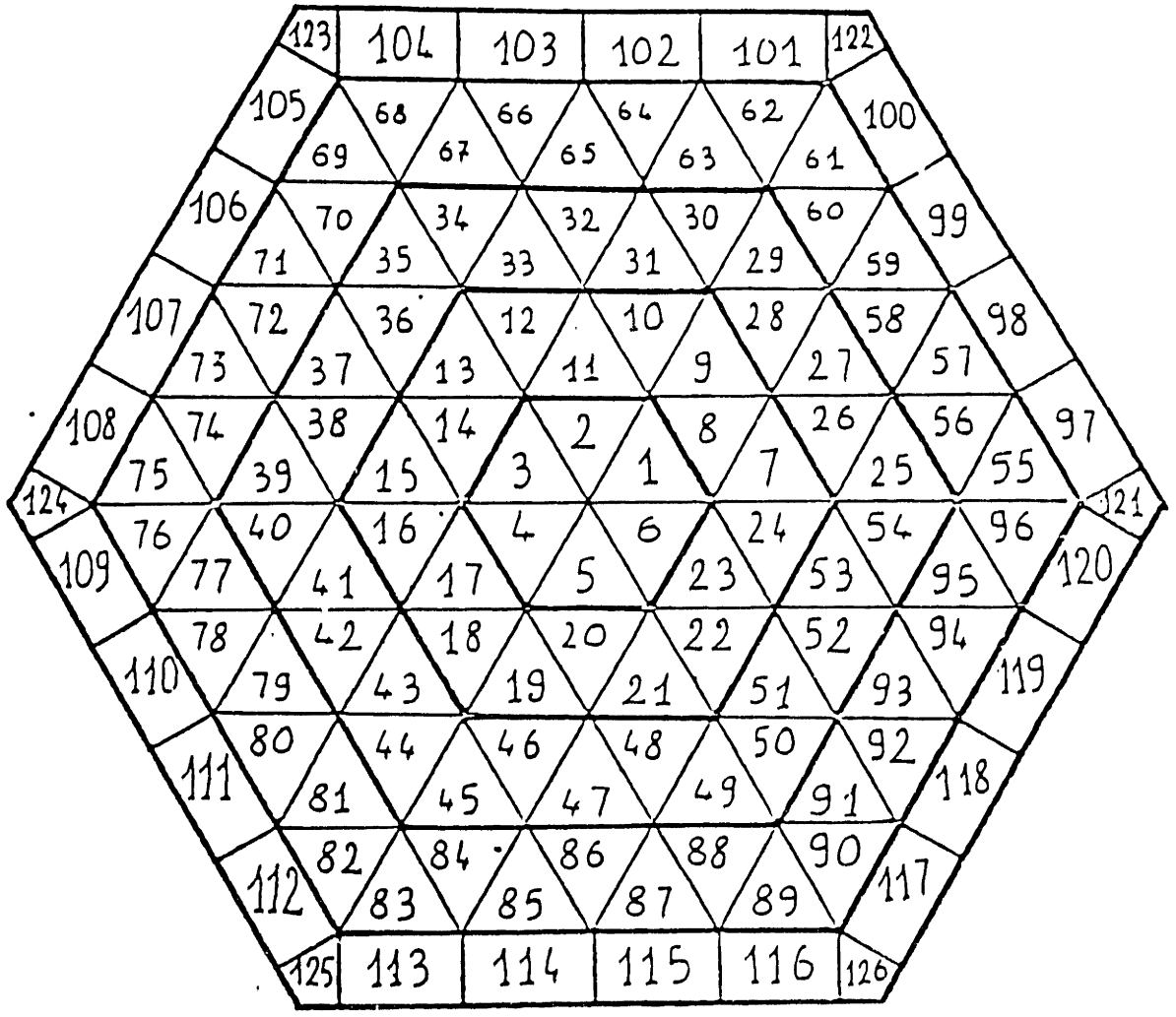

Figure 5.12 Subchannel Numbering Scheme for 61-pin Bundle

Tables 5.3 and 5.4 depicts the reduced $\varepsilon^*_{I\eta}$ and C_{IL} for H/D = 8 and H/D = 4 bundles, respectively. Figures 5.13 and 5.14 compare the calculation results at the minimum MSI with the data at three Reynolds numbers for the interior injection case and for H/D = 8 and H/D = 4 bundles, respectively. Similarly, Figures 5.15 and 5.16 compare the edge injection results at two Reynolds numbers. These figures show that the comparison between calculations and data for Chiu's results are not as good as that of the 37-pin experiments especially for the edge injection cases in which the data display much higher maximum values than that of the DRV calculations. However, the DRV calculations can still quantitatively match the trend of the data quite well.

Figures 5.17 and 5.18 illustrate $\varepsilon^*_{I\eta}$ and C_{IL} reduced from the data as functions of Re_b for H/D = 8 and H/D = 4 bundles, respectively. The predictions of the Chiu-Burns correlation are also presented in these two figures for comparison. For H/D = 8 bundle, the correlation overpredicts $\varepsilon^*_{I\eta}$ (30%) and underpredicts C_{IL} (20%) in the turbulent region. For H/D = 4 bundle, the correlation underpredicts both $\varepsilon^*_{I\eta}$ (15%) and C_{IL}(15%) in the turbulent region.

Figure 5.19 and 5.20 compare the new $\varepsilon^*_{I\eta}$ and C_{IL} reduced in this study with the old $\varepsilon^*_{I\eta}$ and C_{IL} reported by Chiu (1978c). For $\varepsilon^*_{I\eta}$, the two sets of data are almost identical for H/D = 4 bundle, while the new reduced $\varepsilon^*_{I\eta}$'s show lower values (-15%) in the turbulent region for H/D = 8 bundle. For C_{IL}, the new reduced results are a smoother function of Reynolds number.

Table 5.3 Reduced $\varepsilon^*_{1\eta}$ and C_{1L} for 61-pin Bundle with H/D = 8

Re_b	Interior Injection Results (6)*				Edge Injection Results (115)			
	Inj. Depth	Input C_{1L}	Minimum MSI for $\varepsilon^*_{1\eta}$	$\varepsilon^*_{1\eta}$	Inj. Depth	Input $\varepsilon^*_{1\eta}$	Minimum MSI for C_{1L}	C_{1L}
666	16"	0.08	10.18	0.048	22.5"	-	-	-
999	16"	0.13	9.31	0.075	22.5"	0.08	10.26	0.139
1331	16"	0.14	12.11	0.087	22.5"	0.09	12.93	0.150
1664	16"	0.15	10.47	0.100	22.5"	0.10	13.90	0.155
1997	16"	0.18	9.95	0.107	22.5"	0.11	9.27	0.176
2663	-	-	-	-	22.5"	0.11	12.50	0.199
3328	16"	0.21	11.85	0.094	22.5"	0.10	15.52	0.208
4660	16"	0.22	9.73	0.112	22.5"	0.11	16.25	0.228
6656	16"	0.25	10.48	0.108	22.5"	0.11	11.27	0.252
8653	16"	0.27	9.92	0.122	22.5"	0.12	16.39	0.284
10650	-	-	-	-	22.5"	0.13	13.86	0.293

* injection subchannel

Table 5.4 Reduced $\varepsilon^*_{1\eta}$ and C^*_{1L} for 61-pin Bundle with H/D = 4

Re_b	Interior Injection Results (6)*				Edge Injection Results (115)			
	Inj. Depth	Input C_{1L}	Minimum MSI for $\varepsilon^*_{1\eta}$	$\varepsilon^*_{1\eta}$	Inj. Depth	Input $\varepsilon^*_{1\eta}$	Minimum MSI for C_{1L}	C_{1L}
855	14"	0.20	10.30	0.128	14"	0.14	30.70	0.196
1283	14"	0.28	8.76	0.138	14"	0.14	21.32	0.252
1710	14"	0.32	7.44	0.156	14"	0.16	16.45	0.280
2138	14"	0.36	8.17	0.156	14"	0.16	16.75	0.288
2565	15.4"	0.36	7.20	0.152	14"	0.15	14.46	0.306
3420	15.4"	0.52	6.60	0.168	14"	0.17	26.67	0.362
4275	15.4"	0.44	6.59	0.200	14"	0.20	12.98	0.354
5985	15.4"	0.48	5.59	0.252	14"	0.25	14.18	0.402
8550	15.4"	0.50	5.42	0.270	14"	0.27	15.66	0.438
11120	15.4"	0.54	4.89	0.304	14"	0.30	20.79	0.482
13680	15.4"	0.51	5.48	0.284	14"	0.30	17.81	0.462
13680	-	-	-	-	14"	0.30	17.27	0.480
16250	-	-	-	-	14"	0.30	16.83	0.470

* injection subchannel

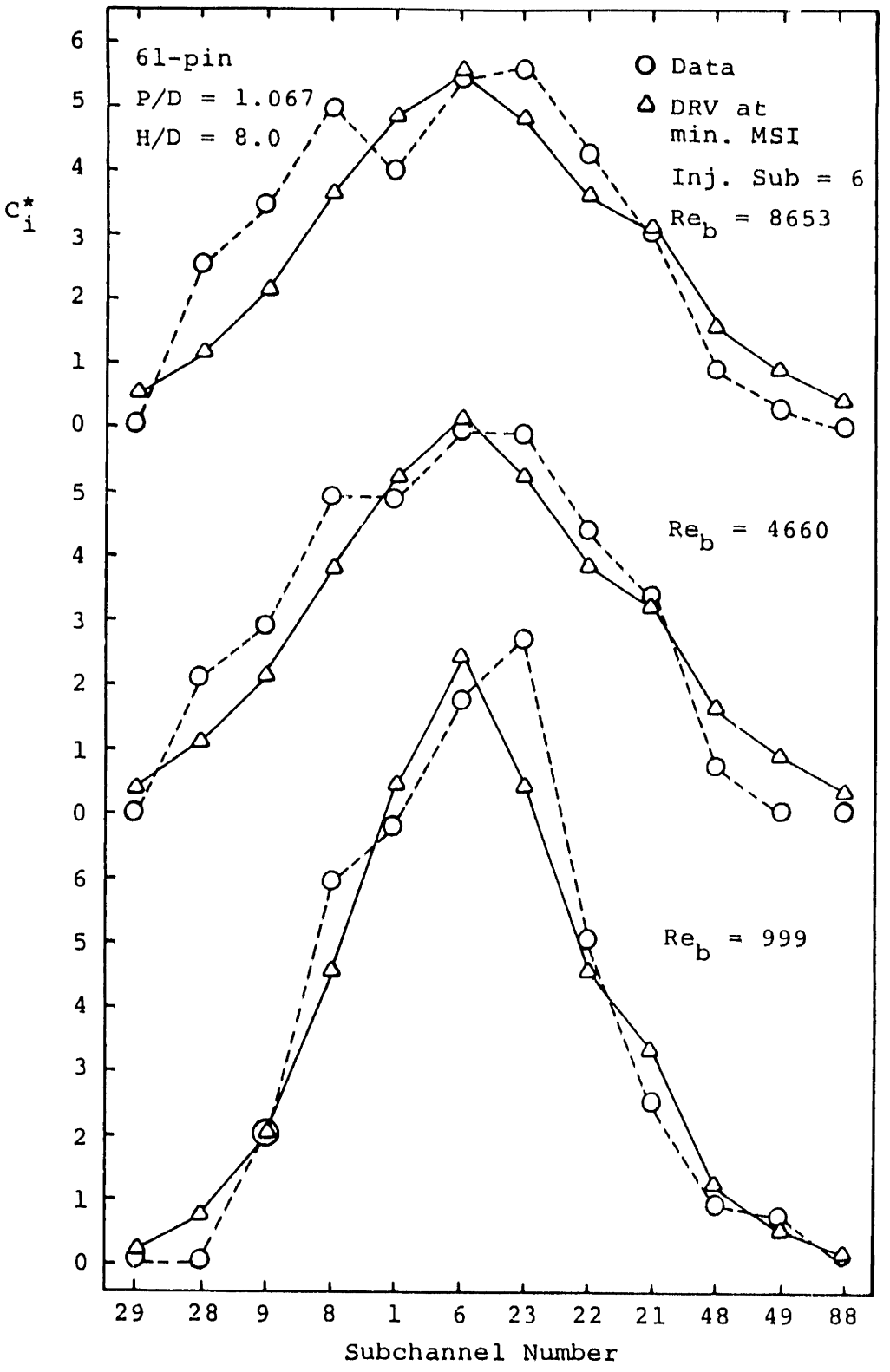

Figure 5.13 Comparison between DRV Calculations at Minimum MSI and Data for 61-pin H/D=8 Interior Injection Cases

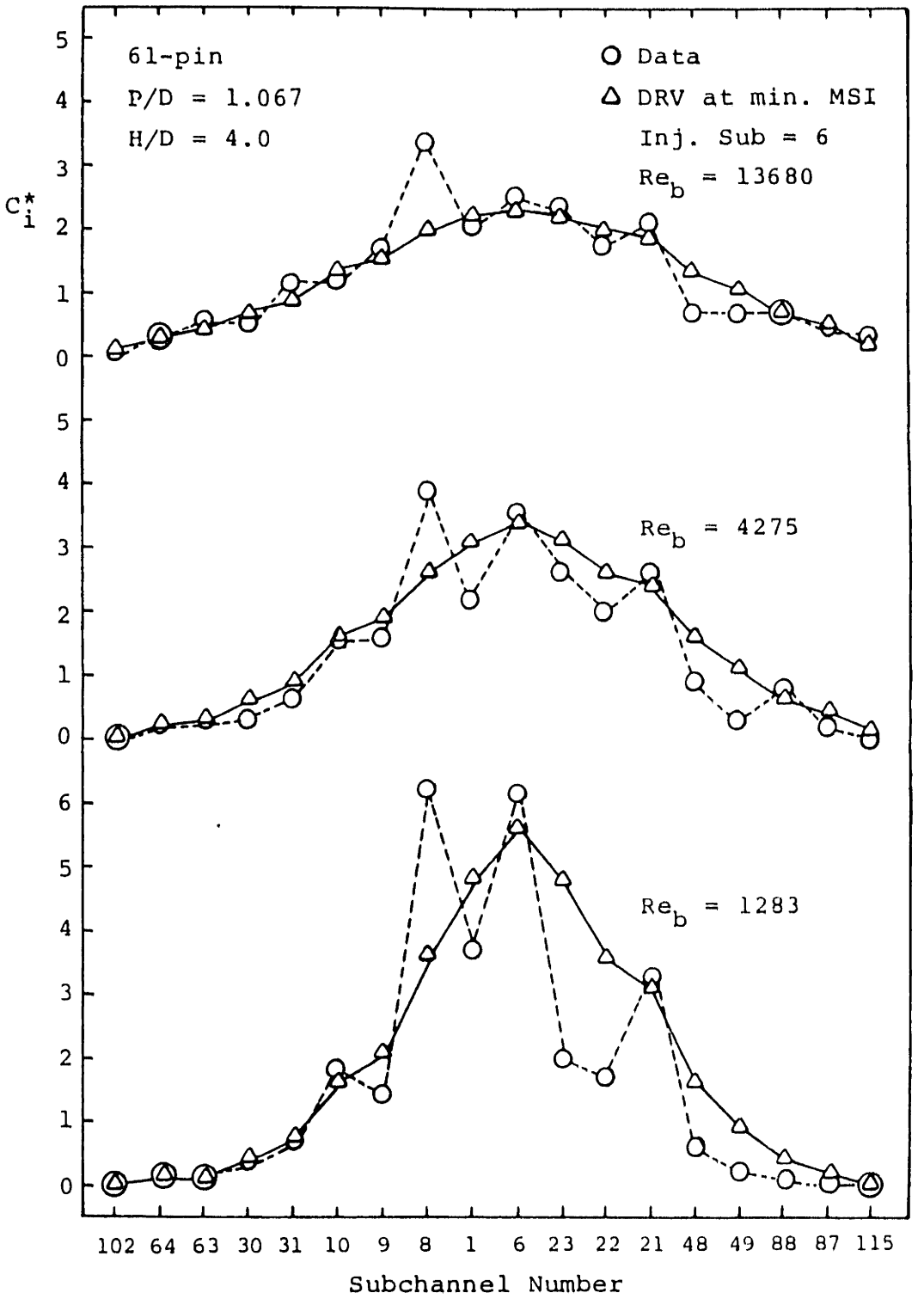

Figure 5.14 Comparison between DRV Calculations at Minimum MSI and Data for 61-pin H/D = 4 Interior Injection Cases

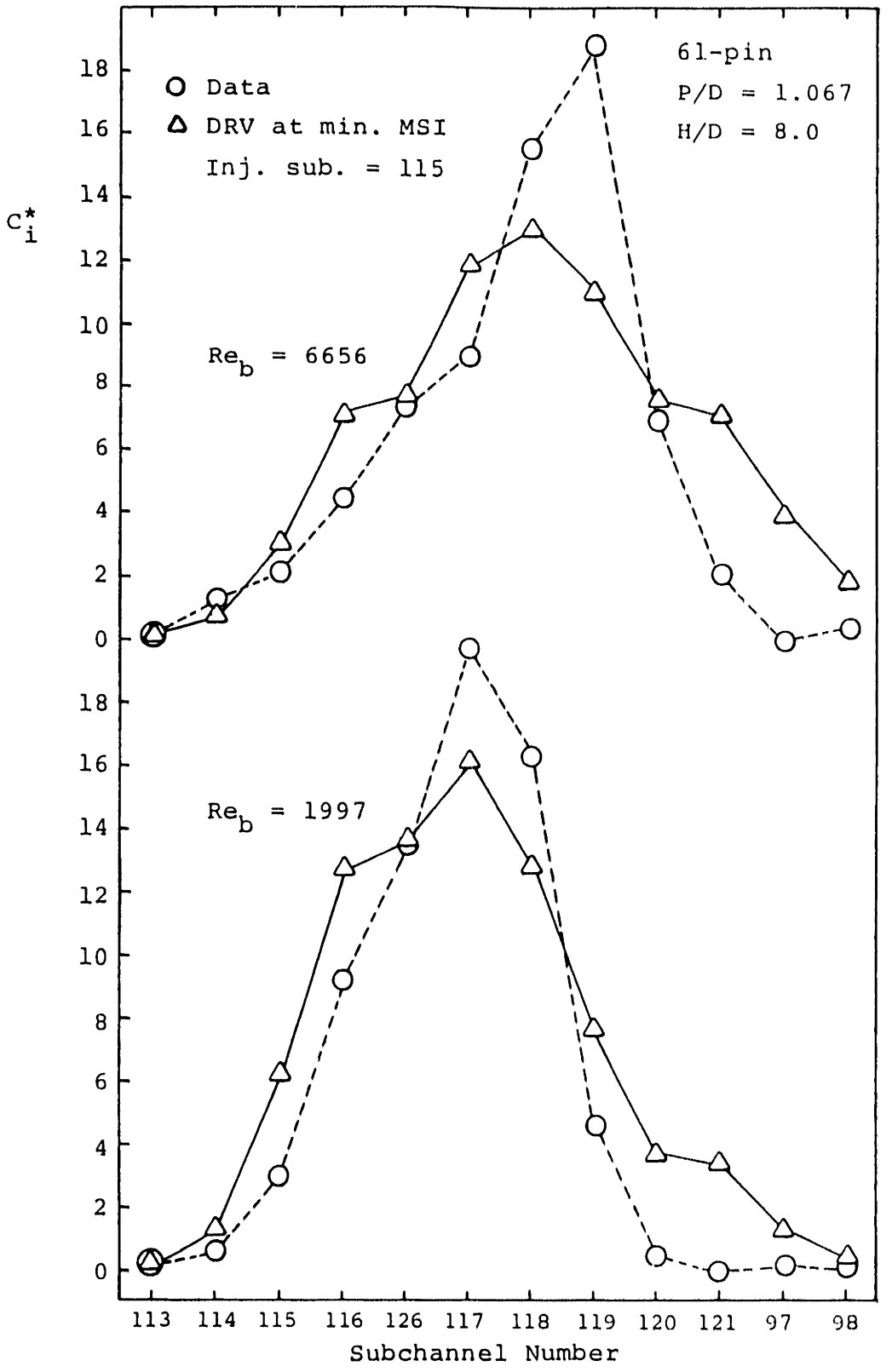

Figure 5.15 Comparison between DRV Calculations at Minimum MSI and Data for 61-pin H/D = 8 Edge Injection Cases

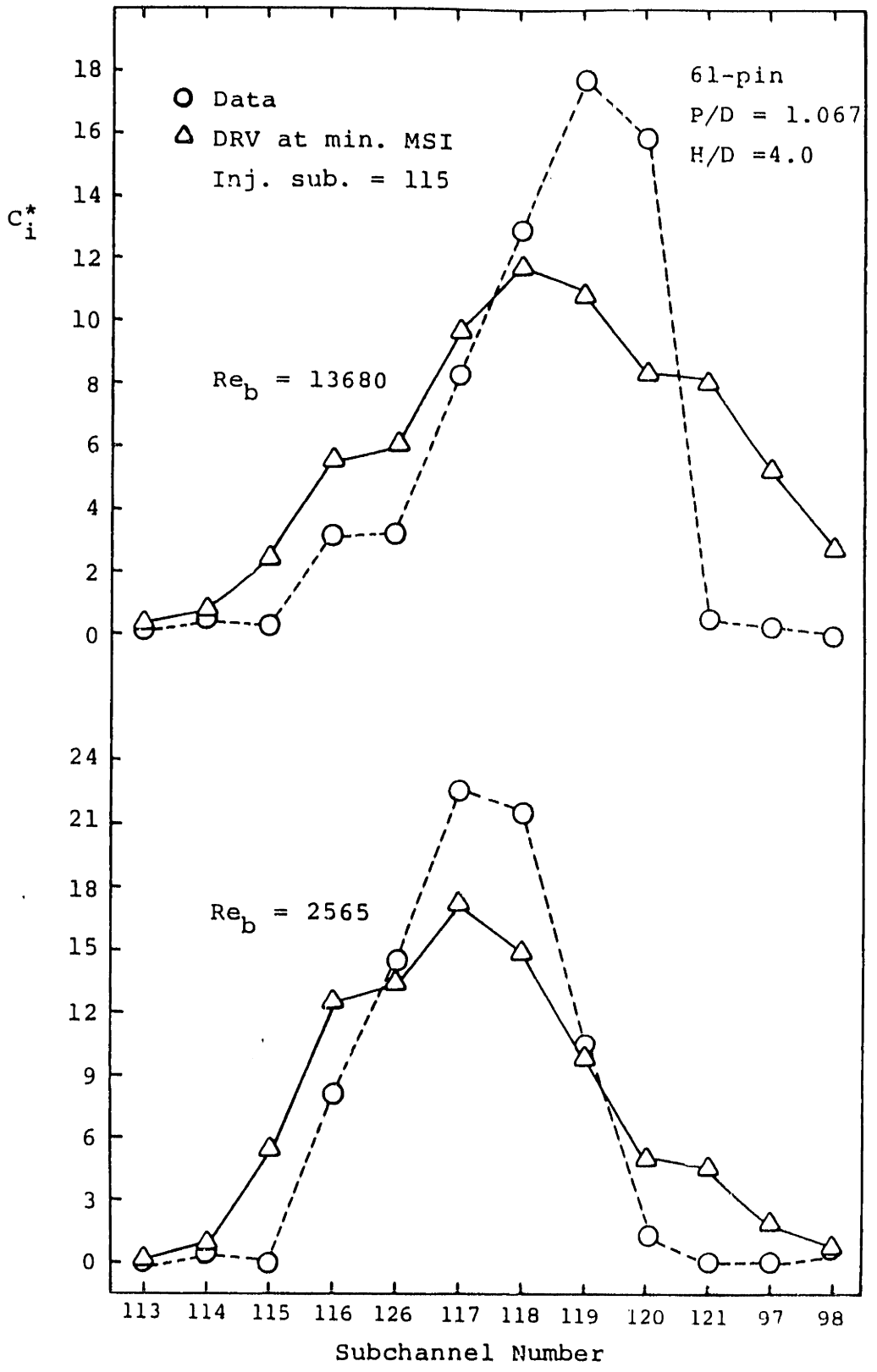

Figure 5.16 Comparison between DRV Calculations at Minimum MSI and Data for 61-pin H/D = 4 Edge Injection Cases

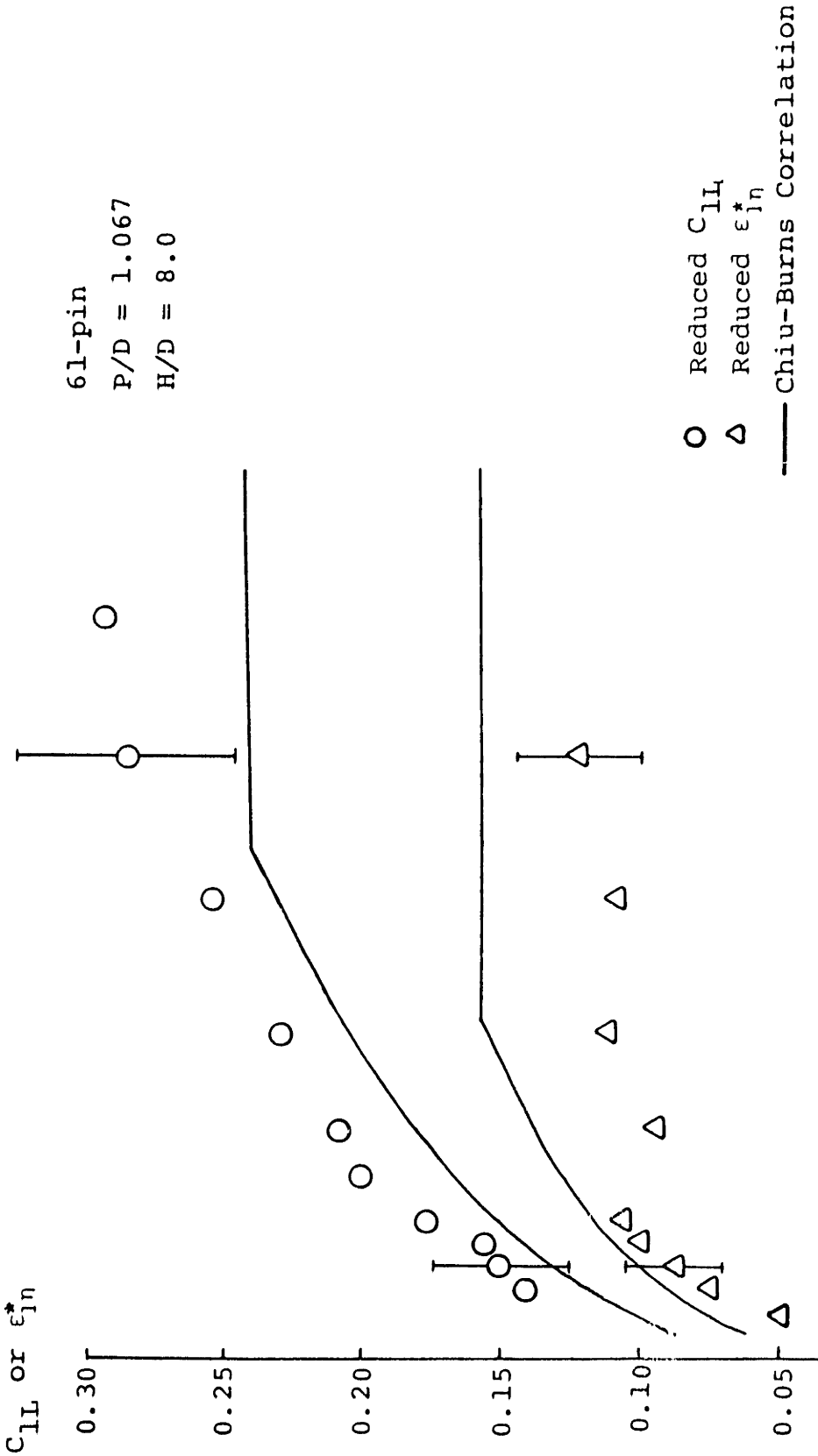

Figure 5.17 Reduced Mixing Parameters for 61-pin H/D = 8 Bundle

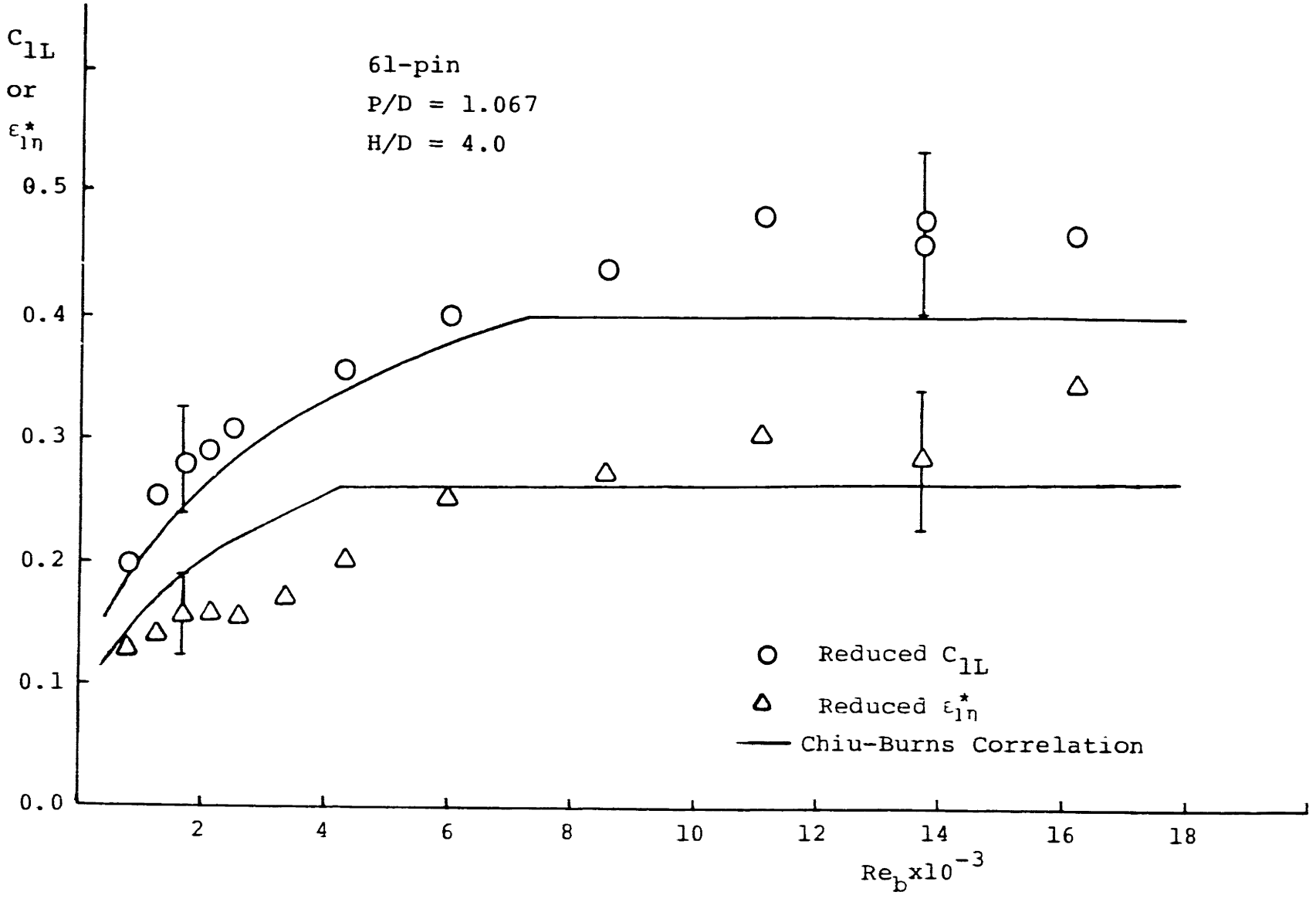

Figure 5.18 Reduced Mixing Parameters for 61-pin H/D = 4 Bundle

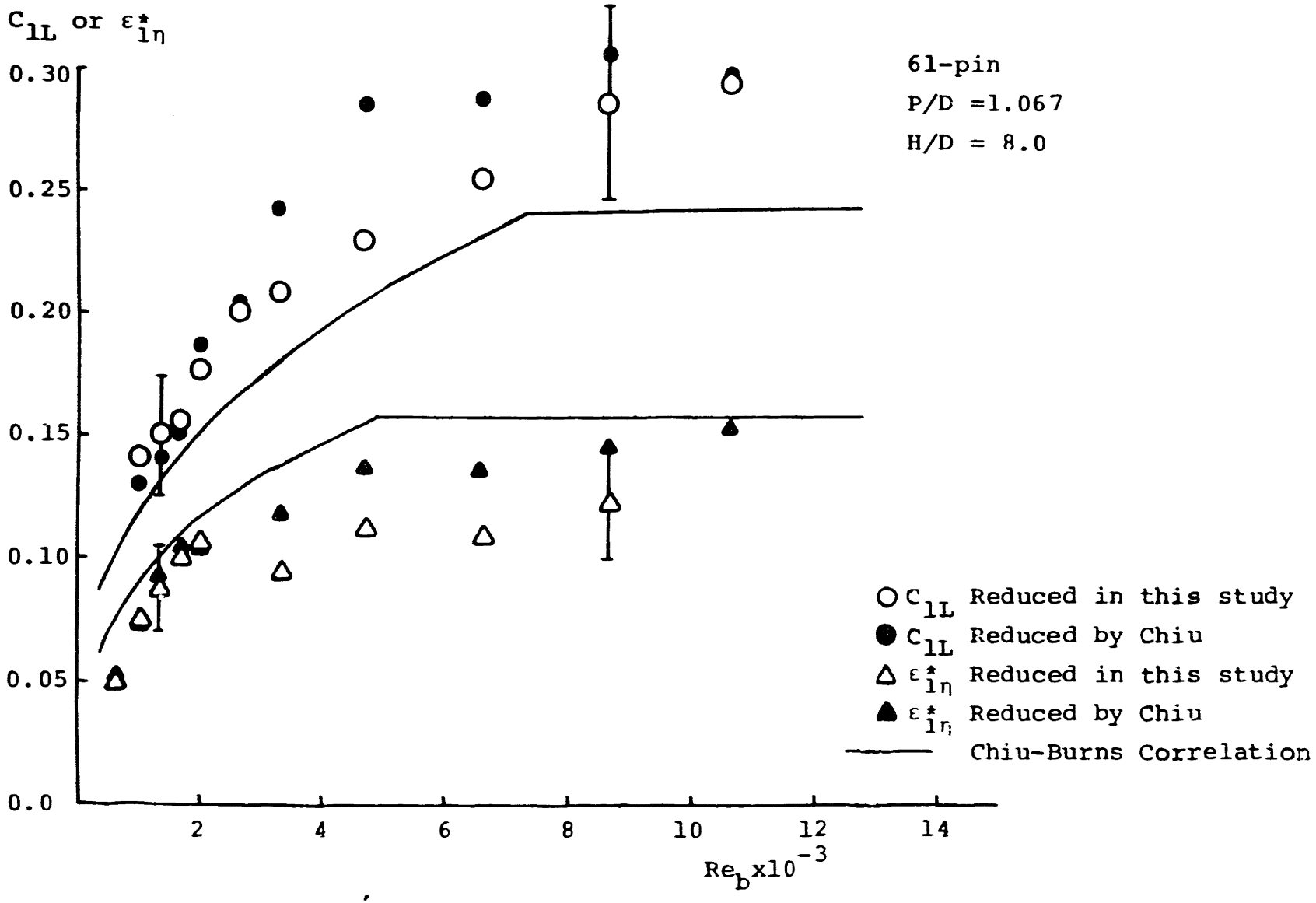

Figure 5.19 Comparison between New (this study) and old (Chiu) Mixing Parameters for 61-pin H/D = 8 Bundle

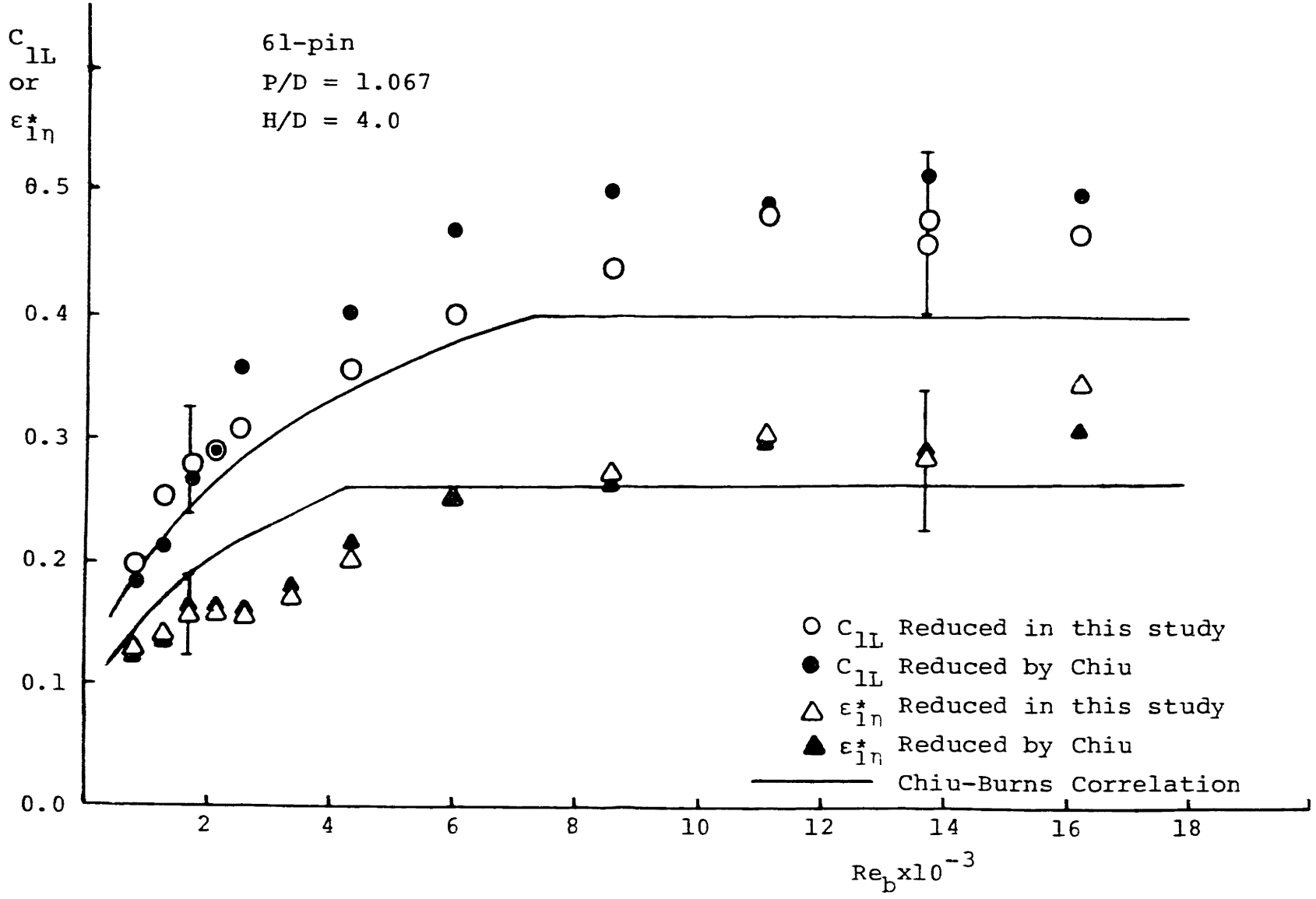

Figure 5.20 Comparison between New (this study) and Old (Chiu) Mixing Parameters for 61-pin H/D =4 Bundle

5.2.4 Discussion

Figures 5.4, 5.8, 5.10 and 5.11 show a clear trend of $\varepsilon^*_{l\eta}$ and C_{lL} as functions of Re_b. As Re_b increases, these parameters increase to a saturated value. The critical turbulent Reynolds numbers, Re_{bT}, from equation (4.34b) are 12820 for 37 pin bundle (P/D = 1.154) and 11140 for 61 pin bundle (P/D = 1.067), respectively. One might conclude that these parameters are constant values for $Re_b > Re_{bT}$. Since only one or two data points are in the laminar region ($Re_b \leq Re_{bL}$, Re_{bL}= 400 for P/D = 1.067; Re_{bL} = 550 for P/D = 1.154) it is not possible to conclude whether these parameters are constants in the laminar region.

As for the Chiu-Burns correlation, the discrepancy between predictions and data are around 15% - 30% for the turbulent values of these parameters. In addition to this flaw, we would like to have a consistent model for the transition region similar to the subchannel friction factor correlation as pointed out in the first chapter. The correlations are then required to be redeveloped to accomplish these two improvements. This will be performed in the next chapter.

5.3 Error Analysis of Mixing Parameters Results

The objective of this section is to estimate the error associated with the experimental determination of the mixing parameters. The total error inherent in the determination of the mixing parameter $\varepsilon^*_{l\eta}$ and C_{lL} is comprised of three parts:

1) the error involved in obtaining the dimensionless salt concentration, C^*_i;

2) the error involved in the code calibration; and

3) the error involved by using this reduced value as the sodium heat mixing parameter.

5.3.1 Error Involved in C_i^* : Experimental Error

The dimensionless salt concentration is defined by

(c.f. equation (3.5))

$$C_i^* \equiv \frac{C_i}{\frac{1}{m_o}\left[\sum_{j=\text{interior}} m_j C_j + \sum_{k=\text{edge}} m_k c_k\right]} \tag{5.18}$$

where

m_j, m_k = interior and edge subchannel flow rates

m_o = injection subchannel flow rate

= m_j for interior injection

= m_k for edge injection

C_i, C_j, C_k = detected subchannel salt concentrations

For interior injection, since almost all the salt tracer is confined in the interior region at the bundle exit level, C_i^* can be expressed as

$$C_i^* \simeq \frac{C_i}{\sum_{j=\text{interior}} C_j} \tag{5.19}$$

Therefore, since

$$\frac{\delta C_i^*}{C_i} = \frac{\delta C_i}{C_i},$$

the error associated with C_i^*, is caused by the uncertainty in determining C_i only.

For edge injection, approximately half the amount of injected salt diffused into the central region, then since $\sum_j C_j \simeq \sum_j C_k$ and $m_o = m_k$

$$C_i^* = \frac{C_i}{\sum_j \frac{m_j}{m_o} C_j + \sum_k C} = \frac{C_i}{\frac{X_1}{X_2} \sum_j C_j + \sum_k C_k} \simeq \frac{C_i}{(1 + \frac{X_1}{X_2}) \sum_j C_j} \qquad (5.20)$$

Therefore,

$$\frac{\delta C_i^*}{C_i^*} = \frac{\delta C_i}{C_i} + \frac{\delta(\frac{X_1}{X_2})}{1 + \frac{X_1}{X_2}} \simeq \frac{\delta C_i}{C_i} + \frac{\delta(\frac{X_1}{X_2})}{2} \qquad (5.21)$$

since in general $X_1 \simeq X_2$.

Equation (5.21) shows that the error associated with $\frac{X_1}{X_2}$ will induce error in C_i^*. However, since equation (5.20) shows that this error influences all the C_i^* in the same direction, it is systematic in nature.

5.3.1.1 Error Caused by Misdetermination of C_i

The error associated with C_i is caused by two affects: the fluctuation in the data and the spatial nonuniformity of subchannel salt concentration. Both of these are random errors and should be combined in statistical manner.

The standard deviation of the probe resistance after combining calibration and mixing data was estimated to be 10. The nominal value of the difference between the calibration correction and mixing data,

which were used to reduce to salt concentration, was about 100 for most subchannels that are important to this experiment. Therefore, the error associated with C_i is 10/100 = 10%. Note that in [Chiu(1978c)] the mean probe resistance of 1200 was used as the nominal value which is now not considered to be correct.

The nonuniformity of subchannel concentration would cause at most 5% error when the detected value was used as the real average value as estimated by Chiu (1978c). The total error involved in determining C_i is then $\sqrt{(5)^2+ (10)^2}$ = 11%

To investigate how this error in concentration affected the mixing parameters reduced from this data, the prediction maps by DRV for different assumed values of $\varepsilon^*_{1\eta}$ were compared e.g., map A calculated by $\varepsilon^*_{1\eta}$= 0.060 and map B calculated by $\varepsilon^*_{1\eta}$= 0.065. It was found that the percentage difference of the dimensionless concentration in most subchannels between these two maps were about the same as the percentage difference of the mixing parameters input, i.e., the difference in salt concentration in most subchannels between map A and map B is about 10%. The random nature of these experimental errors in different subchannels would mitigate their effect in reducing mixing parameters. Specifically, if all the concentration were overdetermined (or underdetermined), then the error associated with the reduced mixing parameters would be very small. This is because only the relative distribution was the key feature in determining the mixing parameters picked up at minimum MSI. On the other hand, if all the high concentrations were overdetermined and all the low concentrations

were underdetermined, then the error associated with the reduced mixing parameters would be about 10%. A reasonable estimate of the error of mixing parameters in this part might be half of the error associated with salt concentration,i.e., 6%.

5.3.1.2 Error Caused by Misdetermination of Flow Split Parameters

As discussed in the beginning of this section, only in the edge injection case would the C_i^* be affected by this flow split parameters misdetermination. Note that the experimental results of flow split parameters were used to calculate C_i^*. The error associated with these experimental X_i's are 5% in the turbulent flow regime, and 10% in the transition/laminar region, as described in Chapter 3. By equation (5.21), this would give 5% and 10% error in C_i^*, respectively.

Chiu (1978c) had studied this kind of systematic error. The conclusion is about half the percentage error was induced in reducing them to mixing parameters. Hence, 3% and 5% error were imposed on C_{1L} by this misdetermination, respectively.

5.3.2 Error Involved in the Code Calibration

The maldistribution of the concentration map caused by the 30° injection flow disturbance and the strong local sweeping flow near the injection position will introduce uncertainty in the determination of ε_{In}^* and C_{1L} as reduced by the DRV code. In addition, one might expect that the uncertainty could also be introduced by the flow split correlations used in the DRV. For the interior case, since almost no salt is diffusing into the edge region, only equation (5.13) is

crucial. Because no flow split parameters were involved in equation (5.13), the reduced $\varepsilon^*_{1\eta}$ was not affected by the flow split parameters. For the edge injection case, since only the edge subchannels were used for calculating MSI, the ratio $(\frac{X_1}{X_2})$ in equation (5.14) would have only slight influence in reducing C_{1L}. We conclude that the reduced $\varepsilon^*_{1\eta}$ and C_{1L} were quite insensitive to the flow split parameters used, and this uncertainty will not be further considered.

5.3.2.1 Interior Injection Case: $\varepsilon^*_{1\eta}$

In this case, all except the two lowest flow rate runs showed that the peak concentration occurs in subchannel 2. This implied that the maldistribution was caused by the strong local sweeping flow at the injection position rather than the injection disturbance. The results of DRV run for the same sets of data with injection subchannel set to be 1 and 2 were compared in section 5.2.2.1, which showed that the differences between these two sets of reduced parameters were about 10%. The real value showed be between these two results as we recommended, hence we conclude that the error caused by this maldistribution is about 5%.

5.3.2.2 Edge Injection Case: C_{1L}

In contrast to the $\varepsilon^*_{1\eta}$ case, the injection disturbance was expected to be dominant in this case. Since the injection flow was in the same direction as the swirl flow direction, it would increase the swirl effect, thereby increasing the reduced value of C_{1L}. Symolon (1981) studied this effect, and the total error was believed to be less than 5%.

Note that in our work the injection depth was 32" which was four lead lengths and therefore longer than all previous similar works. The longer the injection depth, the less the data reduction error because the disturbance effect is mitigated. However, the injection depth should not be too long; otherwise, too flat a salt concentration distribution might cause large uncertainty in data reduction. Our 32" length is believed to be near optimum.

5.3.3 Error Involved by Methodology

In the LMFBR, sodium instead of water is used as a coolant, and heat mixing instead of salt tracer mixing occurs. As discussed in section 5.1, this would introduce about 9% error in $\varepsilon^*_{1\eta}$ and no error in C_{1L}.

5.3.4 Conclusion

The total error for $\varepsilon^*_{1\eta}$ and C_{1L} are summarized from above discussions to be

for $\varepsilon^*_{1\eta}$:

6% (experimental) + 5% (maldistribution)

+ 9% (methodology) = 20%

for C_{1L}:

$$6\% \text{ (experimental)} + 5\% \text{ (maldistribution)} + \begin{cases} 5\% \text{ (flowsplit maldetermination for } Re_b < 6000) = 16\% \\ 3\% \text{ (flowsplit maldetermination for } Re_b > 6000) = 14\% \end{cases}$$

Table 5.5 depicts these error estimates. The error bar shown in Figures 5.4, 5.8, 5.14 and 5.15 are from those results.

Table 5.5
Summarization of Errors Associated with Mixing Parameters

Cause	$\delta C_i^*/C_i^*$				Maldis-tribution	Method-ology	Total
	$\delta C_i/C_i$			$\frac{\delta(X_1/X_2)}{2}$			
	Data Fluctuation	Non-uniformity	Total on re-duced value				
$\varepsilon_{1\eta}^*$	10%	5%	6%	--	5%	9%	20%
C_{1L}	10%	5%	6%	5% (Re < 6,000) 3% (Re > 6,000)	5%	--	16% (Re < 6,000) 14% (Re > 6,000)

CONSTITUTIVE CORRELATIONS FOR WIRE-WRAPPED SUBCHANNEL ANALYSIS UNDER FORCED AND MIXED CONVECTION CONDITIONS

by

SHIH-KUEI CHENG

B. S. National Tsing-Hua University
(1975)

M. S. National Tsing-Hua University
(1979)

Submitted to the Department of
Nuclear Engineering
in Partial Fulfillment of the
Requirements for the Degree of

DOCTOR OF PHILOSOPHY

at the

© MASSACHUSETTS INSTITUTE OF TECHNOLOGY

August 1984

Signature of the Author Shih-Kuei Cheng
Department of Nuclear Engineering
July 24, 1984

Certified by Neil E. Todreas
Professor Neil E. Todreas
Thesis Supervisor

Accepted by A. F. Henry
Allen F. Henry
Chairman, Departmental
Graduate Committee

MASSACHUSETTS INSTITUTE
OF TECHNOLOGY

OCT 29 1984

LIBRARIES

CHAPTER 6

MIXING PARAMETER CORRELATIONS

6.1 Physical Meaning of Mixing Parameters

The mixing parameters required for the ENERGY code as the input parameters discussed in Chapter 2 are, dimensionless effective eddy diffusivity (DEED), $\varepsilon^*_{l\eta}$; dimensionless eddy diffusivity for the edge region, $\varepsilon^*_{2\eta}$; edge transverse velocity ratio (ETVR), C_{lL}, and conduction shape factor, κ. Correlations for dimensionless effective eddy diffusivity and edge transverse velocity ratio have been developed by Chiu (1978e) and Burns (1980); however, a different length scale, the interior subchannel equivalent hydraulic diameter, De_l, was used by these authors in defining DEED. Their parameter was denoted as ε^*_{lL} in all the paper or reports presented before this work, i.e.,

$$\varepsilon^*_{lL} \equiv \frac{\varepsilon}{V_l De_i} \tag{6.1}$$

where ε is the effective eddy diffusivity between subchannels. The effective eddy diffusivity between edge subchannels was simply assumed to be the same value as that between interior subchannels in their approach.

In this study, $\varepsilon^*_{l\eta}$ is defined as

$$\varepsilon^*_{l\eta} \equiv \frac{\varepsilon}{V_l \eta_{ij}}$$

The reasons for changing the definition for this parameter are as follows:

1) The characteristic length used to derive a dimensionless parameter for eddy diffusivity should be a distance related to two subchannels rather than an equivalent hydraulic diameter for one subchannel. The simplest length is the centroid to centroid distance η_{ij}. This has been pointed out by Nijsing and Eifler (1974) for bare rod cases; and

2) $\varepsilon^*_{l\eta}$ is a parameter reduced directly from the energy conservation equation, and has a physical meaning which is similar to the mixing Stanton number, M_{ij} = transverse mass flux/axial mass flux, in the literature. This has been discussed in chapter 2.

To further illustrate the physical meaning of $\varepsilon^*_{l\eta}$ and the assumption used for the ENERGY code to simulate the energy transfer by turbulent interchange and wire sweeping for the interior gap, Figure 6.1 shows the actual transverse velocity (averaged over the gap at one axial position) at one interior gap, $V_{T,ACT}$, along one axial lead length from WARD's air flow data measured by Roidt et al. (1980). The flow oscillates as the wire travels around the rod and is symmetric for each one-half lead length. This oscillating flow transports fluid from subchannel i to subchannel j over a portion of the axial length and from subchannel j to subchannel i over the remaining length. Figure 6.1 assigns the convention of positive $V_{T,ACT}$ to flow from subchannel i to j. Since the flow behavior from 0 to 180° and 180° to 360° are inversely symmetric, the following relation between flow velocities exists.

$$V_{T,ACT_{i-j}} = \left| V_{T,ACT_{j-i}} \right| \qquad (6.2)$$

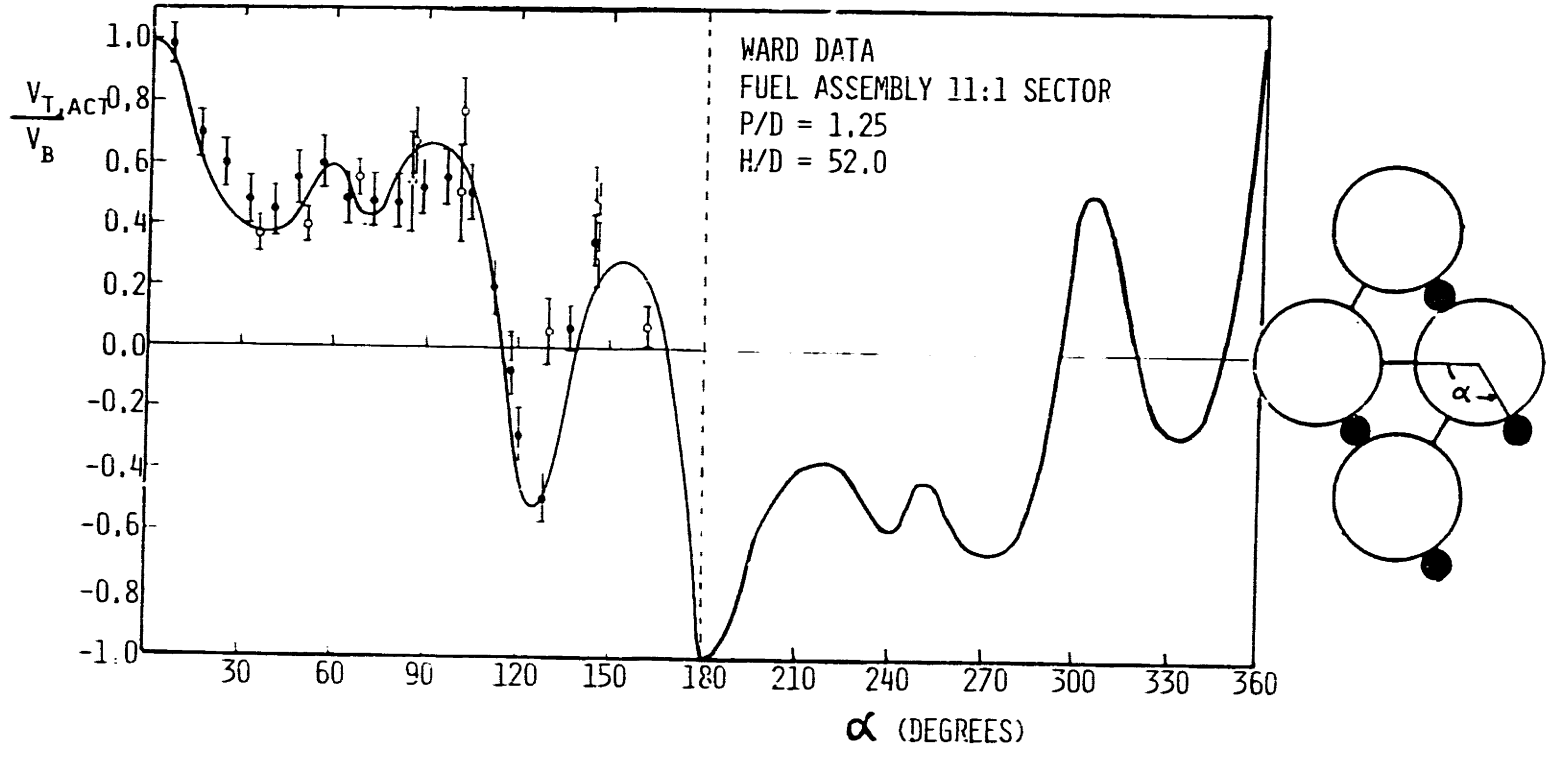

Figure 6.1 TYPICAL TRANSVERSE VELOCITY AT THE INTERIOR GAP AS A FUNCTION OF WIRE POSITION

Hence, one pseudo average transverse velocity $\tilde{V}_T$ can be considered which transports fluid both from subchannel i to j and from j to i as

$$\tilde{V}_T = \frac{1}{H} \int_0^H V_{T,ACT_{i-j}} dz = \frac{1}{H} \int_0^H V_{T,ACT_{j-i}} dz \tag{6.3a}$$

or since

$$\left| V_{T,ACT} \right| = V_{T,ACT_{i-j}} + \left| V_{T,ACT_{j-i}} \right|$$

$$\tilde{V}_T = \frac{1}{2H} \int_0^H \left| V_{T,ACT} \right| dz \tag{6.3b}$$

This velocity $\tilde{V}_T$ is constant over the lead length H and is related to the parameter W'^{W}_{ij}, the mass interchange rate per unit axial length, discussed in chapter 2, by

$$W'^{W}_{ij} = \rho \tilde{V}_T c \tag{6.4}$$

Superimposing the turbulent interchange mass rate per unit area, W'_{ij}/c, to $\rho\tilde{V}_T$ and dividing by the axial mass flux ρV_l, we obtain the parameter $\varepsilon^*_{l\eta}$. In addition to the approximation of using $\tilde{V}_T$ as the transport mechanism, we assume that the energy carried by $\tilde{V}_T$ is the average subchannel enthalpy. This energy transfer term is then shown in the energy equation (2.34) as the term associated with $\varepsilon^*_{l\eta}$.

The parameter $\varepsilon^*_{2\eta}$ is defined similarly to $\varepsilon^*_{l\eta}$ except that it only accounts for the turbulent interchange between the edge subchannels. $\varepsilon^*_{2\eta} = \varepsilon^*_{l\eta}$ is not assumed as in the old approach because the wire sweeps

the flow in one direction in the edge region and has no contribution to $\varepsilon^*_{2\eta}$; however, the wire might enhance the turbulence interchange because of the flow scattering by the wire.

The transverse velocity at the gap between edge subchannels along one axial lead length is shown in Figure 6.2 [Lafay and Benant(1975)]. The velocity has a maximum value as the wire approaches the gap at 120° clockwise from the gap and a minimum value as the wire leaves the gap at 30° counterclockwise from the gap. Other investigators [Chen et al.(1974), Lorenz et al. (1977)] also have observed this phenomenon. To simulate this flow, the ENERGY code uses an axially uniform transverse velocity $\overline{V}_T$ along the assembly wall, which can be obtained from the continuity consideration.

$$\overline{V}_T = \frac{1}{H} \int_0^H V_{T,ACT} \Big|_{edge} \, dz \tag{6.5}$$

Note that only H appears in the denominator of the right hand side of equation (6.5) while, 2H appears in that of equation (6.4). The straight solid line in Figure 6.2 represents this $\overline{V}_T$. One can see that $\overline{V}_T$ is higher than the velocity following the wire direction, $V_A \tan\theta$, as shown in the dashed line. Detailed investigation of the available data for $\overline{V}_T$ shows that for H/D less than 15.0, $\overline{V}_T$ is less than $V_A \tan\theta$ while for H/D higher than 15.0, $\overline{V}_T$ is higher than $V_A \tan\theta$. Consistent with this, the ratio of $\overline{V}_T$ to $\overline{V}_A \tan\theta$ increases as H/D increases. The parameter C_{1L} is defined as the ratio of $\overline{V}_T$ and the average axial velocity in the edge subchannel, V_2.

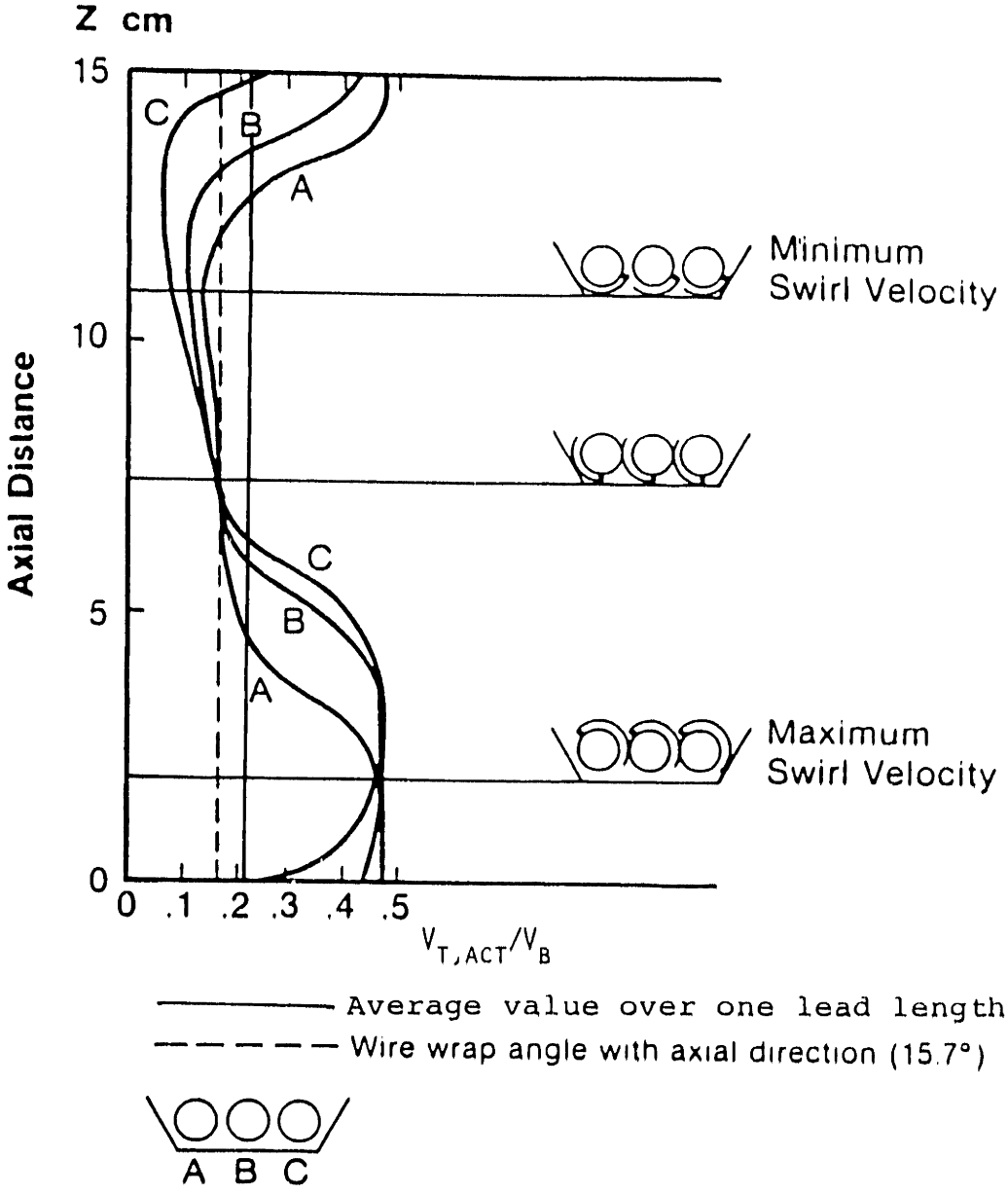

Figure 6.2 Typical Transverse Velocity at the Edge Gap (19-pin, P/D = 1.19, H/D = 18.75, H = 15 cm, from Lafay and Benant (1975))

The physical meaning of κ was discussed in chapter 2.(c.f. equation (2.11)).

In the following sections, the turbulent interchange mechanism is a bare rod bundle will be first discussed and a value for $\varepsilon^*_{2\eta}$ will be recommended. The models and correlations for $\varepsilon^*_{1\eta}$ and C_{1L} will then be developed. Finally, the correlation for κ will be suggested.

6.2 Recommended Value for $\varepsilon^*_{2\eta}$

The turbulent interchange between subchannels in a bare rod bundle has been studied by many investigators. The correlations for W'_{ij} between triangular and triangular (T-T) subchannels, triangular to square (T-S) subchannels, and square to square (S-S) subchannels have been developed by Rogers and Tahir (1975). They are

for T-T
$$\frac{W'_{ij}}{\mu} = 0.0018\ Re_i^{0.9}\ \left(\frac{c}{D}\right)^{-0.4} \tag{6.6}$$

for T-S
$$\frac{W'_{ij}}{\mu} = 0.0027\ Re_i^{0.9}\ \left(\frac{c}{D}\right)^{0.05}\left[1+\left\{\frac{.101(1+c/D)^2-1}{1.273(1+c/D)^2-1}\right\}^{1.5}\right] \tag{6.7}$$

and

for S-S
$$\frac{W'_{ij}}{\mu} = 0.0050\ Re_i^{0.9}\ \left(\frac{c}{D}\right)^{0.106} \tag{6.8}$$

The relationship between (W'_{ij}/μ) and the dimensionless eddy diffusivity for turbulent interchange, $\varepsilon^*_{\eta T}$, can be easily obtained by the definition of $\varepsilon^*_{\eta T}$,

$$\varepsilon^*_{\eta T} \equiv \frac{W'_{ij}/c}{\rho V_i} = \frac{(W_{ij}/c)De_i}{\frac{\mu\rho V_i De_i}{\mu}} = \left(\frac{W'_{ij}}{\mu}\right)\left[\frac{\frac{De_i}{c}}{Re_i}\right] \tag{6.9}$$

Using equations (6.6), (6.8), and (6.9) we can write $\varepsilon^*_{\eta T}$ as

$$\varepsilon^*_{\eta T} = a\left(\frac{De_i}{c}\right)\left(\frac{c}{D}\right)^b Re_i^{-0.1} \tag{6.10}$$

where for T-T $a = 0.0018$, $b = -0.4$

S-S $a = 0.0050$, $b = 0.106$

The definition of $\varepsilon^*_{\eta T}$ is the same as the mixing Station number M_{ij} for turbulent interchange. The mixing parameter β used in the COBRA series of codes is defined as

$$\beta = \frac{W'_{ij}}{\overline{G}} = M_{ij}\frac{G_i}{\overline{G}} = \varepsilon^*_{\eta}\frac{G_i}{\overline{G}} \tag{6.11}$$

where $\overline{G} = (G_i + G_j)/2$

If the velocities in two channels are not very different, β is the same as $\varepsilon^*_{\eta T}$. Considering the error associated with the data for these mixing parameters, which is around 20%, one can not distinguish between β and $\varepsilon^*_{\eta T}$ from the data. The parameter β has also been studied by some investigators, e.g., Rowe and Angle (1967) suggested

$$\beta = 0.0062\left(\frac{de_i}{c}\right)Re_i^{-0.1} \tag{6.12}$$

and Castellana et al. (1973) suggested that β for a square array with $P/D = 1.334$ should be

$$\beta = 0.0071\left(\frac{de_i}{c}\right)Re_i^{-0.1} \tag{6.13}$$

In the most recent version of the COBRA code, a constant value, 0.01 is used for β for all geometry and flow regions in LMFBR subchannel analysis [Khan(1982)].

The exponent for Reynolds number, -0.1, is from the theoretical derivation rather than fitting from the experimental data. The eddy diffusivity for the turbulent core in a tube can be derived as

$$\varepsilon_{H_{ij}} \propto \nu Re \sqrt{(f/2)} \tag{6.14}$$

Typically, if one uses $f = aRe^{-0.2}$ for turbulent flow, $\varepsilon_{H_{ij}} \propto Re^{0.9}$. Dividing $\varepsilon_{H_{ij}}$ by the mass flux, one obtains β or $\varepsilon^*_{\eta T} \propto Re^{-0.1}$. However, based on the scatter of the available data, one can not conclude the Reynolds number dependence of this parameter. Hence, we would assume that $\varepsilon^*_{\eta T}$ has no dependence on the Reynolds number, and developed a simpler correlation for $\varepsilon^*_{\eta T}$ (or β) which depends only on geometry. Figure 6.3 illustrates some available data as function of c/D. The Rogers and Tahir correlation for ε^*_{η}, equation (6.10), is also present for comparison. For the T-T array, the low c/D data of Petrunik (1968) and Walton (1969) do not appear consistent. Since Walton's result is consistent with other data at larger c/D, Petrunik's lowest c/D result is not used in the correlation proposed below.

$$\text{For T-T} \qquad \varepsilon^*_{\eta T} = 0.0016\left(\frac{c}{D}\right)^{-0.5} \tag{6.15}$$

$$\text{S-S} \qquad \varepsilon^*_{\eta T} = 0.0056\left(\frac{c}{D}\right)^{-0.3} \tag{6.16}$$

Figure 6.3 shows that for T-T, $\varepsilon^*_{\eta T}$ is about 0.008 - 0.02. The Typical results for $\varepsilon^*_{l\eta}$ are around 0.02 to 0.12 with P/D = 1.25, H/D = 48 to P/D = 1.067, H/D = 8. Hence for an interior subchannel, (T-T), the turbulent interchange part is around 10% of $\varepsilon^*_{l\eta}$.

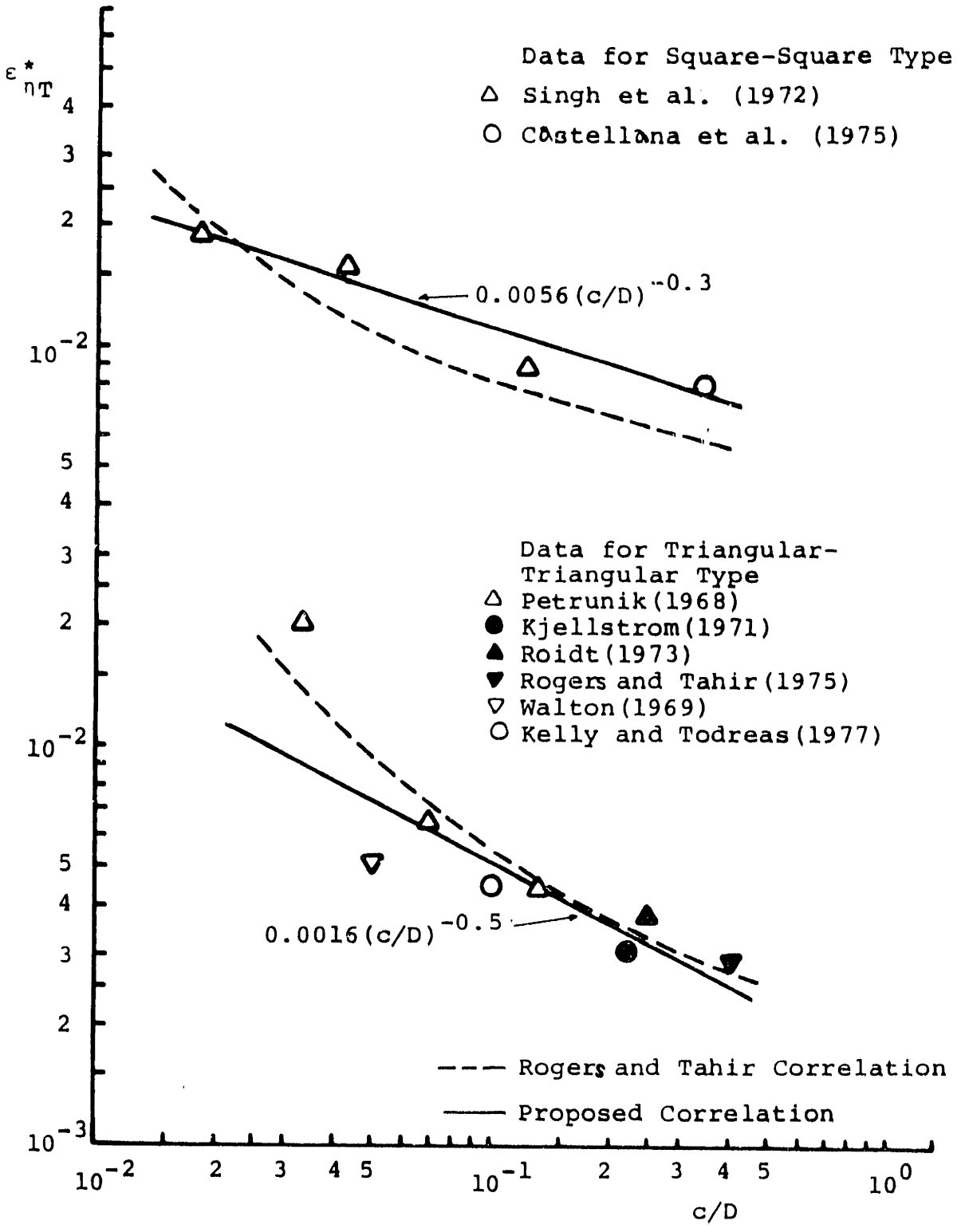

Figure 6.3 Turbulent Interchange Mixing Parameter for Bare Rod Bundle

The parameter $\varepsilon^*_{2\eta}$ is the turbulent interchange between edge subchannels. Rehme (1980a, 1982) has measured the detail turbulent structure in this kind of geometry. No global $\varepsilon^*_{2\eta}$ data, however, are available in the literature. From the data for T-T and S-S, we recommend that 0.01 can be used for $\varepsilon^*_{2\eta}$. This is consistent with what is used for β in the COBRA code.

6.3 Models for DEED and ETVR

6.3.1 Literature Review

The purpose of this section is to propose models for the transverse velocities $\tilde{V}_T$ and $\overline{V}_T$ and then formulate the correlations for DEED and ETRV from this model. The following is some previous work for modelling the wire sweeping flow.

Rogers and Todreas (1968) and Todreas and Turi (1972) performed detailed literature reviews on correlations for M_{ij} defined as V_T/V_A, where $V_T \equiv 2\tilde{V}_T$ for the interior gap and $V_T = \overline{V}_T$ for the edge gap for wire-wrapped rod bundles. The latter have showed that the most general form of the basic flow sweeping equation should be

$$M_{ij} = \alpha_f \frac{\pi(D + D_w)}{H} = \alpha_f \tan\theta \qquad (6.17)$$

where α_f is the fraction of the total subchannel free flow area swept out by wire wraps, i.e., Ar/A's; θ is the wire angle.

Rogers and Tarasuk (1968) assumed that the axial flow pressure drop over the axial distance traveled by mixing flow is approximately equal to the pressure drop experienced by the mixing flow as it passes from subchannel i to subchannel j. This leads to

$$M_{ij} = \left(\frac{2f_i}{K_m} \frac{(D + Dw)}{De_i} \theta_{ij}\right)^{1/3} \tag{6.18}$$

where f_i = subchannel friction factor

θ_{ij} = angular displacement between centroids of adjacent subchannels

K_m = transverse resistance coefficient to cross flow, function of (H/D) correlated differently for different kind of bundles.

Ginsberg (1972) recommended a forced-flow mixing model using the following expression for the forced-flow mixing rate

$$M_{ij} = F(P/D,\ H/D,\ Re)\ \frac{\pi(D+Dw)}{H}\ \delta_{ij} \tag{6.19}$$

where the correlation factor, function F, must be obtained experimentally. δ_{ij} = + 1, -1, and 0 when flow is transported from subchannel i to subchannel j, from subchannel j to i, and when no wire passes through i, j boundary, respectively. Thus, the model described above specifies a pulse type axial distribution of interchannel mixing rate. The model has been tested with only very limited experimental data.

The COBRA-WC wire-wrap model [Donovan et al. (1979)] is based on the assumption that the crossflow induced by the wire wrap passing through a gap is some fraction of the subchannel flow. The expression developed for the ratio of the transverse to axial flow rate was

$$\frac{W_{forced}/c}{G_i} = \left(\frac{\delta}{\Delta x}\right) \pi(D+D_w) \tag{6.20}$$

$$= DUR \tan\theta$$

where Δx = the axial node length

δ = the arbitrary parameter, usually set to $\Delta x/H$

DUR = $\delta(H/\Delta x)$

If one uses $\delta = \Delta x/H$, i.e., DUR = 1, then equation (6.20) becomes

$$\frac{W_{forced}/c}{G_i} = M_{ij} = \frac{\pi(D+D_w)}{H} = \tan\theta \tag{6.21}$$

Equation (6.21) implies that the flow is exactly following the wire direction. In the COBRA code, the forced cross flow is held constant while solving the transversed momentum equations for the remaining cross flows.

Previous to this study, at MIT Chiu (1978e) developed a model for the sweeping flow based on the assumption that the only driving force for this flow was the flow wake effect behind the wire. Chiu's result can be represented in the following form.

$$\frac{V_T}{V_A} = C\left(\frac{gap}{\eta}\right)^{n/2}\left(\frac{A_r}{A_s'}\right)^{1/2}\sin\theta \tag{6.22}$$

where C = 0.235, n = -1 for the interior gap and C = 3.342, n = 0.7 for the edge gap. Note that V_T for the interior gap is $\tilde{V}_T$ while for the edge gap V_T is $\overline{V}_T$ as discussed before.

The above models are only valid in the turbulent region in which M_{ij} does not depend upon Reynolds number. As for the transition region Burns (1980) suggested a model following Chiu's argument but with a Reynolds number dependence. The Reynolds number exponential dependence was taken from bare rod bundle friction factor data measured by Rehme (1973) and was evaluated after some manipulation to be 0.35, i.e,

$$\frac{V_T}{V_A} \propto Re_b^{0.35} \tag{6.23}$$

6.3.2 Models for the Transverse Velocity

Since the final correlations for the mixing parameters DEED and ETVR are empirically determined from the available data, we will not develop very complicated models for these parameters. Instead, only important geometrical parameters will be extracted and the constants of proportionality will be fitted from the data.

The general form for V_T/V_A, equation (6.17), is adopted for our purpose. Intuitively one recognizes that the flow more or less follows the wire direction. This gives equation (6.17) directly, i.e.,

$$\frac{V_T}{V_A} = \alpha_f \tan\theta \tag{6.24}$$

Here, we realize that α_f is a parameter related to A_r/A_s', which makes $V_T/V_A = 0$ as wire diameter goes to zero. Rather that using α_f directly proportional to A_r/A_s', the relation

$$\alpha_f = C_m \left(\frac{A_r}{A_s'}\right)^{1/2} \tag{6.25}$$

where C_m could be function of D_w/D or H/D or both,

is proposed based on the following consideration.

Consider a wire-wrapped rod bundle and the pressure field associated with the wires shown in Figure 6.4. Because of the presence of wire, the flow is stagnant in front of the wire while a wake region

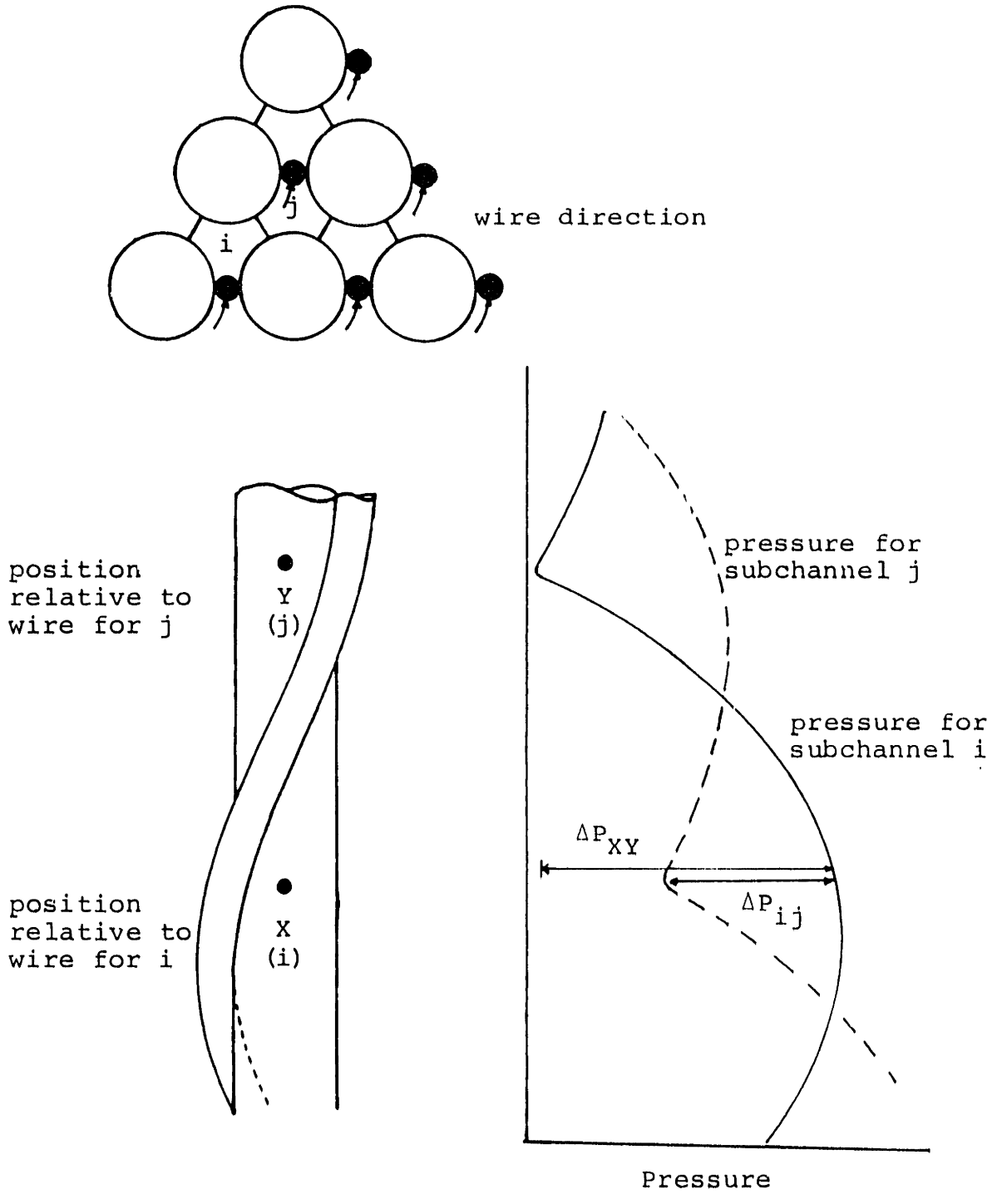

Figure 6.4 Pressure Distribution Relative to Wire Position

is produced downstream of the wire position. This produces the following static pressure distribution: a peak upstream of the wire (corresponding to X position) and a dip downstream of the wire (corresponding to Y position) shown in the right hand side of Figure 6.4. For the wire positions as located in the plan view at the top of Figure 6.4, subchannel i is in a position similar to position x while subchannel j is in a position similar to y. Pressure distribution curves A and B correspond to subchannel j and i, respectivley. The pressure drop from subchannel i to j is seen to not differ much from the pressure drop from X to Y.

The pressure drop ΔP_{XY} can be estimated from the typical wire drag force formulation as

$$\Delta P_{XY} = \frac{F_r}{A_s'} = C_d\left(\frac{\rho V_A^2}{2}\right)\frac{A_r}{A_s'} \tag{6.26}$$

where C_d = drag coefficient of wire

A_r = wire projected area

A_s' = bare subchannel flow area

If we assume that ΔP_{ij} can be related to V_T by the following form

$$\Delta P_{ij} = K_{ij}\left(\frac{\rho V_T^2}{2}\right) \tag{6.27}$$

where K_{ij} is the resistance coefficient for transverse flow, then from

$$\Delta P_{ij} \approx \Delta P_{XY} \tag{6.28}$$

we have

$$K_{ij}\left(\frac{\rho V_T}{2}\right) \approx C_d\left(\frac{\rho V_A^2}{2}\right)\frac{A_r}{A_s'} \tag{6.29}$$

i.e.,

$$\frac{V_T}{V_A} \propto \left(\frac{C_d}{K_{ij}}\right)^{1/2}\left(\frac{A_r}{A_s'}\right)^{1/2} \tag{6.30}$$

Therefore, we conclude that V_T/V_A is proportional to $(A_r/A_s')^{1/2}$. The The constant $(C_d/K_{ij})^{1/2}$ can be incorporated into the proportional constant and determined by the data.

The pressure distribution of Figure 6.4, however, does not exist between adjacent edge subchannels, because the wires are in phase in the edge region. Since a parameter related to A_r/A_s' is also required to make V_T/V_A go to zero as wire diameter goes to zero in the edge region, and since use of the parameter $(A_r/A_s')^{1/2}$ makes C_{1L} fit data well as will be shown in section 6.4, the parameter $(A_r/A_s)^{1/2}$ is also used to formulate (V_T/V_A) in the edge region.

Therefore, the final form for the the transverse velocity is then

$$\frac{V_T}{V_A} = C_m\left(\frac{A_r}{A_s'}\right)^{1/2}\tan\theta \tag{6.31}$$

6.3.3 Correlations for DEED and ETVR

The transverse velocity V_T in equation (6.31) represents either $\tilde{V}_T$ for the interior gap or $\bar{V}_T$ for the edge gap. The corresponding empirical constant C_m is determined from the data base of each geometrical region.

The DEED is comprised of both $\tilde{V}_T$ and a turbulent terchange part

W'_{ij}. However, since the turbulent interchange part of DEED contributes about 10% as discussed in Section 6.2, it can be assumed that

$$\varepsilon^*_{1\eta} \simeq \frac{\tilde{V}_T}{V_A} = C_{m1}\left(\frac{A_{r1}}{A'_1}\right)^{1/2} \tan\theta \tag{6.32}$$

Note that C_{m1} is determined from the data whih includes the turbulent interchange contribution.

On the other hand, ETVR is defined to encompass only the flow sweeping effect so that the parameter C_{1L} is directly expressed in terms of equation (6.31), i.e.,

$$C_{1L} = \frac{\bar{V}_T}{V_A} = C_{m2}\left(\frac{A_{r2}}{A'_2}\right)^{1/2} \tan\theta \tag{6.33}$$

Similar to the subchannel friction factor correlations, the correlations for DEED and ETRV are separated into three flow regions, i.e., turbulent ($Re_b \geq Re_{bT}$) transition ($Re_{bL} < Re_b < Re_{bT}$) and laminar ($Re_b \leq Re_{bL}$). Since the data indicate that both DEED and ETVR are independent of Reynolds number in the turbulent region, the empirical constants in this region denoted as C_{m1T} and C_{m2T}, would be formulated only as functions of geometry. For the laminar region, although the data are not sufficient to confirm that both DEED and EVTR are Reynolds number independent, we assume that they are independent for consistency with the flow split approach and easy formulation of the correlations. The empirical constants for the laminar flow region, denoted as C_{m1L} and C_{m2L}, would then be functions of geometry only.

In the transition region, both DEED and ETVR increase with Reynolds number. The empirical constants for the transition region, denoted as C_{m1tr} and C_{m2tr} would be formulated as functions of both geometry and Reynolds number. A superposition method which combines the laminar and turbulent values would be developed for DEED and ETVR in the transition region in the next section.

6.4 Empirical Constants for DEED and ETVR

6.4.1 Empirical Constants for the Turbulent Region: C_{m1T} and C_{m2T}

In addition to the mixing experiments investigated in chapter 5, i.e., 37-pin data from this study and Chiu's two 61-pin data, the other mixing experiments for wire-wrapped rod bundles using different techniques have been discussed in detail by Khan et al. (1974) and Khan (1980). The data from these experiments will be used to calibrate constants C_{m1} and C_{m2}.

DEED

Table 6.1 depicts the $\varepsilon^*_{1\eta}$ data available in the literature. The data of Okamoto (1970), Hines (1971), Collingham (1971), Skok (1973) were taken from Khan's (1974) reduction results for ε^*_1 by the old DRV code, which were transferred to $\varepsilon^*_{1\eta}$ by equation (5.17b) and the new flow split correlations. The Data from KfK [Baumann (1969), Hoffman (1973, 1975)] were reduced by their MISTRAL II code to get μ with units of % per cm, defined as the total mass interchange rate (% of axial flow) per unit length over all the gaps surrounding one subchannel. For an interior subchannel (3 gaps), μ can be related to $\varepsilon^*_{1\eta}$ by

Table 6.1 Available Data for ε^*_{ln} in the Turbulent Region

Organiz-ation	Investigators	N_r	$D_{(cm)}$	$D_{w(cm)}$	P/D	H/D	Experiment Type	ε_{ln}	C_{mlT}
MIT	Cheng*	37	15.04	2.26	1.154	13.4	Salt tracer	0.065	0.343
	Chiu(1978c)**	61	12.73	0.80	1.067	4.0	"	0.294	0.60
	"	"	"	"	"	8.0	"	0.294	0.50
	Symolon(1981a)	61	6.35	1.59	1.250	24.0	"	0.047	0.38
	"	"	"	"	"	48.0	"	0.026	0.42
KfK	Baumann(1969)	61	6.00	1.00	1.167	16.67	Ht'd pin air	0.044	0.28
	Hoffman(1973)	61	6.00	1.90	1.317	16.67	Ht'd pin, Na	0.065	0.33
	"	"	"	"	"	33.33	"	0.033	0.33
	"	"	"	"	"	50.00	"	0.020	0.30
	Hoffman(1975)	61	6.0	1.20	1.200	16.67	"	0.054	0.32
	"	"	"	"	"	33.33	"	0.023	0.28
	"	"	"	"	"	50.00	"	0.013	0.24
WARD	Roldt(1980)**	217	63.5	15.9	1.250	52.0	Cobra probe+	0.017	0.30
	"	61	63.5	4.50	1.070	7.9	tracer, air	0.140	0.53
ORNL	Fontana(1974)	19	5.84	1.42	1.244	52.0	Ht'd pin, Na	0.020	0.35
HEDL	Collingham(1971)	217	5.84	1.40	1.240	52.0	Salt tracer	0.014	0.25
GE	Hines(1971)	127	6.35	1.78	1.280	24.0	Hot Water	0.043	0.33
Japan	Okamoto(1970)	91	6.30	1.39	1.221	40.48	Salt tracer	0.018	0.25
France	Skok(1973)	7	21.0	3.0	1.142	14.29	Hot Water	0.046	0.26
	"	"	"	"	"	21.43	"	0.030	0.26
	"	"	"	"	"	28.57	"	0.023	0.26
	"	"	16.9	6.0	1.355	26.63	"	0.023	0.18

* This work
** Data reduced by the Author

$$\mu(\%/cm) \equiv \frac{W'_{ij}}{\dot{m}_i} = \left(\frac{W'_{ij}/c}{\dot{m}_i/A_i}\right)\frac{c}{A_i} = 3\varepsilon^*_{l\eta}\left(\frac{c}{A_i}\right) \tag{6.34a}$$

i.e.,

$$\varepsilon^*_{l\eta} = \left(\frac{\mu}{3}\right)\left(\frac{A_i}{c}\right) \tag{6.34b}$$

where A_i and c are in cm^2 and cm, respectively.

The data of Roidt et al. (1980) are from the measured transverse velocity at an interior gap. Using their results presented as Figure 6.1, we can calculate $\bar{V}_T/V_A$ from equation (6.3). The $\varepsilon^*_{l\eta}$ for these bundles can be estimated to be approximately equal to $(\bar{V}_T/V_A)$. The parameter C_{mlT} for all these bundles calculated by equation (6.34) are also present in Table 6.1. The reported error associated with the $\varepsilon^*_{l\eta}$'s listed in Table 6.1 is 20 - 30%.

Figure 6.5 illustrates C_{mlT} as a function of c/D. Although the data scattering for high c/D, the trend suggests that C_{mlT} increases as c/D decreases. As for the H/D effects for C_{mlT}, the data of Chiu's two bundles (P/D = 1.067, H/D = 4.8), Symolon's two bundles (P/D = 1.25, H/D = 24, 48), Hoffman's three bundles (P/D = 1.317, H/D = 16.67, 33.33, 50.0) and Skok's three bundles (P/D = 1.142, H/D = 14.29, 21.43, 28.57) show that these effects are very weak. The reason for the strong dependence on (c/D) of $\varepsilon^*_{l\eta}$ might be that the transverse resistance plays an important role for $\varepsilon^*_{l\eta}$ as seen from equation (6.30). The transverse resistance is strongly affected by the gap to diameter ratio, c/D, hence so is $\varepsilon^*_{l\eta}$.

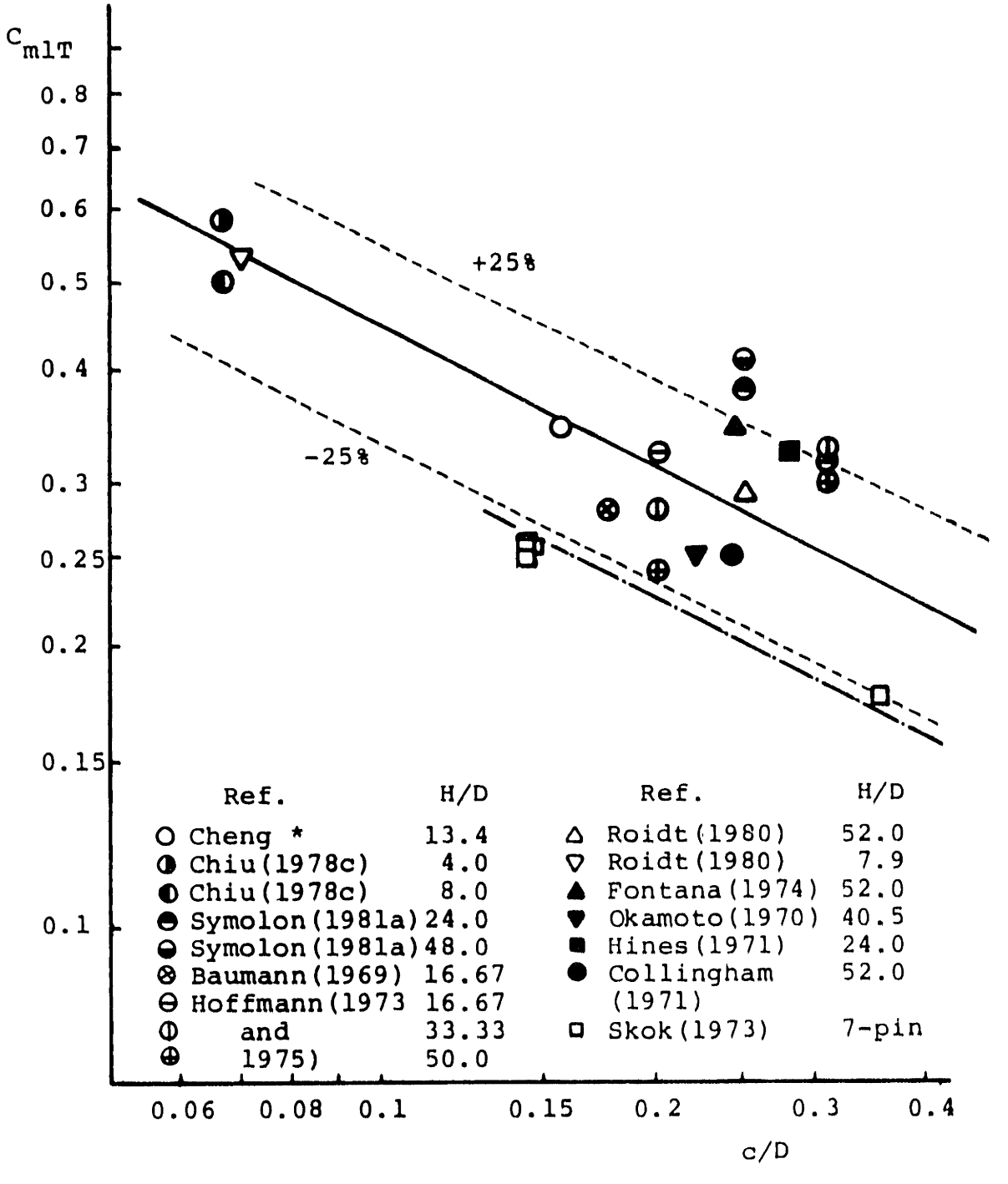

Figure 6.5 Data and Calibrating Results for C_{mlT} (i.e., $\varepsilon^*_{1\eta}$) in the Turbulent Region

Therefore, C_{mlT} would be correlated as function of (c/D) only.

Since in a 7-pin bundle all the interior subchannels are adjacent to the edge subchannels, the $\varepsilon^*_{l\eta}$ reduced from these bundles does not fully represent the $\varepsilon^*_{l\eta}$ between interior and interior subchannels. As shown in Figure 6.5, the $\varepsilon^*_{l\eta}$ from Skok's 7-pin experiments are consistently lower than that from experiments with higher pin number ($\geq$19). Therefore, the results of Skok's experiments are seperated from the other results and correlated seperately for 7-pin bundle application.

The results for C_{mlT}, as illustrated in Figure 6.5 in correlation form are

$$\text{for } N_R \geq 19 \qquad C_{mlT} = 0.14\left(\frac{c}{D}\right)^{-0.5} \tag{3.35a}$$

$$\text{for } N_R = 7 \qquad C_{mlT} = 0.1\left(\frac{c}{D}\right)^{-0.5} \tag{3.35b}$$

These correlations can predict most of the data within ± 25% error except for Symolon's data, which are still within 35% of the prediction. Symolon recalibrated Hanson's salt injection experiment, which were the first experiments performed at MIT using this technique. Because of inexperience with this technique at that time, the larger error of the data might be expected.

ETVR

Table 6.2 depicts the C_{lL} data available in the literature. The data of Skok (1973), Fontana (1974), Pederson (1974) and Lorenz (1974) were also taken from Khan's (1974) reduction results for C_l by the old DRV code, which were transfered to C_{lL} by the flow split correlation.

Table 6.2 Available Data for C_{1L} in the Turbulent Region

Organization	Investigators	N_r	D(cm)	D_w(cm)	P/D	H/D	Experiment Type	C_{1L}	C_{m2T}
MIT	Cheng*	37	15.04	2.26	1.154	13.4	Salt tracer	0.268	1.65
	Chiu(1978C)**	61	12.73	0.80	1.067	4.0	"	0.470	1.14
	"	"	"	"	"	8.0	"	0.284	1.38
	Symolon(1981A)	61	6.35	1.59	1.250	24.0	"	0.22	1.98
	"	"	"	"	"	48.0	"	0.18	3.33
	Symolon(1981)	217	5.89	1.47	1.250	51.72	"	0.11	2.22
	Chen(1974)	61	6.35	1.59	1.250	24.0	LDA	0.22	1.98
	"	"	"	"	"	48.0	"	0.13	2.42
ANL	Pederson(1974)	91	6.35	1.27	1.210	48.0	Hotwater	0.136	2.73
	Lorenz(1977)	91	12.7	3.05	1.240	48.0	Salt tracer	0.137	2.53
ORNL	Fontana(1974)	19	5.84	1.42	1.244	52.0	Ht'd pin, Na	0.115	2.28
France	Lafay(1975)	19	8.00	1.50	1.188	18.75	FV+	0.247	1.93
France	Skok(1973)	7	21.0	3.0	1.142	14.29	Hot Water	0.20	1.30
	"	"	"	"	"	21.43	"	0.15	1.46
	"	"	"	"	"	28.57	"	0.13	1.69

* This work

** Data Reduced by the Author

\+ Flow Visualization Technique

(c.f. equations (5.10),(5.12)) Chen's (1974) data were measured by a laser doppler anemometer (LDA) at Re_b = 4500. Observing the data in the transition region from our study, we find that the value for C_{1L} at this Reynolds number is around 90% of its turbulent value. Hence, the reported value divided by 0.9 is estimated to be the turbulent value. Collingham's (1971) 217-pin edge injection data reduced by Khan (1974) are not included in this table because they are apparently much lower than (40%) all the other data for bundle geometry resembling a fuel assembly. The bundle size effect could not be confirmed since the recent Symolon (1981) 217 pin data showed consistent values with the data from the small size bundle with similar geometry. The parameter C_{m2T} for all these bundles calculated by equation (6.33) is also present in Table 6.2. The reported errors associated with C_{1L}'s listed in Table 6.2 are around 20%.

Figure 6.6 illustrates C_{m2T} as a function of H/D. The trend of C_{m2T} in this figure strongly suggests that it is a function of H/D only. As H/D increases, C_{m2T} increases. Only slight scatter of these values is indicated at the H/D ≈ 50 end, at which all the data are from a geometry similar to a fuel assembly.

The characteristic of the transverse velocity in the edge gap is not the same as that in the interior gap. The pressure driving source illustrated in Figure 6.3 does not exist in the edge gap since all the wires are in phase. Hence the transverse velocity in the edge gap is mainly created by the wire sweeping. As the data show, these wire-sweeping effects create flow with an average angle with respect to the rod axis less than the comparable wire angle for low H/D and

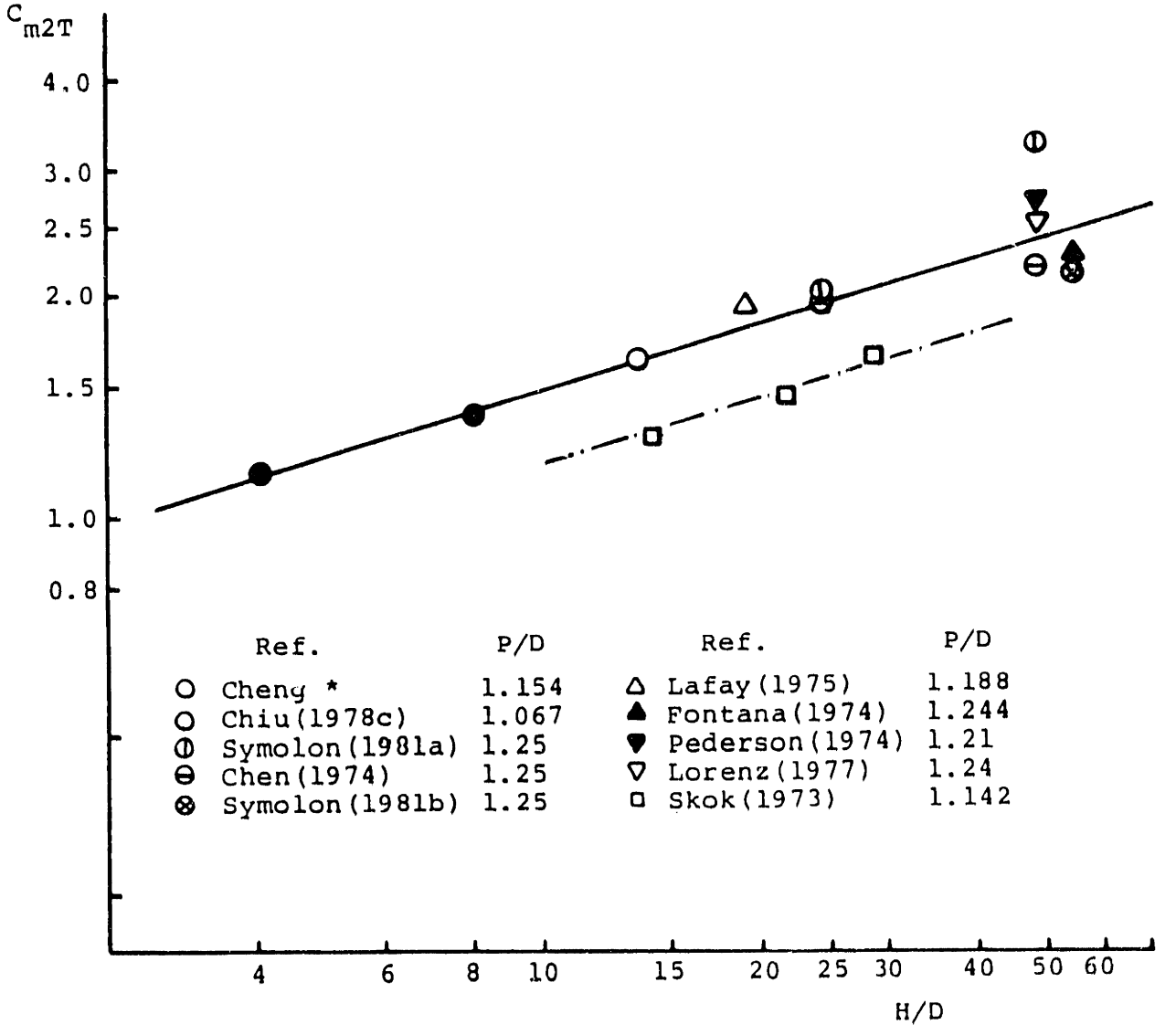

Figure 6.6 Data and Calibrating Results for C_{m2T} (i.e., C_{1L}) in the Turbulent Region

greater than the wire orientation for high H/D. The breaking point for this phenomenon is around H/D = 15.

Similar to the $\varepsilon^*_{1\eta}$ case, consistently lower values of C_{1L} for 7-pin bundles from Skok's data than that from other bundles' data are found. Since all the edge gaps in a 7-pin bundle connect an edge subchannel to a corner subchannel, the transverse velocity might be retarded by this character. Again, the results of Skok's experiments are correlated seperately for 7-pin bundle application.

The fitted results for C_{m2T} as illustrated in Figure 6.6 are

$$\text{for } N_R \geq 19 \quad C_{m2T} = 0.75(H/D)^{0.3} \tag{6.36a}$$

$$\text{for } N_R = 7 \quad C_{m2T} = 0.6(H/D)^{0.3} \tag{6.36b}$$

These correlations can predict all the data for C_{1L} within ± 15%.

The consistency between the H/D dependence of C_{m2T} and W_{sT}, the swirl flow constant in the subchannel friction factor models, (c.f. equations, (4.20), (4.64)) is worth pointing out. Comparing equation (4.20) to (6.33) one finds that $\sqrt{W_{sT}}$ corresponds to C_{m2T}. Although the absolute magnitude is quite different for these two parameters, the dependence of (H/D) for these parameters is almost the same, i.e., the parameter $\sqrt{W_{sT}}$ is almost proportional to $(H/D)^{0.3}$ from equation (4.64).

To illustrate the parameter behavior of $\varepsilon^*_{1\eta}$ and C_{1L}, Figures 6.7 and 6.8 illustrate the predicted $\varepsilon^*_{1\eta}$ and C_{1L} as functions of P/D and H/D, respectively. Some data from Tables 6.1 and 6.2 are also present in these figures for comparison.

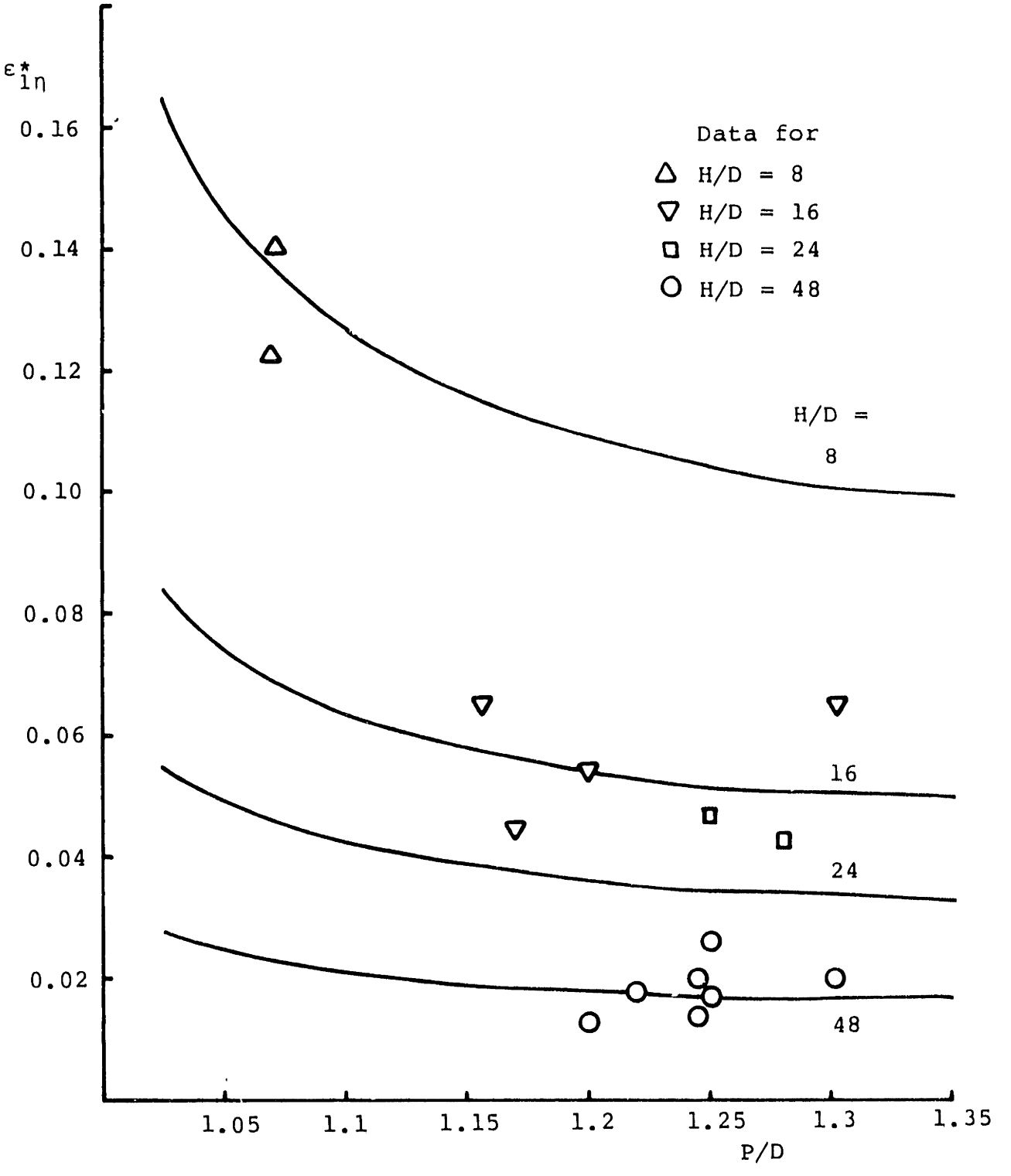

Figure 6.7 Parametric Behavior of $\varepsilon^*_{1\eta}$ in the Turbulent Region

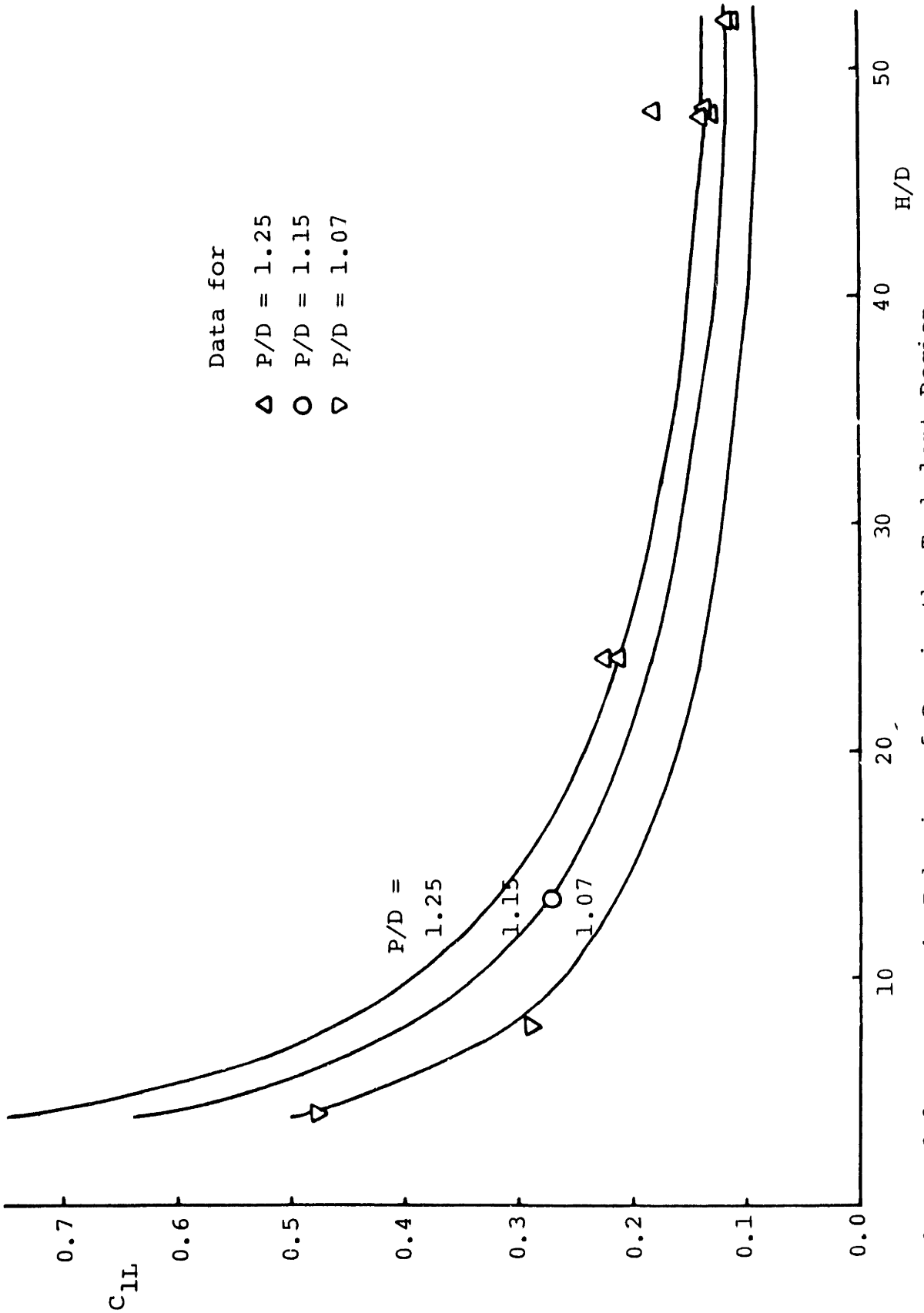

Figure 6.8 Parametric Behavior of C_{1L} in the Turbulent Region

6.4.2 Empirical Constants for the Laminar Region: C_{m1L} and C_{m2L}

Only Chiu (1978) and Symolon (1981) performed similar experiments to the mixing experiments, in this study at low flow rates. Using a laser doppler anemometer, Chen (1974) measured transverse and axial velocities in the edge region at $Re_b = 430$ in two 61-pin bundles with P/D = 1.25 and H/D = 24 and 48. These are the only available data for the mixing parameters $\varepsilon^*_{1\eta}$ and C_{1L} in the laminar region.

Because of the insufficient data base in the laminar region, assumptions of the relation between laminar and turbulent values for these parameters have to be made. We assume that the ratios between laminar and turbulent values of $\varepsilon^*_{1\eta}$ and C_{1L} are the same for both parameters, i.e.,

$$\frac{\varepsilon^*_{1\eta}\Big|_{\text{laminar}}}{\varepsilon^*_{1\eta}\Big|_{\text{turbulent}}} = \frac{C_{1L}\Big|_{\text{laminar}}}{C_{1L}\Big|_{\text{turbulent}}} = C_{mLT} \tag{6.37}$$

The parameter C_{mLT} can be estimated from the data described above. However, since large scatter is found in Symolon's data for low flow rates, estimation of C_{mLT} from his data is not achievable. Further, the lowest flow rates in Chiu's experiments were beyond the laminar laminar region (i.e., $Re_b = 860$ vs 400). The laminar values of $\varepsilon^*_{1\eta}$ or C_{1L} of Chiu's bundle were estimated by extrapolating the data in the transition region to $Re_b \approx 400$. As for Chen's data, the corrected turbulent values for C_{1L} listed in Table 6.2 are used to calculate C_{mLT}. Table 6.3 lists the calculated results of C_{mLT} for these bundles.

Table 6.3 Available Data for C_{mLT}

Investigators	N_r	P/D	H/D	C_{mLT} for $\epsilon^*_{l\eta}$	C_{mLT} for C_{lL}
Cheng*	37	1.154	13.4	~0.6	~0.6
Chiu(1978c)	61	1.067	4.0	~0.3	~0.3
	"	"	8.0	~0.3	~0.3
Chen(1974)	61	1.25	24.0	-	~0.68
	"	"	48.0	-	~0.63

* This work

Investigating C_{mLT} in Table 6.3, one finds that this parameter is an increasing function of P/D. The following correlation can satisfactorily fit these values as function of P/D.

$$C_{mLT} = 1.5\left(\frac{c}{D}\right)^{0.6} \tag{6.38}$$

The laminar values of $\varepsilon^*_{l\eta}$ and C_{lL} can then be calculated from equation (6.38) and their corresponding turbulent values.

Equation (6.38) gives C_{mLT} a value from 0.3 to 0.7 as P/D varies from 1.067 to 1.25. The nominal value of C_{mLT} is around 0.5. This implies that the wire sweeping effect decreases as the flow changes from turbulent to laminar. Note that in the subchannel friction factor correlations, the parameter $\sqrt{W_{sL}/W_{sT}}$, which physically corresponds to C_{mLT}, was calibrated to be 0.55 by the friction factor data. Hence two sets of these correlations are consistent in modelling the hydraulic character for wire-wrapped rod bundles.

6.4.3 Empirical Constants in the Transition Regions: C_{m1tr} and C_{m2tr}

In the transition region, the data show that the mixing parameters $\varepsilon^*_{l\eta}$ and C_{lL} increase as the Reynolds number increases. One can imagine that the wire sweeping effect gradually increases, starting from the value for laminar flow and ending at the value for turbulent flow. Therefore, the following form is formulated for these parameters in the transition region,

$$MP = MP_L + (MP_T - MP_L)\psi_i^{\lambda} \tag{6.39}$$

where MP = mixing parameter $\varepsilon^*_{l\eta}$ or C_{lL}

MP_L = MP in the laminar region

MP_T = MP in the turbulent region

ψ_i = intermittency factor defined in the subchannel friction factor models

$$\equiv \frac{\log (Re_i/Re_{iL})}{\log (Re_{iT}/Re_{iL})}$$

i = 1 for the interior region, i.e., for $\varepsilon^*_{l\eta}$

i = 2 for the edge region, i.e., for C_{lL}

λ = exponent fitted from the data

Note that the ψ_i^λ changes from 0 to 1 as Re_i changes from Re_{iL} to Re_{iT}. The subchannel Reynolds numbers, Re_i's are calculated from the flow split correlation developed in Chapter 4.

By matching the transition data of our 37-pin results and Chiu's two 61-pin results, a value of 2/3 for λ was found to be optimum. The empirical constants C_{m1tr} and C_{m2tr} are then

$$C_{mitr} = C_{miL} + (C_{miT} - C_{miL})\psi_i^{2/3} \qquad (6.40)$$

where i = 1 for $\varepsilon^*_{l\eta}$

= 2 for C_{lL}

Figures 6.9 and 6.10 compare the calculated $\varepsilon^*_{l\eta}$ and C_{lL} and the data for our 37-pin bundle, respectively. Similar comparisons are illustrated in Figures 6.11 and 6.12 for $\varepsilon^*_{l\eta}$ and C_{lL} for Chiu's

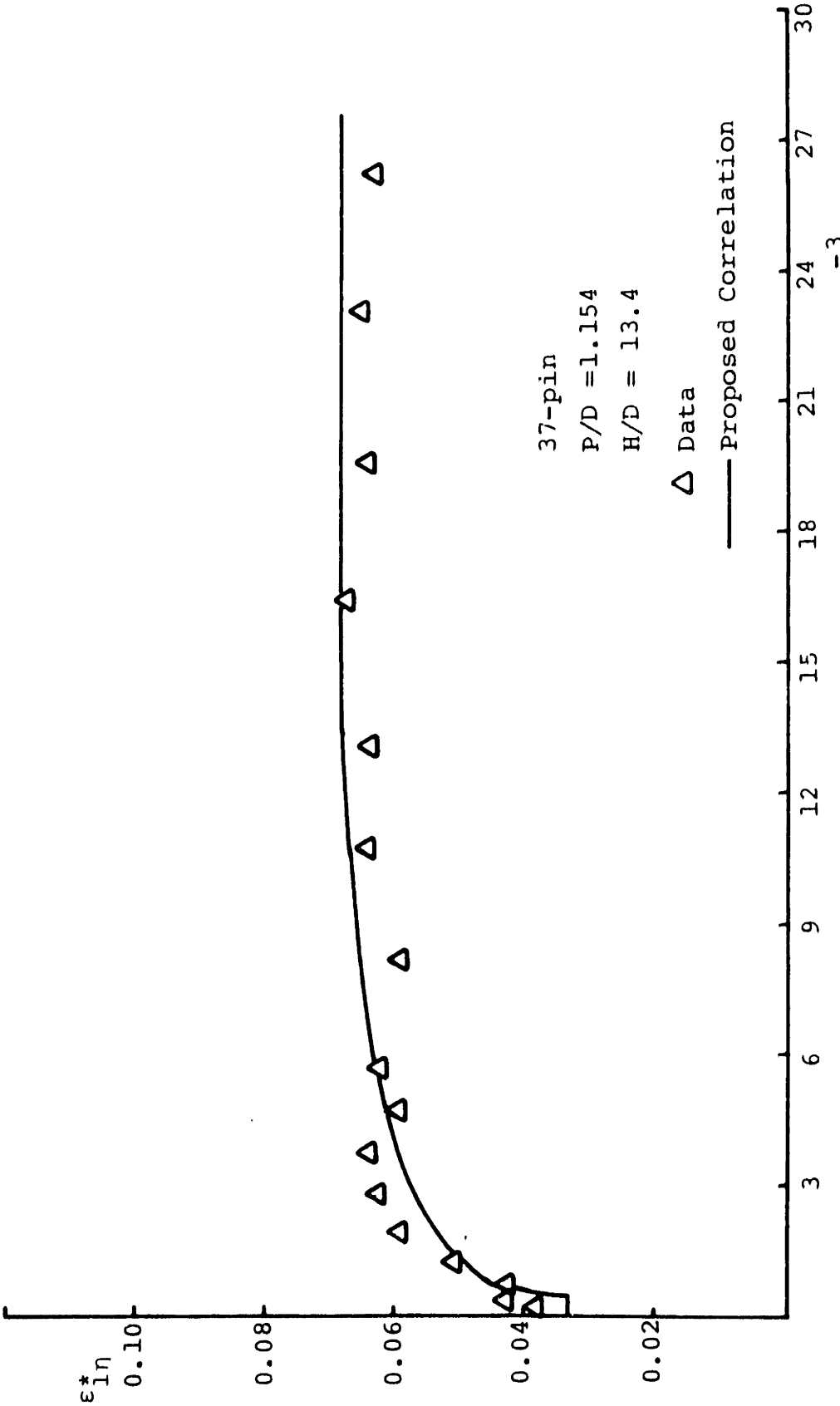

Figure 6.9 Comparison between Proposed Correlation and Data for $\varepsilon^*_{1r_i}$ of 37-pin Results

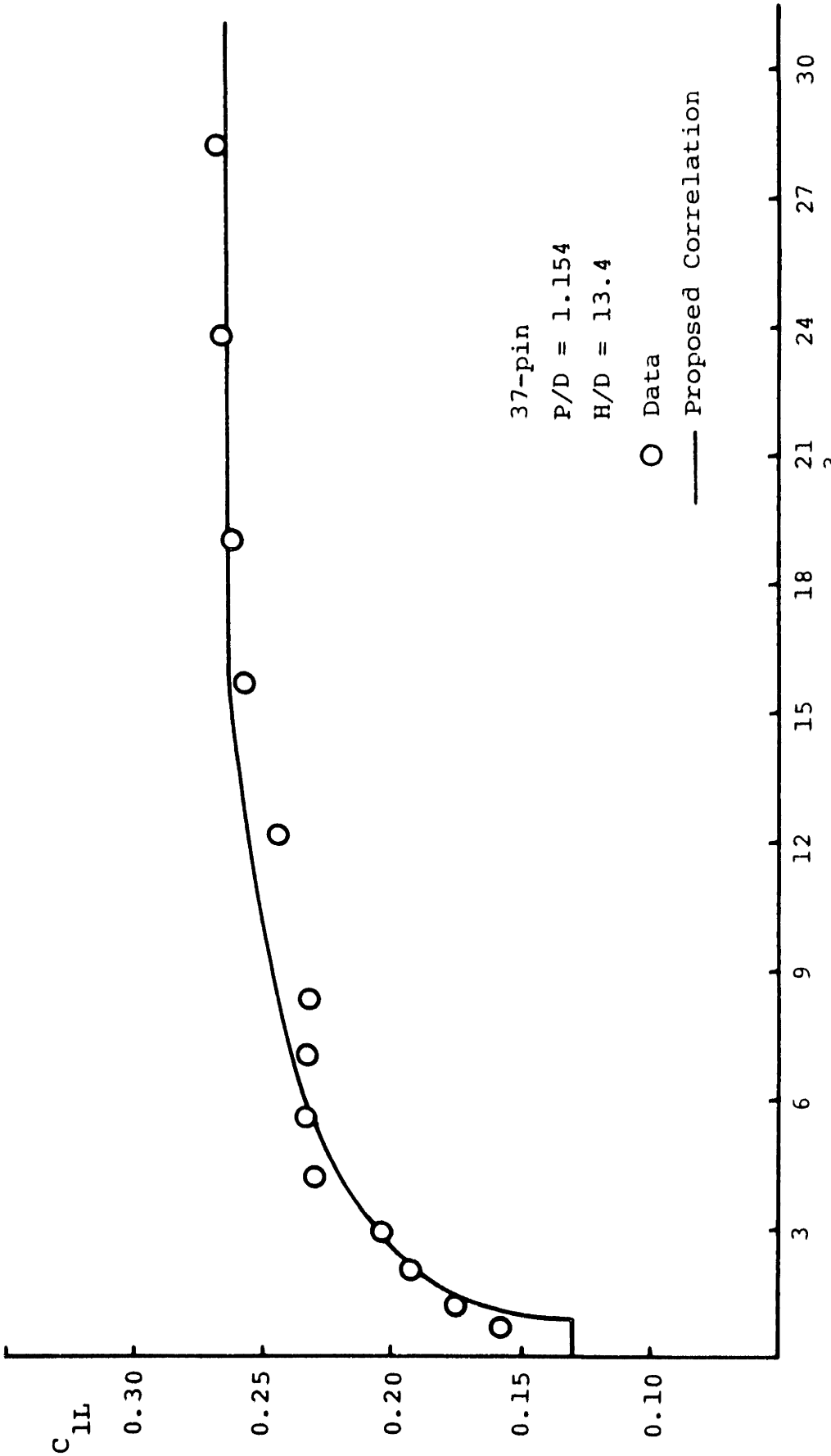

Figure 6.10 Comparison between Proposed Correlation and Data for C_{1L} of 37-pin Results

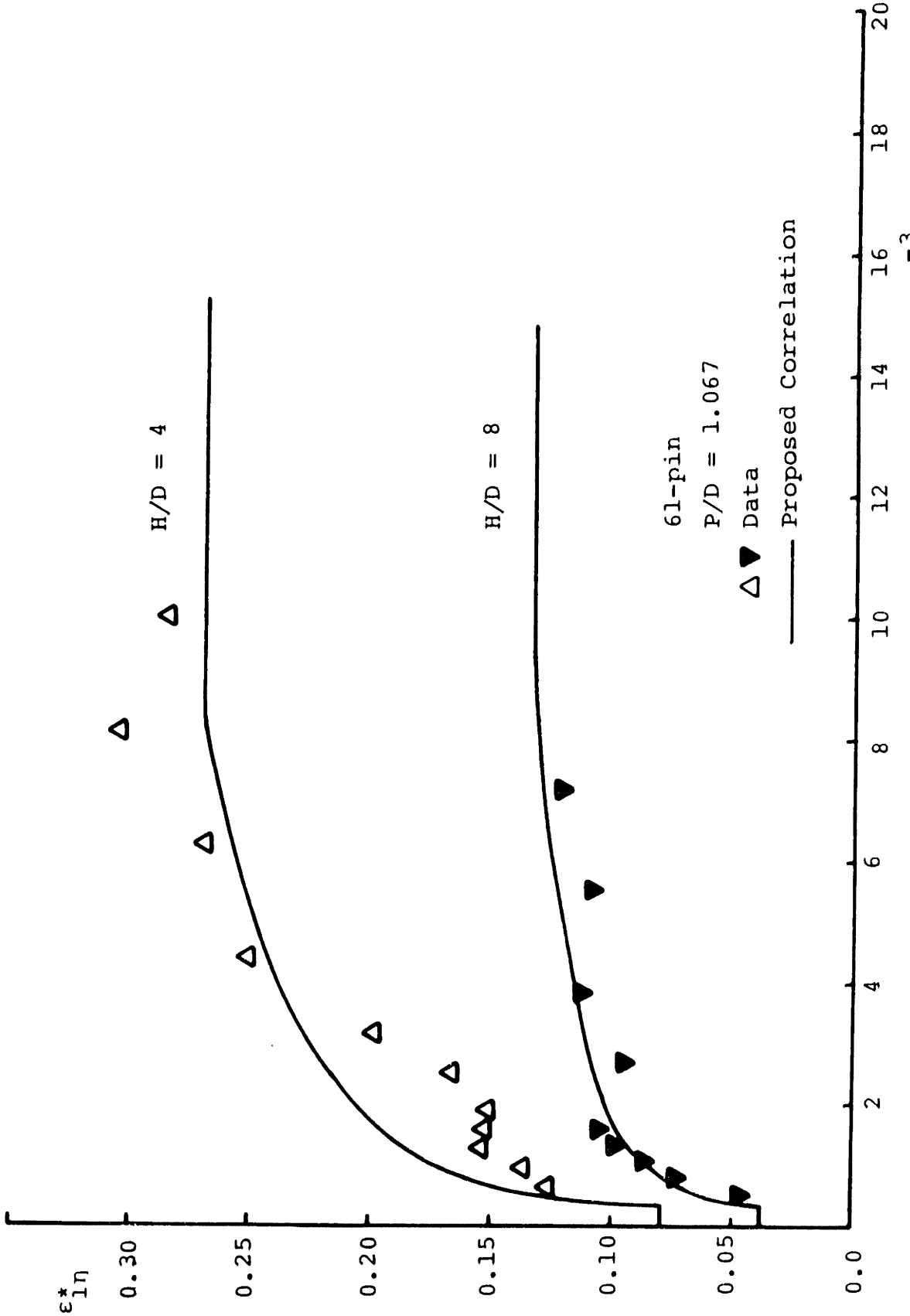

Figure 6.11 Comparison between Proposed Correlation and Data for $\varepsilon^*_{1\eta}$ of 61-pin Results

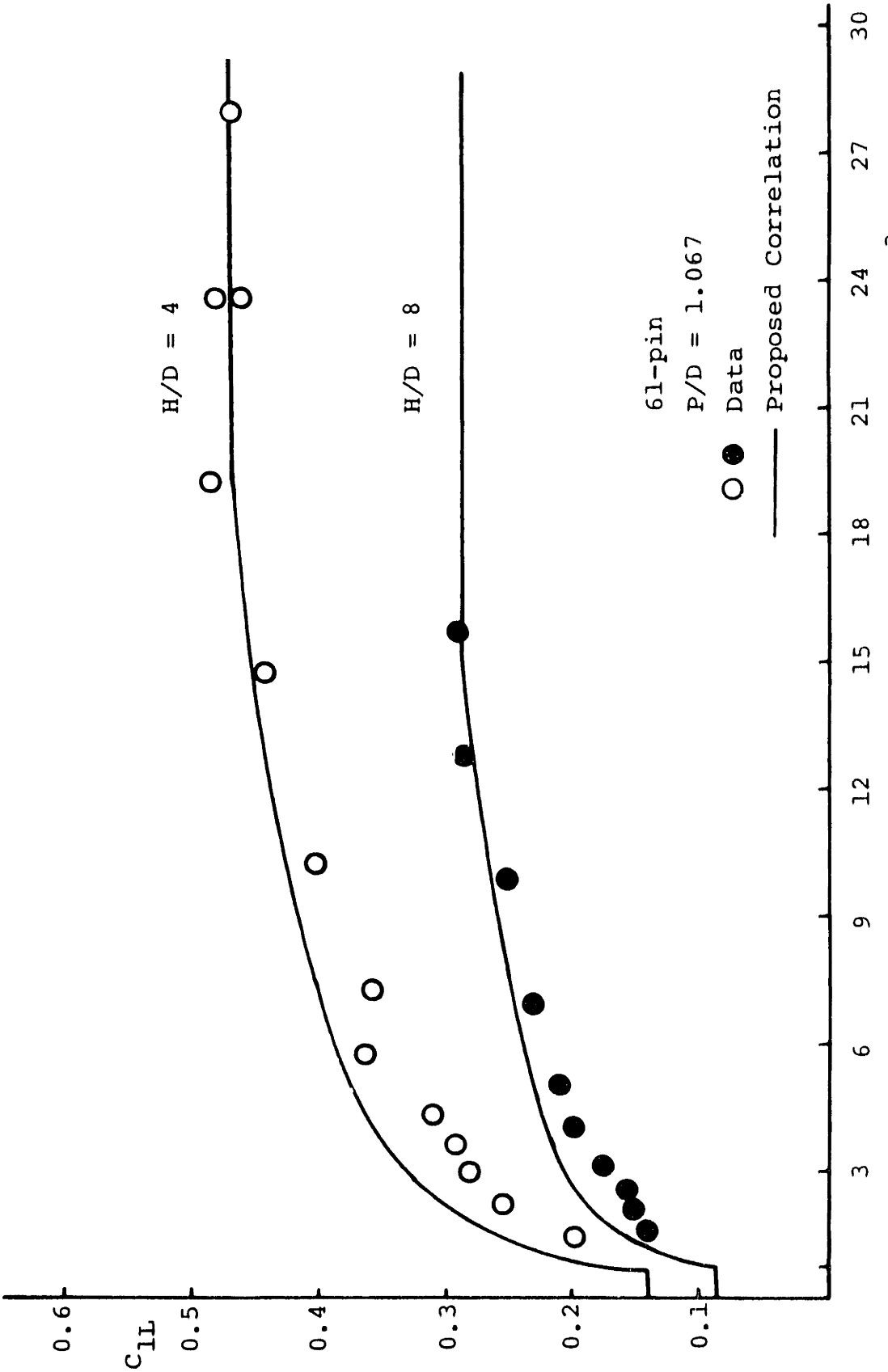

Figure 6.12 Comparison between Proposed Correlation and Data for C_{1L} of 61-pin Results

results, respectively. The trend of our 37-pin results is excellently predicted by this proposed correlation. For $\varepsilon^*_{1\eta}$, fairly good prediction is found for Chiu's H/D = 8 bundle, while overprediction is found for his H/D = 4 bundle. For C_{1L}, the correlation overpredicts all Chiu's data about 15%. Considering the error associated with these data (±20%), we conclude that this correlation can satisfactorily predict $\varepsilon^*_{1\eta}$ and C_{1L} in the transition region.

6.5 Correlation for Conduction Shape Factor, κ

6.5.1 Introduction

The conduction shape factor (SF) discussed in Chapter 2 is defined by equation (2.11),

$$\kappa_{ij} \equiv \frac{\eta_{ij}}{\ell_{ij}}$$

where ℓ_{ij} is the molecular mixing length defined in equation (2.10). In the literature, however, another parameter L_{ij} defined as

$$L_{ij} \equiv \frac{\ell_{ij}}{\eta_{ij}} = \frac{1}{\kappa_{ij}} \tag{6.41}$$

is often used. Since the investigation of SF by either theoretical or experimental study is in itself a large effort, we did not perform these studies in our work. Instead, the available results of SF from literature will be reviewed. By using these results, a correlation for conduction shape factor is recommended. Note that all investigations

described in the next section are for bare rod case only. In turbulent flows the shape factor effect is small compared to the wire driven effective eddy diffusivity. Since the wires will strongly influence the velocity and temperature fields, the importance of the bare rod shape factor results to the wire-wrapped rod bundle is probably limited to the transition or laminar region. However, under these low flow conditions at typical heat fluxes, thermal plume effects appear to induce significant mixing. Further, flow redistribution effects transport significant energy. Therefore, the importance of the shape factor is wire wraped bundles is probably restricted to $Gr_{\Delta T}/Re_b$ envelope. The correlation for shape factor is thus best discussed in Chapter 8 in conjunction with a proposed correlation for the enhancement of the effective eddy diffusivity. Both correlations are tested in Chapter 8 and flow redistribution effects are also assessed against available sodium cooled bundle data.

6.5.2 Conduction Shape Factor in the Literature

France and Ginsberg (1973, 1974) performed an analytical study to investigate the utility and accuracy of the lumped parameter approach to heat transfer analysis in a nuclear reactor subassembly. They found that the molecular mixing lengths are geometry-dependent only. They are shown to be independent of radial power distribution across the subassembly, and asymptotic values which are equal to length scales corresponding to the thermally fully developed condition may be used in the thermally developing entry region which encompasses the entire

axial length of typical nuclear reactor assemblies. Both unheated and heated rod cases for triangular rod arrays were investigated.

Ramm et al. (1974, 1975) investigated thermal mixing flowrates and length scales for pure molecular conduction as well as simultaneous conductive and turbulent intersubchannel transport in triangular rod arrays for unheated and heat rods cases, respectively. They concluded that mixing parameters are only slightly affected by variations in initial and boundary conditions.

Yeung and Wolf (1980) developed an analytical method to determine the theoretical effective mixing length for subchannels in a hexagonal rod bundle. The results showed that the effective mixing length in a strong function of P/D. However, for one P/D, it appears that the asymptotic (fully developed) value of the effective mixing lengths of various subchannel pairs are so close that they can be approximated by a single characteristic value for most practical purposes. By this conclusion, we assume that for one P/D, $\kappa_{11} = \kappa_{12} = \kappa_{22} = \kappa_{23} = \kappa$, i.e., only one κ is used for all kinds of subchannel pairs.

In addition to those theoretical results, Fakuda (1979) performed an electrostatic analog simulation for a single region analysis. He proposed an empirical relation for the mixing length of conduction,

$$\frac{\ell_{ij}}{\eta_{ij}} = \frac{1}{\frac{1.38}{\sqrt{3}} \left(\frac{P-D}{D}\right)^{0.674} \left(\frac{P}{P-D}\right)} \qquad (6.42)$$

Table 6.4 lists the theoretical results of L_{ij} from above investigators for two boundary conditions: heated and unheated rod (plane source) cases as well as Fakuda's correlated value from equation (6.42).

Table 6.4 Theoretical Results for asymptotic

(fully developed)

$$L_{ij} \equiv \frac{\ell_{ij}}{\eta_{ij}}$$

P/D	France & Ginsberg(1973) unheated (plane source)	heated	Ramm et al. (1974) unheated (plane source)	Ramm et al. (1975) heated	Young & Wolf (1980) heated	Fukuda (1979)
1.05	-	-	0.508	0.56	-	0.45
1.08	-	-	-	-	0.69	0.51
1.10	0.628	-	0.590	0.66	-	0.54
1.20	0.697	0.783	0.652	-	-	0.62
1.24	-	-	-	-	0.80	0.636
1.30	0.717	0.817	0.676	0.79	-	0.652

6.5.3 Recommended Correlation for Conduction Shape Factor

Since the velocity and temperature solutions are dependent upon boundary conditions and initial conditions, it should be expected tht molecular mixing length similarly depend on these conditions. In our application for calculating temperature distribution for LMFBR subassembly, the value from heated rod case solution should be used.

Figure 6.13 illustrates L_{ij} listed in Table 6.4 as function of P/D. For the heated rod boundary condition cases, there L_{ij}'s can be fitted similar to equation (6.42) as

$$\frac{1}{L_{ij}} = \kappa = 0.66 \left(\frac{P}{D}\right)\left(\frac{c}{D}\right)^{-0.3} \tag{6.43}$$

Equation (6.43) gives a value of κ varying from 1.25 to 2.0 as P/D varies from 1.25 to 1.025.

6.5 Summary of the Mixing Parameter Correlations

The correlations for the mixing parameters in the forced convection condition, $\varepsilon^*_{1\eta}$, $\varepsilon^*_{2\eta}$, C_{1L}, and κ have been developed in this chapter. In summary,

$$\varepsilon^*_{2\eta} = 0.01$$

$$\varepsilon^*_{1\eta} = C_{m1} \left(\frac{A_{r1}}{A'_1}\right)^{1/2} \tan\theta$$

$$C_{1L} = C_{m2} \left(\frac{A_{r2}}{A'_2}\right)^{1/2} \tan\theta$$

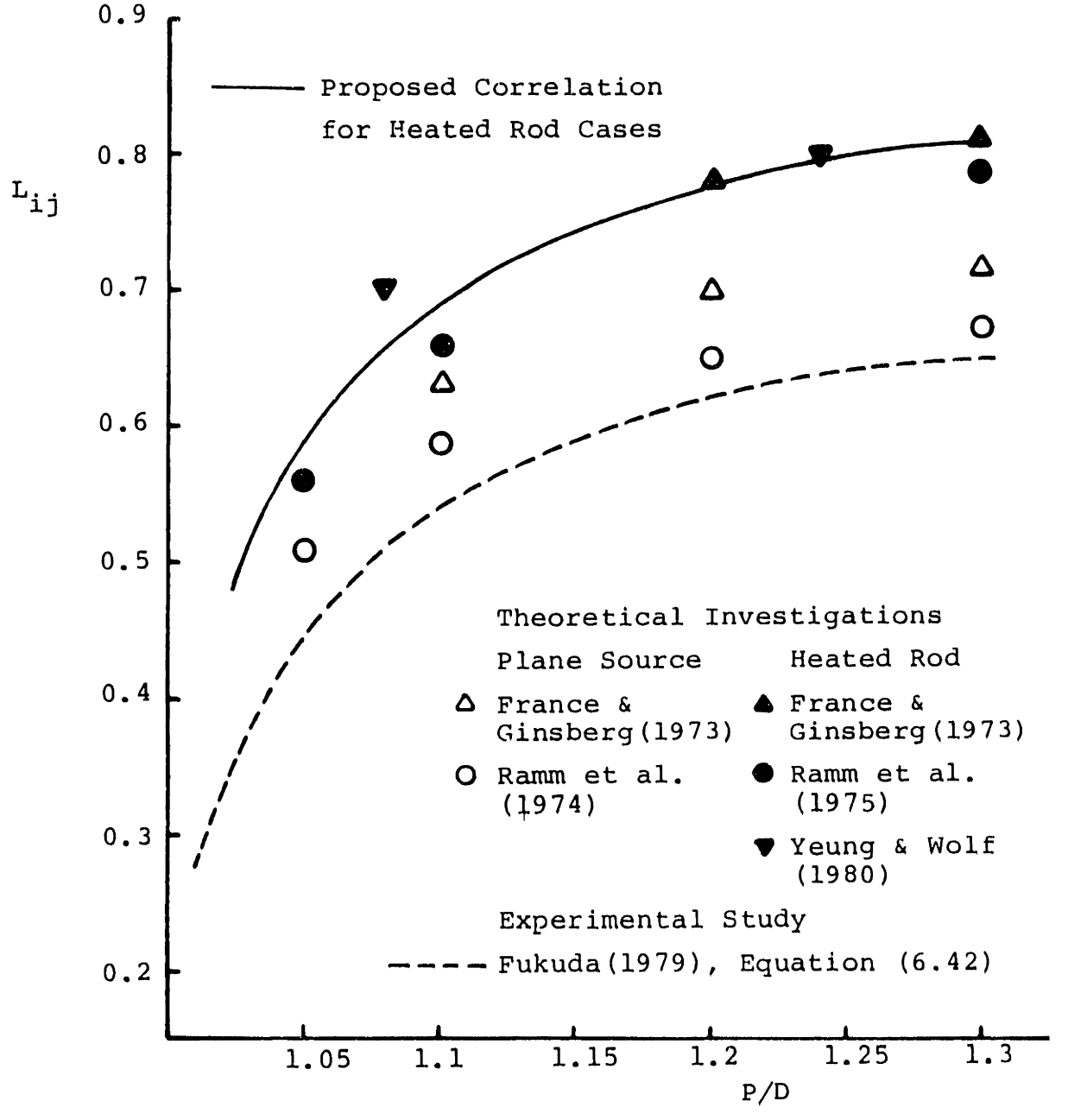

Figure 6.13 Available Investigations and Fitting Result for Conduction Shape Factor $\kappa \equiv L_{ij}$

where

for the turbulent region ($Re_b \geq Re_{bT}$)

$$N_r \geq 19$$

$$C_{m1T} = 0.14(\frac{c}{D})^{-0.5}$$

$$C_{m2T} = 0.75(\frac{H}{D})^{0.3}$$

$$N_r = 7$$

$$C_{m1T} = 0.1(\frac{c}{D})^{-0.5}$$

$$C_{m2T} = 0.6(\frac{H}{D})^{0.3}$$

for the laminar region ($Re_b \leq Re_{bL}$)

$$C_{miL} = 1.5(\frac{c}{D})^{0.6} C_{miT}$$

for the transition region

$$C_{mitr} = C_{miL} + (C_{miT} - C_{miL})\psi_i^{2/3}$$

and

$$\kappa = 0.66(\frac{P}{D})(\frac{c}{D})^{-0.3}$$

The above correlations can predict the data within ±25% for $\varepsilon^*_{1\eta}$ and ±15% for C_{1L} in the following geometrical ranges,

$$7 \leq N_r \leq 217$$

$$1.067 \leq P/D \leq 1.317$$

$$4 \leq H/D \leq 52$$

$$400 \leq Re_b \leq 10^6$$

CHAPTER 7

The ENERGY-IV CODE

7.1 Structure of the ENERGY-IV code

A new version of the ENERGY series code, ENERGY-IV, was written for predicting coolant temperature distributions in wire-wrapped rod assemblies used in the Liquid Metal Fast Breeder Reactor. The ENERGY-IV Code is applicable to both steady-state forced and mixed convection operation for a single isolated assembly. (The SUPERENERGY Code, [Basehore (1980)] is applicable to core wide forced convection analysis.) ENERGY-IV is an empirical code designed to be fast running. Hence the core designer can use it as an inexpensive thermal hydraulic design or diagnosis tool.

The main structure of the ENERGY-IV is similar to the old versions, ENERGY-I, II, III; however, most of the statements have been revised. Figure 7.1 depicts the flow chart for ENERGY-IV, in which the names of the subroutines are identified. Figure 7.2 briefly describes the structure of the subroutines and their functions. Because of the implementation of the subroutine NUMB, (originally developed by Basehore (1980)), which assigns the subchannel and rod scheme in a hexagonal assembly, the code automatically generates the noding and connection logic. This dramatically simplifies the required input information. Figure 7.3 shows the rod identification number assigned by the subroutine NUMB for a 61-pin bundle. The subchannel identification number was shown in Figures 3.17 and 5.12 for 37-pin and 61-pin bundles, respectively. The correlations for the required forced

Figure 7.1 Flow Chart for the ENERGY-IV

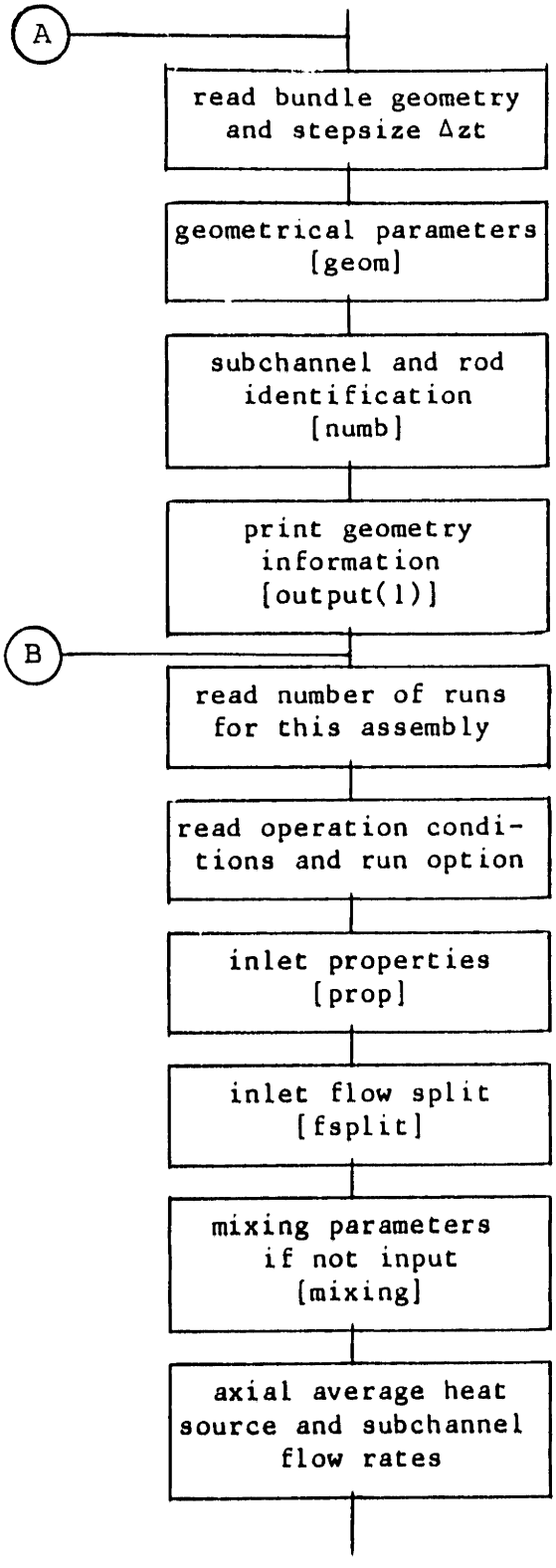

Figure 7.1 Continued

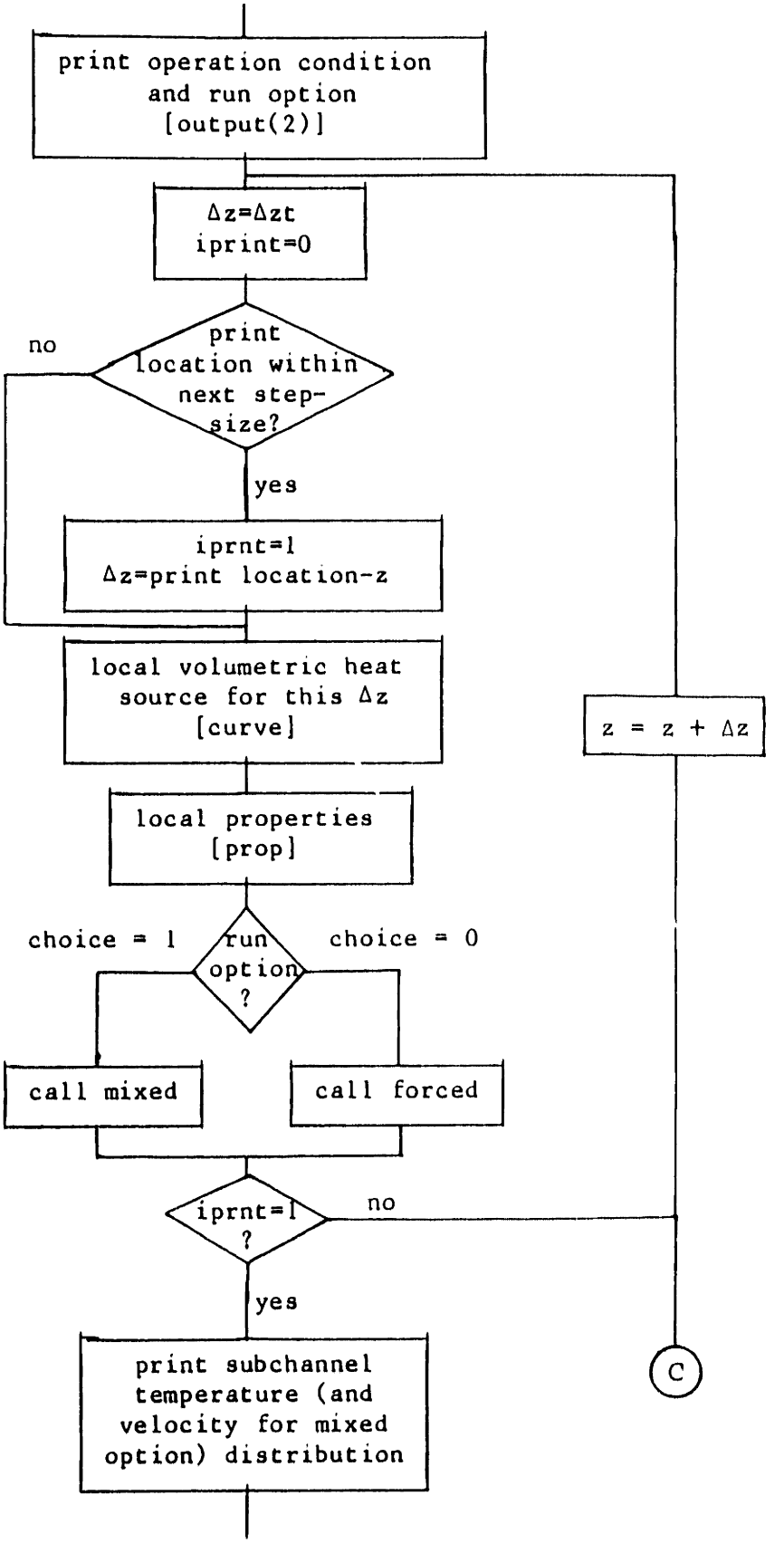

Figure 7.1 Continued

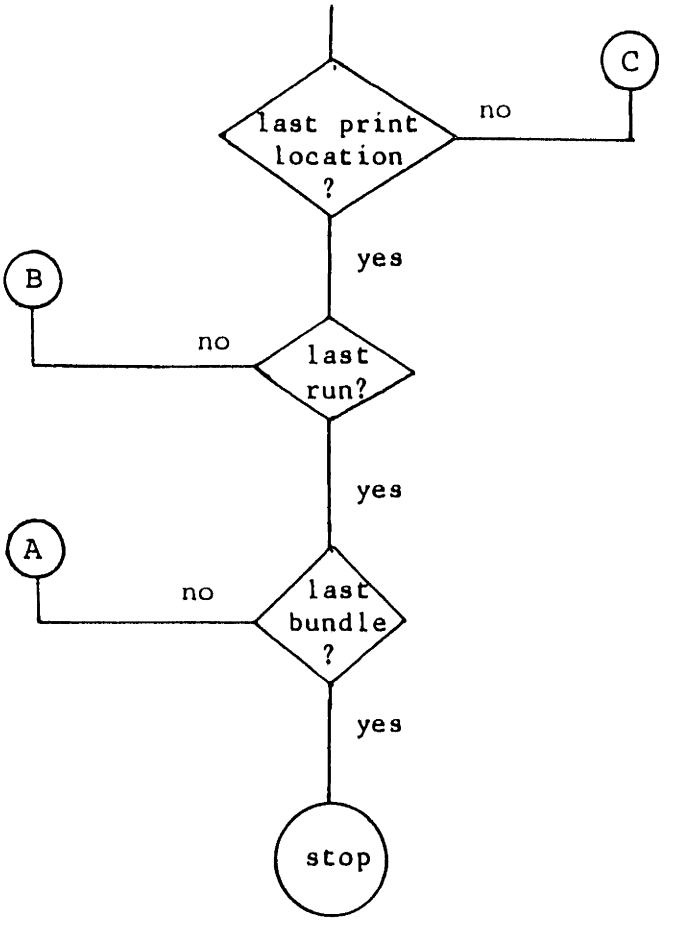

Figure 7.2 Functions of the Subroutines in ENERGY-IV

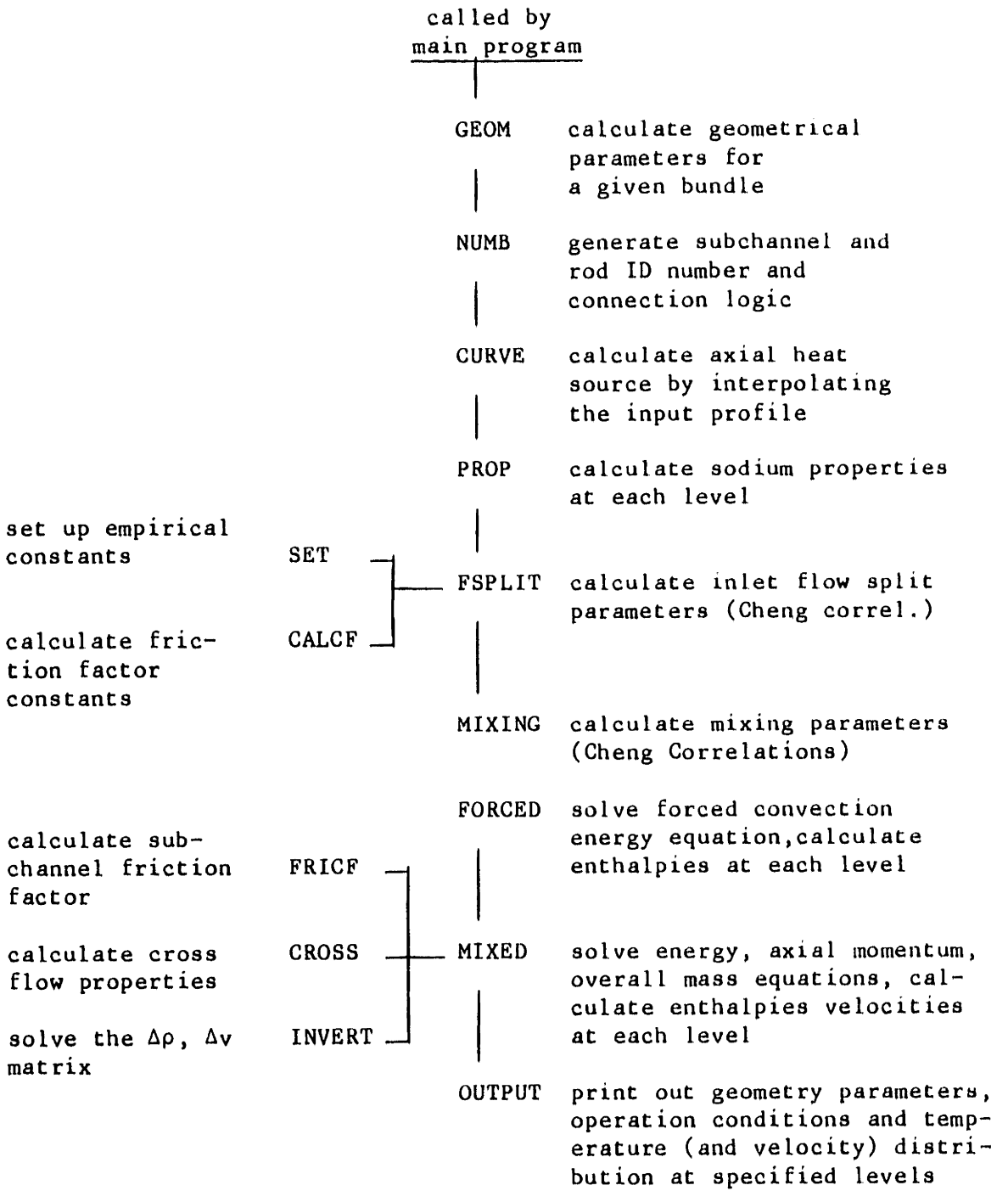

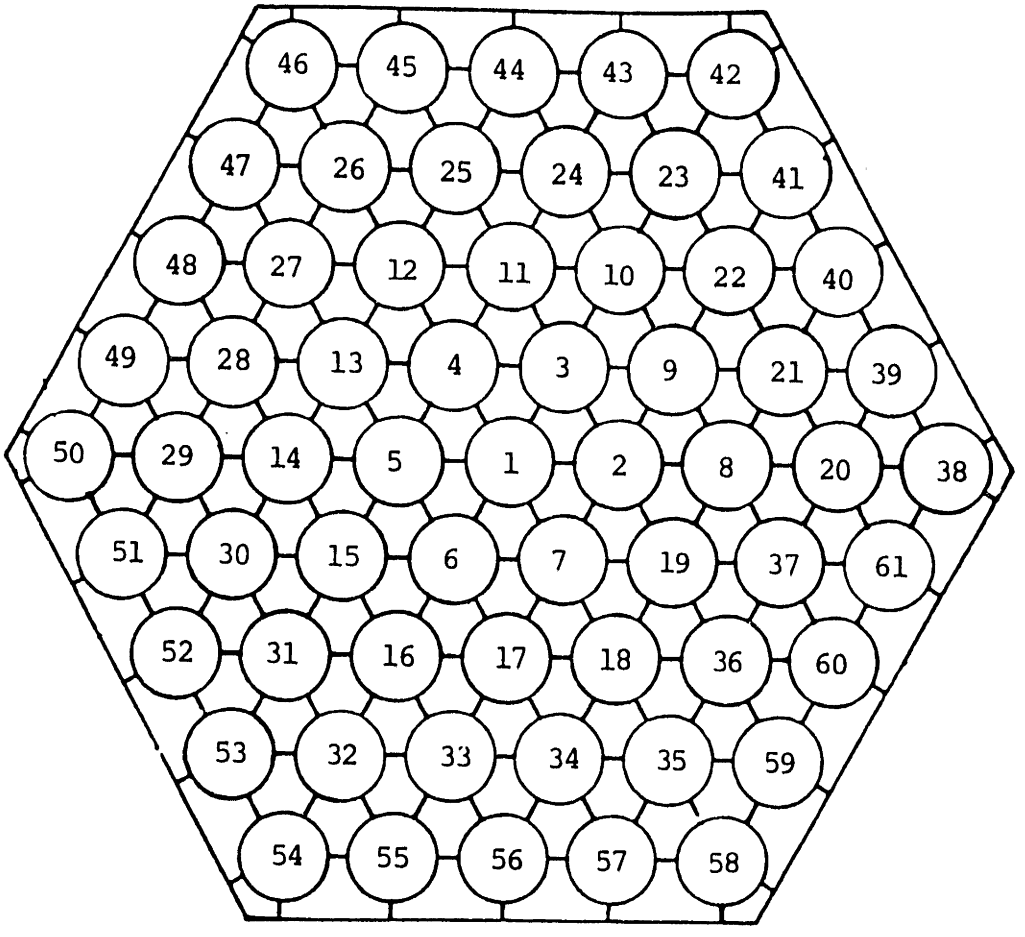

Figure 7.3 Rod Identification Number Assigned by Subroutine NUMB

convection input parameters: flow split parameters (X_i), subchannel friction factors (f_i), and mixing parameters ($\varepsilon^*_{1\eta}$, $\varepsilon^*_{2\eta}$, C_{1L} and κ) developed in Chapter 4 and Chapter 6 were implemented in the subroutines FSPLIT, FRICF and MIXING, respectively. Additionally, the correlation for the enhanced mixing due to thermal plumes ($\varepsilon^*_{\eta M}$) developed in Chapter 8 was implemented in the main program. The sodium properties at each level are calculated by the subroutine PROP.

The subroutines FORCED and MIXED are formulated according to the different equations derived in Chapter 2 for the forced convection condition and the mixed convection condition, respectively. They solve the subchannel enthalpies (and velocities for the mixed convection option) at each axial level. The calculation results are printed out at the user specified levels. Appendix D1 describes the input format for ENERGY-IV and Appendix D2 lists this code.

In the next two sections, the numerical methods used for the forced and mixed convection option will be discussed.

7.2 Numerical Method for the Forced Convection Option

A numerical marching scheme is used to solve the forced convection energy equations. For each axial step, the enthalpies on the right hand side of equations (2.34), (2.35), and (2.36) are evaluated at the node inlets. The enthalpy rise for each subchannel over the axial step may then be computed explicitly. This explicit method eliminates the need for a simultaneous solution. As a result, a substantial reduction in computational storage and running time is possible when compared to implicit formulations.

The disadvantage of this explicit method is that the axial node length size is stablity limited. The right hand side of equations (2.34), (2.35) and (2.36) must remain positive in the most limiting case, since the coolant enthalpy should never be negative. This limiting case occurs when the heat generation term is zero and when h_i, h_j and h_k are small compared to h_n (n = 1, 2, 3). For an interior subchannel, this criterion becomes

$$0 < h_l(z + \Delta z) = h_l - \Delta z(\frac{C}{A_l})[\frac{\kappa\alpha}{v_l \eta_{ll}} + \varepsilon^*_{l\eta}](-3h_l) \tag{7.1}$$

The conduction term in equation (7.1) can be further expressed as

$$\frac{\kappa\alpha}{v_l \eta_{ll}} = \frac{1}{Re_b}\left[(\frac{De_b}{\eta_{ll}})(\frac{\kappa}{X_l})\frac{1}{P_r}\right] \equiv \frac{K^*_l}{Re_b} \tag{7.2}$$

therefore,

$$\Delta z < \frac{1}{3(\frac{C}{A_l})[\frac{K^*_l}{Re_b} + \varepsilon^*_{l\eta}]} \tag{7.3}$$

Equation (7.3) shows that the limiting Δz is dependent upon Re_b: as Re_b decreases, the maximum allowable Δz decreases. Quantitatively, for Re_b = 1000, the limiting Δz is about 0.5 inch. Since the Re_b for most forced convection cases are higher than 1000, 0.5 inch is sufficient and recommended for the axial stepsize. For $1000 > Re_b > 500$, a stepsize of 0.25 inch is recommended.

The running time of the ENERGY-IV code for the forced convection option for a 61-pin bundle with around 100 axial nodes is less than 2 seconds in an IBM-370 computer.

7.2 Numerical Method for the Mixed Convection Option

The mixed convection option solves the energy, axial momentum and mass conservation equations simultaneously as discussed in chapter 2. A marching scheme is also employed in this option. The conservation equations for any subchannel contain three unknowns $\Delta\rho$, Δv, and ΔP. The pressure is assumed to be a constant in the transverse direction at any axial level. Thus for an N-channel problem, there exist 2N + 1 unknowns (N $\Delta\rho$'s, N Δv's, and one ΔP) with 2N + 1 equations. Figure 7.4 illustrates the equations and unknowns in matrix form for a 3-channel problem. (c.f. equations (2.47) and (2.48)). Note that the unknowns $\Delta\rho_i$ and Δv_i appear within the coefficient matrix. The quantities ρ_i, v_i, and h_i in the terms EEX_i and MEX_i are the average values within each node. They are approximated as

$$h_i = h_{iz} + \frac{1}{2} R_i \Delta\rho_i, \text{ where } R \equiv \left(\frac{\partial h}{\partial \rho}\right)_p \qquad (2.45d)$$

$$\rho_i = \rho_{iz} + \frac{1}{2} \Delta\rho_i \qquad (2.46a)$$

$$v_i = v_{iz} + \frac{1}{2} \Delta v_i \qquad (2.46b)$$

The quantities H_i^* and V_i^* are calculated by these average values. (c.f. equation (2.19)). These situations make the calculations of the $\Delta\rho$'s and Δv's an iterative procedure.

The technique used in the original version of ENERGY-III to solve the matrix equation was Gaussian Elimination. This method is very inefficient when dealing with a sparse matrix such as the one employed here. Greene (1980) suggested a simple technique applicable only to

Figure 7.4 Equation in Matrix Form for Mixed Convection Option

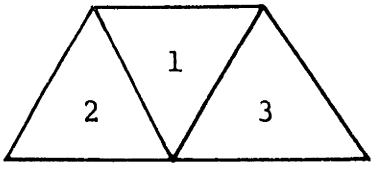

$$
\begin{vmatrix}
S_1 & T_1 & 0 & 0 & 0 & 0 & 0 \\
E_1 & F_1 & 0 & 0 & 0 & 0 & 1 \\
0 & 0 & S_2 & T_2 & 0 & 0 & 0 \\
0 & 0 & E_2 & F_2 & 0 & 0 & 1 \\
0 & 0 & 0 & 0 & S_3 & T_3 & 0 \\
0 & 0 & 0 & 0 & E_3 & F_3 & 1 \\
C_{\rho 1} & C_{v1} & C_{\rho 2} & C_{v2} & C_{\rho 3} & C_{v3} & 0
\end{vmatrix}
\begin{vmatrix} \Delta\rho_1 \\ \Delta v_1 \\ \Delta\rho_2 \\ \Delta v_2 \\ \Delta\rho_3 \\ \Delta v_3 \\ 0 \end{vmatrix}
=
\begin{vmatrix} Q_1\Delta z + EEX_1 \\ G_1 + MEX_1 \\ Q_2\Delta z + EEX_2 \\ G_2 + MEX_2 \\ Q_3\Delta z + EEX_3 \\ G_3 + MEX_3 \\ 0 \end{vmatrix}
$$

Energy equation: equation (2.47)

Momentum equation: equation (2.48)

Overall Continuity equation:

$$\sum_{}^{N} (C_{\rho i}\Delta\rho_i + C_{vi}\Delta v_i) = 0$$

where $C_{\rho i} = v_i + \Delta v_i$

$C_{vi} = \rho_i$

the matrix form under consideration, for solving the matrix problem. Referring to the matrix of Figure 7.4, the technique is as follows:

1. Subtract row 1 from row 2 to eliminate E_1
2. Subtract row 1 from the last row to eliminate $C_{\rho 1}$
3. Subtract row 2 from row 1 to eliminate T_1
4. Subtract row 2 from the last row to eliminate C_{v1}

This procedure is repeated with rows 3 and 4 et cetera. At this point, the matrix has non zero terms on the diagonal and in the last column. All other entries are zero. After clearing the last column by repeated subtractions of the last row from the remaining rows, and normalizing the diagonal entries to 1, the right hand side vector will contain $\Delta\rho_i$, Δv_i, and ΔP.

The $\Delta\rho$'s and Δv's are set to zero for the first iteration. The newly calculated $\Delta\rho$'s and Δv's are used to calculate the coefficient in the matrix and update the quantities in the right hand side of the matrix equation in Figure 7.4. This procedure is continued until the deviation in the overall continuity equation is reduced to within a specified tolerance. The proposed convergence criterion is

$$\frac{\sum^{N} \Delta(\rho vA)}{\sum^{N} (\rho vA)} < 10^{-7} \qquad (7.4)$$

This method, however, was found to be unable to yield a solution satisfying equation (7.4) for low flow rate cases, say $Re_b < 1000$. The resultant $\sum^{N} \Delta(\rho vA) / \sum^{N} (\rho vA)$ oscillates around a value much higher than 10^{-7}.

To improve the convergence of the solution, a relaxation factor (RLF) was introduced. Rather than directly insert the newly calculated $\Delta\rho$'s and Δv's into the matrix equation, the modified values,

$$\Delta\rho = RLF(\Delta\rho)_{new} + (1-RLF)(\Delta\rho)_{old} \tag{7.5a}$$

$$\Delta v = RLF(\Delta v)_{new} + (1-RLF)(\Delta v)_{old} \tag{7.5b}$$

were used. The RLF is initially set to be 1.0. If after 20 iterations (around 10 iterations should make the solution converge; otherwise, it starts oscillating) the solution is not converged, the code automatically subtracts 0.1 from RLF and restarts the iteration procedure from the intial guesses, i.e, $\Delta\rho$, $\Delta v = 0$. This procedure is continued until the solution converges. The resulting RLF value is stored and used as the initial value for the calculation at the next node. The minimum RLF is set to be 0.3. If a value of 0.3 for RLF can not make the solution converge, an error message will be printed out. The lowest value of RLF observed was 0.4, occuring at a Reynolds number of $Re_b \approx 500$. This procedure is illustrated by the flow chart of the subroutine MIXED in Figure 7.5.

When the density and velocity increments have been calculated, the velocities and densities are calculated by incrementing the fields at the previous axial level, i.e.,

$$\rho_{z+\Delta z} = \rho_z + \Delta\rho$$

$$v_{z+\Delta z} = v_z + \Delta v$$

The enthalpy field is calculating using $\Delta\rho$ and the partial derivative $(\partial h/\partial\rho)p$,

Figure 7.5 Flow Chart of Subroutine MIXED

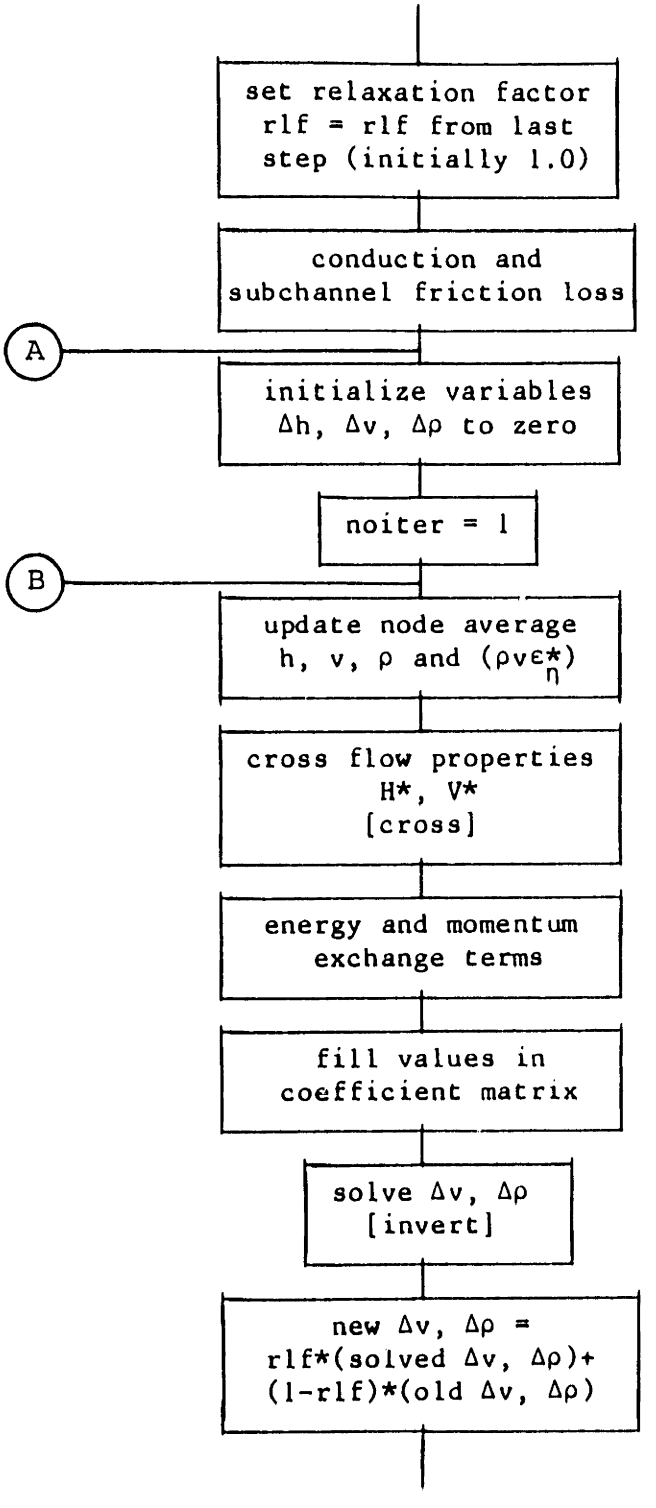

Figure 7.5 Continued

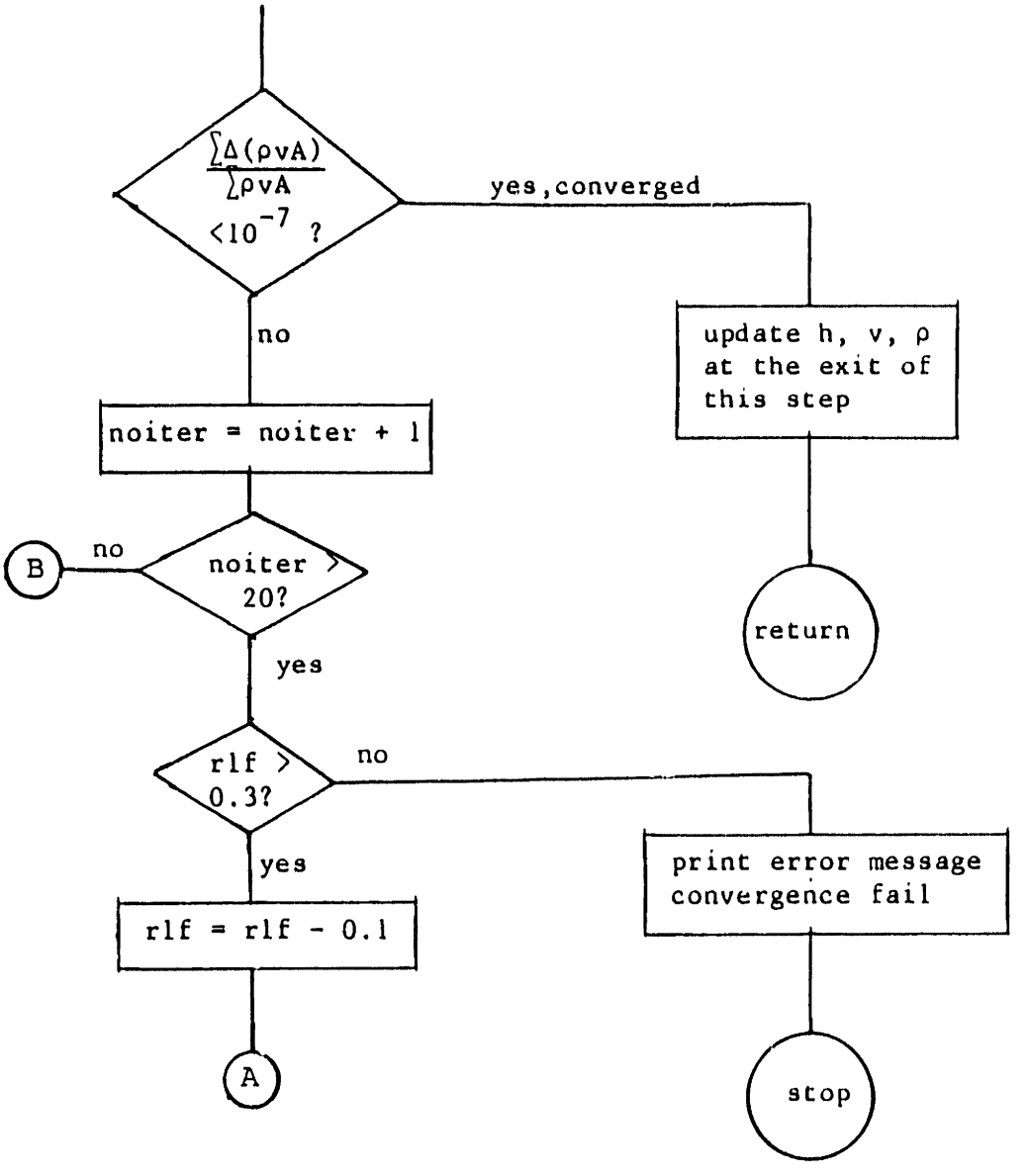

$$h_{z+\Delta z} = h_z + \left(\frac{\partial h}{\partial \rho}\right)_p \Delta\rho$$

The entire procedure is repeated at each axial level until the last printing location is reached.

The running time for the mixed convection option is proportional to the number of axial and radial nodes used. The stepsize was found to be not stability limited. Typically, 0.5 inch is recommended. For a 61-pin bundle with 126 nodes, the running time is about 0.5 second for each node. If the bundle length is 5 ft, i.e., 120 axial nodes, the running time is about 1 minute.

CHAPTER 8

VALIDATION OF THE ENERGY IV CODE

8.1 Introduction

The ENERGY-IV code is applicable to both forced and mixed convection conditions. In the forced convection condition, the buoyancy induced cross flow is negligible and a very simple method using only the energy equation and an explicit numerical scheme is employed. In the mixed convection condition, the buoyancy induced cross flow reduces the normalized peak temperature rise, defined as

$$\Delta T^* = \frac{T_i - T_{in}}{T_{out} - T_{in}} , \tag{8.1}$$

where T_i = subchannel temperature rise

T_{in} = bundle inlet temperature

T_{out} = bundle outlet temperature

and a more complicated method solving the overall mass, axial momentum, and energy conservation equations simultaneously in an implicit way is employed.

The operation condition at which the normalized peak temperature rise reduces from the forced convection value was investigated by Engel et al. (1982) in their blanket bundle. They developed a simple correlation to specify the transition between the forced convection and mixed convection regimes, i.e.,

$$\frac{Gr_{\Delta T}}{Re_b} = 0.04 \tag{8.2}$$

where $Gr_{\Delta T}$ = Grashof number based on temperature rise $\equiv \dfrac{g\beta(\frac{\Delta T_b}{L})\ De_b^{\,4}}{\nu^2}$

$\Delta T_b = T_{out} - T_{in}$

L = heated length

For a blanket assembly, the typical $Gr_{\Delta T}$ is around 400. Hence the mixed convection region is reached when the Re_b is less than 10000. For a fuel assembly, the typical $Gr_{\Delta T}$ is around 600. Assuming equation (8.2) is applicable, the mixed convection region is reached when the Re_b is less than 15000. Based on the flow regimes defined in chapter 4, one might roughly conclude that typically the turbulent flow regime corresponds to the forced convection condition while the transition and laminar flow regimes corresponds to the mixed convection condition. Note that if $Gr_{\Delta T}$ decreases to a lower value, the Re_b will proportionally decrease to make the flow condition mixed.

The correlations for the required input parameter for the ENERGY IV have been developed in Chapters 4 and 6. The data used to calibrate these correlations were obtained in the forced covection condition. Although the individual models of the ENERGY-IV, such as, flow split, interchannel mixing and conduction shape factor, have been established this way, the combined thermal-hydraulic models in the ENERGY-IV are required to be validated by the temperature data of sodium cooled heated pin tests.

For the forced convection condition, these correlations are used without any modification. However, for the mixed convection condition, some modifications are required for these (forced convection) input parameters because of the existence of different thermal-hydraulic characteristics. First, since the friction factor increases as the buoyancy effect becomes important [Symolon (1982)], the subchannel friction factor used in the mixed convection regime should take into

account this buoyancy effect. Second, thermal plumes which surround the rods and interact with each other promoting turbulent mixing between channels have been visually observed by Bates and Khan (1980) and Symolon (1982) in their low flow rate tests. These thermal plumes are zones of locally heated fluid which rise more rapidly than the bulk fluid in the subchannel due to their lower density [Bates and Khan (1980)]. Thus an additional mixing parameter, $\varepsilon^*_{\eta M}$, defined similar to $\varepsilon^*_{2\eta}$ is required to represent the enhanced mixing between subchannels due to this thermal plume effect.

As discussed near the end of Chapter 6, the validity of using the bare rod conduction shape factor in the wire wrapped rod bundle needs to be evaluated. Typically, the conduction effect is not important in the forced convection regime; however, it contributes a large amount of energy transfer in some region of the mixed convection regime as we should discuss later in section 8.5.

In this chapter, the recent published out of pile temperature data from four different organizations: Westinghouse Advance Reactor Division (WARD), Oak Ridge National Laboratory (ORNL), Toshiba Corporation (Japan), and Grenoble (France), are used for testing the combined thermal-hydraulic models in ENERGY-IV. The thermal plume effect in the mixed convection regime will be modelled by adding a thermal plume mixing parameter (TPMP), $\varepsilon^*_{\eta M}$, to the interchannel mixing $\varepsilon^*_{1\eta}$ and $\varepsilon^*_{2\eta}$. This TPMP is estimated by matching the ENERGY-IV predictions to the mixed conveciton temperature data. A correlations is then proposed for $\varepsilon^*_{\eta M}$ as a function of geometry, $Gr_{\Delta T}$ and Re_b.

Finally, the relative importance of wire sweeping mixing, molecular conduction, thermal plume mixing and flow redistribution due to buoyancy, in the energy transfer between subchannels will be compared.

8.2 Description of the Tests Used for Validation

Table 8.1 depicts the characteristics of the test bundles for those four organizations. The WARD and Grenoble (FETUNA) bundles are similar to the blanket assembly while the ORNL and Toshiba bundles are similar to the fuel assembly. All tests used heated pins and were cooled by sodium. All bundles except the Toshiba bundle operated with a radial power skew in a row by row sense, i.e., each row of pins can operate at an independent power level. Figure 8.1 shows 9 rows for a 61-pin bundle. Table 8.2 describes the normalized power factor of each row for different power skew used in the WARD and ORNL 61-pin and 19 pin bundles. The radial power factor used in the Toshiba bundle will be described later. The corresponding subchannel identification number used in the ENERGY-IV (calculated by subroutine NUMB) for a 61-pin bundle is shown in Figure 8.2.

The test sections and thermocouple locations where the measured temperature data were obtained which will be used for ENERGY-IV validation purpose are briefly described as follows.

WARD 61-pin

Figure 8.3 shows the test section and axial loation of the thermocouples for the WARD 61-pin simulated blanket assembly tests.

Table 8.1 Characteristics of Test Bundles

Bundle	Nr	D (in)	Dw (in)	P/D	W/D	H/D	Heated length (in)	Axial power profile	Radial power skew	Flow regime
WARD 61-pin [Engel(1980)]	61	0.519	0.037	1.082	1.078	7.7	45.0	cosine 1.4/1*	1/1,2/1, 2.8/1**	Forced Mixed
ORNL 19-pin [Fontana(1974)]	19	0.230	0.056	1.244	1.244	52.2	21.0	uniform	1/1,3/1	Forced
ORNL 61-pin [Morris(1980)]	61	0.230	0.056	1.244	1.244	52.2	36.0	cosine 1.38/1	1/1,1.5/1 2/1,3/1	Forced Mixed
Toshiba 37-pin [Namekawa(1984)]	37	0.256	0.052	1.210	1.210	47.2	36.6	cosine 1.21/1	1/1,1.4/1 2/1	Forced Mixed
Grenoble 91-pin [Rameau(1980)]	91	0.622	0.042	1.067	1.067	11.4	59.0	cosine	1/1,2.5/1	Mixed

* maximum to average
** maximum to minimum

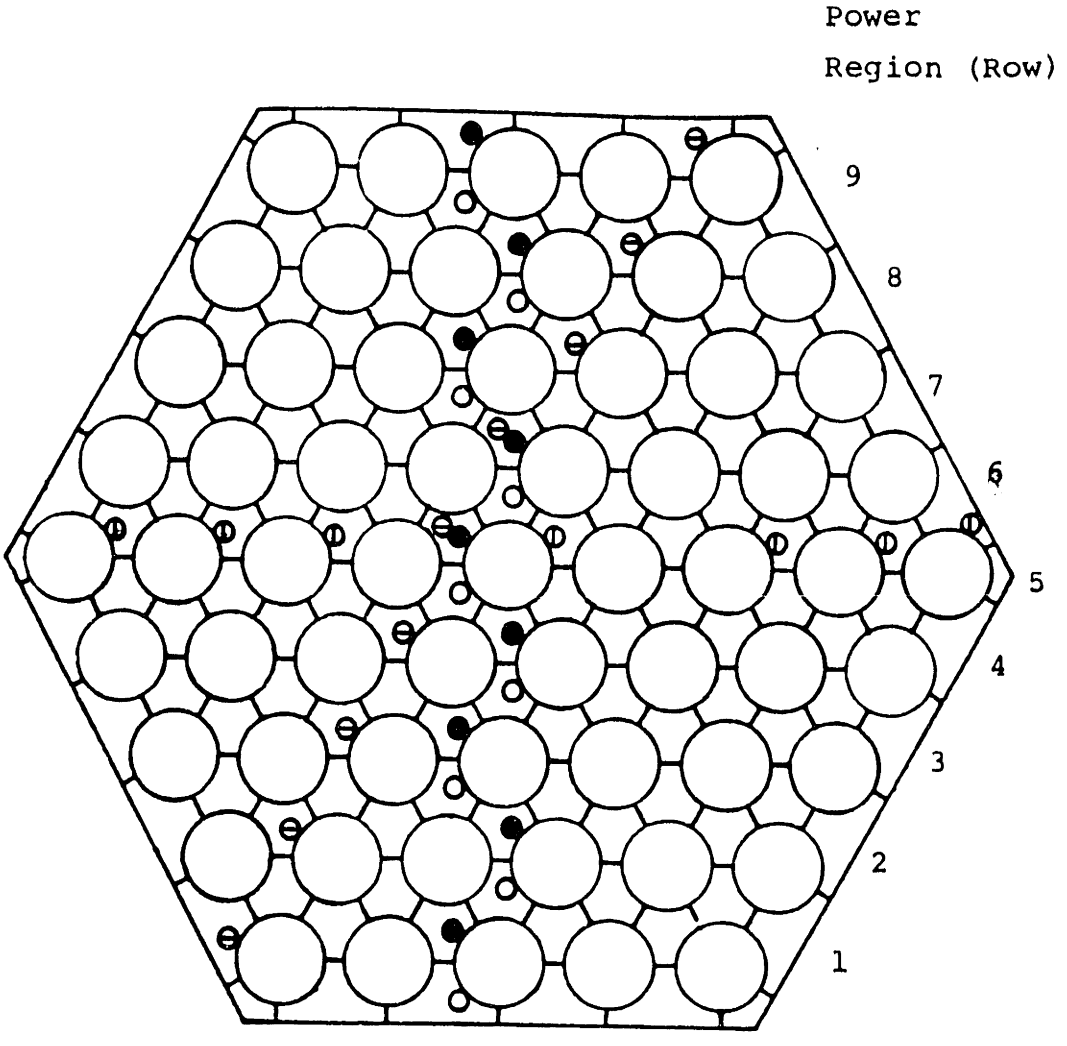

Figure 8.1 Power Regions and Thermocouple Locations for WARD and ORNL 61-pin Bundles

Table 8.2 Normalized Power Factor for Different Power Skew in WARD and ORNL Tests

Bundle	Radial Power Skew	Row 1	2	3	4	5	6	7	8	9
WARD	2/1	0.710	0.745	0.800	0.870	0.960	1.060	1.180	1.300	1.450
61-pin	2.8/1	0.635	0.678	0.713	0.796	0.882	1.026	1.220	1.473	1.776
ORNL	1.5/1	0.83	0.83	0.95	0.95	0.95	0.95	1.07	1.19	1.19
61-pin	2/1	0.72	0.72	0.84	0.96	0.96	1.08	1.20	1.20	1.32
	3/1	0.49	0.62	0.74	0.86	0.99	1.11	1.24	1.48	1.48
ORNL 19-pin	3/1	0.50	0.75	1.00	1.25	1.75				

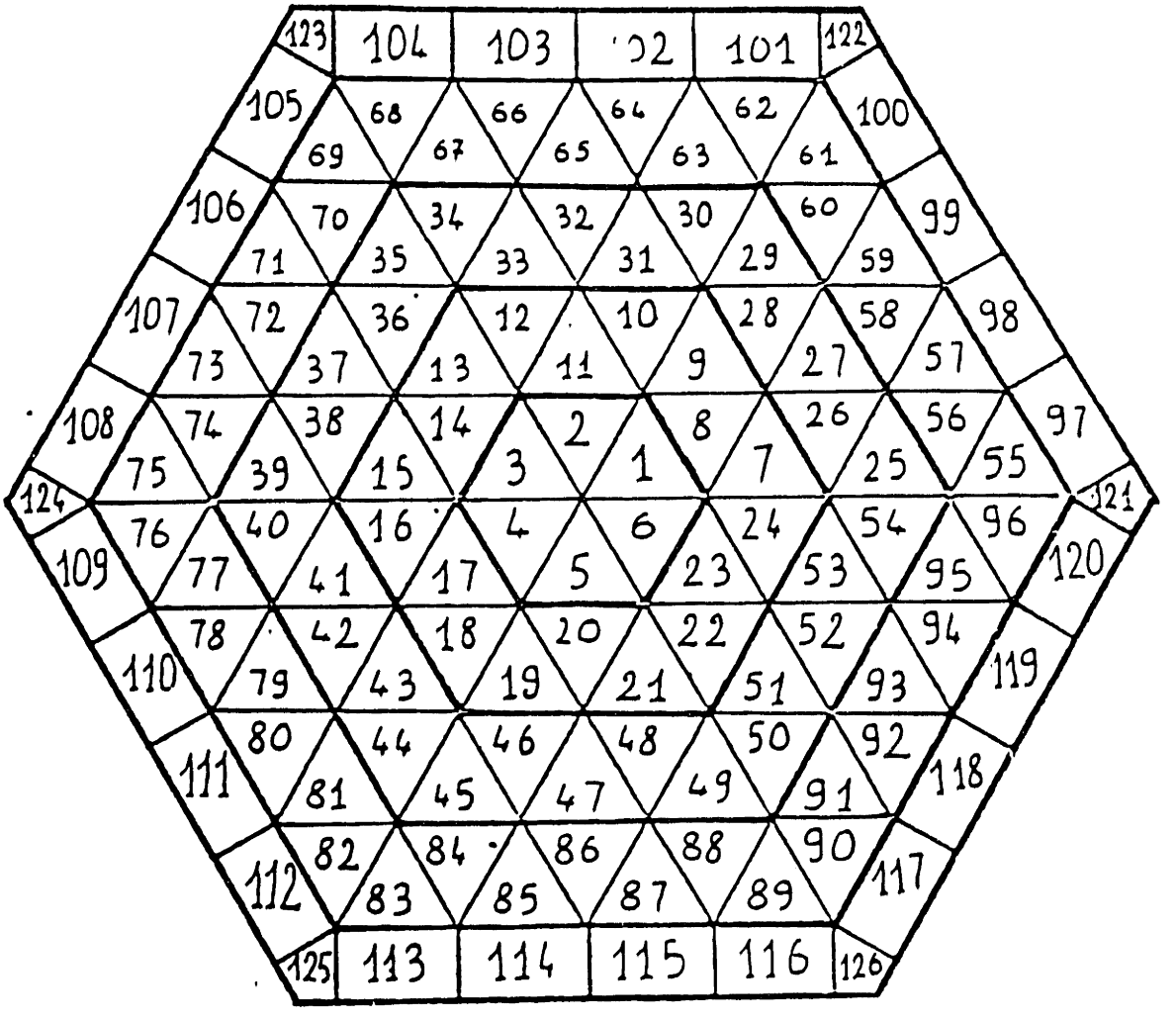

Face A

Figure 8.2 Subchannel Identification Number for a 61-pin Bundle by Subroutine NUMB

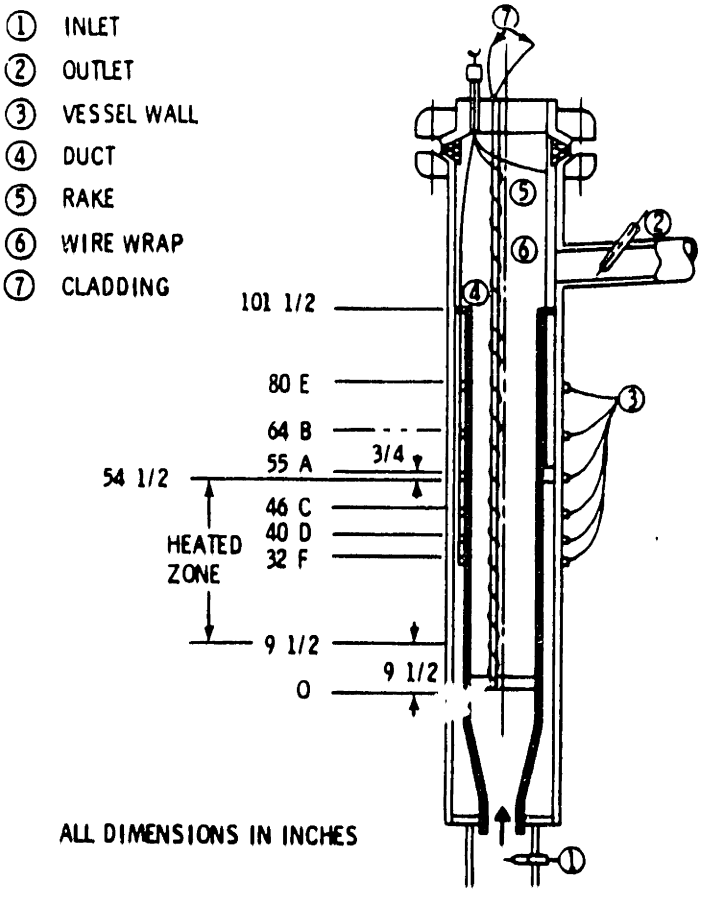

Figure 8.3 Test Section and Thermocouple Positions for WARD 61-pin Bundle Tests

[Engel et al. (1978, 1980, 1981), Markley and Engel (1981)]. The coolant enters the bundle 9.5 inches below the plane where the rods are heated so as to provide a fully developed flow field at the entrance to the heated section. Within each pin there is a resistance coil of nichrome wire wound so as to provide a chopped cosine axial heat flux profile over a 45-inch length. Thermocouples are located at three axial elevations in the heated zone and at three axial elevations above the heated zone. Only the data measured at levels E (25 inches downstream of the end of the heated zone), A (outlet of heated zone), and F (heated zone midplane) will be used for the validation. The thermocouples are implemented in the wire wraps. The position of these wire wrap thermocouples at levels E, A, F, are shown in Figure 8.1. They are distributed flat to flat across the bundle. Also there are thermocouples for most of the edge pins to measure the temperature in the edge subchannels.

ORNL 19 pin

The ORNL THORS-2A data [Fontana et al (1973, 1974)] was taken in the 19-pin bundle shown in Figure 8.4. The heated length of the rods is 21 inches. The cold entrance length is approximately 6 inches. Thermocouples are located in the rod walls and also in the wire wraps. An exit rake is located 3 inches above the exit of the heated bundle and is instrumented with thermocouples which directly measure coolant temperatures at the center of various subchannels (c.f. Figure 8.4). The axial power profile is uniform. The hexaganol duct is surrounded by guard heaters to minimize heat losses.

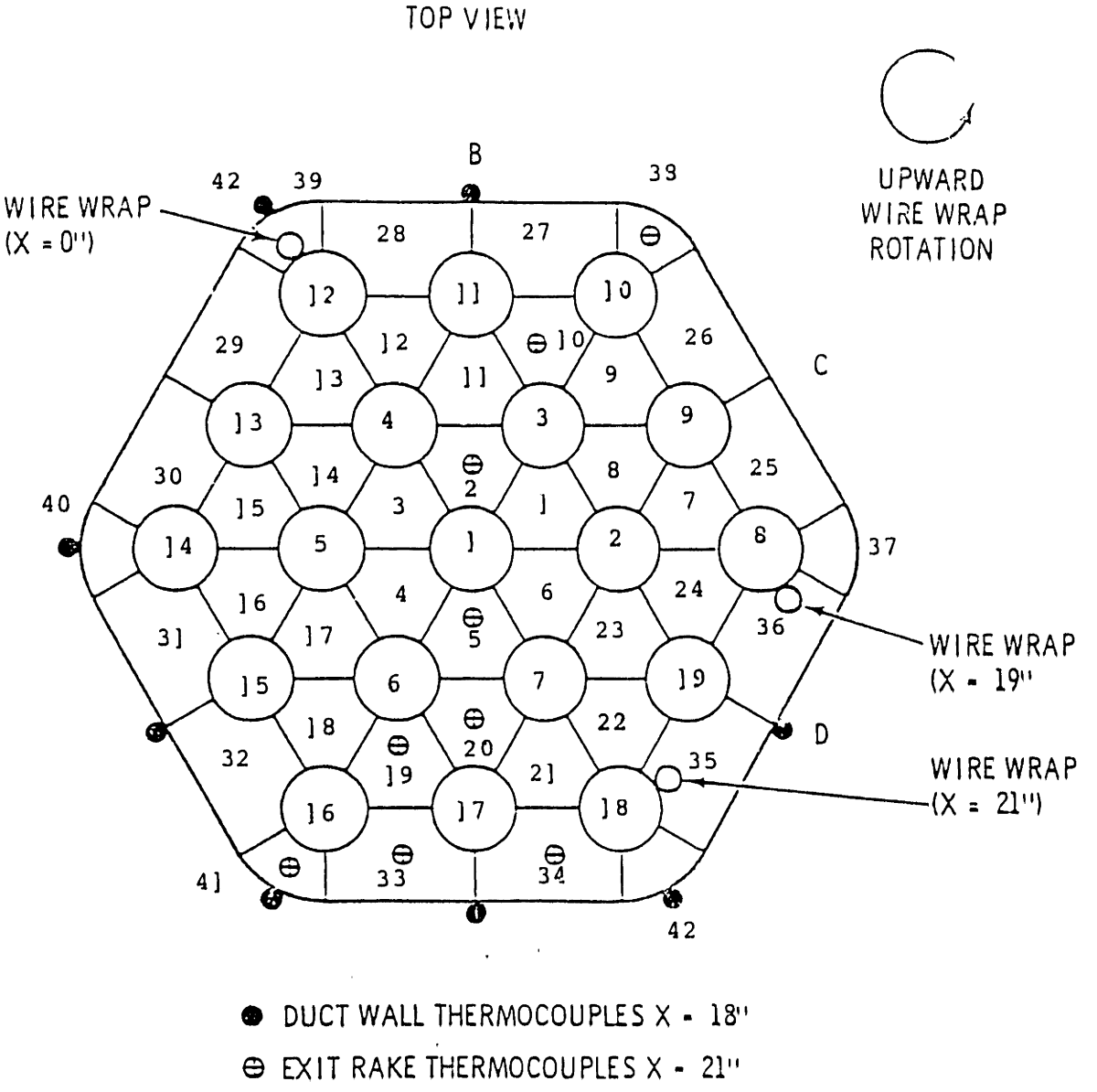

Figure 8.4 Rod and Subchannel Identification Number and Thermocouple Locations for ORNL 19-pin THORS 2A Bundle

ORNL 61-pin

The geometry of the THORS-9A 61-pin test bundle [Morris et al. (1980)] is similar to the THORS 2A test bundle except for the total number of pins and an axial varying power profile. The bundle was fabricated axially with a 9 inches cold entrance length and a 36 inches heated length that was followed by a 1 inch unheated length. Thermocouples were implemented in wire wraps and the assembly wall. The data at the 21-inch, 25-inch and 37-inch levels will be used for comparison. Note that the start of the heated length is defined to be the zero inch level. The thermocouple locations at these levels are also shown in Figure 8.1. They are distributed corner to corner across the bundle.

Toshiba 37-pin

The Toshiba test assembly [Namekawa et al. (1984)] contains 37 simulator rods within a hexaganol can, which is installed in a containment tube. There are many horizontal plates in the containment tube to prevent heat loss, since sodium is filled between the hexagonal can and containment tube. The cold entrance length is 15.7 inches following by a 36.6 inch heated length. Electrical power is supplied to the heated rods by three power control units. The axial power profile is a chopped consine shape with a 1.21 maximum to average ratio. The rod bundle is grouped into three divided regions, which correspond to three power control units. Radial power skew within the bundle is produced by the three divided regions as shown in Figure 8.5 The power factors for Region I, II, III are: 1.18, 1.0, 0.84, and

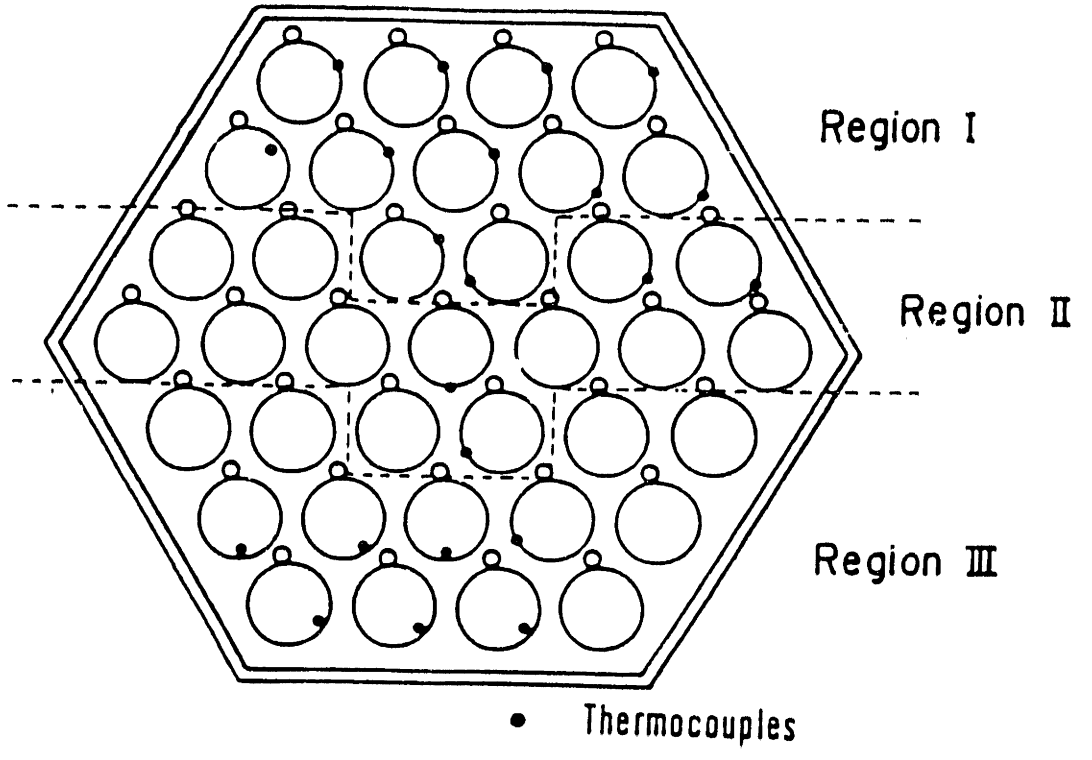

Figure 8.5 Thermocouple Locations and Power Regions for Toshiba 37-pin Bundle

1.36, 1.0, 0.694 for 1.4/1 and 2/1 power skew, respectively. The corresponding subchannel numbering scheme used in the ENERGY-IV is the same as that in Figure 3.17. Numerous thermocouples were embedded in the simulator rods to measure heat transfer characteristics within the rod bundle. The thermocouples were grouped into distinct horizontal planes at position L_1 (24.0 inches downstream of the inlet of heated zone) and L_2 (36.0 inches downstream of the inlet of heated zone.) The thermocouple locations are also shown in Figure 8.5.

Grenoble 91-pin

The Grenoble (FETUNA) GR.91 mock-up [Rameau (1984)] consists of an electricity heated 91-pin bundle within a hexagonal wrapper, which is surrounded by a jacket. The heated length is 53.15 inches. About 150 thermocouples were used to measure the temperature field in the bundle and wrapper tube. Only the mixed convection condition temperature data measured at the end of heated length were reported.

8.3 Validation of the ENERGY-IV in the Forced Convection Condition

Table 8.3 describes the operation conditions for the cases used to validate the ENERGY-IV in the forced convection condition. Two cases with "Edge" under column run are for the temperature distribution in the edge subchannels, while all the other ten cases are for the temperature distribution across the bundle: flat to flat for WARD and Toshiba bundles and corner to corner for the ORNL bundles. The temperature data and calculation results are represented by a

Table 8.3 Cases Used for Forced Convection Validation

Bundle	Run	Bundle Flow Rate (GPM)	Average Rod Power(kW/ft)	Power Skew	Re_b	T_{in} (F)	$\Delta T_b^{\dagger}$ (F)
WARD	223	36.8	1.143	2.8/1	8900	600	178
61-pin	415	36.8	1.143	2/1	8900	600	178
	226	36.8	1.143	1/1	8900	600	178
	Edge	36.8	1.143	2.8/1	8900	600	178
ORNL	14-101	54.0	5.0	3/1	67000	600	75
19-pin	Test 2	53.0	5.0	1/1	66000	600	77
	Edge	54.0	10.0	3-pin	67000	600	24
ORNL	19-101	104.0	4.44	3/1	49000	700	203
61-pin	1-4	156.0	6.67	1/1	73000	700	203
Toshiba	G37P22	15.72	0.484	2/1	8000	402	83
37-pin	E37P17	16.02	0.474	1.4/1	8300	409	80
	B37P02	23.57	0.475	1/1	12000	412	54

† Energy balance value

normalized temperature rise, ΔT^*, defined by equation (8.1). The temperature can be calculated from this ΔT^* utilizing the values of $\Delta T_b (\equiv T_{out} - T_{in})$ and T_{in} in Table 8.3.

8.3.1 Comparisons between Data and Predictions for WARD Bundle

Figures 8.6, 8.7, 8.8 compare the ENERGY-IV predictions with the temperature data for Runs 223, 403, and 226, respectively. For all three power skews, the ENERGY-IV results are observed to excellently predict the data. The maximum difference between the ENERGY-IV predictions and data occurs in the outlet of heated zone data (level "A") of Run 223 which has 2.8/1 power skew. A 0.07 overprediction for ΔT_b^* was found for this maximum difference (1.48 versus 1.41). Since ΔT_b = 178°F for this case, this gives a 12.5°F temperature difference.

The predictions of the COTEC code for Run 223 are also present in Figure 8.6 for comparison. The COTEC results have same degree of accuracy as that of the ENERGY-IV results in predicting levels "A" and "F" data. However, the level E data are not as well predicted by the COTEC as the ENERGY-IV does. The COTEC model might use a lower value for the interchannel mixing, which makes the gradient across the bundle of its predictions higher than that of the data.

To investigate the sensitivity of the ENERGY-IV prediction to $\varepsilon_{1\eta}^*$ Figures 8.9, 8.10, and 8.11 illustrate the ENERGY-IV results with $\varepsilon_{1\eta}^*$ values at +25% and -25% of the correlation value (0.122). Note that the accuracy of the correlation for $\varepsilon_{1\eta}^*$ is ±25% as discussed in chapter 6. At outlet of the heated zone (level "A"), this ±25% change in $\varepsilon_{1\eta}^*$

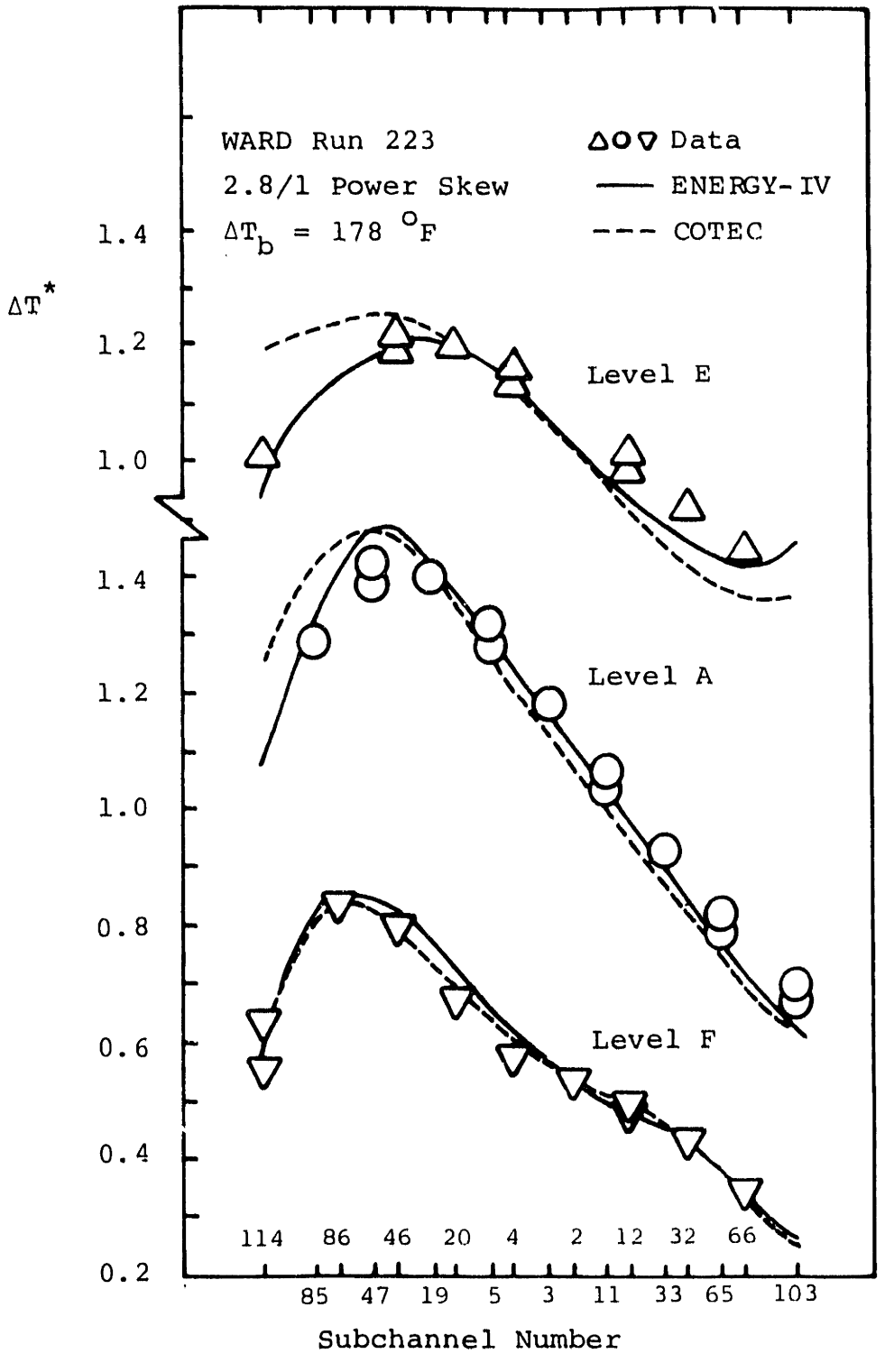

Figure 8.6 Measured and predicted Temperature Rise for WARD Run 223

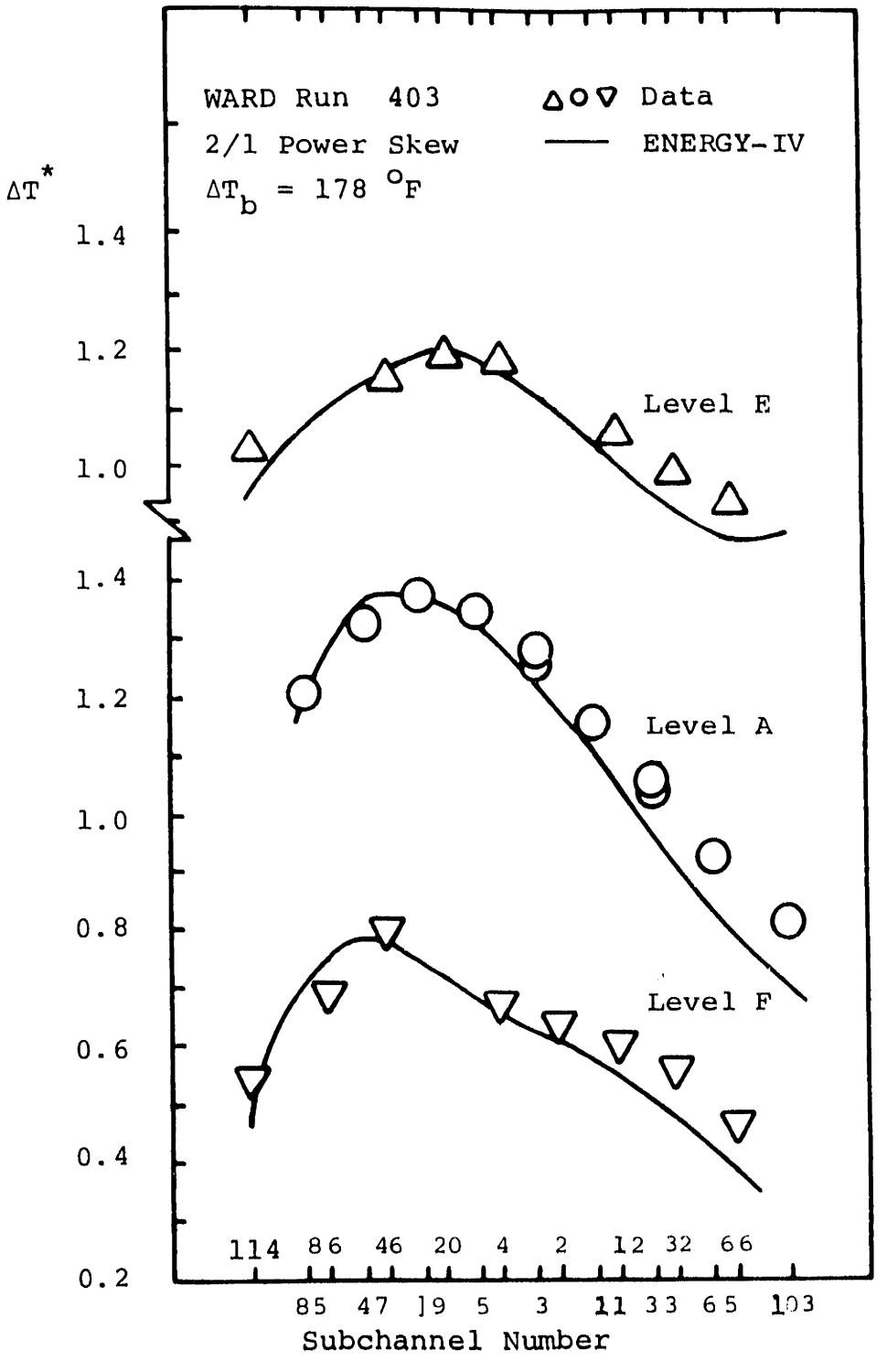

Figure 8.7 Measured and Predicted Temperature Rise for WARD Run 403

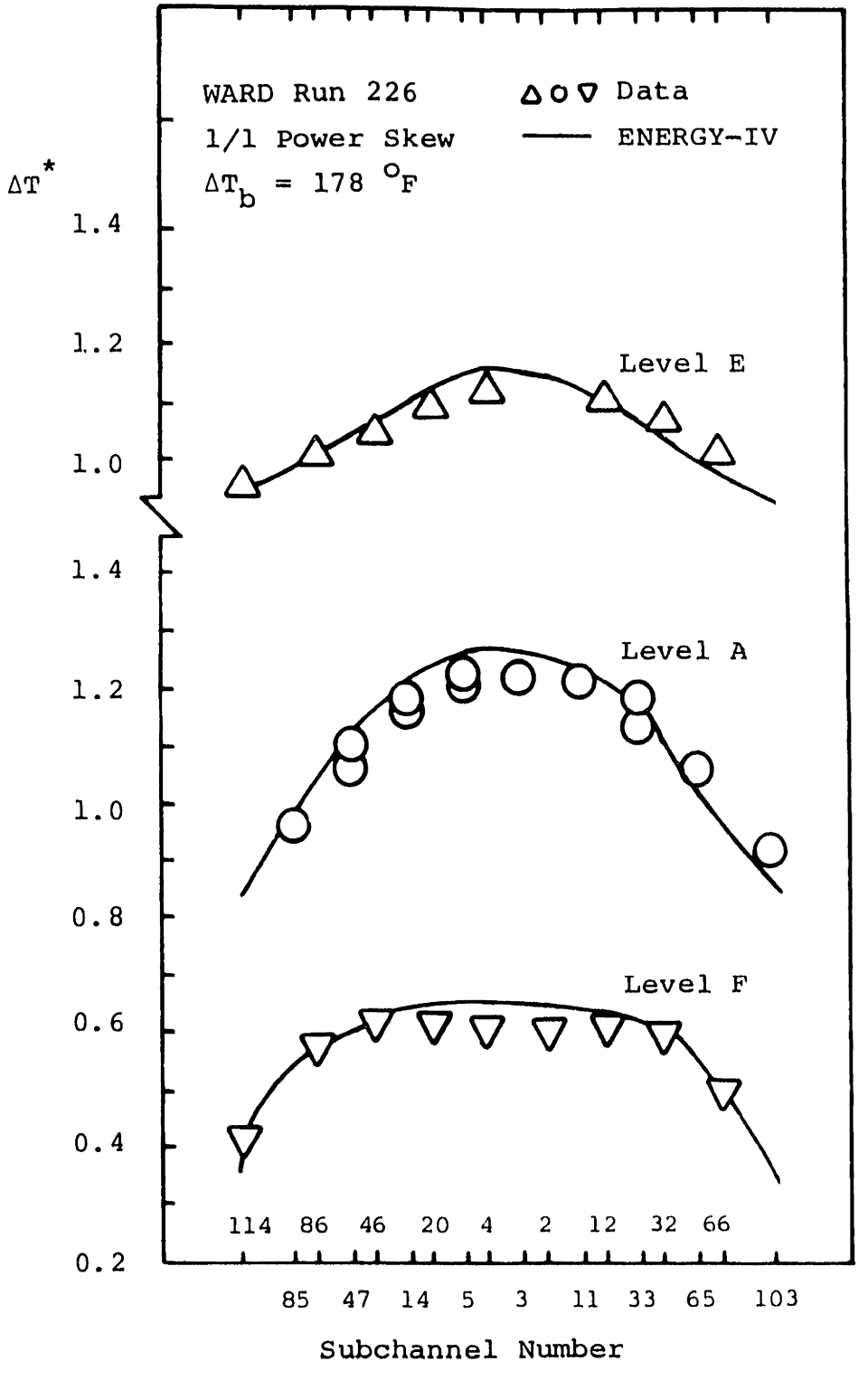

Figure 8.8 Measured and predicted Temperature Rise for WARD Run 226

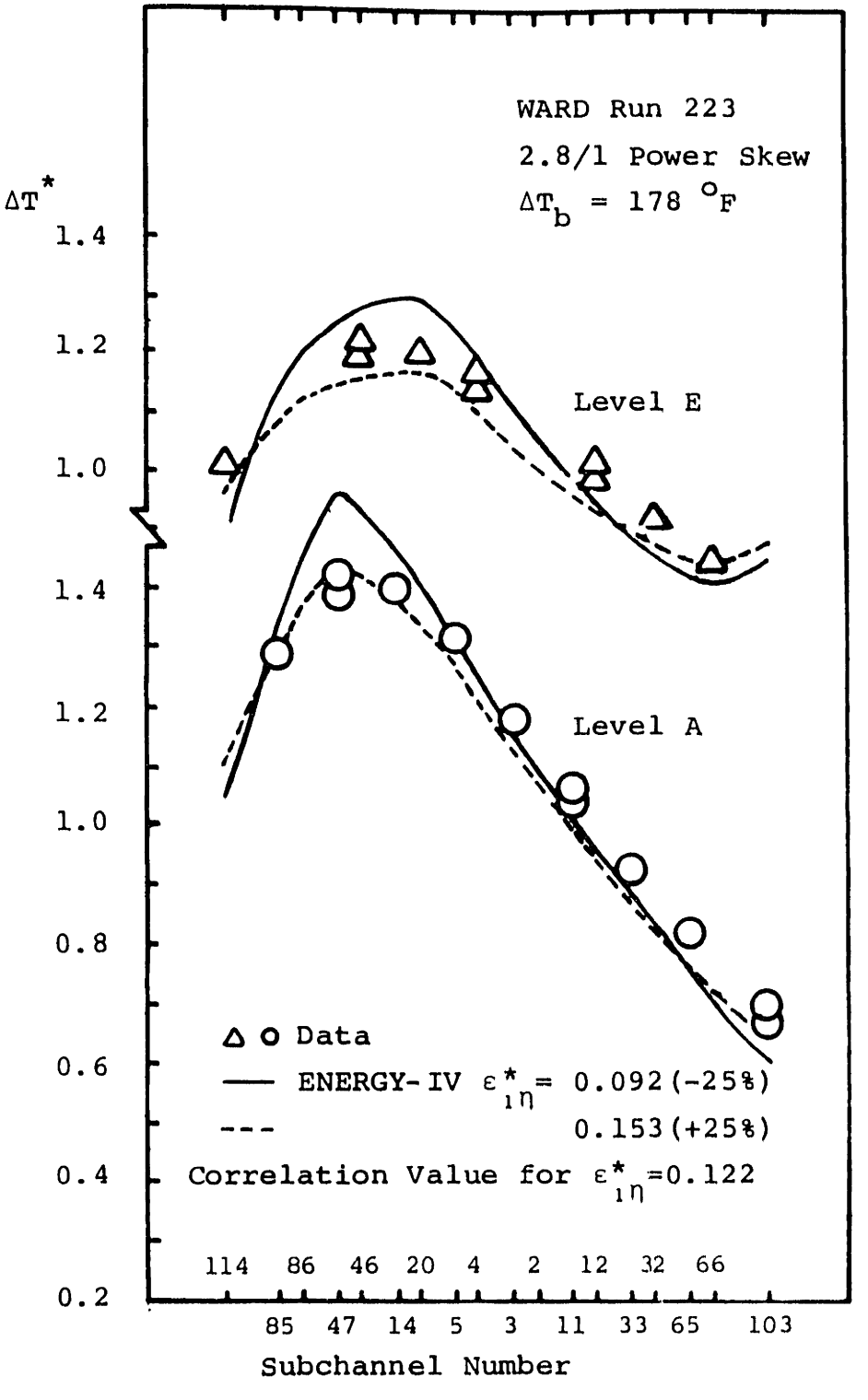

Figure 8.9 Sensitivity of the ENERGY-IV Results to $\varepsilon^*_{1\eta}$ for WARD Run 223

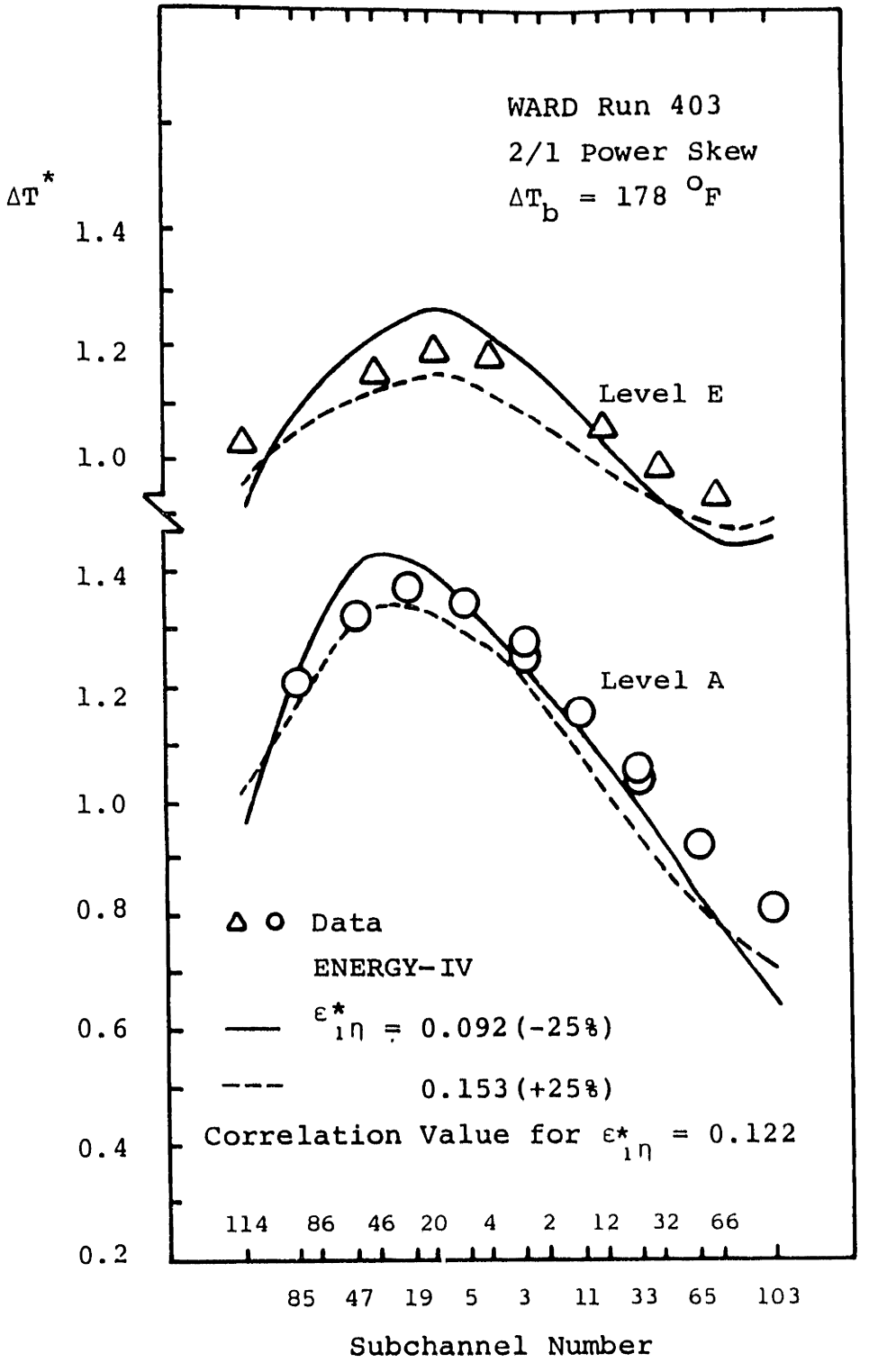

Figure 8.10 Sensitivity of the ENERGY-IV Results to $\varepsilon^*_{1\eta}$ for WARD Run 403

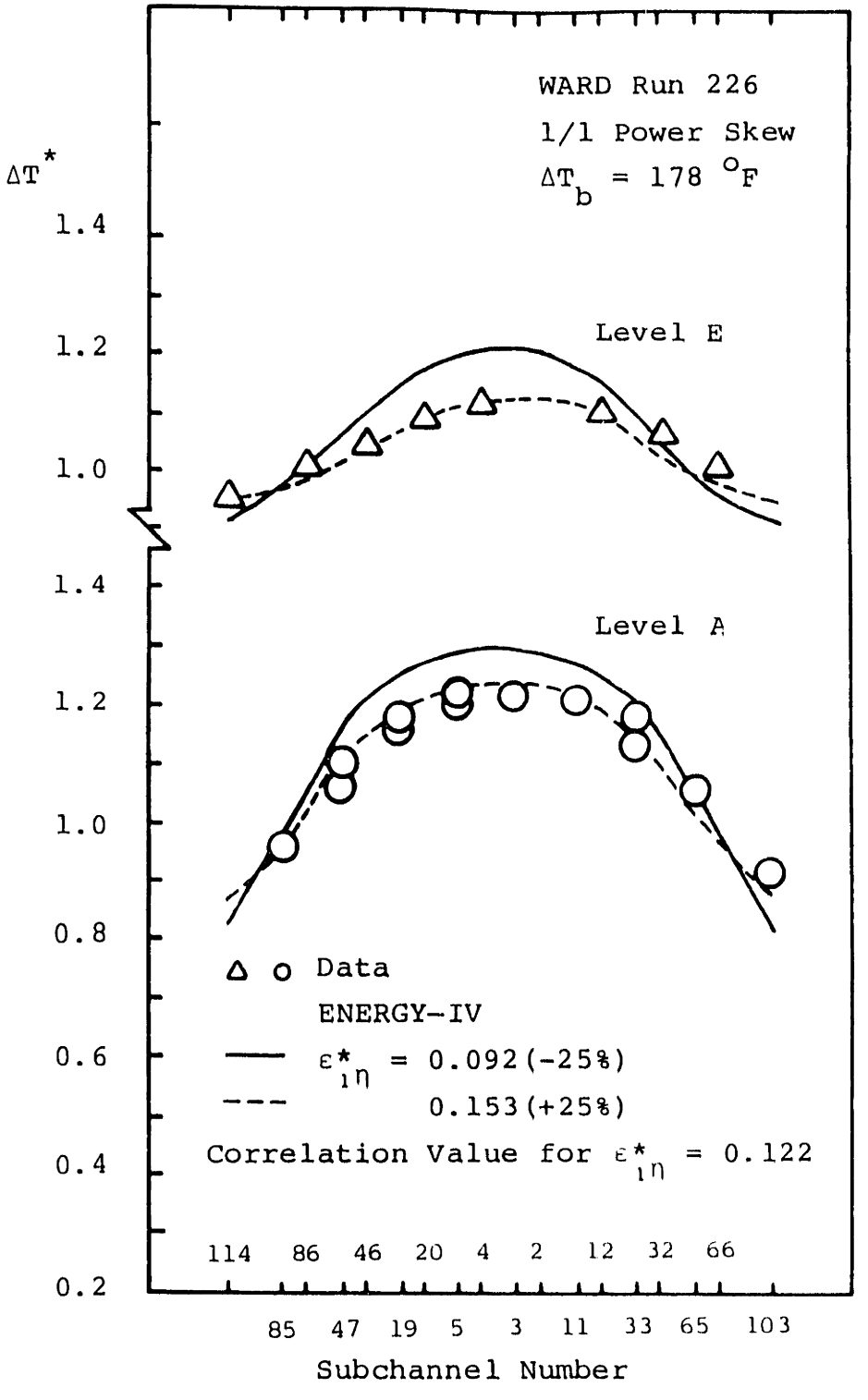

Figure 8.11 Sensitivity of the ENERGY-IV Results to $\varepsilon^*_{1\eta}$ for WARD Run 226

changes the calculated maximum ΔT^* $\bar{+}$0.065 (44%), 0.045 (3.5%), and 0.03 (2.4%) corresponding to temperature differences +12°F, 8°F, and 5°F, for 2.8/1, 2/1, and 1/1 power skew, respectively.

Apparently, this temperature sensitivity to $\varepsilon^*_{l\eta}$ is much less than that for the salt concentration calculation in Chapter 5, which gave -20% of dimensionless salt concentration for +25% of $\varepsilon^*_{l\eta}$ and +34% of dimensionless salt concentration for -25% of $\varepsilon^*_{l\eta}$. The reason for this drastic difference is that the salt injection case is basically a local point source, while the heated pin case is a global (axially and radially) heat source. This global heat source diminishes the influence of $\varepsilon^*_{l\eta}$ to the calculated temperature distribution. Hence the $\varepsilon^*_{l\eta}$ reduced from the point source experiments will be much more accurate than that reduced from the heated pin experiment. Note that most of the reduced $\varepsilon^*_{l\eta}$ values used for calibrating our proposed correlation were from the point source experiments.

Despite the fact that the calculation results for the heated pin bundle are not as sensitive to $\varepsilon^*_{l\eta}$ as that for the point source case, $\varepsilon^*_{l\eta}$ is still the most important input parameter to accomplish good predictions. As seen from Figures 8.9, 8.10 and 8.11, most of the data, especially in the high temperature region, fall inside the calculation results using $^+$25% and -25% of the correlation value of $\varepsilon^*_{l\eta}$.

As for the temperature distribution along the edge subchannels, Figure 8.12 compares the data, the ENERGY-IV predictions, and the COTEC

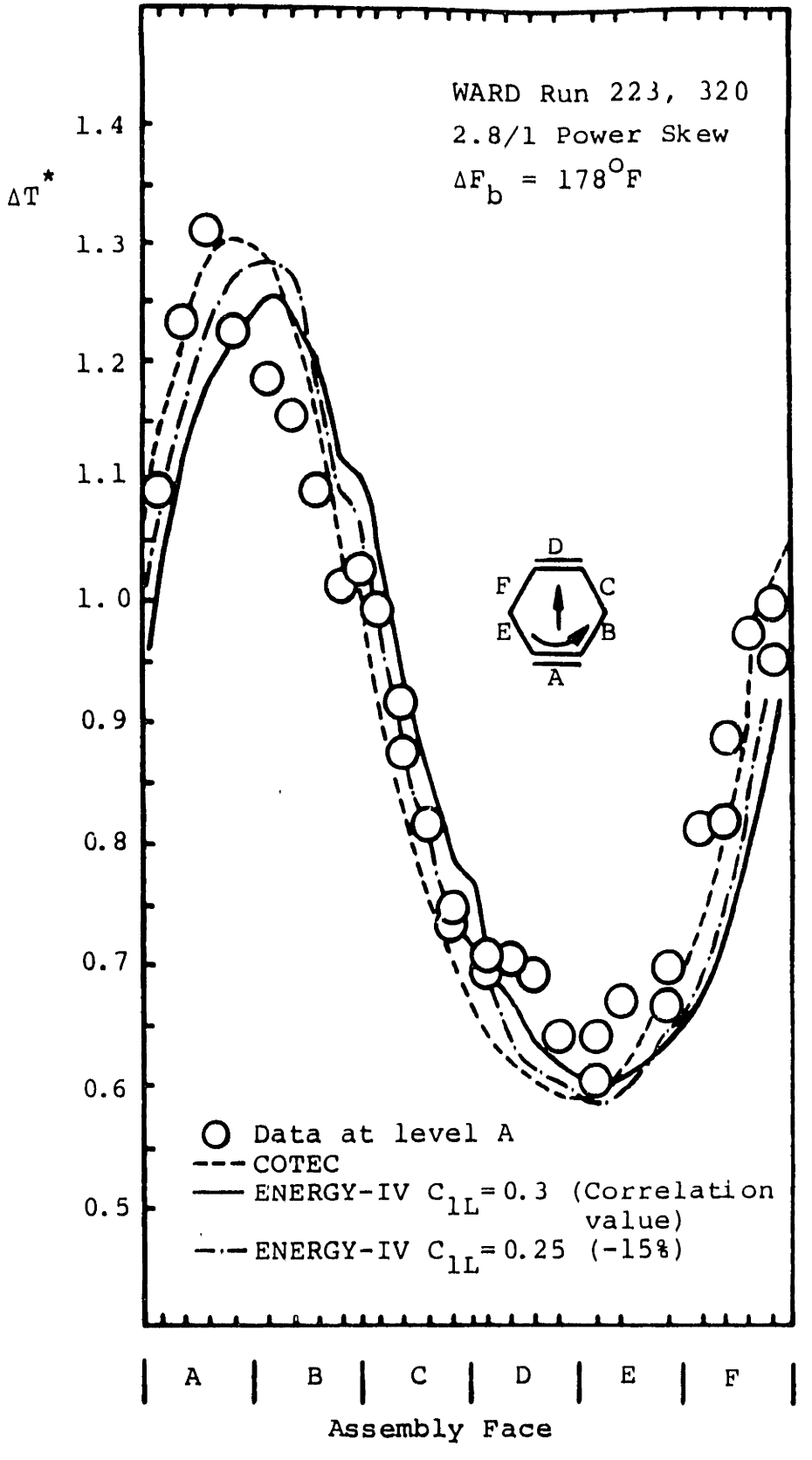

Figure 8.12 Measured and Predicted Temperature Rise in Edge Subchannels for WARD Bundle

predictions. Two ENERGY-IV results are shown in this figure, one with C_{1L} = 0.3 (correlation value), the other one with C_{1L} = 0.25 (-15% of the correlation value). Note that the accuracy of the correlation for C_{1L} is ±15%. The results with C_{1L} = 0.25 predicts the data better, although the maximum ΔT^* only increases 2% and its location moves backward one subchannel comparing the results with C_{1L} = 0.3. Similar to the $\varepsilon^*_{1\eta}$, this sensitivity is much less than that for salt injection calculation. The difference between the maximum ΔT^* for the data and for the calculation results with the correlation value of C_{1L} (0.30) is about 0.06, which gives 11°F temperature difference since ΔT_b = 178°F. The COTEC results match the data quite well. Incidentally, the COTEC calculation looks like a ENERGY-IV calculation with C_{1L} = 0.20 (-30% of correlation value).

8.3.2 Comparison between Data and Predictions for the ORNL Bundles

ORNL 19-pin

Figures 8.13 and 8.14 compare the ENERGY-IV prediction to the data for a 3/1 and 1/1 power skew, in the 19 pin THORS-2A bundle. The ENERGY-IV calculation predicts the 3/1 power skew data well, but it slightly overpredicts the peak temperature of the 1/1 power skew data by a value of 3°F (0.004 of ΔT*).

The COBRA calculations [Khan et al. (1982), Donovan et al. (1979)] are also present in these figures for comparison. The input parameters used in the COBRA (-WC or -IV) are listed in Table 8.4. This set of input parameters have been validated by Khan et al. (1982) to be

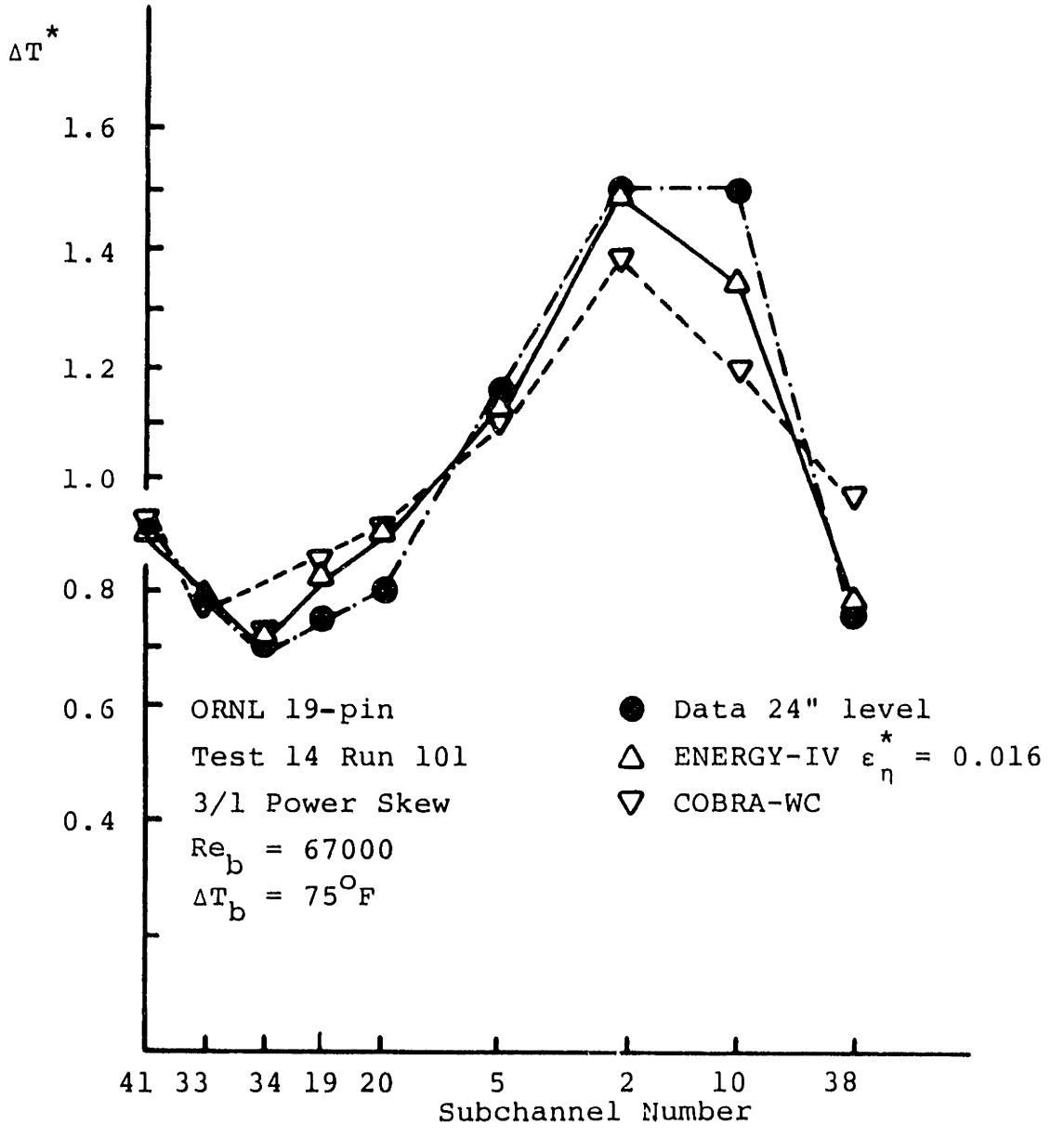

Figure 8.13 Measured and Predicted Temperature Rise for ORNL 19-pin 3/1 Power Skew

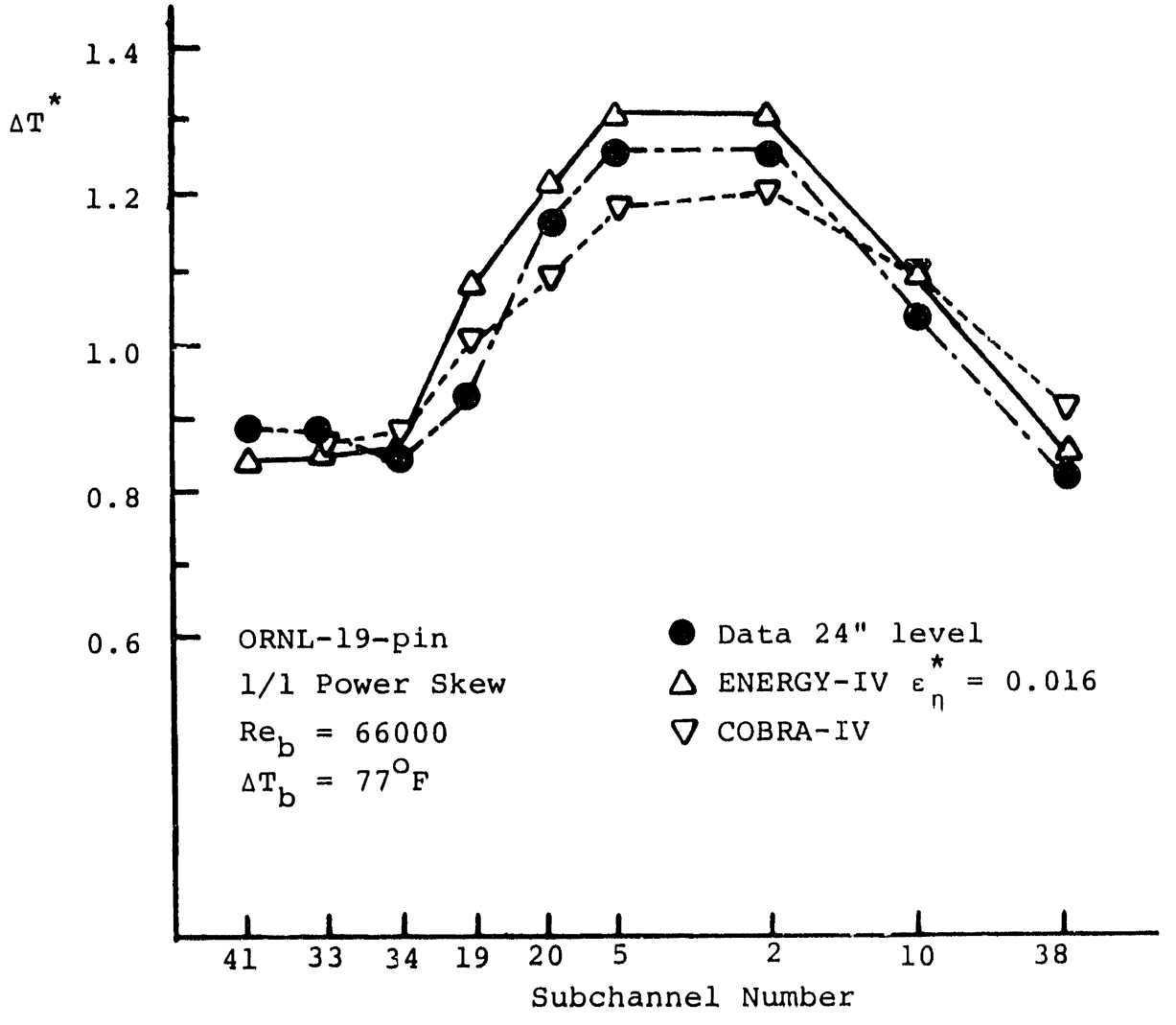

Figure 8.14 Measured and Predicted Temperature Rise for ORNL 19-pin Uniform Power Distribution

Table 8.4 Input Parameters for COBRA-WC (or -IV)

Parameter	Blanket	Fuel
wire-wrap sweep flow coefficient, DUR	1.0	1.0
crossflow resistance, K_{IJ}	0.5	0.5
momentum length, S/ℓ	0.5	0.5
conduction shape factor, G	0.5	0.5
fraction of bundle flat-to-flat tolerance accommodated at the wall	0.0	0.0
turbulent mixing parameter, β	0.01	0.01[a] 0.00[b]
subchannel friction factors, f	$f = \frac{M f_{smooth}}{X_i^2} \frac{d_i}{d_{bundle}}$	

where

i = 1 for interior channels

i = 2 for wall channels

M = Novendstern's friction factor multiplier for wire wrapped rod bundles

f_{smooth} = smooth tube friction factor

X_i = flow split from (Khan 1980; Chiu 1978; Wang and Todreas 1981)

(a) For prediction of coolant temperature distribution across the assembly.

(b) For prediction of peak coolant temperature within the assembly.

applicable to wire-wrapped rod bundle in both forced an mixed flow required. Unless otherwise specified, all the COBRA predictions presented in this chapter use these input parameters. As shown in these two Figures, the COBRA results underpredict the data.

The sensitivity of the ENERGY calculations to ε^*_{ln} can be estimated by the following discussion. As ε^*_{ln} changes from the correlation value, 0.016, to the +50% value, 0.024, the peak temperatures predicted by the ENERGY-IV coincide with the data for the uniform power skew case, i.e., the maximum ΔT^* decreases a value of 0.04 or 3°F, For the 3/1 power skew case, the maximum ΔT^* decreases 0.06 or 4.5°F as ε^*_{ln} increases 50%.

Figure 8.15 shows the comparison between the ENERGY-IV calculation and the temperature data in the edge subchannels for three edge pins heated. The trend of the data and the peak temperature location are well predicted by the ENERGY-IV. The maximum temperature difference is about 14°F in the peak temperature subchannel.

ORNL-61 pin

Figures 8.16 and 8.17 compare the data, the ENERGY-IV results and the COBRA-WC results for the ORNL-61 pin bundle with 3/1 power skew and uniform power skew, respectively. Excellent predictions by the ENERGY-IV are observed. The maximum difference between the data and ENERGY-IV results is about ΔT^* equal to 0.06, which gives a temperature difference of 12°F with ΔT_b = 203°F. As seen from these figures, the ENERGY-IV has a better capability in predicting the data than that of the COBRA-WC.

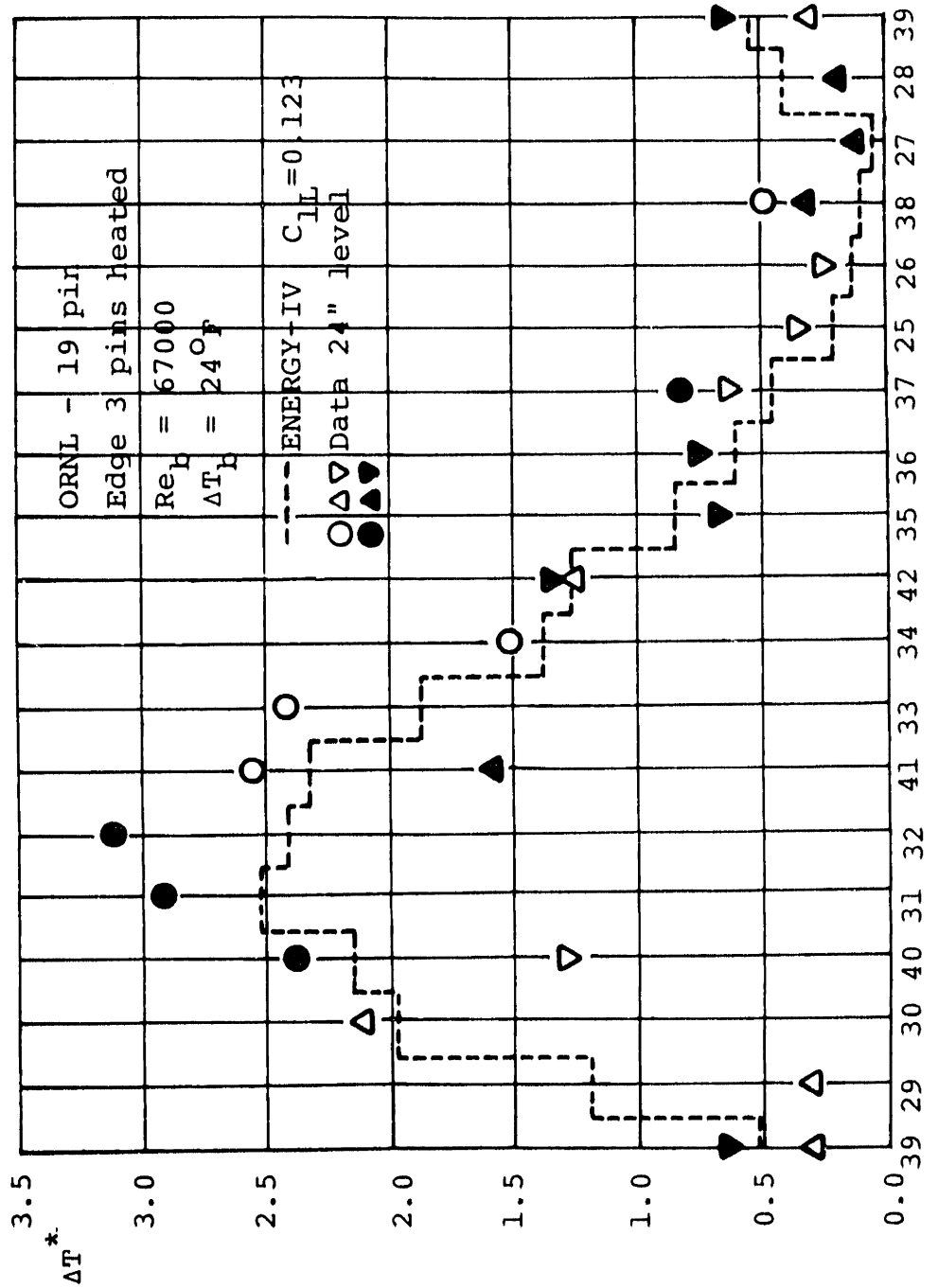

Figure 8.15 Measured and Predicted Temperature Rise in the Edge Subchannel for ORNL 19-pin Bundle

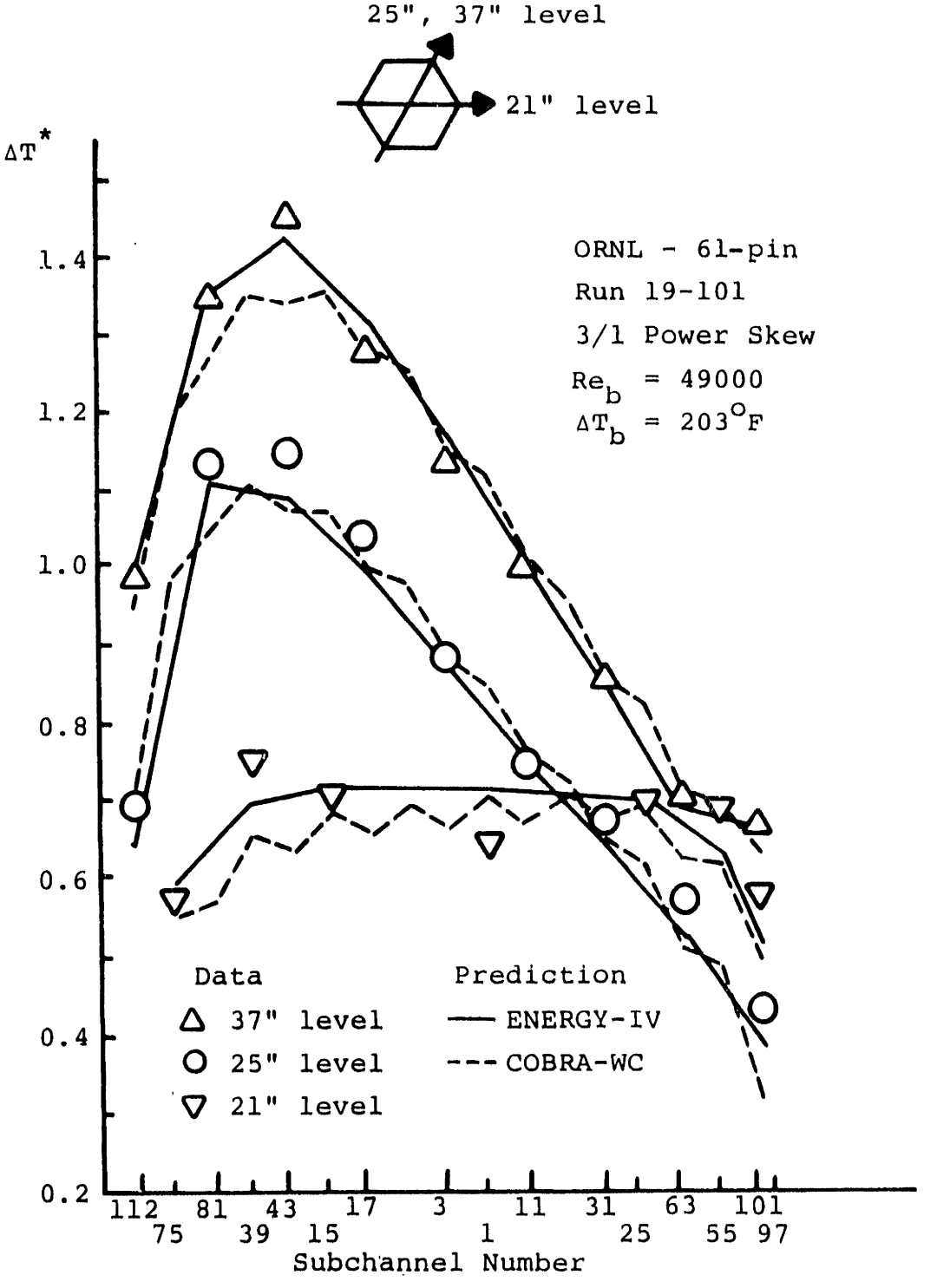

Figure 8.16 Measured and Predicted Temperature Rise for ORNL - 61-pin Run 19-101

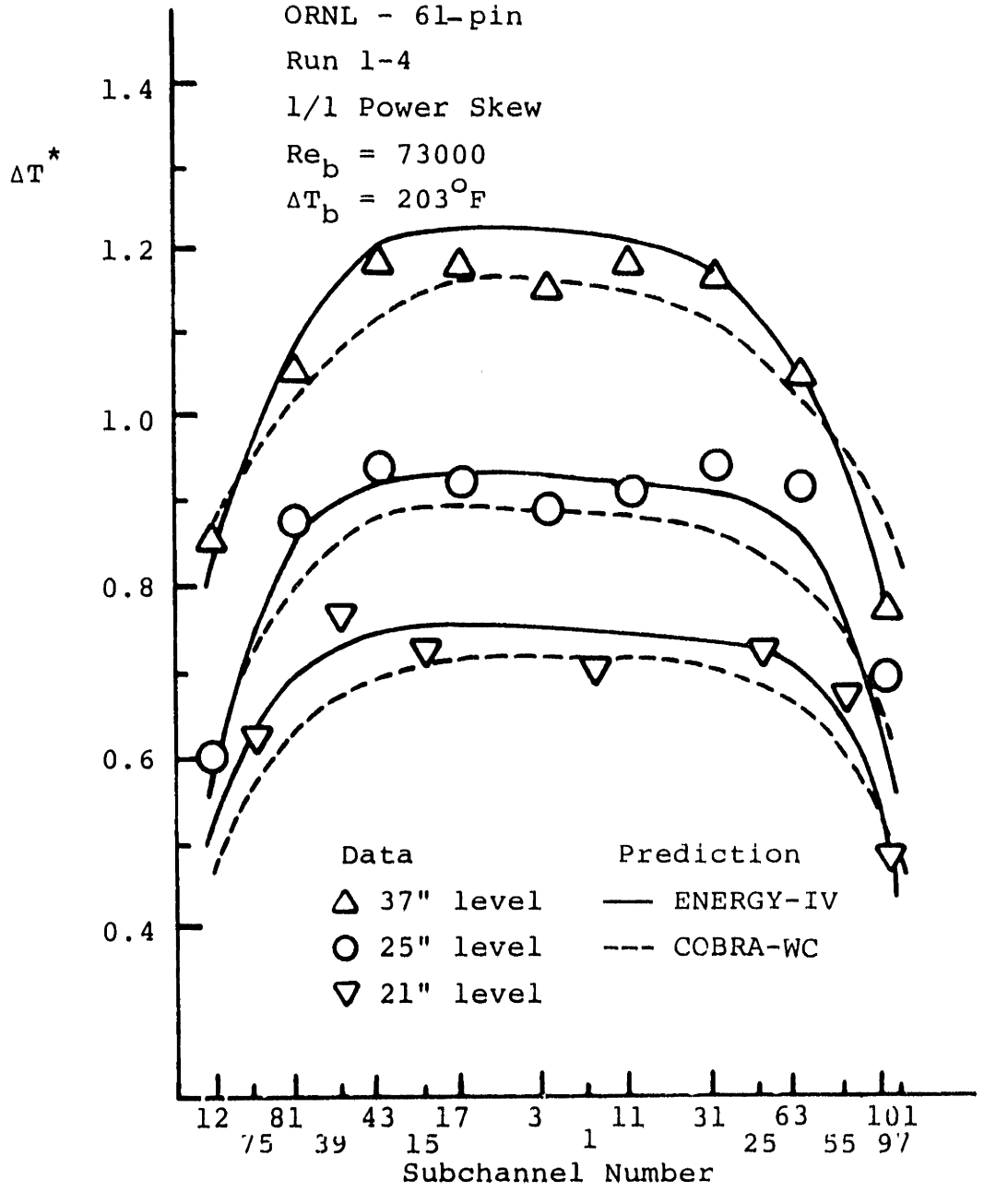

Figure 8.17 Measured and Predicted Temperature Rise for ORNL - 61-pin Run 1-4

Figure 8.19 shows the sensitivity of the calculation results of ENERGY-IV to $\varepsilon^*_{l\eta}$. With a ±35% (±0.05) change of $\varepsilon^*_{l\eta}$, the average change in ΔT in the high temperature region is about ± 0.04 or ±8°F.

8.3.3 Comparison between Data and Predictions for Toshiba Bundle

Figure 8.19 illustrates the comparison among the data at high flow rates of Toshiba bundle with different power skews, the ENERGY-IV predictions and the COBRA predictions. The COBRA input parameters for calculating Toshiba cases are depicted in Table 8.5. The maximum temperatures in different power skews are accurately predicted by both the ENERGY-IV and the COBRA codes. ENERGY-IV predicts well the temperatures in the high power region, while it overpredicts the temperatures in the lower power region, especially for the 2/1 power skew case. The COBRA predictions have just the opposite trends. The overall behavior of these data, however are satisfied by the predictions.

8.3.4 Conclusions

The validation of the ENERGY-IV for the forced convection condition has been illustrated in the previous sections with geometries ranging from typical fuel assembly geometries to blanket assembly geometries and power skew across the assemblies ranging from uniform to 3/1. The predictions of the ENERGY-IV are found to be more accurate than, or at least similar to that of the COBRA. The maximum temperature difference between the ENERGY predictions and the data are less than 7% of the bulk temperature rise (ΔT_b),i.e., 12.5°F for the most severe case.

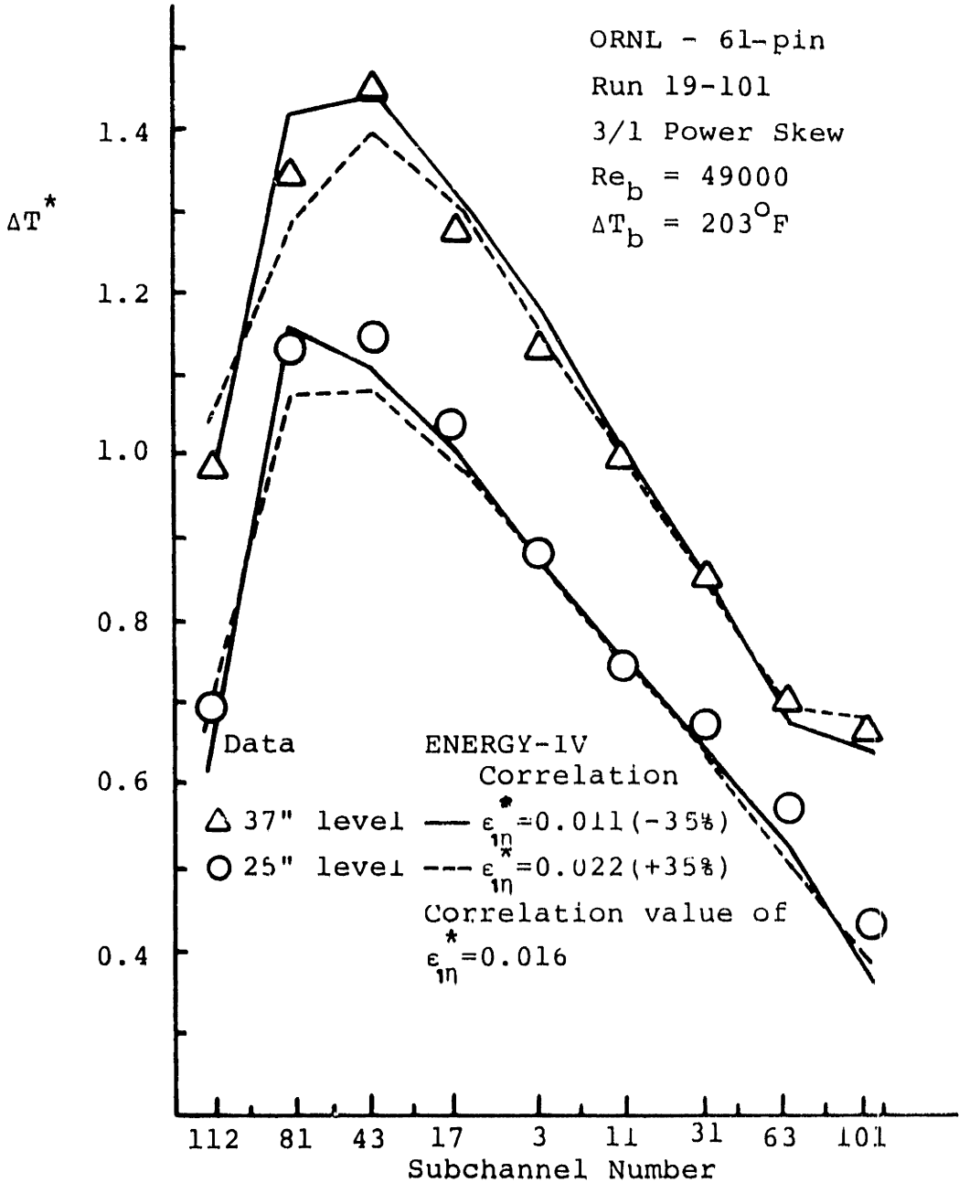

Figure 8.18 Sensitivity of $\varepsilon^*_{1\eta}$ to the ENERGY-IV Results for ORNL - 61-pin Run 19-101

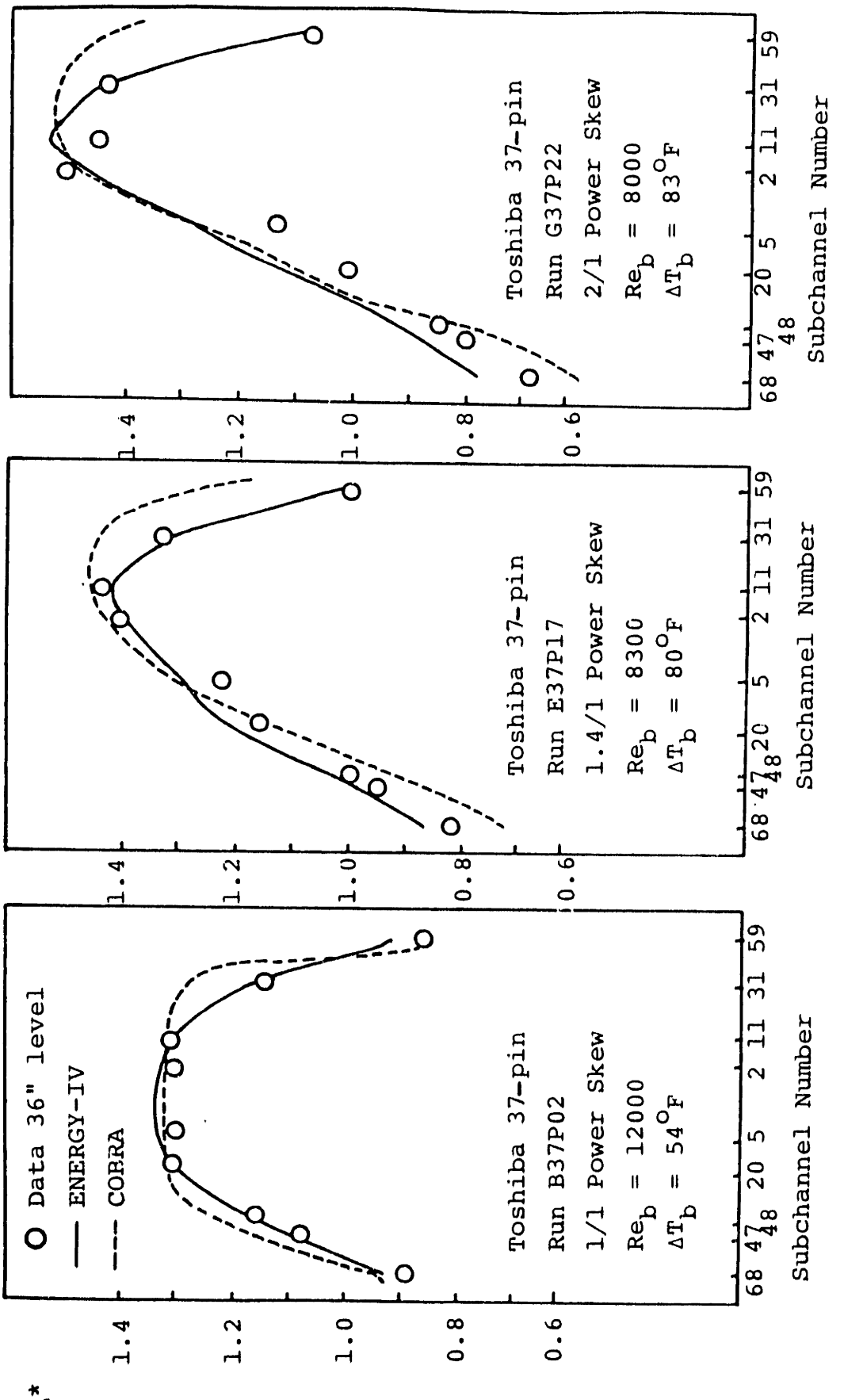

Figure 8.19 Measured and Predicted Temperature Rise for Toshiba 37-pin Bundle

Table 8.5 Input Parameters Used in COBRA-IV for Toshiba Tests

Summary of COBRA-IV input parameters

Parameter	
Turbulent mixing parameter	0.02 (Re ≥ 1200) 0.00 (Re < 1200)
Transverse momentum parameter	0.5
Wire wrap sweeping parameter	0.03
Conduction. factor	0.5
Friction factor	$f = 41.7/Re + 0.12/Re^{0.159}$ (Re ≥ 1200) $f = 37.3/Re^{0.872}$ (Re < 1200)

The favorable comparison of ENERGY-IV to COBRA is not suprising when one realized that the empirical input parameters for the ENERGY-IV are much better calibrated than those for the COBRA-WC code. Although a much more complicated method is used in the COBRA-WC, a simplified method as employed in ENERGY-IV with fine calibrated input parameters can do a better job in the forced convection region. However, the COBRA-WC code is intended to be a bench-mark code which is assumed to be applicable outside its validation range, while the ENERGY-IV is a totally empirical code which can only be used inside the validation range as a fast running design tool.

As for the sensitivity of the calculation results of the ENERGY-IV to $\varepsilon^*_{l\eta}$. Table 8.6 shows the changes of maximum ΔT^* calculated by the ENERGY-IV for different power skews for both blanket and Fuel bundles. The temperature difference caused by 25% change of $\varepsilon^*_{l\eta}$ is about 6 - 12°F for typical fuel and blanket operation conditions, respectively.

8.4 Validation of the ENERGY-IV in the Mixed Convection Condition

The major difference between the forced convection option and the mixed convection option of the ENERGY-IV code is that flow redistribution due to the buoyancy force is modelled in the mixed convection option. This is accomplished by solving the overall mass, energy, and axial momentum conservation equations with the assumption of a uniform pressure across the bundle. Since the momentum equation is used, the subchannel friction factors are required as input parameters in addition to the input parameters required for the energy

Table 8.6 Sensitivity of the ENERGY-IV Calculation to $\varepsilon^*_{1\eta}$

Bundle	$\varepsilon^*_{1\eta}$	Change of $\varepsilon^*_{1\eta}$	Change of the Maximum ΔT^* Power Skew 3/1	2/1	1/1
WARD (Blanket)	0.122	per 25%	0.065	0.045	0.030
		per 0.01	0.021	0.015	0.010
ORNL (Fuel)	0.016	per 25%	0.030	-	0.020
		per 0.01	0.075	-	0.050

equation in the forced convection condition, i.e., the inlet flow split parameter, X_i, the dimensionless effective eddy diffusivity, $\varepsilon^*_{1\eta}$, $\varepsilon^*_{2\eta}$, the edge transverse velocity ratio, C_{1L}, and the conduction shape factor, κ. Use of these parameters in the equations for the mixed convection option was discussed in chapter 2.

As mentioned before, the conduction shape factor for wire-wrapped rod bundle is still an open quesion. In the following ENERGY-IV calculations, the bare rod values for κ developed in chapter 6 will be assumed to be applicable in wire-wrapped rod bundle. In section 8.5, it will be shown that this assumption is satisfactory.

In addition to these features, thermal plume effects, which enhance the mixing between subchannels, contribute a significant amount of energy transfer in the mixed convection regime. An estimation of this thermal plume mixing expressed as the parameter $\varepsilon^*_{\eta M}$ is required for the ENERGY-IV calculation.

In this section, the phenomena generated by the buoyancy effects, i.e., subchannel friction factor in the mixed convection condition, flow redistribution and thermal plume mixing will be discussed first. After a correlation for $\varepsilon^*_{\eta M}$ is proposed, the predictions of the ENERGY-IV code are compared to the data. Meanwhile the sensitivity of the ENERGY-IV predictions to the $\varepsilon^*_{\eta M}$ parameter will also be investigated. The data base selected for the validation of the ENERGY-IV in the mixed convection condition are depicted in Table 8.7.

Table 8.7 Cases Used for Mixed Convection Validation

Bundle	Run	Flow (GPM)	Rod (kW/ft)	Power Skew	Re_b	$Gr_{\Delta T}$	$\frac{Gr_{\Delta T}}{Re_b}$	T_{in} (F)	$\Delta T_b^{\dagger}$ (F)
WARD	221	18.1	0.571	2.8/1	4390	400	0.091	600	181
61-pin	229	4.8	0.150	2.8/1	1160	390	0.336	600	178
	231	2.3	0.075	2.8/1	560	410	0.732	600	186
	401	4.89	0.146	2/1	1180	375	0.318	605	171
	731	3.34	0.094	2/1	800	350	0.438	602	162
	720	2.29	0.062	2/1	520	360	0.692	600	165
	227	4.90	0.147	1/1	1180	370	0.314	602	171
	732	3.44	0.096	1/1	820	340	0.415	602	159
ORNL	19-105	4.2	0.270	3/1	2250	620	0.276	729	308
61-pin	18-105	4.2	0.278	2/1	2270	650	0.286	736	318
	17-105	4.3	0.281	1.5/1	2320	640	0.276	739	314
	12-114	2.2	0.067	1/1	1110	260	0.234	722	144
Toshiba	G37P25	5.24	0.484	2/1	3070	280	0.091	399	250
37-pin	L37P43	2.39	0.302	2/1	1500	450	0.300	401	345
	F37P20	5.24	0.477	1.4/1	3060	280	0.092	400	246
	F37P27	2.85	0.289	1.4/1	1700	320	0.188	400	274
	C37P06	5.47	0.364	1/1	2920	170	0.058	378	178
	E37P13	1.54	0.119	1/1	880	230	0.261	404	208
Grenoble	1a	24.11	0.352	1/1	3420	404	0.118	600	148
91-pin	1b	12.24	0.177	1/1	1740	400	0.230	600	146
	1c	4.45	0.062	1/1	630	380	0.603	600	140
	2	12.61	0.186	2.5/1	1790	410	0.230	600	150

† Energy balance value

8.4.1 Phenomena Caused by Buoyancy Effects in the Mixed Convection Condition

8.4.1.1 Subchannel Friction Factors

The subchannel friction factor correlations developed in chapter 4 are for the forced convection condition only. In the mixed convection condition, buoyancy increases the velocity gradient near the wall, thus increasing the friction factor. Hence the forced convection subchannel friction factor needs to be modified to take into account these buoyancy effects.

The effects of buoyancy on the friction factor in a circular tube was studied by Bishop et al. (1980). An analytical solution of the conservation equations was found for fully developed flow. From the solution for the velocity field, the friction factor was obtained. An algebraic fit to the analytical results was found to be:

$$\frac{f}{f_o} \equiv \left[1 + 2.97 \times 10^{-3} \frac{Gr_q}{Re}\right]^{0.655} \equiv F \qquad (8.3)$$

where f = friction factor taking into account buoyancy effects

f_o = forced convection friction factor

Gr_q = Grashof Number based on heat flux

$\equiv \beta g D_e^{\,4} q''/k\nu^2$

Equation (8.3) will be assumed to be also applicable to the subchannel friction factor. The subchannel mixed convection friction factors are taken equal to the forced convection correlations multiplied by the factor F. The local (subchannel) value of the

Grashof number based on subchannel heat flux is used for calculating F. The parameter generally used in this chapter is a global Grashof number based on bundle axial averaged temperature gradient, $(\Delta T_b/L)$. The bundle average Gr_q can be related to $Gr_{\Delta T}$ as

$$Gr_q = \frac{Re\ Pr}{4\ (\frac{De_b}{D_H})}\ Gr_{\Delta T} \qquad (8.4)$$

where $D_H \equiv \frac{4A_b}{P_H}$

A_b = Bundle flow area

P_H = Bundle heated perimeter

An estimate of the value of F for typical sodium mixed convection conditions is

$$\frac{De_b}{D_H} \approx 1.0$$

$$Pr \approx 0.004$$

$$Gr_{\Delta T} \simeq 500 \text{ for typical operation,}$$

hence $(Gr_q/Re) \approx 0.5$. Substituting this value of (Gr_q/Re) into equation (8.3), yields F = 1.001. Thus only about a 0.1% increase in friction factor due to buoyancy effects is anticipated. We therefore conclude that for typical mixed convection operation, the increase in subchannel friction factors due to buoyancy effects is negligible. However, this correction factor was implemented in the ENERGY-IV for completeness of the correlation.

8.4.1.2 Flow Redistribution

The flow redistribution due to buoyancy effects is modelled by the ENERGY-IV in a much simpler way than that in the COBRA code as discussed in chapter 2. The COBRA code calculates the diversion cross flow utilizing the transverse momentum equation. This equation is not used in the ENERGY-IV code.

The validity of the simple model for calculating flow redistribution in ENERGY-IV can be checked by comparing the axial velocity fields at different axial levels calculated by ENERGY-IV to those calculated by COBRA-WC. Figure 8.20 compares the axial velocity distribution across the bundle from high power region to low power region at different axial levels for the WARD Run 229 with Re_b = 1160 and $Gr_{\Delta T}$ = 390. Two ENERGY-IV calculation results, one for $\varepsilon^*_{1\eta}$ = 0.082 (forced convection correlation values) and the other one for $\varepsilon^*_{1\eta}$ = 0.20 (including a 0.118 increment to the correlation value), are presented. As we should see later, the 0.118 increment is the enhancement due to the thermal plume effects. This figure shows that the velocity distributions calculated by ENERGY-IV are very close to those calculated by COBRA, especially for the $\varepsilon^*_{1\eta}$=0.20 case in which the values are almost the same for the central region. Discrepancies between the COBRA and ENERGY-IV ($\varepsilon^*_{1\eta}$ = 0.20) predictions, however, are found in the edge subchannels and the interior subchannels adjacent to the edge subchannels. Dips in the interior subchannels next to the edge region are always exhibited in the COBTA results. This might be the reason that the velocities in the edge subchannels for the COBRA

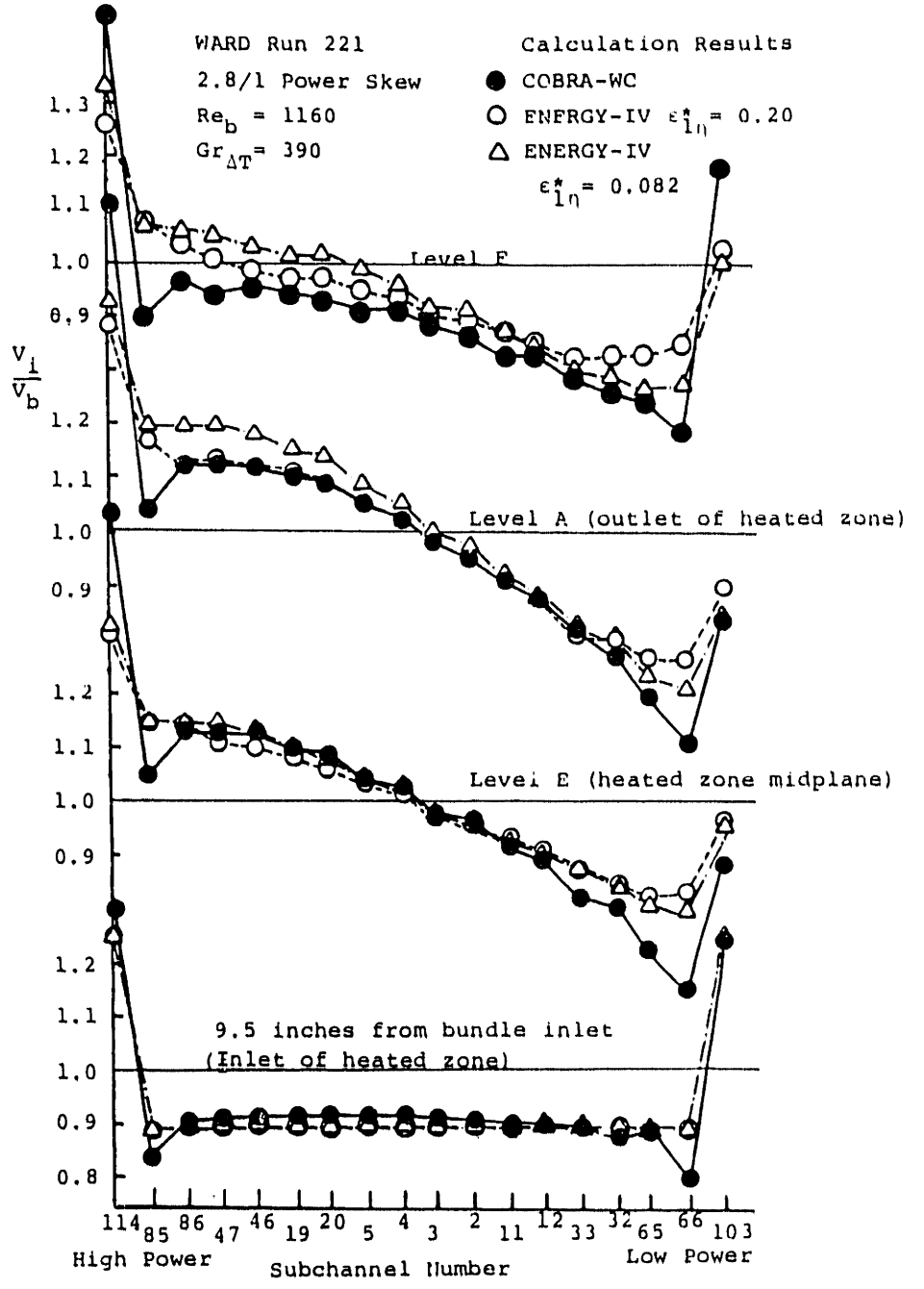

Figure 8.20 Velocity Distributions Calculated by COBRA-WC and ENERGY-IV in the Mixed Convection Condition

results are higher than those for the ENERGY-IV results. This situation must be caused by the pressure distribution calculated by COBRA, which generates this solution through the transverse momentum equation. The physical reason for this phenomenon, however, is not clear to us.

8.4.1.3. Mixing Enhanced by Thermal Plume Effects

Thermal plumes have been visually observed by Bates and Khan(1980) and Symolon (1982) for heated bundles in low flow rate operations. In this study, use of only the forced convection value of $\varepsilon^*_{l\eta}$ in the ENERGY-IV code were always found to overpredict the maximum ΔT^* of the mixed convection data. Since ENERGY-IV predicts the forced convection temperature data very well, and the flow redistribution seems to be correct as discussed in the last subsection, we conclude that an additional mixing mechanism exists in the mixed convection regime. The thermal plume phenomenon is probably the origin for this mixing mechanism.

A Thermal Plume Mixing Parameter (TPMP), $\varepsilon^*_{\eta M}$, was defined similar to $\varepsilon^*_{l\eta}$, i.e.,

$$\varepsilon^*_{\eta M} = \frac{\text{transverse mass flux due to thermal plume effects}}{\text{axial mass flux}}$$

to quantitatively represent the enhanced mixing caused by thermal plumes. Symolon (1982) investigated a simple model for this mixing mechanism. According to similar fundamental consideration, Appendix E1 presents a model for $\varepsilon^*_{\eta M}$ which indicates that $\varepsilon^*_{\eta M}$ should be a

function of bundle geometry, $Gr_{\Delta T}/Re$, and local relative power density. Although $\varepsilon^*_{\eta M}$ should be a local phenomenon which depends on local power to flow ratio, we recommend use of a bundle global value for simplicity. Use of a local value of $\varepsilon^*_{\eta M}$ as a function of relative power density was investigated but found not to improve the predictions significantly.

Cases listed in Table 8.7 were used to estimate the thermal plume enhanced mixing parameter $\varepsilon^*_{\eta M}$ as a function of geometry, $Gr_{\Delta T}/Re$, and power skew by matching the ENERGY-IV calculating to the data. The power skew influence on this global $\varepsilon^*_{\eta M}$ was found to be insignificant. The correlation constructed for $\varepsilon^*_{\eta M}$ according to this procedure was,

$$\varepsilon^*_{\eta M} = 0.1\left(\frac{c}{D}\right)^{-0.5}\left(\frac{Gr_{\Delta T}}{Re_b}\right) \qquad (8.5)$$

For ENERGY-IV calculations in the mixed convection condition, the appropriate total interchannel mixing parameter is the sum of this enhanced parameter, $\varepsilon^*_{\eta M}$, and the forced convection dimensionless eddy diffusivity, $\varepsilon^*_{\eta F}$, ($\varepsilon^*_{1\eta}$ for the interior subchannel and $\varepsilon^*_{2\eta}$ for the edge subchannel)

8.4.2 Comparisons between Data and Predictions in the Mixed Convection Condition

8.4.2.1 WARD Bundle

Figure 8.21 illustrates the comparison among the data, the ENERGY-IV predictions and the COBRA predictions for WARD Run 221. Figure 8.22 compares the calculation results of ENERGY-IV with four

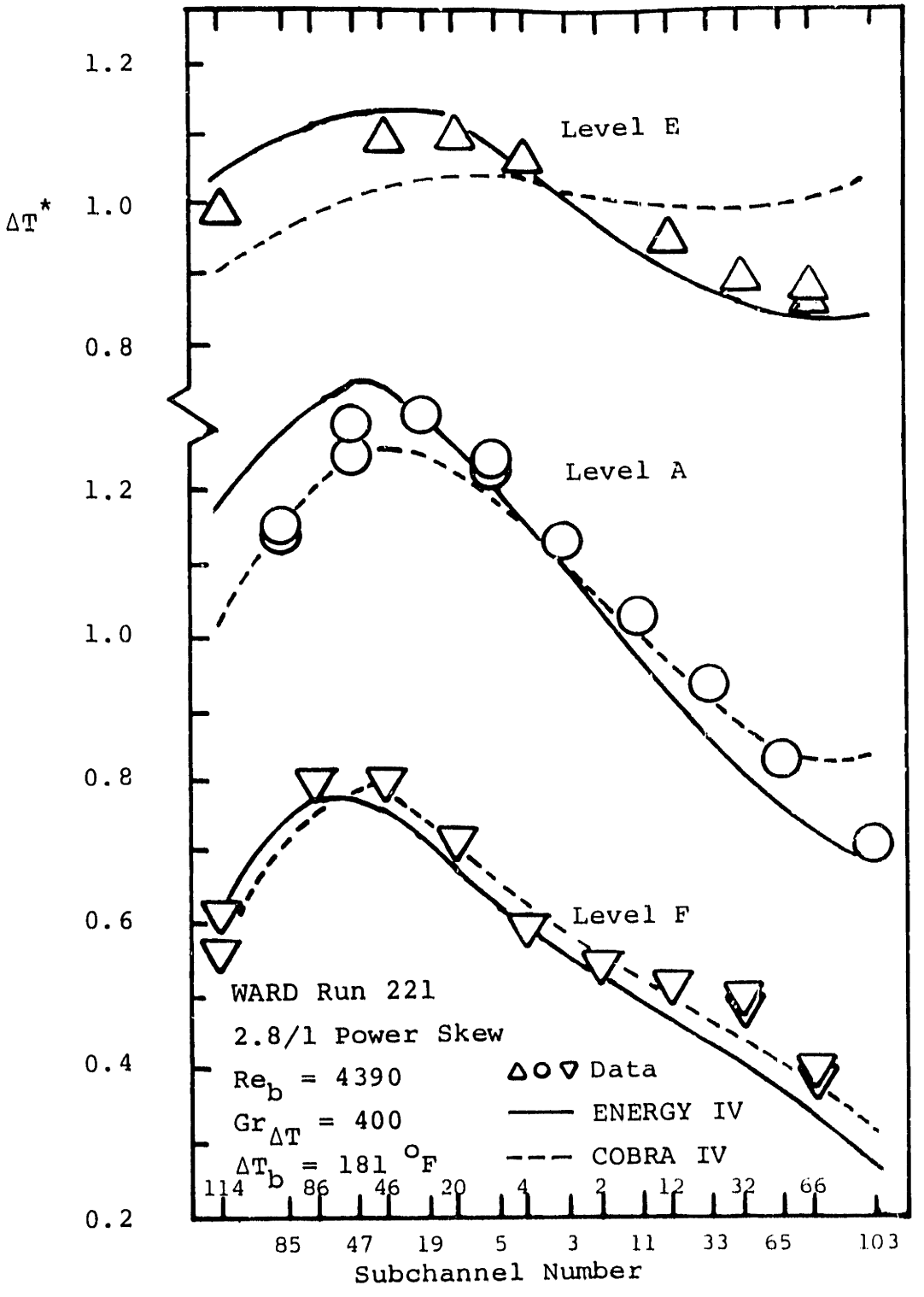

Figure 8.21 Measured and Predicted Temperature Rise for Ward Run 221

different options: recommended ε^*_η (i.e., $\varepsilon^*_{\eta F} + \varepsilon^*_{\eta M}$), $\varepsilon^*_{\eta F}$ only, recommended ε^*_η plus one additional $\varepsilon^*_{\eta M}$ increment (i.e., $\varepsilon^*_{\eta F} + 2\varepsilon^*_{\eta M}$) and the forced convection method with $\varepsilon^*_{\eta F}$ (i.e., no flow redistribution). Similarly, Figures 8.23 and 8.24, and Figures 8.25 and 8.26 illustrate the comparisons and sensitivity of the computed ΔT^* to $\varepsilon^*_{\eta M}$ for WARD Run 229 and Run 231, respectively. The COBRA-IV predictions for Run 231 were not available in the literature.

Figures 8.22, 8.24, and 8.25 not only show the sensitivity of the calculation results to $\varepsilon^*_{\eta M}$ but also compare the effects of flow redistribution to the temperature distribution. The flow redistribution reduces the maximum ΔT^* by values of 0.05, 0.17, and 0.22 for Runs 221, 229, and 231, corresponding to $Gr_{\Delta T}/Re_b$ = 0.091, 0.336, and 0.732, respectively. As the $Gr_{\Delta T}/Re_b$ increases, the flow redistribution effect becomes more and more dominant in establishing the temperature distribution. The maximum ΔT^* decreases by 0.04, 0.035, and 0.025 for each $\varepsilon^*_{\eta M}$ increment, (0.032, 0.117, and 0.256) for Run 221, 229, and and 231, respectively.

The sensitivity study of $\varepsilon^*_{1\eta}$ illustrates the way we estimated $\varepsilon^*_{\eta M}$ for each case. For these three cases, the temperature data in the low power region were always higher than the predictions even when high $\varepsilon^*_{\eta M}$ were used. Use of a mean square indicator method such as that in chapter 5 might not be adequate since a very high $\varepsilon^*_{\eta m}$ would be required to match the temperature data in low power region to give a minimum mean square indicator. Instead, we estimate $\varepsilon^*_{\eta M}$ by engineering judgements based on two considerations: the maximum temperature rise

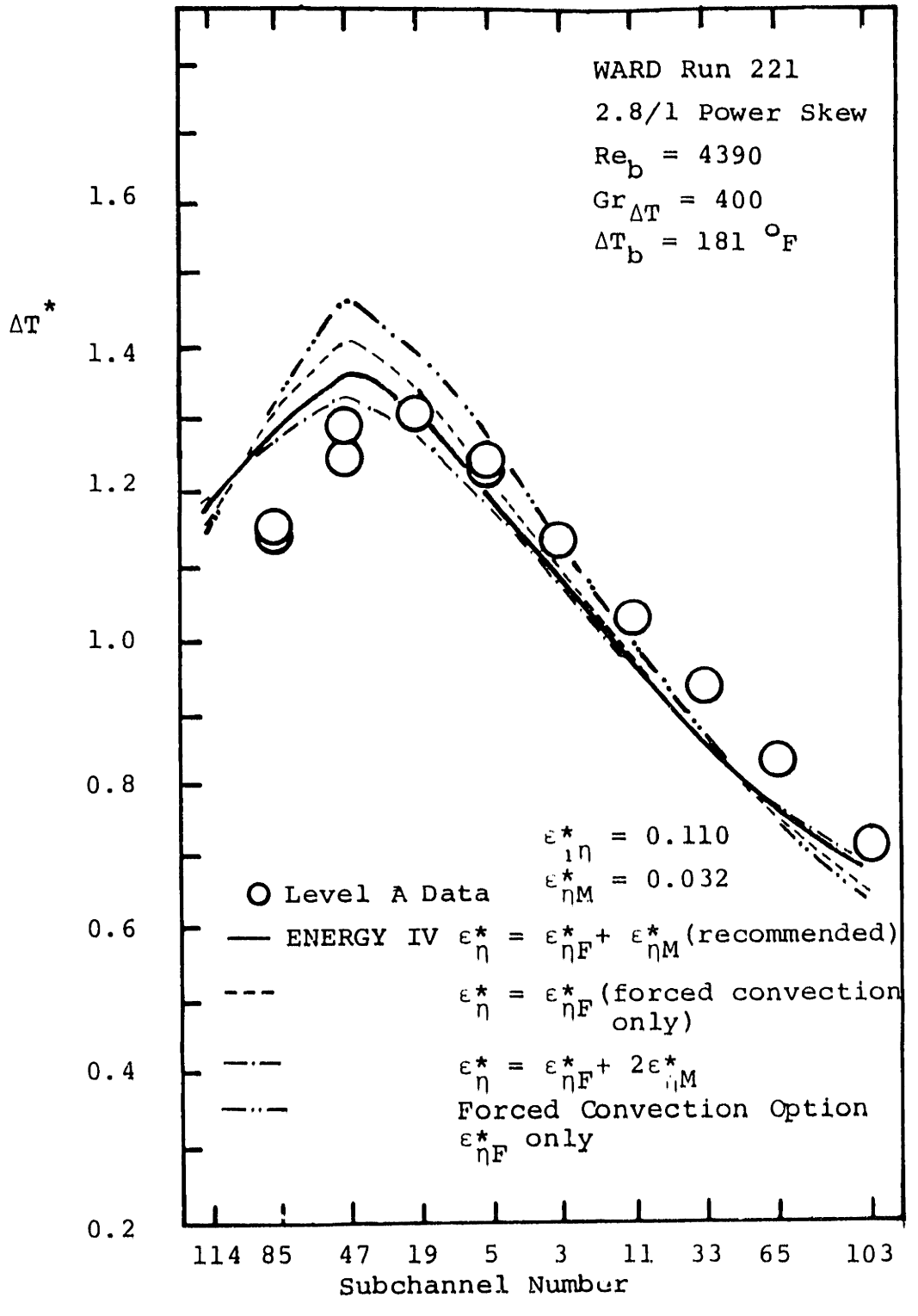

Figure 8.22 Sensitivity of $\varepsilon^*_{\eta M}$ to ENERGY-IV Results for WARD Run 221

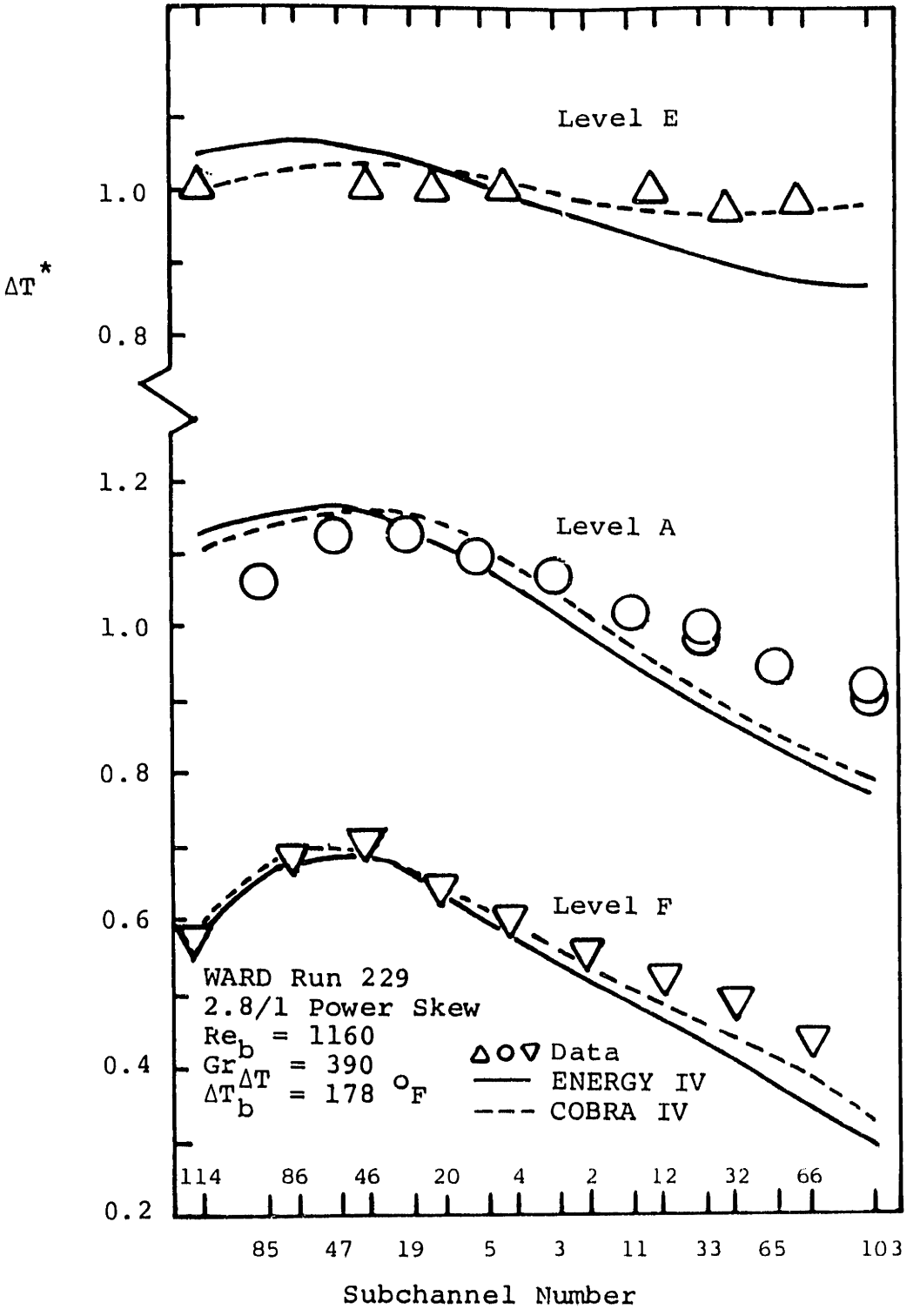

Figure 8.23 Measured and Predicted Temperature Rise for WARD Run 229

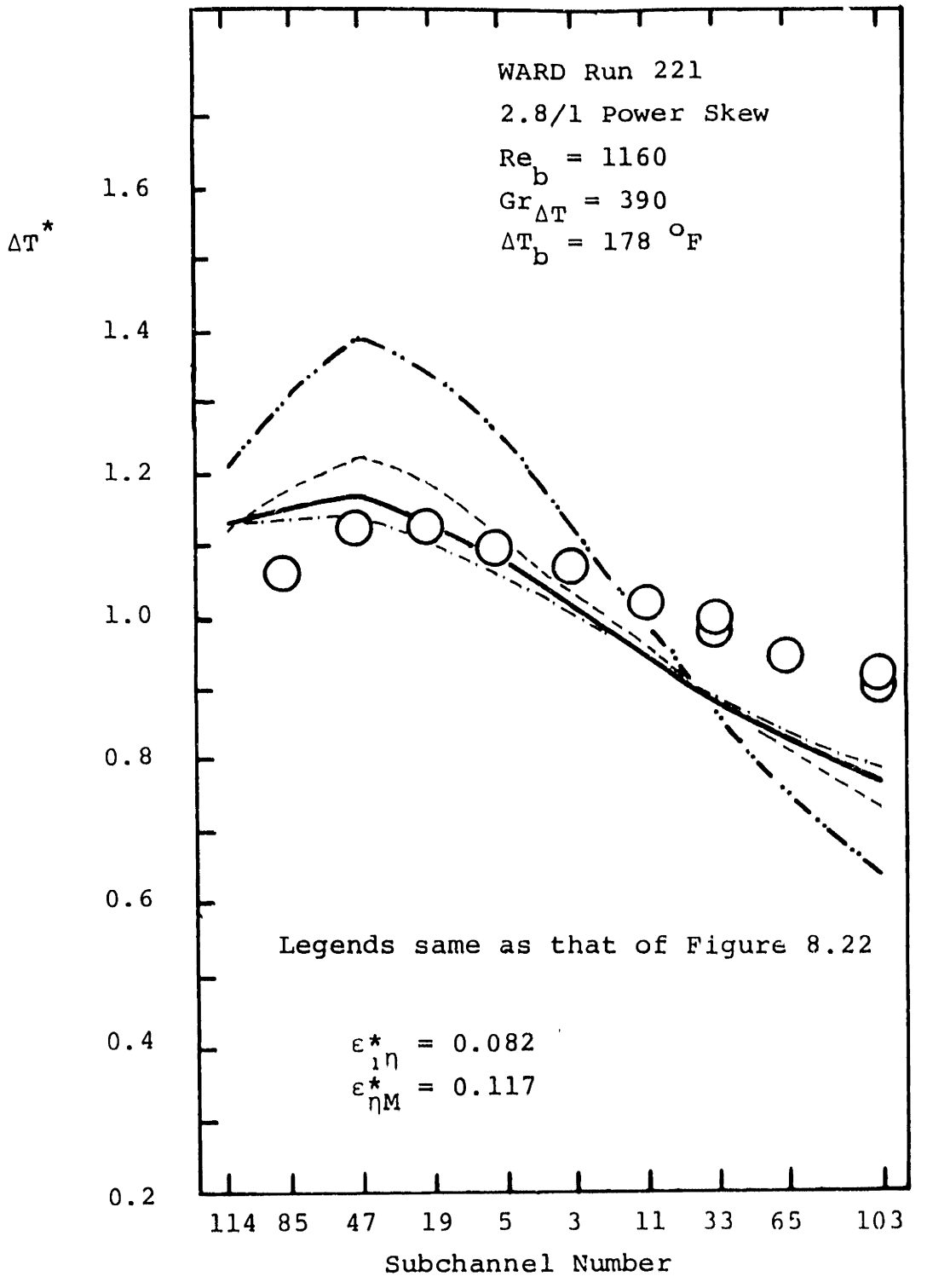

Figure 8.24 Sensitivity of the ENERGY IV Results to $\varepsilon^*_{\eta M}$ for WARD Run 229

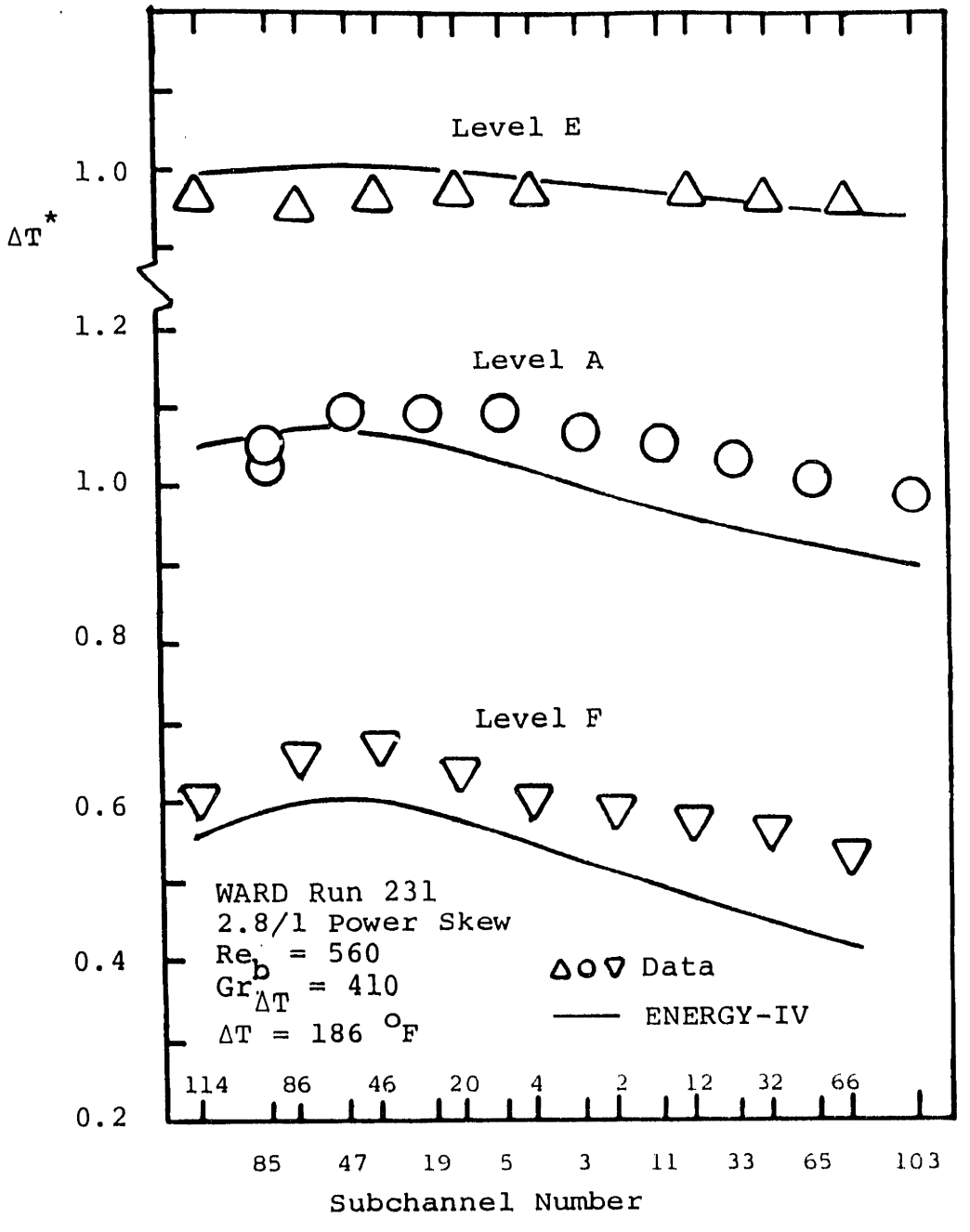

Figure 8.25 Measured and Predicted Temperature Rise for Ward Run 231

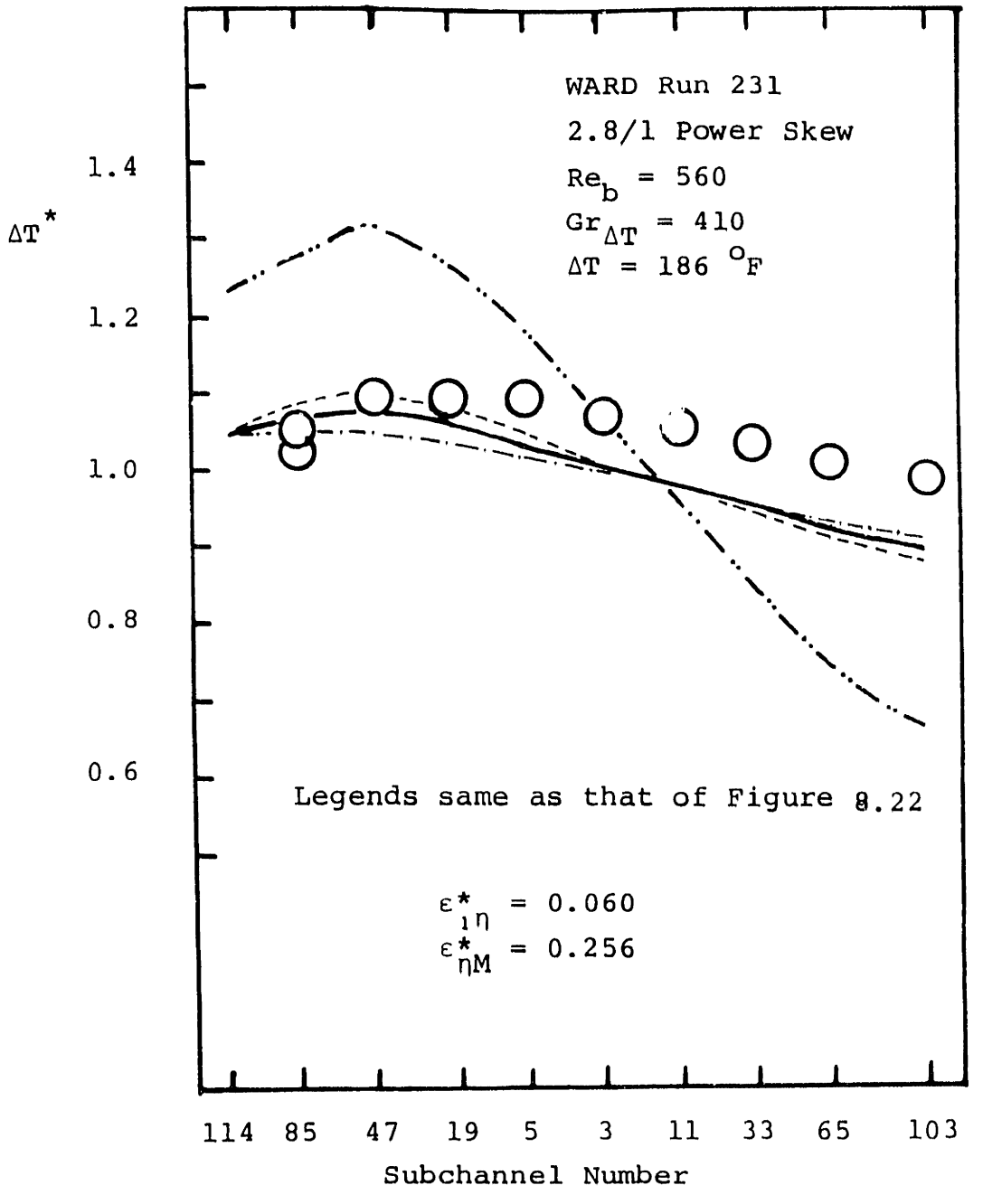

Figure 8.26 Sensitivity of ENERGY-IV Results to $\varepsilon^*_{\eta M}$ for WARD Run 231

should be reasonably predicted, and the shape of temperature profiles should be comparable. This method was found to allow securing consistent $\epsilon^*_{\eta M}$ values for all the other cases and lead to the proposed correlation, equation (8.5).

As shown in Figures 8.21 and 8.23, Th predictions of ENERGY-IV have the same degree of accuracy as that of COBRA-IV. For the high $Gr_{\Delta T}/Re_b$ case in Figure 8.25 (Run 231, $Gr_{\Delta T}/Re_b = 0.732$), the shape of the data is predicted by the ENERGY-IV; however, all the ΔT^* data at level A are higher than 1.0 indicating that an energy balance error might exist in the measured data.

For 2/1 power skew cases, Figures 8.27, 8.28, 8.29 compare the data and ENERGY-IV predictions for Runs 401, 731, and 720 respectively. The mixed convection calculations by ENERGY-IV using $\epsilon^*_{\eta F}$ only are also presented in these figures. Similar comparisons for uniform power skew cases, Run 227 and Run 732, are illustrated in Figures 8.30 and 8.31, respectively. As observed from these figures, the sensitivity of $\epsilon^*_{\eta M}$ is almost the same as for different power skews.

The ENERGY-IV code predicts all these WARD cases very well except for the level A data of 2/1 power skew cases and Run 229 (2.8 power skew). Although the maximum ΔT^*'s for these cases are well predicted, the prediction of the subchannel location of maximum temperature are shifted to the high power side, and underpredictions are found in the lower power region. This situation, however, is not observed in the prediction for other bundles with similar power skews as we will see

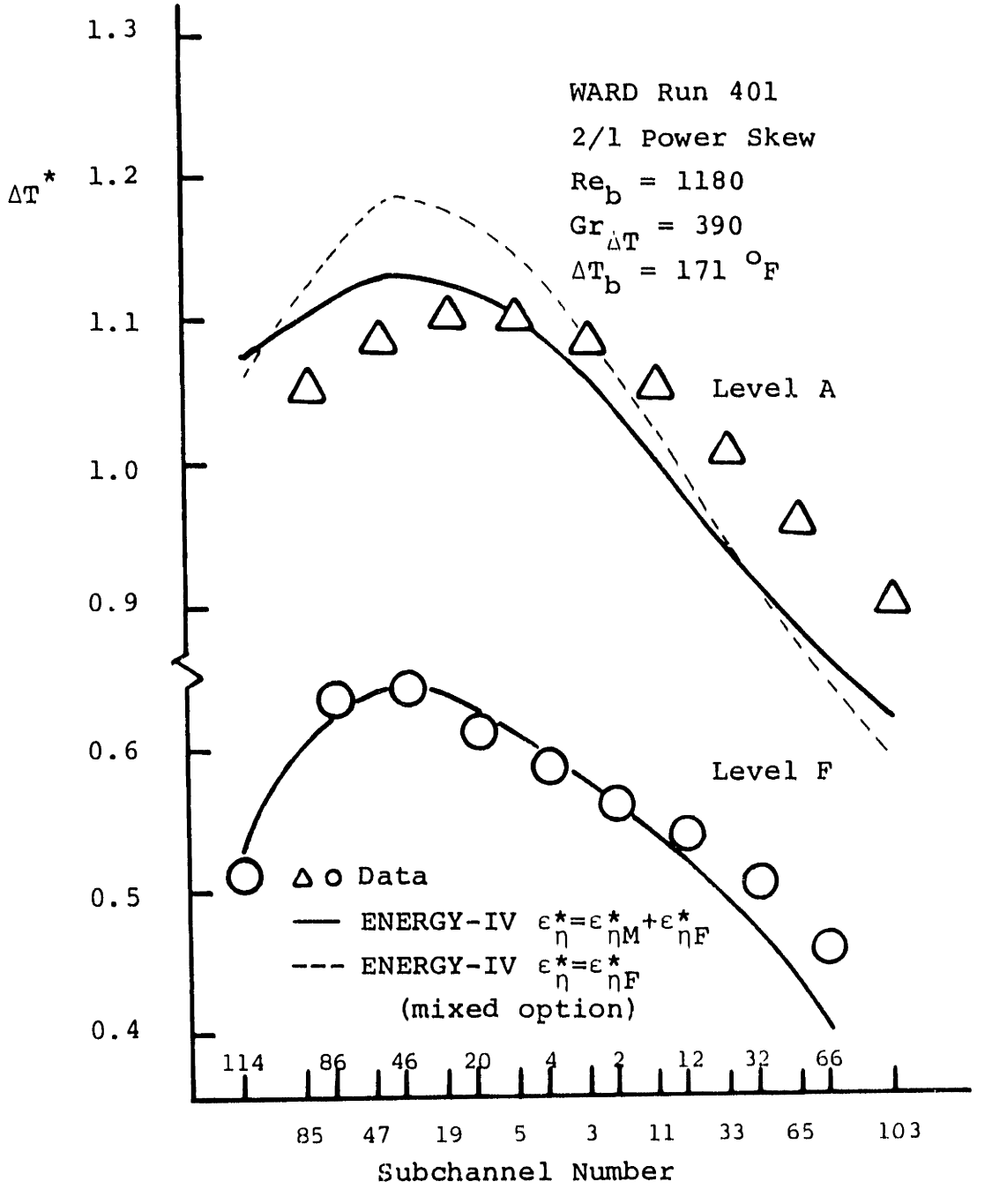

Figure 8.27 Measured and predicted Temperature for WARD Run 401

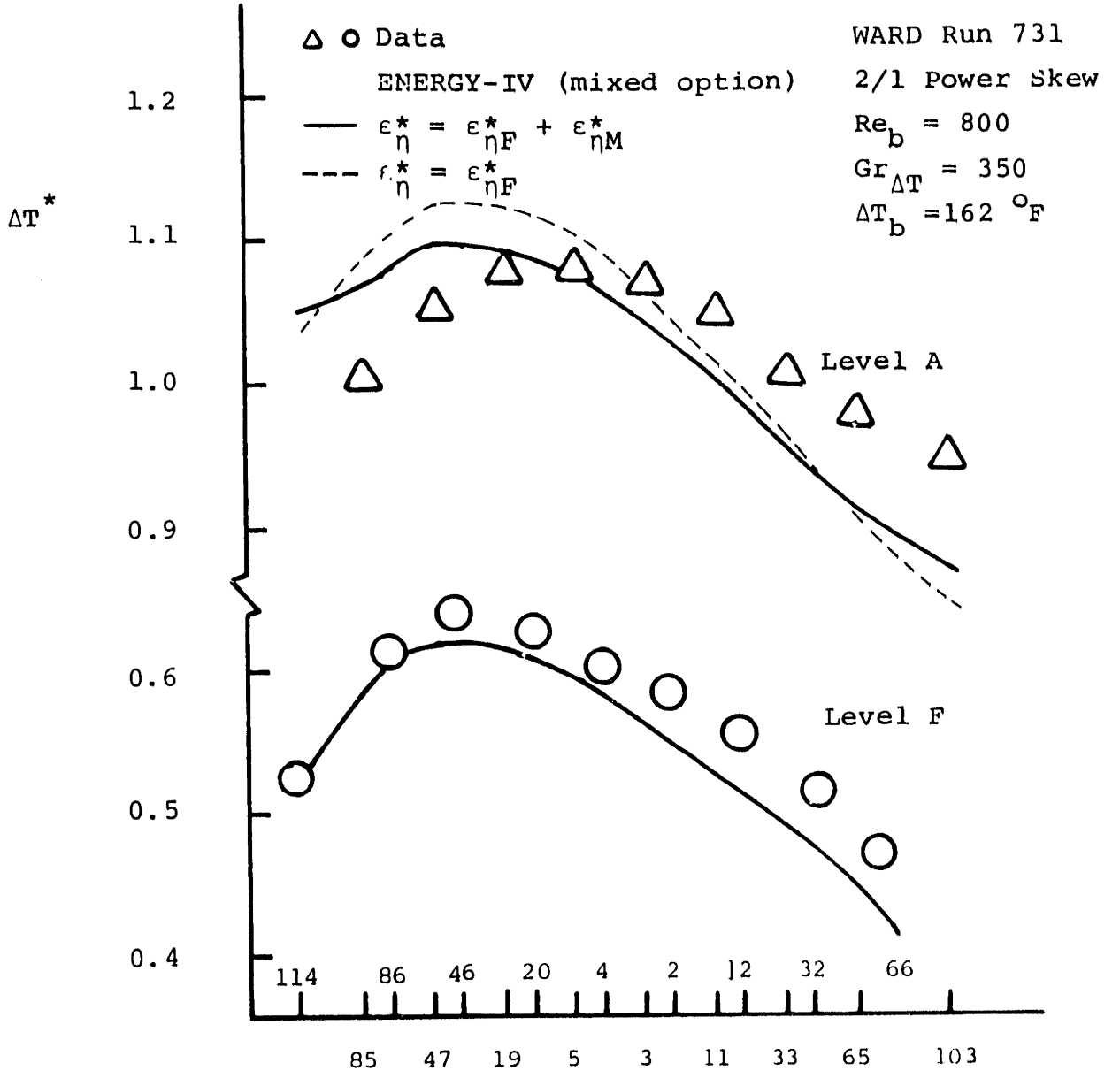

Figure 8.28 Measured and Predicted Temperature Rise for WARD Run 731

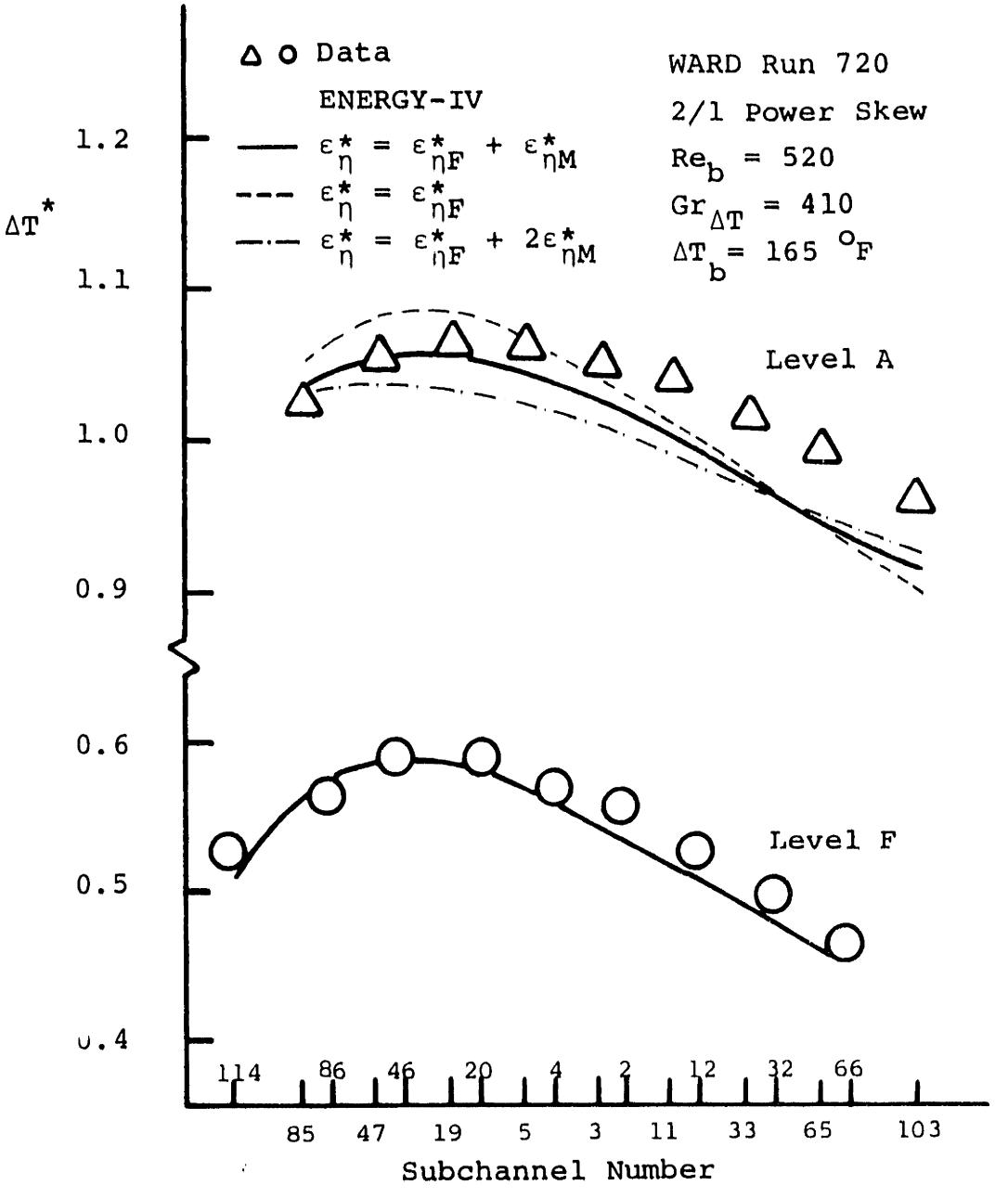

Figure 8.29 Measured and Predicted Temperature Rise for WARD Run 720

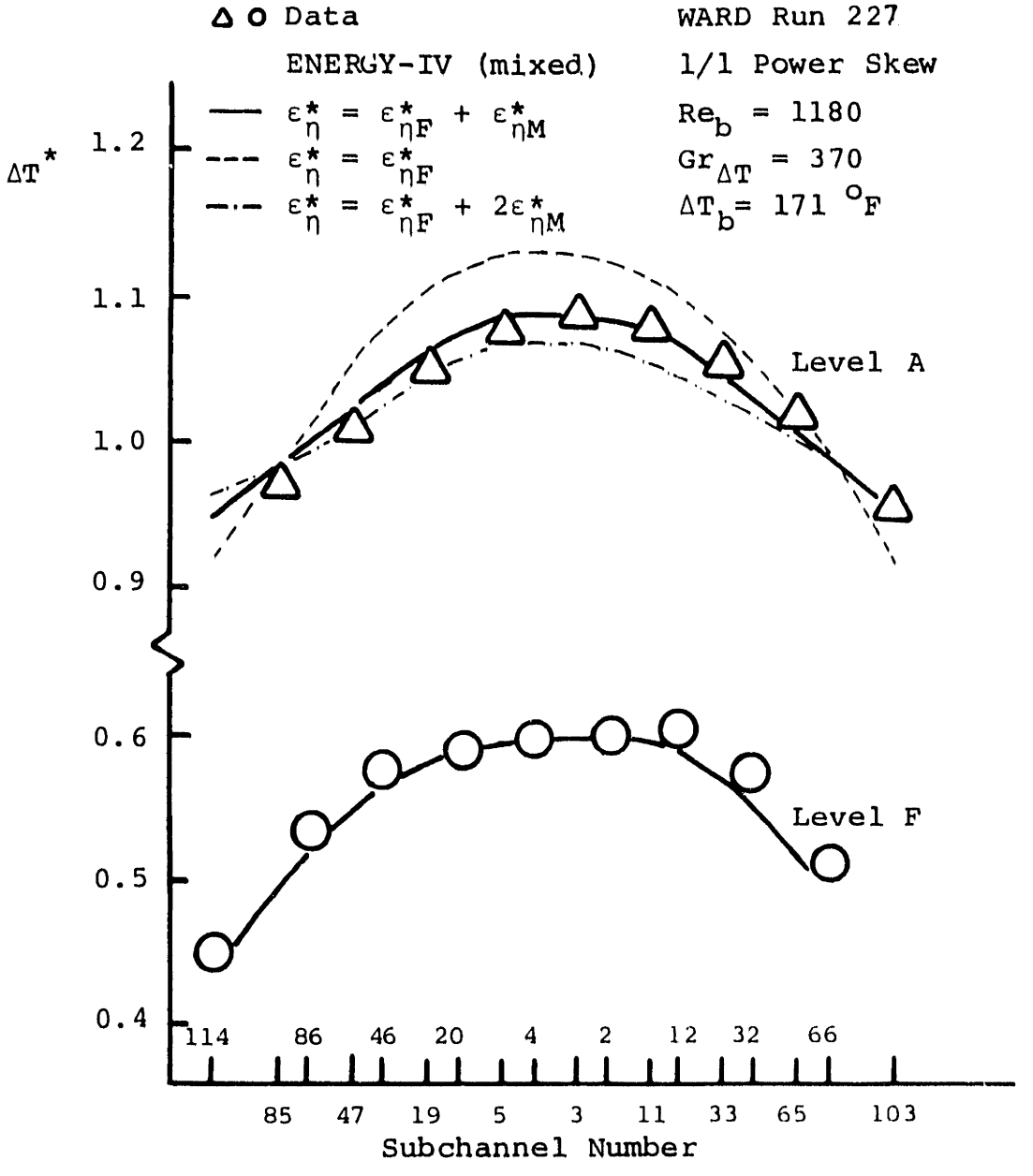

Figure 8.30 Measured and Predicted Temperature Rise for WARD Run 227

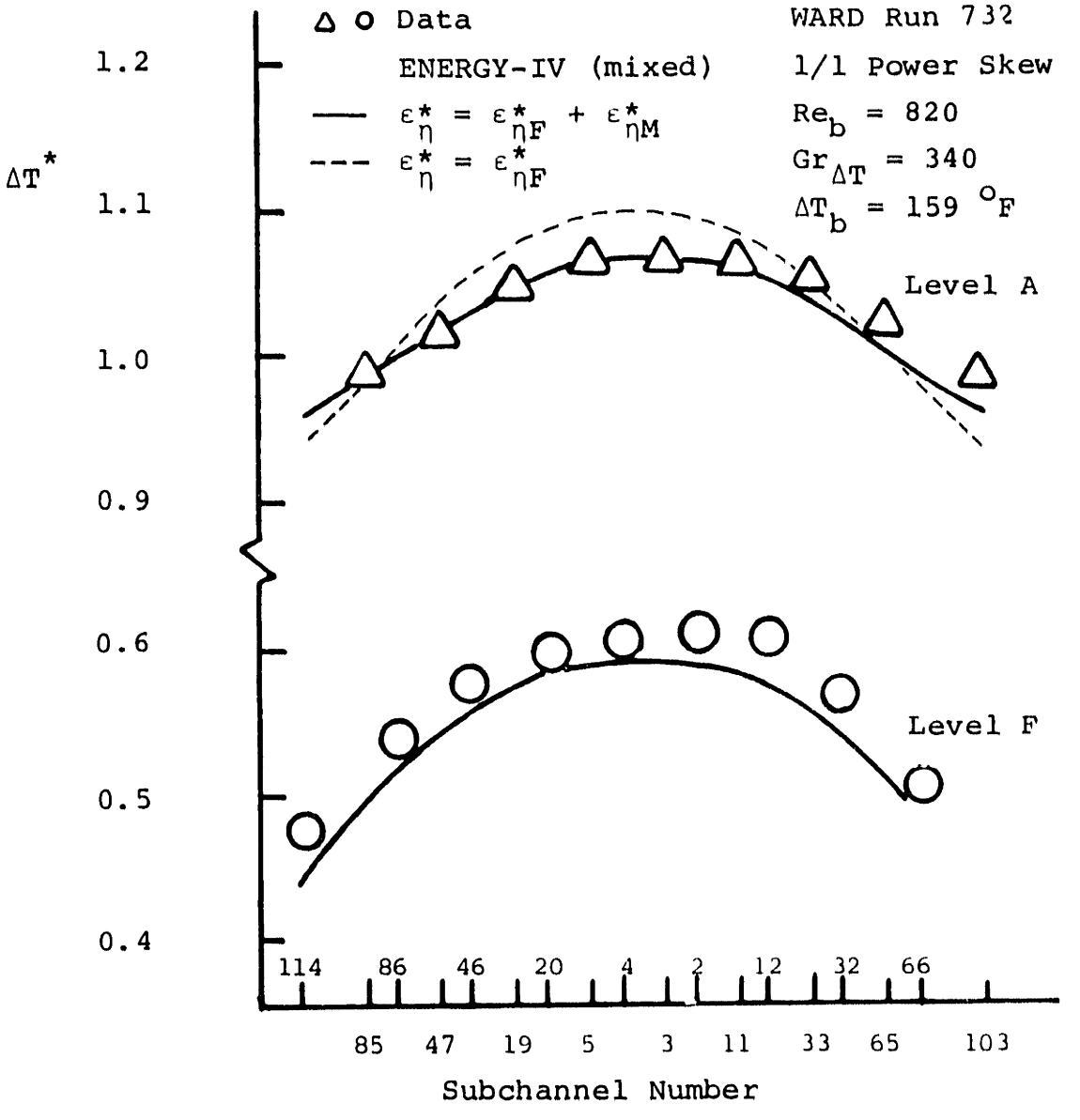

Figure 8.31 Measured and Predicted Temperature Rise for WARD Run 732

later. The maximum temperature difference between the predictions and data occurs in Run 229 with about 11% underprediction of ΔT_b in the farest subchannel of low power side. This gives about a 20°F difference. As for the peak temperature rise, the ENERGY-IV can predict within 7% of ΔT_b for all cases.

8.4.2.2 ORNL-61 pin Bundle

Figures 8.32, 8.33, 8.34 illustrate the comparisons among the data and the ENERGY-IV calculations with $\varepsilon^*_\eta = \varepsilon^*_{\eta F} + \varepsilon^*_{\eta M}$, $\varepsilon^*_\eta = \varepsilon^*_{\eta F}$, and $\varepsilon^*_\eta = \varepsilon^*_{\eta F} + 2\varepsilon^*_{\eta M}$ for ORNL 61-pin bundle Test 19 Run 105 (3/1 power skew), Test 18 Run 105 (2/1 power skew), and Test 17 Run 105 (1.5/1 power skew), respectively. The data of ΔT^* in these Figures were calculated from the temperature data corrected by energy balance considerations and the energy balance ΔT_b. The measured $(T_{out} - T_{in})$ were 290°F, 290°F, and 291°F, while the same ΔT_b from the energy balance were 308°F, 318°F, and 314°F, for these three cases, respectively. Hence energy lossed of about 6% - 9% appear to exist for the tests. The outlet temperature was measured at a distance of 61 inches from the start of the heated section of the bundle. Hence if heat loss was proportional to the averge temperature along the bundle length, the data at the 37" level could be corrected to account this loss by multiplying them by a factor of $\{1+[(37 \times$ average temperature over heated length)/(37 x average temperature over heated length + (61-37) x outlet temperature)$]$ x percentage of total energy loss$\}$.

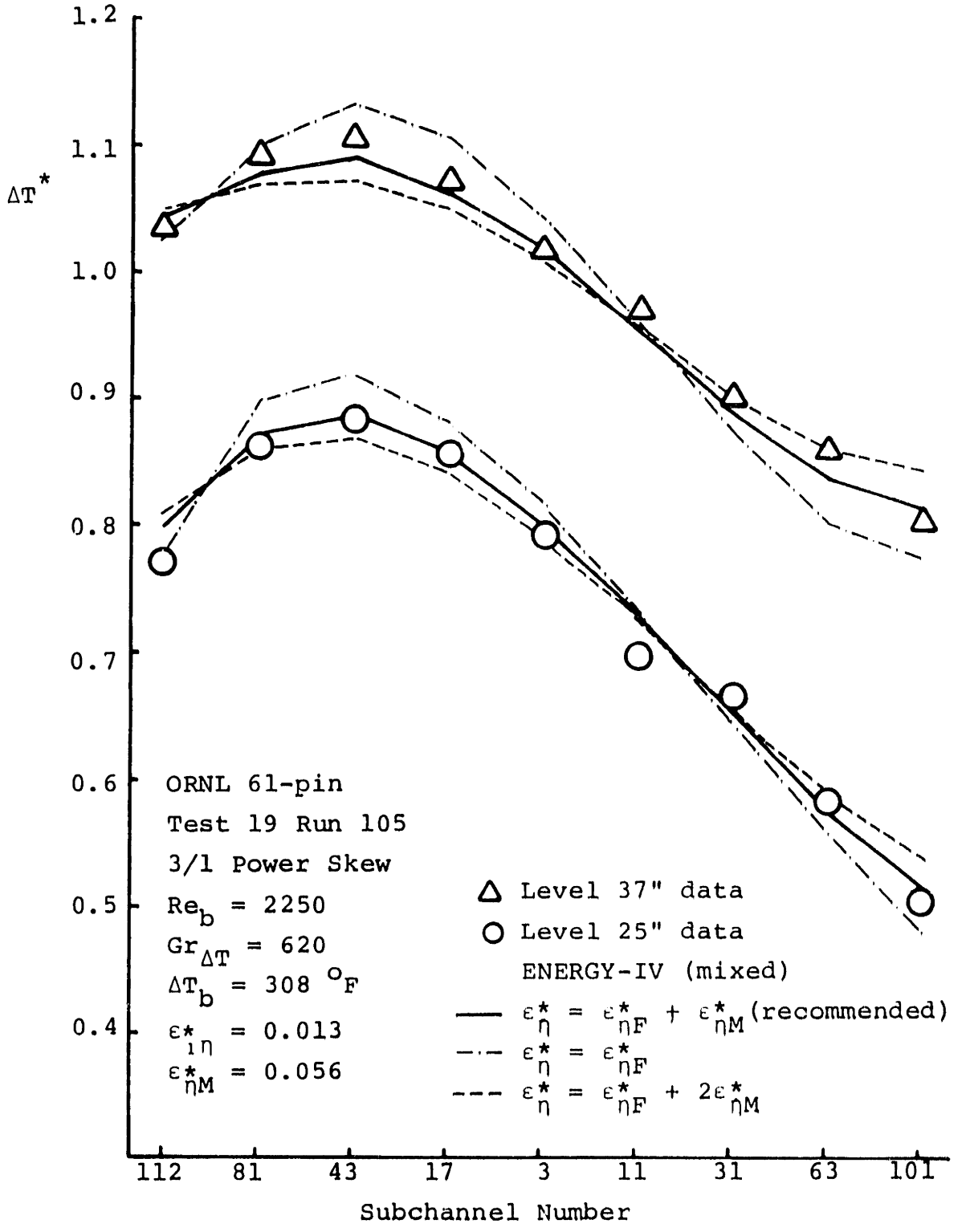

Figure 8.32 Measured and Predicted Temperature Rise for ORNL 61-pin Bundle Test 19 Run 105

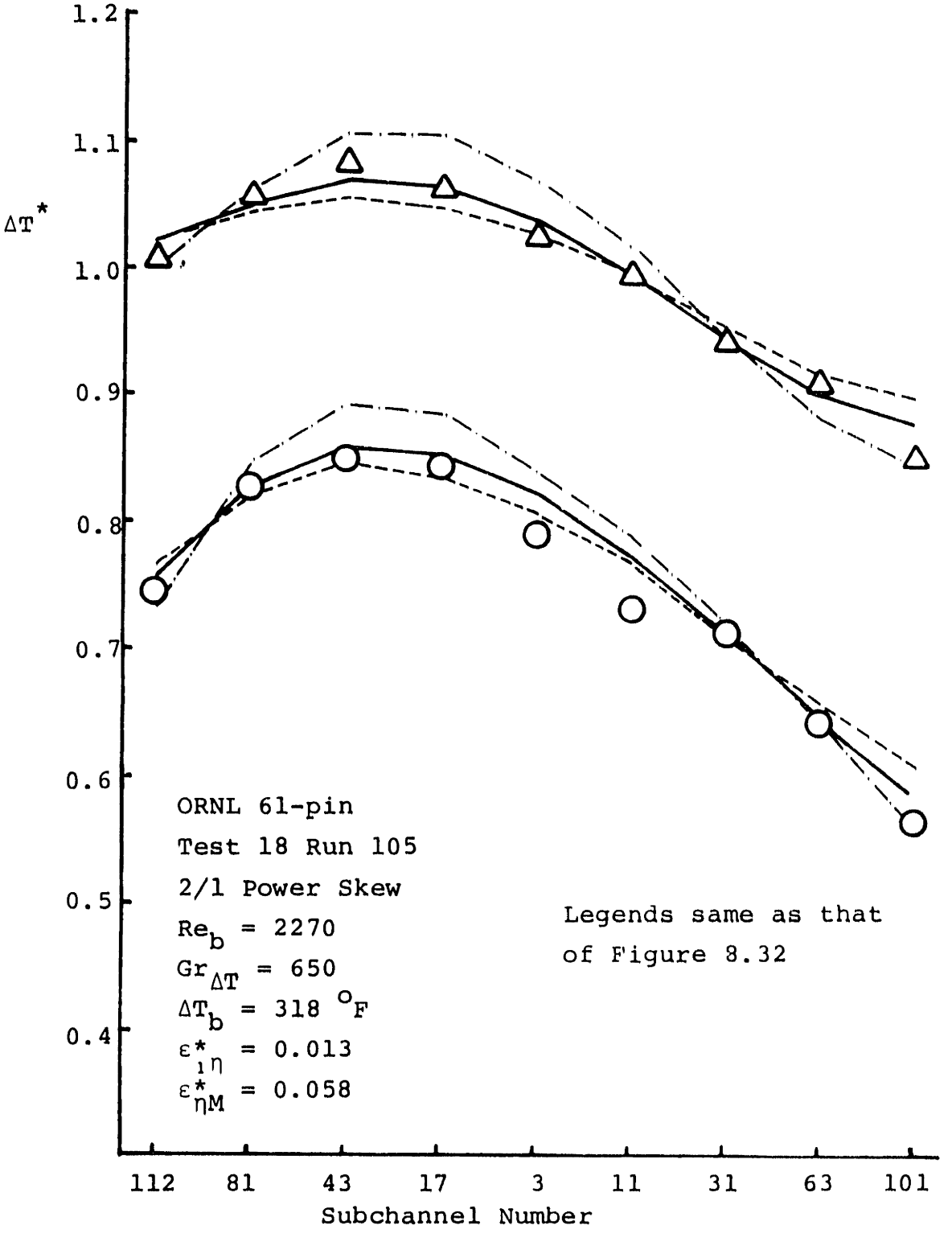

Figure 8.33 Measured and Predicted Temperature Rise for ORNL 61-pin Bundle Test 18 Run 105

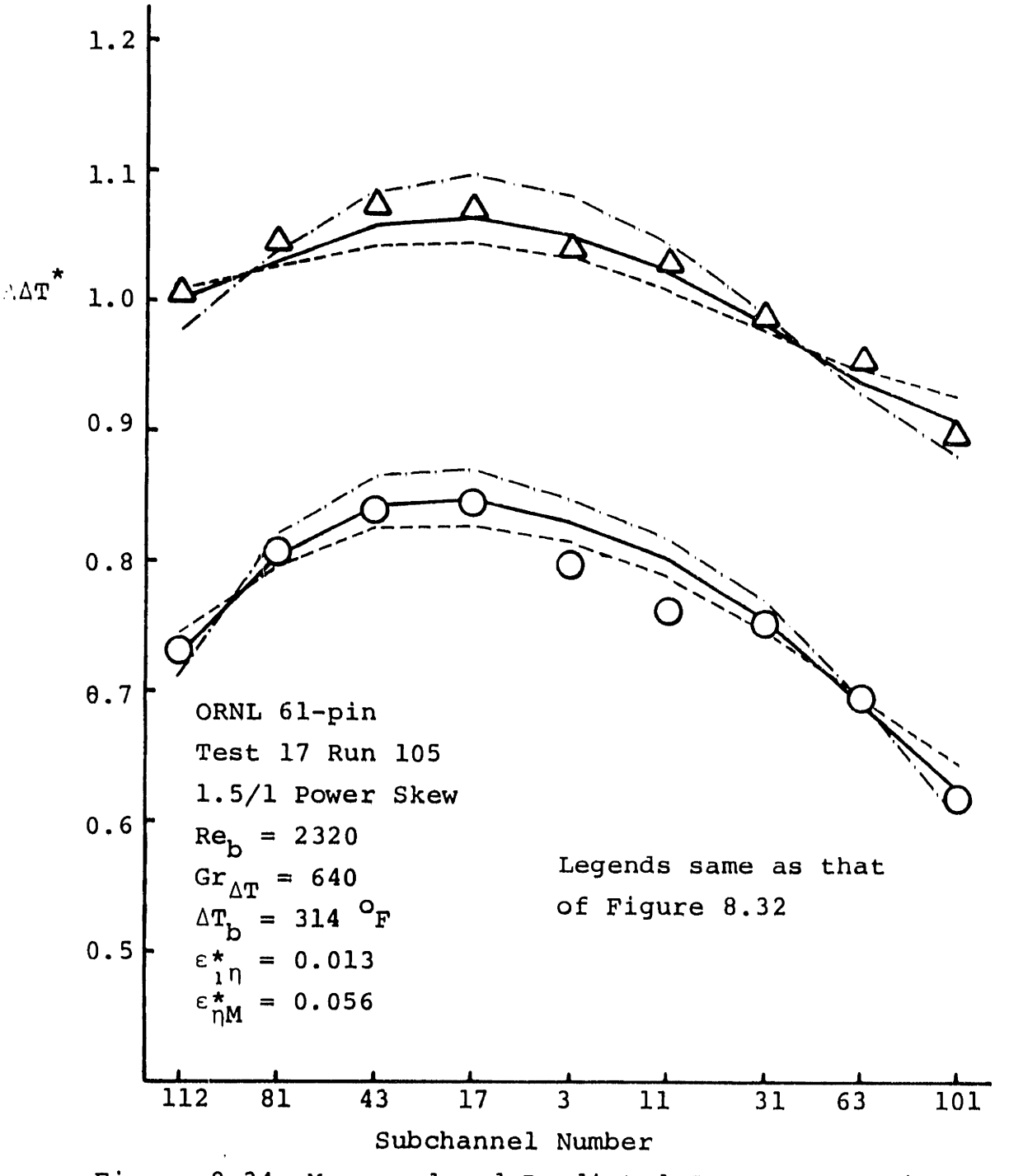

Figure 8.34 Measured and Predicted Temperature Rise for ORNL 61-pin Bundle Test 17 Run 105

A similar correction factor could be developed for data at the 25" level. Note that the profiles of the temperture distribution would not be changed by these corrections. The correction values for temperatures were about 5% of ΔT_b, i.e., about 15°F. As seen from these Figures, ENERGY-IV excellently predicts these corrected data. The maximum difference between the data and predictions is about 2% of ΔT_b, i.e., 6°F. The COBRA-WC predictions performed by Khan et al. (1981) for Test 19 Run 105 were almost exactly the same as the ENERGY-IV calculations with $\varepsilon_\eta^* = \varepsilon_{\eta F}^*$ only. Figure 8.35 illustrates the COBRA-WC results, the ENERGY-IV with $\varepsilon_\eta^* = \varepsilon_{\eta F}^*$ only, and the ΔT^* calculated from the reportedtemperature data (not corrected by above heat balance method). Figure 8.36 illustrates similar comparisons for uniform power skew case, Test 12 Run 114.

8.4.2.3 Toshiba Bundle

Figure 8.37 illustrates the comparisons among the data, the ENERGY-IV calculations and the COBRA calculations for Toshiba 37-pin tests with different power skews at Re_b near 3000. The sensitivity of predicted ΔT^* to variations of $\varepsilon_{\eta M}^*$ for these tests are illustrated in Figure 8.38. Figure 8.39 illustrate comparisons similar to Figure 8.36 for the low flow rate tests, Re_b = 900 to 1500. The ENERGY-IV predicts all these data as well as COBRA does as observed from these comparisons. The maximum temperature rises are well predicted by the ENERGY-IV, except that an underprediction of 4% ΔT_b was observed in Run F37P20. The maximum ΔT^* difference between predictions and data

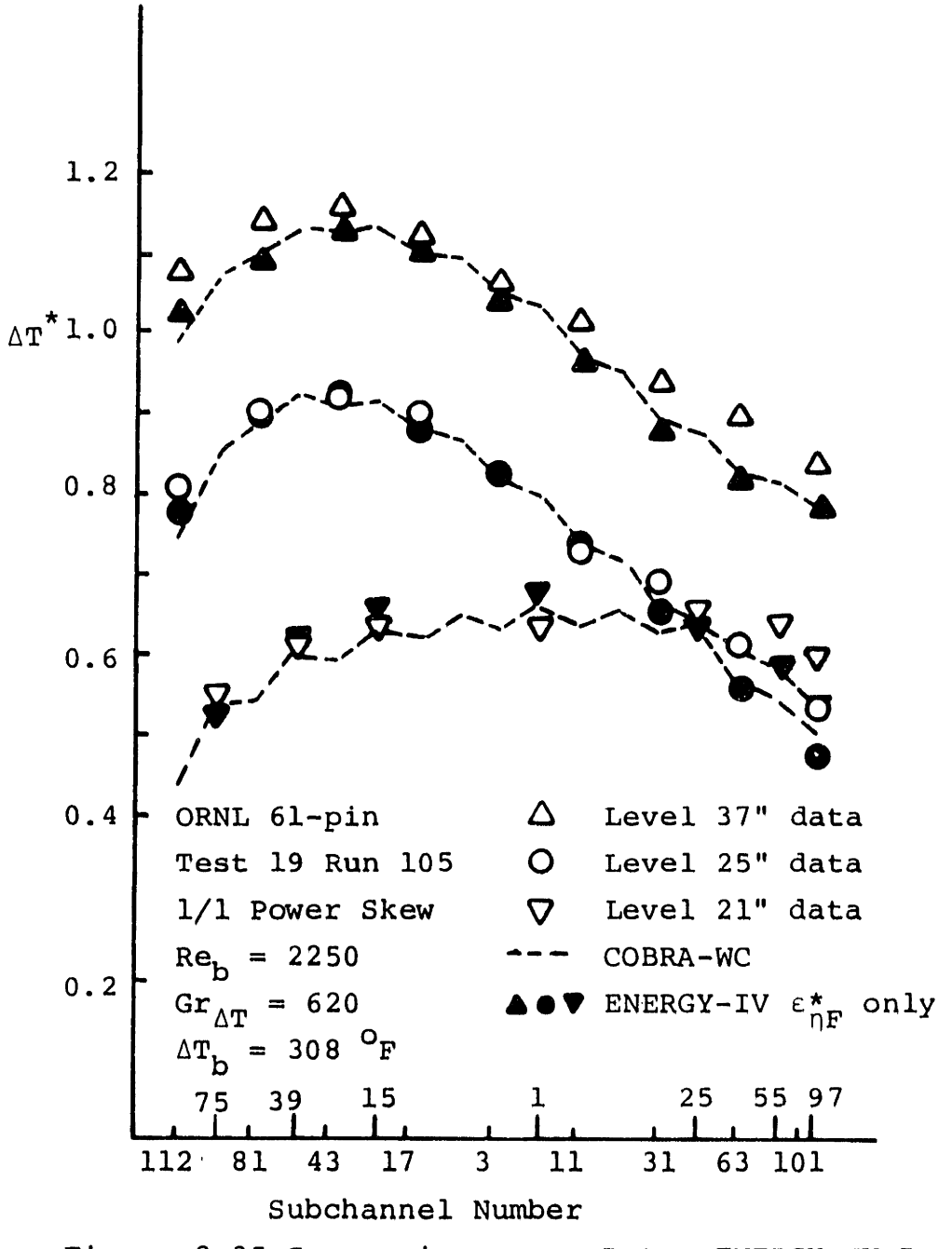

Figure 8.35 Comparsion among Data, ENERGY-IV Results ($\varepsilon^*_{\eta F}$ only) and COBRA-WC Results for Test 19 Run 105

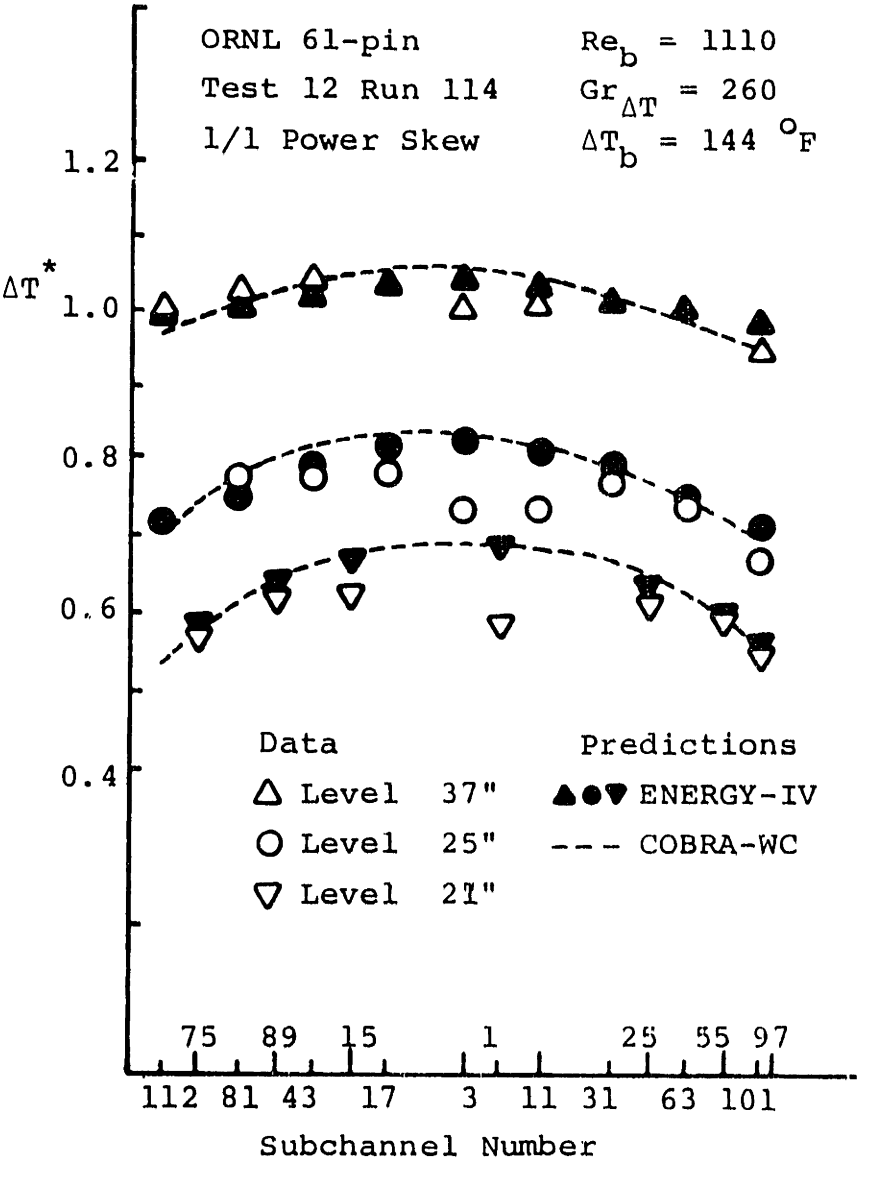

Figure 8.36 Measured and Predicted Temperature Rise for ORNL 61-pin undle Test 12 Run 114

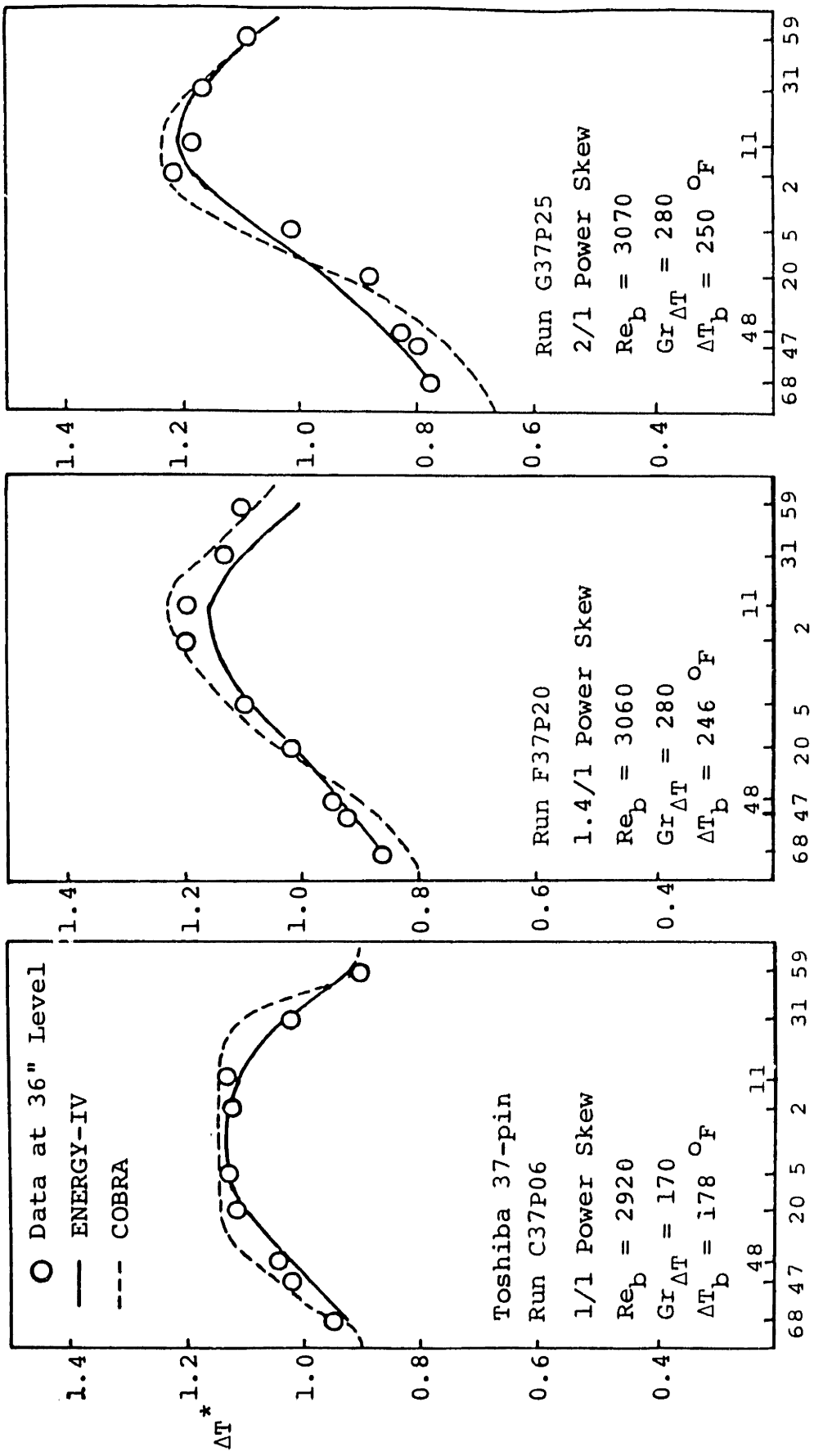

Figure 8.37 Measured and Predicted Temperature Rise for Toshiba 37-pin Test at Re_b=3000

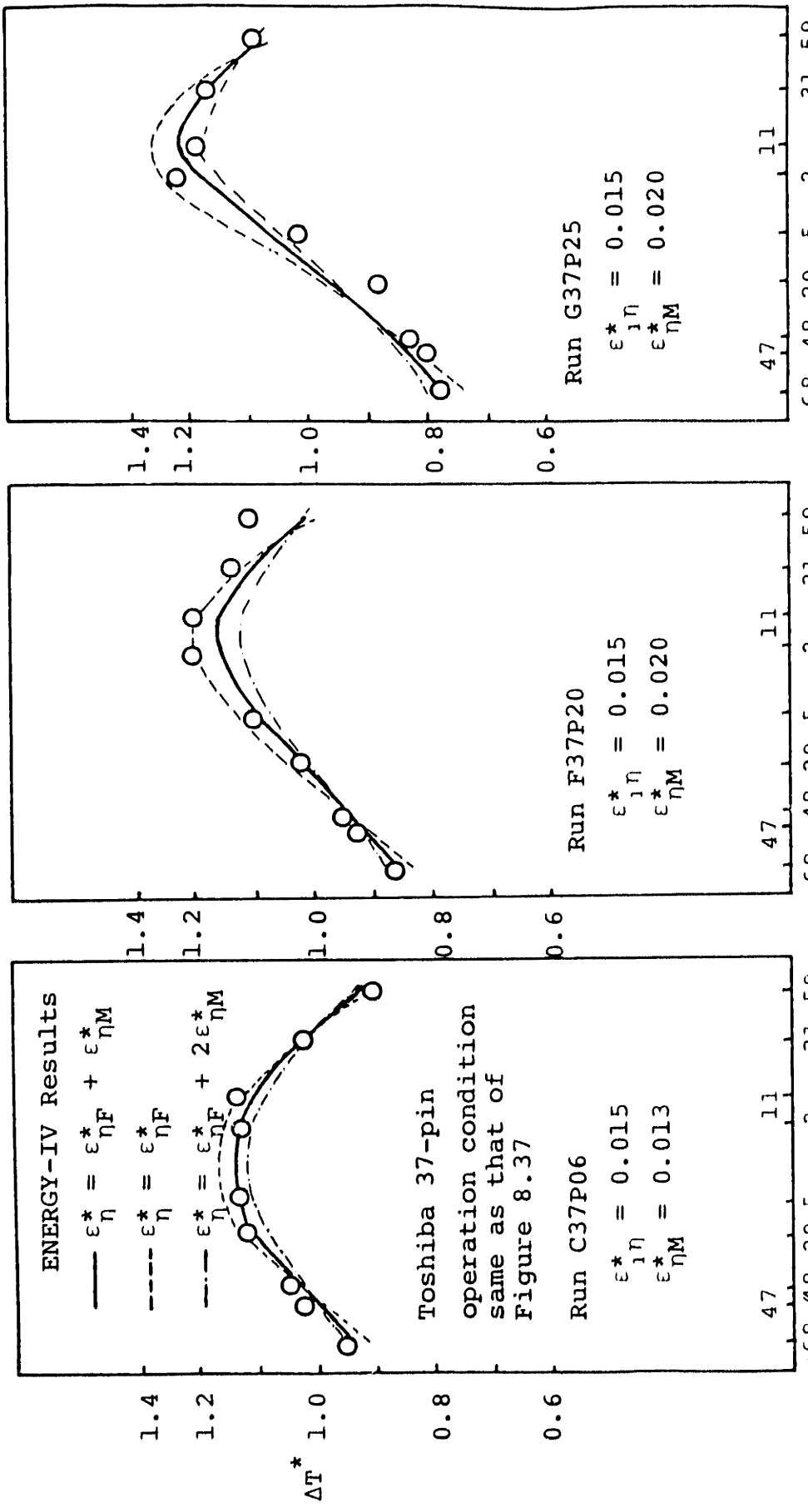

Figure 8.38 Sensitivity of the ENERGY-IV Results to $\varepsilon^*_{\eta M}$ for Toshiba Tests

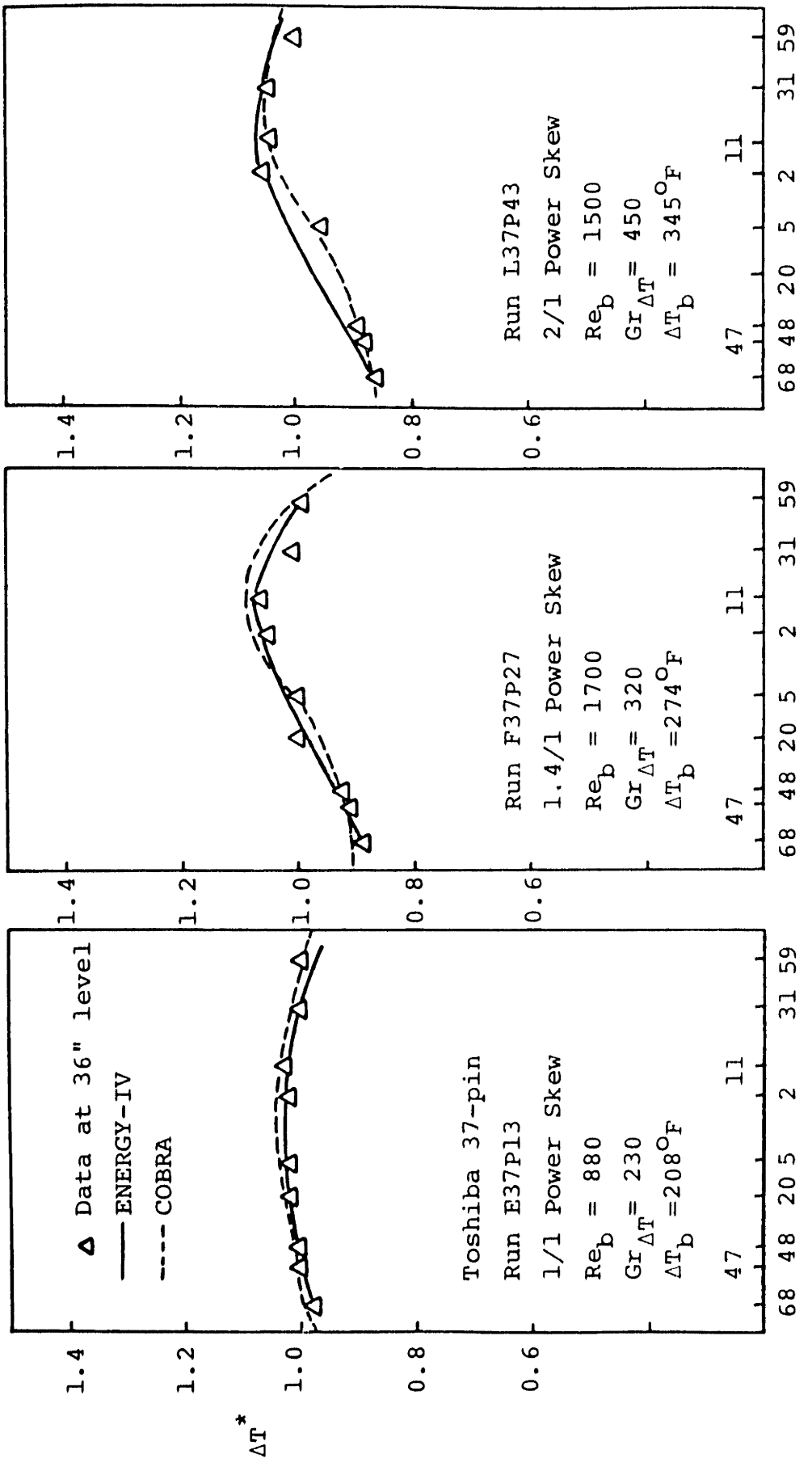

Figure 8.39 Measured and Predicted Temperature Rise for Toshiba 37-pin Low Flow Tests

occured in the low power region of Run G37P25. A 9% difference of ΔT^* was found in subchannel 20 in this case. This gives a temperature difference of 22.5°F.

8.4.2.4 Grenoble (FETUNA) Bundle

Figure 8.40 illustrates the comparisons among the data, the ENERGY-IV predictions and the predictions of the investigators' computer code, BACCHUS [Rameau (1984)], for the uniform power skew of FETUNA tests with different Re_b. The data were better predicted by ENERGY-IV than by BACCHUS. Figure 8.41 compares the ENERGY-IV predictions to the data for two power skews, 2.5/1 and 1/1 at Re_b = 1790. BACCHUS results are not available for the 2.5/1 power skew case since it is only a 2D code. About a 10% ΔT_b difference between ENERGY-IV predictions and data were found in the 2.5/1 power skew case.

8.4.3 Conclusions

The validation for the ENERGY-III code for the mixed convection condition has been illustrated in the previous subsections. The ranges of geometries and power skews are the same as that considered for the forced convection condition. The mixed convection operation conditions examined range from Re_b = 4400 to Re_b 520 and $Gr_{\Delta T}$ = 650 to $Gr_{\Delta T}$ = 170. The ranges of the parameter $(Gr_{\Delta T}/Re_b)$ is 0.058 to 0.732.

An additional mixing mechanism due to thermal plume effects was considered in the mixed convection flow regime. These thermal plumes

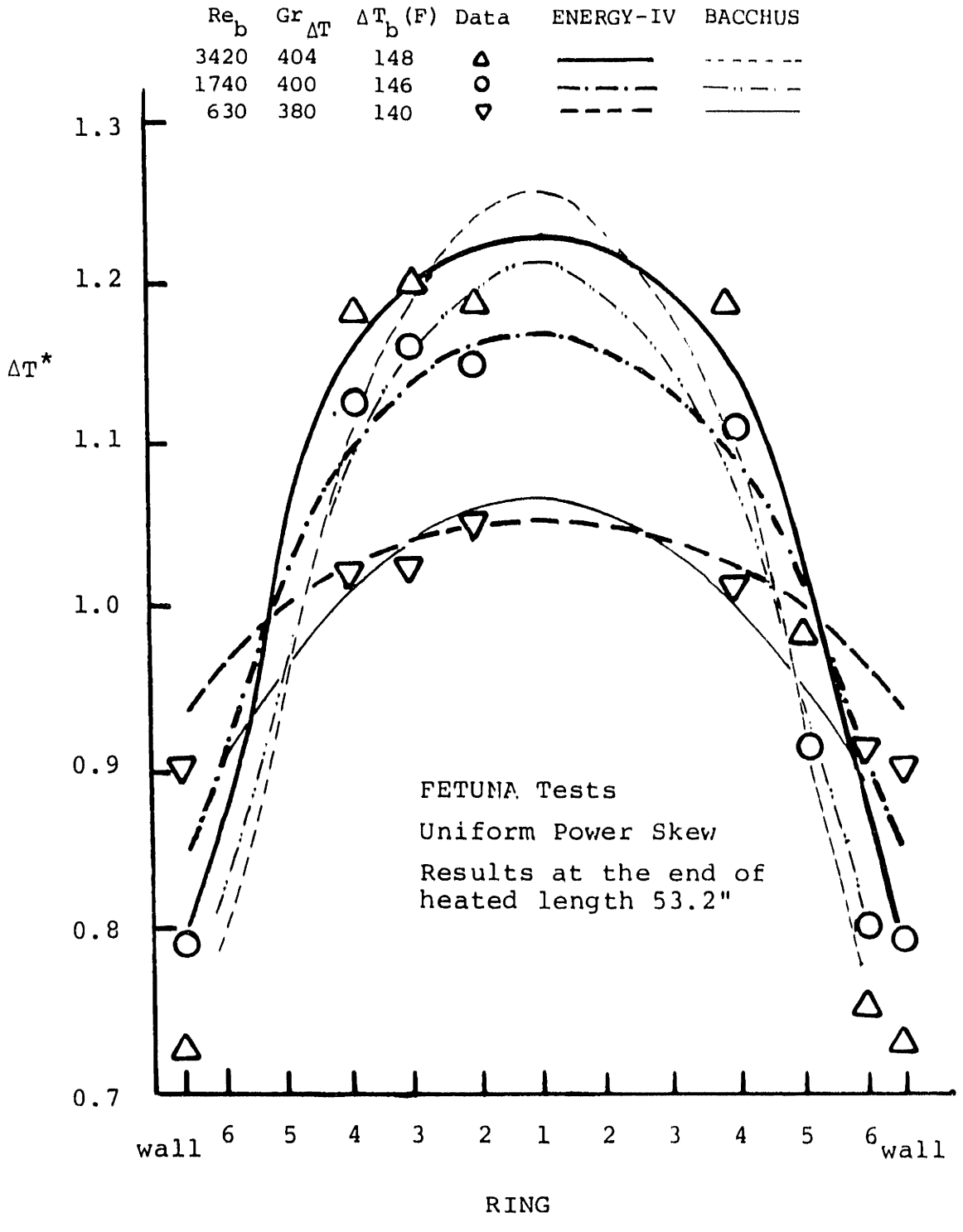

Figure 8.40 Measured and Predicted Temperature Rise for FETUNA Tests with Uniform Power Skew

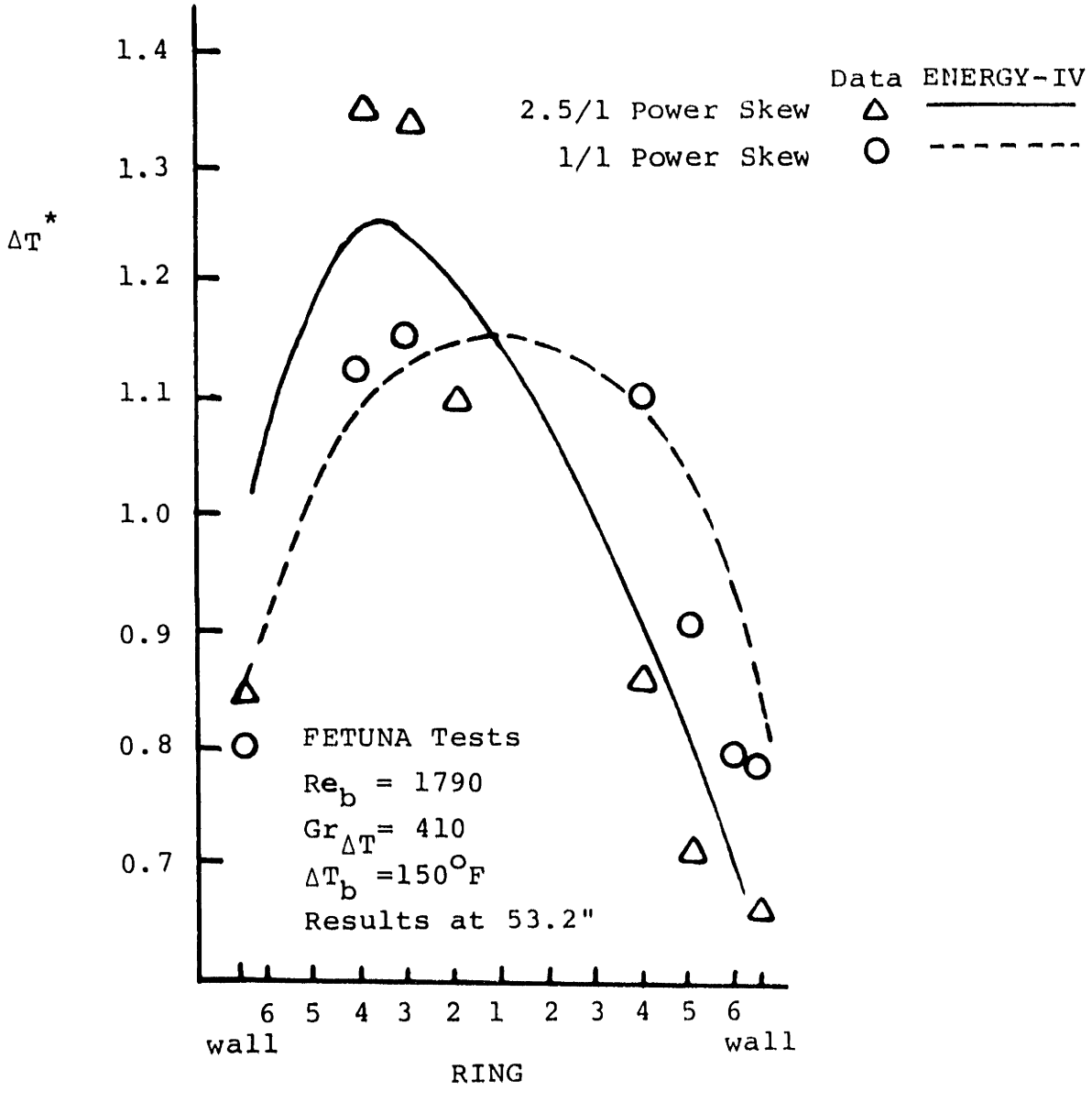

Figure 8.41 Measured and Predicted Temperature Rise for FETUNA Tests at Re_b = 1740

are caused by buoyancy effects when $Gr_{\Delta T}/Re_b$ becomes significant, say ≥ 0.04. To match the ENERGY-IV calculations to the data base in Table 8.7, the following correlation was found to be satisfactory,

$$\varepsilon^*_{\eta M} = 0.1 \left(\frac{c}{D}\right)^{-0.5} \left(\frac{Gr_{\Delta T}}{Re_b}\right) \tag{8.5}$$

The forced convection mixing parameter $\varepsilon^*_{1\eta}$ and $\varepsilon^*_{2\eta}$ are enhanced by $\varepsilon^*_{\eta M}$ when the mixed convection option of the ENERGY-IV code is used.

With these mixing parameters and the conduction shape factor suggested from base rod results, the predictions of ENERGY-IV in the mixed convection condition were confirmed to have the same degree of accuracy as that of COBRA. The peak temperature rises were predicted within 7% of the bundle average temperature rise. The maximum difference between predictions and data occured in the lower power region of the power skew cases. About 10% differences between measured and predicted ΔT^* were observed for the most severe cases. This gave the maximum difference between predicted temperture and data a value of 23°F.

8.5 Relative Importance of Energy Transfer Mechanisms in the Mixed Convection Condition

As discussed in the last section, four energy transfer mechanisms exist in the mixed convection flow regime, i.e., wire sweeping and turbulent mixing, molecular conduction, thermal plume mixing, and convective energy transfer due to flow redistribution. In this

section, the relative importance of the mechanisms will be investigated, and the regimes in which these parameters dominate will be identified.

For the molecular conduction, a parameter called the interior dimensionless thermal diffusivity, α_l^*, comparable to $\varepsilon_{l\eta}^*$, can be established from the energy equation for interior subchannels,(c.f. equation (2.27))

$$\Delta h_l = \frac{Q_l \Delta z}{\rho v_l} + \frac{c\Delta z}{A_l}\left[\left(\frac{\kappa\alpha}{v_l \eta}\right) + \varepsilon_{l\eta}^*\right](h_i + h_j + h_k - 3h_l) \qquad (2.27)$$

and

$$\alpha_l^* \equiv \frac{\kappa\alpha}{v_l \eta} \qquad (8.6)$$

Expressing α_l^* in dimensionless parameters, we get

$$\alpha_l^* = \frac{\frac{\kappa\alpha}{\eta}}{\left(\frac{v_b De_b}{\nu}\right)\left(\frac{v_l}{v_b}\right)\left(\frac{\nu}{De_b}\right)} = \frac{1}{Re_b}\frac{1}{P_r}\left(\frac{\kappa}{X_l}\right)\left(\frac{De_b}{\eta}\right) \qquad (8.7)$$

For the thermal plume mixing, a correlation equation (8.5) has been developed to evaluate $\varepsilon_{\eta M}^*$. Note that $\varepsilon_{\eta M}^*$ is dependent upon both $Gr_{\Delta T}$ and Re_b, while $\varepsilon_{l\eta}^*$ and α_l^* are only dependent upon Re_b. These parameters have similar meaning relative to energy transfer and can be directly compared to each other. Table 8.8 describes these parameters as functions of Re_b for the blanket assembly with a typical $Gr_{\Delta T}$ of 400 and fuel assembly with a typcial $Gr_{\Delta T}$ of 600.

Regarding convective transfer by flow redistributive (FRD), no obvious parameter is available. The energy transfer by the flow

Table 8.8 Comparisons among $\varepsilon^*_{l\eta}$, α^*_l and $\varepsilon^*_{\eta M}$ for Balnket and Fuel Assemblies

	$\left(\frac{De_b}{\eta}\frac{\kappa}{\bar{X}_l}\frac{1}{P_r}\right)$	$Gr_{\Delta T}$		Re_b					
				2×10^4	10^4	5×10^3	2×10^3	10^3	5×10^2
Blanket (WARD)	185.6	400	$\varepsilon^*_{l\eta}$	0.122	0.122	0.120	0.100	0.075	0.055
			α^*_l	0.009	0.019	0.037	0.093	0.186	0.371
			$\varepsilon^*_{\eta M}$	0.007	0.014	0.028	0.070	0.140	0.280
Fuel (ORNL)	80.5	600	$\varepsilon^*_{l\eta}$	0.016	0.016	0.016	0.013	0.012	0.011
			α^*_l	0.004	0.008	0.016	0.040	0.080	0.161
			$\varepsilon^*_{\eta M}$	0.006	0.012	0.024	0.060	0.120	0.240

redistribution is a global phenomenon characterized by the cross flow enthalpy, H^*, and cross flow velocity, V^*, in equations (2.47) and (2.48), respectively. Here, a simple method is suggested to estimate the relative importance of energy transfer by flow distribution, FRD, to ε_η^* by examining the changes in maximum ΔT^* due to these two mechanisms. From the sensitivity study of $\varepsilon_{\eta M}^*$ in the mixed convection option, the changes of maximum ΔT^* due to the changes of ε_η^* can be estimated. For each of the cases, the changes of the maximum ΔT^* at the end of heated length due to flow redistribution effects can be estimated by running ENERGY-IV with both the forced convection option (no flow distribution) and with mixed convection option (with flow redistribution) using same values of ε_η^*, e.g., $\varepsilon_{1\eta}^*$ and $\varepsilon_{2\eta}^*$ were used for both runs. The relative importance in energy transfer of FRD to $\varepsilon_{1\eta}^*$ could then be estimated by dividing the change of maximum ΔT^* due to FRD effects to the change of maximum ΔT^* due to one increment of $\varepsilon_{1\eta}^*$ in ε_η^*, which is estimated by (change of maximum ΔT^* due one increment of $\varepsilon_{\eta M}^*$)$\times(\varepsilon_{1\eta}^* / \varepsilon_{\eta M}^*)$.

This relative importance of FRD to $\varepsilon_{1\eta}^*$ was found to be quite insensitive to both bundle geometries and power skew. On the other hand, it is a strong function of $Gr_{\Delta T}/Re_b$. Table 8.9 illustrates the changes of maximum ΔT^* due to FRD and one $\varepsilon_{1\eta}^*$ increment effects and the relative importance of FRD compared to $\varepsilon_{1\eta}^*$ as a function of $Gr_{\Delta T}/Re_b$.

Based on the relative importance of FRD compared to $\varepsilon_{1\eta}^*$ determined in the previous paragraph and the expressions for α_1^* and $\varepsilon_{\eta M}^*$ (c.f. Table 8.8), the relative importance of each of these four energy

Table 8.9 Relative Importance on Energy Transfer of Flow Redistribution to $\varepsilon^*_{l\eta}$

$\frac{Gr_{\Delta T}}{Re_b}$	Change of maximum ΔT^* per $\varepsilon^*_{l\eta}$	Change of maximum ΔT^* due to FRD†	Relative Importance of FRD to $\varepsilon^*_{l\eta}$
0.09	0.15	0.05	0.33
0.34	0.03	0.18	6.0
0.73	0.01	0.21	21.0

† Difference between ENERGY-IV result with forced convection option and that with mixed convection option using same $\varepsilon^*_\eta = \varepsilon^*_{\eta F}$

transfer mechanisms compared to $\varepsilon^*_{l\eta}$ as the base are illustrated in Figures 8.42 and 8.44 for blanket assembly and fuel assembly, respectively. At very high Re_b operation, only $\varepsilon^*_{l\eta}$ is important for energy transfer. As Re_b decreases, conduction, thermal plume and FRD become important. At very low Re_b operation, FRD becomes so important that all the other mechanisms are relatively insignificant. Note that the FRD and $\varepsilon^*_{\eta M}$ curves will shift to higher Re_b as $Gr_{\Delta T}$ increases as shown in Figure 8.43 for a blanket assembly.

Using Figures 8.42 and 8.43, the relative effect on energy transfer for each mechanism with respect to the total effect of all four energy transfer mechanisms as function of Re_b and $Gr_{\Delta T}$ can be estimated for blanket assembly. For example, Figure 8.45 illustrates the conduction effect relative to the total effect as a function of Re_b for blanket assembly at $Gr_{\Delta T} = 400$. The way to calculate (effect of α^*_l/total effect) is simply to divide the value of $(\alpha^*_l/\varepsilon^*_{l\eta})$ by the sum of the values of all four affects, e.g., at $Re_b = 1000$, $\alpha^*_l/\varepsilon^*_{l\eta} = 2.5$, $\varepsilon^*_{\eta M}/\varepsilon^*_{l\eta} = 1.9$, $FRD/\varepsilon^*_{l\eta} = 7.5$, hence $2.5/(2.5+1.9+7.5+1) = 19.4\%$. Similar curves can be constructed with different values of $Gr_{\Delta T}$ from Figure 8.43. By this method the two regions where α^*_l and $\varepsilon^*_{\eta M}$ are significant were identified in Figures 8.46 and 47 for blanket and fuel assemblies, respectively. A 15% or greater effect with respect to the total effect of energy transfer was uses as the criterion of significance.

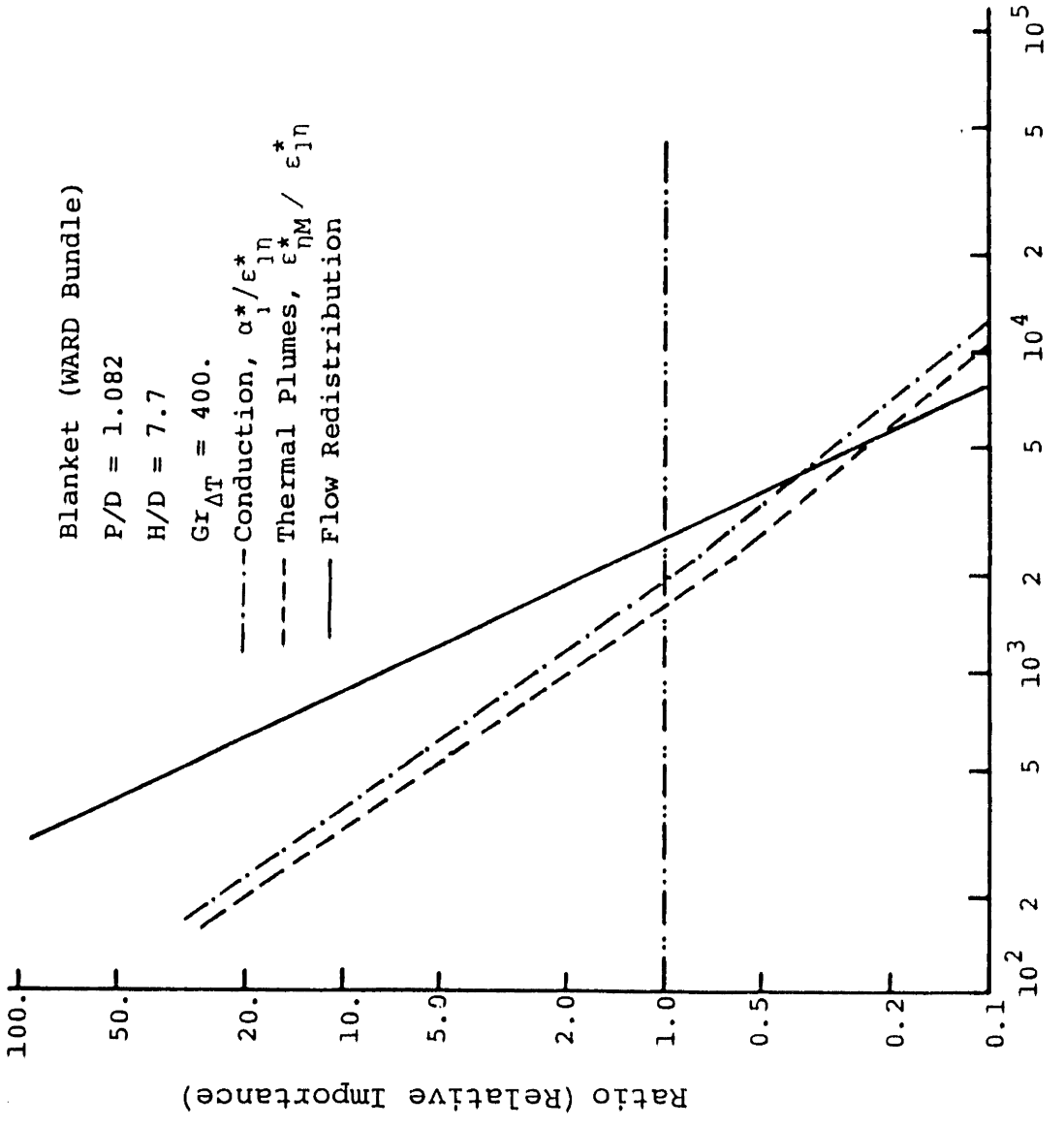

Figure 8.42 Relative Importance of Energy Transfer Mechanisms for Blanket Assembly

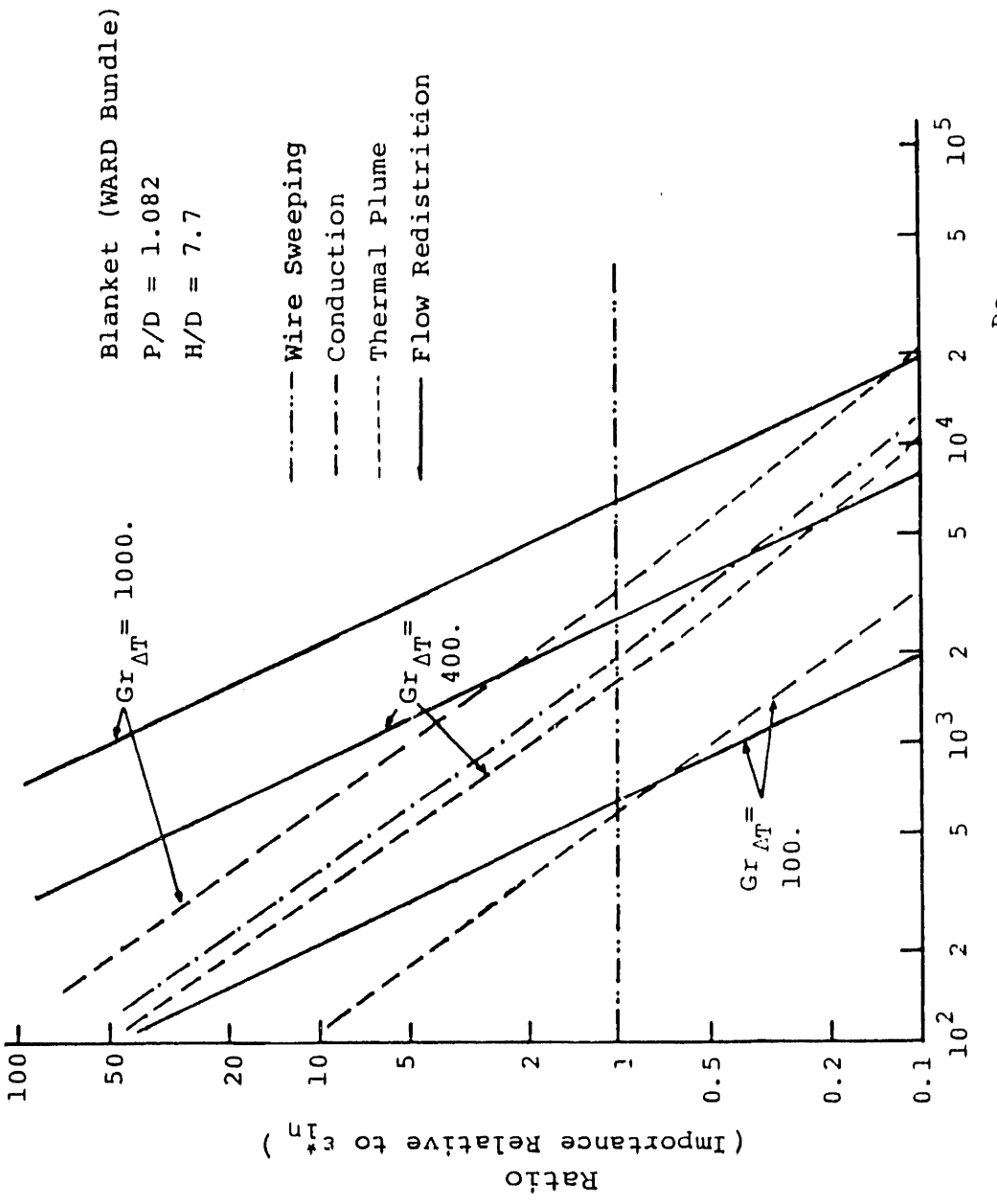

Figure 8.43 Relative Important of Energy Transfer Mechanisms for Blanket Bundle with Different $Gr_{\Delta T}$

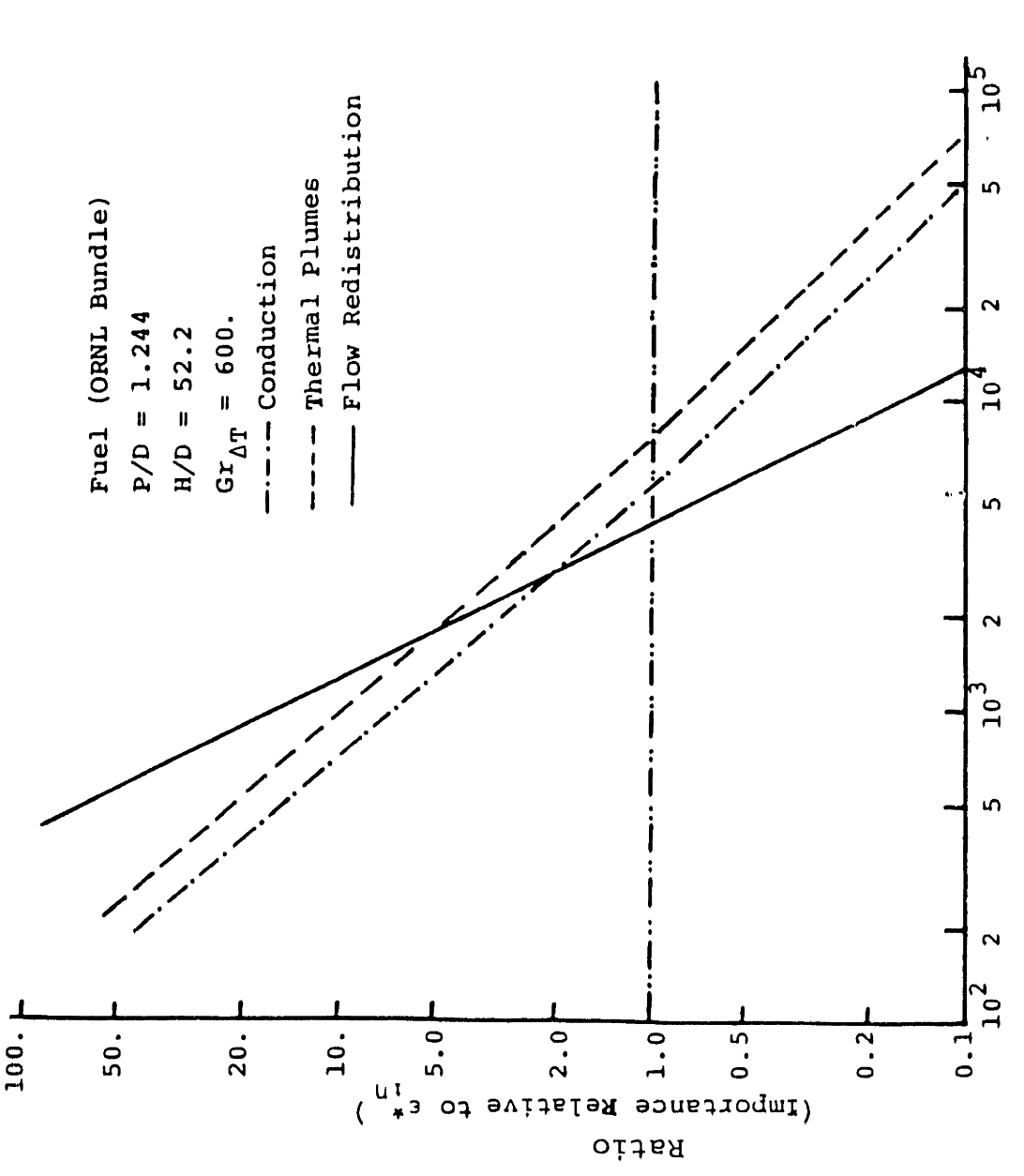

Figure 8.44 Relative Importance of Energy Transfer Mechanisms for Fuel Assembly

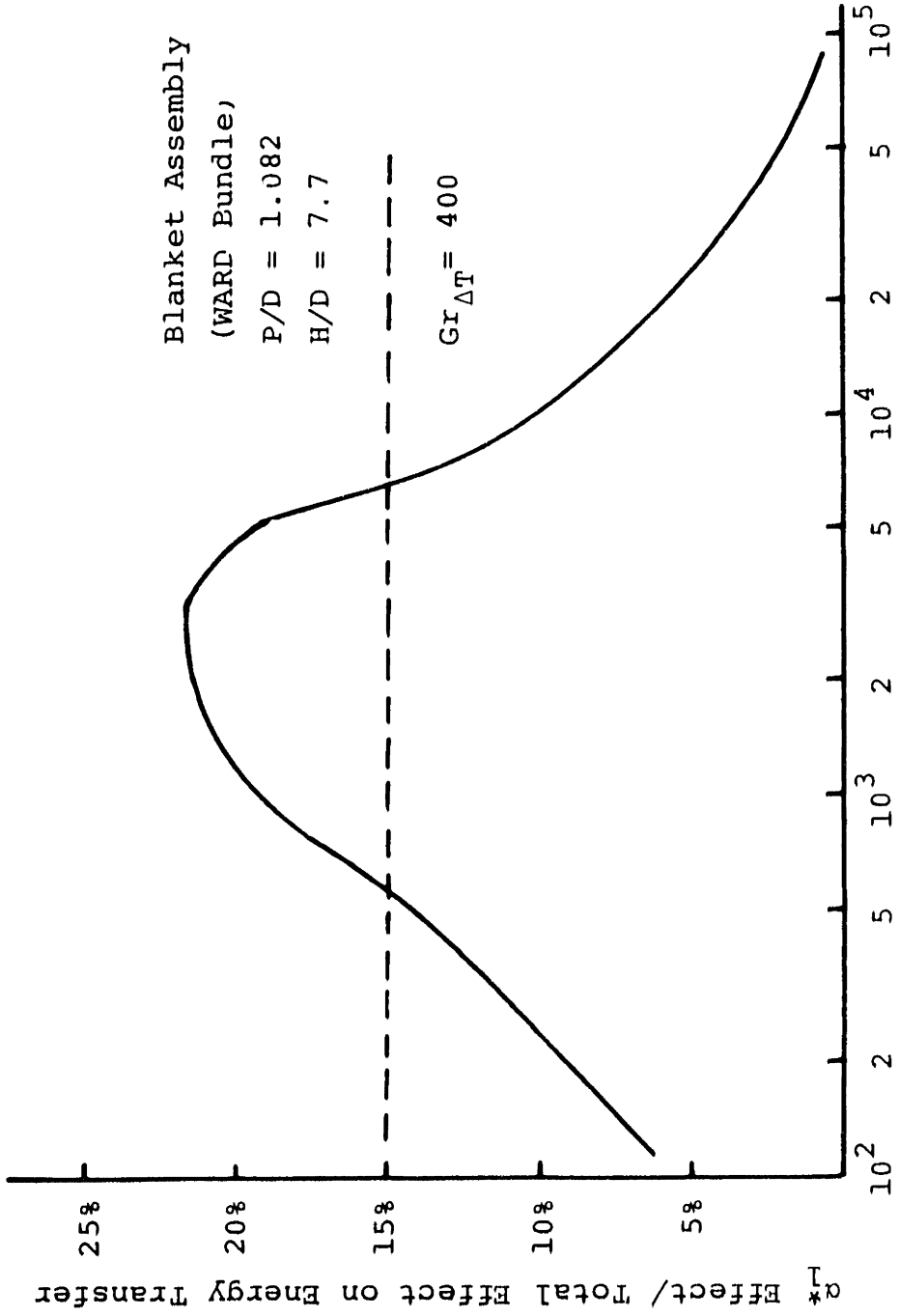

Figure 8.45 α_1^* Effect on the Total Energy Transfer

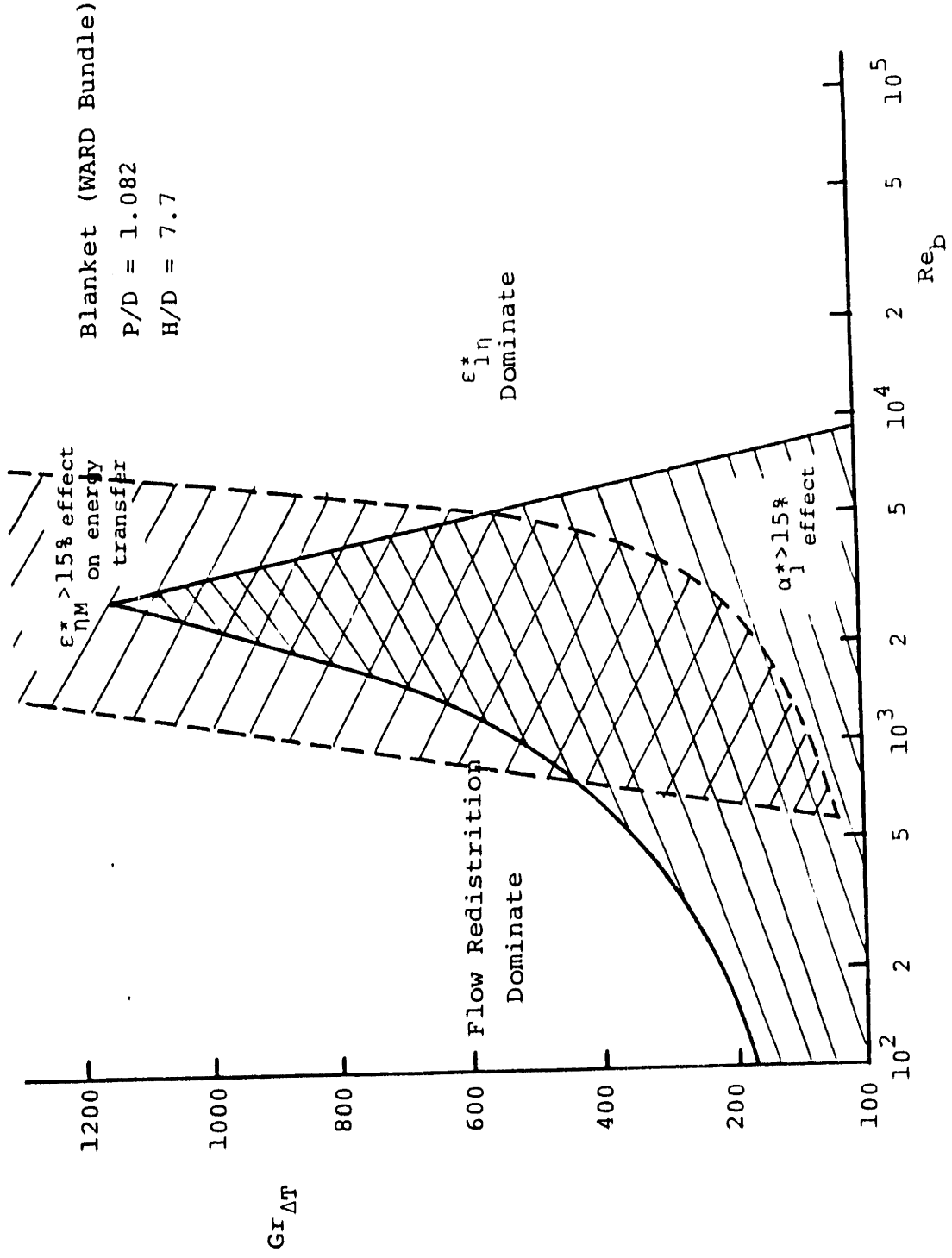

Figure 8.46 Operation Regions in which Different Energy Transfer Mechanisms Are Important for Blanket Assembly

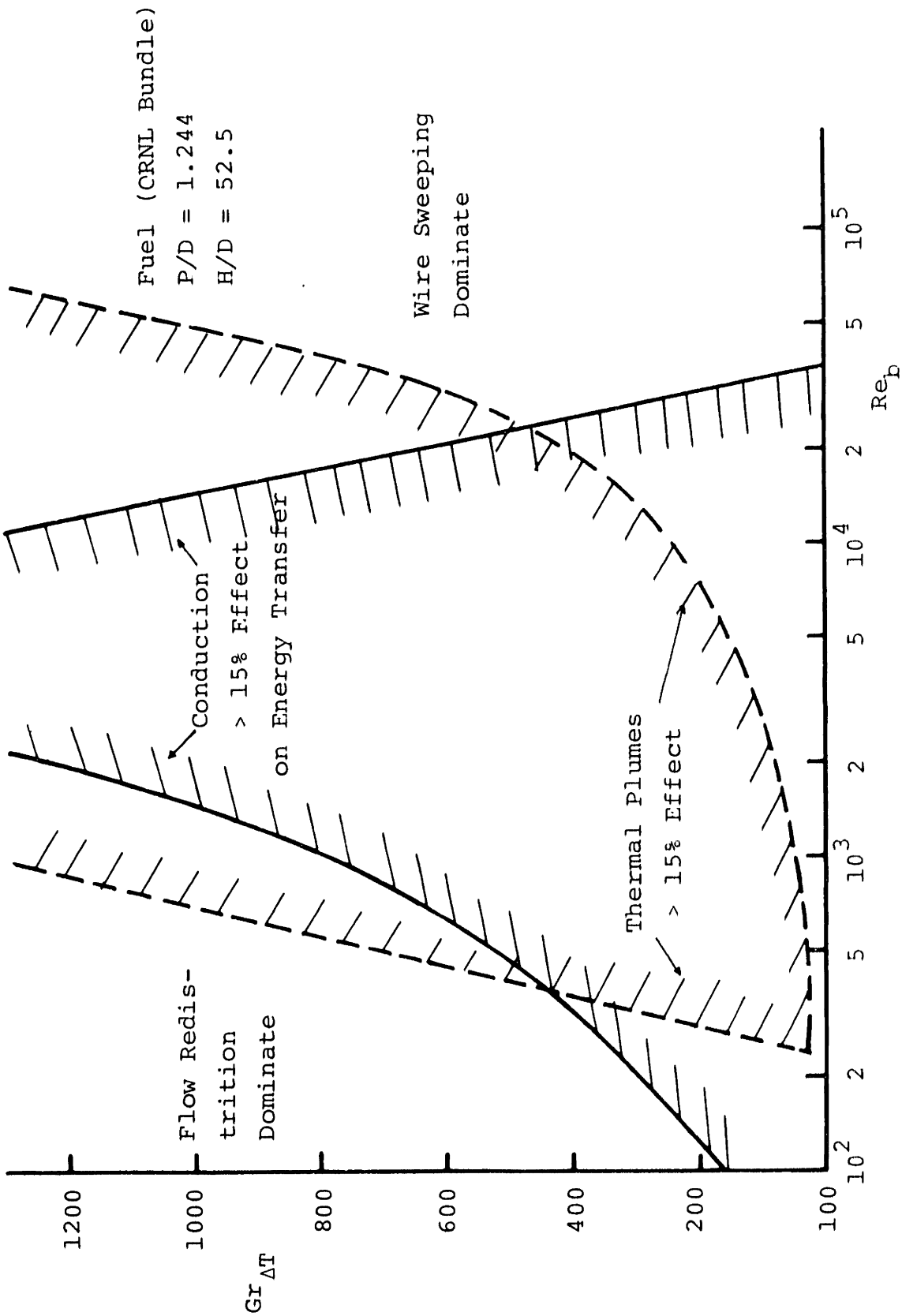

Figure 8.47 Operation Regions in which Different Energy Transfer Mechanisms Are Important for Fuel Assembly

Outside these two regions, FRD dominates the energy transfer at low Re_b operation, while $\varepsilon^*_{1\eta}$ dominates the energy transfer at high Re_b operation. This is because at high $Gr_{\Delta T}/Re_b$, all the other mechanisms are small comparing to FRD, while at low $GR_{\Delta T}/Re_b$ and high Re_b, $\varepsilon^*_{\eta M}$ is the only important mechanism. For $Gr_{\Delta T}$ lower than a particular value ($\tilde{}$100), the buoyancy effects become so small that FRD and $\varepsilon^*_{\eta M}$ are negligible. On the other hand, for $Gr_{\Delta T}$ higher than particular values (e.g., 1100 for blanket bundle) the buoyancy effects become so large that α^*_1 becomes negligible.

As seen from Figures 8.46 and 8.47, the conduction effects are significant ($\geq$ 15% between Re_b = 700 to 6000, and Re_b = 600 to 2000 for typical blanket assembly and fuel assembly operations, respectively. Note that for low $Gr_{\Delta T}$ operation, conduction effect is always significant even for very low Re_b as shown in these figures. In these regions, use of the bare rod case conduction shape factor for the wire-wrapped rod bundle may require further investigation. However, the validation studies in the last two sections showed that satisfactory predictions were obtained using this conduction shape factor. Therefore, we conclude that the correlation for conduction factor proposed in Chapter 6 is applicable for predicting wire-wrapped rod bundle behavior.

CHAPTER 9

SUMMARY, CONCLUSION AND RECOMMENDATION

9.1 Introduction

In this study the following tasks have been completed

9.1.1 Formulation of a Simple Subchannel Analysis Code, the ENERGY-IV

A two region approach is used to model the thermal-hydraulics in an LMFBR wire-wrapped assembly. In the interior region the wire-sweeping effects on energy transfer are modeled by an enhanced eddy diffusivity, in dimensionless form $\varepsilon^*_{1\eta}$, while in the edge region the wire sweeping flow is modeled by a uniform dimensionless transverse velocity ratio, C_{1L}. Using these models, a set of difference equations are derived from the general subchannel conservation equations and input parameters for this subchannel analysis method are identified. Based on this set of equations, a new version in the ENERGY series of codes, ENERGY-IV, is constructed. ENERGY-IV is applicable to both forced convection and mixed convection conditions. In the forced convection condition only the energy conservation equation is used, while in the mixed convection condition the overall mass, energy, and momentum conservation equations are solved with the assumption of equal pressure drop across the bundle. An improved numerical method is implemented in the code to make the solution converge in the mixed convection condition.

9.1.2 Data Base for Input Parameters

Flow split, pressure drop and salt mixing data are obtained in a 37-pin wire wrapped rod bundle with P/D = 1.154 and H/D = 13.4 using water as the working fluid. The isokinetic extraction method, pitot-static probe pressure measurement method and salt tracer injection were used in these experiments to obtain this data. These experiments are performed to fill the gap in the available data base for the input parameters of the ENERGY-IV code. The published world data base for these parameters have been collected and thoroughly reviewed.

9.1.3 Models and Correlations for Input Parameters

The input parameters required for the ENERGY-IV are the inlet flow split parameter, $X_i \equiv V_i/V_b$, where V_i is the (constant) velocity in each specific type of subchannel (interior, edge or corner), and V_b is the bundle average velocity; the subchannel friction factor, f_i; the dimensionless effective eddy diffusivity, $\varepsilon^*_{1\eta}$ for the interior region and $\varepsilon^*_{2\eta}$ for the edge region, which are defined as the ratio of the effective transverse mass flux at the gap carrying subchannel average enthalpy to the average axial mass flux; the edge transverse velocity ratio, $C_{1L} \equiv V_T/V_2$, where V_T is the uniform transverse velocity, and V_2 is the axial velocity in the edge subchannel; and the conduction shape factor κ. It is found that in the mixed convection condition an addition mixing mechanism due to thermal plume effects contributes a significant amount of energy transfer. Using a definition analogous to that of $\varepsilon^*_{1\eta}$, a parameter called thermal plume

mixing parameter, $\varepsilon^*_{\eta M}$, is introduced to quantitatively represent this effect. The models for all these parameters accounting both the geometric and flow regime affects are proposed and correlations using those models are calibrated by the data base.

9.1.4 Validation of the ENERGY-IV Code

Recent published out of pile sodium cooled heated pin data are collected and reviewed for the validation for the ENERGY-IV model an its input parameters. These data cover ranges of geometry from blanket to fuel assembly (P/D = 1.07, H/D = 8.0 to P/D = 1.25, H/D = 52), and of flow regimes from forced to mixed convection (Re_b = 70000 to 500, and $Gr_{\Delta T}/Re_b$ = 0.01 ot 0.73). The energy transfer mechanisms in the mixed convection condition, namely, the wire-sweeping effect, conduction effect, thermal plume effect, and flow redistribution effect are investigated and estimated by the validated input parameter correlations and the ENERGY-IV model. Operation regions in which these parameters are significant are then identified.

9.2 Summary

In what follows the accomplishments and conclusions are summarized.

9.2.1 Experimental Results

The experimental results for edge flow split parameter (X_2), bundle average friction factor (f_b), dimensionless effective eddy diffusivity ($\varepsilon^*_{l\eta}$), and edge transverse velocity ratio (C_{lL}), are

shown in Figures 3.10, 3.12, 5.6, and 5.10, respectively. Experimental errors are estimated for these results and are shown by the error bars in these figures. The parameters $\varepsilon^*_{l\eta}$ and C_{lL} are reduced from a new version of data reduction code using the ENERGY-IV model.

9.2.2 Models and Correlations of Input Parameters

Consistent Models for subchannel friction factors and transverse velocities at the gaps have been proposed. The correlations for subchannel friction factors, f_i, flow split parameters, X_i and mixing parameters $\varepsilon^*_{l\eta}$ and C_{lL} are formulated based on these models, respectively. These models are seperately considered in three flow regimes, namely, laminar, transition, and turbulent flow regime. The flow regmes are artificially defined from the behavior of bundle average friction factors in hexagonal rod bundles (both bare and wire-wrapped).

Below a particular Re_{bL} which depends on the bundle geometry, the bundle average friction factor is proportional to $1/Re_b$. This regime is defined as the laminar region. Above a particular Re_{bT}, which also depends of the bundle geometry, the bundle average friction factor is proportional to $1/Re_b^a$. This regime is defined as the turbulent region. From the data base, parameter a has a value ranging from 0.15 to 0.25, with an average value of 0.18. The region between these two Re_b's is defined as the transition regime. According to the bundle average friction factor data base, the following correlations are found to satisfactorily predict Re_{bL} and Re_{bT},

$$\log\left(\frac{Re_{bL}}{300}\right) = 1.7\left(\frac{P}{D} - 1.0\right) \tag{4.34a}$$

and

$$\log\left(\frac{Re_{bT}}{10000}\right) = 0.7\left(\frac{P}{D} - 1.0\right) \tag{4.34b}$$

Hence, the three flow regimes are

Turbulent: $Re_b \geq Re_{bT}$

Transition: $Re_{bT} > Re_b > Re_{bL}$

Laminar: $Re_b \leq Re_{bL}$

Models for all input parameters in the laminar region are similar to those in the turbulent region with only different Reynolds number dependence in specific cases. The empirical constants in the laminar region are assumed to be strongly connected to the turbulent region because of the insufficient data base in the laminar region. Correlations for the transition region are formulated by superposing laminar and turbulent of values relevant parameters weighting by an intermittency factor ψ_i. The intermittency factor which physically represents the fraction of the flow field which is turbulent in a specified flow subchannel is defined as

$$\psi_i \equiv \frac{\log Re_i - \log Re_{iL}}{\log Re_{iT} - \log Re_{iL}}$$

where Re_{iF} = subchannel Reynolds number at Laminar/transition (F=L) or transition/turbulent (F=T) point

$$= Re_{bF}\,(De_i/De_b)X_{iF}$$

9.2.2.1 Subchannel Friction Factor and Flow Split parameter

Again the two region approach is used to establish models for subchannel friction factor. In the interior region, the total drag force exerting on the fluid is comprised of rod surface friction and wire form drag. In the edge region, only the friction loss due to the swirl flow along both rod surface and wire is considered. The form drag of wire is assumed to be negligible since flow in the edge subchannel is more or less following the wire direction. The magnitude of swirl flow in th edge region is calculated from a transverse velocity V_T and the axial average velocity V_A. The relation between V_T and V_A is formulated similar to the models for transverse velocity at the gaps for the mixing parameters $\varepsilon^*_{1\eta}$ and C_{1L},

$$\left(\frac{V_T}{V_A}\right)^2 = W_s \left(\frac{A_{r2}}{A'_2}\right) \tan^2\theta \qquad (4$$

These models are also formulated so as to be able to be reduced to bare rod cases when the wire diameter goes to zero. The subchannel friciton factors are then expressed as,

for the turbulent and laminar regions

$$f_1 = \frac{1}{Re_1^m}\left[K_1\left(\frac{P'_{w1}}{P_{w1}}\right) + W_d\left(\frac{3A_{r1}}{A'_1}\right)\left(\frac{De_1}{H}\right)\left(\frac{De_1}{D_w}\right)^m\right] \qquad (4.31)$$

$$= \frac{C_{f1}}{Re_1^m}$$

$$f_2 = \frac{1}{Re_2^m}\left[K_2\left(1+W_s\left(\frac{A_{r2}}{A_2'}\right)\tan^2\theta^{\frac{3-m}{2}}\right)\right] = \frac{C_{f2}}{Re_2^m} \qquad (4.32)$$

$$f_3 = \frac{1}{Re_3^m}\left[K_3\left(1+W_s\left(\frac{A_{r3}}{A_3'}\right)\tan^2\theta^{\frac{3-m}{2}}\right)\right] = \frac{C_{f3}}{Re_3^m} \qquad (4.33)$$

where

Re_i = subchannel Reynolds number

A_{ri} = wire projection area in subchannel i

A_1' = bare subchannel flow area

θ = wire direction

P_{W1}' = subchannel wetted perimeter without wire

P_{W1} = subchannel wetted perimeter with wire

K_i = empirical constant from bare rod subchannel friction factor

W_d = wire drag constant

W_s = swirl flow constant

m = 1.0 for the laminar flow region

m = 0.18 for the turbulent flow region;

for the transition region

$$f_{itr} = f_{iL}\,(1-\psi_i)^{\gamma} + f_{iT}\,\psi_i^{\gamma} \qquad (4.35)$$

where

$f_{iL} = C_{fiL}/Re_i$

$f_{iT} = C_{fiT}/Re_i^{0.18}$

γ = empirical constant fitted by data

The flow split parameters can be obtained from above subchannel friction factor with the assumption of equal pressure across the bundle, i.e.,

$$\Delta P_1 = \Delta P_2 = \Delta P_3 = f_i \frac{L}{De_i} \frac{\rho V_i^2}{2}$$

hence

$$\frac{f_1}{De_1} X_1^2 = \frac{f_1}{De_2} X_2^2 = \frac{f_3}{De_3} X_3^2 \tag{4.36}$$

Using the available data base, the following results for the empirical constants in equations (4.31) - (4.35) are obtained which are valid over the following parameter ranges:

$$19 \leq N_r \leq 217$$

$$1.0 \leq P/D \leq 1.42$$

$$4.0 \leq H/D \leq 52.0$$

$$50 \leq Re_b \leq 10^6$$

Fitted results (subscript T and L refering to the turbulent and laminar region respectively):

$$K_{iT} \text{ (or } K_{iL}) = a + b_1(\frac{P}{D} - 1.0) + b_2(\frac{P}{D} - 1.0)^2 \tag{4.54}$$

where a, b_1, b_2 are listed in Table 9.1

$$W_{dT} = \left[29.5 - 140.0\ (\frac{Dw}{D}) + 401.0\ (\frac{Dw}{D})^2\right](\frac{H}{D})^{-0.85} \tag{4.63}$$

$$W_{sL} = 20.0 \log(\frac{H}{D}) - 7.0 \tag{4.64}$$

$$W_{dL} = 1.4\ W_{dT} \tag{4.67}$$

$$W_{sL} = 0.3\ W_{sT} \tag{4.68}$$

$$\gamma = 1/3$$

Table 9.1

Coefficients for Bare Rod Friction Factor Constants K_i

		$1.0 \leq P/D \leq 1.1$			$1.1 < P/D \leq 1.5$		
flow regimes	subchannel kind	a	b_1	b_2	a	b_1	b_2
Laminar	Interior	26.00	888.2	-3334.	62.97	216.9	-190.2
	Edge	26.18	554.5	-1480.	44.40	256.7	-267.6
	Corner	26.98	1636.	-10050	87.26	38.59	- 55.12
Turbulent	Interior	0.09378	1.398	-8.664	0.1458	0.03632	-0.03333
	Edge	0.09377	0.8732	-3.341	0.1430	0.04199	-0.04428
	Corner	0.1004	1.625	-11.85	0.1499	0.006706	-0.009567

The correlation can predict the bundle average friction factor data within ±14% with a 92% confidence interval and all the flow split data within ±5%.

9.2.2.2 Dimensionless Effective Eddy Diffusivity $\varepsilon^*_{l\eta}$ and Edge Transverse Velocity Ratio C_{lL}.

The proposed model for the transverse velocity at the gap based on pressure distribution consideration is

$$\frac{V_T}{V_A} \propto \left(\frac{A_r}{A'}\right)^{1/2} \tan\theta \tag{6.31}$$

According to their definition both $\varepsilon^*_{l\eta}$ and C_{lL} are directly proportional to V_T/V_A. Hence the correlations for them are for the turbulent and lamiar regions

$$\varepsilon^*_{l\eta} = C_{ml}\left(\frac{A_{rl}}{A'_l}\right)^{1/2} \tan\theta \tag{6.32}$$

and

$$C_{lL} = C_{m2}\left(\frac{A_{r2}}{A'_2}\right)^{1/2} \tan\theta \tag{6.33}$$

for the transition region

$$MP = MP_L + (MP_T - MP_L)\psi_i^{\lambda} \tag{6.39}$$

where MP = mixing parameters $\varepsilon^*_{l\eta}$ or C_{lL}

λ = fitted from data

Using the available data ase, the following results for the empirical constants in equations (6.32) and (6.33) are obtained,

Range of Validity

$$1.067 \leq P/D \leq 1.35$$

$$4 \leq H/D \leq 52$$

$$400 \leq Re_b \leq 10^6$$

Fitted results

for $N_r \geq 19$

$$C_{m1T} = 0.14 \left(\frac{c}{D}\right)^{-0.5} \tag{6.35a}$$

$$C_{m2T} = 0.75 \left(\frac{H}{D}\right)^{0.3} \tag{6.36a}$$

for $N_r = 7$

$$C_{m1T} = 0.1 \left(\frac{c}{D}\right)^{-0.5} \tag{6.35b}$$

$$C_{m2T} = 0.6 \left(\frac{H}{D}\right)^{0.3} \tag{6.36b}$$

and

$$\lambda = 2/3$$

$$C_{miL} = 1.5 \left(\frac{c}{D}\right)^{0.6} C_{miT} \tag{6.38}$$

where $c = P-D$ = gap between rods

$i = 1$ or 2

The above correlations can predict the data within ±25% for $\varepsilon^*_{1\eta}$ and ±15% for C_{1L}.

9.2.2.3 Dimensionless Eddy Diffusivity for the Edge Region $\varepsilon^*_{2\eta}$

The mixing due to turbulent interchange only in a bare rod bundle has also been investigated. The parameter with similar definition to $\varepsilon^*_{1\eta}$ is denoted as $\varepsilon^*_{\eta T}$. Based on the available data base correlations for $\varepsilon^*_{\eta T}$ between triangular to triangular subchannels and between square to square subchannels are proposed under the assumption that they are Reynolds number independent, i.e.,

$$\text{for T-T} \quad \varepsilon^*_{\eta T} = 0.0016 \left(\frac{C}{D}\right)^{-0.5} \tag{6.15}$$

$$\text{S-S} \quad \varepsilon^*_{\eta T} = 0.0056 \left(\frac{C}{D}\right)^{-0.3} \tag{6.16}$$

$\varepsilon^*_{2\eta}$ is $\varepsilon^*_{\eta T}$ between edge subchannels. Equations (6.15) and (6.16) which relate to different shaped channels are therefore not directly applicable. A value of 0.01 is recommended for $\varepsilon^*_{2\eta}$ for simplicity and consistent with the input parameter for the COBRA code.

9.2.2.4 Conduction Shape Factor κ

The literature investigating the conduction shape factor for bare rod cases has been reviewed. A correlation for this parameter as function of geometry only is proposed from the available investigations, i.e.,

$$\kappa = 0.66 \left(\frac{P}{D}\right)\left(\frac{c}{D}\right)^{-0.3} \tag{6.42}$$

No studies are available for κ in the wire wrapped rod bundle. Equation (6.42) is assumed to be applicable to the wire wrapped cases. As the validation results show, use of equation (6.42) can give satisfactory predictions.

9.2.2.5 Thermal Plume Mixing Parameter $\varepsilon^*_{\eta M}$

A simple model for the mixing enhanced by therml plume effects in the mixed convection condition is presented. It indicates that $\varepsilon^*_{\eta M}$ is a function of geometry, $(Gr_{\Delta T}/Re_b)$, and power skew, where

$Gr_{\Delta T} \equiv (\beta g De_b^4 (\Delta T_b/L)/\nu^2)$. $\varepsilon^*_{\eta M}$ is estimated by matching the ENERGY-IV calculations to the temperature data from out of pile sodium cooled heated pin experiments. The following correlation is found to be satisfactory,

$$\varepsilon^*_{\eta M} = 0.1 \left(\frac{c}{D}\right)^{-0.5} \left(\frac{Gr_{\Delta T}}{Re_b}\right) \qquad (8.5)$$

9.2.3 Validation of the ENERGY-IV Code

The ENERGY-IV code has been developed to be fast running with satisfactory prediction capability. The running time of the ENERGY-IV for the forced convection option for a 61-pin bundle with 100 axial nodes is less than 2 seconds. For the mixed convection option, the running time is about 0.5 second for each axial node in a 61-pin with 126 radial nodes. With 100 axial nodes, this takes about 50 seconds. For a similar number of nodes, the COBRA-WC code requires about 5 minutes for the forced convection option and probably hours for the mixed convection option. However, COBRA-WC has transient, multiassembly capibility.

In the forced convection condition, ENERGY-IV predicts data better than COBRA-WC does. The maximum difference of the normalized

temperature rise, ΔT^*, between the ENERGY-IV results and temperature data is about 7%. All the data are predicted within ±12.5 °F.

In the mixed convection option, ENERGY-IV has the same degree of accuracy as that of COBRA-WC. The maximum difference for peak ΔT^* between predictions and data is about 7%. The maximum difference for ΔT^* between predictons and data is about 10%, which occurs in the lower power region of the power skew cases. Futhermore, the locations of the maximum temperature rise are not well predicted for power skew cases of WARD data. However, the ENERGY-IV predicts all the data within ±22.5°F.

9.2.4 Mechanisms for Energy Transfer in the Mixed Convection Condition

Four mechanisms for energy transfer in the mixed convection condition have been investigated as discussed in section 9.1.4. The relative importance of the effect on energy transfer of each mechanism has been studied. Figure 8.43 shows the relative importance of these mechanisms for a blanket assembly. Figure 8.46 identifies operation regions in which the effects of these mechanisms on energy transfer are significant for a blanket assembly. Similar figures for the fuel assembly have also been constructed.

9.3 Recommendation

Although the input parameter in the forced convection condition have been satisfactorily correlated and validated, further invesigations regarding input parameters κ and $\varepsilon^*_{\eta M}$ in the mixed convection condition are recommended.

9.3.1 Conduction Shape Factor

The influence of the wire wrap on the temperature and velocity fields should be studied to check the applicability of th bare rod conduction shape factor to the wire wrap bundle. Also, the buoyancy effects in the mixed convection condition might affect the value of conduction shape factor. A theoretical study might be worthwhile to investigate this phenomenon.

9.3.2 Thermal Plume Mixing Parameter

The fundamental model for the thermal plume mixing mechanism is still an open question. A model should be developed to correctly account for the power skew effect and $Gr_{\Delta T}/Re$ effect. Experimental studies to enable development of a better understanding of this phenomenon and for validating the model are necessary.

REFERENCES

Axford, R. A. (1964), "Multiregion Analysis of Temperature Fields and Heat Fluxes in Tube Bundles with Internal, Solid, Nuclear Heat Sources," Rep. No. LA-3167 Los Alamos Sci. Lab., Univ. California, Los Alamos, N.M. (1964), 82 pp.

Axford, R. A. (1967), "Two-Dimensional, Multiregion Analysis of Temperature Fields in Reactor Tube Bundles," Nuclear Engineering and Design, 6, (1967) 25-42.

Bartholet, T. G., et al (1976), "11:1 Scale Wire-Wrap Rod Bundle Air Flow Test, Side Subchannels," WARD-D-0129, Jan. 1976.

Basehore, K.L. and Todreas, N.E. (1980), "SUPERENERGY-2: A Multiassembly Steady-State Computer Code for Thermal-Hydraulic Analysis," COO-2245-57 TR, MIT, Aug. 1980.

Bates, J. M. and Khan, E. U. (1980), "Investigation of Combined Free and Forced Convection in a 2×6 Rod Bundle During Controlled Flow Transients," AIChE Symposium Series, Heat Transfer, Orlando (1980).

Baumann, W., Cosal, V., Hoffmann, H., Moller, R. and Rust, K. (1968), "Brennelemente mit Wendelformigen Abstandshalter fur Schnelle Brutreaktoren," KfK-768 (1968). Also EURFNR-571.

Baumann, W. and Moller, R. (1969), "Experimental Study of Coolant Cross-Mixing in Multirod-Bundles," Atomkernergie, 14-56 (1969).

Baumann, W. (1972), "MISTRAL-II, Thermohydraulische Mischstromung-salgorithmen fur Strabbundel," KfK-1065, June 1972.

Biancheria, A. and Markley, R.A. (1973), "Design Analysis of the LMFBR Radial Blanket," Westinghouse Advanced Reactors Design, WARD-3045T2B-9, March 1973.

Bishop, A. A., Nelson, P. A. and McCabe, E. A. (1962), "Thermal and Hydraulic Design of the CVTR-fuel Assemblies," CVNA-115, June 1962.

Bishop, A. A. and Todreas, N. E. (1980), "Hydraulic Characteristics of Wire-Wrapped Rod Bundles," Nuclear Engineering and Design, 62, (1980) 271-293.

Bishop, A. A., Willis, J. M. and Markley, R. A. (1980), "Effects of Buoyance on Laminar Vertical Upward Flow Friction Factors in Cylindrical Tubes," Nuclear Engineering and Design, 62, (1980) 365-369.

Burns, K.J. (1980), "Thermal Hydraulic Studies of a 37-pin LMFBR Wire Wrapped Rod BUndle," S.M. Thesis, Nuclear Engineering Department, MIT, July 1980.

References (Continued)

Bunrs, K.J. et al. (1980a) "Laminar/Transition Sweeping Flow Mixing Model for Wire Wrapped LMFBR Assemblies," DOE/ET/37240-81TR, July 1980.

Burns, K.J. and Todreas, N.E. (1980b), "Laboratory Manual for Static Pressure Drop Experiments in LMFBR Wire Wrapped Rod Bundles," DOE/ET/37240-77TR, July 1980.

Carajilescov, P. and Fernandez, E. F. (1982), "Semi-Empirical Model for Friction Factors in LMFBR Wire-Wrapped Rod Bundles," 2nd Int'l Topical Meeting on Nuclear Reactor Thermal-Hydraulics, Santa Barbara, CA. (1982).

Carelli, M. D. and Willis, J. M. (1981), "The CRAB-II Computer Program and Its Verification," Presented at LMFBR Thermal-Hydraulic Information Meeting in Monterey, CA, (March 1981).

Castellana, F.S., Adams, W.T. and Casterline, J.E. (1974), "Single-Phase Subchannnel Mixing in Simulated Nuclear Fuel Assembly," Nuclear Enginering and Design, Vol. 26, pp 242-249 (1974)

Chan, Y.N., Hawley, J.T. and Todreas, N.E. (1980) "Input Parameters to Code Which Analyze LMFBR Wire Wrapped Bundle," COO-2245-17TR, Rev. II, MIT, December 1980.

Chan, Y.N. and Todreas, N.E. (1980a), "Laboratory Manual for Salt Mixing Test in 37- and 217-pin Bundles," COO-2245-62TR, Rev. I, MIT, Aug. 1980

Chen, Y. B., Ip, K. and Todreas, N. E. (1974), "Velocity Measurements in Edge Subchannels of Wire-Wrapped LMFBR Fuel Assemblies," COO-2245-11TR, MIT, (Sept. 1974).

Cheng, S.-K. (1982), this study in Chapter 2.

Chiu, C. and Todreas, N. E. (1978a), "Flow Split Meeasurements in LMFBR Blanket Assemblies," COO-2245-41TR, MIT, April 1978.

Chiu, C., Hawley, J., Rohsenow, W. M. and Todreas, N. E. (1978b) "Pressure Drop Measurements in Wire-Wrapped Blanket Assemblies," COO-2245-42TR, July 1978.

Chiu, C., Rohsenow, W. M. and Todreas, N. E. (1978c), "Mixing Experiments in LMFBR Wire-Wrapped Blanket Assemblies," COO-2245-43TR, April 1978.

Chiu, C., Rohsenow, W. M. and Todreas, N. E. (1978d), "Turbulent Sweeping Flow Mixing Model for Wire-Wrapped LMFBR Assemblies," COO-2245-55TR, Rev. 1, MIT, 1978.

Chiu, C., Rohsenow, W. M. and Todreas, N. E. (1978e), "Flow-Split Model for LMFBR Wire-Wrapped Assemblies,"COO-2245-56TR, Rev. 1, MIT, Apr.1978.

References (Continued)

Chiu, T. (1979), "Fluid Mixing Studies in a Hexagonal 37-Pin Wire-Wrapped Rod Bundle," S. M. Thesis, Dept. Nuclear Engineering, MIT, (Sept. 1979).

Chiu, K.W. (1979a), "Fabrication Detail for Wire-Wrapped Fuel Assembly Components," COO-2245-27TR, Rev.II, MIT, Sep. 1979.

Collingham, R. E., Thorne, W. L. and McCormack, J. D. (1971), "217-pin Wire Wrapped Bundle Coolant Mixing Test," HEDL-TME 71-146, Nov. 1971. Also NED, 24, 1973, pp 393-409.

Cooper, A. A. (1981), "HAMNA: A Steady-State Thermal Hydraulic Code for Sodium Cooler Rod Cluster Analysis," AEEW-R1103 (1981).

Cushman, R. A. and McGinnis, F. D. (1969), "Experimental Breeder Reactor No. II Reactor Heat Transfer: Experience with an Operating Liquid Metal Fast Breeder Reactor," CEP Symposium Series No. 91, 65, (1969).

Davidson, C. R. (1971), "Hydraulic Tests on the 217-Rod Full-Sized Wire-Wrapped Fuel Assembly," TR-095-211-006, Atomic International Supporting Document (1971).

Deissler, R. G. and Taylor, M. T. (1957), "Analysis of Axial Turbulent Flow and Heat Transfer Through Banks of Rods or Tubes," Reactor Ht. Conference of 1956, TID-7529 (Pt. 1) Book 2, (1957) 416-461.

deStordeur, A. N. (1961), "Drag Coefficients for Fuel-Element Spacers," Nucleonics 19(6), 74-79, (June 1961).

Domanus, H. M., Schmitt, R. C. and Sha, W. T. (1977), "Numerical Results Obtained from the Three Dimensional Transient Single Phase Version of the COMMIX Computer Code," NUREG-0355, ANL, Argonne, IL. October, 1977.

Donovan, T. E., George, T. L. and Wheeler, C. L. (1979), COBRA-IV Wire-Wrap Data Comparisons," PNL-2938, UC-79e Feb. (1979).

Dwyer, O. E. and Berry, H. C. (1972), "Heat Transfer to Liquid Metals Flowing Turbulently and Longitudinally Through Closely-Spaced Rod Bundles, Part I," Nuclear Engineering and Design, 23, (1972) 273-294.

Efthimiadis, A. (1983), "Mixed Convectiuon and Hydrodynamic Modeling of Flows in Rod Bundle," Ph. D. Thesis, Nuclear Engineering Department, MIT, May, 1984.

Eifler, W. and Nijsing, R. (1965), " Fundamental Studies of Fluid Flow and Heat Transfer in Fuel Element Geometries. Paet II. Experimental Investigation of Velocity Distribution and Flow Resistance in a Triangular Array of Parallel Rods." Report EUR 2193, European Atomic Energy Community (1965); cf. Nuclear Engineering and Design, 5, (1967) 22-42.

References (Continued)

Eifler, W. and Nijsing, R. (1967), "Experimental Investigation of Velocity Distribution and Flow Resistance in triangular Array of Parallel Rods," Nuclear Engineering and Design, 5, (1967) 22-42.

Engel, F. C. and Markley, R. A. (1978), "Buoyancy Effects on Sodium Coolant Temperature Profiles Measured in an Electrically Heated Mock-up of a 61-Rod Breeder Reactor Blanket Assembly, ASME Paper 78-WA/HT-25 (1978).

Engel, F. C., Markley, R. A. and Bishop, A. A.(1979), "Laminar, Transition, and Turbulent Parallel Flow Pressure Drop Across Wire-Wrap-Spaced Rod Bundles," Nuclear Science and Engineering, 69 (1979) 290-296.

Engel, F. C., Minushkin, B., Atkins, R. J. and Markley, R. A. (1980), "Characterization of Heat Transfer and Temperature Distributions in an Electrically Heated Model of an LMFBR Blanket Assembly," Nuclear Engineering and Design, 62, (1980) 335-347.

Engel, F. C., Markley, R. A. and Minushkin, B. (1981), "Temperature Profiles in Natural and Forced Circulation of Sodium Through a Vertical LMFBR Blanket Test Assembly," AIChE Symposium Series, Milwaukee (1981).

Engel, F. C. and Markley, R. A. (1981), "Parameter Studies of Peak Temperature Rise for LMFBR Blanket Rod Bundles," Nuclear Engineering and Design, 68, (1981) 347-357.

Engel, F. C., Markley, R. A. and Bishop, A. A. (1982), "The Effects of Radial Heat Flux Gradients and Flow Regimes on the Peak Sodium Temperature Rise in Wire-Wrapped Rod Bundles," Kiamesha Lake Meeting, NY, (Sept. 1982).

Fajeau, M. (1969), "Programme Flica-Etude Thermodynamique d'un Reacteur ou d'une Boucle d'Essai," CEA-R-3716, 1969.

Fakori-Monazah, M. R. and Todreas, N. E. (1977), "Measurement and Analysis of Flow Wall Shear Stress in an Interior Subchannel of Triangular Array Rods," COO-2245-49TR, MIT (Aug. 1977).

Fontana, M. H. et al. (1973), "Temperature Distribution in a 19-Rod Simulated LMFBR Fuel Assembly in a Hexagonal Duct (Fuel Failure Mockup Bundle 2A)- Record of Experimental Data," ORNL-TM-4113, UC-79, Sep. 1973.

Fontana, M. H. et al (1974), "Temperature Distribution in the Duct Wall and at the Exit of a 19-Rod Simulated LMFBR Fuel Assembly (FFM Bundle 2A), Nuclear Technology, 24, (Nov. 1974).

References (Continued)

France, D. M. and Ginsberg, T. (1973), "Evaluation of Lumped Parameter Heat Transfer Techniques for Nuclear Reactor Applications," Nuclear Science and Engineering, 51, (1973) 41-51.

France, D. and Ginsberg, T. (1974), "Comparison of Analytic and Lumped Parameter Solutions for Steady-State Heat Transfer in Fuel Rod Assemblies," Progress in Heat and Mass Transfer, Vol. 7, (1974)

Fukuda (1979), private communication with T. Greene, unpublished work at ORNL, October, 1979.

Galloway, L. R. and Epstein, N. (1965), "Longitudinal Flow Between Cylinders in Square and Triangular Arrays and in a Tube with Square-Edged Entrances," AIChE Symposium Series No. 6, London (1965) 4-15.

George, T. L., Basehore, K. L. and Prather, W. A. (1980), "COBRA-WC Model and Predictions for A Fast Reactor Natural Circulation Transient," AIChE Symposium Series, Heat Transfer, Orlando (1980).

Ginsberg, T. (1972), "Forced-Flow Interchannel Mixing Model for Fuel Rod Assemblies Utilizing a Helical Wire-Wrap Spacer System," Nuclear Engineering and Design, 22, (1972) 28-42.

Ginsberg, T. and Lorentz, J. J. (1973), "Experimental Mixing Studies in Simulated Wire-Wrap Fuel Assemblies," International Meeting Reactor Heat Transfer Oct. 9-11, 1973, Karlsruhe.

Glazer, S., Chiu, C. and Todreas, N. E. (1977), "Collection and Evaluation of Salt Mixing Data with the Real Time Data Acquisition System," COO-2245-36TR, MIT, April 1977.

Graves, A. W. (1971), "Friction Factor and Rod Bundle Entrance and Exit Loss Coefficient for 217-Rod FBR Fuel Assembly Water Test Model," TR-095-211-009, (Aug. 1971).

Greene, T. E. (1980), "Development and Evaluation of Techniques for Thermal-Hydraulic analysis of LMFBR Fuel Assemblies," M.S. Thesis, Nuclear Engineering Department, MIT, July, 1980.

Gunn, D. J. and Darling, C. W. W. (1963), "Fluid Flow and Energy Losses in Non-Circular Conduits," Transactions Institute of Chemical Engineers, (41), No. 4 (1963) 163-173.

Hawley, J. T., Chiu, C., Rohsenow, W. M. and Todreas, N. E. (1980), "Subchannel and Bundle Friction Factors and Flow Split Parameters for Laminar, Transition and Turbulent Longitudinal Flows in Wire Wrap Spaced Hexagonal Arrays," DOE/ET/37240-79TR, MIT, Nuclear Engineering Department, (August 1980).

References (Continued)

Hawley, J. T., Chiu, C. and Todreas, N. E. (1980a), "M.I.T. Extraction Method for Measuring Average Subchannel Axial Velocities in Reactor Assemblies," DOE/ET/37240-80TR, MIT,July 1980.

Hines, D. P., Boyd, L. R. and Marian, V. R. (1971), "In-Core Boiling or Over Temperature Detector Development," General Electirc NEDC-13650 (1971).

Hoffmann, H. (1973), "Experimentelle Untersuchungen zur Kuhlmittelquervermichung und zum Druckabfall in Stabbundeln mit Wendelformigen Abstandshaltern," KfK-1832, (December 1973).

Hoffmann, H. and Baumgartner, E. (197_), "Experimental Investigations of the Thermodynamic Behavior of Fast Breeder Reactor Fuel Elements with Different Spacer Types," from "Fuel and Fuel Elements for Fast Reactors," International Atomic Energy Agency, Vienna, (1974).

Ibragimov, M. K. et al. (1967), "Calculation of Hydraulic Resistivity Coefficients for Turbulent Fluid Flow in Channels of Non-Circular Cross Section," Atomnaya Energiya 23 (4) 300-305 (1967).

Itoh, K. (1981), Personal Communication to Professor N. E. Todreas.

Johannsen, K. (1981), "Longitudinal Flow Over Tube Bundles," NATO Advanced Study Institute on "Low Reynolds Number Forced Convection in Channel and Bundles," Ankara, Turkey, July 13-24, (1981).

Jones, O. C., Yao, S.-C. and Henry, R. E. (1976), "SIMPLE-2: A Computer Code for Calculation of Steady Thermal Behavior of Rod Bundles with Flow Sweeping," ASME paper 76-HT-8 (1976).

Kelly, J. and Todreas, N. E. (1977), "Turbulent Interchange in Triangular Array Bare Rod Bundles," COO-2245-45TR, MIT, July 1977.

Khan, E. U. et al (1974), "Analysis of Mixing Data Relevant to Wire Wrapped Fuel Assembly Thermal-Hydraulic Design," COO-2245-12TR, Dept. Nucl. Eng., MIT, (Sept. 1974).

Khan, E. U. (1975), "A Porous Body Model for Predicting Temperature Distribution in Wire-Wrapped Fuel Rod Assemblies," Nuclear Engineering and Design, 35 (1975) 1-12.

Khan, E. U. (198), "LMFBR In-Core Thermal-Hydraulics: The State of the Art and U.S. Research and Development Needs," PNL-3337, UC-32, April 1980.

Khan, E. U. (1982), "A Validation Study of COBRA-WC for LMFBR Steady-State and Transient Analysis," Presented in Kiamesha Lake Meeting, Sep. 1982.

References (Continued)

Kim, S. N. (1982), "LMFBR Thermal Hydraulic Code Develpoment and Evaluation," S. M. Thesis, MIT, Nuclear Engineering Department, Oct. 1982.

Kjellstrom, B. (1971), "Transport Process in Turbulent Cjannel Flow," Final Report AE-RL-1344, Nykoping, Sweden (1971).

Lafay, J. and Benant, B. (1975), "Local Pressure Measurements and Peripheral Flow Visualization in a Water 19-Rod Bundle Compound with FLICA IB Calculations: Influence of Helical Wire-Wrap Spacer System," ASME Paper 75-HT-22, (1975).

Levchenko, Y. D., Subbotin, V. I. and Ushakov, P. A. (1967), "The Distribution of Coolant Velocities and Wall Stresses in Closely Packed Rods," (transl.) Atomonaya Energiya 22, (1967) 218.

LeTourneau, B. W., Grimble, R. E. and Zerbe, J. E. (1957), "Pressure Drop for Parallel Flow Through Rod Bundles," Trans. Am. Soc. Mech. Engrs. 79, (1957), 1751-1758.

Lorenz, J. J. and Ginsberg, T. (1972), "Results and Analysis of 7-Pin Wire-Wrap Mixing Test," ANS Transactions, Vol. 15, No. 2, (Nov. 1972).

Lorenz, J. J. and Ginsbert, T. (1977), "Coolant Mixing and Subchannel Velocities in an LMFBR Fuel Assembly," Nuclear Engineering and Design, 40, (1977) 315-326.

Magee, P. M. and Nilsson (1971), K. A., "Pressure Drop in Wire-Wrapped Rod Bundles," ANS Transactions, 14, No. 1, 254, (1971).

Malak, J., Hejna, J. and Schmid, J. (1975), "Pressure Losses and Heat Transfer in Non-Circular Channels with Hydraulically Smooth Walls," Int. Journal of Heat and Mass Transfer, Vol. 18, (1975) 139-149.

Markley, R. A. and Engel, F. C. (1981a), "Parameter Studies of Peak Temperature Rise for LMFBR Blanket Rod Bundles," LMFBR Core T/H Information Meeting, Monterey, CA, (March 1981).

Markley, R. A. and Engel, F. C. (1981b), "Blanket Sodium Heat Transfer Test Data and Evaluation," LMFBR Core T/H Information Meeting, Monterey, CA, (March 1981).

Markley, R. A. and Engel, F. C. (1981c), "Experimental Activities in LMFBR Core Design Thermal-Hydraulics," First IAHR Meeting on Liquid Metals Thermal-Hydraulics, MIT, Cambridge, MA, Oct. 5-6, (1981).

Markley, R. A. (1982), personal communication to S.-K. Cheng

References (Continued)

Marten, K., Yonekawa, S. and Hoffmann, H. (1982), "Experimental Investigation on Pressure Drop in Tightly Packed Bundles with Wire Wrapped Rods," IAHR Second International Specialists Meeting on Thermal-Hydraulics in LMFBR Rod Bundles, Rome, Sept. 15-17, (1982).

Maubach, K. (1970), "Reibungsgesetze Turbulenter Stromungen," Chem. Ing. Techn. 42, 995-1004 (1970).

McAreavey, C. G. and Betts, C. (1979), "A Review of Theoretical and Experimental Studies Underlying the Thermal-Hydraulic Design of Fast Reactor Fuel Elements," Specialist Meeting on Thermodynamics of FBR Fuel Subassemblies under Nominal and Non-Nominal Operating Conditions, Karlsruhe, Feb. 5-7, (1979).

Miyaguchi, K. and Takahashi, J. (1979), "Thermal-Hydraulic Experiments with Simulated LMFBR Sub-Assemblies under Nominal and Non-Nominal Operating Conditions," Specialists Meeting on Thermodynamics of FBR Fuel Subassemblies under Nominal and Non-Nominal Operating Conditions, Karlsruhe, Feb. 5-7, (1979)

Morris, H. M., APPLIED HYDRAULICS IN ENGINEERING, The Ronald Press Company, NY (1963).

Morris, R. H., et al. (1980), "Single-Phase Sodium Tests in 61-pin Full-Length Simulated LMFBR Assembly- Record of Phase 1 Experimental Data for THOR Bundle 9," ORNL/TM-7313, (1980)

Namekawa, F., Ito, A. and Mawatari, K. (1984), "Buoyancy Effects on Wire-Wrapped Rod Bundle Heat Transfer in an LMFBR Fuel Assembly," Nuclear Engineering Laboratory, Toshiba Corporation, Japan, to be plished in 1984 National Heat Transfer Conference.

Nijsing, R. and Eifler, W. (1974), "A Computational Method for the Steady State Thermohydraulic Analysis of Fuel Rod Bundles with Single Phase Cooling," Nuclear Engineering and Design, 30 (1974) 145-185.

Novendstern, E. H. (1972a), "Mixing Model for Wire Wrap Fuel Assemblies," ANS Winter Meeting, Nov. 12-17, 1972, Washington, D. C. Also ANS Transactions, 15 866 (1972).

Novendstern, E. H. (1972), "Turbulent Flow Pressure Drop Model for Fuel Rod Assemblies Utilizing a Helical Wire Wrap Spacer System," Nuclear Engineering and Design, 22 19 (1972).

Ohtake, T., Uruwashi, S. and Takahashi, K. (1976), "Velocity Measurements in the Subchannel of the Wire-Spaced Subassembly," Nuclear Technology, 30 333 (1976).

References (Continued)

Okamoto, Y., Hishida, M and Akino, N. (1970), "Hydraulic Performance in Rod-Bundle of Fast Reactor Fuels. Pressure Drop, Vibration and Mixing Coefficient," IAEA/SM-130/5 (1970).

Oosthuizen, R. H. (1974), "Turbulent Combined Convective Flow Over a Vertical Plane Surface," 5th International Heat Transfer Conference, Tokyo, 1974.

Panknin, W., et al. (1974), "Forced Convection Heat Treansfer in the Transition from Laminar to Turbulent Flow in Closely Spaced Circular Tube Bundles," Heat Transfer 1974, Vol. 2 pp 325-329, Scripta Book Co., Washington, D.C., 1974.

Pedersen, D. R., Pierce, R. D., Wilson, R. E. and Roop, C. J. (1974) "Crossflow Mixing in a 91-Element Bundle," ANL/RAS 74-2, (Feb. 1974).

Pedersen, D. R., Pierce, R. D., Lorentz, J. J. and Roop, C. J. (1974a), "Experimental Investigation of the Hydraulic Entrance Length and Subchannel Velocity Profiles in a 91-Element Wire-Wrapped Subassembly," ANL/RAS 74-5, (Apr. 1974).

Petrunik, K. (1968), "Turbulent Mixing Measurement for Single Phase Air, Single Phase Water, and Two Phase Air-Water Flows in Adjacent Rectangualr Subchannels," M.A. Sc. Thesis, University of Windsor, Ont. (1968).

Pirelli, D. (1982), "Pressure Drop Characteristics of PEC Reactor Fuel Element," Presented at Second IAHR Specialist Meeting on LMFBR Rod Bundle Thermal-Hydraulics, Rome, Sept. 15-17, (1982).

Potter, R. et al., (1976), "SABRE-1- A Computer Program for the Calculation of Three Dimensional Flows in Rod Clusters," United Kingdom Atomic Energy aauthority (July 1976)

Presser, K. H. (1967), "Warmeubergang und Druckverlust an Reaktorbrennlementen in Form langsdurchstrounter Rundstrabbundel," Jul-486-RB, KFA Julich (1967). Also, International Journal of Heat and Mass Transfer, 14 1235-1259 (1971).

Rameau, B. and Menant, B. (1984), "Sodium Thermalhydraulics under Natural and Mixed Convection in Bundle Geometry- Experimental Results and Analysis," CEA-Centre D'etudes Nucleaires de Grenoble, France, to be published.

Ramm, H., Johannsen, K. and Todreas, N. E. (1974), "Single Phase Transport within Bare-Rod Arrays at Laminar, Transition and Turbulent Flow Condition," Nuclear Engineering and Design, 30, 186-204(1974).

Ramm, H. and Johannsen, K. (1975), "Evaluation of Interchannel Heat Transport in Bare Liquid-Metal Cooled Rod Arrays of Equilateral Triangular Arrangement," ASME paper 75-HT-32 (1975).

References (Continued)

Rehme, K. (1967), "Geometry-Dependence of the Pressure Loss in Rod Bundles with Coiled Wire Spacers and Longitudinal Flow," Ph. D. Dissertation, U. Karlsruhe, Germany, (December 1967).

Rehme, K. (1970), "Widerstandsbeitwerte von Gitterabstandshaltern fur Reaktorbrennelemente," ATKE 15 (2) 127-130 (1970).

Rehme, K. (1971), "Laminarstromung in Stabbundeln," Chemi Ingenieur Technik, 43 17 (1971).

Rehme, K. (1972a), "Pressure Drop Performance of Rod Bundles in Hexagonal Arrangements," Int. Journal of Heat and Mass Transfer, 15 2499-2517 (1972).

Rehme, K. (1973), "Pressure Drop Correlations for Fuel Element Spacers," Nucl. Tech. (17) Jan. 1973.

Rehme, K. (1972), "Simple Method of Predicting Friction Factors of Turbulent Flow in Non-Circular Channels," Int. Journal of Heat and Mass Transfer, 16 933-950 (1973).

Rehme, K. (1978a), "The Structure of Turbulent Flow Through a Wall Subchannel of a Rod Bundle," Nuclear Engineering and Design, 45 311-323 (1978).

Rehme, K. (1978b), "Turbulente Stromung in eihem Wandkanal eines Stabbundels," KfK-2617 (1978).

Rehme, K. (1978c), "Geschwindigkeits-und Turbulenzverteilungen in einem Wandkanal eines Stabbundels," KfK-2637 (1978).

Rehme, K. (1980a), "Turbulent Momentum Transport in Rod Bundles," Nuclear Engineering and Design, 62 137-146 (1980).

Rehme, K. and Trippe, G. (1980), "Pressure Drop and Velocity Distribution in Rod Bundles with Spacer Grids," Nuclear Engineering and Design, 62 349-359 (1980).

Rehme, K. (1982), "Distributions of Velocity and Turbulence in Parallel Flow along an Asymmetric Rod Bundle," Nuclear Technology, 59 (Oct. 1982).

Reihman, T. C. (1969), "An Experimental Study of Pressure Drop in Wire Wrapped FFTF Fuel Assemblies," BNWL-1207, (Sept. 1969).

Reihman, T. C. (1982), "Experimental Study of Pressure Drop in Wire-Wrapped Road Bundle," Presented at 1982 AIAA/ASME Joint Fluids, Plasma, Thermophysics and Heat Transfer Conference, St. Louis, MO, June 7-11, (1982).

References (Continued)

Rogers, J. T. and Tarasuk, W. R. (1968), "Coolant Mixing in Reactor Fuel Bundles. Part II. Forced Mixing by Flow Sweeping," R68-CAP 32, Canadian General Electric (Sept. 1968).

Rogers, J. T. and Todreas, N. E. (1968), "Coolant Interchannel Mixing in Reactor Fuel Rod Bundles Single-Phase Coolants," Heat Transfer in Rod Bundles, ASME (1968).

Rogers, J. T. and Tahir, A. E. E. (1975), "Turbulent Interchange Mixing in Rod Bundle and The Role of Secondary Flows," ASME paper 75-HT-31 (1975).

Roidt, R. M. et al. (1973), "Experimental Determination of Turbulent Exchange Coefficients in Model Reactor Rod Bundle," ASME paper 73-HT-51, Aug. 1973.

Roidt, R. M., Carelli, M. D. and Markley, R. A. (1980), "Experimental Investigations of the Hydraulic Field in Wire-Wrapped LMFBR Core Assemblies," Nuclear Engineering and Design, 62 295-321 (1980).

Rowe, D. S. and Angle, C. W. (1967), "Cross-Flow Mixing between Parallel Flow Channels During Boilng, COBRA- Computer Programm for Coolant Boiling in Rod Arrays," (Part I) BNWL-371, March 1967.

Sangster, W. A. (1968), "Calculation of Rod Bundle Pressure Loss," ASME Paper 68 WA/TH-35 (1968).

Schmid, J. (1966), "Longitudinal Laminar Flow in an Array of Circular Cylinders," International Journal of Heat and Mass Transfer, Vol. 9 925-937 (1966).

Seban, R. A. and Hunsbedt, A. (1973), "Friction and Heat Transfer in the Swirl Flow of Water in an Annulus," International Journal of Heat and Mass Transfer, 16 303-310 (1973).

Sha, W. T. and Schmidt, R. C. (1975), "THI-3D: A Computer Program for Steady State Thermal Hydraulic Multichannel Analysis," ANL-8112 (Dec. 1975).

Sheynina, A. V. (1967), "Hydraulic Resistance of Bundles of Cores in Axial Fluid Flow," Liquid Metals, pp 210-223, Atomizdat, Moscow (1967), KfK-tr-365. Also "Resistance to Axial Flow of Fluids Past Rod Clusters, NASA TT F-522, Tr. of Liquid Metals, Atomizdat, Moscow (1967).

Simonek, J. (1966), "Prisperec K problematia prestupu tepla v proutkovem palivovem clanku," Jaderna energie 12 (7), 246-249 (1966).

Singh, K. and St Pierre C. C. (1972), "Single Phase Turbulent Mixing in Simulated Rod Bundle Geometries," Trans. CSME 1 (2) 73-80 (June 1972)

References (Continued)

Skok, J. (1973), "Mixing of the Fluid due to Helicoidal Wires on Fuel Pins in a Triangular Array," Progress in Heat and Mass Transfer, 7 (1973).

Sparrow, E. M. and Loefler, J. R. (1959), "Longitudinal Laminar Flow Between Cylinders Arranged in Regular Array," American Institute of Chemical Engineering Journal, 5 No. 3, 1959.

Spencer, D. R. and Markley, R. A. (1980), "Friction Factor Correlation for 217-Pin Wire Wrap Spaced LMFBR Fuel Assemblies," ANS Transactions, 39 1014, 1980.

Spriggs, H. D. (1973), "Comments on Transition from Laminar to Turbulent Flow," Ind. Eng. Chem. Fundam., 12, 3, 286 (1973).

Straub, G. (1976), "Berechnung der Temperatur- und Geschwindigkeitsfelder in Parallel angestromten Brennstabbundlen Schneller natriumgekuhlter Brutreaktoren," Dissertation, IKE, TU Stuttgart 1976.

Subbotin, V. I. et al (1960), "Hydraulischer Widerstand bei durch Flussigkeiten langsumstromten Stabbundeln," Kernenergie, 4, 658-660 (1961). Cf. Atomnaya Energiya, 9, 308 (1960).

Subbotin, V. I., Gabrianovich, B. N. and Sheinina, A. V. (1972), "Hydraulic Resistance with Longitudinal Streamline Flow for Bundles of Plain and Finned Rods," Atomnaya Energiya, Vol. 33, No. 5, pp 889-892, (Nov. 1972).

Sutherland, W. A. and Kays, W. M. (1965), "Heat Transfer in Parallel Rod Arrays," Report GEAP-4637 of General Electric Company, San Jose, CA (1965).

Symolon, P. D. and Todreas, N. E. (1980), "A Manual for Use with the Computer Code SUPERENERGY- Data Reduction Version," COO-2245-74TR, MIT, Feb. 1980.

Symolon, P. D. and Todreas, N. E. (1981), "Fluid Mixing Studies in a Hexagonal 217-pin Wire Wrapped Rod Bundle," DOE/ET/37240-84TR, MIT, (Feb. 1981).

Symolon, P. D. and Todreas, N. E. (1981a), "Fluid Mixing Studies in a Hexagonal 61 pin Wire Wrapped Rod Bundle," Coo-2245-51TR, Rev. I, MIT, (Feb. 1981).

Symolon, P. D. (1982), "Mixed Convection in Vertical Rod Bundles," Ph.D. Thesis, Nuclear Engineering Department, MIT (Aug. 1982).

Symolon, P. D. (1982a) personal communication to S.-K. Cheng.

References (Continued)

Todreas, N. E. and Turi, J. A. (1972), "Interchannel Mixing in Wire Wrapped Liquid Metal Fast Reactor Fuel Assemblies," Nucl. Tech. Vol. 13 (Jan 1972).

Todreas, N. E., (1984), 22.313 Class Notes, Nuclear Engineering Department, MIT, Jan. 1984.

Ullrich, R. (1974), "Analyse der Ansgebildeten Laminarstromung in Langsangestromten Endlichen, Hexagonalen Stabbundeln," Doktor-Ingenieur Dissertation, Inst. Kerntech., Technische Universitat Berlin, Berlin, (1974).

Wakasugi, K. and Kakehi, I. (1971), "Pressure Drop Performance of Fuel Pin Bundle with Spiral Wire Spacer," Jl. Nucl. Sci. and Tech. 8 (3) 167-172 (March 1971).

Walton, F. B. (1969), "Turbulent Mixing Measurements for Single Phase Air-Water Flows in Adjacent Triangualr Subchannels," M.A. Sc. Thesis, University of Windsor, Windsor, Ont. (1069)

Wang, S. F. and Todreas, N. E. (1980), "Flow Split, Pressure Drop, and Mixing Experiments in a 61-pin Shaved-Wire Blanket Assembly," DOE/ET/37240-86TR, MIT (Oct. 1980).

Wang, S. F. and Todreas, N. E. (1981), "Computer Model for M.I.T. Correlations for Friction Factors, Flow Splits and Mixing Parameters in LMFBR Wire-Wrapped Rod Assemblies," COO-2245-87TR, MIT, Feb. 1981.

Wantland, J. L. (1974), "ORRIBLE - A Computer Program for Flow and Temperature Distribution in 19-Rod LMFBR Fuel Subassemblies," Nucl. Tech. Vol. 24, (Nov. 1974).

Wei, J. P. (1979), "FLUMIX II: A Computer Program for Steady-State Thermal Hydraulic Analysis of Wire-Wrapped Rod Bundle," GEFR 00436, General Electric Company (1979)

Wheeler, C. L., Rowe, D. S. and Smith, J. D. (1974), "An Experimental Study of Axial and Cross Flow Velocity in a 7-Pin Wire Wrapped Bundle, BNWL-1804, (Feb. 1974).

Wheeler, C. L. et al. (1976), "COBRA-IV-1: An Interin Version of COBRA for Thermal Hydraulic Analysis of Rod Bundle Nuclear Fuel Elements and Cores," BNWL-1962, Pacific Northwest Laboratory, Richland, WA. (1976)

Yang, J. W. (1976), "A Note on Turbulent-Laminar Transition for Flow in Triangular Rod Bundles," Nucl. Sci. and Eng., Vol. 62, No. 3, 579-582 (1976).

References (continued)

Yeung, M. R. and Wolf, L., (1980), "Evaluation of Conduction Mixing Lengths for Subchannel Analysis of Finite LMFBR Bundles," Nuclear Engineering and Design, 62 371-378 (1980).

Yoshikawa, N. et al. (1981), "ASFRE: A Computer Code for Single-Phase Subchannel Thermal Hydraulic Analysis of LMFBR Single Subassembly," PNC Report, PNC N941 81-74, April 1981.

APPENDIX A1

NORMALIZED FLOW SPLIT MAP RESULTS OF FLOW SPLIT EXPERIMENT

RUN 1

M_L = 32.5 GPM

Re_b = 3,470

X_1 = 0.763

X_2 = 1.307

Mass Balance Error = -12%

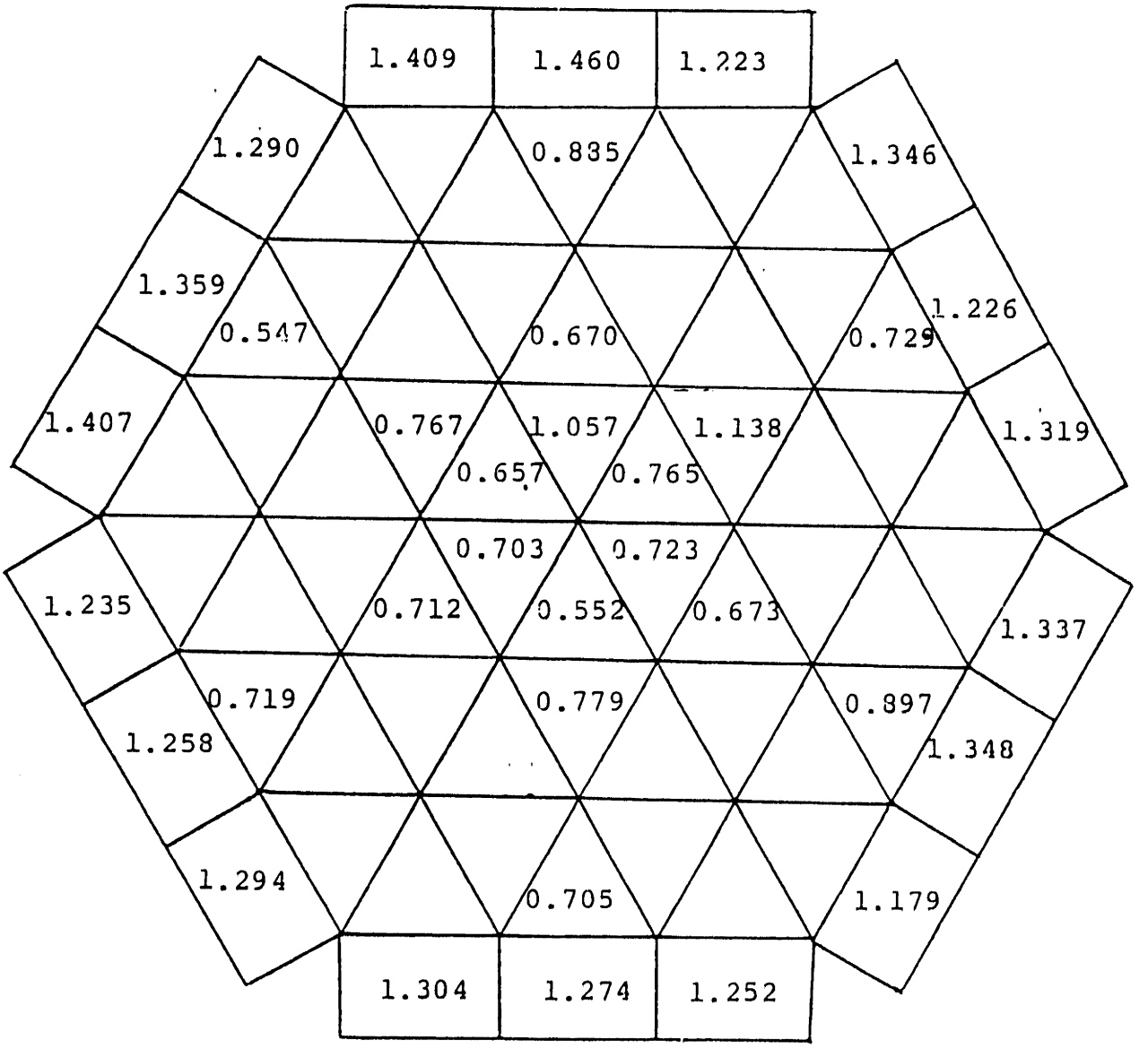

RUN 2

M_L = 42.8 GPM

Re_b = 4,570

X_1 = 0.800

X_2 = 1.259

Mass Balance Error = -5.0%

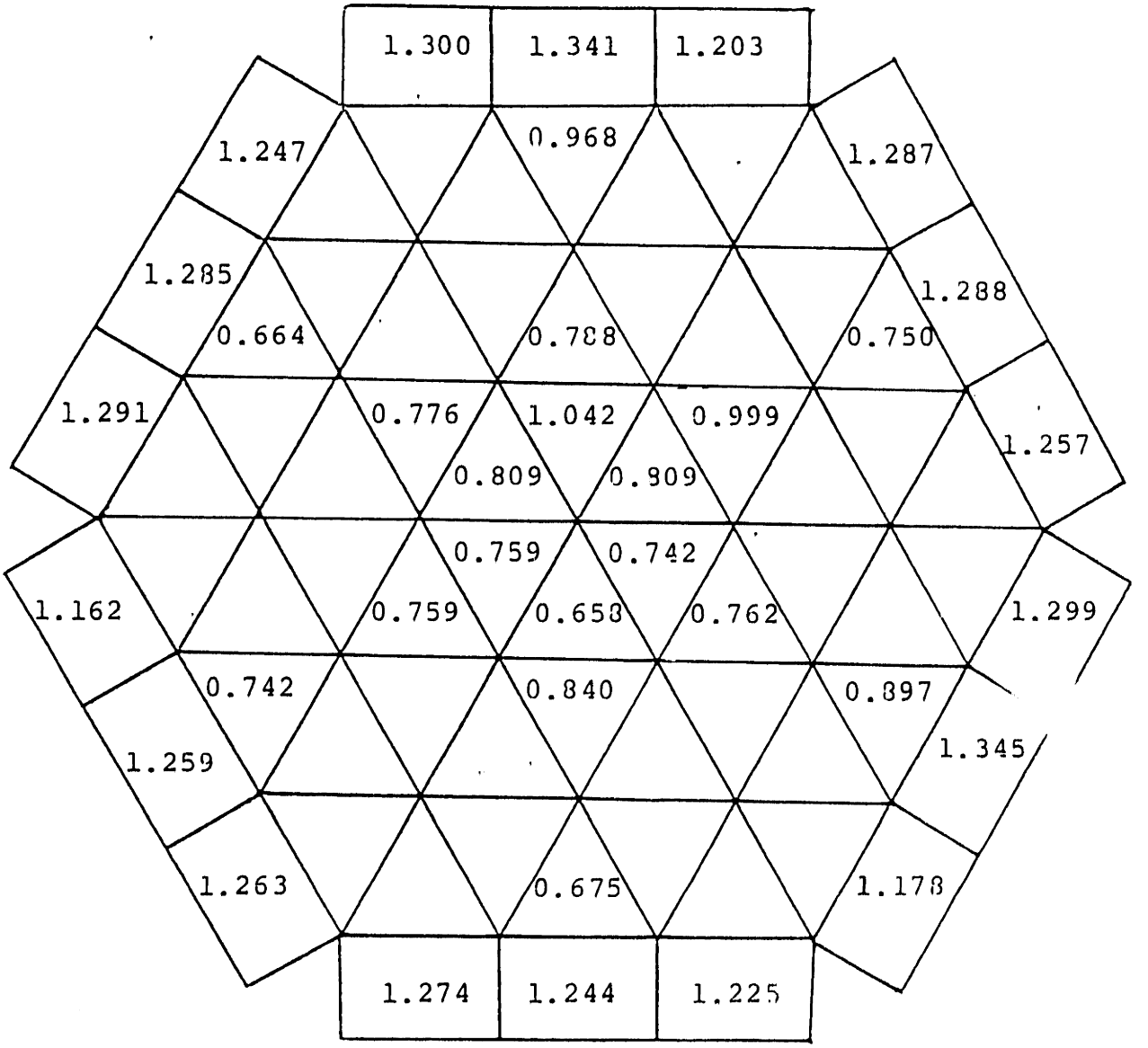

RUN 3

M_L = 52.4 GPM

Re_b = 5,600

X_1 = 0.841

X_2 = 1.206

Mass Balance Error = -3.5%

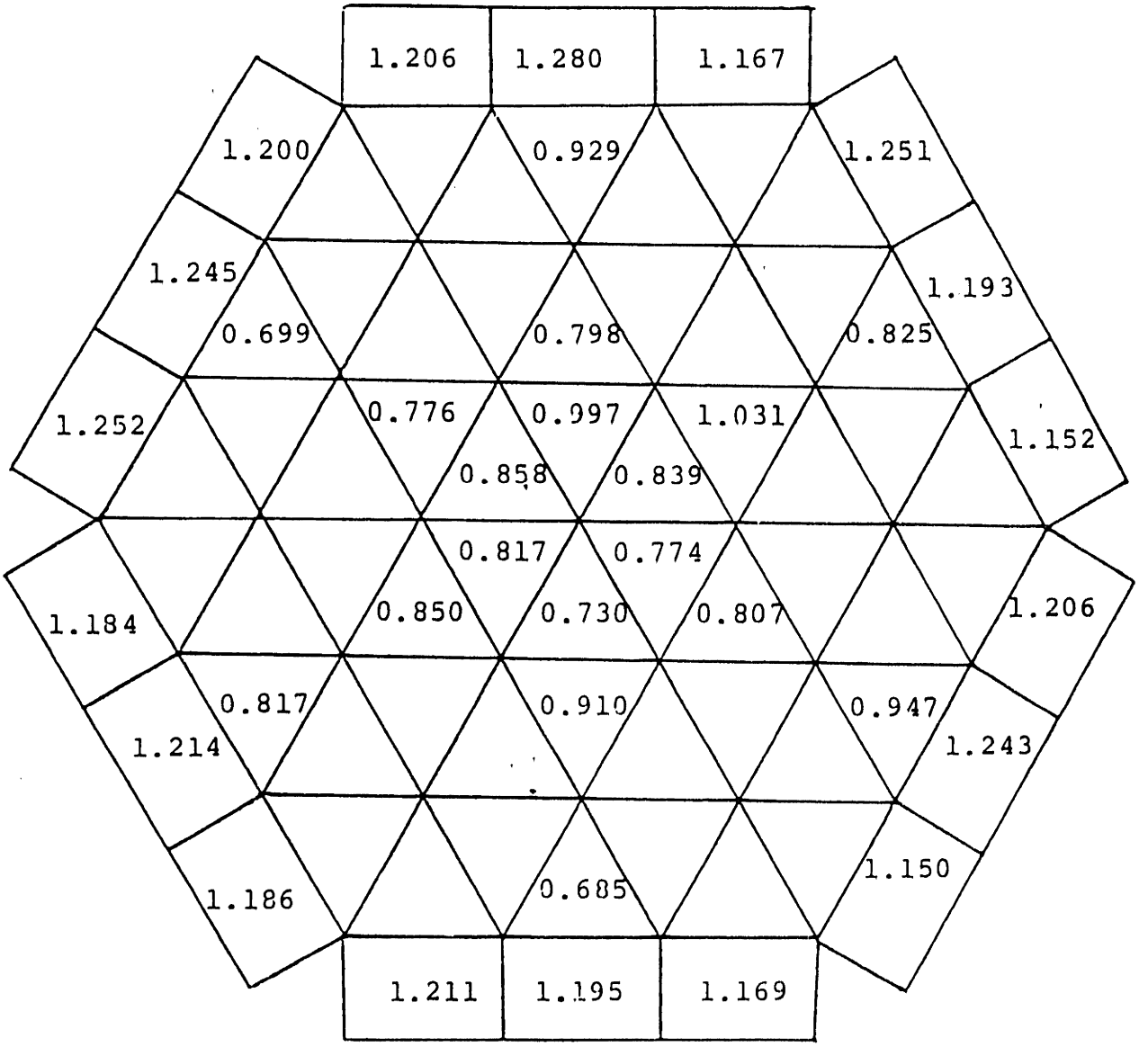

RUN 4

M_L = 56 GPM

Re_b = 5,950

X_1 = 0.864

X_2 = 1.175

Mass Balance Error = -1.6%

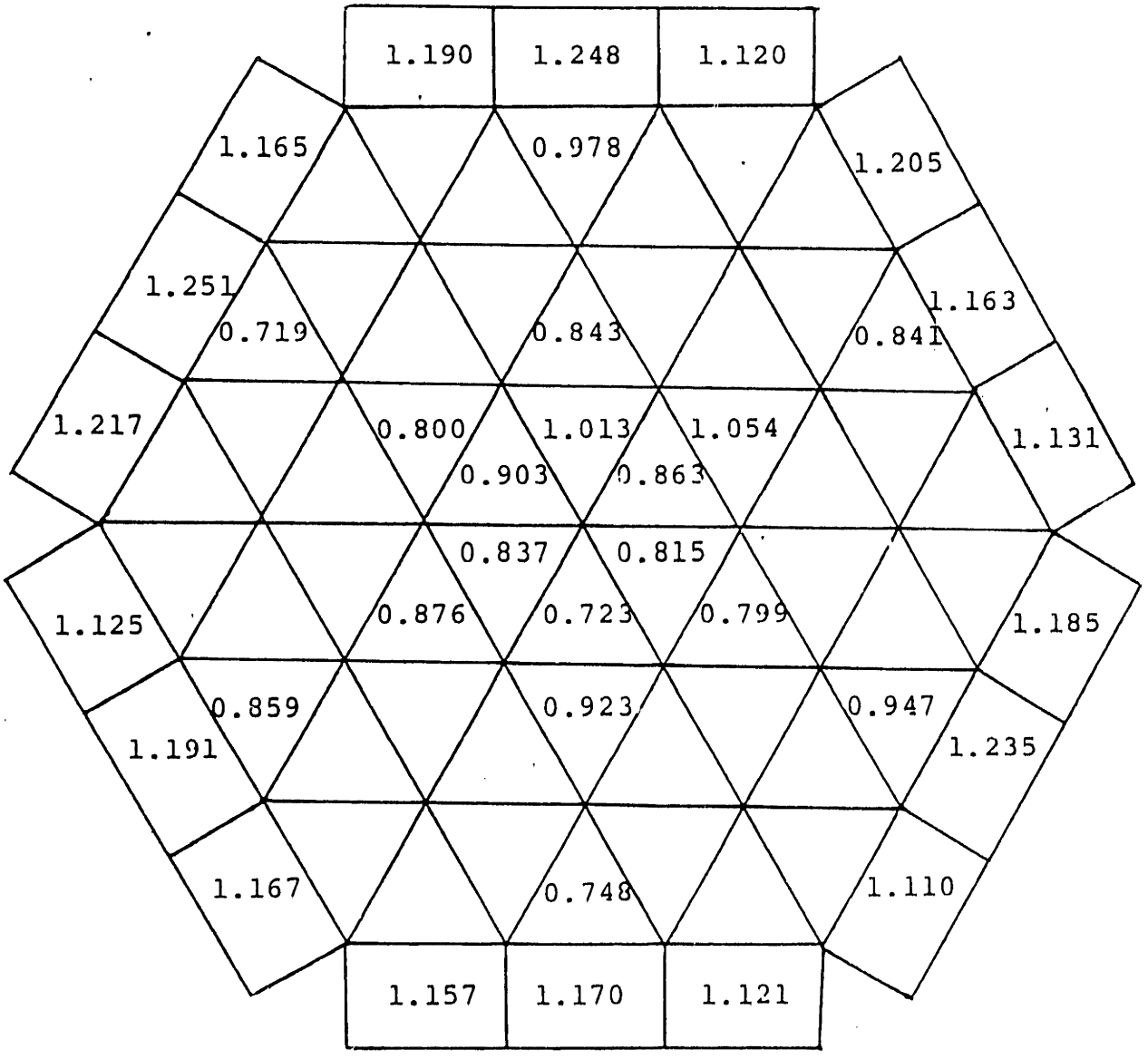

RUN 5

M_L = 70 GPM

Re_b = 7,440

X_1 = 0.875

X_2 = 1.161

Mass Balance Error = -2.2%

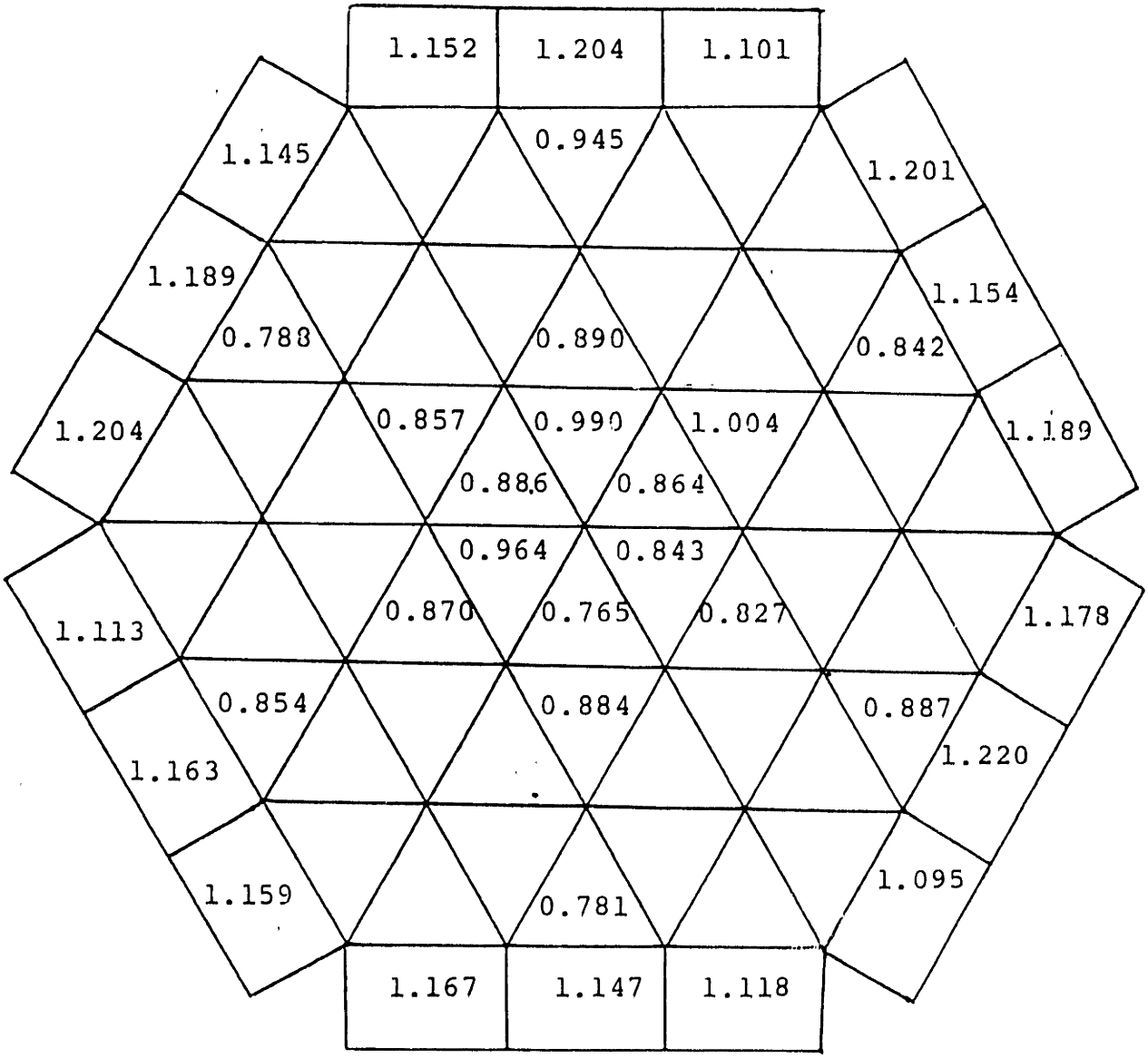

RUN 6

M_L = 70 GPM

Re_b = 7,630

X_1 = 0.879

X_2 = 1.155

Mass Balance Error = -1.4%

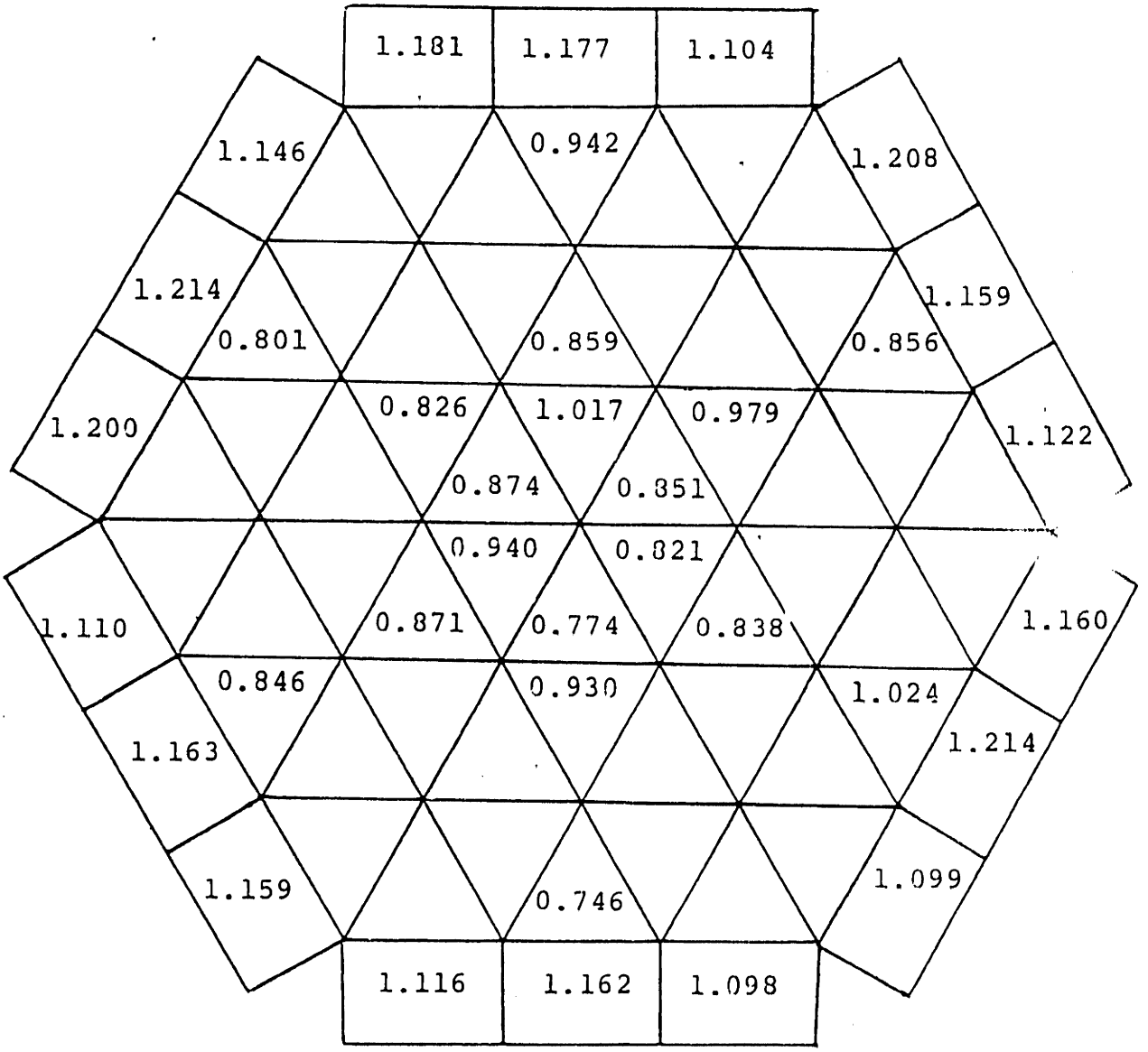

RUN 7

M_L = 81 GPM

Re_b = 8,620

X_1 = 0.894

X_2 = 1.136

Mass Balance Error = -2.8%

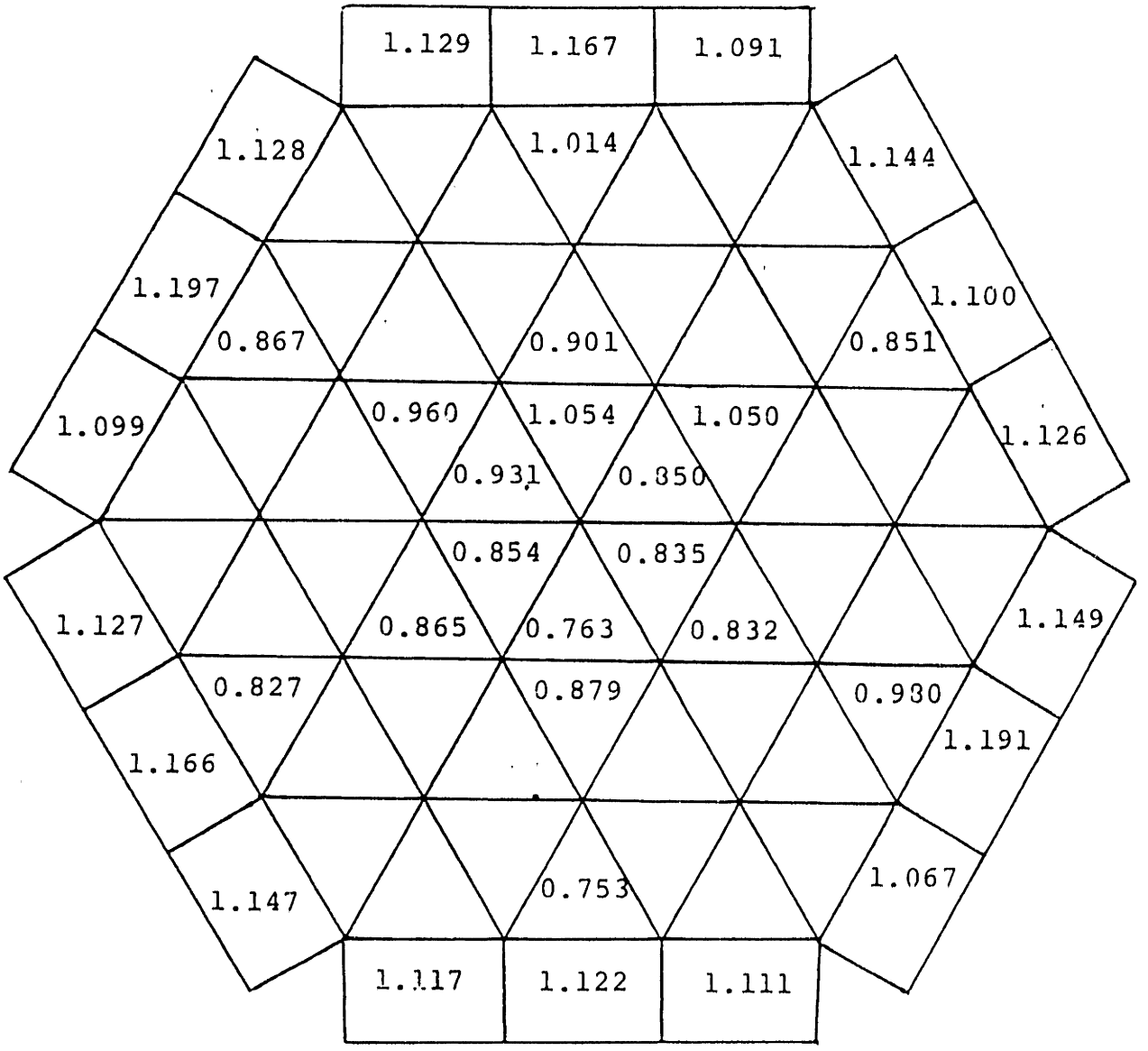

RUN 8

M_L = 100 GPM

Re_b = 10,480

X_1 = 0.915

X_2 = 1.110

Mass Balance Error = -3.7%

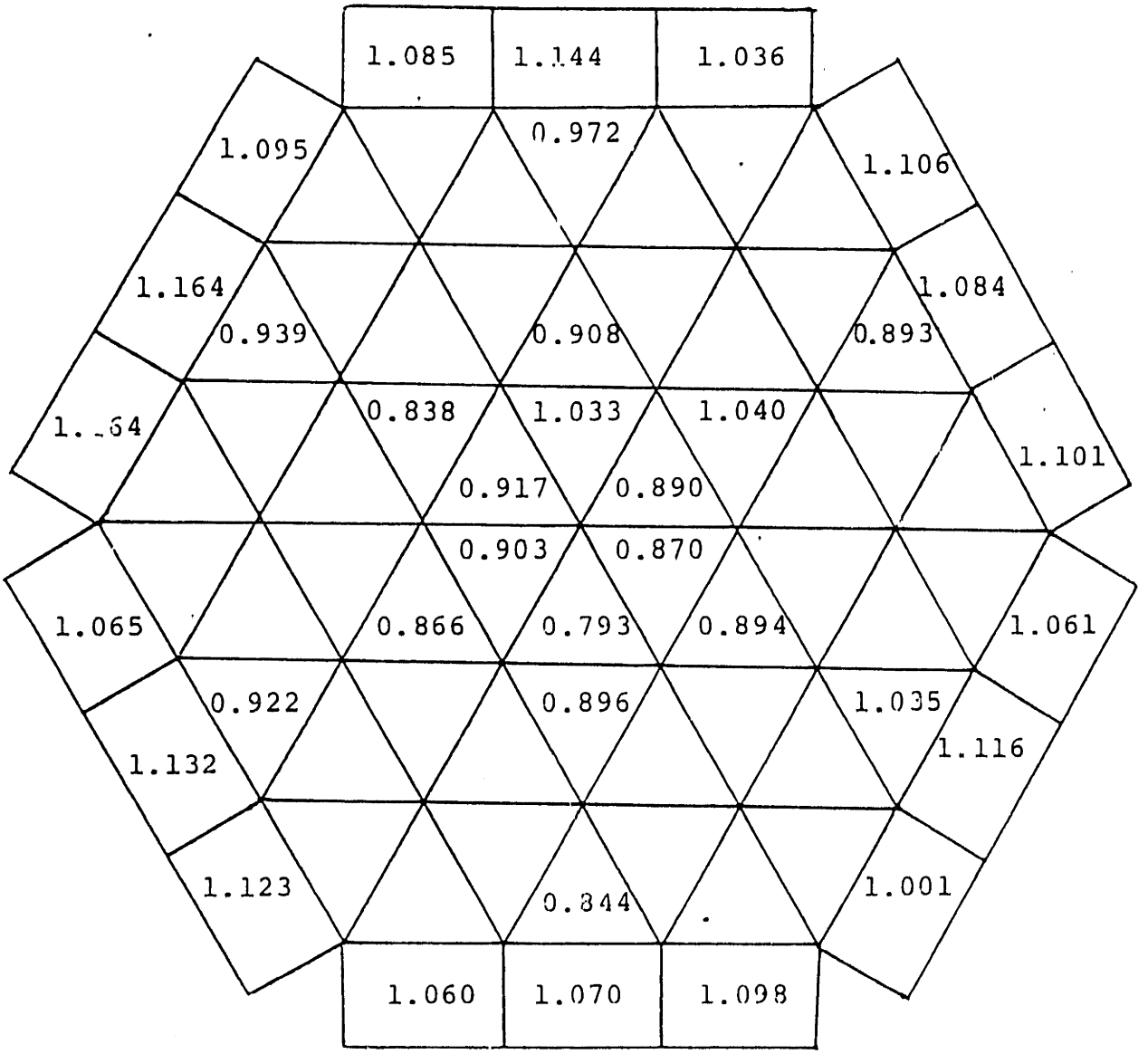

RUN 9

M_L = 105 GPM

Re_b = 11,380

X_1 = 0.916

X_2 = 1.109

Mass Balance Error = -3.5%

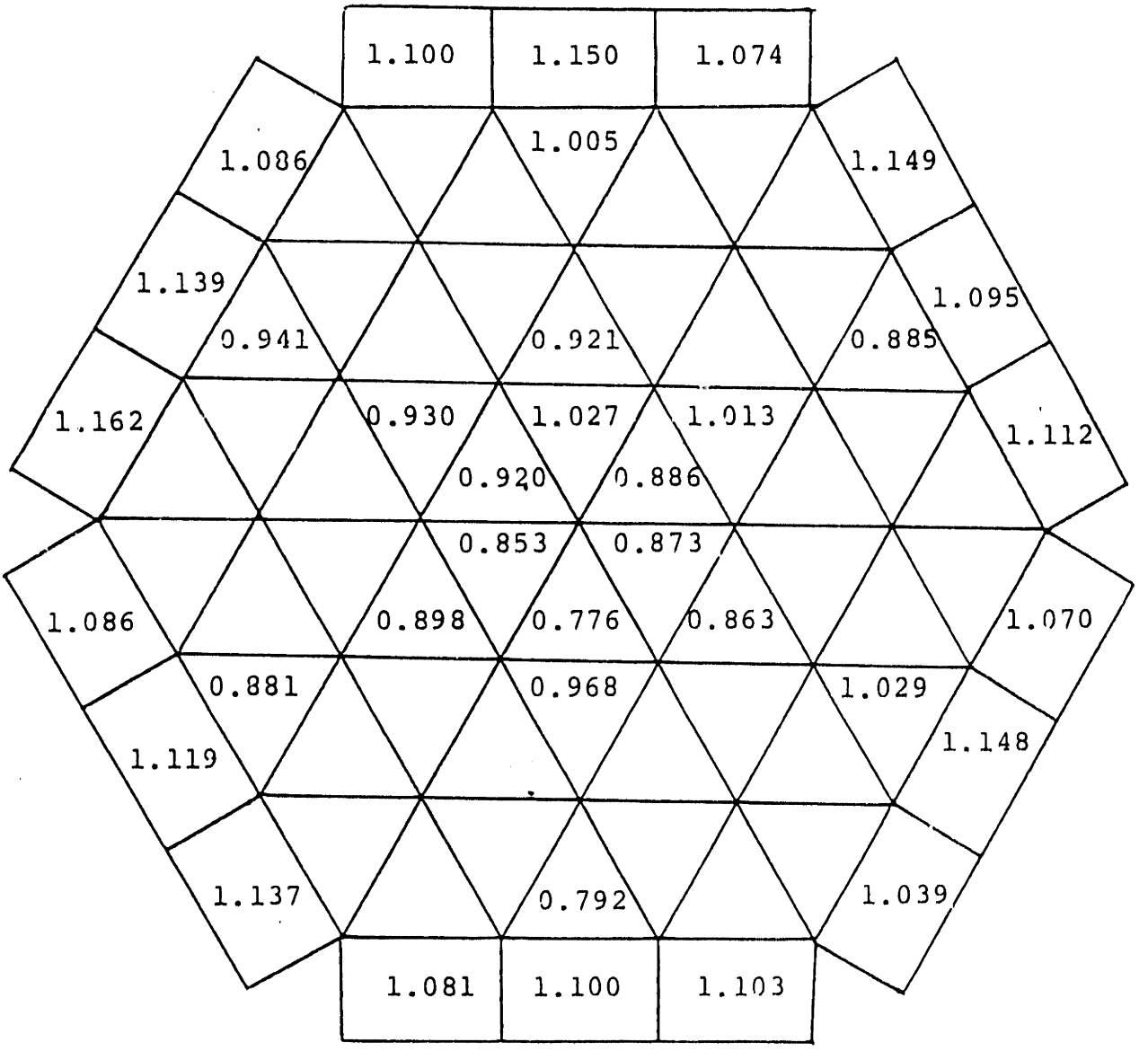

RUN 10

M_L = 121 GPM

Re_b = 10,740

X_1 = 0.949

X_2 = 1.079

Mass Balance Error = -3.6%

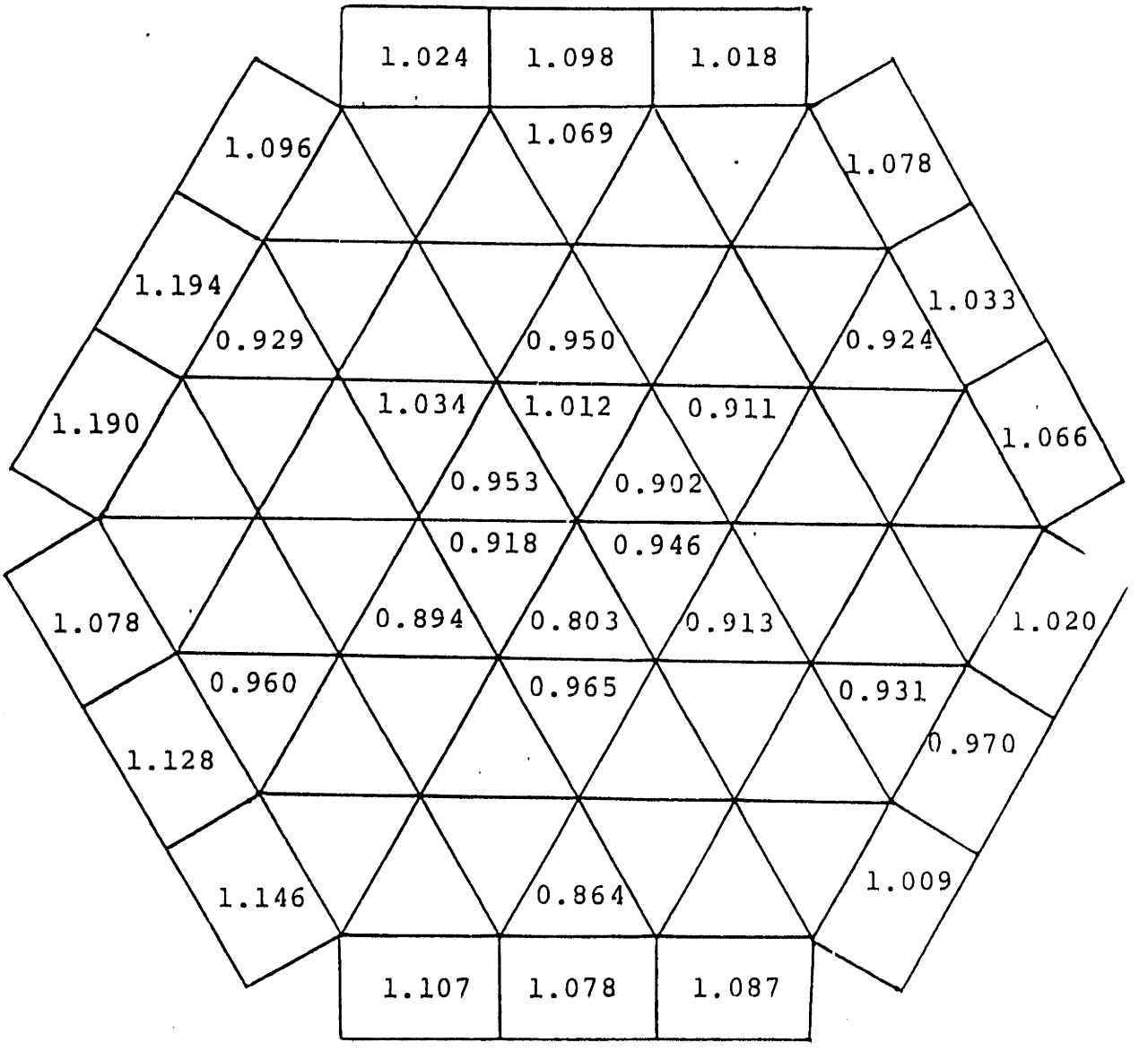

RUN 11

M_L = 142 GPM

Re_b = 12,840

X_1 = 0.936

X_2 = 1.082

Mass Balance Error = -4.4%

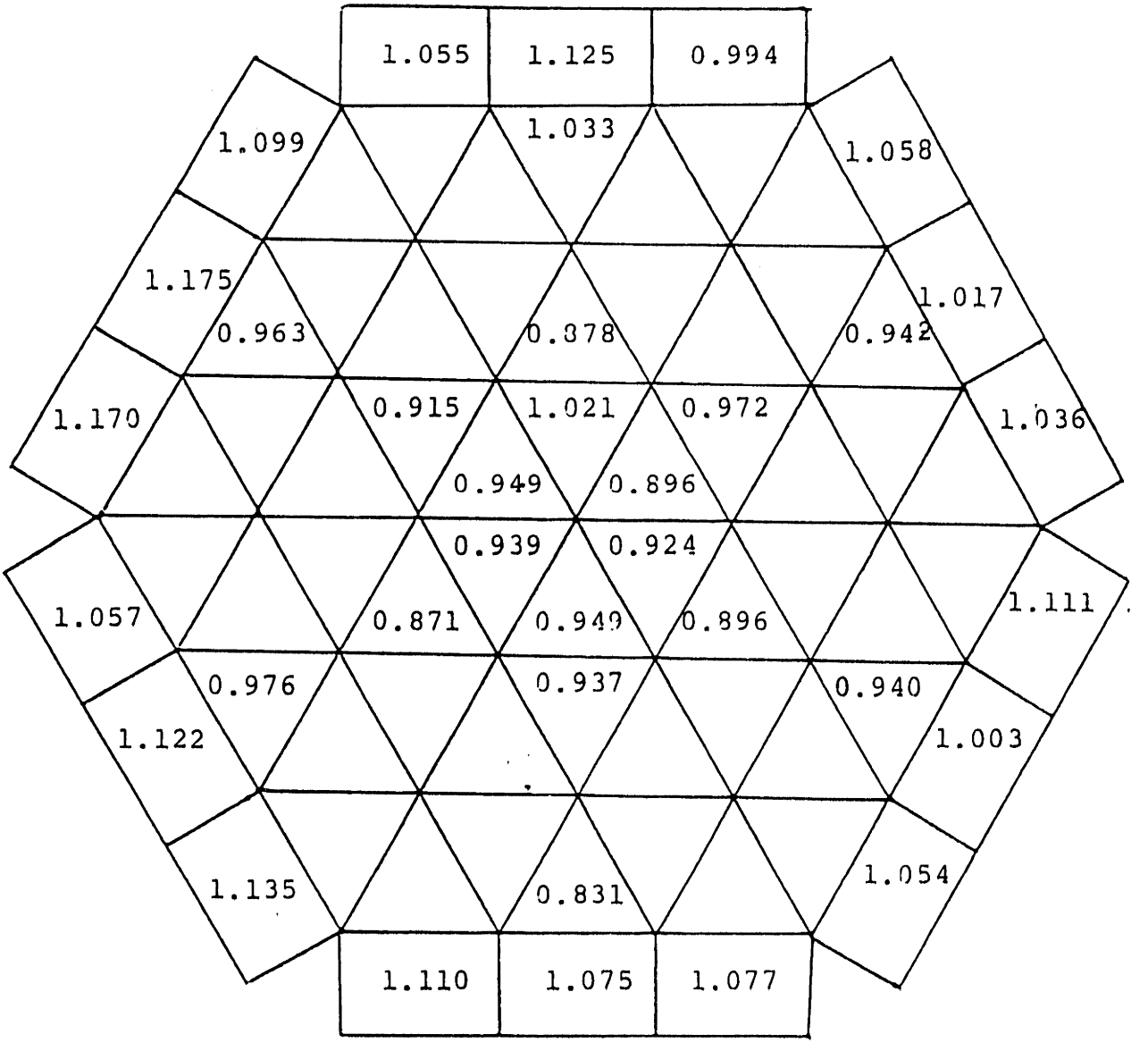

RUN 12

M_L = 173 GPM

Re_b = 16,170

X_1 = 0.934

X_2 = 1.085

Mass Balance Error = -2.8%

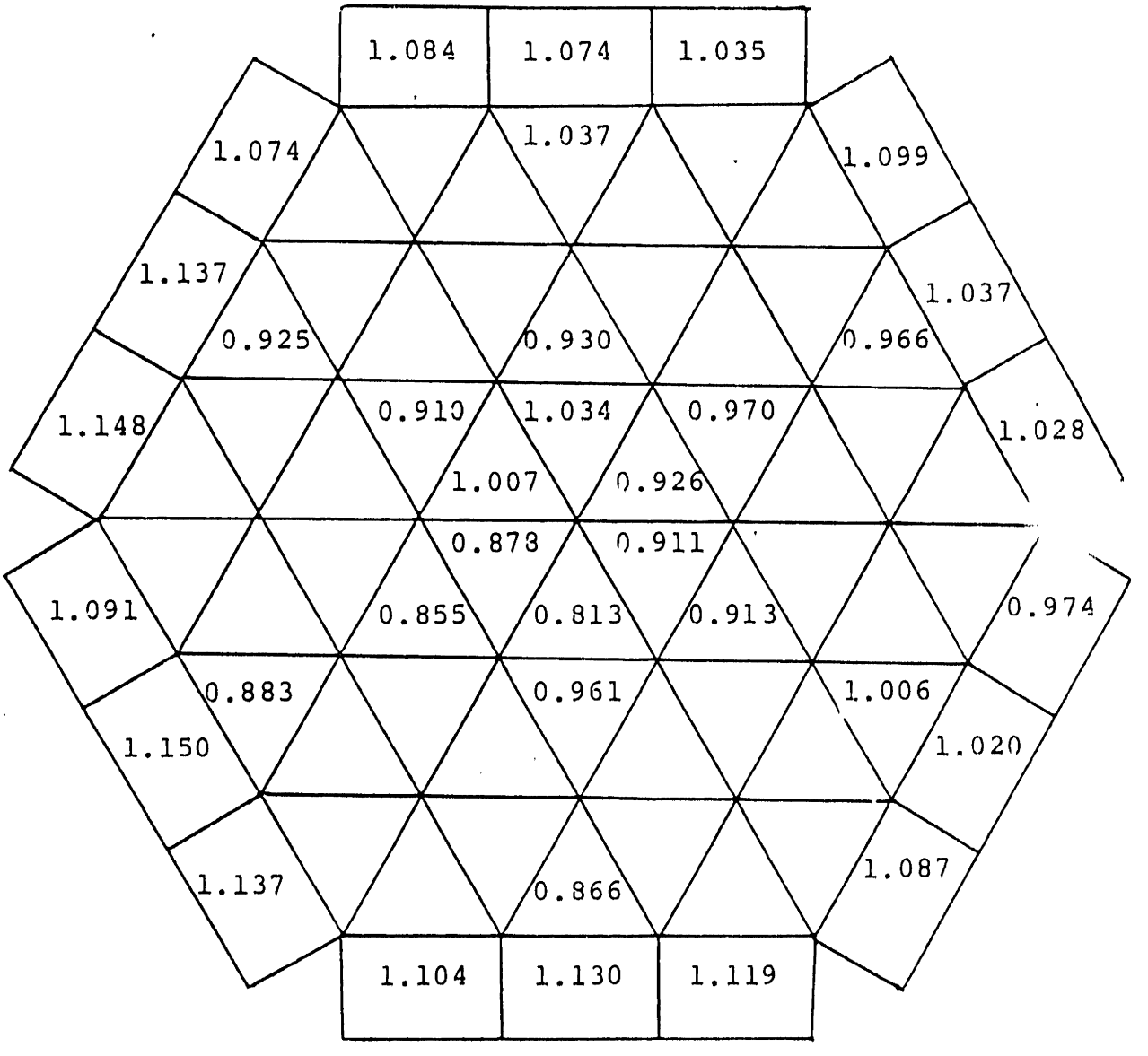

RUN 13

M_L = 197 GPM

Re_b = 18,960

X_1 = 0.939

X_2 = 1.078

Mass Balance Error = -3.4%

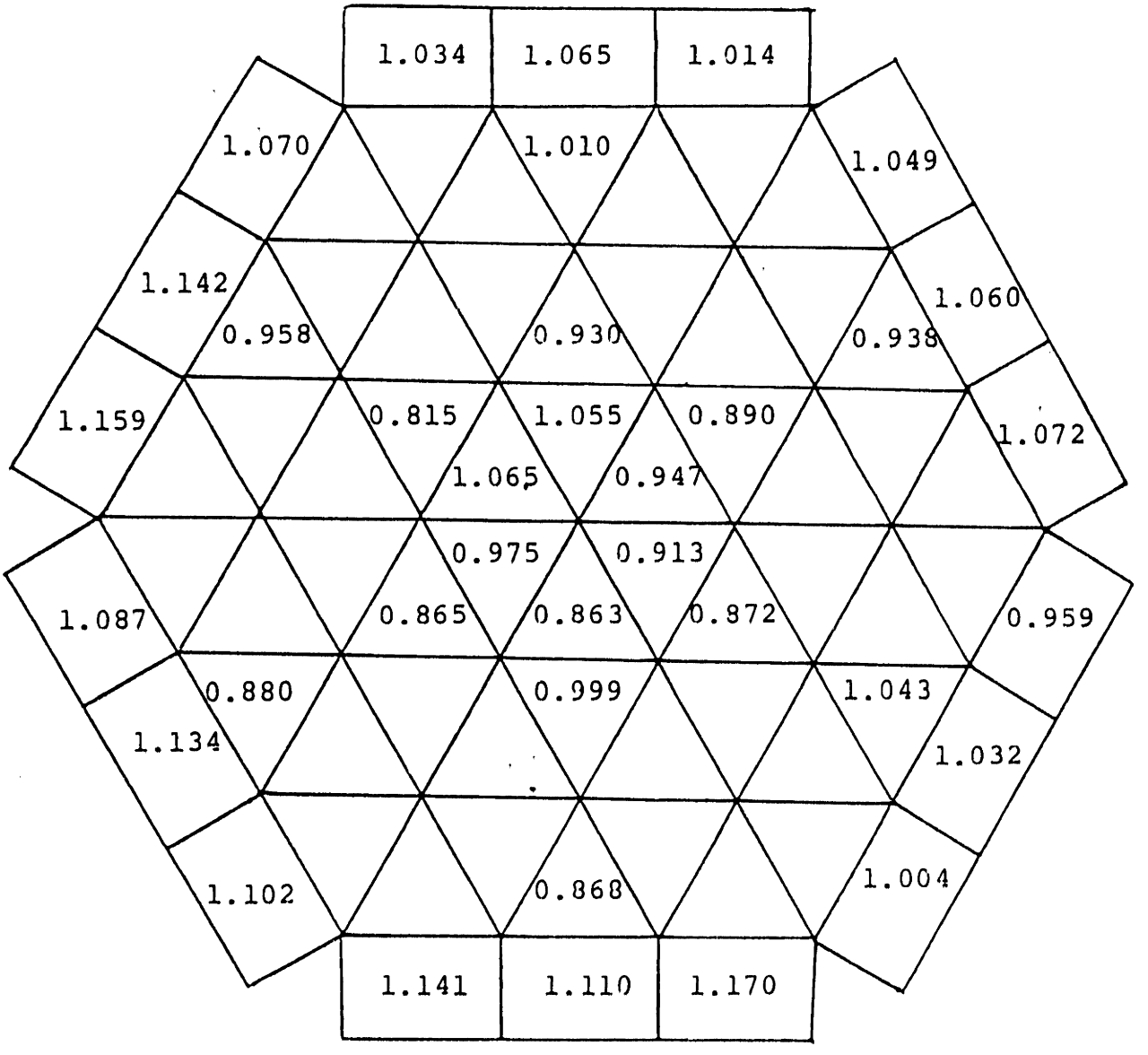

RUN 14

M_L = 224 GPM

Re_b = 21,600

X_1 = 0.962

X_2 = 1.048

Mass Balance Error = -2.2%

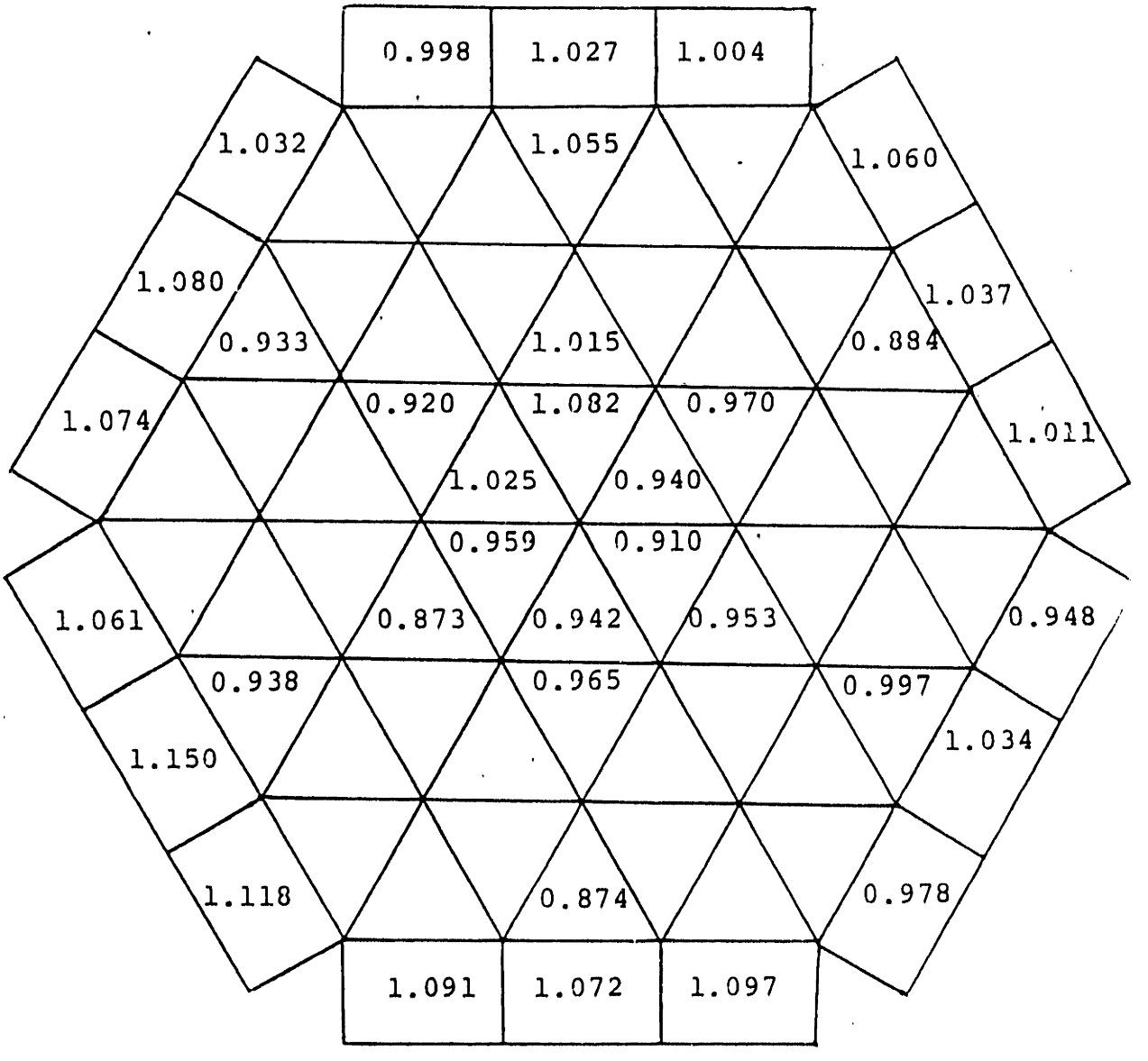

RUN 15

M_L = 220 GPM

Re_b = 22,510

X_1 = 0.953

X_2 = 1.060

Mass Balance Error = -2.0%

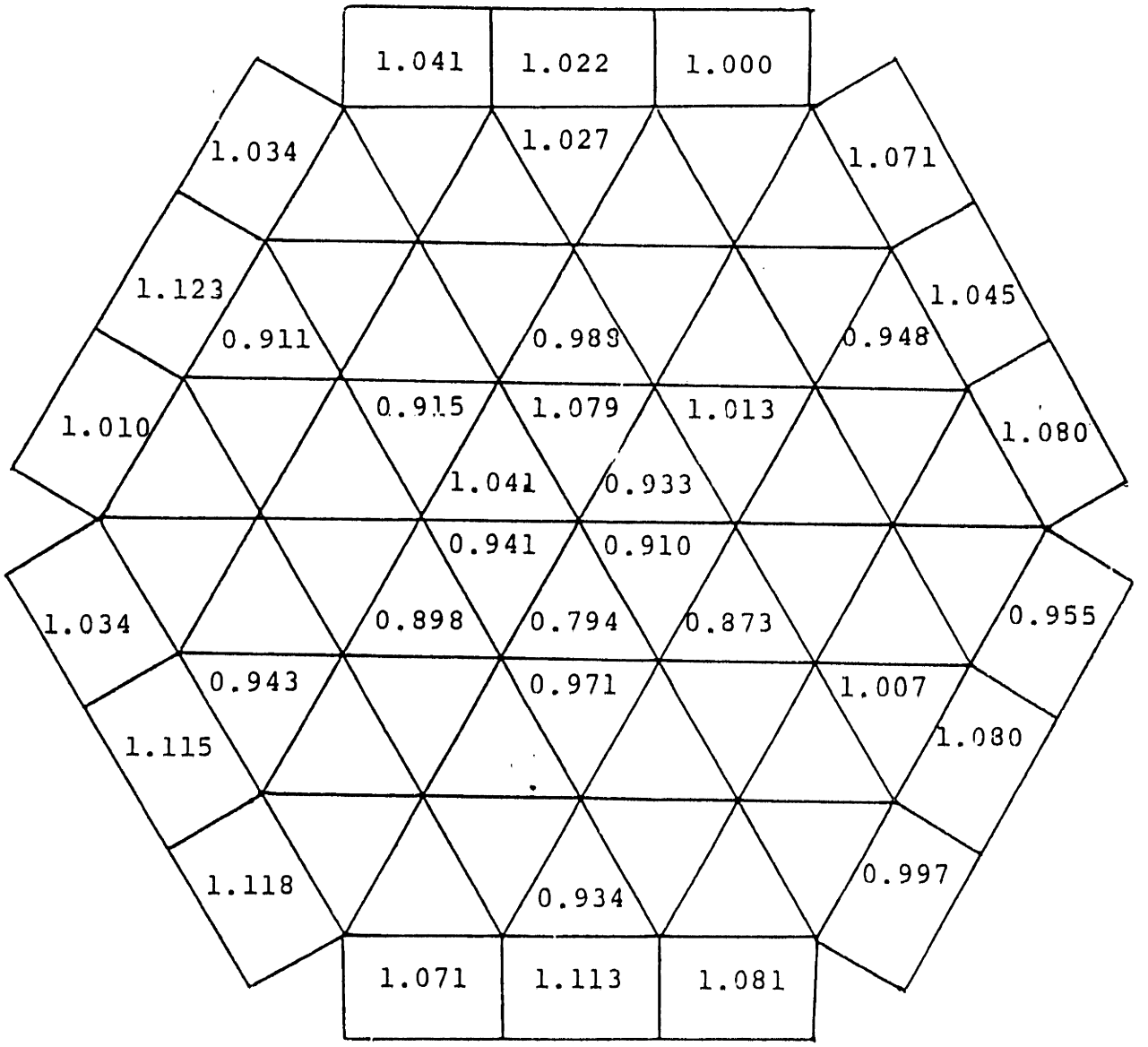

RUN 16

$M_{I,}$ = 215 GPM

Re_b = 26,300

X_1 = 0.967

X_2 = 1.042

Mass Balance Error = +0.9%

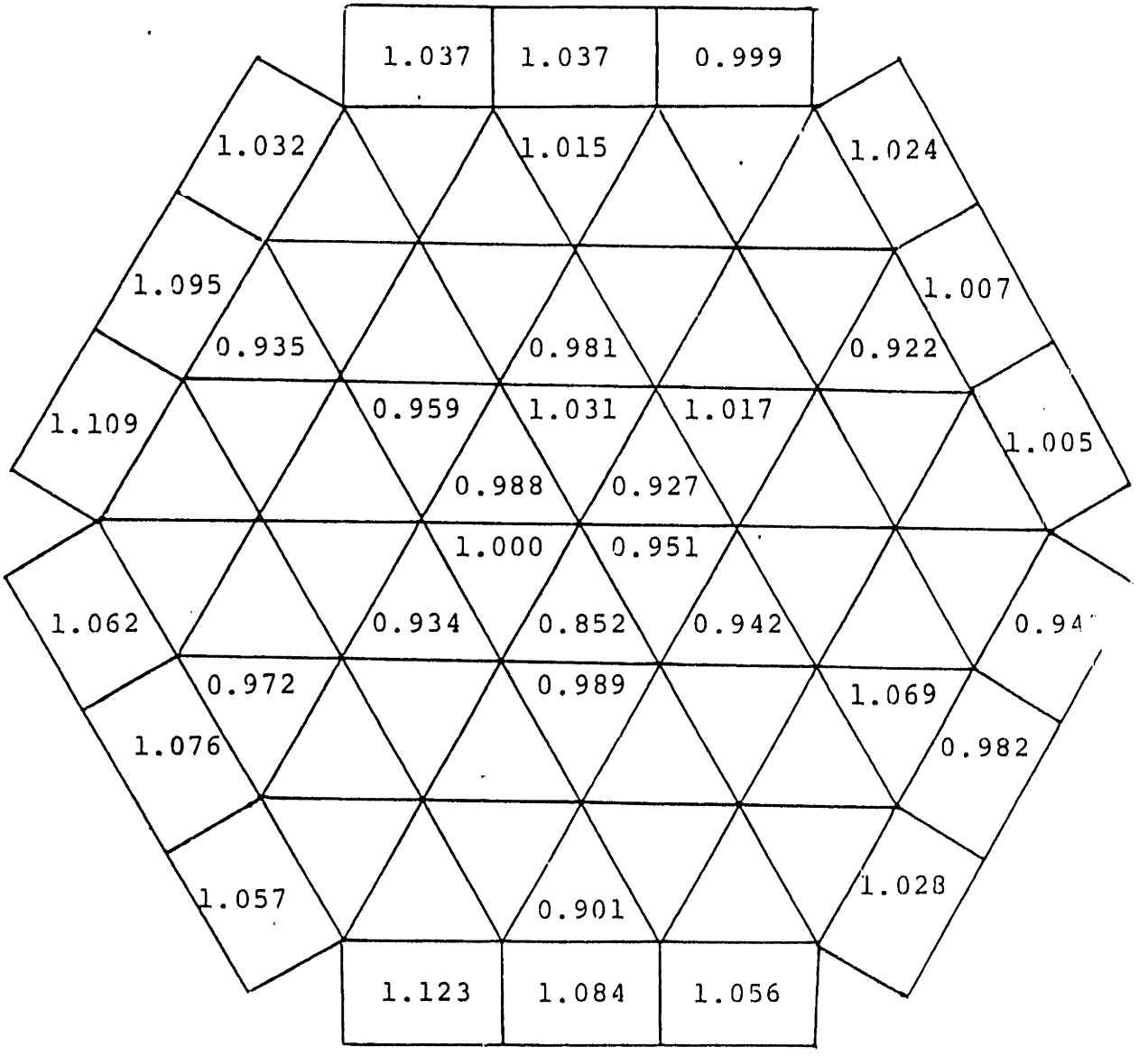

APPENDIX A2

EXPERIMENTAL DIMENSIONLESS SALT CONCENTRATION MAPS

Note: ◯ - Injection subchannel

37 pin p/d= 1.154 h/d= 13.40
inj. subchannel = 1
inj. depth (in) = 32.0
bundle reynolds no.= 220
mass balance ratio = 1.702
dimensionless ratios of salt concentration*100.0:

0.3 0.0 0.0 0.1 0.2

0.1 0.1 0.4 1.6 0.1

0.0 0.1 1.2 0.9

0.1 0.0 1.6 6.8 6.3 0.1

0.2 0.7 6.6 5.8 4.4

0.1 0.0 0.7 5.6 13.6 2.2 0.0

0.0 0.1 2.7 (5.3) 3.7 2.3

0.0 0.1

0.0 0.2 0.4 6.4 4.2 0.5

0.1 0.0 0.0 2.1 5.7 2.0 0.1

0.0 0.0 0.1 0.7 0.4

0.0 0.0 0.1 0.5 0.9 0.2

0.0 0.1 0.1 0.2

0.0 0.0 0.0 0.1 0.0

0.0 0.0 0.1 0.0 0.0

37 pin p/d= 1.154 h/d= 13.40
inj. subchannel = 1
inj. depth (in) = 32.0
bundle reynolds no.= 29600
mass balance ratio = 1.430
dimensionless ratios of salt concentration*100.0:

0.5 0.1 0.5 0.3 0.0

0.3 1.0 2.5 0.5 0.0

0.7 2.0 2.5 0.2

0.0 1.5 3.3 3.9 1.1 0.0

0.7 3.1 4.9 4.6 1.4

0.4 1.4 4.6 5.3 3.7 1.3 0.1

0.3 1.6 4.0 (3.8) 3.8 0.9

0.0 0.0

0.2 2.7 2.9 3.7 1.2 0.6

0.0 0.5 1.2 2.9 2.2 1.2 0.0

0.5 0.9 0.6 0.9 0.6

0.5 0.7 0.9 1.4 0.5 0.0

0.6 0.6 0.1 0.0

0.3 0.1 0.3 0.0 0.0

0.7 0.6 0.5 0.0 0.0

37 pin p/d= 1.154 h/d= 13.40
inj. subchannel = 1
inj. depth (in) = 32.0
bundle reynolds no.= 430
mass balance ratio = 1.805
dimensionless ratios of salt concentration*100.0:

0.3 0.0 0.3 0.3 0.3

0.2 0.4 0.4 1.8 0.3

0.0 1.3 1.7 0.4

0.0 0.4 1.4 6.7 6.4 0.3

0.2 1.0 4.0 5.4 3.8

0.2 0.0 1.1 6.2 7.0 1.7 0.0

0.1 0.4 3.2 (7.7) 3.5 1.7

0.9 0.0

0.3 0.9 1.3 4.4 2.1 1.0

0.0 0.2 0.5 1.9 4.5 2.4 0.3

0.0 0.3 0.8 0.7 0.6

0.1 0.1 0.0 0.4 0.4 0.1

0.0 0.2 0.2 0.2

0.0 0.4 0.0 0.0 0.1

0.5 0.0 0.1 0.0 0.0

37 pin p/d= 1.154 h/d= 13.40
inj. subchannel = 71
inj. depth (in) = 32.0
bundle reynolds no.= 430
mass balance ratio = 2.007
dimensionless ratios of salt concentration*100.0:

1.0 0.2 0.0 9.2 18.3

0.0 0.6 1.3 1.1 15.7

0.4 0.7 1.2 7.2

0.5 1.1 0.0 0.0 4.5 13.1

0.9 0.5 0.0 1.4 3.5

1.1 0 2 0.5 0.2 2.8 16.8 7.7

0.2 0.0 0.0 0.3 2.3 12.7

0.2 7.7

0.7 0.0 0.0 0.0 1.0 14.9

0.8 0.9 0.0 0.0 0.0 9.6 7.8

0.0 0.1 0.6 1.0 9.6

0.0 0.9 0.7 0.0 1.0 (1.7)

0.2 1.1 0.5 2.4

0.0 1.2 0.9 2.6 0.1

2.7 0.6 0.5 0.5 0.3

37 pin p/d= 1.154 h/d= 13.40
inj. subchannel = 1
inj. depth (in) = 32.0
bundle reynolds no.= 860
mass balance ratio = 1.348
dimensionless ratios of salt concentration*100.0:

0.1 0.2 0.4 0.2 0.0

0.0 0.4 0.6 0.6 0.1

0.0 0.2 0.9 0.8

0.1 0.2 2.2 4.9 2.2 0.2

0.7 1.8 3.4 3.9 1.2

0.0 0.5 3.0 7.4 6.4 1.8 0.4

0.6 1.5 4.1 (6.1) 1.9 1.2

0.1 0.2

0.0 1.9 4.8 5.7 1.7 0.4

0.2 0.2 1.5 6.0 4.3 0.8 0.3

0.2 0.7 0.6 0.9 0.4

0.3 0.0 0.5 0.1 0.6 0.0

0.1 0.4 0.1 0.1

0.0 0.0 0.0 0.0 0.2

0.0 0.0 0.0 0.4 0.3

37 pin p/d= 1.154 h/d= 13.40
inj. subchannel = 71
inj. depth (in) = 32.0
bundle reynolds no.= 860
mass balance ratio = 1.532
dimensionless ratios of salt concentration*100.0:

0.0 0.0 7.6 12.5 17.3

0.0 0.3 0.3 3.7 14.1

0.0 0.4 0.7 7.7

0.0 0.0 0.0 0.4 2.6 10.8

0.5 0.1 0.0 0.0 6.5

0.0 0.0 0.2 0.0 1.5 8.9 7.5

0.4 0.2 0.2 0.2 1.1 10.5

0.0 6.3

0.2 0.0 0.2 0.3 4.2 11.4

0.0 0.0 0.0 0.2 0.0 9.3 5.0

0.2 0.6 0.4 3.9 7.3

0.0 0.0 0.0 1.5 7.3 (4.2)

1.1 0.2 0.5 5.9

0.0 2.9 0.0 1.6 0.9

0.0 0.0 0.2 0.0 0.5

A21

37 pin p/d= 1.154 h/d= 13.40
inj. subchannel = 1
inj. depth (in) = 32.0
bundle reynolds no.= 1500
mass balance ratio = 1.393
dimensionless ratios of salt concentration*100.0:

0.0 0.0 0.5 0.3 0.2

0.1 0.2 1.2 1.0 0.3

0.4 0.5 1.5 1.1

0.2 0.6 3.1 5.0 1.3 0.3

0.8 2.3 3.6 4.3 1.6

0.0 0.8 3.2 6.5 4.3 1.5 0.0

0.6 1.9 4.2 (5.1) 3.2 0.8

0.0 0.0

0.0 2.6 3.5 4.2 1.2 0.3

0.3 0.2 1.8 5.4 3.5 0.7 0.3

0.5 0.7 0.7 0.6 0.0

0.4 0.0 0.8 0.8 0.3 0.0

0.3 0.1 0.4 0.3

0.0 0.0 0.1 0.0 0.1

0.0 0.1 0.2 0.1 0.1

37 pin p/d= 1.154 h/d= 13.40
inj. subchannel = 71
inj. depth (in) = 32.0
bundle reynolds no.= 1500
mass balance ratio = 1.051
dimensionless ratios of salt concentration*100.0:

0.4 4.9 11.9 10.3 8.7

0.0 0.0 0.0 4.9 9.2

0.3 0.6 0.3 6.7

0.0 0.0 0.0 0.0 8.8 9.7

0.0 0.3 0.0 1.3 7.6

0.0 0.0 1.0 0.0 1.2 8.9 7.4

0.3 0.0 0.0 0.3 1.9 11.7

0.0 6.6

0.0 0.0 0.0 0.2 3.5 11.0

0.0 0.7 0.0 0.0 0.8 7.0 5.8

0.3 0.0 0.0 4.5 9.3

0.3 0.0 0.7 0.4 5.8 (2.1)

1.2 0.9 1.3 4.8

0.0 1.5 1.7 1.9 1.1

0.0 0.4 0.0 0.3 0.7

37 pin p/d= 1.154 h/d= 13.40
inj. subchannel = 1
inj. depth (in) = 32.0
bundle reynolds no.= 2200
mass balance ratio = 1.151
dimensionless ratios of salt concentration*100.0:

0.0 0.1 0.0 0.0 0.1

0.6 0.4 1.2 1.3 0.1

0.8 1.0 1.7 1.1

0.4 0.8 2.8 4.0 1.4 0.2

0.4 2.3 4.0 4.5 1.9

0.2 0.4 3.1 5.5 4.0 0.6 0.4

0.1 2.0 4.2 (3.7) 2.9 0.7

0.0 0.5

1.0 2.5 3.1 3.7 1.4 0.7

0.0 0.7 1.4 5.1 3.0 0.5 0.2

0.0 1.1 1.0 1.1 0.2

0.3 0.4 1.2 1.0 0.8 0.3

0.3 0.2 0.0 0.2

0.3 0.2 0.5 0.3 0.1

0.0 0.0 0.3 0.1 0.1

37 pin p/d= 1.154 h/d= 13.40
inj. subchannel = 71
inj. depth (in) = 32.0
bundle reynolds no.= 2200
mass balance ratio = 1.265
dimensionless ratios of salt concentration*100.0:

2.2 7.3 11.2 10.4 9.6

0.0 0.5 2.1 6.5 9.0

0.9 0.5 0.8 7.3

0.0 0.0 0.0 1.0 6.9 8.4

0.0 0.0 0.0 0.3 6.1

0.0 0.0 0.0 0.5 3.5 10.4 7.4

0.0 0.0 0.3 1.1 2.5 8.9

0.0 6.9

0.0 0.0 0.0 0.2 4.2 9.0

0.0 0.0 0.0 0.0 1.7 9.6 6.4

0.0 0.0 0.3 3.2 4.6

0.0 0.0 0.3 0.9 6.8 (2.7)

0.0 0.5 0.8 4.3

0.3 0.0 0.0 1.6 0.2

0.0 0.0 0.3 0.3 0.2

37 pin p/d= 1.154 h/d= 13.40
inj. subchannel = 1
inj. depth (in) = 3..0
bundle reynolds no.= 3200
mass balance ratio = 1.360
dimensionless ratios of salt concentration*100.0:

0.0 0.2 0.2 0.2 0.1

0.2 0.6 1.6 1.4 0.2

0.5 1.1 1.9 0.7

0.2 1.3 2.8 3.9 1.5 0.3

0.3 2.6 3.8 4.6 1.8

0.0 0.8 3.8 5.2 3.6 0.8 0.2

0.1 1.9 4.5 (3.7) 2.8 1.0

0.0 0.7

0.3 2.7 3.2 3.5 1.4 0.1

0.3 0.8 1.5 5.1 2.7 0.9 0.2

0.1 1.1 1.0 0.9 0.2

0.1 0.6 1.5 1.1 0.7 0.1

0.3 0.5 0.0 0.0

0.2 0.4 0.4 0.4 0.0

0.0 0.0 0.1 0.3 0.2

37 pin p/d= 1.154 h/d= 13.40
inj. subchannel = 71
inj. depth (in) = 32.0
bundle reynolds no.= 3200
mass balance ratio = 1.335
dimensionless ratios of salt concentration*100.0:

4.5 10.6 9.1 9.8 10.5

2.1 0.8 2.7 7.6 8.7

0.8 1.5 2.0 7.9

0.5 0.3 0.0 1.0 3.4 6.9

0.0 0.1 0.0 1.9 6.8

0.3 0.0 0.0 0.2 1.7 8.4 5.7

0.0 0.0 0.3 0.0 0.6 8.2

0.5 5.5

0.7 0.0 0.0 2.6 3.0 8.3

1.0 0.0 0.0 0.0 1.0 9.4 5.4

0.3 0.0 1.9 3.1 5.4

0.0 0.5 0.3 1.1 5.1 (1.4)

1.0 0.0 2.1 3.6

0.0 0.3 0.3 1.5 0.0

1.2 0.3 1.0 0.2 0.1

37 pin p/d= 1.154 h/d= 13.40
inj. subchannel = 1
inj. depth (in) = 32.0
bundle reynolds no.= 4300
mass balance ratio = 1.126
dimensionless ratios of salt concentration*100.0:

0.1 0.8 0.2 0.3 0.3

0.0 0.7 1.9 1.8 0.4

0.2 1.5 2.5 0.9

0.0 1.4 3.1 3.9 1.5 0.6

0.5 2.7 3.9 4.4 1.4

0.3 1.2 3.5 4.8 3.5 1.0 0.2

0.1 1.9 4.0 (4.1) 3.6 1.1

0.1 0.1

0.4 2.7 2.7 3.3 1.2 0.3

0.0 0.3 1.4 4.3 2.2 1.0 0.3

0.2 1.2 0.9 1.0 0.2

0.1 0.6 1.3 1.5 0.9 0.0

0.2 0.4 0.0 0.2

0.1 0.4 0.5 0.4 0.1

0.0 0.0 0.0 0.0 0.0

37 pin p/d= 1.154 h/d= 13.40
inj. subchannel = 71
inj depth (in) = 32.0
bundle reynolds no.= 4300
mass balance ratio = 0.939
dimensionless ratios of salt concentration*100.0:

4.3 9.1 9.6 9.0 8.4

0.3 0.6 0.9 6.8 7.3

0.7 1.0 1.0 7.4

0.3 0.0 0.3 1.6 5.1 6.1

0.0 1.3 0.0 1.0 6.0

0.0 0.0 3.7 0.3 4.4 11.3 5.2

0.3 0.0 0.3 0.8 2.0 6.2

0.7 5.0

0.0 0.0 0.0 0.3 3.4 9.0

1.0 0.0 0.0 0.2 2.7 8.1 4.9

0.0 0.0 0.3 3.3 3.0

0.0 0.0 0.0 0.7 5.4 (2.2)

0.0 0.0 1.7 4.1

0.3 0.0 0.0 1.2 1.1

0.0 0.4 1.6 1.6 1.3

37 pin p/d= 1.154 h/d= 13.40
inj. subchannel = 1
inj. depth (in) = 32.0
bundle reynolds no.= 5400
mass balance ratio = 1.307
dimensionless ratios of salt concentration*100.0:

0.1 0.2 0.3 0.2 0.1

0.0 0.7 1.8 1.6 0.2

0.4 1.1 2.3 0.8

0.2 1.1 2.9 4.2 1.5 0.3

0.5 2.6 4.0 4.3 1.2

0.0 1.1 3.9 5.8 4.0 1.0 0.0

0.4 2.3 4.1 (4.6) 3.0 0.9

0.0 0.0

0.3 3.0 3.7 4.1 1.1 0.2

0.2 0.3 2.2 5.3 2.6 1.0 0.0

0.2 1.3 1.2 0.8 0.1

0.0 0.3 1.9 2.6 1.1 0.0

0.5 0.5 0.1 0.1

0.0 0.3 0.3 0.2 0.0

0.0 0.0 0.0 0.0 0.0

37 pin p/d= 1.154 h/d= 13.40
inj. subchannel = 71
inj. depth (in) = 32.0
bundle reynolds no.= 5400
mass balance ratio = 1.383
dimensionless ratios of salt concentration*100.0:

4.5 7.4 8.2 7.8 7.4

1.6 0.7 2.4 6.5 6.7

1.0 2.7 2.4 5.9

0.2 1.5 0.0 2.2 7.1 6.0

1.4 0.5 0.6 1.9 4.9

0.5 0.5 0.0 0.2 2.3 8.3 6.0

0.4 0.4 2.0 1.1 2.5 7.2

0.2 4.8

0.0 2.6 0.2 1.2 2.9 7.1

0.2 0.7 0.0 0.0 1.8 7.6 3.5

1.2 0.2 0.4 2.7 4.1

0.5 0.7 0.9 2.8 5.5 (1.7)

0.2 0.9 2.3 4.2

0.2 1.3 0.0 3.0 1.1

0.0 0.0 1.3 0.9 1.0

37 pin p/d= 1.154 h/d= 13.40
inj. subchannel = 1
inj. depth (in) = 32.0
bundle reynolds no.= 6500
mass balance ratio = 1.444
dimensionless ratios of salt concentration*100.0.

0.6 0.2 0.5 0.4 0.4

0.4 0.8 1.9 0.9 0.2

1.0 1.4 2.5 1.4

0.0 1.2 3.7 4.6 1.4 0.1

1.0 2.8 4.6 3.9 0.8

0.3 0.7 3.6 5.4 3.8 1.0 0.2

0.5 1.4 3.9 (4.2) 3.0 0.3

0.2 0.1

0.3 2.1 3.6 3.8 0.9 0.6

0.0 0.4 2.0 4.5 2.4 1.7 0.1

0.7 0.7 0.3 0.4 0.3

0.0 0.7 1.2 1.0 0.6 0.0

0.3 0.5 0.2 0.3

0.0 0.4 0.2 0.2 0.0

0.5 0.2 0.3 0.0 0.0

37 pin p/d= 1.154 h/d= 13.40
inj. subchannel = 71
inj. depth (in) = 32.0
bundle reynolds no.= 6500
mass balance ratio = 1.112
dimensionless ratios of salt concentration*100.0:

5.0 8.4 9.3 8.5 7.8

1.0 1.2 0.7 7.4 7.2

0.8 1.0 2.4 8.2

0.5 0.3 0.7 1.0 8.0 6.6

0.0 0.3 0.9 2.6 7.4

0.0 0.0 0.0 0.2 2.5 7.2 6.4

0.0 0.0 0.0 1.2 3.4 7.5

0.0 5.2

0.0 0.2 0.0 1.5 3.4 7.6

0.0 0.0 0.0 1.1 2.2 8.6 4.1

0.0 0.0 0.5 3.0 4.3

0.0 0.0 0.0 0.8 4.7 (2.8)

0.0 0.0 0.5 3.7

0.3 0.0 0.0 1.8 0.6

0.0 0.0 0.5 0.0 0.3

37 pin p/d= 1.154 h/d= 13.40
Inj. subchannel = 1
Inj. depth (in) = 32.0
bundle reynolds no.= 9400
mass balance ratio = 1.584
dimensionless ratios of salt concentration*100.0:

0.1 0.1 0.6 0.5 0.4

0.1 0.6 2.4 1.4 0.2

0.2 1.2 2.0 1.9

0.1 0.7 3.6 3.8 0.9 0.1

0.9 2.7 4.4 3.7 1.2

0.2 1.2 3.9 5.6 4.0 1.3 0.1

0.2 2.1 4.4 (4.9) 3.0 1.0

0.0 0.0

0.1 2.9 4.0 3.6 1.1 0.5

0.1 0.2 2.4 4.6 2.6 1.2 0.0

0.3 1.1 1.1 0.9 0.2

0.1 0.2 1.6 1.3 0.9 0.0

0.3 0.2 0.1 0.0

0.0 0.4 0.0 0.0 0.0

0.1 0.0 0.0 0.0 0.0

37 pin p/d= 1.154 h/d= 13.40
Inj. subchannel = 71
Inj. depth (in) = 32.0
bundle reynolds no.= 9400
mass balance ratio = 1.197
dimensionless ratios of salt concentration*100.0:

6.4 7.5 8.8 8.0 7.2

2.4 0.7 3.1 7.7 6.7

1.0 1.9 2.5 8.3

0.0 0.0 0.0 0.9 7.6 6.2

0.2 0.0 0.9 1.2 6.8

0.3 0.0 0.0 0.6 0.7 6.6 5.3

0.0 0.2 0.0 0.4 2.8 6.4

0.0 4.8

0.0 0.0 0.0 1.1 3.4 6.8

0.0 0.0 0.0 0.0 1.3 8.7 4.3

0.0 0.0 0.9 2.4 4.1

0.2 0.0 0.0 1.1 4.3 (0.7)

0.2 0.0 1.2 3.8

0.7 0.0 0.0 2.8 0.4

0.4 0.5 0.0 1.6 1.0

37 pin p/d= 1.154 h/d= 13.40
inj. subchannel = 1
inj. depth (in) = 32.0
bundle reynolds no.= 12200
mass balance ratio = 1.566
dimensionless ratios of salt concentration*100.0:

0.2 0.4 0.8 0.7 0.6

0.1 0.8 2.9 1.6 0.4

0.2 1.3 2.1 2.4

0.1 1.0 3.7 4.2 0.9 0.1

1.0 2.8 4.4 4.1 1.2

0.2 1.2 3.6 5.4 4.1 1.5 0.2

0.2 1.2 3.6 (4.0) 2.9 0.8

0.4 0.2

0.2 2.9 3.2 3.3 1.1 0.5

0.1 0.3 1.9 4.2 2.3 1.1 0.1

0.2 1.0 0.3 0.9 0.2

0.2 0.2 1.3 0.8 0.8 0.0

0.1 0.3 0.4 0.1

0.0 0.3 0.3 0.1 0.1

0.6 0.0 0.1 0.0 0.0

37 pin p/d= 1.154 h/d= 13.40
inj. subchannel = 71
inj. depth (in) = 32.0
bundle reynolds no.= 12200
mass balance ratio = 1.620
dimensionless ratios of salt concentration*100.0:

7.4 6.9 7.5 6.7 5.8

2.4 1.6 3.4 6.4 5.5

1.2 3.1 1.8 7.2

0.2 1.4 0.2 0.7 6.8 5.2

0.4 0.5 0.2 2.3 6.2

0.0 0.0 0.0 1.0 2.2 6.6 5.1

0.0 0.3 0.0 0.1 2.3 6.1

0.4 4.2

0.2 0.4 0.3 1.0 3.6 6.2

0.0 0.4 0.4 0.3 1.4 7.2 3.4

0.2 0.2 0.9 3.8 4.1

0.2 0.4 0.2 2.1 5.6 (2.7)

0.4 2.0 2.0 3.1

0.6 0.2 0.6 0.0 0.8

0.9 0.0 0.2 1.1 0.9

37 pin p/d= 1.154 h/d= 13.40
inj. subchannel = 1
inj. depth (in) = 32.0
bundle reynolds no.= 14800
mass balance ratio = 1.672
dimensionless ratios of salt concentration*100.0:

0.0 0.3 0.5 0.5 0.5

0.1 0.7 1.7 1.1 0.3

0.2 1.2 1.8 1.5

0.1 0.9 3.2 3.7 0.9 0.1

0.9 2.6 4.4 3.4 1.3

0.3 1.3 3.7 5.6 3.8 1.6 0.3

0.6 2.7 3.8 (4.1) 3.1 0.6

0.1 0.2

0.7 3.0 3.9 3.4 1.1 0.5

0.1 0.4 2.2 4.4 2.2 1.3 0.0

0.5 1.2 0.8 0.8 0.1

0.1 0.3 1.9 1.6 1.1 0.1

0.4 0.3 0.0 0.1

0.2 0.4 0.5 0.3 0.0

0.0 0.0 0.2 0.0 0.0

37 pin p/d= 1.154 h/d= 13.40
inj. subchannel = 71
inj. depth (in) = 32.0
bundle reynolds no.= 14800
mass balance ratio = 1.402
dimensionless ratios of salt concentration*100.0:

8.4 8.2 8.1 7.2 6.3

3.4 0.9 1.8 6.5 5.8

1.1 1.6 1.7 7.2

0.2 0.0 0.2 0.8 6.6 5.4

0.0 0.1 0.2 2.5 6.1

0.2 0.4 0.0 0.0 2.2 5.5 5.3

0.0 0.0 0.0 0.5 2.7 5.6

0.0 4.5

0.0 0.2 0.5 1.1 3.3 6.1

0.2 0.0 0.0 0.0 1.1 7.7 3.6

0.0 0.0 0.9 3.0 3.6

0.4 0.0 0.0 1.3 4.2 (1.7)

0.2 0.4 1.0 3.3

0.2 0.2 0.0 1.7 1.0

0.0 1.1 0.2 0.6 0.8

37 pin p/d= 1.154 h/d= 13.40
inj. subchannel = 1
inj. depth (in) = 32.0
bundle reynolds no.= 18600
mass balance ratio = 1.583
dimensionless ratios of salt concentration*100.0:

0.4 0.7 0.6 0.6 0.5

0.2 0.7 2.5 1.8 0.3

0.7 1.5 2.3 1.9

0.1 1.5 3.7 4.6 0.9 0.1

1.0 3.0 5.2 3.9 1.4

0.0 1.3 3.7 5.2 4.0 1.7 0.1

0.5 1.7 3.6 (3.2) 3.0 0.6

0.3 0.0

0.9 2.5 3.2 3.1 0.9 0.3

0.1 0.3 2.0 3.8 1.9 0.9 0.0

0.4 0.9 0.7 0.8 0.2

0.2 0.3 1.4 1.2 0.7 0.2

0.2 0.4 0.2 0.0

0.1 0.8 0.1 0.0 0.0

0.3 0.0 0.0 0.1 0.0

37 pin p/d= 1.154 h/d= 13.40
inj. subchannel = 71
inj. depth (in) = 32.0
bundle reynolds no.= 18600
mass balance ratio = 1.502
dimensionless ratios of salt concentration*100.0:

7.9 6.7 7.3 6.7 6.1

3.7 1.3 1.3 7.1 5.7

2.1 1.9 2.4 7.2

1.0 0.2 0.0 0.9 6.4 5.4

1.2 0.3 0.4 2.0 5.3

0.0 0.0 0.8 1.9 2.0 7.4 4.3

0.2 0.2 0.0 0.2 3.1 5.4

0.0 3.6

0.6 0.2 0.2 1.3 3.2 6.1

0.4 0.0 0.0 0.0 1.2 6.9 3.0

0.2 0.2 0.9 4.0 3.5

0.0 0.0 0.4 1.7 5.6 (0.7)

0.2 0.6 2.1 3.2

0.0 0.2 0.6 2.5 0.5

0.0 0.0 0.6 1.5 1.0

37 pin p/d= 1.154 h/d= 13.40
inj. subchannel = 1
inj. depth (in) = 32.0
bundle reynolds no.= 22100
mass balance ratio = 1.423
dimensionless ratios of salt concentration*100.0:

0.3 0.5 0.8 0.6 0.4

0.1 0.8 2.8 1.4 0.2

0.5 1.3 2.3 1.7

0.3 1.3 3.8 4.2 1.0 0.0

1.0 3.1 4.4 4.0 1.5

0.1 1.3 4.2 5.5 3.7 1.3 0.3

0.4 1.6 3.6 (3.9) 2.8 0.7

0.2 0.0

0.5 2.7 4.1 3.2 0.9 0.1

0.0 0.1 2.1 4.0 2.2 0.9 0.0

0.6 1.3 0.9 0.7 0.0

0.0 0.3 1.5 1.2 0.5 0.1

0.0 0.2 0.3 0.2

0.1 0.1 0.4 0.0 0.0

0.1 0.1 0.1 0.0 0.0

37 pin p/d= 1.154 h/d= 13.40
inj. subchannel = 71
inj depth (in) = 32.0
bundle reynolds no.= 22100
mass balance ratio = 1.222
dimensionless ratios of salt concentration*100.0:

7.6 7.8 6.8 7.4 8.0

3.6 1.1 1.5 6.2 6.2

1.7 1.3 0.9 5.8

1.6 1.0 0.2 3.2 7.4 4.4

0.0 0.5 0.8 3.0 6.6

0.5 0.0 0.2 0.2 3.3 5.8 3.6

0.0 0.4 0.0 0.9 3.0 5.8

0.5 3.0

0.0 0.0 0.6 1.9 3.4 6.0

0.0 0.0 0.0 0.3 1.7 7.5 2.5

0.0 0.4 1.3 4.3 4.1

0.0 0.0 0.0 1.7 4.5 (1.4)

0.0 0.9 1.8 5.0

0.0 0.0 0.7 1.9 0.6

0.0 0.0 0.0 0.0 0.3

37 pin p/d= 1.154 h/d= 13.40
inj. subchannel = 1
inj. depth (in) = 32.0
bundle reynolds no.= 26000
mass balance ratio = 1.415
dimensionless ratios of salt concentration*100.0:

0.2 0.6 1.0 0.8 0.5

0.2 0.8 2.6 1.2 0.3

0.5 1.7 2.3 1.6

0.4 1.3 3.9 4.2 1.0 0.1

0.8 3.0 4.8 3.9 1.7

0.4 1.3 3.8 5.4 3.7 1.2 0.1

0.3 1.5 3.4 (3.9) 2.8 0.8

0.0 0.0

0.8 2.7 3.3 3.1 0.9 0.3

0.2 0.3 2.1 3.4 2.1 1.0 0.1

0.5 0.8 0.7 0.7 0.0

0.1 0.2 1.0 0.8 0.8 0.1

0.1 0.2 0.0 0.0

0.0 0.4 0.5 0.0 0.1

0.0 0.3 0.2 0.0 0.0

37 pin p/d= 1.154 h/d= 13.40
inj. subchannel = 71
inj. depth (in) = 32.0
bundle reynolds no.= 26000
mass balance ratio = 1.310
dimensionless ratios of salt concentration*100.0:

9.6 7.5 6.9 6.3 5.7

4.2 0.6 0.8 6.0 5.4

2.0 2.1 2.4 5.2

2.3 0.5 0.0 1.4 5.1 5.2

0.0 0.2 1.2 2.6 6.0

0.4 0.0 0.0 0.2 3.1 6.8 4.1

0.0 0.0 0.2 0.0 2.8 6.1

0.4 3.6

0.0 0.0 0.2 2.1 2.6 4.4

0.0 0.0 0.4 0.0 1.2 5.3 3.1

0.0 0.2 0.8 3.1 4.9

0.0 0.0 0.0 3.0 4.6 (1.5)

0.2 1.2 2.7 3.7

0.9 0.0 1.1 1.7 1.0

0.0 0.0 1.4 0.4 0.7

APPENDIX B1

DATA BASE FOR BUNDLE AVERAGE FRICTION FACTOR AND FLOW SPLIT PARAMETER

Note: For the detailed numerical data please refer to the Appendix B1 of Cheng, S.-K. and Todreas, N. E. "Constitutive Correlations for Wire-Wrapped Subchannel Analysis under Forced and Mixed Convection Conditions," DOE/ET/37240-108TR, MIT, August, 1984.

Table A.1 List of Bare Rod Bundle Average Friction Factor Experiments and their detail numerical data

ID	Reference	medium	Nr	D(mm)	P/D	W/D
BAUMANN	Baumann(1968)	water	19	6.620	1.227	1.227
BNWL	Reihman(1969)	water	37	6.350	1.148	1.148
CVTR	Bishop(1962)	water	19	12.650	1.205	1.205
GALLOWAY1	Galloway(1965)	polyethyl	19	11.870	1.105	1.008
GALLOWAY2	Galloway(1965)	polyethyl	19	10.360	1.266	1.082
GALLOWAY3	Galloway(1965)	polyethyl	19	8.680	1.510	1.194
LETOURNEAU	LeTourneau(1957)	water	19	12.700	1.120	1.120
MIKHAYLOV	Mikhaylov(1964)	air	19	11.000	1.200	1.156
REHMEo1c	Rehme(1970)	water	37	12.000	1.275	1.275
REHMEo2c	Rehme(1970)	water	37	12.000	1.392	1.209
REHMEo3c	Rehme(1970)	water	37	12.000	1.417	1.417
REHMEo1g	Rehme(1970)	water	169	6.000	1.317	1.285
REHME1d	Rehme(1972)	water	61	12.000	1.025	1.060
REHME2c	Rehme(1972)	water	37	12.000	1.075	1.095
REHME2d	Rehme(1972)	water	61	12.000	1.084	1.076
REHME3a	Rehme(1972)	water	7	12.000	1.125	1.142
REHME3b	Rehme(1972)	water	19	12.000	1.126	1.142
REHME3d	Rehme(1972)	water	61	12.000	1.124	1.122
REHME4a	Rehme(1972)	water	7	12.000	1.231	1.251
REHME4b	Rehme(1972)	water	19	12.000	1.231	1.252
REHME4c	Rehme(1972)	water	37	12.000	1.235	1.250
REHME5a	Rehme(1972)	water	7	12.000	1.279	1.276
REHME5b	Rehme(1972)	water	19	12.000	1.276	1.308
REHME5c	Rehme(1972)	water	37	12.000	1.275	1.300
REHME6a	Rehme(1972)	water	7	12.000	1.346	1.342
REHME6b	Rehme(1972)	water	19	12.000	1.344	1.341
REHME6c	Rehme(1972)	water	37	12.000	1.345	1.335
REHME7a	Rehme(1972)	water	7	12.000	1.421	1.422
REHME7b	Rehme(1972)	water	19	12.000	1.421	1.425
REHME7c	Rehme(1972)	water	37	12.000	1.420	1.420
REHME7d	Rehme(1972)	water	61	12.000	1.416	1.411
SIMONEK	Simonek(1966)	air	169	5.000	1.400	1.213
SUBBOTIN	Subbotin(1960)	water	19	17.600	1.000	1.000

Table A.2 List of Wire-Wrapped Bundle Average Friction Factor Experiments and their detail numerical data

ID	Reference	medium	Nr	D(mm)	Dw	P/D	W/D	H/D
AI217	Davidson(1971)	water	217	6.390	1.808	1.283	1.283	48.00
BAUMANN1	Baumann(1968)	water	61	6.000	1.000	1.167	1.167	16.70
BAUMANN2	Baumann(1968)	water	61	6.000	1.000	1.167	1.167	25.00
BAUMANN3	Baumann(1968)	water	19	6.620	1.500	1.227	1.227	15.10
BAUMANN4	Baumann(1968)	water	19	6.620	1.500	1.227	1.227	22.70
BNWL1a	Reihman(1969)	water	37	6.350	0.762	1.148	1.171	12.00
BNWL1b	Reihman(1969)	water	37	6.350	0.762	1.148	1.171	24.00
BNWL1c	Reihman(1969)	water	37	6.350	0.762	1.148	1.171	48.00
BNWL1d	Reihman(1969)	water	37	6.350	0.762	1.148	1.171	96.00
BNWL2c	Reihman(1969)	water	37	5.994	1.080	1.215	1.240	50.85
BNWL3b	Reihman(1969)	water	37	6.756	0.406	1.079	1.100	22.56
BNWL3c	Reihman(1969)	water	37	6.756	0.406	1.079	1.100	45.11
BNWL6c	Reihman(1969)	water	37	4.978	0.597	1.145	1.158	61.22
BNWL7c	Reihman(1969)	water	37	6.096	1.016	1.196	1.220	50 00
BNWL8c	Reihman(1969)	water	37	7.620	0.914	1.150	1.178	40.00
BNWL9b	Reihman(1969)	water	37	6.350	2.012	1.376	1.434	24.00
BNWL9c	Reihman(1969)	water	37	6.350	2.012	1.376	1.434	48.00
BNWL11c	Reihman(1969)	water	19	6.350	0.762	1.156	1.184	48.00
BNWL12c	Reihman(1969)	water	217	6.350	0.762	1.135	1.143	48.00
CHENG	Cheng(1982)	water	37	15.040	2.260	1.154	1.164	13.40
CHIU1	Chiu(1978a)	water	61	12.730	0.800	1.067	1.069	4.00
CHIU2	Chiu(1978a)	water	61	12.730	0.800	1.067	1.069	8.00
CVTR1	Bishop(1962)	water	19	13.610	1.630	1.120	1.120	25.25
CVTR2	Bishop(1962)	water	19	12.930	2.310	1.179	1.179	25.25
CVTR31	Bishop(1962)	water	19	12.650	2.590	1.205	1.205	8.03
CVTR32	Bishop(1962)	water	19	12.650	2.590	1.205	1.205	16.07
CVTR33	Bishop(1962)	water	19	12.650	2.590	1.205	1.205	24.10
CVTR34	Bishop(1962)	water	19	12.650	2.590	1.205	1.205	30.12
CVTR4	Bishop(1962)	water	19	12.070	3.180	1.263	1.263	25.25
FFTFs	Spencer(1980)	water	217	5.840	1.420	1.252	1.242	51.74
HOFFMANN1	Hoffmann(1973)	sodium	61	6.000	1.900	1.317	1.317	16.67
HOFFMANN2	Hoffmann(1973)	sodium	61	6.000	1.900	1.317	1.317	33.33
HOFFMANN3	Hoffmann(1973)	sodium	61	6.000	1.900	1.317	1.317	50.00
JEFR19m	Okamoto(1970)	water&Na	19	6.300	1.390	1.221	1.221	40.48
JEFR91m	Okamoto(1970)	water&Na	91	6.300	1.390	1.221	1.221	40.48
JEFR91a	Wakasugi(1971)	water	91	6.300	1.200	1.221	1.167	14.29
JEFR91b	Wakasugi(1971)	water	91	6.300	1.200	1.221	1.167	20.63
JEFR91c	Wakasugi(1971)	water	91	6.300	1.200	1.221	1.167	30.16
JEFR91d	Wakasugi(1971)	water	91	6.300	1.200	1.221	1.167	41.27
JOYO1ca	Itoh(1981)	water	91	6.300	1.270	1.216	1.164	15.03
JOYO1cb	Itoh(1981)	water	91	6.300	1.270	1.216	1.164	22.54
JOYO1cc	Itoh(1981)	water	91	6.300	1.270	1.216	1.164	32.22
JOYO1cd	Itoh(1981)	water	91	6.300	1.270	1.216	1.164	45.08
JOYO2c	Itoh(1981)	water	127	5.500	0.900	1.176	1.178	53.27
JOYO4c	Itoh(1981)	water	127	5.500	0.900	1.176	1.178	38.00

MONJU5c	Itoh(1981)	water	169	6.500	1.320	1.214	1.188	47.39
MARTEN11	Marten(1982)	water	37	15.980	0.660	1.041	1.041	8.38
MARTEN12	Marten(1982)	water	37	15.980	0.660	1.041	1.041	12.60
MARTEN13	Marten(1982)	water	37	15.980	0.660	1.041	1.041	17.01
MARTEN21	Marten(1982)	water	37	15.510	1.120	1.072	1.072	8.34
MARTEN22	Marten(1982)	water	37	15.510	1.120	1.072	1.072	12.54
MARTEN23	Marten(1982)	water	37	15.510	1.120	1.072	1.072	16.68
MARTEN31	Marten(1982)	water	37	15.110	1.530	1.101	1.101	8.31
MARTEN32	Marten(1982)	water	37	15.110	1.530	1.101	1.101	12.31
MARTEN33	Marten(1982)	water	37	15.110	1.530	1.101	1.101	16.61
PEC91a	Pirelli(1982)	water	91	6.700	1.200	1.180	1.180	20.90
PEC91b	Pirelli(1982)	water	91	6.700	1.200	1.180	1.180	23.88
REHME11b	Rehme(1967)	water	19	12.000	1.500	1.125	1.125	8.33
REHME11c	Rehme(1967)	water	37	12.000	1.500	1.125	1.125	8.33
REHME11d	Rehme(1967)	water	61	12.000	1.500	1.125	1.125	8.33
REHME12b	Rehme(1967)	water	19	12.000	1.500	1.125	1.125	12.50
REHME12c	Rehme(1967)	water	37	12.000	1.500	1.125	1.125	12.50
REHME12d	Rehme(1967)	water	61	12.000	1.500	1.125	1.125	12.50
REHME13b	Rehme(1967)	water	19	12.000	1.500	1.125	1.125	16.67
REHME13c	Rehme(1967)	water	37	12.000	1.500	1.125	1.125	16.67
REHME13d	Rehme(1967)	water	61	12.000	1.500	1.125	1.125	16.67
REHME14b	Rehme(1967)	water	19	12.000	1.500	1.125	1.125	25.00
REHME14c	Rehme(1967)	water	37	12.000	1.500	1.125	1.125	25.00
REHME14d	Rehme(1967)	water	61	12.000	1.500	1.125	1.125	25.00
REHME15b	Rehme(1967)	water	19	12.000	1.500	1.125	1.125	50.00
REHME15c	Rehme(1967)	water	37	12.000	1.500	1.125	1.125	50.00
REHME15d	Rehme(1967)	water	61	12.000	1.500	1.125	1.125	50.00
REHME21a	Rehme(1967)	water	7	12.000	2.800	1.233	1.233	8.33
REHME21b	Rehme(1967)	water	19	12.000	2.800	1.233	1.233	8.33
REHME21c	Rehme(1967)	water	37	12.000	2.800	1.233	1.233	8.33
REHME22a	Rehme(1967)	water	7	12.000	2.800	1.233	1.233	12.50
REHME22b	Rehme(1967)	water	19	12.000	2.800	1.233	1.233	12.50
REHME22c	Rehme(1967)	water	37	12.000	2.000	1.233	1.233	12.50
REHME23a	Rehme(1967)	water	7	12.000	2.800	1.233	1.233	16.67
REHME23b	Rehme(1967)	water	19	12.000	2.800	1.233	1.233	16.67
REHME23c	Rehme(1967)	water	37	12.000	2.800	1.233	1.233	16.67
REHME24a	Rehme(1967)	water	7	12.000	2.800	1.233	1.233	25.00
REHME24b	Rehme(1967)	water	19	12.000	2.800	1.233	1.233	25.00
REHME24c	Rehme(1967)	water	37	12.000	2.800	1.233	1.233	25.00
REHME25a	Rehme(1967)	water	7	12.000	2.800	1.233	1.233	50.00
REHME25b	Rehme(1967)	water	19	12.000	2.800	1.233	1.233	50.00
REHME25c	Rehme(1967)	water	37	12.000	2.800	1.233	1.233	50.00
REHME31a	Rehme(1967)	water	7	12.000	3.300	1.275	1.275	8.33
REHME31b	Rehme(1967)	water	19	12.000	3.300	1.275	1.275	8.33
REHME31c	Rehme(1967)	water	37	12.000	3.300	1.275	1.275	8.33
REHME32a	Rehme(1967)	water	7	12.000	3.300	1.275	1.275	12.50
REHME32b	Rehme(1967)	water	19	12.000	3.300	1.275	1.275	12.50
REHME32c	Rehme(1967)	water	37	12.000	3.300	1.275	1.275	12.50
REHME33a	Rehme(1967)	water	7	12.000	3.300	1.275	1.275	16.67
REHME33b	Rehme(1967)	water	19	12.000	3.300	1.275	1.275	16.67

REHME33c	Rehme(1967)	water	37	12.000	3.300	1.275	1.275	16.67
REHME34a	Rehme(1967)	water	7	12.000	3.300	1.275	1.275	25.00
REHME34b	Rehme(1967)	water	19	12.000	3.300	1.275	1.275	25.00
REHME34c	Rehme(1967)	water	37	12.000	3.300	1.275	1.275	25.00
REHME35a	Rehme(1967)	water	7	12.000	3.300	1.275	1.275	50.00
REHME35b	Rehme(1967)	water	19	12.000	3.300	1.275	1.275	50.00
REHME35c	Rehme(1967)	water	37	12.000	3.300	1.275	1.275	50.00
REHME41a	Rehme(1967)	water	7	12.000	4.100	1.343	1.343	8.33
REHME41b	Rehme(1967)	water	19	12.000	4.100	1.343	1.343	8.33
REHME42a	Rehme(1967)	water	7	12.000	4.100	1.343	1.343	12.50
REHME42b	Rehme(1967)	water	19	12.000	4.100	1.343	1.343	12.50
REHME42c	Rehme(1967)	water	37	12.000	4.100	1.343	1.343	12.50
REHME43a	Rehme(1967)	water	7	12.000	4.100	1.343	1.343	16.67
REHME43b	Rehme(1967)	water	19	12.000	4.100	1.343	1.343	16.67
REHME43c	Rehme(1967)	water	37	12.000	4.100	1.343	1.343	16.67
REHME44a	Rehme(1967)	water	7	12.000	4.100	1.343	1.343	25.00
REHME44b	Rehme(1967)	water	19	12.000	4.100	1.343	1.343	25.00
REHME44c	Pehme(1967)	water	37	12.000	4.100	1.343	1.343	25.00
REHME45a	Rehme(1967)	water	7	12.000	4.100	1.343	1.343	50.00
REHME45b	Rehme(1967)	water	19	12.000	4.100	1.343	1.343	50.00
REHME45c	Rehme(1967)	water	37	12.000	4.100	1.343	1.343	50.00
REHME51a	Rehme(1967)	water	7	12.000	5.000	1.417	1.417	8.33
REHME51b	Rehme(1967)	water	19	12.000	5.000	1.417	1.417	8.33
REHME51c	Rehme(1967)	water	37	12.000	5.000	1.417	1.417	8.33
REHME52a	Rehme(1967)	water	7	12.000	5.000	1.417	1.417	12.50
REHME52b	Rehme(1967)	water	19	12.000	5.000	1.417	1.417	12.50
REHME52c	Rehme(1967)	water	37	12.000	5.000	1.417	1.417	12.50
REHME53a	Rehme(1967)	water	7	12.000	5.000	1.417	1.417	16.67
REHME53b	Rehme(1967)	water	19	12.000	5.000	1.417	1.417	16.67
REHME53c	Rehme(1967)	water	37	12.000	5.000	1.417	1.417	16.67
REHME54a	Rehme(1967)	water	7	12.000	5.000	1.417	1.417	25.00
REHME54b	Rehme(1967)	water	19	12.000	5.000	1.417	1.417	25.00
REHME54c	Rehme(1967)	water	37	12.000	5.000	1.417	1.417	25.00
REHME55a	Rehme(1967)	water	7	12.000	5.000	1.417	1.417	50.00
REHME55b	Rehme(1967)	water	19	12.000	5.000	1.417	1.417	50.00
REHME55c	Rehme(1967)	water	37	12.000	5.000	1.417	1.417	50.00
TCHIU	Burns(1980)	water	37	12.720	1.910	1.156	1.177	21.00
TOLIS	Efthimiadis(1983)	water	19	18.920	4.600	1.245	1.245	35.20
WARDa	Carelli(1981)	water	61	12.700	0.635	1.050	1.050	20.00
WARDb	Engel(1979)	water&Na	61	12.850	0.940	1.082	1.080	7.78

Table A.3 List of Wire-Wrapped Bundle Flow Split Experiments and their detail numerical data

ID	Reference	method	Nr	D(mm)	Dw	P/D	W/D	H/D
AI217	Davidson(1971)	TOF	217	6.390	1.810	1.283	1.227	48.00
ANLCT7	Ginsberg(1973)	IEM	7	12.700	2.790	1.200	1.220	48.00
ANLCT91	Lorenz(1977)	IEM	91	12.700	3.050	1.240	1.240	48.00
ANLRAS91	Pederson(1974)	TOF	91	6.350	1.270	1.210	1.210	48.00
CHEN1	Chen(1974)	LDA	61	6.350	1.590	1.250	1.250	24.00
CHEN2	Chen(1974)	LDA	61	6.350	1.590	1.250	1.250	48.00
CHENG	Cheng(1982)	IEM	37	15.040	2.260	1.154	1.164	13.40
CHIU1	Chiu(1978a)	IEM	61	12.730	0.800	1.067	1.069	4.00
CHIU2	Chiu(1978a)	IEM	61	12.730	0.800	1.067	1.069	8.00
PNC37a	Ohtake(1976)	air&pitot	37	31.600	6.000	1.190	1.190	34.80
SYMOLON	Symolon(1981)	IEM	217	5.893	1.470	1.250	1.250	51.72
TOLIS	Efthimiadis(1983)	Hot-wire	19	18.920	4.600	1.245	1.245	35.20
UK1	McAreavey(1979)	Yawmeter	37	10.000	2.500	1.250	1.250	14.80
WARDfs	Bartholet(1976)	air&pitot	217	63.600	15.880	1.257	1.257	51.68

APPENDIX B2

INPUT, OUTPUT AND LISTING FOR WWCR PROGRAM

Inputs for WWCR Program
(all inputs are free format)

Card 1 nrod, d, dw, pdr, wdr, hdr

Information for bundle geometry

nrod = rod number
d = rod diameter (cm)
dw = wire diameter, 0 for bare rod bundle (cm)
pdr = pitch to rod diameter ratio, P/D
wdr = edge pitch to rod diameter ratio, W/D
hdr = lead length to rod diameter ratio, H/D

Card 2 beta

Option for using equations to calculate flow split parameters

beta = 1.0, theoretical solution of eqs. (2.27) (2.28)
beta = 0.05, approximate empirical eq. (2.32)

Card 3 nre, re(1), re(2),..., re(nre)

nre = number of Reynolds number to be calculated
re(i)= Reynolds number

Card 4-6 another set of input

etc.

Typical output for WWCR program

Description of Bundle Geometry

Number of Rods	N	=	37
Rod Dimeter(mm)	D	=	15.040
Wire Diameter(mm)	Dw	=	2.260
Interior Pitch to Rod Diameter Ratio	P/D	=	1.154
Edge Pitch to Rod Diameter Ratio	W/D	=	1.164
Lead Length to Rod Diameter Ratio	H/D	=	13.400

Equivalent Diamater

Equi. Dia. for Bundle Average	Deb	=	6.298
Equi. Dia. for Interior Subchannel	De1	=	5.792
Equi. Dia. for Edge Subchannel	De2	=	7.383
Equi. Dia. for Corner Subchannel	De3	=	5.288

Results for Laminar anr Turbulent Flow Condition
Cfi is the friction factor constant (fi=Cfi/Rei**m)
Xi is the flow split parameters

		Interior Subchannel	Edge Subchannel	Corner Subchannel	Bundle Average
Laminar	CfiL =	79.78	89.07	103.54	81.11
Turbulent	CfiT =	0.2273	0.2416	0.2456	0.2306
Laminar	XiL =	0.860	1.251	0.552	
Turbulent	XiT =	0.955	1.080	0.862	

(continue)

Prediction for Friction Factors (fi) and Flow Split Parameters (Xi) at given Bundle Reynolds no. (Reb)

	Interior Subchannel	Edge Subchannel	Corner Subchannel	Bundle Average
Reb = 200.0				
fi =	0.5045E+00	0.3037E+00	0.1116E+01	0.4056E+00
Xi =	0.860	1.251	0.552	
Reb = 400.0				
fi =	0.2523E+00	0.1518E+00	0.5581E+00	0.2028E+00
Xi =	0.860	1.251	0.552	
Reb = 450.0				
fi =	0.2430E+00	0.1590E+00	0.4906E+00	0.2023E+00
Xi =	0.876	1.223	0.589	
Reb = 500.0				
fi =	0.2229E+00	0.1506E+00	0.4369E+00	0.1881E+00
Xi =	0.883	1.212	0.603	
Reb = 600.0				
fi =	0.1918E+00	0.1351E+00	0.3600E+00	0.1646E+00
Xi =	0.891	1.199	0.621	
Reb = 800.0				
fi =	0.1526E+00	0.1135E+00	0.2685E+00	0.1339E+00
Xi =	0.902	1.180	0 649	
Reb = 1000.0				
fi =	0.1292E+00	0.9984E-01	0.2163E+00	0.1152E+00
Xi =	0.909	1.167	0.671	
Reb = 1500.0				
fi =	0.9862E-01	0.8106E-01	0.1511E+00	0.9019E-01
Xi =	0.921	1.146	0.711	
Reb = 2000.0				
fi =	0.8359E-01	0.7135E-01	0.1208E+00	0.7764E-01
Xi =	0.927	1.133	0.737	
Reb = 3000.0				
fi =	0.6867E-01	0.6129E-01	0.9234E-01	0.6498E-01
Xi =	0.936	1.118	0.771	
Reb = 5000.0				
fi =	0.5659E-01	0.5267E-01	0.7094E-01	0.5450E-01
Xi =	0.943	1.104	0.805	
Reb = 8000.0				
fi =	0.4937E-01	0.4721E-01	0.5912E-01	0.4809E-01
Xi =	0.948	1.094	0.828	
Reb = 12000.0				
fi =	0.4485E-01	0.4362E-01	0.5221E-01	0.4401E-01
Xi =	0.951	1.088	0.842	
Reb = 18000.0				
fi =	0.4105E-01	0.4047E-01	0.4669E-01	0.4052E-01
Xi =	0.953	1.084	0.854	
Reb = 20000.0				
fi =	0.3913E-01	0.3894E-01	0.4378E-01	0.3878E-01
Xi =	0.955	1.080	0.862	
Reb = 25000.0				
fi =	0.3759E-01	0.3741E-01	0.4205E-01	0.3725E-01
Xi =	0.955	1.080	0.862	

```
c
c  ********************* WWCR program *********************
c  main program for wire wrapped friction factor correlation
c  this program predicts subchannel friction factors fi
c  and flow split parameters Xi
      common nrod,d,dw,pdr,wdr,hdr,at,de(3),deb,
     &  s(3),g(6),cft(4),cfl(4),x(3),xl(3),xt(3)
      common/blc/ a1l(3),a2l(3),b1l(3,5),b2l(3,5)
      common/btc/ a1t(3),a2t(3),b1t(3,5),b2t(3,5)
      common/wwc/ a1,b11,b12,c,a2,b2,el,rlt1,rlt2
      dimension re(50),f(4)
c  input geometry and Reynolds numbers
   10 read(5,*,end=999) nrod,d,dw,pdr,wdr,hdr
      read(5,*) beta
      read(5,*) nre,(re(i),i=1,nre)
c  ******************************************************
c  set all the empical constants
      call set
c  ******************************************************
c  calculate needed geometrical parameters
      call geom
c  ******************************************************
c  print out input information and equivalent diameter
      write(6,610)
      write(6,620) nrod,d,dw
      write(6,630) pdr,wdr,hdr
      write(6,640) deb,(de(i),i=1,3)
c  ******************************************************
c  calculate laminar and turbulent friction factor constants
      call calcf(1.0,cfl,xl)
      call calcf(0.18,cft,xt)
c  ******************************************************
c  print out the preliminary results for laminar and turbulent
c  friction factor constants and flow split parameters
      write(6,710)
      write(6,720)
      write(6,730) (cfl(i),i=1,4)
      write(6,740) (cft(i),i=1,4)
      write(6,750) (xl(i),i=1,3)
      write(6,760) (xt(i),i=1,3)
c  ******************************************************
      if(nre.eq.0) go to 10
c  print out head discription if nre >= 1
      write(6,810)
      write(6,720)
c  friction factor and flow split parameters for a given
c  bundle Reynolds number
      do 100 i=1,nre
      call flows(el,beta,re(i))
      call fricf(el,re(i),f)
      write(6,820) re(i)
      write(6,830) (f(j),j=1,4)
      write(6,840) (x(j),j=1,3)
c
  100 continue
      write(6,900)
c
      go to 10
  610 format(6x,'Description of Bundle Geometry',/)
  620 format(6x,'Number of Rods',23x,'N    = ',i5,/,
```

```
     &  6x,'Rod Dimeter(mm)',22x,'D    = ',f7.3,/,
     &  6x,'Wire Diameter(mm)',20x,'Dw   = ',f7.3)
  630 format(6x,'Interior Pitch to Rod Diameter Ratio P/D = ',f7.3,/,
     &  6x,'Edge Pitch to Rod Diameter Ratio     W/D = ',f7.3,/,
     &  6x,'Lead Length to Rod Diameter Ratio    H/D = ',f7.3,/)
  640 format(6x,'Equivalent Diamater',/,
     &  6x,'Equi. Dia. for Bundle Average        Deb = ',f7.3,/,
     &  6x,'Equi. Dia. for Interior Subchannel   De1 = ',f7.3,/,
     &  6x,'Equi. Dia. for Edge Subchannel       De2 = ',f7.3,/,
     &  6x,'Equi. Dia. for Corner Subchannel     De3 = ',f7.3,///)
  710 format(12x,'Results for Laminar and Turbulent Flow Condition',/,
     &  11x,'Cfi is the friction factor constant (fi=Cfi/Rei**m)',/,
     &  11x,'Xi  is the flow split parameters',/)
  720 format(23x,'Interior',6x,'Edge',7x,'Corner',7x,'Bundle',/,
     &  22x,'Subchannel',2x,'Subchannel',2x,'Subchannel',4x,
     &  'Average',/)
  730 format(6x,'Laminar   CfiL = ',1x,f6.2,3(6x,f6.2))
  740 format(6x,'Turbulent CfiT = ',1x,f6.4,3(6x,f6.4))
  750 format(6x,'Laminar    XiL = ',1x,f6.3,2(6x,f6.3))
  760 format(6x,'Turbulent  XiT = ',1x,f6.3,2(6x,f6.3))
  810 format(1h1,/,12x,'Prediction for Friction Factors (fi) and Flow
     &  Split',/,12x,'Parameters (Xi) at given Bundle Reynolds
     &  no. (Reb)',/)
  820 format(6x,'Reb =',f9.1)
  830 format(17x,'fi = ',e10.4,3(2x,e10.4))
  840 format(17x,'Xi = ',2x,f6.3,3(6x,f6.3))
  900 format(1h1)
  999 stop
      end
c
c  ***************************************************
c
      subroutine calcf(em,cf,xx)
c
c  ***************************************************
c
c  This subroutine calculates laminar(m=1) or turbulent(m=0.18)
c  friction factor constant cfi for i=1,2,3 and 4(bundle)
c  and flow split parameter Xi
      common nrod,d,dw,pdr,wdr,hdr,at,de(3),deb,
     &  s(3),g(6),cft(4),cfl(4),x(3),xl(3),xt(3)
      common/wwc/ a1,b11,b12,c,a2,b2,el,rlt1,rlt2
      dimension cf(4),xx(3)
      e1=2.0-em
      e2=1.0/e1
      e3=(1.0+em)/e1
      e4=(3.0-em)/2.
      x1=dw/d
c turbulent constants c1 and c2
      cc1=(a1+x1*(b11+x1*b12))/hdr**c
      cc2=a2+b2*alog10(hdr)
      if(em.eq.1.0) then
      fk1=fkl(1,pdr)*g(5)
      fk2=fkl(2,wdr)
      fk3=fkl(3,wdr)
c  laminar constants c1 and c2
      cc1=rlt1*cc1
      cc2=rlt2*cc2
      else
      fk1=fkt(1,pdr)*g(5)
```

```
      fk2=fkt(2,wdr)
      fk3=fkt(3,wdr)
      end if
      g1=g(1)*g(4)**em
c  subchannel friction factor constant cf1
      cf(1)=fk1+cc1*g1
      cf(2)=fk2*(1.0+cc2*g(2))**e4
      cf(3)=fk3*(1.0+cc2*g(3))**e4
c  bundle average friction factor constant cfb(cf4)
      sd3=s(3)*(de(3)/deb)**e3
      sd2=s(2)*(de(2)/deb)**e3
      sd1=s(1)*(de(1)/deb)**e3
      temp=sd3*(1.0/cf(3))**e2
      temp=temp+sd2*(1.0/cf(2))**e2
      temp=temp+sd1*(1.0/cf(1))**e2
      cf(4)=(1.0/temp)**e1
c  flow split parameter
      t1=cf(1)**e2/de(1)**e3
      t2=cf(2)**e2/de(2)**e3
      t3=cf(3)**e2/de(3)**e3
      x12=t2/t1
      x32=t2/t3
      xx(2)=1.0/(s(2)+x12*s(1)+x32*s(3))
      xx(1)=xx(2)*x12
      xx(3)=xx(2)*x32
      return
      end
c
c  ******************************************************
c
      function fkl(i,pdr)
c
c  ******************************************************
c
c  this function calculates laminar friction factor
c  constants KL(i)
      common /blc/a1(3),a2(3),b1(3,5),b2(3,5)
      xu=pdr-1.0
      if(xu.le.0.1) then
      fkl=a1(i)+xu*(b1(i,1)+xu*b1(i,2))
      else
      fkl=a2(i)+xu*(b2(i,1)+xu*b2(i,2))
      end if
      return
      end
c
c  ******************************************************
c
      function fkt(i,pdr)
c
c  ******************************************************
c
c  this function calculates turbulent friction factor
c  constants KT(i)
      common /btc/a1(3),a2(3),b1(3,5),b2(3,5)
      xu=pdr-1.0
      if(xu.le.0.1) then
      fkt=a1(i)+xu*(b1(i,1)+xu*b1(i,2))
      else
      fkt=a2(i)+xu*(b2(i,1)+xu*b2(i,2))
```

```
      end if
      return
      end
c
c  ****************************************************
c
      subroutine flows(el,beta,re)
c
c  ****************************************************
c
c  This subroutine calculates flow split parameters
c  x1,x2,x3 for a given Reynolds number re
      common nrod,d,dw,pdr,wdr,hdr,at,de(3),deb,
     &  s(3),gg(6),cft(4),cfl(4),x(3),xl(3),xt(3)
c  laminar case, bundle Re<=400
      if(re.le.400.0) then
      x(2)=xl(2)
      x(1)=xl(1)
      x(3)=xl(3)
c  turbulent case, bundle Re>=2.e4
      else if(re.ge.2.e4) then
      x(2)=xt(2)
      x(1)=xt(1)
      x(3)=xt(3)
      else
c  trasition case 400<bundle Re<2.e4
      el=1/1.82
      e2=1.18/1.82
      tl1=cfl(1)/(de(1)*de(1))
      tl2=cfl(2)/(de(2)*de(2))
      tl3=cfl(3)/(de(3)*de(3))
      tt1=cft(1)**el/de(1)**e2
      tt2=cft(2)**el/de(2)**e2
      tt3=cft(3)**el/de(3)**e2
      phi=alog10(re/400.)/alog10(50.)
      dre=deb/re
      t11=tl1*dre*(1.-phi)**el
      t12=tt1*dre**0.0989*phi**(el/1.82)
      t1=t11+t12*beta
      t21=tl2*dre*(1.-phi)**el
      t22=tt2*dre**0.0989*phi**(el/1.82)
      t2=t21+t22*beta
      t31=tl3*dre*(1.-phi)**el
      t32=tt3*dre**0.0989*phi**(el/1.82)
      t3=t31+t32*beta
      x12=t2/t1
      x32=t2/t3
      x2=1.0/(s(2)+x12*s(1)+x32*s(3))
      x1=x2*x12
      x3=x2*x32
c  if beta not equal 1, use empical flow split
      if(beta.ne.1.0) then
      x(2)=x2
      x(1)=x1
      x(3)=x3
      else
c  if beta is 1, use Newton's iteration to solve
c  mass balance and same pressure drop equations
      dret=dre**0.18
      dn1=1.0/alog10(xt(1)*50./xl(1))
```

```
      dn2=1.0/alog10(xt(2)*50./x1(2))
      dn3=1.0/alog10(xt(3)*50./x1(3))
      tt1=tt1**1.82
      tt2=tt2**1.82
      tt3=tt3**1.82
      nit=0
c  Newton's iteration starts
   10 p1=alog10(x1*re/(x1(1)*400.))*dn1
      p1d=dn1/x1
      p1m=1.-p1
      p1e=p1**el
      p1me=p1m**el
      p2=alog10(x2*re/(x1(2)*400.))*dn2
      p2d=dn2/x2
      p2m=1.-p2
      p2e=p2**el
      p2me=p2m**el
      p3=alog10(x3*re/(x1(3)*400.))*dn3
      p3d=dn3/x3
      p3m=1.-p3
      p3e=p3**el
      p3me=p3m**el
c  ri is fi*xi**2/del,pressure eq. is ri-rj=0
      r1=t11*dre*p1me*x1+tt1*x1**1.82*dret*p1e
      rd1=t11*dre*p1me+t11*dre*x1*el*(-p1d)*p1me/p1m+
     &  1.82*tt1*x1**0.82*dret*p1e+tt1*x1**1.82*dret*el*
     &  p1d*p1e/p1
      r2=t12*dre*p2me*x2+tt2*x2**1.82*dret*p2e
      rd2=t12*dre*p2me+t12*dre*x2*el*(-p2d)*p2me/p2m+
     &  1.82*tt2*x2**0.82*dret*p2e+tt2*x2**1.82*dret*el*
     &  p2d*p2e/p2
      r3=t13*dre*p3me*x3+tt3*x3**1.82*dret*p3e
      rd3=t13*dre*p3me+t13*dre*x3*el*(-p3d)*p3me/p3m+
     &  1.82*tt3*x3**0.82*dret*p3e+tt3*x3**1.82*dret*el*
     &  p3d*p3e/p3
c  f is mass balance eq, h,g are pressure drop eqs.
      f=x1*s(1)+x2*s(2)+x3*s(3)-1.0
      f1=s(1)
      f2=s(2)
      f3=s(3)
      g=r1-r2
      g1=rd1
      g2=-rd2
      g3=0.
      h=r3-r2
      h1=0.
      h2=-rd2
      h3=rd3
      xj=det(f1,f2,f3,g1,g2,g3,h1,h2,h3)
      x1n=x1+det(-f,f2,f3,-g,g2,g3,-h,h2,h3)/xj
      x2n=x2+det(f1,-f,f3,g1,-g,g3,h1,-h,h3)/xj
      x3n=x3+det(f1,f2,-f,g1,g2,-g,h1,h2,-h)/xj
      if((x2n-x2).le.1.e-5) then
      x(2)=x2n
      x(1)=x1n
      x(3)=x3n
      go to 999
      else if(nit.gt.100) then
      write(6,230)
      go to 999
```

```
      else
      x1=x1n
      x2=x2n
      x3=x3n
      nit=nit+1
      go to 10
      end if
      end if
      end if
  230 format(1x,'no. of iteration > 100, iteration terminated')
  999 return
      end
c
c  ************************************************************
c
      function det(a11,a12,a13,a21,a22,a23,a31,a32,a33)
c
c  ************************************************************
c
      det=a11*a22*a33+a12*a23*a31+a13*a21*a32-
     &  a13*a22*a31-a11*a23*a32-a33*a12*a21
      return
      end
c
c  ************************************************************
c
      subroutine fricf(el,re,f)
c
c  ************************************************************
c
c  this subroutine calculates bundle average friction factor
c  and subchannel friction factor for a given Reynolds number
c  subscript 1,2,3 for subchannel, 4 for bundle average
      common nrod,d,dw,pdr,wdr,hdr,at,de(3),deb,
     &  s(3),gg(6),cft(4),cfl(4),x(3),xl(3),xt(3)
      dimension f(4),res(4)
      do 100 j=1,3
      res(j)=re*x(j)*de(j)/deb
  100 continue
      res(4)=re
      do 200 i=1,4
      fl=cfl(i)/res(i)
      ft=cft(i)/res(i)**0.18
      if(re.le.400) then
      f(i)=fl
      else if(re.ge.2.e4) then
      f(i)=ft
      else
c  for transition case calculating intermittence factors, phi
      if(i.le.3) phi=alog10(x(i)*re/(xl(i)*400.))/
     &  alog10(xt(i)*50./xl(i))
      if(i.eq.4) phi=alog10(re/400.0)/alog10(50.)
      f(i)=fl*(1.-phi)**el+ft*phi**el
      end if
  200 continue
      return
      end
c
c  ************************************************
c
```

```
      subroutine geom
c
c  ********************************************
c
c  this subroutine calculates the geometrical parameters for
c  bare or wire wrap hexagonal bundles
      common nrod,d,dw,pdr,wdr,hdr,at,de(3),deb,
     &  s(3),g(6),cft(4),cfl(4),x(3)
      data pi,sqrt3/3.1415926,1.7320508/
      nring=(3.+sqrt(12.*nrod-3.))/6.-1.
      nch1=6*nring**2
      nch2=6*nring
      nch3=6
      p=pdr*d
      w=(wdr-0.5)*d
c  bare rod bundle geometrical parameters
      asp1=sqrt3*p**2/4.-pi*d**2/8.
      asp2=p*w-pi*d**2/8.
      asp3=w**2/sqrt3-pi*d**2/24.
      pwp1=pi*d/2.
      pwp2=p+pwp1
      pwp3=pwp1/3.+2.*w/sqrt3
      if (dw.eq.0.) then
      as1=asp1
      as2=asp2
      as3=asp3
      pw1=pwp1
      pw2=pwp2
      pw3=pwp3
      de(1)=4.*asp1/pwp1
      de(2)=4.*asp2/pwp2
      de(3)=4.*asp3/pwp3
      do 80 j=1,4
   80 g(j)=0.0
      g(5)=1.0
      g(6)=1.0
      else
c  wire-wrapped bundle geometrical parameters
      h=hdr*d
      wirln=sqrt(h**2+(pi*(d+dw))**2)
      delta=wirln/h
      sinth=pi*(d+dw)/wirln
      costh=1./delta
      tanth=sinth/costh
      tanth2=tanth*tanth
      cosin=delta
      pcd=pi*cosin*dw*dw/8.
      as1=asp1-pcd
      as2=asp2-pcd
      as3=asp3-pcd/3.
      pcd=pcd*4./dw
      pw1=pwp1+pcd
      pw2=pwp2+pcd
      pw3=pwp3+pcd/3.
      de(1)=4.*as1/pw1
      de(2)=4.*as2/pw2
      de(3)=4.*as3/pw3
      sinth2=sinth*sinth
      ar=pi*(d+dw)*dw/2.0
      g(1)=(ar/asp1)*(de(1)/h)
```

```
      g(2)=(ar/asp2)*tanth2
      g(3)=(ar/(asp3*3.))*tanth2
      g(4)=de(1)/dw
      g(5)=pwp1/pw1
      end if
c  bundle total flow area, equiv. dia. and s
      at=nch1*as1+nch2*as2+nch3*as3
      pwt=nch1*pw1+nch2*pw2+nch3*pw3
c  Rehme's parameter prb=nrod*pi*(d+dw)/pwt
      deb=4.*at/pwt
      s(1)=nch1*as1/at
      s(2)=nch2*as2/at
      s(3)=1.0-s(2)-s(1)
      return
      end
c
c  ******************************************************
c
      subroutine set
c
c  ******************************************************
c
c  this sub sets all the constants needed for the correlations
      common/blc/ a11(3),a21(3),b11(3,5),b21(3,5)
      common/btc/ a1t(3),a2t(3),b1t(3,5),b2t(3,5)
      common/wwc/ a1,b11,b12,c,a2,b2,e1,rlt1,rlt2
c  bare rod laminar friction factor coeffients
      a11(1)   = 0.2600e2
      b11(1,1)= 0.8882e3
      b11(1,2)=-0.3334e4
      a21(1)   = 0.6297e2
      b21(1,1)= 0.2169e3
      b21(1,2)=-0.1902e3
      a11(2)   = 0.2618e2
      b11(2,1)= 0.5545e3
      b11(2,2)=-0.1480e4
      a21(2)   = 0.4440e2
      b21(2,1)= 0.2567e3
      b21(2,2)=-0.2676e3
      a11(3)   = 0.2698e2
      b11(3,1)= 0.1636e4
      b11(3,2)=-0.1005e5
      a21(3)   = 0.8726e2
      b21(3,1)= 0.3859e2
      b21(3,2)=-0.5512e2
c  bare rod turbulent friction factor coefficients
      a1t(1)   = 0.9378e-1
      b1t(1,1)= 0.1398e1
      b1t(1,2)=-0.8664e1
      a2t(1)   = 0.1458
      b2t(1,1)= 0.3632e-1
      b2t(1,2)=-0.3333e-1
      a1t(2)   = 0.9377e-1
      b1t(2,1)= 0.8732
      b1t(2,2)=-0.3341e1
      a2t(2)   = 0.1430
      b2t(2,1)= 0.4199e-1
      b2t(2,2)=-0.4428e-1
      a1t(3)   = 0.1004
      b1t(3,1)= 0.1625e1
```

```
      b1t(3,2)=-0.1185e2
      a2t(3)   = 0.1499
      b2t(3,1)= 0.6706e-2
      b2t(3,2)=-0.9567e-2
c  wire wrapped turbulent constrants for c1; a1,b11,b12,c
c  for c2; a2,b2; for transition el; for laminar rlt1,rlt2
c  rlt1=c11/c1t; rlt2=c21/c2t
      a1       = 29.5
      b11      =-140.0
      b12      = 401.0
      c        = 0.85
      a2       =-3.5
      b2       = 10.0
      el       = 1.0/3.0
      rlt1     = 1.4
      rlt2     = 0.3
      return
      end
```

APPENDIX C1

REVISED DRV CODE LISTING

```
c   *** data reduction version of energy series code  ***
c   *** for 37 and 61 pin salt injection  experiments ***
      common/array/ enthal(130),temp(130),flo(130),q(130),qavg(130),
     &              dhdz(130),v(130),mrod(130,3),lc(130,3),prad(61),
     &              axl(60),paxl(60),name(20),prtloc(20)
      common/varbl/ floww,qbar,bunlen,htlen,delz,delzt,reb,pdp,varprt,
     &              grt,choice,imix,noax,nrun,nstep,n2,nk1,nk2
      common/geom/  nrod,d,dw,pdr,wdr,hdr,nring,nchanl,nch1,nch2,nch3,
     &              at,de(3),deb,asp(3),as(3),ar(3),ph(3),eta(4),tanth,
     &              cg,dg,s(3),g(6)
      common/prop/  tin,hin,pref,rhoin,rho(130),viscos(130),dhdro(130),
     &              tavg,cpavg,conavg,beavg,viscin,conbr,cpbr,tout,faxl,
     &              tb,rhoavg,qc
      common/empco/ cft(4),cfl(4),xl(3),xt(3),x(3),rel(3),ret(3),
     &              es1,es2,c11,shape,es1t,es11,c11t,c111
      dimension m(130),yc(130),y(130),y1(130)
c
      read(5,*) nrod,d,dw,pdr,wdr,hdr,nsteps,adj,nchoice,nprt
      read(5,*) es2,shape
      call geom
      call numb
      call output(1)
      read(5,*) (m(i),i=1,nchanl)
   10 read(5,*,end=999) ninj,bunlen,reb,bal,es1,c11
      read(5,*) (y(m(k)),k=1,nchanl)
      call fsplit(1.0,reb)
      n2=nch1+nch2
      nk1=nch1+1
      nk2=n2+1
      bunlen=bunlen/12.
      delz=bunlen/nsteps
      tin=0.0
      hin=0.0
      vin=reb*0.038/deb
      sum1=0.0
      do 100 i=1,nchanl
      q(i)=0.0
      if(i.le.nch1) xs=x(1)
      if(i.gt.nch1.and.i.le.n2) xs=x(2)
      if(i.gt.n2) xs=x(3)
      flo(i)=62.2*xs*vin
      sum1=sum1+y(i)
  100 continue
      cpavg=1.0
      write(6,300) ninj,reb,bal,es1,c11
      call prnt1(nrod,y)
      write(6,301)
      jxs=0
      iflat=0
  105 continue
      jxs=jxs+1
      if(ninj.le.nch1) then
      es1=es1+adj
      if(iflat.eq.1) es1=res1*1.25
      if(iflat.eq.2) es1=res1*0.75
      else
      c11=c11+adj
      if(iflat.eq.1) c11=rc11*1.25
      if(iflat.eq.2) c11=rc11*0.75
      end if
```

```
      do 120 i=1,nchanl
      temp(i)=tin
      enthal(i)=hin
  120 continue
      temp(ninj)=700.
      enthal(ninj)=700.
      do 200 nstep=1,nsteps
      call forced
  200 continue
      sum2=0.0
      do 210 i=1,nchanl
      yc(i)=(temp(i)-tin)/(700.-tin)*100.
      sum2=sum2+yc(i)
  210 continue
      cind=0.0
      if(nchoice.eq.0) then
      do 230 i=1,nchanl
c      yc(i)=yc(i)*sum1/sum2
      cind=cind+(yc(i)-y(i))**2
  230 continue
      else
      do 240 i=nk1,nchanl
      cind=cind+(yc(i)-y(i))**2
  240 continue
      end if
      cind=sqrt(cind)
      if(iflat.ge.1) go to 260
      write(6,310) es1,c11,cind,sum1,sum2
      if(jxs.eq.1.or.cind.lt.reind) then
      reind=cind
      res1=es1
      rc11=c11
      do 250 i=1,nchanl
      y1(i)=yc(i)
  250 continue
      go to 105
      else
      if(jxs.eq.2) then
      es1=res1
      c11=rc11
      adj=-adj
      go to 105
      else
  260 write(6,400)
      write(6,405) ninj
      write(6,404) bunlen*12.
      write(6,406) reb
      write(6,407) x(1),x(2),x(3)
      if(iflat.eq.0) then
      write(6,410) res1
      write(6,420) rc11
      write(6,430) reind
      write(6,440)
      call prnt1(nrod,y1)
      else
      write(6,410) es1
      write(6,420) c11
      write(6,430) cind
      write(6,440)
      call prnt1(nrod,yc)
```

```
      end if
      if(nprt.eq.0) go to 10
      iflat=iflat+1
      if(iflat.le.2) go to 105
      end if
      end if
      go to 10
  300 format(1h1,i4,2x,f9.2,3f8.3,//)
  301 format(1h0//)
  310 format(5x,5f10.3)
  400 format(1h1/////,
     &  5x,'Energy DRV results at minimum square indicator')
  405 format(5x,'injection subchannel                    = ',i4)
  404 format(5x,'injection depth (in)                    = ',f5.1)
  406 format(5x,'bundle average Reynolds number          = ',e10.4)
  407 format(5x,'flow split parameters          X1       = ',f6.3,/,
     &       5x,'                               X2       = ',f6.3,/,
     &       5x,'                               X3       = ',f6.3)
  410 format(5x,'effective eddy diffusity   E*1eta = ',f6.3)
  420 format(5x,'transverse velocity ratio  C1L    = ',f6.3)
  430 format(5x,'min. mean square indicator MSI    = ',f6.2)
  440 format(5x,'dimensionless ratios of salt concentration*100.0:'//)
  999 stop
      end
c
      subroutine prnt1(nrod,y)
      dimension y(130)
c
      if(nrod.eq.37) then
      write(6,81) y(75),y(60),y(59),y(58),y(74)
      write(6,81) y(61),y(34),y(32),y(30),y(57)
      write(6,83) y(35),y(33),y(31),y(29)
      write(6,84) y(62),y(36),y(12),y(10),y(28),y(56)
      write(6,81) y(37),y(13),y(11),y(9),y(27)
      write(6,86) y(63),y(38),y(14),y(2),y(8),y(26),y(55)
      write(6,84) y(39),y(15),y(3),y(1),y(7),y(25)
      write(6,90) y(76),y(73)
      write(6,84) y(40),y(16),y(4),y(6),y(24),y(54)
      write(6,86) y(64),y(41),y(17),y(5),y(23),y(53),y(72)
      write(6,81) y(42),y(18),y(20),y(22),y(52)
      write(6,84) y(65),y(43),y(19),y(21),y(51),y(71)
      write(6,83) y(44),y(46),y(48),y(50)
      write(6,81) y(66),y(45),y(47),y(49),y(70)
      write(6,81) y(77),y(67),y(68),y(69),y(78)
      end if
      if(nrod.eq.61) then
      write(6,110) y(123),y(104),y(103),y(102),y(101),y(122)
      write(6,110) y(105),y(68),y(66),y(64),y(62),y(100)
      write(6,120) y(69),y(67),y(65),y(63),y(61)
      write(6,130) y(106),y(70),y(34),y(32),y(30),y(60),y(99)
      write(6,110) y(71),y(35),y(33),y(31),y(29),y(59)
      write(6,140) y(107),y(72),y(36),y(12),y(10),y(28),y(58),y(98)
      write(6,130) y(73),y(37),y(13),y(11),y(9),y(27),y(57)
      write(6,150) y(108),y(74),y(38),y(14),y(2),y(8),y(26),y(56),y(97)
      write(6,140) y(75),y(39),y(15),y(3),y(1),y(7),y(25),y(55)
      write(6,160) y(124),y(121)
      write(6,140) y(76),y(40),y(16),y(4),y(6),y(24),y(54),y(96)
      write(6,150) y(109),y(77),y(41),y(17),y(5),y(23),y(53),y(95),y(120)
      write(6,130) y(78),y(42),y(18),y(20),y(22),y(52),y(94)
      write(6,140) y(110),y(79),y(43),y(19),y(21),y(51),y(93),y(119)
```

```
      write(6,110) y(80),y(44),y(46),y(48),y(50),y(92)
      write(6,130) y(111),y(81),y(45),y(47),y(49),y(91),y(118)
      write(6,120) y(82),y(84),y(86),y(88),y(90)
      write(6,110) y(112),y(83),y(85),y(87),y(89),y(117)
      write(6,110) y(125),y(113),y(114),y(115),y(116),y(126)
      end if
   80 format(1h1//////)
   81 format(1h0,12x,5f6.1)
   83 format(1h0,15x,4f6.1)
   84 format(1h0,9x,6f6.1)
   86 format(1h0,6x,7f6.1)
   90 format(1h0,3x,f6.1,36x,f6.1)
  110 format(1h0,15x,6f6.1)
  120 format(1h0,18x,5f6.1)
  130 format(1h0,12x,7f6.1)
  140 format(1h0,9x,8f6.1)
  150 format(1h0,6x,9f6.1)
  160 format(1h0,3x,f6.1,48x,f6.1)
      return
      end
```

Appendix D1 Input and Output for ENERGY IV

The input format used in the ENERGY-IV code is free format. In the following, each group means a new line in the input file. The number of lines within each group is not limited.

Group 1 Bundle Geometry parameters: nrod, d, dw, pdr, wdr, hdr, bunlen, htlen, delzt

nrod = N_r, number of pins

d = D, rod diameter (inch)

dw = D_w, wire diameter (inch)

pdr = P/D, pitch to rod diameter ratio

wdr = W/D, edge pitch to rod diameter ratio, i.e., $(D_g + D)/D$

hdr = H/D, wire lead length to rod diameter ratio

bunlen = bundle length (inch), use for calculating axial power profile

htlen = heated length (inch)

delzt = axial stepsize (inch), 0.5 is the recommended value

Group 2 Number of runs for this bundle: norun

Group 3 Description of this run, format 20A4

This information will be printed out before each run. Also it is purposely implemented to make sure the input information is complete. Error message in reading will be printed if input information is not complete.

Group 4 Operation Conditions: Floww, gbar, tin, pref

floww = bundle flow rate (gpm)

gbar = average power per pin (kw/ft)

tin = inlet temperature (°F)

pref = inlet pressure (psi)

Group 5 Option for axial and radial power input: iax,irad

iax = option for axial power profile

= 0 no input needed for Group 5.1, use the axial power profile of last run

= 1 input Group 5.1 for axial power profile

irad = option for radial power profile

= 0 no input needed for Group 5.2, use the radial power profile of last run

= 1 input Group 5.2 for radial power profile

= 2 no input needed for Group 5.2, the code defaults uniform power distribution

Group 5.1 Axial power profile: noax, (axl(i), pax(i), i=1, noax)

noax = number of axial points for input axial profile

axl(i) = relative (to bundle length) position

pax(i) = relative value (to rod average) of power at axl(i)

Group 5.2 Radial Power Profile: (i, prad(i), j=1, nrod)

i = rod identification number (c.f. Figure 7.3)

prad (i) = power factor for rod i

Group 6 Run option: choice, imix

choice = choice of solution scheme, forced or mixed (integer)

= 0 forced convection option

= 1 mixed convection option

imix = option for use of mixing paramters

= 0 no input needed for mixing parameters (Gropu 6.1) default forced convection correlation values with mixing enhanced by $\varepsilon^*_{\eta M}$, i.e. $\varepsilon^*_{\eta} = \varepsilon_{\eta F} + \varepsilon^*_{\eta M}$

= 1 no input needed for mixing parameters, default forced correlation values only, i.e., $\varepsilon^*_{\eta} = \varepsilon^*_{\eta F}$

= 2 mixing parameters specified by users, Group 6.1 must be inputted

Group 6.1 Mixing parameters specified by users: es1, es2, c1ℓ, shape

es1 = $\varepsilon^*_{1\eta}$, Dimensionless effective eddy diffusivity for interior region

es2 = $\varepsilon^*_{2\eta}$, dimensionless effective eddy diffusivity for edge region

C1ℓ = C_{1L}, edge transverse velocity ratio

shape = κ, conduction shape factor

Group 7 Printout locations: novar, (prtloc(i), i=1, novar)

novar = number of axial locations at which subchannel temperatures (and velocities for mixed option) will be printed out

prtloc(i) = axial position for print out (inch)

Repeat Group 3 - Group 7 for next run in this bundle, etc, till norun sets are complete

Code will automatically start to read Group 1 after norun runs are calculated. Users can repeat input information for another bundle etc., in one input file.

The output of the ENERGY-IV is separated into three parts for each bundle. The geometry informations are printed out first. For each run, the operation conditions are printed out and follows by the output of subchannel temperatures (and velocities) at each printout location.

APPENDIX D2

ENERGY-IV CODE LISTING

```
c  ***************************************************************************
c                              energy IV
c  This is an improved and updated version of the energy III code. Only
c  subchannel representation is presented in this code. Both the forced
c  and mixed convection problems may be analyzed. The English unit is
c  used in this code. Recommended input parameters : flow split para-
c  meters, mixing parameters, and subchannel friction factors are from
c  Cheng's latest correlations. They are implemented in this code.
c  Copyright 1984, Massachusetts Institute of Technology
c                    February, 1984  by Shih-Kuei Cheng
c  ***************************************************************************
c
c  nomenclature
c  Note     inch is used for input all the length, but foot is used in code
c  ar(k)    wire projection area(ft**2)
c  as(k)    average subchannel flow area(ft**2)
c  asp(k)   bare subchannel flow area(ft**2)
c  at       bundle total average flow area(ft**2)
c  axl(j)   axial position for input axial power profile, x/l
c  beavg    themal expansion coefficient
c  bunlen   totalbundle length for calculation(ft)
c  cfl(k)   laminar subchannel friction factor constant
c  cft(k)   turbulent subchannel friction factor constant
c  cg       gap between rods(ft)
c  choice   option for forced or mixed solution scheme
c  coeff    matrix for solving mixed option coupling equations
c  conavg   bundle average conductivity at one axial position(btu/hr/ft/F)
c  conbr    average conductivity over whole bundle length(btu/hr/ft/F)
c  cpavg    bundle average specific heat at one axial position(btu/lbm)
c  cpbr     average specific heat over whole bundle length(btu/lbm)
c  c11      edge transverse velocity ratio, c111: laminar, c11t: turbulent
c  d        rod diameter(ft)
c  de(k)    subchannel equivalent hydraulic diameter(ft)
c  deb      bundle average equivalent hydraulic diameter(ft)
c  delz     axial step size(ft)
c  dg       gap between rod and wall
c  dhdro(i) dh/d(rho) at constant pressure
c  dhdz(i)  dh/dz for forced concevtion; dh for mixed convection
c  dw       wire diameter(ft)
c  enthal(i) node inlet enthalpy(btu/lbm)
c  es1      interior effective eddy diffusivity, E1*eta, es1l: laminar,
c           es1t: turbulent
c  es2      edge effective eddy diffusivity, E2*eta
c  eta(x)   centroid distance between subchannels(ft)
c           x=1 triangular-triangular subchannel
c           x=2 triangular-edge subchannel
c           x=3 edge-edge subchannel
c           x=4 edge-corner subchannel
c  flo(i)   forced convection: subchannel mass flux(lbm/hr/ft**2)
c           mixed convection: subchannel mass flow rate(lbm/hr)
c  floww    bundle mass flow rate(lbm/hr), gpm used for input
c  flr(i)   increase of mass flow rate after one axial step(lbm/hr)
c  g(n)     geometrical parameters used in friction factor correlations
c  gbar     bundle average mass flux(lbm/hr/ft**2)
c  gg       gravitational acceleration(ft/hr**2)
c  grt      Grashof number based on dTb/dz, (g*beta*de**4*dTb/dz/mu)
c  h        lead length(ft)
c  havg(i)  average enthalpy for each axial node(btu/lbm)
c  hdr      h/d
c  hhf      sodium saturated enthalpy at gived pressure
```

```
c  hin      bundle inlet enthalpy(btu/lbm)
c  htlen    heated length(in)
c  lc(i,m) neighboring subchannel identifying number
c  mrod(i,m) neighboring rod identifying number
c  nchanl   total number of subchannels
c  nch1     total number of interior subchannels
c  nch2     total number of edge subchannels
c  nch3     total number of corner subchannels
c  n1       number of interior subchannels up to (nring-1) ring
c  n2       nch1+nch2
c  novar    number of axial positions to be print out
c  nring    number of rings of subchannels
c  nrod     number of rods
c  nsteps   total number of axial steps
c  p        rod pitch(ft)
c  paxl(j) axial power factor at axl(j)
c  pdr      p/d
c  pdp      pressure drop from inlet to print location(psia)
c  ph(k)    subchannel heat perimeter
c  pp       given pressure for saturated data(psia)
c  prad(m) radial power factor
c  pref     inlet reference pressure(psia)
c  prtloc(j) axial locations for print out calculation results(ft)
c  q(i)     volumetric heat source(btu/hr/ft**3)
c  qbar     average heat flux(btu/hr/ft**2), kw/ft used for input
c  ravg(i) average density for each axial node(lbm/ft**3)
c  re       subchannel Reynolds number
c  reb      bundle average Reynolds number
c  rel(k)   subchannel critical laminar Reynolds number
c  ret(k)   subchannel critical turbulent Reynolds number
c  rho(i)   inlet density for each node(lbm/ft**3)
c  rhoin    bundle inlet density(lbm/ft**3)
c  row      last row of matrix for solving mixed solution scheme
c  shape    shape factor
c  tanth    tangent of wire angle
c  tavg     bundle average temperature calculateed by summing method(F)
c  tb       byndle average temperature by heat balance(F)
c  temp(i) inlet temperature for each axial node(F)
c  tin      bundle inlet temperature(F)
c  tt       sodium saturated temperature at given pressure(F)
c  v(i)     inlet velocity for each axial node(ft/hr)
c  vavg(i) average velocity for each axial node(ft/hr)
c  viscin   bundle inlet viscosity at one axial position(lbm/ft/hr)
c  viscos(i) viscosity for each node(lbm/ft/hr)
c  w        d/2+dg(ft)
c  wdr      (d+dg)/d
c  x(k)     flow split parameters
c  xl(k)    laminar flow split parameters
c  xt(k)    turbulent flow split parameters
c
c  ***************************************************************************
      common/array/ enthal(186),temp(186),flo(186),q(186),qavg(186),
     &              dhdz(186),v(186),mrod(186,3),lc(186,3),prad(91),
     &              axl(60),paxl(60),name(20),prtloc(20)
      common/varbl/ floww,qbar,bunlen,htlen,delz,delzt,reb,pdp,varprt,
     &              grt,choice,imix,noax,nrun,nstep,n2,nk1,nk2
      common/geom/  nrod,d,dw,pdr,wdr,hdr,nring,nchanl,nch1,nch2,nch3,
     &              at,de(3),deb,asp(3),as(3),ar(3),ph(3),eta(4),tanth,
     &              cg,dg,s(3),g(6)
      common/prop/  tin,hin,pref,rhoin,rho(186),viscos(186),dhdro(186),
```

```
     &               tavg,cpavg,conavg,beavg,viscbr,conbr,cpbr,tout,faxl,
     &               tb,rhoavg,qc
      common/empco/ cft(4),cfl(4),xl(3),xt(3),x(3),rel(3),ret(3),
     &               es1,es2,c11,shape,est,esl,clt,cll,esm
      common/cros/  flr(186),havg(186),vavg(186),ravg(186),vstar,hstar
      integer choice
c
c ***************************************************************************
c
c   read input data
c
c ***************************************************************************
c
c  ** geometry input data ***
c
    1 read(5,*,end=999) nrod,d,dw,pdr,wdr,hdr,bunlen,htlen,delzt
c
c  ** geometrical parameters ***
c
      call geom
c
c  ** numbering subchannel and its neighbor ***
c
      call numb
c
c  ** print out geometrical parameters ***
c
      call output(1)
c
c  ** subchannel number and axial step size **
c
      n2=nch1+nch2
      nk1=nch1+1
      nk2=n2+1
      bunlen=bunlen/12.
      htlen=htlen/12.
      delzt=delzt/12.
c
c  ** run number for this geometry and axial step number **
c
      read(5,*) noruns
c
c  ** operation condition ***
c
      do 900 nrun=1,noruns
      read(5,2) (name(i),i=1,20)
    2 format(20a4)
      read(5,*) floww,qbar,tin,pref
      read(5,*) iax,irad
      if(iax.eq.1) read(5,*) noax,(axl(i),paxl(i),i=1,noax)
      if(irad.eq.1) read(5,*) (i,prad(i),j=1,nrod)
      if(irad.eq.2) then
      do 3 i=1,nrod
    3 prad(i)=1.0
      end if
c
c  ** run option ***
c
      read(5,*) choice,imix
      if(imix.gt.1) read(5,*) es1,es2,c11,shape
```

```
c
c  ** location for print out **
c
      read(5,*) novar,(prtloc(i),i=1,novar)
c
c ****************************************************************
c
c   preliminary calculation
c
c ****************************************************************
c
c  ** inlet temperature distribution and inlet properties ***
c
      nstep=0
c
c  change unit of flow rate from gpm to lbm/hr in prop
c  change unit of heat flux from kw/ft to btu/hr/ft**2 in prop
c  initiate temperature and enthalpy at inlet postion in prop
c
      call prop
c
c  ** flow split parameters ***
c
      gbar=floww/at
      reb=gbar*deb/viscbr
      beta=1.0
c  beta is the option for flow split equations
c  1 means iteration solution, 0.05 means empical equations
      call fsplit(beta,reb)
c
c  ** mixing parameters ***
c
      grt=(32.174*3600.**2)*abs(beavg)*(tout-tin)/htlen
     &  *deb**4/(viscbr/rhoavg)**2
      if(imix.le.1) then
      call mixing(reb)
      if (imix.eq.0.and.choice.eq.1) then
      esm= 0.1*(pdr-1)**(-0.5)*grt/reb
      es1=es1+esm
      es2=es2+esm
      end if
      end if
c
c  ** axial average volumetric heat source and mass flux ***
c
      do 10 i=1,nch1
      p1=prad(mrod(i,1))+prad(mrod(i,2))+prad(mrod(i,3))
      qavg(i)=qbar*p1*ph(1)/3.0/as(i)
   10 flo(i)=gbar*x(1)
      do 20 i=nk1,n2
      p2=prad(mrod(i,1))+prad(mrod(i,2))
      qavg(i)=qbar*p2*ph(2)/2.0/as(2)
   20 flo(i)=gbar*x(2)
      do 30 i=nk2,nchanl
      qavg(i)=qbar*prad(mrod(i,1))*ph(3)/as(3)
   30 flo(i)=gbar*x(3)
c
c *** print out operation condition ***
c
      call output(2)
```

```
c
c  ***************************************************************
c
c   main calculation
c
c  ***************************************************************
c
      pdp=0.0
      zaxl=0.0
      ivar=1
      varprt=prtloc(1)/12.
c
c  ** main calculational loop ***
c
      delz=delzt
  100 nstep=nstep+1
      zaxl=zaxl+delz
      delz=delzt
      iprnt=0
c
c  check to see if a printout is required within next step
c  reset delz to make next axial position meet the print location
c  iprnt=1 indicates when a printout is needed at the end of next step
c
      if((varprt-zaxl).le.delzt) then
      iprnt=1
      delz=varprt-zaxl
      end if
c
c  ** axial power factor; local volumetric heat generation **
c
      zbar=zaxl+delz/2.0
      zbar=zbar/bunlen
      call curve(faxl,zbar,paxl,axl,noax)
      do 110 i=1,nchanl
  110 q(i)=qavg(i)*faxl
c
c  ** local properties for mixed convection scheme ***
c
       call prop
c
c  **  calculate enthalpies at inlet of next axial step ***
c
      if(choice .eq. 0) call forced
      if(choice .eq. 1) call mixed
c
c  print out temperatue and velocity (only for mixed option)
c  distribution; reset print location to next required position
c
      if(iprnt.eq.1) then
      call output(3)
c
      ivar=ivar+1
      if(ivar.gt.novar) go to 900
      varprt=prtloc(ivar)/12.
      end if
      go to 100
  900 continue
      go to 1
  999 stop
```

```
      end
c
c  ****************************************************************
c
      subroutine curve(fx,x,f,y,n)
c
c  ****************************************************************
c
c  calculate values from interpolating of known data
c
      dimension f(n),y(n)
      do 10 k=1,n
      if(x.le.y(k)) goto 20
   10 continue
   20 if(k.eq.1) k=k+1
      b=(f(k)-f(k-1))/(y(k)-y(k-1))
      fx=f(k-1)+b*(x-y(k-1))
      return
      end
c
c*****************************************************************************
c
      subroutine forced
c
c  *************************************************************************
c
c  this subroutine calculates forced convection solution
c
      common/array/ enthal(186),temp(186),flo(186),q(186),qavg(186),
     &              dhdz(186),v(186),mrod(186,3),lc(186,3),prad(91),
     &              axl(60),paxl(60),name(20),prtloc(20)
      common/varbl/ floww,qbar,bunlen,htlen,delz,delzt,reb,pdp,varprt,
     &              grt,choice,imix,noax,nrun,nstep,n2,nk1,nk2
      common/geom/  nrod,d,dw,pdr,wdr,hdr,nring,nchanl,nch1,nch2,nch3,
     &              at,de(3),deb,asp(3),as(3),ar(3),ph(3),eta(4),tanth,
     &              cg,dg,s(3),g(6)
      common/prop/  tin,hin,pref,rhoin,rho(186),viscos(186),dhdro(186),
     &              tavg,cpavg,conavg,beavg,viscbr,conbr,cpbr,tout,faxl,
     &              tb,rhoavg,qc
      common/empco/ cft(4),cfl(4),xl(3),xt(3),x(3),rel(3),ret(3),
     &              es1,es2,c11,shape,esit,esil,c1lt,c1ll,esm
      integer choice
c ****************************************************************************
c
c  initial calculations
c
      almr=conavg/cpavg
      sa=shape*almr
      ex11=(cg/as(1))*(sa/flo(1)/eta(1)+es1)
      ex12=(cg/as(1))*(sa/flo(1)/eta(2)+es1)
      ex21=(cg/as(2))*(sa/flo(nk1)/eta(2)+(x(1)/x(2))*es1)
      ex22=(dg/as(2))*(sa/flo(nk1)/eta(3)+es2)
      ex23=(dg/as(2))*(sa/flo(nk1)/eta(4)+es2)
      exc2=(dg/as(2))*c11
      ex32=(dg/as(3))*(sa/flo(nk2)/eta(4)+(x(2)/x(3))*es2)
      exc3=(dg/as(3))*(x(2)/x(3))*c11
c
c* energy equations
c  interior subchannels
c
```

```
      do 100 i=1,nch1
      ii=lc(i,1)
      jj=lc(i,2)
      kk=lc(i,3)
      exa=ex11
      if(kk.gt.nch1) exa=ex12
 100  dhdz(i)=q(i)/flo(i)+ex11*(enthal(ii)+enthal(jj)
     &   -2.0*enthal(i))+exa*(enthal(kk)-enthal(i))
c
c  edge subchannels
c
      do 110 i=nk1,n2
      ii=lc(i,1)
      jj=lc(i,2)
      kk=lc(i,3)
      duma=ex22
      dumb=ex22
      if(jj.gt.n2) duma=ex23
      if(kk.gt.n2) dumb=ex23
 110  dhdz(i)=q(i)/flo(i)+(exc2+duma)*(enthal(jj)-enthal(i))
     & +ex21*(enthal(ii)-enthal(i))+dumb*(enthal(kk)-enthal(i))
c
c  corner subchannels
c
      do 120 i=nk2,nchanl
      jj=lc(i,1)
      kk=lc(i,2)
 120  dhdz(i)=q(i)/flo(i)+(exc3+ex32)*(enthal(jj)-enthal(i))
     &   +ex32*(enthal(kk)-enthal(i))
c
c  update enthalpies
c
      do 200 i=1,nchanl
      dh=dhdz(i)*delz
      temp(i)=temp(i)+dh/cpavg
 200  enthal(i)=enthal(i)+dh
c
      return
      end
c
c  ***********************************************************************
c
      subroutine fsplit(beta,re)
c
c  ***********************************************************************
c
c  This subroutine calculates flow split parameters
c  x1,x2,x3 for a given Reynolds number re
      common/geom/  nrod,d,dw,pdr,wdr,hdr,nring,nchanl,nch1,nch2,nch3,
     &              at,de(3),deb,asp(3),as(3),ar(3),ph(3),eta(4),tanth,
     &              cg,dg,s(3),gg(6)
      common/empco/ cft(4),cfl(4),xl(3),xt(3),x(3),rel(3),ret(3),
     &              es1,es2,c11,shape,es1t,es11,c11t,c111,esm
      common/blc/ a11(3),a21(3),b11(3,5),b21(3,5)
      common/btc/ a1t(3),a2t(3),b1t(3,5),b2t(3,5)
      common/wwc/ a1,b11,b12,c,a2,b2,el,rlt1,rlt2
c
c  set constants
      call set
c  friction factor constants, 4 for bundle average
```

```
c  laminar case
      call calcf(1.0,cf1,x1)
c  turbulent case
      call calcf(0.18,cft,xt)
c  laminar RebL
      reb1=300.*10.**(1.7*(pdr-1.0))
      rebt=10000.*10.**(0.7*(pdr-1.0))
c  subchannel laminar and turbulent Re
      do 5 i=1,3
      re1(i)=reb1*(de(i)/deb)*x1(i)
      ret(i)=rebt*(de(i)/deb)*xt(i)
   5  continue
c  laminar case, bundle Re<=RebL
      if(re.le.reb1) then
      x(2)=x1(2)
      x(1)=x1(1)
      x(3)=x1(3)
c  turbulent case, bundle Re>=rebt
      else if(re.ge.rebt) then
      x(2)=xt(2)
      x(1)=xt(1)
      x(3)=xt(3)
      else
c  trasition case RebL<bundle Re<rebt
      e1=1/1.82
      e2=1.18/1.82
      t11=cf1(1)/(de(1)*de(1))
      t12=cf1(2)/(de(2)*de(2))
      t13=cf1(3)/(de(3)*de(3))
      tt1=cft(1)**e1/de(1)**e2
      tt2=cft(2)**e1/de(2)**e2
      tt3=cft(3)**e1/de(3)**e2
      phi=alog10(re/reb1)/alog10(rebt/reb1)
      dre=deb/re
      t11=t11*dre*(1.-phi)**e1
      t12=tt1*dre**0.0989*phi**(e1/1.82)
      t1=t11+t12*beta
      t21=t12*dre*(1.-phi)**e1
      t22=tt2*dre**0.0989*phi**(e1/1.82)
      t2=t21+t22*beta
      t31=t13*dre*(1.-phi)**e1
      t32=tt3*dre**0.0989*phi**(e1/1.82)
      t3=t31+t32*beta
      x12=t2/t1
      x32=t2/t3
      x2=1.0/(s(2)+x12*s(1)+x32*s(3))
      x1=x2*x12
      x3=x2*x32
c  if beta not equal 1, use empical flow split
      if(beta.ne.1.0) then
      x(2)=x2
      x(1)=x1
      x(3)=x3
      else
c  if beta is 1, use Newton's iteration to solve
c  mass balance and same pressure drop equations
      dret=dre**0.18
      dn1=1.0/alog10(xt(1)*rebt/(x1(1)*reb1))
      dn2=1.0/alog10(xt(2)*rebt/(x1(2)*reb1))
      dn3=1.0/alog10(xt(3)*rebt/(x1(3)*reb1))
```

```
      tt1=tt1**1.82
      tt2=tt2**1.82
      tt3=tt3**1.82
      nit=0
c  Newton's iteration starts
   10 p1=alog10(x1*re/(x1(1)*rebl))*dn1
      p1=abs(p1)
      p1d=dn1/x1
      p1m=1.-p1
      p1e=p1**el
      p1me=p1m**el
      p2=alog10(x2*re/(x1(2)*rebl))*dn2
      p2=abs(p2)
      p2d=dn2/x2
      p2m=1.-p2
      p2e=p2**el
      p2me=p2m**el
      p3=alog10(x3*re/(x1(3)*rebl))*dn3
      p3=abs(p3)
      p3d=dn3/x3
      p3m=1.-p3
      p3e=p3**el
      p3me=p3m**el
c  ri is f1*xi**2/del,pressure eq. is r1-rj=0
      r1=tl1*dre*p1me*x1+tt1*x1**1.82*dret*p1e
      rd1=tl1*dre*p1me+tl1*dre*x1*el*(-p1d)*p1me/p1m+
     &  1.82*tt1*x1**0.82*dret*p1e+tt1*x1**1.82*dret*el*
     &  p1d*p1e/p1
      r2=tl2*dre*p2me*x2+tt2*x2**1.82*dret*p2e
      rd2=tl2*dre*p2me+tl2*dre*x2*el*(-p2d)*p2me/p2m+
     &  1.82*tt2*x2**0.82*dret*p2e+tt2*x2**1.82*dret*el*
     &  p2d*p2e/p2
      r3=tl3*dre*p3me*x3+tt3*x3**1.82*dret*p3e
      rd3=tl3*dre*p3me+tl3*dre*x3*el*(-p3d)*p3me/p3m+
     &  1.82*tt3*x3**0.82*dret*p3e+tt3*x3**1.82*dret*el*
     &  p3d*p3e/p3
c  f is mass balance eq, h,g are pressure drop eqs.
      f=x1*s(1)+x2*s(2)+x3*s(3)-1.0
      f1=s(1)
      f2=s(2)
      f3=s(3)
      g=r1-r2
      g1=rd1
      g2=-rd2
      g3=0.
      h=r3-r2
      h1=0.
      h2=-rd2
      h3=rd3
      xj=det(f1,f2,f3,g1,g2,g3,h1,h2,h3)
      x1n=x1+det(-f,f2,f3,-g,g2,g3,-h,h2,h3)/xj
      x2n=x2+det(f1,-f,f3,g1,-g,g3,h1,-h,h3)/xj
      x3n=x3+det(f1,f2,-f,g1,g2,-g,h1,h2,-h)/xj
      if((x2n-x2).le.1.e-6) then
      x(2)=x2n
      x(1)=x1n
      x(3)=x3n
      go to 999
      else if(nit.gt.100) then
      write(6,230)
```

```
      go to 999
      else
      x1=x1n
      x2=x2n
      x3=x3n
      nit=nit+1
      go to 10
      end if
      end if
      end if
  230 format(1x,'no. of iteration > 100, iteration terminated')
  999 return
      end
c
c  ***********************************************************
      function det(a11,a12,a13,a21,a22,a23,a31,a32,a33)
c  ***********************************************************
c
      det=a11*a22*a33+a12*a23*a31+a13*a21*a32-
     &  a13*a22*a31-a11*a23*a32-a33*a12*a21
      return
      end
c
c  ***************************************************
c
      subroutine calcf(em,cf,xx)
c
c  ***************************************************
c
c  This subroutine calculates laminar(m=1) or turbulent(m=0,18)
c  friction factor constant cfi for i=1,2,3 and 4(bundle)
c  and flow split parameter Xi
      common/geom/  nrod,d,dw,pdr,wdr,hdr,nring,nchanl,nch1,nch2,nch3,
     &              at,de(3),deb,asp(3),as(3),ar(3),ph(3),eta(4),tanth,
     &              cg,dg,s(3),g(6)
      common/wwc/ a1,b11,b12,c,a2,b2,el,rlt1,rlt2
      dimension cf(4),xx(3)
      e1=2.0-em
      e2=1.0/e1
      e3=(1.0+em)/e1
      e4=(3.0-em)/2.
      x1=dw/d
c  turbulent constants c1 and c2
      cc1=(a1+x1*(b11+x1*b12))/hdr**c
      cc2=a2+b2*alog10(hdr)
      if(em.eq.1.0) then
      fk1=fkl(1,pdr)*g(5)
      fk2=fkl(2,wdr)
      fk3=fkl(3,wdr)
c  laminar constants c1 and c2
      cc1=rlt1*cc1
      cc2=rlt2*cc2
      else
      fk1=fkt(1,pdr)*g(5)
      fk2=fkt(2,wdr)
      fk3=fkt(3,wdr)
      end if
      g1=g(1)*g(4)**em
c  subchannel friction factor constant cfi
      cf(1)=fk1+cc1*g1
```

```
      cf(2)=fk2*(1.0+cc2*g(2))**e4
      cf(3)=fk3*(1.0+cc2*g(3))**e4
c  bundle average friction factor constant cfb(cf4)
      sd3=s(3)*(de(3)/deb)**e3
      sd2=s(2)*(de(2)/deb)**e3
      sd1=s(1)*(de(1)/deb)**e3
      temp=sd3*(1.0/cf(3))**e2
      temp=temp+sd2*(1.0/cf(2))**e2
      temp=temp+sd1*(1.0/cf(1))**e2
      cf(4)=(1.0/temp)**e1
c  flow split parameter
      t1=cf(1)**e2/de(1)**e3
      t2=cf(2)**e2/de(2)**e3
      t3=cf(3)**e2/de(3)**e3
      x12=t2/t1
      x32=t2/t3
      xx(2)=1.0/(s(2)+x12*s(1)+x32*s(3))
      xx(1)=xx(2)*x12
      xx(3)=xx(2)*x32
      return
      end
c
c  ******************************************************
      function fkl(i,pdr)
c  ******************************************************
c
c  this function calculates laminar friction factor
c  constants KL(i)
      common /blc/a1(3),a2(3),b1(3,5),b2(3,5)
      xu=pdr-1.0
      if(xu.le.0.1) then
      fkl=a1(i)+xu*(b1(i,1)+xu*b1(i,2))
      else
      fkl=a2(i)+xu*(b2(i,1)+xu*b2(i,2))
      end if
      return
      end
c
c  ******************************************************
      function fkt(i,pdr)
c  ******************************************************
c
c  this function calculates turbulent friction factor
c  constants KT(i)
      common /btc/a1(3),a2(3),b1(3,5),b2(3,5)
      xu=pdr-1.0
      if(xu.le.0.1) then
      fkt=a1(i)+xu*(b1(i,1)+xu*b1(i,2))
      else
      fkt=a2(i)+xu*(b2(i,1)+xu*b2(i,2))
      end if
      return
      end
c
c  ******************************************************
c
      subroutine set
c
c  ******************************************************
c
```

```
c  this sub sets all the constants needed for the correlations
      common/blc/ a11(3),a21(3),b11(3,5),b21(3,5)
      common/btc/ a1t(3),a2t(3),b1t(3,5),b2t(3,5)
      common/wwc/ a1,b11,b12,c,a2,b2,e1,rlt1,rlt2
c  bare rod laminar friction factor coeffients
      a11(1)  = 0.2600e2
      b11(1,1)= 0.8882e3
      b11(1,2)=-0.3334e4
      a21(1)  = 0.6297e2
      b21(1,1)= 0.2169e3
      b21(1,2)=-0.1902e3
      a11(2)  = 0.2618e2
      b11(2,1)= 0.5545e3
      b11(2,2)=-0.1480e4
      a21(2)  = 0.4440e2
      b21(2,1)= 0.2567e3
      b21(2,2)=-0.2676e3
      a11(3)  = 0.2698e2
      b11(3,1)= 0.1636e4
      b11(3,2)=-0.1005e5
      a21(3)  = 0.8726e2
      b21(3,1)= 0.3859e2
      b21(3,2)=-0.5512e2
c  bare rod turbulent friction factor coefficients
      a1t(1)  = 0.9378e-1
      b1t(1,1)= 0.1398e1
      b1t(1,2)=-0.8664e1
      a2t(1)  = 0.1458
      b2t(1,1)= 0.3632e-1
      b2t(1,2)=-0.3333e-1
      a1t(2)  = 0.9377e-1
      b1t(2,1)= 0.8732
      b1t(2,2)=-0.3341e1
      a2t(2)  = 0.1430
      b2t(2,1)= 0.4199e-1
      b2t(2,2)=-0.4428e-1
      a1t(3)  = 0.1004
      b1t(3,1)= 0.1625e1
      b1t(3,2)=-0.1185e2
      a2t(3)  = 0.1499
      b2t(3,1)= 0.6706e-2
      b2t(3,2)=-0.9567e-2
c  wire wrapped turbulent constrants for c1; a1,b11,b12,c
c  for c2; a2,b2; for transition e1; for laminar rlt1,rlt2
c  rlt1=c11/c1t; rlt2=c21/c2t
      a1      = 29.5
      b11     =-140.0
      b12     = 401.0
      c       = 0.85
      a2      =-7.0
      b2      = 20.0
      e1      = 1.0/3.0
      rlt1    = 1.4
      rlt2    = 0.3
      return
      end
c
c  ***********************************************
c
      subroutine geom
```

```
c
c  ***********************************************
c
c  this subroutine calculates the geometrical parameters for
c  bare or wire wrap hexagonal bundles
      common/geom/  nrod,d,dw,pdr,wdr,hdr,nring,nchanl,nch1,nch2,nch3,
     &              at,de(3),deb,asp(3),as(3),ar(3),ph(3),eta(4),tanth,
     &              cg,dg,s(3),g(6)
      data pi,sqrt3/3.1415926,1.7320508/
c
      nring=(3.+sqrt(12.*nrod-3.))/6.-1.
      nch1=6*nring**2
      nch2=6*nring
      nch3=6
      nchanl=nch1+nch2+nch3
c  change unit from inch to feet
      d=d/12.0
      dw=dw/12.0
      p=pdr*d
      w=(wdr-0.5)*d
      cg=p-d
      dg=w-d/2.
c  bare rod bundle geometrical parameters
      asp(1)=sqrt3*p**2/4.-pi*d**2/8.
      asp(2)=p*w-pi*d**2/8.
      asp(3)=w**2/sqrt3-pi*d**2/24.
      ph(1)=pi*d/2
      ph(2)=ph(1)
      ph(3)=ph(1)/3.
      ph1=ph(1)
      ph2=p+ph(1)
      ph3=ph(1)/3.+2.*w/sqrt3
      eta(1)=p/sqrt3
      eta(2)=(eta(1)+w)/2
      eta(3)=p
      eta(4)=(p+w/sqrt3)/2.
      if (dw.eq.0.) then
      as(1)=asp(1)
      as(2)=asp(2)
      as(3)=asp(3)
      de(1)=4.*as(1)/ph1
      de(2)=4.*as(2)/ph2
      de(3)=4.*as(3)/ph3
      do 80 j=1,4
   80 g(j)=0.0
      g(5)=1.0
      g(6)=1.0
      else
c  wire-wrapped bundle geometrical parameters
      h=hdr*d
      wirln=sqrt(h**2+(pi*(d+dw))**2)
      cosin=wirln/h
      sinth=pi*(d+dw)/wirln
      costh=1./cosin
      tanth=sinth/costh
      tanth2=tanth*tanth
      pcd=pi*cosin*dw*dw/8.
      as(1)=asp(1)-pcd
      as(2)=asp(2)-pcd
      as(3)=asp(3)-pcd/3.
```

```
      pcd=pcd*4./dw
      pw1=ph1+pcd
      pw2=ph2+pcd
      pw3=ph3+pcd/3.
      de(1)=4.*as(1)/pw1
      de(2)=4.*as(2)/pw2
      de(3)=4.*as(3)/pw3
      aar=pi*(d+dw)*dw/2.0
      ar(1)=aar/3.
      ar(2)=aar/2.
      ar(3)=ar(1)
      g(1)=(aar/asp(1))*(de(1)/h)
      g(2)=(ar(2)/asp(2))*tanth2
      g(3)=(ar(3)/asp(3))*tanth2
      g(4)=de(1)/dw
      g(5)=ph1/pw1
      end if
c  bundle total flow area, equiv. dia. and s
      at=nch1*as(1)+nch2*as(2)+nch3*as(3)
      pwt=nch1*pw1+nch2*pw2+nch3*pw3
c  Rehme's parameter prb=nrod*pi*(d+dw)/pwt
      deb=4.*at/pwt
      s(1)=nch1*as(1)/at
      s(2)=nch2*as(2)/at
      s(3)=1.0-s(2)-s(1)
      return
      end
c
c  ***********************************************************************
c
      subroutine mixed
c
c  ***********************************************************************
c
c  this subroutine does the mixed convection solution
c
      common/array/ enthal(186),temp(186),flo(186),q(186),qavg(186),
     &              dhdz(186),v(186),mrod(186,3),lc(186,3),prad(91),
     &              axl(60),paxl(60),name(20),prtloc(20)
      common/varbl/ floww,qbar,bunlen,htlen,delz,delzt,reb,pdp,varprt,
     &              grt,choice,imix,noax,nrun,nstep,n2,nk1,nk2
      common/geom,  nrod,d,dw,pdr,wdr,hdr,nring,nchanl,nch1,nch2,nch3,
     &              at,de(3),deb,asp(3),as(3),ar(3),ph(3),eta(4),tanth,
     &              cg,dg,s(3),g(6)
      common/prop/  tin,hin,pref,rhoin,rho(186),viscos(186),dhdro(186),
     &              tavg,cpavg,conavg,beavg,viscbr,conbr,cpbr,tout,faxl,
     &              tb,rhoavg,qc
      common/empco/ cft(4),cfl(4),xl(3),xt(3),x(3),rel(3),ret(3),
     &              es1,es2,c11,shape,esit,esil,c1lt,c1ll,esm
      common/cros/  flr(186),havg(186),vavg(186),ravg(186),vstar,hstar
      common/mixu/  coeff(372,4),row(374),aaa(186),delv(186),delr(186),
     &              fr(186),rves(186),gg,ndp1,jtot,ndim,rlf
      integer choice
      real*8 coeff,row
c
c-----------------------------------------------------------------------
c   parameter initialization prior to first axial step
c-----------------------------------------------------------------------
      if(nstep.gt.1) go to 50
      ndim=2*nchanl
```

```
      ndp1=ndim+1
      jtot=ndim+2
      gg=32.174*3600.*3600.
      rlf=1.0
      do 10 i=1,nchanl
      if(i.le.nch1) aaa(i)=as(1)
      if(i.gt.nch1.and.i.le.n2) aaa(i)=as(2)
      if(i.gt.n2) aaa(i)=as(3)
      rho(i)=rhoin
      v(i)=flo(i)/rho(i)
   10 continue
   50 continue
c-----------------------------------------------------------------------
c  start calculation for each axial step
c-----------------------------------------------------------------------
      exch1=delz*cg/as(1)
      exch21=delz*cg/as(2)
      exch2=delz*dg/as(2)
      exch3=delz*dg/as(3)
c-----------------------------------------------------------------------
c  conduction factors
c-----------------------------------------------------------------------
      sf=shape*conavg/cpavg
      sf1=sf/eta(1)
      sf2=sf/eta(2)
      sf3=sf/eta(3)
      sf4=sf/eta(4)
c-------------------------------------------------------
c  subchannel friction factor and mixing parameters
c-------------------------------------------------------
      do 90 i=1,nchanl
      if(i.le.nch1) then
      isub=1
      des=de(1)
      qp=q(i)*as(1)/ph(1)
      else if(i.le.n2) then
      isub=2
      des=de(2)
      qp=q(i)*as(2)/ph(2)
      else
      isub=3
      des=de(3)
      qp=q(i)*as(3)/ph(3)
      end if
      re=rho(i)*v(i)*des/viscos(i)
      gr=des**4*gg*abs(beavg)*qp*rho(i)**2/(conavg*viscos(i)**2)
      fr(i)=fricf(isub,re,gr)*delz/des
   90 continue
c-------------------------------------------------------------
c  initialize array for iteration in this step
c-------------------------------------------------------------
      ifg=0
  101 if(ifg.eq.1) rlf=rlf-0.1
      do 95 i=1,nchanl
      dhdz(i)=0.0
      flr(i)=0.0
      delr(i)=0.0
      delv(i)=0.0
   95 continue
c-------------------------------------------------------------
```

```
c  start iteration for dv dr and dp
c-----------------------------------------------------------------
      ifg=0
      noiter=1
  100 continue
c-----------------------------------------------------------------
c  update average properties of an axial node
c-----------------------------------------------------------------
      do 110 i=1,nchan1
      havg(i)=enthal(i)+0.5*dhdz(i)
      vavg(i)=v(i)+0.5*delv(i)
      ravg(i)=rho(i)+0.5*delr(i)
      rves(i)=ravg(i)*vavg(i)*es1
  110 continue
c-----------------------------------------------------------------
c  entering loop to fill matrix for dr dv and dp
c-----------------------------------------------------------------
      nnmc=0
      do 120 i=1,nchan1
      if(i.le.n2) then
      ii=lc(i,1)
      jj=lc(i,2)
      kk=lc(i,3)
      else
      jj=lc(i,1)
      kk=lc(i,2)
      ii=lc(i,3)
      end if
c-----------------------------------------------------------------
c  cross flow properties: hstar, vstar
c-----------------------------------------------------------------
      call cross(i,ii,jj,kk)
c-----------------------------------------------------------------
c  exchange terms for interior channels with interior neighbors
c-----------------------------------------------------------------
      if(i.le.nch1) then
      exi=0.5*(rves(i)+rves(ii))
      exj=0.5*(rves(i)+rves(jj))
      exk=0.5*(rves(i)+rves(kk))
      if(kk.le.nch1) then
      ee1=exch1*((sf1+exi)*(havg(ii)-havg(i))
     &    +(sf1+exj)*(havg(jj)-havg(i))+(sf1+exk)*(havg(kk)-havg(i)))
      ee2=0.0
      em1=exch1*(exi*(vavg(ii)-vavg(i))+exj*(vavg(jj)-vavg(i))
     &    +exk*(vavg(kk)-vavg(i)))
      em2=0.0
      else
c-----------------------------------------------------------------
c  interior channels with edge neighbors
c-----------------------------------------------------------------
      ee1=exch1*((sf1+exi)*(havg(ii)-havg(i))+(sf1+exj)*
     &    (havg(jj)-havg(i))+(sf2+rves(i))*(havg(kk)-havg(i)))
      ee2=0.0
      em1=exch1*(exi*(vavg(ii)-vavg(i))+exj*(vavg(jj)-vavg(i))
     &     +rves(i)*(vavg(kk)-vavg(i)))
      em2=0.0
      end if
      else
c-----------------------------------------------------------------
c  edge channels and corner channels
```

```
c-----------------------------------------------------------------
      rv2=ravg(i)*vavg(i)
      rvj=ravg(jj)*vavg(jj)
      rvk=ravg(kk)*vavg(kk)
      exj2=0.5*es2*(rv2+rvj)
      exk2=0.5*es2*(rv2+rvk)
      rjvj=rvj*c11
      rivi=rv2*c11
      if(i.le.n2) then
      if(jj.le.n2) then
      sfa=sf3
      else
      sfa=sf4
      end if
      if(kk.le.n2) then
      sfb=sf3
      else
      sfb=sf4
      end if
      ee1=exch21*(sf2+rves(ii))*(havg(ii)-havg(i))+exch2*((sfa+exj2)
     &    *(havg(jj)-havg(i))+(sfb+exk2)*(havg(kk)-havg(i)))
      ee2=exch2*(rjvj*(havg(jj)-hstar)-rivi*(havg(i)-hstar))
      em1=exch21*rves(jj)*(vavg(ii)-vavg(i))+exch2*(exj2*(vavg(jj)-
     &    vavg(i))+exk2*(vavg(kk)-vavg(i)))
      em2=exch2*(rjvj*(vavg(jj)-vstar)-rivi*(vavg(i)-vstar))
      else
c-----------------------------------------------------------------
c  corner channels
c-----------------------------------------------------------------
      ee1=exch3*((sf4+exj2)*(havg(jj)-havg(i))
     &    +(sf4+exk2)*(havg(kk)-havg(i)))
      ee2=exch3*(rjvj*(havg(jj)-hstar)-rivi*(havg(i)-hstar))
      em1=exch3*(exj2*(vavg(jj)-vavg(i))+exk2*(vavg(kk)-vavg(i)))
      em2=exch3*(rjvj*(vavg(jj)-vstar)-rivi*(vavg(i)-vstar))
      end if
      end if
c-----------------------------------------------------------------
c  set up coefficient matrix
c-----------------------------------------------------------------
      nnmc=nnmc+2
      vdv=v(i)+delv(i)
      enmh=enthal(i)-hstar
c       rrh=dhdro(i)*(rho(i)+delr(i))+enmh
      coeff(nnmc,1)=gg*delz/2.+vdv*(vdv-vstar)+(1./16.)*fr(i)*
     &  (vdv+delv(i))**2
      coeff(nnmc,2)=rho(i)*((2.+fr(i)/2.)*v(i)+(1.+fr(i)/8.)*
     &  delv(i)-vstar)
      coeff(nnmc-1,1)=vdv*(dhdro(i)*(rho(i)+delr(i))+enmh)
      coeff(nnmc-1,2)=rho(i)*enmh
      coeff(nnmc,3)=gg
      coeff(nnmc-1,3)=0.0
      row(nnmc-1)=aaa(i)*vdv
      row(nnmc)=aaa(i)*rho(i)
      coeff(nnmc-1,4)=q(i)*delz+ee1+ee2
      coeff(nnmc,4)=-rho(i)*gg*delz-0.5*fr(i)*rho(i)*v(i)*v(i)
     &  +em1+em2
  120 continue
      row(ndp1)=0.0
      row(jtot)=0.0
c-----------------------------------------------------------------
```

```
c  solve dh droh dp by elimination method
c-----------------------------------------------------------------------
      call invert(coeff,row,ndim,nchanl,jtot,ndp1)
c-----------------------------------------------------------------------
c  convergence check use average of old and new values for new iteration
c-----------------------------------------------------------------------
      nr=0
      crosum=0.0
      do  130 i=1,nchanl
      nr=nr+2
      delv(i)=rlf*coeff(nr,4)+(1.-rlf)*delv(i)
      delr(i)=rlf*coeff(nr-1,4)+(1.-rlf)*delr(i)
      dhdz(i)=dhdro(i)*delr(i)
      flr(i)=aaa(i)*((v(i)+delv(i))*delr(i)+rho(i)*delv(i))
      crosum=crosum+flr(i)
  130 continue
      if(abs(crosum)/floww.lt.0.1e-6.and.noiter.gt.1) go to 200
c-----------------------------------------------------------------------
c  chenk maximum iterations
c-----------------------------------------------------------------------
      noiter=noiter+1
      if(noiter.gt.20) go to 300
      go to 100
 200  continue
c-----------------------------------------------------------------------
c   converged; calculate exit properties
c-----------------------------------------------------------------------
      do 210 i=1,nchanl
      v(i)=v(i)+delv(i)
      rho(i)=rho(i)+delr(i)
      flo(i)=rho(i)*v(i)
      enthal(i)=enthal(i)+dhdz(i)
      temp(i)=temp(i)+dhdz(i)/cpavg
  210 continue
      pdp=pdp+row(jtot)/144.+rhoavg*delz/144.
      return
c-----------------------------------------------------------------------
c* error messages
c-----------------------------------------------------------------------
  300 continue
      if(rlf.gt.0.3) then
      ifg=1
      go to 101
      else
      print 310
      end if
  310 format(1x,'convergence failed in mixed option !!!')
      stop
      end
c
c  ***************************************************************************
      subroutine cross(i,mm1,mm2,mm3)
c  ***************************************************************************
c
      common/varbl/ floww,qbar,bunlen,htlen,delz,delzt,reb,pdp,varprt,
     &              grt,choice,imix,noax,nrun,nstep,n2,nk1,nk2
      common/cros/  flr(186),havg(186),vavg(186),ravg(186),vstar,hstar
c
      i1 = i
      i2 = i
```

```
      i3 = i
      crsf11 = flr(i)-flr(mm1)
      crsf12 = flr(i)-flr(mm2)
      crsf13 = flr(i)-flr(mm3)
      if(crsf11.gt..0) i1 = mm1
      if(crsf12.gt..0) i2 = mm2
      if(crsf13.gt..0) i3 = mm3
      crsf11 = abs(crsf11)
      crsf12 = abs(crsf12)
      crsf13 = abs(crsf13)
c
      if(i.le.n2) then
      crsumm = crsf11+crsf12+crsf13
      if(crsumm.le.1.e-6) go to 100
      hstar = (crsf11*havg(i1)+crsf12*havg(i2)+crsf13*havg(i3))/crsumm
      vstar = (crsf11*vavg(i1)+crsf12*vavg(i2)+crsf13*vavg(i3))/crsumm
      else
      crsumm=crsf12+crsf13
      if(crsumm.lt.1.e-6) goto 100
      hstar=(crsf12*havg(i2)+crsf13*havg(i3))/crsumm
      vstar=(crsf12*vavg(i2)+crsf13*vavg(i3))/crsumm
      end if
      return
c
  100 hstar = havg(i)
      vstar = vavg(i)
      return
      end
c
c  ***********************************************************************
      subroutine invert(a,row,ndim,nchanl,jtot,ndp1)
c  ***********************************************************************
c
      real*8 a,row
      dimension a(372,4),row(374)
c  hard-wired matrix solver
      do 10 i=1,nchanl
      i2=2*i
      i2m=i2-1
c  f is a multiplication factor,
      f=a(i2,1)/a(i2m,1)
      a(i2,2)=a(i2,2)-a(i2m,2)*f
      a(i2,4)=a(i2,4)-a(i2m,4)*f
c  begin cleaning out the last row
      f=row(i2m)/a(i2m,1)
      row(i2)=row(i2)-f*a(i2m,2)
      row(jtot)=row(jtot)-f*a(i2m,4)
      f=row(i2)/a(i2,2)
      row(ndp1)=row(ndp1)-f*a(i2,3)
      row(jtot)=row(jtot)-f*a(i2,4)
      f=a(i2m,2)/a(i2,2)
      a(i2m,3)=-f*a(i2,3)
   10 a(i2m,4)=a(i2m,4)-f*a(i2,4)
c  finish last row
      row(jtot)=row(jtot)/row(ndp1)
c clean out column 3
      do 20 i=1,ndim
   20 a(i,4)=a(i,4)-a(i,3)*row(jtot)
c  divide by diagonal terms
      do 30 i=1,nchanl
```

```
      i2=2*i
      i2m=i2-1
      a(i2,4)=a(i2,4)/a(i2,2)
   30 a(i2m,4)=a(i2m,4)/a(i2m,1)
      return
      end

c
c  ***************************************************************
c
      function fricf(i,re,gr)
c
c  ***************************************************************
c
c  this subroutine calculates subchannel friction factors for
c  mixed convection option
c
      common/empco/ cft(4),cfl(4),xl(3),xt(3),x(3),rel(3),ret(3),
     &              es1,es2,c11,shape,es1t,es11,c11t,c111,esm
      common/wwc/ a1,b11,b12,c,a2,b2,el,rlt1,rlt2
c
c  multiplication factor for correction f in mixed convection
c
      fac=(1.0+2.97e-3*gr/re)**0.655
      if(re.le.rel(i)) then
      fricf=(cfl(i)/re)*fac
      else if(re.ge.ret(i)) then
      fricf=(cft(i)/re**0.18)*fac
      else
      phi=alog10(re/rel(i))/alog10(ret(i)/rel(i))
      fricf=((cfl(i)/re)*(1.-phi)**el+(cft(i)/re**0.18)*phi**el)*fac
      end if
      return
      end

c
c  ***************************************************************
c
      subroutine mixing(re)
c
c  ***************************************************************
c
c  this subroutine calculates mixing parameters: es1,es2,c11,kapa
c
      common/geom/  nrod,d,dw,pdr,wdr,hdr,nring,nchanl,nch1,nch2,nch3,at,
     &              de(3),deb,asp(3),as(3),ar(3),ph(3),eta(4),tanth,cg,dg,
     &              s(3),g(6)
      common/empco/ cft(4),cfl(4),xl(3),xt(3),x(3),rel(3),ret(3),
     &              es1,es2,c11,shape,es1t,es11,c11t,c111,esm
c
c  geometrical parameters
      at1=sqrt(ar(1)/asp(1))
      at2=sqrt(ar(2)/asp(2))
      gm1=(cg/d)**(-0.5)*at1*tanth
      gm2=hdr**0.3*at2*tanth
c   critical Reynolds number
      reb1=300.*10.**(1.7*(pdr-1.0))
      rebt=10000.*10.**(0.7*(pdr-1.0))
c  set up constants
      if(nrod.gt.7) then
```

```
      cm1t=0.14
      cm2t=0.75
      else
      cm1t=0.10
      cm2t=0.60
      end if
      cm1t=1.5*(pdr-1.)**0.6
      cm11=cm1t*cm1t
      cm21=cm1t*cm2t
c
c  effective eddy diffusivity and swirl flow ratio
c
      es2=0.01
      es1t=cm1t*gm1
      es11=cm11*gm1
      c11t=cm2t*gm2
      c111=cm21*gm2
      if(re.ge.rebt) then
      es1=es1t
      c11=c11t
      else if(re.le.reb1) then
      es1=es11
      es2=0.0
      c11=c111
      else
      re1=re*x(1)*de(1)/deb
      re2=re*x(2)*de(2)/deb
      phi1=alog10(re1/rel(1))/alog10(ret(1)/rel(1))
      phi2=alog10(re2/rel(2))/alog10(ret(2)/rel(2))
      es1=(es1t-es11)*phi1**0.666667+es11
      c11=(c11t-c111)*phi2**0.666667+c111
      end if
c  parameter kapa
      shape=0.66*pdr*(cg/d)**(-0.3)
      return
      end
c
c  ***************************************************************
c
      subroutine numb
c
c  ***************************************************************
c
c  subroutine for numbering automatically the
c  subchannels for a hexgonal rod bundle
c
      common/array/ enthal(186),temp(186),flo(186),q(186),qavg(186),
     &              dhdz(186),v(186),mrod(186,3),lc(186,3),prad(91),
     &              ax1(60),pax1(60),name(20),prtloc(20)
      common/geom/  nrod,d,dw,pdr,wdr,hdr,nring,nchan1,nch1,nch2,nch3,
     &              at,de(3),deb,asp(3),as(3),ar(3),ph(3),eta(4),tanth,
     &              cg,dg,s(3),g(6)
c
      nring=(3.+sqrt(12.*nrod-3))/6.-1
      notrg=6*nring*nring
      notg1=6*(nring-1)*(nring-1)
      nog01=3*(nring-1)*nring
      lstch=notrg+6*(nring+1)
      nfwch=notrg+1
      nlwch=lstch-6
```

```
c
c  treatment of triangular subchannel
c
      do 7 i=1,notrg
      z=(i-1)/6
      n=sqrt(z)+1.0001
      notr0=6*n*n
      notr1=6*(n-1)*(n-1)
      notr2=6*(n-2)*(n-2)
      not01=3*n*(n-1)
      not12=3*(n-1)*(n-2)
      iq=(i-notr1-1)/(2*n-1)+0.0001
      iy=1.6-1/n
      ir=i-notr1-iq*(2*n-1)+0.0001
      if(i-notr1-1) 901,902,901
  901 if(i.eq.notr0) goto 903
      j=ir/2
      if(ir-j*2) 905, 905, 904

c  treatment of a triangular subchannel
c  facing the inner ring
c
  905 iz=1.0001/(notr0-i)
      lc(i,1)=notr2+iq*(2*n-3)+ir-1
      lc(i,2)=i-1
      lc(i,3)=i+1
      mrod(i,1)=1+not12+iq*(n-1)+ir/2
      mrod(i,2)=mrod(i,1)+1-6*iz*(n-1)
      mrod(i,3)=not01+iq*n+ir/2+2
      goto 7
c
c  general treatment of a triangular subchannel facing
c  the outer ring (not first or last one of a ring)
c
  904 lc(i,1)=i-1
      lc(i,2)=i+1
      mrod(i,1)=iy+not12+iq*(n-1)+(ir+1)/2
      mrod(i,2)=1+not01+iq*n+(ir+1)/2
      mrod(i,3)=mrod(i,2)+1
  908 if(n.eq.nring) goto 906
c
c  the third adjacent subchannel is a wall subchannel
c
      lc(i,3)=notr0+iq*(2*n+1)+ir+1
      goto 7
c
c  the third adjacent subchannel is a triangular subchannel
c
  906 lc(i,3)=notr0+iq*n+(ir+1)/2
      goto 7
c
c  treatment of the last subchannel of a ring
c
  903 lc(i,1)=notr1+1
      lc(i,2)=notr0-1
      mrod(i,1)=1+iy+not12
      mrod(i,2)=2+not01
      mrod(i,3)=1+3*n*(n+1)
      goto 908
c
```

```
c  treatment of the first subchannel of a ring
c
  902 lc(i,1)=notr1+2
      lc(i,2)=notr0
      mrod(i,1)=1+iy+not12
      mrod(i,2)=2+not01
      mrod(i,3)=mrod(i,2)+1
      goto 908
    7 continue
c
c  treatment of edge subchannels
c
      do 8 i=nfwch,nlwch
      mrod(i,3)=nrod+1
      iz=1.0001/(lstch-5-1)
      iq=(i-notrg-1)/nring+0.0001
      ir=i-notrg-iq*nring+0.0001
c
c  common treatment to all edge subchannel
c
      lc(i,1)=notg1+iq*(2*nring-1)+2*ir-1
      mrod(i,1)=1+nog01+iq*nring+ir
      mrod(i,2)=mrod(i,1)+1-6*iz*nring
      if(ir.eq.1) goto 911
      if(ir.eq.nring) goto 912
c
c  subchannel not adjacent to any corner subchannel
c
      lc(i,2)=i-1
      lc(i,3)=i+1
      goto 8
c
c  subchannel following a corner subchannel
c
  912 lc(i,2)=i-1
      lc(i,3)=(1-iz)*(lstch+iq-4)+iz*(i+1)
      goto 8
c
  911 lc(i,2)=lstch+iq-5
      lc(i,3)=i+1
    8 continue
c
c  treatment of corner subchannels
c
      do 9 k=1,6
      i=nlwch+k
      iq=k-1
c
c  common treatment to all corner subchannels
c
      lc(i,3)=lstch+1
      mrod(i,1)=2+nog01+iq*nring
      mrod(i,2)=lstch+1
      mrod(i,3)=lstch+1
      if(iq) 913,914,913
c
c  treatment of all corner subchannels but the first one
c
  913 lc(i,1)=notrg+iq*nring
      lc(i,2)=lc(i,1)+1
```

```
      goto 9
c
c  treatment of the first corner subchannel
c
  914 lc(i,1)=i-1
      lc(i,2)=notrg+1
    9 continue
c
      return
      end
c
c  ***********************************************************************
c
      subroutine prop
c
c  ***********************************************************************
c
      common/array/ enthal(186),temp(186),flo(186),q(186),qavg(186),
     &              dhdz(186),v(186),mrod(186,3),lc(186,3),prad(91),
     &              axl(60),paxl(60),name(20),prtloc(20)
      common/varbl/ floww,qbar,bunlen,htlen,delz,delzt,reb,pdp,varprt,
     &              grt,choice,imix,noax,nrun,nstep,n2,nk1,nk2
      common/geom/  nrod,d,dw,pdr,wdr,hdr,nring,nchanl,nch1,nch2,nch3,
     &              at,de(3),deb,asp(3),as(3),ar(3),ph(3),eta(4),tanth,
     &              cg,dg,s(3),g(6)
      common/prop/  tin,hin,pref,rhoin,rho(186),viscos(186),dhdro(186),
     &              tavg,cpavg,conavg,beavg,viscbr,conbr,cpbr,tout,faxl,
     &              tb,rhoavg,qc
      common/empco/ cft(4),cfl(4),xl(3),xt(3),x(3),rel(3),ret(3),
     &              es1,es2,c11,shape,es1t,es11,c11t,c111,esm
      integer choice
      dimension pp(50),tt(50),hhf(50)
c  data for pressure, saturated temperature and enthalpy for sodium
      data pp/0.52e-4,0.1333e-3,0.3177e-3,0.7093e-3,0.1495e-2,0.2127e-2,
     &      0.2989e-2,0.3528e-2,0.4153e-2,0.4874e-2,0.5706e-2,0.6661e-2,
     &      0.7757e-2,0.9010e-2,0.1044e-1,0.1207e-1,0.1392e-1,0.1601e-1,
     &      0.1838e-1,0.2106e-1,0.2408e-1,0.2746e-1,0.3127e-1,0.3553e-1,
     &      0.4029e-1,0.4560e-1,0.5152e-1,0.5810e-1,0.6541e-1,0.7351e-1,
     &      0.8247e-1,0.9237e-1,0.1033,0.1153,0.1286,0.1431,0.1590,
     &      0.1765,0.1956,0.2164,0.1392,0.2909,0.3520,0.5079,0.7195,
     &      1.002,1.373,1.855,2.470,3.249/
      data tt/500.,540.,580.,620.,660.,680.,700.,710.,720.,730.,740.,
     &      750.,760.,770.,780.,790.,800.,810.,820.,830.,840.,850.,860.,
     &      870.,880.,890.,900.,910.,920.,930.,940.,950.,960.,970.,980.,
     &      990.,1000.,1010.,1020.,1030.,1040.,1060.,1080.,1120.,1160.,
     &      1200.,1240.,1280.,1320.,1360./
      data hhf/303.8,316.3,328.8,341.2,353.6,359.7,365.9,368.9,372.0,
     &      375.1,378.1,381.2,384.2,387.3,390.3,393.4,396.4,399.5,402.5,
     &      405.5,408.6,411.6,414.6,417.7,420.7,423.7,426.7,429.8,432.8,
     &      435.8,438.8,441.8,444.8,447.8,450.8,453.8,456.9,459.9,462.9,
     &      465.9,468.9,474.9,480.9,492.9,504.9,516.8,528.8,540.8,552.9,
     &      564.9/
c  ***********************************************************************
c
c  correlations for viscosity, specific heat, conductivity, density
c  source: ANL-CEN-RSD-76-1; supplement 1, LMFBR safety (UC-79P)
c  "Properties for LMFBR Safety Analysis," April, 1976
c
      vf(t)=2.87728-7.59499e-3*t+9.97288e-6*t*t-6.03425e-9
     &  *t**3+1.34854e-12*t**4
```

```
      cpf(t)=0.344021-7.03539e-5*t+2.68131e-8*t*t
      ckf(t)=54.306-1.878e-2*t+2.0914e-6*t*t
      rf(t)=59.566-7.9504e-3*t-0.2872e-6*t*t+0.06035e-9*t**3
      dcpt(t)=0.344021-14.07078e-5*t+8.04393e-8*t**2
      dr(t)=-7.9504e-3-0.5744e-6*t+0.18105e-9*t**2
c
c  find inlet thermophsical properties given tin
c
      if(nstep.eq.0) then
      call curve(hin,tin,hhf,tt,50)
c
c  bundle inlet properties
c
      tb=tin
      rhoin=rf(tin)
      do 5 i=1,nchanl
      temp(i)=tin
    5 enthal(i)=hin
c
c  change unit of floww and qbar
c  average properties over whole bundle length
c  calculate the bundle mean temperature
c
      qbar=qbar*3412.76/(3.14159*d)
      floww=floww*rhoin*8.0208
      ptot=0.0
      do 10 i=1,nrod
   10 ptot=ptot+prad(i)
      qc=qbar*ptot*3.14159*d/floww
      t1=tin+0.5*htlen*qc/cpf(tin)
      tout=tin+htlen*qc/cpf(t1)
      tbar=(tout+tin)/2.
      cpbr=cpf(tbar)
      conbr=ckf(tbar)
      viscbr=vf(tbar)
      beavg=dr(tbar)/rf(tbar)
      rhoavg=rf(tbar)
      else
c
c*  calculate properties at local condit.
c
      summ1=0.0
      summ2=0.0
      do 110 i=1,nchanl
      aa=as(1)
      if(i.gt.nch1) aa=as(2)
      if(i.gt.n2) aa=as(3)
      summ1=summ1+flo(i)*aa*temp(i)
      summ2=summ2+flo(i)*aa
  110 continue
      tavg=summ1/summ2
c
c  conductivity cp  density at local position
c
      rhoavg=rf(tavg)
      cpavg=cpf(tavg)
      conavg=ckf(tavg)
      tb=tb+qc*faxl*delz/cpavg
      if(choice.gt.0) then
      beavg=dr(tavg)/rf(tavg)
```

```
      do  140  i=1,nchanl
      viscos(i)=vf(temp(i))
      dhdro(i)=dcpt(temp(i))/dr(temp(i))
  140 continue
      end if
      end if
      return
      end
c
c  ********************************************************************
c
      subroutine output(n)
c
c  ********************************************************************
c
c  this subroutine print out the output
      common/array/ enthal(186),temp(186),flo(186),q(186),qavg(186),
     &              dhdz(186),v(186),mrod(186,3),lc(186,3),prad(91),
     &              axl(60),paxl(60),name(20),prtloc(20)
      common/varbl/ floww,qbar,bunlen,htlen,delz,delzt,reb,pdp,varprt,
     &              grt,choice,imix,noax,nrun,nstep,n2,nk1,nk2
      common/geom/  nrod,d,dw,pdr,wdr,hdr,nring,nchanl,nch1,nch2,nch3,
     &              at,de(3),deb,asp(3),as(3),ar(3),ph(3),eta(4),tanth,
     &              cg,dg,s(3),g(6)
      common/prop/  tin,hin,pref,rhoin,rho(186),viscos(186),dhdro(186),
     &              tavg,cpavg,conavg,beavg,viscbr,conbr,cpbr,tout,faxl,
     &              tb,rhoavg,qc
      common/empco/ cft(4),cfl(4),xl(3),xt(3),x(3),rel(3),ret(3),
     &              es1,es2,c11,shape,es1t,es11,c1lt,c111,esm
      integer choice
      dimension tot(186)
c
      go to (1,2,3) n
c
c  geometrical parameters
c
    1 a=12.
      b=144.
      write(6,100)
      write(6,110)
      write(6,120) nrod,d*a,dw*a
      write(6,130) pdr,wdr,hdr
      write(6,140) pdr*d*a,hdr*d*a,dg*a
      write(6,150) nchanl,nch1,nch2,nch3
      write(6,160) at*b,(as(i)*b,i=1,3)
      write(6,170) deb*a,(de(i)*a,i=1,3)
      return
c
c  operation conditions and run option
c
    2 write(6,210) nrun,(name(i),i=1,20)
      write(6,220) floww,qbar,pref,tin,tout
c
c  power distribution
c
      write(6,230)
      ir=nrod/3
      mr=mod(nrod,3)
      nr1=ir+mr-mr/2
      nr2=nr1+ir+mr/2
```

```
      do 10 i=1,ir
      i1=i+nr1
      i2=i+nr2
      write(6,240) i,prad(i),i1,prad(i1),i2,prad(i2)
   10 continue
      if(mr.eq.1) write(6,240) nr1,prad(nr1)
      if(mr.eq.2) write(6,240) nr1,prad(nr1),nr2,prad(nr2)
      write(6,250)
      ia=noax/3
      ma=mod(noax,3)
      na1=ia+ma-ma/2
      na2=na1+ia+ma/2
      do 20 i=1,ia
      i1=i+na1
      i2=i+na2
      write(6,260) axl(i),paxl(i),axl(i1),paxl(i1),
     &  axl(i2),paxl(i2)
   20 continue
      if(ma.eq.1) write(6,260) axl(na1),paxl(na1)
      if(ma.eq.2) write(6,260) axl(na1),paxl(na1),axl(na2),
     &  paxl(na2)
c
      write(6,310) reb
      write(6,311) grt
      if(choice.eq.0) write(6,320)
      if(choice.eq.1) write(6,325)
      write(6,326) delzt*12.
      write(6,330) (x(i),i=1,3)
      if(imix.eq.0) write(6,340)
      if(imix.gt.0) write(6,345)
      write(6,350) es1,es2,c11,shape
      return
c
c  temperature and velocity distributions
c
    3 write(6,410) varp,t*12.
      s1=0.0
      s2=0.0
      do 25 i=1,nchanl
      aa=as(1)
      if(i.gt.nch1) aa=as(2)
      if(i.gt.n2) aa=as(3)
      s1=s1+flo(i)*temp(i)*aa
      s2=s2+flo(i)*aa
   25 continue
      tavg=s1/s2
      write(6,411) tavg
      if(choice.eq.1) write(6,413) tb
c       if(choice.eq.1) write(6,412) pdp
      write(6,416)
c  mixed convection energy balance correction
      if(choice.eq.1) then
      do 27 i=1,nchanl
   27 temp(i)=temp(i)*tb/tavg
      end if
      do 30 i=1,nchanl
   30 tot(i)=(temp(i)-tin)/(tout-tin)
      is=nchanl/2
      ns1=is+mod(nchanl,2)
      do 40 i=1,is
```

```
      i1=i+ns1
      write(6,420) i,temp(i),tot(i),i1,temp(i1),tot(i1)
   40 continue
      if(choice.eq.1) then
      write(6,430)
      do 50 i=1,nchanl
      vb=floww/at/rhoin
   50 tot(i)=v(i)/vb
      do 60 i=1,is
      i1=i+ns1
   60 write(6,421) i,v(i)/3600.,tot(i),i1,v(i1)/3600.,tot(i1)
      end if
      return
c
  100 format(6x,'ENERGYIV Output',//)
  110 format(6x,'Description of Bundle Geometry',/)
  120 format(6x,'Number of Rods',23x,'N    = ',i5,/,
     &  6x,'Rod Diameter(in)',21x,'D    = ',f7.3,/,
     &  6x,'Wire Diameter(in)',20x,'Dw   = ',f7.3)
  130 format(6x,'Interior Pitch to Rod Diameter Ratio P/D = ',f7.3,/,
     &       6x,'Edge Pitch to Rod Diameter Ratio     W/D = ',f7.3,/,
     &       6x,'Lead Length to Rod Diameter Ratio    H/D = ',f7.3)
  140 format(6x,'Rod Pitch(in)                         P   = ',f7.3,/,
     &       6x,'Wire Lead Length(in)                 H   = ',f7.3,/,
     &       6x,'Gap between Rod and Wall(in)         Dg  = ',f7.3,/)
  150 format(6x,'Number of Subchannels',/,
     &       6x,'Total    = ',i3,3x,'Interior = ',i3,3x,'edge     = ',
     &       i3,3x,'Corner   = ',i3)
  160 format(6x,'Average Flow Area(in**2)',/,
     &       6x,'   Asb   = ',f6.3,'   As1   = ',f6.3,'   As2   = ',
     &       f6.3,'   As3   = ',f6.3)
  170 format(6x,'Equivalent Diameter(in)',/,
     &       6x,'   Deb   = ',f6.3,'   De1   = ',f6.3,'   De2   = ',
     &       f6.3,'   De3   = ',f6.3)
  210 format(1h0,//,5x,'Operation Conditions',//,6x,'Run',2x,i3,2x,20a4,
     &       //)
  220 format(6x,'Bundle Mass Flow Rate(lbm/hr)              = ',e10.4,/,
     &       6x,'Average Rod Heat Flux(btu/hr/ft**2)       = ',e10.4,/,
     &       6x,'Inlet Pressure(psia)                      = ',f8.2,/,
     &       6x,'Inlet Temperature(F)                      = ',f8.2,/,
     &       6x,'Average Outlet Temperature(F)             = ',f8.2,///)
  230 format(6x,'Radial Power Profile',//,
     &       6x,'Rod ID   Power    Rod ID   Power    Rod ID   Power',/,
     &       6x,'Number   Factor   Number   Factor   Number   Factor',/,
     &       /)
  240 format(6x,3(i5,4x,f5.3,4x))
  250 format(1h0,/,6x,'Axial Power Profile',//,
     &       6x,'Relative Power    Relative Power    Relative Power',/,
     &       6x,'Position Factor   Position Factor   Position Factor',
     &       //)
  260 format(6x,3(f6.3,3x,f5.3,4x))
  310 format(1h0,//,6x,'Bundle Average Reynolds Number     Reb = ',e10.4)
  311 format(6x,       'Bundle Grashof Number based on DT GrT = ',e10.4)
  320 format(1h0,   5x,'Solution Scheme Used       convection = forced')
  325 format(1h0,   5x,'Solution Scheme Used       convection = mixed')
  326 format(6x,       'Axial Stepsize Used(inch)              = ',f6.3)
  330 format(6x,'Empirical Parameters Used',//,
     &       6x,'Flow Split Parameters: (from Cheng Correlations)',/,
     &       6x,'    Interior Subchannel                  X1 = ',f7.3,/,
     &       6x,'    Edge Subchannel                      X2 = ',f7.3,/,
```

```
   &        6x,'     Corner Subchannel                          X3 = ',f7.3,//)
340 format(6x,'mixing Parameters Used: (from Cheng Correlations)',/)
345 format(6x,'mixing Parameters Used: (Manually Input)',/)
350 format(6x,'Interior Effective Eddy Diffusivity E*1eta = ',f7.3,/,
   &        6x,'Edge Effective Eddy Diffusivity     E*2eta = ',f7.3,/,
   &        6x,'Edge Transverse Velocity Ratio         C1L = ',f7.3,/,
   &        6x,'Conduction Shape Factor               kapa = ',f7.3)
410 format(1h0///,5x,'Calculation Results at Axial Position ',f7.2,
   &        '  inches')
411 format(6x,     'Average Temperature at this Level       ',f7.2,
   &        '  F')
413 format(6x,     'Heat Balance Temperature at this level ',f7.2,
   &        '  F')
412 format(6x,     'Pressure Drop from Inlet                ',f7.3,
   &        '  psia' ,//)
416 format(6x,'Temperature Distribution',//,
   &6x,' Channel            (T-Tin)/     Channel            (T-Tin)/',
   &/,6x,'ID Number   T(F)   (Tb-Tin)    ID Number   T(F)   (Tb-
   &Tin)',//)
420 format(6x,2(i6,3x,f7.2,4x,f5.3,7x))
421 format(6x,2(i6,3x,f7.3,4x,f5.3,7x))
430 format(1h0,///,6x,'Axial Velocity Distribution',//,
   &        6x,' Channel      V          V/          Channel      V          V
   &/',/,   6x,'Id Number (ft/sec)     Vb        ID Number (ft/sec)     V
   &b',//)
    end
```

Appendix E1 Simple Model for Thermal Plumes Mixing Parameter

Symolon (1982) developed an expression for velocity fluctuation due to buoyancy effects based on the mixing length model suggested by Oosthizen (1974),

$$\left|v'\right| \propto \sqrt{\ell^2 \beta g \left|\frac{dT}{dy}\right|} \tag{E1.1}$$

where v' = velocity fluctuation in transverse direction

ℓ = mixing length

$\frac{dT}{dy}$ = temperature gradient in transverse direction

From the eddy diffusivity approach,

$$\varepsilon_H \frac{dT}{dy} = \overline{v'T'} \propto \left|v'\right| \left|T'\right| \tag{E1.2}$$

where ε_H = equivalent eddy diffusivity for thermal plume effects

$$\left|T'\right| = \ell \left|\frac{dT}{dy}\right|$$

Substituting equation (E1.1) into equation (E1.2), we have

$$\varepsilon_H \propto \ell^2 \sqrt{\beta g \left|\frac{dT}{dy}\right|} \tag{E1.3}$$

Next a nondimensional parameter Y^* is defined as

$$Y^* \equiv \frac{\left|\frac{dT}{dy}\right|}{\frac{\Delta T_b}{L}}$$

$$= \frac{\text{transverse temperature gradient}}{\text{Axial temperature gradient}} \tag{E1.4}$$

Equation (E.3) becomes

$$\varepsilon_H \propto \ell^2 \sqrt{\beta\, g(\frac{\Delta T_b}{L})Y^*}$$

$$\propto \frac{\ell^2}{De^2}\,\nu \sqrt{\frac{\beta g De^4(\frac{\Delta T_b}{L})}{\nu^2}\,Y^*}$$

$$\propto \frac{\ell^2}{De^2}\,\nu \sqrt{Gr_{\Delta T}\,Y^*} \qquad \text{(E1.5)}$$

The definition of thermal plume mixing parameter, $\varepsilon^*_{\eta M}$, is similar to ε^*_η, i.e.,

$$\varepsilon^*_{\eta M} \equiv \frac{\varepsilon_H}{V\eta} \qquad \text{(E1.6)}$$

Substituting equation (E1.5) into equation (E1.6), we get

$$\varepsilon^*_{\eta M} \propto \left[(\frac{\ell^2}{De^2})(\frac{De}{\eta})\right](\frac{1}{Re_b})\sqrt{Gr_{\Delta T}Y^*} \qquad \text{(E1.7)}$$

As it stands now, the correlation is difficult to apply since Y^* is an unknown parameter. However, Y^* can be simply estimated to be proportional to power skew and Re_b because transverse temperature gradient should be proportional to power skew and axial temperature gradient should be inversely proportional to Re_b. Therefore, equation (E1.7) becomes,

$$\varepsilon^*_{\eta M} \propto \left[(\frac{\ell^2}{De^2})(\frac{De}{\eta})\right]\,\frac{Gr_{\Delta T}}{Re_b}\,\phi \qquad \text{(E1.8)}$$

where ϕ = power skew parameter.

The parameter in [ ] is realized to be a function of geometry (e.g., P/D or c/d). Therefore, $\varepsilon^*_{\eta M}$ is concluded to be function of (c/D), $(Gr_{\Delta T}/Re_b)$ and power skew.

Although $\sqrt{Gr_{\Delta T}/Re_b}$ and $\sqrt{\phi}$ appear in the derivation, it was found in the validation study reported in Section 8.4 that for sodium $\varepsilon^*_{\eta M}$ is proportional to $Gr_{\Delta T}/Re_b$ and insensitive to power skew. This suggests that further investigation of the $\varepsilon^*_{\eta M}$ model is necessary to better understand this phenomenon.